

Cardiff University

School of Chemistry



**Red Emitting Iridium(III) and Rhenium(I) Complexes
Developed for Photonic Applications**

Thesis submitted for the degree of Doctor of Philosophy by:

Christopher Edward Elgar

June 2021

CARDIFF UNIVERSITY

SCHOOL OF CHEMISTRY

ABSTRACT

DOCTOR OF PHILOSOPHY

By Christopher Edward Elgar

This thesis outlines the design, synthesis, and characterisation of novel 2-arylquinoxalines and 2-arylquinoline fluorophores alongside their coordination with iridium(III) and rhenium(I) producing red emissive phosphors. The photophysical properties of the complexes are discussed, which could see possible applications in fields of LEECs and bioimaging.

Chapter 2 describes the effects of different electron withdrawing and electron donating groups substituted into differing positions around the cyclometalated 2-phenylquinoxaline ligand and the subsequent results in the tuneability of emission wavelength of iridium(III) complexes.

Chapter 3 outlines the effect of benzannulation in the cyclometalating ligand with a series of 2-(naphthyl)quinoxaline based cyclometalated iridium(III) complexes. The emission shifted to deeper red upon extending the conjugation, with mixed ^3LC and $^3\text{MLCT}$ character, differing in amounts between naphthalene isomers.

Chapter 4 describes the cyclometalation of a series of 2-(naphthyl)quinoline cyclometalating ligands on iridium, describing the effects of substitution of the quinoline on the tuneability of emission. Detailed characterisation of the excited state has shown 1-naphthyl complexes possess more $^3\text{MLCT}$ character and can demonstrate successful TTA-UC with DPA.

Chapter 5 describes the synthesis and characterisation of eight novel bidentate quinoline ligands, and their coordination to iridium as ancillary ligands. The result of detail the affects of extending the conjugation of the ancillary ligand, and how it is affecting the photophysical properties, with an emission range of 40 nm tuneability in 2-(naphth-2-yl)quinoline complexes.

Chapter 6 takes the bidentate ligands from the previous chapter and chelates them with rhenium(I), forming neutral complexes, upon which they demonstrate $^3\text{MLCT}$ emission from the solid state.

Finally, Chapter 7 outlines the design, synthesis and characterisation of a cyclometalated iridium(III) complex incorporating a TTA-UC annihilator moiety. The complex is weakly upconverting in pure solution. The photophysical characterisation suggests back energy pathways between the annihilator moiety and the $^3\text{MLCT}$ states dominate the desired upconversion fluorescence.

Contents

Chapter 1 - Introduction	1
1.1 Introduction	2
1.2 Photoluminescence	3
1.2.1 Jablonski diagrams	3
1.2.2 Stokes shift	4
1.2.3 Kasha's rule	5
1.2.4 Quantum yield (Φ).....	5
1.2.5 Luminescent lifetimes (τ).....	6
1.2.6 Energy transfer	7
1.2.7 Emission quenching.....	8
1.3 Photoluminescent measurements.....	9
1.4 Luminophores	10
1.4.1 Organic fluorophores	10
1.4.2 Luminescent metal complexes.....	11
1.4.3 Summary	18
1.5 References.....	19
Chapter 2 - Iridium(III) Complexes of Substituted Phenyl-Quinoxalines.	23
2.1 Introduction	24
2.1.1 Cyclometalated iridium complexes.....	24
2.1.2 Photonic applications for cationic iridium(III) complexes.....	27
2.1.3 Quinoxalines	34
2.2 Aims	38
2.3 Results and discussions	39
2.3.1 Ligand synthesis and characterisation	39
2.3.2 Complex synthesis and characterisation	40
2.3.3 X-ray crystal structure of $[\text{Ir}(\text{L}^1)_2(\text{bpy})]\text{PF}_6$ and $[\text{Ir}(\text{L}^2)_2(\text{bpy})]\text{PF}_6$	45
2.3.4 Electronic properties	49
2.4 Conclusions.....	55

2.5 Experimental	57
2.5.1 Synthesis of α -bromoacetophenone precursors ⁸⁹	58
2.5.2 Synthesis of phenylquinoxaline ligands	58
2.5.3 Synthesis of cyclometalated Ir(III) complexes	61
2.6 References.....	63
Chapter 3 - Iridium(III) Complexes of 2-(Naphthyl)Quinoxalines.	67
3.1 Introduction	68
3.1.1 Extended conjugation in ligand design.....	68
3.2 Aims	70
3.3 Results and Discussion	71
3.3.1 Ligand synthesis and characterisation	71
3.3.2 Complex synthesis and characterisation	72
3.3.3 X-Ray crystallography.....	73
3.3.4 Electrochemistry	75
3.3.5 Photophysical measurements	76
3.4 Conclusions.....	81
3.5 Experimental	83
3.5.1 2-Bromo-1-(naphthalen-1-yl)ethan-1-one (1).....	83
3.5.2 2-Bromo-1-(naphthalen-2-yl)ethan-1-one (2).....	84
3.5.3 2-Bromo-1-(4-fluoronaphthalen-1-yl)ethan-1-one (3).....	84
3.5.4 2-Bromo-1-(4-methoxynaphthalen-1-yl)ethan-1-one (4)	84
3.5.5 2-(naphthalen-1-yl)-quinoxaline (LH ¹). ³⁰	84
3.5.6 2-(naphthalen-2-yl)-quinoxaline (LH ²). ³¹	85
3.5.7 2-(4-fluoronaphthalen-1-yl)-quinoxaline (LH ³).	85
3.5.8 2-(4-methoxynaphthalen-1-yl)-quinoxaline (LH ⁴).	85
3.5.9 General procedure for the synthesis of [(Ir(L ^x) ₂ μ -Cl) ₂].	86
3.5.10 [Ir(L ¹) ₂ (bpy)]PF ₆	86
3.5.11 [Ir(L ²) ₂ (bpy)]PF ₆	86
3.5.12 [Ir(L ³) ₂ (bpy)]PF ₆	87

3.5.13 [Ir(L ⁴) ₂ (bpy)]PF ₆	87
3.6 References.....	89
Chapter 4 - Red Emissive Iridium Complexes Based upon 2-(Naphthyl)Quinoline Ligand Architecture.....	91
4.1 Introduction	92
4.1.1 Quinolines.....	92
4.1.2 Triplet-triplet-annihilation energy up conversion	97
4.1.3 Transient absorption spectroscopy	99
4.2 Aims of the Chapter.....	100
4.3 Results and Discussions.	102
4.3.1 Ligand synthesis and characterisation.	102
4.3.2 Complex synthesis and characterisation.	104
4.3.3 X-Ray crystallography	108
4.3.4 Electrochemical properties.....	113
4.3.5 Electronic properties	114
4.3.6 Density Functional Theory	125
4.4 Conclusions.....	126
4.5 Experimental	128
4.5.1 General Synthesis of 2-(2-naphthyl)quinoline-4-carboxylic acids	129
4.5.2 General synthesis of ethyl 2-(naphthalen-2-yl)quinoline-4-carboxylate derivatives	131
4.5.3 Iridium(III) Dimer formation ⁶³	133
4.5.4 General Synthesis of [Ir(L) ₂ (bpy)]PF ₆ complexes	134
4.6 References.....	138
Chapter 5 - Iridium(III) Complexes of <i>Bis</i> -Imine Ligands; 2-(Pyridin-2-yl)Quinoline and 2-(Pyrazin-2-yl)Quinoline.	142
5.1 Introduction	143
5.1.1 Asymmetric <i>bis</i> -cyclometalated iridium(III) complexes	143
5.1.2 Bidentate chelating quinoline ligands	145
5.2 Aims of the Chapter.....	146

5.3 Results and Discussions	148
5.3.1 Ligand synthesis and characterisation	148
5.3.2 Complex synthesis and characterisation	149
5.3.3 Electronic properties	159
5.4 Conclusions.....	168
5.5 Experimental	169
5.5.1 Ligand synthesis.....	169
5.5.2 General procedure for the synthesis of $[\text{Ir}(\text{L})_2(\text{MeCN})_2]\text{BF}_4$	172
5.5.3 General procedure for the synthesis of $[\text{Ir}(\text{1/2nq})_2(\text{L}^{1-8})]^+$	172
5.6 References.....	181
Chapter 6 - Rhenium(I) Complexes of <i>Bis-Imine</i> Ligands; 2-(Pyridin-2-yl)Quinoline and 2-(Pyrazin-2-yl)Quinoline.	183
6.1 Introduction	184
6.1.1 Rhenium(I) tricarbonyl chemistry.....	184
6.1.2 Photonic applications for Re(I) complexes	185
6.2 Aims of the chapter.	190
6.3 Results and Discussions	191
6.3.1 Rhenium tricarbonyl complex synthesis and characterisation	191
6.3.2 Electrochemical properties.....	197
6.3.3 Rhenium complex absorption and emission properties	200
6.4 Conclusions.....	202
6.5 Experimental	203
6.5.1 $[\text{Re}(\text{CO})_3(\text{L}^1)\text{Br}]$	203
6.5.2 $[\text{Re}(\text{CO})_3(\text{L}^2)\text{Br}]$	204
6.5.3 $[\text{Re}(\text{CO})_3(\text{L}^3)\text{Br}]$	204
6.5.4 $[\text{Re}(\text{CO})_3(\text{L}^4)\text{Br}]$	204
6.5.5 $[\text{Re}(\text{CO})_3(\text{L}^5)\text{Br}]$	205
6.5.6 $[\text{Re}(\text{CO})_3(\text{L}^6)\text{Br}]$	205
6.5.7 $[\text{Re}(\text{CO})_3(\text{L}^7)\text{Br}]$	206

6.5.8 [Re(CO) ₃ (L ⁸)Br].	206
6.6 References	207
Chapter 7 - Towards an Intramolecular Energy Upconverting Assembly....	210
7.1 Introduction	211
7.1.1 TTA-UC efficiency	211
7.1.2 Intramolecular TTA-UC	212
7.1.3 Functionalisation strategies of DPA.	215
7.2 Aims of the Chapter	217
7.3 Results and Discussions	219
7.3.1 Design strategies	219
7.3.2 Synthesis and characterisation of 2-amino-9,10-diphenylanthracene	220
7.3.3 Ligand synthesis and characterisation	222
7.3.4 Complex synthesis and characterisation	225
7.3.5 Ligand absorption and emission properties	227
7.3.6 Complex absorption and emission properties.	229
7.3.7 Degassed emission measurements	232
7.4 Conclusions.	235
7.5 Experimental	236
7.5.1 2-(anthracen-2-yl)isoindoline-1,3-dione (1)	236
7.5.2 2-(9,10-dibromoanthracen-2-yl)isoindoline-1,3-dione (2)	237
7.5.3 2-(9,10-diphenylanthracen-2-yl)isoindoline-1,3-dione (3)	237
7.5.4 2-amino-9,10-diphenylanthracene (4)	237
7.5.5 N-(anthracen-2-yl)-2-phenylquinoline-4-carboxamide (9)	238
7.5.6 N-(9,10-dibromoanthracen-2-yl)-2-phenylquinoline-4-carboxamide (10)	238
7.5.7 N-(9,10-diphenylanthracen-2-yl)-2-phenylquinoline-4-carboxamide (LH)	239
7.5.8 [Ir(L) ₂ (μ-Cl)] ₂ (11)	239
7.5.9 [Ir(L) ₂ (MeCN) ₂]BF ₄ (12)	239

7.5.10 [Ir(L) ₂ (bpy)]PF ₆ (IrDPA)	240
7.6 References.....	241
Chapter 8 - Summary and Future Work	244
8.1 Summary.....	245
8.2 Future Work	246
8.2.1 2-(Pyridin-2-yl)quinoline and 2-(pyrazin-2-yl)quinoline ligands.	246
8.2.2 [Re(CO) ₃ (L ^x)Br]	246
8.2.3 Ir-DPA.....	247

Acknowledgements

Firstly, I would like to thank to my supervisor, Professor Simon Pope, for all his support and guidance during my studies. I'd also like to extend my thanks to my industrial supervisors at STG Aerospace, Dr Andrew Hallett and Dr Sean O'Kell as well as KESS 2 for providing funding for the project.

Secondly, to all the people in the inorganic department who made my time studying memorable. My appreciation goes to my fellow members of the Pope Group; Sam, Adam and Kaitlin, Natalia, and Deemah for making days in the lab so enjoyable, with a special mention for one of my MChem students, and latterly fellow PhD student, Sophie for her persistence and perseverance during her MChem project on substituted quinoxaline complexes. The support and friendship from Ella and Gupps has been amazing in surviving lockdowns and long days of writing!

Lastly, I'd like to thank my parents for their unwavering support from the moment I told them I was quitting my career to return to studying they have always been there for me when I've needed them. Lastly, my Grandma, I say "Yes Grandma, I've finally finished school!"

Table of Figures

Figure 1.1 - Jablonski diagram.....	3
Figure 1.2 – Diagram showing Stokes Shift (left) and a Jablonski diagram representing Stokes Shift (right).....	5
Figure 1.3 – Three common quantum yield standards, with details of quantum yields, solvents used and excitation wavelengths ²¹	6
Figure 1.4 – Schematic representation of RET and Dexter energy transfer processes.	7
Figure 1.5 - Simplified set up of a spectrofluorometer	9
Figure 1.6 – Common organic emitting polyaromatic compounds. Measurements made in cyclohexane ³³	10
Figure 1.7 – Recent examples of organic fluorophores with a range of different emission wavelengths ³⁶⁻³⁸	11
Figure 1.8 – Schematic representing the major emission pathways for metal complexes.	12
Figure 1.9 - Three examples of fluorescent complexes ⁴⁴⁻⁴⁶	12
Figure 1.10 – Examples of phosphorescent complexes of Cr(III) ^{55,56} and Cu(I) ⁵⁹ Phosphorescent d ⁶ complexes of the second and third row transition metals.....	14
Figure 1.11 – Examples of recent Ru(II) complexes ^{75,76}	15
Figure 1.12 – Examples of recently published Os(II) complexes ^{78,79}	15
Figure 1.13 - Archetypal rhodium (III) and iridium (III) complexes. ⁸³	16
Figure 1.14 – Platinum complexes and their photophysical properties ⁹⁰⁻⁹²	17
Figure 1.15 – Examples of phosphorescent Pd(II), Au(III) and Au(I) complexes ^{94,96,97}	17
Figure 2.1 – Nonoyama's synthesis of Benzo[h]quinoline-10-yl-N iridium dimer ¹⁰	24
Figure 2.2 -Formation of neutral Ir(III) complexes from [Ir(N [^] C) ₂ (μ-Cl)] ₂ and two equivalents of L [^] X. Some forms of L [^] X are shown below.	25
Figure 2.3 – General procedure for splitting iridium dimers to form a cationic complex.....	25
Figure 2.4 – a) Using a silver salt to abstract chlorides. b) substitution of the weakly coordinated solvent ligands in a <i>bis</i> -MeCN complex. Insert – Tight ion pairing seen by Schneider <i>et al</i> in 2{[Ir(ppy) ₂ (bpy)][Cl]}•2CH ₂ Cl ₂ •[H ₃ O] ⁺ •[Cl] ⁻ ¹⁷ and confirmed by single crystal diffraction. Image taken from Housecroft and Constable ¹⁸	26
Figure 2.5 – The emission tuneability of Ir(III) come from the choice of ligands around the coordination sphere. Examples of three such complexes are seen	

above. i) Neutral heteroleptic blue ^{20,21} , ii) homoleptic green emitter ^{22,23} and iii) an orange emitting cationic complex ^{24,25}	27
Figure 2.6 – General scheme by Henwood and Zysman-Colman ³⁶ for the architecture seen in OLED (Left) and LEEC (Right). PEDOT – poly(3,4-ethylenedioxythiophene), PSS – Poly(styrenesulfonate).	28
Figure 2.7 – Left: Structure of the red emitting layer for LEEC applications from Monkman <i>et al</i> ⁴⁵ . Middle + right: (A) + (B) Structure of ppz complexes synthesised by Thompson <i>et al</i> . (C) red emitting Ir(III) complex tested by Thompson <i>et al</i> in LEEC devices ⁴⁷	30
Figure 2.8 – Above – Iridium(III) complexes synthesised by Li <i>et al</i> . ⁵⁵ Below: Confocal microscopy images of a) HeLa cells untreated, b) Same cells incubated with 20 μ M solutions in DMSO/PBS (pH 7, 1/49, v/v) for 10 min at 25 °C. c) Differential Interference Contrast (DIC) images of b). d) Overlaid confocal and DIC microscopy showing iridium complex located in the cytoplasm of the cells.	31
Figure 2.9 – Left Top - Complex used for chemodosimeter detection of HOCl by Lu and Nabeshima ⁵⁶ showing non-emissive Ir-ANMM state and the emissive cleaved complex. Left lower – reaction between o-nitroaniline and HOCl. Right: Confocal microscopy images of HeLa Cells (a) incubated with 20 μ M Ir-ANMM and (b) Ir-ANMM cells treated with 50 μ M HOCl.	32
Figure 2.10 – (a) Huang <i>et al</i> ⁵⁷ PLIM images with HepG 2 cells incubated with iridium(III) complex (10 μ M, λ_{ex} 405 nm) in different oxygen levels. (b) The average lifetime distributions from PLIM. (c) Complex with intercalating ancillary ligand..	33
Figure 2.11 – Left: A simplified Jablonski diagram from the work of Elias <i>et al</i> summarising the generation of ROS. ⁵⁹ Right: PDT Agent trailed <i>in vivo</i> by Hou <i>et al</i> . ⁶⁰	33
Figure 2.12 – The bicyclic heterocyclic quinoxaline and some examples of the quinoxaline motif in use against HIV ⁶¹ , anticancer ⁶² and the isolate natural product, izumiphenazine C ⁶³	34
Figure 2.13 – Classical quinoxaline synthetic routes.....	35
Figure 2.14 - Top: Mixed isomers that would result from the α,β -diketone condensation with 1,2-diaminobenzene. Below: One pot copper catalysed three component route to single isomers presented by Baohua <i>et al</i> ⁶¹	35
Figure 2.15 – Red emitting quinoxaline complexes for OLED use, Complexes (i) and (ii) were synthesised by Lee <i>et al</i> ⁶⁴ , and complex (iii) was synthesised by Johannes <i>et al</i> . ⁶⁵	36
Figure 2.16 – Quinoxaline complexes synthesised by Pope <i>et al</i> in 2013 ⁶⁶	37

Figure 2.17 – Ligands and complexes published by Pope <i>et al</i> in investigations into tuneable red emission. ^{87,88}	38
Figure 2.18 – Synthetic route used for ligand synthesis: a: 1,4-dioxane, diethyl ether, dropwise addition, 2 hours, room temperature; b: Ethanol, 24 hours, 78 °C.	39
Figure 2.19 – $[(L^n)_2Ir(\mu-Cl)_2Ir(L^n)_2]$ synthesis following Nonoyama route ¹⁰ . ^a two eq L^nH , one eq $IrCl_3 \cdot xH_2O$, 2-methoxyethanol, 125 °C, 48 hours.	40
Figure 2.20 – Top: Dimer Splitting synthesis. ^b i) 2-methoxyethanol, 125 °C, 16 hours. ii) sat. $NH_4PF_6(aq)$. Bottom: Synthesised cyclometalated iridium(III) complexes in this work.....	41
Figure 2.21 – $^{19}F\{^1H\}$ NMR spectrum for $[Ir(L^3)_2(bpy)]PF_6$ – PF_6 signal (-72.6 ppm) omitted for clarity. Insert – the different coordination isomers.	42
Figure 2.22 – Upfield aromatic singlet shifts seen in 1H NMR spectra upon complexation and proposed assignments.	43
Figure 2.23 - X-ray structure of $[Ir(L^1)_2(bpy)]PF_6$ $\{C_{48}F_6H_{47}IrN_6O_{0.5}P$, $M_r = 1053.08$, triclinic, $P-1$ (No. 2), $a = 10.1665(3)$ Å, $b = 13.4268(4)$ Å, $c = 17.3892(9)$ Å, $\alpha = 105.700(4)$ °, $\beta = 100.845(3)$ °, $\gamma = 93.671(2)$ °, $V = 2227.67(16)$ Å ³ , $T = 100(2)$ K, $Z = 2$, $Z' = 1$, $m(CuK\alpha) = 6.716$ mm ⁻¹ , 28306 reflections measured, 8018 unique ($R_{int} = 0.1024$) which were used in all calculations. The final wR_2 was 0.1882 (all data) and R_1 was 0.0720 ($I > 2(I)$)}.	46
Figure 2.24 – X-ray structure of $[Ir(L^2)_2(bpy)]PF_6$ $\{C_{46}H_{40}F_{10}IrN_6OP$, $M_r = 1106.01$, monoclinic, $P2_1/n$ (No. 14), $a = 10.2004(2)$ Å, $b = 21.6662(6)$ Å, $c = 18.8506(5)$ Å, $\beta = 90.842(2)$ °, $\alpha = \gamma = 90$ °, $V = 4165.61(18)$ Å ³ , $T = 100(2)$ K, $Z = 4$, $Z' = 1$, $m(Mo K\alpha) = 3.335$ mm ⁻¹ , 189265 reflections measured, 9560 unique ($R_{int} = 0.0529$) which were used in all calculations. The final wR_2 was 0.0726 (all data) and R_1 was 0.0288 ($I > 2(I)$)}.	48
Figure 2.25 - UV-Vis spectra for $L^{1-6}H$ recorded in MeCN at $ca.10^{-5}$ M.	49
Figure 2.26 – Emission spectra for Ligands $L^{1-6}H$ obtained in aerated acetonitrile. $\lambda_{ex} = 330$ nm	51
Figure 2.27 - UV-Vis spectra for isolated complexes, $[Ir(L^{1-6})(bpy)]PF_6$, recorded in acetonitrile at $ca.10^{-5}$ M.	52
Figure 2.28 – Steady state emission spectra for isolated complexes, $[Ir(L^{1-6})(bpy)]PF_6$. Samples run in MeCN at $ca.10^{-5}$ M. $\lambda_{ex} = 450$ nm	53
Figure 2.29 - Steady state emission spectra for mixed isomer complexes, $[Ir(L^{3-4})(bpy)]PF_6$. Samples run in MeCN at $ca.10^{-5}$ M. $\lambda_{ex} = 450$ nm	54

Figure 3.1 – The effect on emission of extending the cyclometalating ligand. ^a Measured in aerated MeCN ² , ^b Measured in aerated MeOH ⁴ , ^c Measured in aerated MeCN ⁵ , ^d Degassed MeCN ⁶ , ^e Measured in degassed DCM ⁷	68
Figure 3.2 – Neutral complexes investigating increased conjugation in the aryl ring of the cyclometalating ligand. Left: Ir(1npy) ₃ from Wallentin <i>et al</i> ⁸ . Middle: [Ir(1npy) ₂ (acac)] from Cao <i>et al</i> ^{11,12} . Right [Ir(2npy) ₂ (acac)] from Lee <i>et al</i> ¹⁰	69
Figure 3.3 – Three complexes synthesised and characterised by Sun <i>et al</i> ¹³ to explore the effects of conjugation in the aryl group of the cyclometalating ligand in cationic emitters. Emission recorded in degassed MeCN solutions.....	70
Figure 3.4 - Synthetic route used for ligand synthesis: a: 1,4-dioxane, dropwise addition, 2 hours, room temperature; b: Ethanol, 24 hours, 78 °C.....	71
Figure 3.5 – Complexes synthesised in this chapter.	72
Figure.3.6 - X-ray structure of [Ir(L ¹) ₂ (bpy)]PF ₆ . Crystal Data: C ₅₈ H ₆₀ IrN ₆ O ₃ PF ₆ , M _r = 1226.29, triclinic, P-1 (No. 2), a = 11.7003(3) Å, b = 14.5700(4) Å, c = 15.4795(4) Å, α = 110.590(2)°, β = 91.143(2)°, γ = 94.368(2)°, V = 2460.01(12) Å ³ , T = 100(2) K, Z = 2, Z' = 1, μ(MoK _α) = 2.824, 83320 reflections measured, 11256 unique (R _{int} = 0.0652) which were used in all calculations. The final wR ₂ was 0.0947 (all data) and R ₁ was 0.0356 (I > 2(I)).	75
Figure 3.7 - Cyclic Voltammograms of [Ir(L ¹) ₂ (bpy)]PF ₆ and [Ir(L ²) ₂ (bpy)]PF ₆ . All potentials measured in deoxygenated DCM solutions at 200 mVs ⁻¹ with 0.1 M [NBu ₄][PF ₆] as supporting electrolyte calibrated with Fc/Fc ⁺	76
Figure 3.8 – Left: UV-Vis spectra for LH ¹⁻⁴ recorded in MeCN at ca.10 ⁻⁵ M. Right: Emission spectrums for Ligands LH ¹⁻⁴ obtained in aerated acetonitrile at ca.10 ⁻⁵ M. λ _{ex} = 330 nm.	76
Figure 3.9 - UV-Vis spectra for [Ir(LH ¹⁻⁴)(bpy)]PF ₆ recorded in aerated MeCN at ca.10 ⁻⁵ M.	78
Figure 3.10 – Steady state emission spectra for complexes [Ir(L ¹⁻⁴) ₂ (bpy)]PF ₆ , recorded in aerated MeCN at λ _{ex} = 500 nm.	79
Figure 3.11 – Low temperature emission measurements (solid line), recorded in 4:1 ethanol/methanol glass, overlaid with room temperature measurements (dashed lines) recorded in MeCN solution. (λ _{ex} = 500 nm)	80
Figure 4.1 – Heterocyclic quinoline and examples of antimalarials, quinine and hydroxychloroquine ¹ , with natural antiparasitic 2-propylquinoline isolated from <i>Galipea longiflora</i> ²	92
Figure 4.2 – Skarup ¹⁵ , Doebner-Miller ¹⁶ and Conrad-Limpach-Knorr ¹⁷⁻¹⁹ functionalised quinoline synthetic pathways.....	93

Figure 4.3 – Doebner ²² , Niementowski ²¹ , Friedländer ²⁰ and Pfitzinger ²³ Syntheses of 4-functionalised quinolines.....	94
Figure 4.4 – Cationic iridium(III) complexes of Benzo[<i>h</i>]quinoline ²⁹ , 2-phenylquinoline ³¹ and 1-phenylisoquinoline ^{30,31}	95
Figure 4.5 – Amide functionalised quinoline complexes, synthesised by Pope <i>et al</i> ^{β2}	96
Figure 4.6 – Iridium(III) complexes featuring different ancillary ligands synthesised by Pope <i>et al</i> ^{β3,34}	97
Figure 4.7 – Different types of Upconversion processes – adapted from Xu <i>et al</i> ⁴¹ . GS – Ground State, ES – Excited State, Red line – Photon Absorption, blue line – Photon Emission, Dashed line energy transfer processes.	98
Figure 4.8 – Jablonski diagram represented the process of Triplet-Triplet Annihilation.....	98
Figure 4.9 – Examples of known sensitiser – Organic tetraiodohydroxyfluorone ⁴⁶ , octaethylporphyrin complexes ^{48,52} and an iridium(III) sensitiser ⁵³ , capable of upconversion in aqueous solvent.....	99
Figure 4.10 - Principles of Transient Absorption Spectroscopy adapted from Edinburgh Instruments ⁵⁹ . G represents ground state and A and B are distinct excited states.....	100
Figure 4.11 – Pfitzinger ligand synthesis and subsequent Fischer esterification: i) KOH (3 eq), EtOH, 24 hours, 78 °C; ii) Cat. H ₂ SO ₄ , EtOH, 16 hours, 78 °C.....	102
Figure 4.12 – ¹ H NMR spectrum of quinoline ethyl ester, having undergone S _N Ar substitution on the 4-fluoronaphthyl position.	103
Figure 4.13 – Overlaid ¹⁹ F NMR spectra showing starting 5-fluoroisatin and the synthesised acids and esters.	104
Figure 4.14 – ¹ H NMR spectrum of [Ir(L ⁶) ₂ (μ-Cl)] ₂ recorded in CDCl ₃	104
Figure 4.15 – ¹ H- ¹ H COSY NMR spectra for [Ir(L ¹) ₂ (bpy)]PF ₆ (See insert). Top expanded aromatic region. Below: expanded aliphatic region.....	107
Figure 4.16 – Complexes synthesised and characterised in this work.....	107
Figure 4.17 - X-ray structures of [Ir(L ³) ₂ (bpy)]PF ₆ {C ₅₈ H ₄₈ F ₈ IrN ₄ O ₅ P, M _r = 1256.17, triclinic, <i>P</i> -1 (No. 2), a = 12.3219(3) Å, b = 13.6454(2) Å, c = 15.6097(3) Å, α = 81.489(2)°, β = 86.747(2)°, γ = 76.124(2)°, V = 2519.30(9) Å ³ , T = 100(2) K, Z = 2, Z' = 1, μ(MoK _α) = 2.767 mm ⁻¹ , 56370 reflections measured, 11532 unique (R _{int} = 0.0392) which were used in all calculations. The final wR ₂ was 0.0821 (all data) and R ₁ was 0.0315 (I > 2(I)).}	111

Figure 4.18 - X-ray structures of $[\text{Ir}(\text{L}^5)_2(\text{bpy})]\text{PF}_6$ { $\text{C}_{58}\text{F}_6\text{H}_{50}\text{IrN}_4\text{O}_5\text{P}$, $M_r = 1220.19$, monoclinic, $P2_1/n$ (No. 14), $a = 14.8065(3) \text{ \AA}$, $b = 16.0145(3) \text{ \AA}$, $c = 21.9767(4) \text{ \AA}$, $\beta = 105.323(2)^\circ$, $\alpha = \gamma = 90^\circ$, $V = 5025.84(17) \text{ \AA}^3$, $T = 100(2) \text{ K}$, $Z = 4$, $Z' = 1$, $\mu(\text{MoK}\alpha) = 2.766 \text{ mm}^{-1}$, 54477 reflections measured, 11515 unique ($R_{int} = 0.0447$) which were used in all calculations. The final wR_2 was 0.0873 (all data) and R_1 was 0.0395 ($I > 2(I)$).}	112
Figure 4.19 - X-ray structures of $[\text{Ir}(\text{L}^5)_2(\text{bpy})]\text{PF}_6$ { $\text{C}_{55}\text{Cl}_2\text{F}_8\text{H}_{40}\text{IrN}_4\text{O}_4\text{P}$, $M_r = 1266.98$, monoclinic, $I2/a$ (No. 15), $a = 17.9525(6) \text{ \AA}$, $b = 19.6127(9) \text{ \AA}$, $c = 29.2291(9) \text{ \AA}$, $\beta = 93.838(3)^\circ$, $\alpha = \gamma = 90^\circ$, $V = 10268.4(7) \text{ \AA}^3$, $T = 100(2) \text{ K}$, $Z = 8$, $Z' = 1$, $\mu(\text{CuK}\alpha) = 6.982 \text{ mm}^{-1}$, 39479 reflections measured, 8711 unique ($R_{int} = 0.1139$) which were used in all calculations. The final wR_2 was 0.2640 (all data) and R_1 was 0.0893 ($I > 2(I)$).}	112
Figure 4.20 – Cyclic Voltammograms of $[\text{Ir}(\text{L}^{1-6})_2(\text{bpy})]\text{PF}_6$. All potentials measured in deoxygenated DCM solutions at 200 mVs^{-1} with $0.1 \text{ M} [\text{NBu}_4][\text{PF}_6]$ as supporting electrolyte calibrated with Fc/Fc^+	114
Figure 4.21 - UV-Vis spectra for ligands L^{1-7}H recorded in CHCl_3 at $ca. 10^{-5} \text{ M}$	114
Figure 4.22 – Steady state emission spectra for ligands L^{1-7}H obtained in aerated CHCl_3 ($\lambda_{ex} : 330 \text{ nm}$)	115
Figure 4.23 - UV-Vis spectra. R: 2-naphthyl complexes $[\text{Ir}(\text{L}^{1-3})_2(\text{bpy})]\text{PF}_6$, L: 1-naphthyl complexes $[\text{Ir}(\text{L}^{4-7})_2(\text{bpy})]\text{PF}_6$. All spectra recorded in acetonitrile at $ca. 10^{-5} \text{ M}$.	116
Figure 4.24 - Emission spectra complexes $[\text{Ir}(\text{L}^{1-7})_2(\text{bpy})]\text{PF}_6$. Spectra obtained as MeCN solutions at $ca. 10^{-5} \text{ M}$. $\lambda_{ex} = 510 \text{ nm}$	117
Figure 4.25 – Emission spectra for left: $[\text{Ir}(\text{L}^2)_2(\text{bpy})]\text{PF}_6$ and right: $[\text{Ir}(\text{L}^5)_2(\text{bpy})]\text{PF}_6$ in a range of solvents at $\lambda_{ex} = 500 \text{ nm}$	118
Figure 4.26 – Comparison of excitation spectra with absorption spectra (both obtained in MeCN at $ca. 10^{-5} \text{ M}$). * indicates a harmonic from the lamp in the excitation spectra.	119
Figure 4.27 - Luminescence spectra of the complexes recorded as a frozen glass (1:4, MeOH/EtOH) ($\lambda_{ex} = 510 \text{ nm}$).	121
Figure 4.28 - (a) Nanosecond time-resolved transient absorption spectra of compound $[\text{Ir}(\text{L}^4)_2(\text{bpy})]\text{PF}_6$ upon pulsed laser excitation ($\lambda_{ex} = 510 \text{ nm}$, $c = 5 \times 10^{-5} \text{ M}$) and (b) decay trace of compound $[\text{Ir}(\text{L}^4)_2(\text{bpy})]\text{PF}_6$ at 645 nm in acetonitrile under air and nitrogen atmosphere, 20°C .	122
Figure 4.29 - (a) Nanosecond time-resolved transient absorption spectra of compound $[\text{Ir}(\text{L}^5)_2(\text{bpy})]\text{PF}_6$ upon pulsed laser excitation ($\lambda_{ex} = 510 \text{ nm}$, $c = 5 \times 10^{-5} \text{ M}$)	

⁵ M) and (b) decay trace of compound [Ir(L ⁵) ₂ (bpy)]PF ₆ at 625 nm in acetonitrile under air and nitrogen atmosphere, 20 °C.	122
Figure 4.30 - (a) Nanosecond time-resolved transient absorption spectra of compound [Ir(L ⁶) ₂ (bpy)]PF ₆ upon pulsed laser excitation (λ _{ex} = 510 nm, c = 5 × 10 ⁻⁵ M) and (b) decay trace of compound [Ir(L ⁶) ₂ (bpy)]PF ₆ at 645 nm in acetonitrile under air and nitrogen atmosphere, 20 °C.	123
Figure 4.31 - Triplet-triplet annihilation upconversion fluorescence spectra of the photosensitisers, [Ir(L ⁴⁻⁶) ₂ (bpy)]PF ₆ , in aerated acetonitrile where DPA was used as the annihilator. Excitation was achieved with a continuous laser at λ = 532 nm (power density of 5.6 mW) under a deaerated atmosphere. c(sensitiser) = 1 × 10 ⁻⁵ M, c(DPA) = 5 × 10 ⁻⁴ M, 20 °C. The asterisks indicate the scattered laser signal.	124
Figure 4.32 - Photographs of the emission of the selected triplet sensitisers and their upconversion with DPA in deaerated acetonitrile. Excitation was achieved with a continuous laser at λ = 532 nm (power density of 5.6 mW) under a deaerated atmosphere. c(sensitiser) = 1 × 10 ⁻⁵ M, c(DPA) = 5 × 10 ⁻⁴ M, 20 °C. The photographs were taken without any filters.	124
Figure 4.33 – Calculated Kohn-Sham Molecular Orbitals for [Ir(L ²) ₂ (bpy)] ⁺	126
Figure 5.1 – Synthesis of pure mixed ligand Ir(III) dimers, adapted from Nazeeruddin <i>et al</i> ⁸ . (i) acacH, [Bu ₄ N][OH], CH ₂ Cl ₂ , 40 °C overnight, 44%; (ii) (2), HCl (2 M in Et ₂ O), CH ₂ Cl ₂ , RT, 15 min, 86%. TLC plate of acac complexes. C: crude mix from dimer splitting followed by samples after purification.	144
Figure 5.2 – Synthesis <i>Hpic</i> -Br complexes and further post-synthetic modifications employed by Beeby <i>et al</i> . ¹² (i) Acetone, K ₂ CO ₃ , and bromopicolinic acid; (ii) CuI, THF, Et ₃ N, Pd(PPh ₃) ₂ Cl ₂ and triisopropylsilylacetylene.	145
Figure 5.3 – In situ anti addition of an unsaturated bond into μ-OH bond adapted from Tsai <i>et al</i> ¹⁴	145
Figure 5.4 – Cationic complexes synthesised and characterised during investigations into the effects of increased conjugation of ancillary ligands. Emission wavelengths recorded in CH ₂ Cl ₂ . ^{33,36}	146
Figure 5.5 – Synthetic route towards ligand synthesis: i) 33 % NaOH _(aq) (4 eq), stir 15 minutes, room temperature. ii) H ₂ O, HCl (5M). iii) Cat. H ₂ SO ₄ , EtOH, 16 hours, 78 °C.	148
Figure 5.6 - Iridium complexes synthesised and characterised for this work. ...	150
Figure 5.7 – X-ray structure of [Ir(2nq) ₂ (L ⁴)]PF ₆ - C ₇₄ F ₆ H ₇₈ IrN ₅ O _{9.5} P, M _r = 1526.58, triclinic, <i>P</i> -1 (No. 2), a = 14.5944(3) Å, b = 15.8228(4) Å, c = 15.9735(5) Å, α =	

103.713(2)°, $\beta = 92.681(2)^\circ$, $\gamma = 101.881(2)^\circ$, $V = 3488.99(16) \text{ \AA}^3$, $T = 100(2) \text{ K}$, $Z = 2$, $Z' = 1$, $\mu(\text{Mo K}\alpha) = 2.014 \text{ mm}^{-1}$, 91231 reflections measured, 15993 unique ($R_{int} = 0.0803$) which were used in all calculations. The final wR_2 was 0.1337 (all data) and R_1 was 0.0551 ($I > 2(I)$).	151
Figure 5.8 - X-ray structure of $[\text{Ir}(\text{1nq})_2(\text{L}^2)]\text{PF}_6$ - $\text{C}_{66}\text{H}_{57}\text{Cl}_3\text{F}_6\text{IrN}_4\text{O}_7\text{P}$, $M_r = 1461.67$, triclinic, $P-1$ (No. 2), $a = 13.11880(10) \text{ \AA}$, $b = 15.6022(2) \text{ \AA}$, $c = 16.0146(2) \text{ \AA}$, $\alpha = 70.1570(10)^\circ$, $\beta = 83.6410(10)^\circ$, $\gamma = 74.2860(10)^\circ$, $V = 2967.41(6) \text{ \AA}^3$, $T = 100(2) \text{ K}$, $Z = 2$, $Z' = 1$, $\mu(\text{Mo K}\alpha) = 2.491 \text{ mm}^{-1}$, 237955 reflections measured, 18055 unique ($R_{int} = 0.0551$) which were used in all calculations. The final wR_2 was 0.0670 (all data) and R_1 was 0.0261 ($I > 2(I)$).	152
Figure 5.9 - $[\text{Ir}(\text{1nq})_2(\text{L}^2)]\text{PF}_6$ showing hydrogen bonding interactions between solvent and complex, with a maximum D-D distance of 2.84 \AA	155
Figure 5.10 – Packing diagram of left: $[\text{Ir}(\text{1nq})_2(\text{L}^2)]\text{PF}_6$ and right: $[\text{Ir}(\text{2nq})_2(\text{L}^4)]\text{PF}_6$. Both complexes exhibit π - π interactions between aromatic rings highlighted in blue.....	155
Figure 5.11 – Solid state structure of $[\text{Ir}(\text{1nq})_2(\text{L}^2)]\text{PF}_6$ showing Left: quinoline rotation after complexation. Hydrogens have been omitted for clarity. Right: Showing strain of one cyclometalating ligand and selected distances (in \AA) between certain atoms and ring centroids. Counterion and solvents of crystallisation have been omitted for clarity.....	156
Figure 5.12 – Stacked ^1H NMR spectra of $[\text{Ir}(\text{1nq})_2(\text{L}^x)]^+$ (500 MHz, CDCl_3).....	157
Figure 5.13 - NMR spectra for $[\text{Ir}(\text{2nq})_2(\text{L}^2)]\text{PF}_6$ obtained in CD_3OD . Over integration of the quartet at 4.57 ppm is likely a result of H-Bonded water appearing at 4.59 ppm. This peak is seen in each of the spectra obtained in CD_3OD . The solvent was not dried prior to use.....	158
Figure 5.14 – Absorbance spectra for ligands. Spectra obtained in aqueous 0.1 M NaOH (L^{1-6}) at ca. 10^{-5} M . L^{7-8} spectra obtained in MeCN at ca. 10^{-5} M	159
Figure 5.15 - Emission spectra for ligands. Spectra obtained in aqueous 0.1 M NaOH (L^{1-6}) at ca. 10^{-5} M . L^{7-8} spectra obtained in MeCN at ca. 10^{-5} M . $\lambda_{ex} = 325 \text{ nm}$	160
Figure 5.16 - Absorption spectra for $[\text{Ir}(\text{1nq})_2(\text{L}^x)]^+$ obtained in MeCN solution at ca. 10^{-5} M	161
Figure 5.17 - Emission spectra for $[\text{Ir}(\text{1nq})_2(\text{L}^x)]^+$ obtained in MeCN solution at ca. 10^{-5} M ($\lambda_{ex} = 510 \text{ nm}$).	163
Figure 5.18 – Low temperature emission spectra recorded in a MeOH / EtOH (1:4) glass at 77 K ($\lambda_{ex} = 510 \text{ nm}$).	163

Figure 5.19 - Absorption spectra for $[\text{Ir}(\text{2nq})_2(\text{L}^x)]^+$ obtained in MeCN solution at ca. 10^{-5} M.....	164
Figure 5.20 - Emission spectra for $[\text{Ir}(\text{1nq})_2(\text{L}^x)]^+$ obtained in MeCN solution at ca. 10^{-5} M ($\lambda_{\text{ex}} = 510$ nm).	166
Figure 5.21 - Low temperature emission spectra recorded in a MeOH / EtOH (1:4) glass at 77 K ($\lambda_{\text{ex}} = 510$ nm).	167
Figure 6.1 – Example of a synthetic pathway towards a luminescent $[\text{Re}(\text{CO})_3(\text{bpy})(\text{py})]\text{OTf}$ species starting from the dirheniumdecarbonyl ⁹	184
Figure 6.2 – Bidentate ligand coordination, directed by the trans effect resulting in the <i>fac</i> - $[\text{Re}(\text{CO})_3(\text{N}^{\wedge}\text{N})(\text{X})]$ product.....	185
Figure 6.3 - Photoisomerisation of <i>fac</i> - $[\text{Re}(\text{CO})_3(\text{bpy})\text{Cl}]$ to form <i>mer</i> - $[\text{Re}(\text{CO})_3(\text{bpy})\text{Cl}]$ by Ishitani <i>et al.</i> $\text{N}^{\wedge}\text{N}$: bpy. ¹⁰	185
Figure 6.4 – Room temperature emission effects from extended conjugation of the diimine ligands in ^a degassed MeCN. ¹¹ ^b Bisquinoline complex is non emissive at rt in solution – $\lambda_{\text{em}} = 634$ nm at 77 K in an EPA glass. ^{12,13}	186
Figure 6.5 – Tuneability of emission from changing the axial ligands. ^a Spectra recorded as PF_6^- salts in deoxygenated DCM solution ¹⁵ . ^b Spectra recorded in MeCN as ClO_4^- salts ¹⁶ . ^c Recorded in EPA as a CF_3SO_3^- salt ¹³	186
Figure 6.6 - Rhenium (I) imaging agents synthesised by Massi <i>et al</i> ^{24–26}	188
Figure 6.7 - Examples of rhenium(I) tricarbonyls with anticancer properties ^{30,31}	189
Figure 6.8 – Photocatalytic multi-proton, multielectron reduction of CO_2 ^{36,38} ...	190
Figure 6.9 – Synthetic route for rhenium tricarbonyl complexes and the complexes isolated and characterised in this work.	191
Figure 6.10 – X-ray structure of $[\text{Re}(\text{CO})_3(\text{L}^7)\text{Br}] \cdot \text{C}_{20}\text{H}_{14}\text{BrN}_2\text{O}_5\text{Re}$, $M_r = 628.44$, triclinic, <i>P</i> -1 (No. 2), $a = 8.37400(10)$ Å, $b = 13.6124(2)$ Å, $c = 18.4796(2)$ Å, $\alpha = 107.9060(10)^\circ$, $\beta = 94.6350(10)^\circ$, $\gamma = 102.7330(10)^\circ$, $V = 1929.95(4)$ Å ³ , $T = 100(2)$ K, $Z = 4$, $Z' = 2$, $\mu(\text{MoK}\alpha) = 8.402$ mm ⁻¹ , 85283 reflections measured, 9971 unique ($R_{\text{int}} = 0.0332$) which were used in all calculations. The final wR_2 was 0.0379 (all data) and R_1 was 0.0170 ($I > 2(I)$)	192
Figure 6.11 – Packing diagram for $[\text{Re}(\text{CO})_3(\text{L}^7)\text{Br}]$, also showing two separate π - π interactions of aromatic rings highlighted in blue and red.....	192
Figure 6.12 - 2D ¹ H- ¹ H COSY Correlation spectra of $[\text{Re}(\text{CO})_3(\text{L}^8)\text{Br}]$ (Full aromatic region shown).....	195
Figure 6.13 - FTIR spectra showing rhenium complexes of 2-(pyradin-2-yl)quinoline ligands. Inserts – expanded look at the carbonyl region.....	196

Figure 6.14 - Cyclic Voltammograms. [Re(CO) ₃ (L ¹⁻⁸)Br]. All potentials measured in deoxygenated DCM solutions at 200 mVs ⁻¹ with 0.1 M [NBu ₄][PF ₆] as supporting electrolyte calibrated with Fc/Fc ⁺	199
Figure 6.15 - Absorption spectra for rhenium complexes obtained in MeCN solution at ca. 10 ⁻⁵ M.	200
Figure 6.16 - Emission spectra for rhenium Complexes. Spectra obtained from the solid state. λ _{ex} = 420 nm.	202
Figure 7.1 - TTA-UC polyfluorene polymers end capped with Pd(II) porphyrin complexes used in the work by Wegner <i>et al.</i> ²⁸	213
Figure 7.2 – Upconverting MOF design taken from Heinze <i>et al.</i> ³² . Light Blue atoms are the Pd from the [Pd(TCPP)] linker units, grey atoms are Zr of the [Zr ₆ (μ ₃ -OH) ₈ (OH) ₈] secondary binding units, red atoms are oxygen. CA – Caprylic (octanoic) acid.	214
Figure 7.3 – [Zn(II)OEP] and [Ru(CO)(OEP)] TA UC complexes synthesised by Moth--Poulsen <i>et al.</i> ^{5,44}	215
Figure 7.4 - Anthracene cycloaddition pathways.....	216
Figure 7.5 – Retrosynthetic analysis for the synthesis of amino-DPA molecule showing 2 separate routes – a Grignard’s reaction with an amino anthraquinone, or a Suzuki cross coupling between a dibromo species and phenyl boronic acid.	217
Figure 7.6 – Synthesis of 4-(10-(pyridin-4-yl)anthracen-9-yl)aniline by Nitschke <i>et al.</i> ⁵⁸	217
Figure 7.7 – Target ligand design and complex design for the potential of single molecule TTA UC.	219
Figure 7.8 – Synthetic pathway designed for the synthesis of aminoDPA (4). (a) 2-Ethoxyethanol, triethylamine, 80 °C, 16 h. (b) CHCl ₃ , Br ₂ , rt, 1 h. (c) Phenyl boronic acid, [Pd(PPh ₃) ₄], toluene, THF, water, Na ₂ CO ₃ , 85 °C, 16 h. (d) N ₂ H ₄ •H ₂ O, 1,4-dioxane, 101 °C, 16 h.	220
Figure 7.9 – Unsuccessful synthetic routes tried towards LH . (e) SOCl ₂ , rt, 16 h, (f) 4 , CHCl ₃ , DIPEA (2eq), rt, 16 h. (g) MeCN / DCM (1:1), EDC•HCl (5 eq), NHS (5 eq), TEA (0.1 eq), 16 hours, rt.	222
Figure 7.10 – Reactions of 4 to test reactivity; attempted naphthalimide synthesis.	222
Figure 7.11 – Suzuki-Miyaura cross coupling method used for the final synthesis of LH . (h) TEA (2.1 eq), CHCl ₃ , 16 h, rt. (i) Br ₂ , CHCl ₃ , 4 h, rt. (j) Phenyl boronic acid, [Pd(PPh ₃) ₄], toluene, THF, water, Na ₂ CO ₃ , 16 h, 85 °C.	223

Figure 7.12 – NMR (500 MHz) spectra obtained in d_6 -DMSO. Top – 9 , Middle – 10 , Bottom – LH .	224
Figure 7.13 – Synthetic approach to complex synthesis following the Nonoyama iridium dimer formation ⁶⁵ . (k) 2-methoxyethanol, 48 h, 124 °C. (l) $AgBF_4$ (2 eq), MeCN, 16 h, 82 °C. (m) i) 2,2'-bipyridine (1.2 eq), $CHCl_3$, 70 °C, 8 h, ii) MeCN, $[NH_4][PF_6]$, 10 minutes, rt.	225
Figure 7.14 – Low resolution ES+ mass spectrum for IrDPA .	226
Figure 7.15 – Top: projected spectra for IrDPA $[M+2MeOH]^+$ adduct. Below: experimental results.	227
Figure 7.16 – Left: UV-VIS spectra for LH and DPA recorded in aerated DCM at $ca. 10^{-5}$ M. Right: Emission spectra (solid lines) and excitation acquisitions (dotted lines) for LH and DPA recorded in aerated DCM at $ca. 10^{-5}$ M.	227
Figure 7.17 – Left: Emission and excitation spectra for LH showing dependence upon concentration. Right: 10^{-3} M excitation acquisition compared to the absorption of DPA.	229
Figure 7.18 - Absorption spectrum of IrDPA recorded in aerated DCM at $ca. 10^{-5}$ M.	229
Figure 7.19 – Emission (solid line) and excitation (dashed line) spectra for IrDPA recorded in aerated CH_2Cl_2 at $ca. 10^{-5}$ M	230
Figure 7.20 – 77 K emission spectra recorded in 4:1 EtOH : MeOH glass.	231
Figure 7.21 – Possible energy transfer processes seen in the IrDPA molecule. Here, sensitiser refers to the cyclometalated iridium complex, and emitter references to the amino DPA moiety.	232
Figure 7.22 - Emission spectra for IrDPA recorded in degassed CH_2Cl_2 . Insert: Expanded DPA emission region showing upconversion emission from 550 nm excitation. * Indicates scattering from the lamp.	232
Figure 7.23 – TTA-UC between IrDPA and DPA at indicated concentrations. * indicated signal from the scattered lamp.	233
Figure 7.24 – Degassed excitation acquisition spectra for IrDPA + added DPA. Left: $\lambda_{em} = 660$ nm, Right $\lambda_{em} = 411$ nm.	234
Figure 7.25 - Emission spectra for IrDPA with DPA addition at differing λ_{ex} .	234
Figure 8.1 - Possible future complexes to investigate the degree of tuneability from ligand functionalisation.	246
Figure 8.2 – Synthetic route for the substitution of axial halides.	247
Figure 8.3 - Possible future ligand designs.	247

Table of Tables

Table 2.1 – NMR shifts of methyl- and fluoro- substituents of ligands. All spectra obtained in CDCl ₃ unless otherwise stated. ^a – spectrum obtained in d ₆ -Acetone. ^b – Peak integration of 3H unless otherwise stated.....	40
Table 2.2 – Aliphatic shifts from free ligand and complexes for pure synthesised complexes. ^a All spectra obtained in CDCl ₃ unless otherwise indicated. ^b Spectra obtained in d ₆ -Acetone. ^c spectra obtained in d ₃ -MeCN.....	44
Table 2.3 - ¹⁹ F{ ¹ H} NMR spectrum shifts for ligand and complexes.....	44
Table 2.4 – Selected bond lengths and bond angles obtained from crystallographic data from complexes [Ir(L ¹) ₂ (bpy)]PF ₆ and [Ir(L ²) ₂ (bpy)]PF ₆	47
Table 2.5 – ^a All measurements obtained at room temperature in aerated acetonitrile at ca. 1x10 ⁻⁵ M. ^b λ _{ex} = 330 nm; ^c λ _{ex} = 295 nm; ^d Vs standard Quinine Sulphate in 0.05 M H ₂ SO ₄ , λ _{ex} = 350 nm. ⁹³	50
Table 2.6 – ^a All measurements obtained at room temperature in aerated MeCN at ca. 1x10 ⁻⁵ M. ^b λ _{ex} = 450 nm; ^c λ _{ex} = 295 nm; Degassed lifetimes recorded by Haleema Otaif ⁹⁶ ; ^d Vs standard [Ru(bpy) ₃][PF ₆] ₂ in MeCN, λ _{ex} = 450 nm. ⁹³	55
Table 3.1 - Selected bond angles and bond lengths from refinement data for [Ir(L ¹) ₂ (bpy)]PF ₆	74
Table 3.2 - Electrochemical properties of the iridium(III) complexes obtained from cyclic voltammetry. Potentials measured in deaerated DCM solutions at 200 mVs ⁻¹ with 0.1 M [NBu ₄][PF ₆] as supporting electrolyte calibrated with Fc/Fc ⁺ ; ^a E _{1/2} values for fully reversible reduction process.....	75
Table 3.3 - ^a aerated acetonitrile, 10 ⁻⁵ M; ^b λ _{ex} = 330 nm; ^c λ _{ex} = 295 nm; ^d Vs standard Quinine Sulphate in 0.05 M H ₂ SO ₄ , λ _{ex} = 330 nm. ²²	77
Table 3.4 - ^a aerated acetonitrile, 10 ⁻⁵ M; ^b λ _{ex} = 500 nm; ^c λ _{ex} = 295 nm; ^d Vs standard [Ru(bpy) ₃][(PF ₆) ₂] in aerated acetonitrile, 10 ⁻⁵ M, λ _{ex} = 450 nm. ²²	81
Table 4.1 - ¹⁹ F{ ¹ H} NMR spectra shifts for ligand and complexes.....	108
Table 4.2 – Selected bond lengths and bond angles obtained from crystallographic data from complexes [Ir(L ³) ₂ (bpy)]PF ₆ , [Ir(L ⁵) ₂ (bpy)]PF ₆ and [Ir(L ⁶) ₂ (bpy)]PF ₆ . .	110
Table 4.3 – Selected torsion angles between naphthyl and quinoline rings.....	111
Table 4.4 - Electrochemical properties of the iridium(III) complexes obtained from cyclic voltammetry. Potentials measured in deaerated DCM solutions at 200 mVs ⁻¹ with 0.1 M [NBu ₄][PF ₆] as supporting electrolyte calibrated with Fc/Fc ⁺ ; ^a cathodic peak of irreversible process; ^b E _{1/2} values for fully reversible process.	113

Table 4.5 – ^a All measurements run at room temperature in aerated CHCl ₃ at ca. 1x10 ⁻⁵ M. ^b λ _{ex} = 330 nm; ^c λ _{ex} = 295 nm; ^d Vs standard Quinine Sulphate in 0.05 M H ₂ SO ₄ , λ _{ex} = 350 nm. ⁶⁷	116
Table 4.6 – Absorbance and emission data for complexes at room temperature. ^a All measurements run at room temperature in aerated MeCN at ca. 1x10 ⁻⁵ M. ^b λ _{ex} = 510 nm; ^c λ _{ex} = 295 nm; ^d Vs standard [Ru(bpy) ₃](PF ₆) ₂ in MeCN, λ _{ex} = 420 nm ⁶⁷	120
Table 4.7 – Calculated MO contributions for [Ir(L ²) ₂ (bpy)] ⁺ and [Ir(L ⁵) ₂ (bpy)] ⁺ . Q1 and Q2 are the different quinoline ligands on each complex.	126
Table 5.1 – Selected bond lengths and bond angles obtained from crystallographic data for [Ir(1nq) ₂ (L ²)]PF ₆ and [Ir(2nq) ₂ (L ⁴)]PF ₆	153
Table 5.2 – Selected torsion angles from within the cyclometalating ligands for [Ir(1nq) ₂ (L ²)]PF ₆ . [Ir(1nq) ₂ (bpy)]PF ₆ structure taken from the work in Chapter 4.	154
Table 5.3 - ¹⁹ F{ ¹ H} NMR spectra shifts for ligand and complexes. ^a Ligand spectra obtained in d ₆ -DMSO. ^b Iridium complexes of 1nq spectra obtained in CDCl ₃ . ^c Iridium complexes of 2nq spectra obtained in CD ₃ OD.....	159
Table 5.4 - ^a All measurements obtained at room temperature in aerated aqueous 0.1 M NaOH at ca. 1x10 ⁻⁵ M unless otherwise stated. ^b λ _{ex} = 325 nm; ^c λ _{ex} = 295 nm; ^d Vs standard Quinine Sulphate in 0.05 M H ₂ SO ₄ , λ _{ex} = 310 nm. ⁴² ^e Measurements obtained in aerated MeCN. ^f Measurements obtained in aerated CHCl ₃	160
Table 5.5 - ^a All measurements obtained at room temperature in aerated MeCN at ca. 1x10 ⁻⁵ M unless otherwise stated. ^b λ _{ex} = 510 nm; ^c λ _{ex} = 295 nm; ^d Vs standard [Ru(bpy) ₃](PF ₆) ₂ , λ _{ex} = 430 nm. ⁴²	162
Table 5.6 - ^a All measurements obtained at room temperature in aerated MeCN at ca. 1x10 ⁻⁵ M unless otherwise stated. ^b λ _{ex} = 510 nm; ^c λ _{ex} = 295 nm; ^d Vs standard [Ru(bpy) ₃](PF ₆) ₂ , λ _{ex} = 430 nm. ⁴²	165
Table 6.1 - Selected bond lengths, bond angles and ligand torsion angles obtained from crystallographic data from complex [Re(CO) ₃ (L ⁷)Br].	193
Table 6.2 – Metal carbonyl ¹³ C{ ¹ H} NMR spectrum shifts and FTIR peaks assigned to Metal carbonyls for [Re(CO) ₃ (L ¹⁻⁸)Br] complexes. ^a Spectra obtained in d ₆ -acetone.	197
Table 6.3 - Electrochemical properties of the rhenium(I) complexes obtained from cyclic voltammetry. Potentials measured in deaerated DCM solutions at 200 mVs ⁻	

¹ with 0.1 M [NBu₄][PF₆] as supporting electrolyte calibrated with Fc/Fc⁺; ^a $E_{1/2}$ values for fully reversible process; ^b Cathodic peak of irreversible process. 198

Table 6.4 - ^a All measurements obtained at room temperature in aerated MeCN ca. 1×10^{-5} M. ^b Measurements obtained in the solid state, $\lambda_{ex} = 420$ nm. 201

Table 7.1 - ^a All measurements run at room temperature in aerated CH₂Cl₂ at ca. 1×10^{-5} M. ^b $\lambda_{ex} = 387$ nm; ^c $\lambda_{ex} = 374$ nm; ^d $\lambda_{em} = 447$ nm; ^e $\lambda_{ex} = 295$ nm; ^f Vs standard quinine sulfate in 0.05 M H₂SO₄, $\lambda_{ex} = 350$ nm. ⁶⁶ 228

Table 7.2 - ^a All measurements recorded in aerated CH₂Cl₂. $\lambda_{ex} = 387$ nm; ^b Recorded at $\lambda_{em} = 460$ nm; ^c $\lambda_{em} = 430$ nm 229

Table 7.3 - ^a All measurements run at room temperature in aerated CH₂Cl₂ at ca. 10^{-5} M. ^b $\lambda_{ex} = 450$ nm; ^c $\lambda_{em} = 605$ nm; ^d Vs standard [Ru(bpy)₃](PF₆)₂ in MeCN, $\lambda_{ex} = 430$ nm. ⁶⁶ 230

Table 7.4 - **IrDPA** complex lifetime recorded in aerated CH₂Cl₂ at ca. 10^{-5} M.. 231

Table 7.5 - Complex lifetimes recorded in degassed CH₂Cl₂ solution. $\lambda_{ex} = 295$ nm. 235

Table of Equations

Equation 1.1 6

Equation 1.2 6

Equation 1.3 6

Equation 1.4 6

Equation 1.5 7

Equation 1.6 8

Equation 1.7 8

Equation 1.8 10

Equation 2.1 50

Equation 7.1 211

Abbreviations

Spectroscopy and Techniques

ATR – Attenuated total Reflectance

COSY – Correlation Spectroscopy

CV – Cyclic Voltammetry

DFT – Density Functional Theory

ES – Electrospray ionisation

FT – Fourier transform

IR – Infrared

HR – High Resolution

LR – Low resolution

NIR – Near infrared

NMR – Nuclear Magnetic
Resonance

MS – Mass Spectrometry

TA – Transient Absorption

TD – Time Dependent

TLC – Thin Layer Chromatography

UV – Ultraviolet

UV-Vis – Ultraviolet – Visible

XRD – X-ray Diffraction

{¹H} – Proton decoupled

1D – One dimensional

2D – Two dimensional

s – Second

ms – Millisecond

μs – Microsecond

ns – Nanosecond

ps – Picosecond

fs – Femtosecond

cm⁻¹ – Wavenumber

m/z – Mass to Charge ratio

nm – Nanometer

OD – Optical Density

ppm – Parts Per Million

λ - Wavelength

δ – Chemical shift

s – Singlet

d – Doublet

t – Triplet

q – Quartet

m – Multiplet

Photophysics

EDG – Electron Donating Groups

EWG – Electron Withdrawing
Groups

HOMO – Highest Occupied
Molecular Orbital

ILCT – Intraligand Charge Transfer

LC – Ligand Centred transition

LED – Light Emitting Diode

LEEC – Light Emitting
Electrochemical Cell

LLCT – Ligand to Ligand Charge
Transfer

LMCT – Ligand to Metal Charge
Transfer

LUMO – Lowest Unoccupied
Molecular Orbital

MC – Metal Centred transition

MLCT – Metal to Ligand Charge
Transfer

OLED – Organic Light Emitting
Diode

ROS – Reactive Oxygen Species

SOMO – Singly Occupied Molecular
Orbital

PMT – Photo Multiplier Tube

PET – Photoinduced Electron
Transfer

PhOLED – Phosphorescent Organic
Light Emitting Diode

PDT – Photo Dynamic Therapy

TADF – Thermally Activated
Delayed Fluorescence

TTA – Triplet-Triplet Annihilation

UC – Up Conversion

IC – Internal Conversion

ISC – Intersystem crossing

RISC – Reverse intersystem
crossing

SOC – Spin-orbit Coupling

S_0 – Singlet electronic ground state

S_n – Singlet electronic excited state

T_n – Triplet electronic excited state

V – Vibronic state

abs – Absorption

em – Emission

ex – Excitation

k_r – Rate of radiative decay

k_{nr} – Rate of nonradiative decay

RET – Resonance energy transfer

TTET – Triplet – Triplet Energy
Transfer

PL – Photoluminescent
EL – Electroluminescent
EQE – External Quantum Efficiency
 ε – Molar Extinction Coefficient
 Φ – Quantum Yield
 τ - Lifetime

Solvents and Chemicals

1npy – 2-(Naphth-1-yl)pyridine
2npy – 2-(Naphth-2-yl)pyridine
1nq – Ethyl 2-(naphthalen-1-yl)quinoline-4-carboxylate
2nq – Ethyl 2-(naphthalen-2-yl)quinoline-4-carboxylate
AgBF₄ – Silver tetrafluoroborate
AgCl – Silver chloride
AgPF₆ – Silver hexafluorophosphate
acac – Acetylacetonate
biq – 2,2'-Biquinoline
bpy – 2,2'-Bipyridyl
bpz – 2,2'-Bipyrazine
CO – Carbon monoxide
diFppy – 2-(2,4-Difluorophenyl)pyridine
DNA – Deoxyribosenucleic acid
DPA – 9,10-Diphenylanthracene
dppz – Dipyrido[3,2-a:2'3'-c]phenazine

L – Ligand
MgSO₄ – Magnesium sulfate
Na₂SO₄ – Sodium sulfate
[NH₄][PF₆] – Ammonium hexafluorophosphate
OEP – 2,3,7,8,12,13,17,18-Octaethylporphyrin
phen – 1,10-Phenanthroline
PMMA – Poly(Methyl MethAcrylate)
Piq – 1-Phenylisoquinoline
ppy – 2-Phenylpyridine
ppz – 1-Phenylpyrazole
pyq – 2-(Pyridin-2-yl)quinoline
TCCP – 5,10,15,20-Tetrakis-(4-carboxyphenyl)-porphyrin
terpy – 2,2':6',2''-terpyridine
tpphz – Tetrapyrido[3,2-a:2',3'-c:3'',2''-h:2''',3'''-j]phenazine
Me – Methyl
Et – Ethyl
ⁱPr - isopropyl
^tBu – *tert*butyl
OMe – methoxy
Ph – Phenyl
Bn – Benzyl
TIPS – Triisopropyl silyl ether

CHCl ₃ – Chloroform	HCl – Hydrochloric acid
DCM / CH ₂ Cl ₂ – Dichloromethane	H ₂ SO ₄ – Sulfuric acid
DIPEA – Diisopropyl ethylamine	HOCl – Hypochlorous acid
DMF – Dimethylformamide	K ₂ CO ₃ – Potassium carbonate
DMSO – Dimethylsulfoxide	KOH – Potassium hydroxide
EDC•HCL – 1-Ethyl-3-carbodiimide hydrochloride	MeCN – Acetonitrile
EPA – A mixture diethyl ether, pentanes and ethanol	MeOH – Methanol
Et ₂ O – Diethyl ether	NaOH – Sodium hydroxide
Et ₃ N / TEA – Triethylamine	Na ₂ CO ₃ – Sodium carbonate
EtOAc – Ethyl acetate	NHS – N-Hydroxysuccinimide
EtOH – Ethanol	SOCl ₂ – Thionyl chloride
	THF – Tetrahydrofuran

Chapter 1 - Introduction

1.1 Introduction

The work within this thesis explores the development of novel transition metal complexes featuring substituted benzannulated ligand systems developed for photonic applications. The work focuses on the photophysical characterisation of the transition metal complexes, and as such the introduction covers the important underlying principles behind photoluminescent chemistry used in this work. Furthermore, it looks at some recent examples of luminescent transition metal complexes and their properties, such as the ability to emit light across the visible spectrum and into the near infra-red region. There is considerable interest in emissive transition metal complexes¹⁻³ to aid in the development of low energy OLED lighting solutions, photo redox catalysis, solar conversion, and biological applications.⁴⁻⁹

The properties of a compound to emit light can be defined by one of two different processes: incandescence or luminescence¹⁰. In each case, an excited state molecule is returning to its ground state via the release of excess energy as light, with the different processes defined by how the molecules become excited. Incandescence is the emission of light caused by a change in temperature, while luminescence describes the emission of light independent of a change in temperature. Luminescence can be further defined by the excitation energy pathway, with some common examples listed below:

- Photoluminescence – A molecule is excited by a photon.
- Electroluminescence – An excitation caused by an applied electric field.
- Triboluminescence – Transformation of mechanical energy into light energy.
- Chemiluminescence – Emission of light from a chemical reaction.
- Bioluminescence – Emission of light from a living organism.
- Radioluminescence – Excitation caused by bombardment from ionising radiation.

The work in this thesis pertains to photoluminescent molecules, and as such this will be the focus from this point forward.

1.2 Photoluminescence

1.2.1 Jablonski diagrams

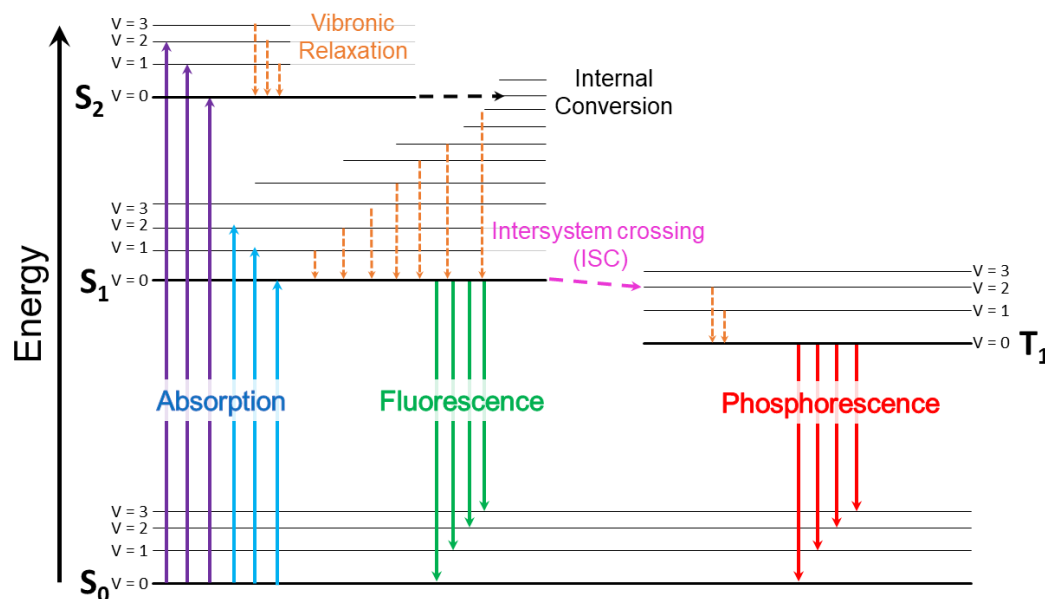


Figure 1.1 - Jablonski diagram

To visualise the possible transition that can occur upon absorption of light, a Jablonski energy level diagram is used (Figure 1.1)¹¹. Named after Alexander Jablonski¹², the diagram details the different energy pathways that can occur upon excitation. Horizontal lines are used to represent the different energy levels of the molecule, with the S_0 representing the molecular ground state. In Figure 1.1, the electronic excited states are labelled as S_n and T_n to represent singlet and triplet multiplicities of the state. Each of these is then subdivided into several different vibrational energy levels, with the bold line representing the lowest vibrational level of each state.

Absorption events are represented by the blue arrows and occur in the order of 10^{-15} s. In keeping with the Franck-Condon principle^{13,14}, each transition between states is represented as a vertical line, since electronic and vibronic transitions are very rapid, they occur near instantaneously with no change in nuclear coordinates. Absorption involves the conversion of a photon into molecular energy, exciting the molecule into a higher vibrational level, typically of the S_1 or S_2 states. Vibronic relaxation is a nonradiative process, whereby the molecule loses excess vibrational energy and returns to the vibrational ground state. These transitions are fast, occurring in the magnitude of $10^{-12} - 10^{-10}$ s. They are shown in the diagram

as the orange dashed arrows. Internal conversion (IC) is a nonradiative transition, occurring between two different electronic levels that share the same spin multiplicity. This is highlighted in the diagram above with the black dashed line. This typically occurs in the timescale of $10^{-11} - 10^{-9}$ s, depending on the energy gap between levels, with the $\mathbf{S}_1 \rightarrow \mathbf{S}_0$ transition typically being the slowest and competing with fluorescence and any nonradiative quenching processes. The conversion between electronic states of different spin multiplicities is known as Intersystem crossing (ISC). Transitions occurring between singlet and triplet states are forbidden by the spin selection rule, but, can occur due to spin-orbit coupling (SOC). Spin-orbit coupling is the interaction between an electron's spin and the magnetic field generated by nearby nuclei. Since the magnitude of the magnetic field is proportional to the size of the atom, the effects of spin-orbit coupling increase with atomic size¹⁵.

The radiative relaxation transitions are known as fluorescence and phosphorescence. Fluorescence is the emission of photons from a $\mathbf{S}_n \rightarrow \mathbf{S}_0$ transition where $\Delta S=0$ and is seen above with the green arrows. Fluorescent lifetimes are typically 10^{-10} and 10^{-8} s. Phosphorescence is indicated by the red arrows and is the emission of photons from a $\mathbf{T}_n \rightarrow \mathbf{S}_0$ transition, where $\Delta S \neq 0$. Since this transition requires a change in spin multiplicity, it is formally spin forbidden and only weakly allowed via spin-orbit coupling interactions. Due to this, the typical timescale possessed by phosphorescent compounds is between milliseconds and seconds. Some phosphorescent materials, such as rare-earth doped strontium aluminates, possess lifetimes measured in minutes or even hours, leading to their use in emergency signage or 'glow-in-the-dark' decorations¹⁶.

1.2.2 Stokes shift

In the 19th century, G. G. Stokes observed that the energy of emission is lower than the energy of absorption¹⁷. Energy can be lost via rapid vibrational relaxation towards the lowest vibrational level of the excited state or via relaxation to higher vibrational levels of the ground state¹¹.

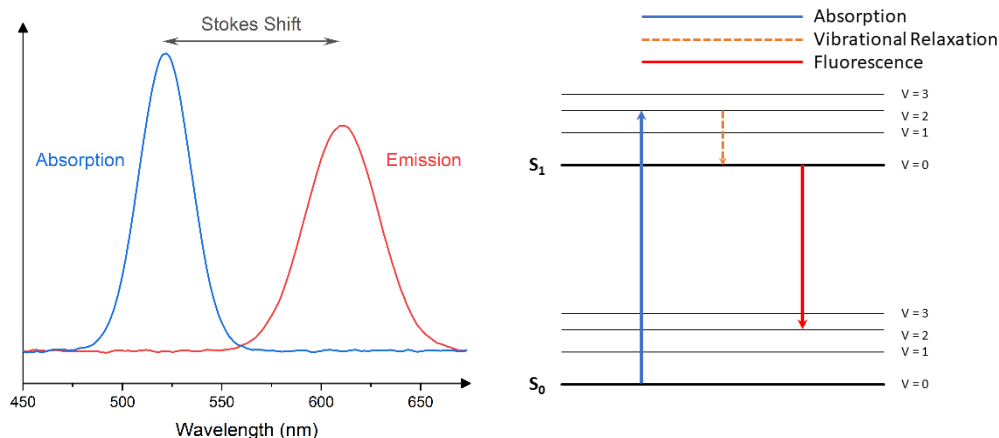


Figure 1.2 – Diagram showing Stokes Shift (left) and a Jablonski diagram representing Stokes Shift (right)

1.2.3 Kasha's rule

Kasha's Rule states, "***The emitting level of a given multiplicity is the lowest excited level of that multiplicity***" and was defined by Michael Kasha's seminal 1950 publication¹⁸. The wavelength of emission from a photoluminescent molecule is independent of the wavelength of absorption. When a molecule is excited to a higher electronic level, S_n , it will quickly undergo vibronic relaxation and internal conversion at a quicker rate than the competing rate of radiative decay back to the ground state (i.e., $S_n \rightarrow S_0$), because the rate of internal conversion is quicker the smaller the energy gap between states (Energy gap law)¹⁹. Since the energy gap between the S_0 and S_1 levels is typically the largest, the rate of internal conversion is slowest, and of comparable magnitude to the rate of fluorescence, and therefore for the $S_1 \rightarrow S_0$ transition, emission is observed. Some molecules, such as azulene, are known to disobey Kasha's rules, and instead emit from the $S_2 \rightarrow S_0$ transition due to a large energy gap between the S_1 and S_2 excited states lowering the rate of internal conversion.

1.2.4 Quantum yield (Φ)

The quantum yield, Φ , is a measure of the ratio between absorbed photons and emitted photons^{11,20}, as described in Equation 1.1. If each photon absorption results in an excitation to the emitting state, and both the radiative and non-radiative processes can depopulate the excited state, then quantum efficiency can also be defined in terms of rate of radiative decay (k_r) and the rate of non-radiative decay (k_{nr}) (Equation 1.2). The larger the Φ , the brighter the emission.

$$\Phi = \frac{\text{Number of photons emitted}}{\text{Number of photons absorbed}} \quad \text{Equation 1.1}$$

$$\Phi = \frac{k_r}{k_r + k_{nr}} \quad \text{Equation 1.2}$$

If k_{nr} is much smaller than k_r then Φ can approach unity. Quantum yield can be calculated experimentally using a standard absorption and emission spectrometers, by comparison to a known standard (Equation 1.3)²¹.

$$\Phi_i = \Phi_R \cdot \left(\frac{I_i}{I_R}\right) \cdot \left(\frac{A_R}{A_i}\right) \cdot \left(\frac{n_i^2}{n_R^2}\right) \quad \text{Equation 1.3}$$

Where Φ_i and Φ_R are the quantum yields of the sample being measured and of the standard respectively, I is the area under the emission spectra of each sample, A is the absorption of each sample at the excitation wavelength and n is the refractive index of the solvents used for the measurements. Typical standards and their quantum yields are seen below (Figure 1.3).

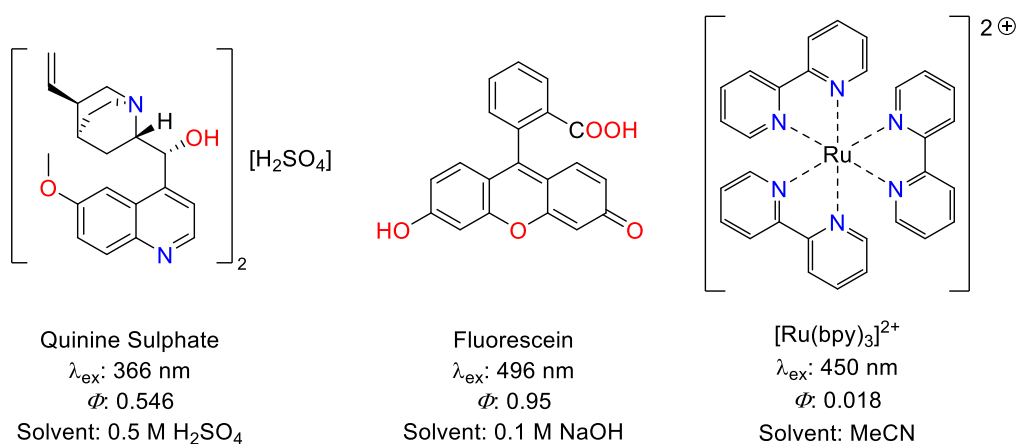


Figure 1.3 – Three common quantum yield standards, with details of quantum yields, solvents used and excitation wavelengths²¹.

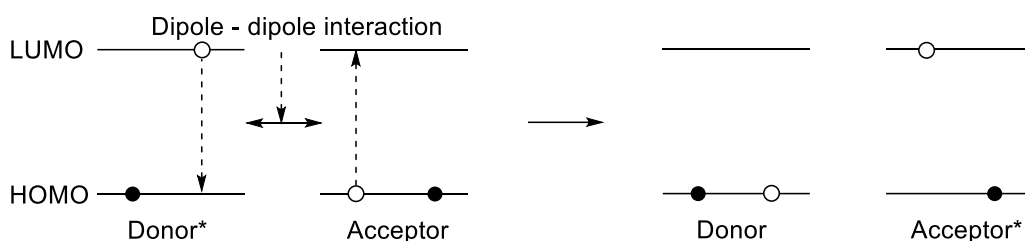
1.2.5 Luminescent lifetimes (τ)

The luminescent lifetime of a molecule is defined by the average amount of time spent in the excited state before returning to the ground state¹¹. It is important to note that τ is an average value since emission is a random process. Fluorescent lifetimes are typically shorter than phosphorescent lifetimes due to the spin forbidden nature of the latter process. The lifetime can be expressed in terms of k_r and k_{nr} as follows:

$$\tau = \frac{1}{k_r + k_{nr}} \quad \text{Equation 1.4}$$

1.2.6 Energy transfer

RET Mechanism



Dexter Mechanism

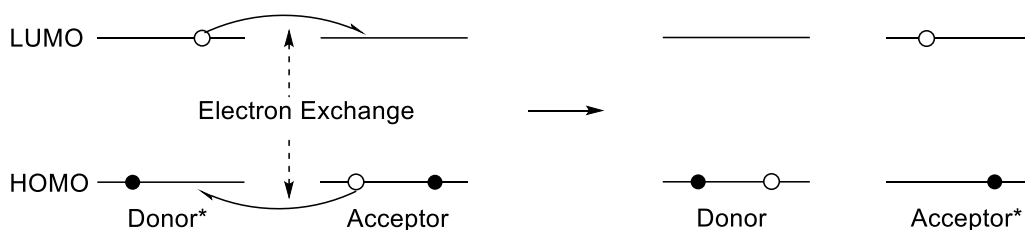


Figure 1.4 – Schematic representation of RET and Dexter energy transfer processes.

Energy transfer between a donor molecule (D) and an acceptor molecule (A) can proceed via Resonance Energy Transfer (RET), or by electron exchange, or both. RET occurs when the absorbance spectrum of the acceptor molecule overlaps with the emission spectrum of the donor molecule²². RET is a nonradiative process that does not proceed via the emission of a photon from the donor molecule and the subsequent absorption by the acceptor molecule. Instead, the donor and acceptor molecule are linked via dipole-dipole interactions, with the extent of energy transfer linked to the distance between the donor and acceptor (r), and the degree of spectral overlap, which can be defined by the Förster radius (R_0). The Förster radius is the distance where half of the excitation energy of the donor molecule can be transferred to the acceptor molecule, and is typically around 30 – 60 Å²³. The rate of energy transfer, $k_T(r)$, describing this relationship is given by the Equation 1.5:

$$k_T(r) = \frac{1}{\tau_D} \left(\frac{R_0}{r} \right)^6 \quad \text{Equation 1.5}$$

Where τ_D is the lifetime of the donor molecule in the absence of energy transfer. Furthermore, the efficiency of a donor and acceptor pair at a fixed distance is defined in Equation 1.6:

$$E = \frac{R_0^6}{R_0^6 + r^6} \quad \text{Equation 1.6}$$

The efficiency of the energy transfer is very clearly dependent upon r , the distance between acceptor and donor molecules¹¹.

Electron exchange, also known as the Dexter Interaction²⁴, is a short-range mechanism of excitation transfer from the HOMO of the electronically excited donor (D^*), to the LUMO of the acceptor (A). This happens in combination with the simultaneous movement of an electron from the HOMO of A to the SOMO of D^* . Unlike RET, which accounts for allowed transitions, Dexter electron exchange can account for forbidden transitions²⁵.

1.2.7 Emission quenching

Quenching is any process by which the emission intensity of luminescence is decreased¹¹. There are several mechanisms that may facilitate this, including the RET discussed above, which is a type of collisional quenching. Collisional quenching, also known as dynamic quenching, is when the excited state of a luminophore collides with another molecule in solution (the quencher) and relaxes back to the ground state in a non-emissive manner. A common source of dynamic quenching is from dissolved molecular oxygen, which can deactivate fluorescent and phosphorescent species in solution^{26,27}. Halide ions can also cause deactivation, perhaps most prominently in quinine solution, where chloride ions are known to quench emission²⁸. Heavier halogens may induce spin-orbit coupling to allow ISC to occur, quenching the fluorescence, such as with Rhodamine Green with a solution containing KI²⁹. The Stern-Volmer equation (Equation 1.7) describes the relationship between fluorescent intensity and quenchers.

$$\frac{I_f^0}{I_f} = 1 + K[Q] = 1 + k_q\tau_0[Q] \quad \text{Equation 1.7}$$

Where I_f and I_f^0 describe the intensity of fluorescence in the presence of and without quencher respectively, K is the Stern-Volmer quenching constant which details the sensitivity towards the quencher, $[Q]$ is the concentration of the quenching agent, k_q is the bimolecular quenching constant and τ_0 is the lifetime of the unquenched molecule.

A second type of quenching is known as static quenching. This is where the quencher and luminophore form a non-emissive complex while still in the ground state¹¹. For example, the DNA intercalating complex $[\text{Ru}(\text{bpy})_2(\text{dppz})]^{2+}$ (bpy: 2,2-bipyridyl, dppz: dipyridophenazine) is non-emissive in aqueous solutions³⁰.

When the complex is intercalated with DNA via the dppz ligand, the emission is 'turned on'. This is because of water hydrogen bonding to the non-coordinating imines in the dppz ligand, quenching the emission. Once intercalated, the environment becomes a lot more hydrophobic and as such the complex becomes emissive.

1.3 Photoluminescent measurements

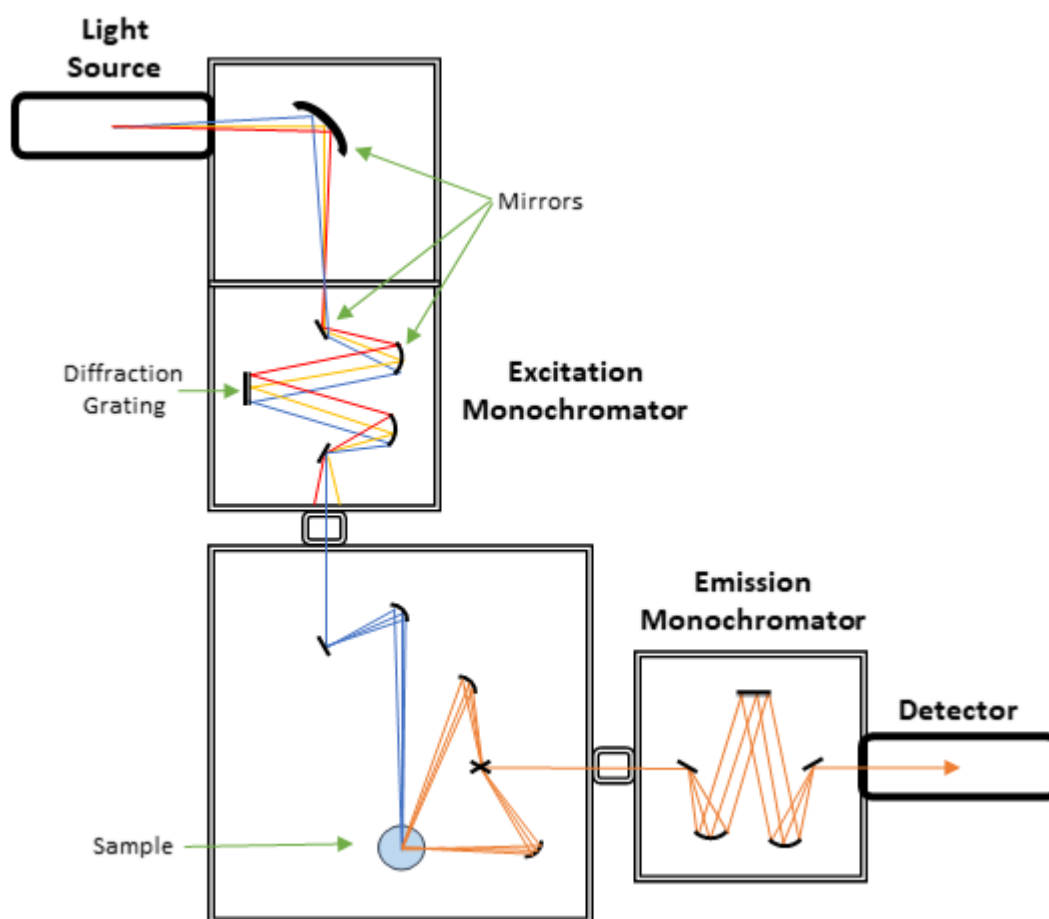


Figure 1.5 - Simplified set up of a spectrofluorometer

Photoluminescent measurements are made on a spectrofluorometer, with a simplified set up show in Figure 1.5. Typical light sources may be arc xenon lamps, mercury lamps, LEDs or laser diodes. The excitation monochromator allows for a single wavelength of light to be sent to the sample, via the use of a diffraction grating. The emission is then directed via a second monochromator to the photo multiplier tube (PMT) where the signal is detected. Measurements are taken as one of two types of experiment: steady state or time-resolved. During steady state

measurements, the sample is under constant illumination. This allows the sample to reach a steady excited state, and allows for the emission spectrum to be recorded¹¹. Steady state measurements show the time averaged emission profile over the decay of the excited state. Conversely, during time-resolved measurements, the sample is excited by short pulses of light before the emission intensity is recorded as a function of time³¹. Typically, a pulse duration is shorter than the emission decay, meaning a high-speed detector is needed. This allows for the collection of luminescent lifetime data, using the following relationship for a single exponential decay:

$$I(t) = I_0 e^{-t/\tau} \quad \text{Equation 1.8}$$

1.4 Luminophores

A luminophore is any molecule that emits light when irradiated³². This can be broken down further into fluorophores and phosphors, which are determined by the multiplicity of the excited state of the emission origin, as mentioned in Section 1.2.1.

1.4.1 Organic fluorophores

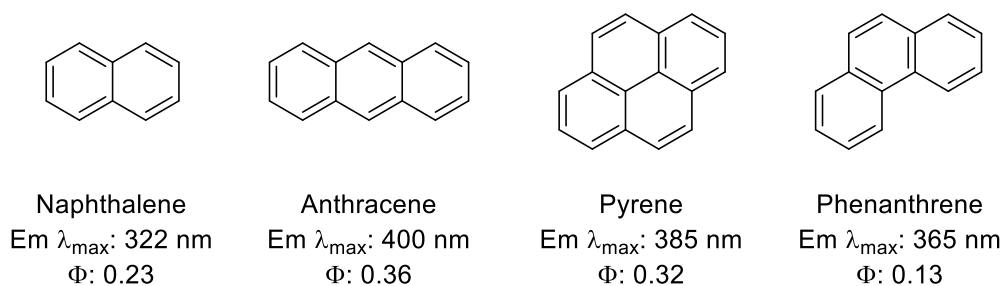


Figure 1.6 – Common organic emitting polyaromatic compounds. Measurements made in cyclohexane³³.

Polyaromatic compounds, such as those seen in Figure 1.6, are commonly used as the basis for organic fluorophores. The conjugated system allows $\pi-\pi^*$ transitions in the visible region of the electromagnetic spectrum^{33,34}. Although typically exhibiting fluorescence emission, some compounds may also exhibit phosphorescent emission, although it is much rarer and is normally readily quenched. Conjugated systems allow for substitution and functionalisation to modify the emission. Typically, larger conjugated systems result in a lower energy emission³³. Substitution of aromatic systems by electron withdrawing or electron donating groups (EWG and EDG respectively) affects the electron density of the aromatic system, resulting in a modulation of the emission properties³⁵. The field of organic fluorophores is still moving forwards. For example, the three structures

in Figure 1.7 were reported in 2021. Compound **A** shows a fluorenone derivative synthesised by Song *et al* for multiphoton absorption studies³⁶. Compound **B** shows a heteroaryl coumarin synthesised for laser induced radical generation studies by Tarkovskii *et al*³⁷. Finally, the perylene based photosensitiser, **C**, was synthesised to be used as a membrane anchoring photo switch for use in photodynamic therapy³⁸.

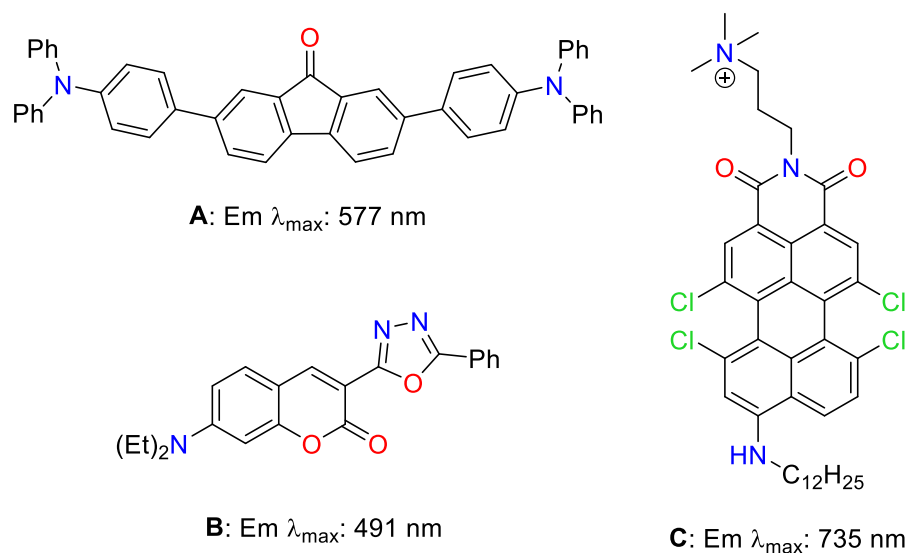


Figure 1.7 – Recent examples of organic fluorophores with a range of different emission wavelengths^{36–38}.

1.4.2 Luminescent metal complexes

Coordination complexes based on the transition metals are attractive luminophores. They possess the ability for fine tuning of electronic and physical properties via ligand design. There are five main electronic transition that can occur^{39,40}.

- Metal Centred (MC) transitions – d-d* transition confined to the metal centre.
- Metal to Ligand Charge Transfer (MLCT) – d- π^* transitions involving a metal centred d-orbital exciting into a ligand π^* -orbital.
- Ligand to Metal Charge Transfer (LMCT) – electronic transition between ligand based π orbitals to a metal centred orbital.
- Intraligand Charge Transfer (ILCT) – a ligand centred (LC) transition involving π - π^* or n- π^* states.

- Ligand to Ligand Charge Transfer (LLCT) – a π - π^* transition between two separate ligands around the metal centre.

The luminescent properties of metal complexes tend to be dominated by phosphorescence, due to the heavy atom effect of the metal centre inducing SOC and populating the triplet states via ISC⁴¹ (Figure 1.8). Although a much rarer phenomenon, fluorescent metal complexes can exist if the rate of SOC is slow, leading to longer lived singlet excited states⁴². Finally, Thermally Activated Delayed Fluorescence (TADF) processes occur when the levels of the **S**₁ and **T**₁ states are energetically close enough for the ambient temperature to induce reverse intersystem-crossing (RISC)⁴³. This can lead to dual fluorescent and phosphorescent complexes.

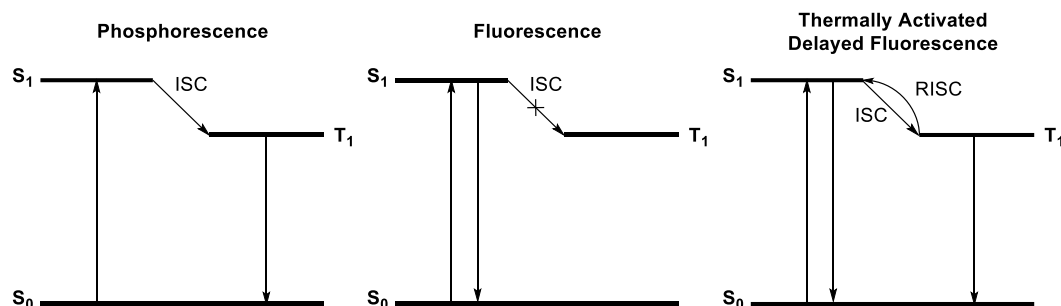


Figure 1.8 – Schematic representing the major emission pathways for metal complexes.

1.4.2.1 Metal complex fluorophores

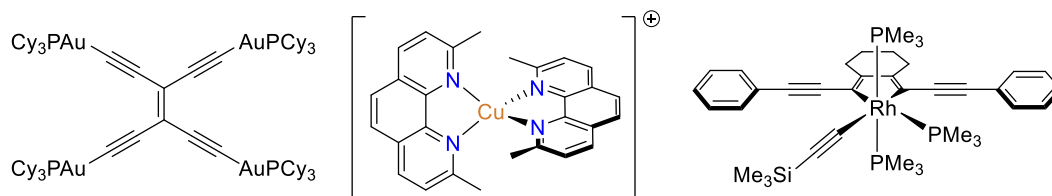


Figure 1.9 - Three examples of fluorescent complexes^{44–46}.

For most metal complexes, fluorescence is difficult to observe. This is due to very short lifetimes and very low quantum yields because of the role the metal centre plays in allowing ISC between the singlet and triplet states. This occurs in around 110 fs⁴⁷. For example, the observed fluorescent lifetimes in $[\text{Ru}(\text{bpy})_3]^{2+}$ and $[\text{Ir}(\text{ppy})_3]$ are reported as being 15 ± 10 fs⁴⁷ and 100 fs⁴⁸ respectively while the fluorescent Φ of $[\text{Ru}(\text{bpy})_3]^{2+}$ is 9×10^{-5} .⁴⁹ (ppy – 2-phenylpyridine)

The complexes in Figure 1.9 all show fluorescent emission. The *tetra*-gold(I) ethynyl complex was synthesised in 2003 by Che *et al*⁴⁶. Despite featuring four heavy gold metal centres, the complex displayed fluorescence with a $\Phi = 0.22$ due

to the symmetrical nature of the ethynyl ligand dominating over the SOC effects⁵⁰. The 3d⁹ electronic configuration of the copper(I) *bis*(neocuproine) induces a Jahn-Teller flattening of the complex alongside steric interactions of the methyl groups, resulting in a splitting of the HOMO and HOMO-1 levels making the ISC process unfavoured⁴⁴. This resulted in a τ of just 13 ps and an Φ of $2.8 \pm 0.8 \times 10^{-5}$. Finally, the rhodium metallocycle was reported by Marder *et al* in 2010⁴⁵. The complex was emissive with a reported τ of 0.33 ns and an Φ of 0.22. In this example, fluorescence is becoming competitive with the rate of ISC, which was found to be slower than normal, at $k_{ISC} = 5 \times 10^8 \text{ s}^{-1}$.

1.4.2.2 Phosphorescent first-row transition metal complexes

First row metals are generally characterised by lower energy ligand field (d-d*) transitions, and weak spin-orbit coupling interactions⁵¹. Due to the weaker ligand field splitting, typically phosphorescence is not seen in solution at room temperature where d-d* transitions result in a distortion of the complex geometry, but may be experienced in glasses at 77 K where distortion becomes less favourable due to a rigid matrix³⁹. The main examples of room temperature phosphorescence are seen with Cu(I) and Cr(III), but phosphorescence is known for other first row metals, including Fe(II)⁵², Ni(II)⁵³ and V(III)⁵⁴.

Cr(III) complexes show a typically red emission.⁵⁵ They also exhibit small Φ in the range of $10^{-3} - 10^{-8}$ at 298 K³⁹. For example, $[\text{Cr}(\text{bpy})_3]^{3+}$, is emissive at 727 nm, with a Φ of 9×10^{-4} (Figure 1.10)⁵⁵. More recent examples include the macrocycle mono-alkynyl complex from the 2021 paper from Ren *et al*, with a λ_{max} of 725 nm⁵⁶.

Cu(I) complexes are known to be emissive via MLCT or intraligand states⁵⁷. The emission from Cu(I) can span the visible spectrum, although much like Cr(III) it is typically emissive in the red region⁵⁸. The neutral copper complex seen in Figure 1.10 was reported by Li *et al* in 2021⁵⁹. A series of diphosphine complexes was synthesised and phosphorescence between 587 and 599 nm in solution (CH_2Cl_2). The emission is assigned as predominantly ³MLCT in character, with some ³LLCT.

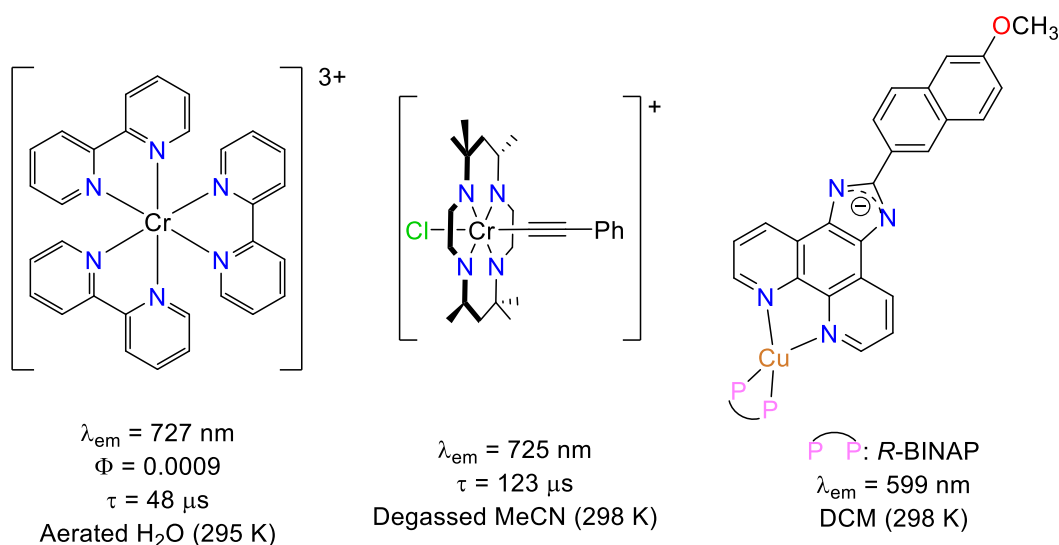


Figure 1.10 – Examples of phosphorescent complexes of Cr(III)^{55,56} and Cu(I)⁵⁹ Phosphorescent d^6 complexes of the second and third row transition metals

With the second and third row transition metals, the larger ligand field splitting gives rise to the more prevalent MLCT transitions. The heavier metal atoms from the second and third row of the periodic table also increase the spin-orbit coupling interactions in comparison to their first row counterparts, which can facilitate the mixing of singlet and triplet excited states via ISC interactions. Up until Adamson and Demas first reported the photo-redox capabilities of $[\text{Ru}(\text{bpy})_3]^{2+}$ in 1971⁶⁰, luminescent research into transition metal complexes was limited to metal carbonyls and Cr(III)⁶¹. Since then, the field of luminescent inorganic chemistry has grown substantially. The d^6 electron configuration is prevalent, with examples seen for a range of metals, including Re(I)^{62,63}, Ru(II)^{64,65}, Os(II)⁶⁶, Rh(III)⁶⁷ and Ir(III)^{68,69}. The chemistry of Ir(III) and Re(I) complexes is discussed in detail over the course of this thesis, and as such is not mentioned here.

The ³MLCT photoluminescent properties of ruthenium polypyridyl complexes, for example complexes with bpy or 1,10-phenanthroline (phen), have been widely reported⁷⁰. Emission for $[\text{Ru}(\text{bpy})_3]^{2+}$ and $[\text{Ru}(\text{phen})_3]^{2+}$ is seen ca. 600 nm, with typical lifetimes around 0.6 – 0.9 μs , and quantum yields $10^{-1} - 10^{-3}$.⁷¹ Because of these properties, Ru(II) complexes have seen uses in the fields of photocatalysis⁷², imaging probes⁷³ and Photo Dynamic Therapy (PDT)⁷⁴. Some recently published examples of emissive Ru(II) polypyridyl complexes can be seen below^{75,76}.

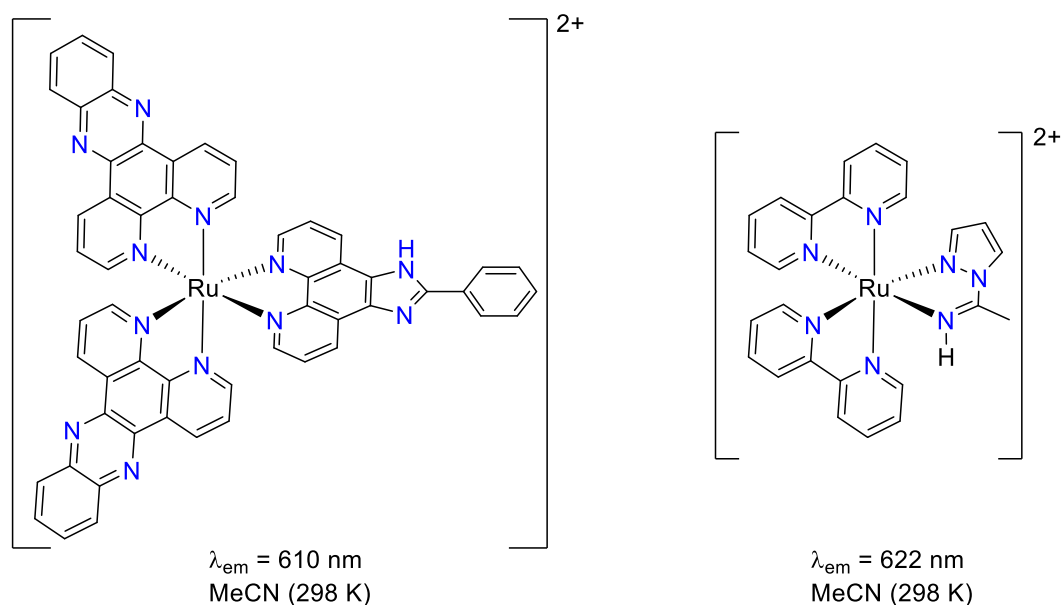


Figure 1.11 – Examples of recent Ru(II) complexes^{75,76}.

Complexes of Os(II) generally show a longer wavelength emission, typically above 700 nm into the near-infrared region. Longer wavelength emission is often coupled with shorter lifetime and lower quantum yields. Typically, τ is in the region of 10-100 ns, while Φ is typically around 10^{-3} .⁷⁷ Recently published examples of Os(II) complexes for cell imaging and PDT can be seen below^{78,79}.

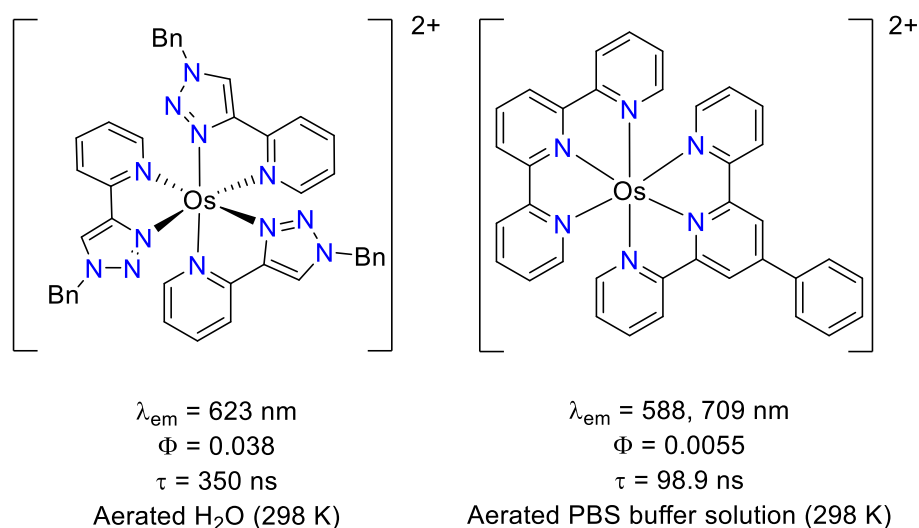


Figure 1.12 – Examples of recently published Os(II) complexes^{78,79}.

Rh(III) cyclometalated complexes are less emissive than their Ir(III) counterparts due to a smaller SOC constant⁸⁰. Also, the luminescent emission is typically ligand centred with a smaller MLCT band^{81,82}.

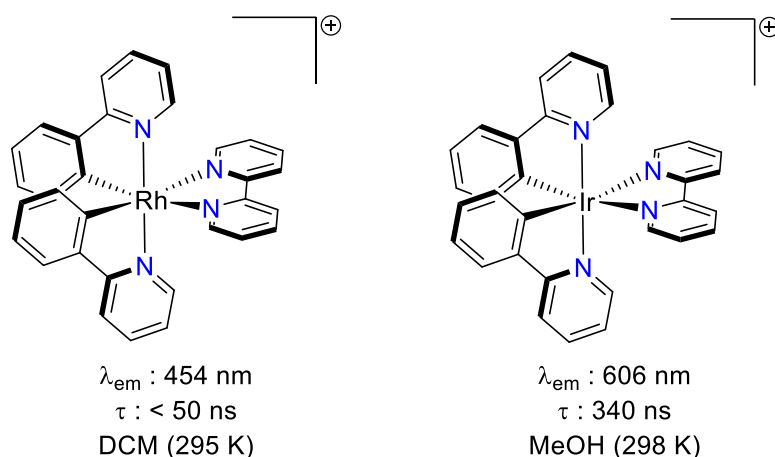


Figure 1.13 - Archetypal rhodium (III) and iridium (III) complexes.⁸³

1.4.2.3 Phosphorescent d^8 and d^{10} complexes of the second and third row transition metals

The luminescent chemistry of the d^8 metals is dominated by platinum(II) complexes^{84–86}, due to the platinum metal atoms heavy atom effect inducing ISC³⁹. The low-lying metal centred excited states are able to facilitate non-radiative relaxation pathways⁸⁷, and as such, room temperature solution phase phosphorescent emission from Pt(II) was only first observed in the 1980s^{88,89}. This means strong field ligands are needed to observe phosphorescence at room temperature, such as ligands with a cyclometalated carbon. Figure 1.14 shows two similar complexes, [Pt(terpy)Cl]Cl and a dipyrind-2-yl-1,3-benzene N[^]C[^]N pincer ligand complex, [Pt(N[^]C[^]N)Cl]. The terpy complex was characterised by Romeo *et al*, and only showed emission in a 4:1 MeOH/EtOH glass at 77 K⁹⁰, with the emission ascribed to both ³MLCT and Metal to metal to ligand charge transfer (MMLCT) excited states, $^3d\sigma^* \rightarrow \pi^*$. When the middle pyridine is substituted for a phenyl group, as shown with the middle complex in Figure 1.14, the compound becomes brightly emissive in solution at 293 K, with high quantum yields. The compound was reported by Wilson *et al*, who were able to assign the emission to $^3\pi-\pi^*$ transitions⁹¹. Pt(II) porphyrin complexes are also emissive in solution, such as the third compound in Figure 1.14, reported by Sujatha *et al* in 2019⁹². The complex exhibits phosphorescence which can be almost entirely quenched by O₂ leading to the applications as a sensor for dissolved oxygen.

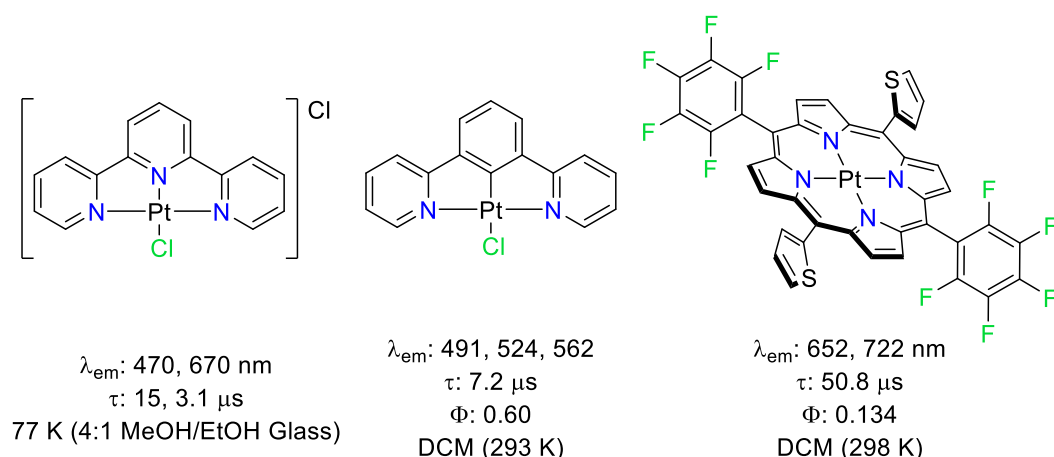


Figure 1.14 – Platinum complexes and their photophysical properties^{90–92}.

Due to the weaker nature of ligand field splitting for Pd(II), the non-emissive metal centred transitions tend to dominate in the solution phase at 298 K⁹³. The $^3\pi-\pi^*$ emissive Pd(II) complex seen in Figure 1.15 was reported by Che *et al* in 2016⁹⁴.

Similarly, gold(III) complexes are also typically not emissive at 298 K in solution, again due to the weaker ligand field splitting favouring the non-emissive metal centred transitions⁹⁵. However, there are examples where the ligand field is strong enough for emission to occur, such as the N-confused metalloporphyrins (Figure 1.15) from the 2008 paper by Furuta *et al*⁹⁶. The complex is dual emissive, with weaker fluorescent peaks being seen at 650 and 707 nm, while the dominant λ_{max} emission is seen at 789 nm.

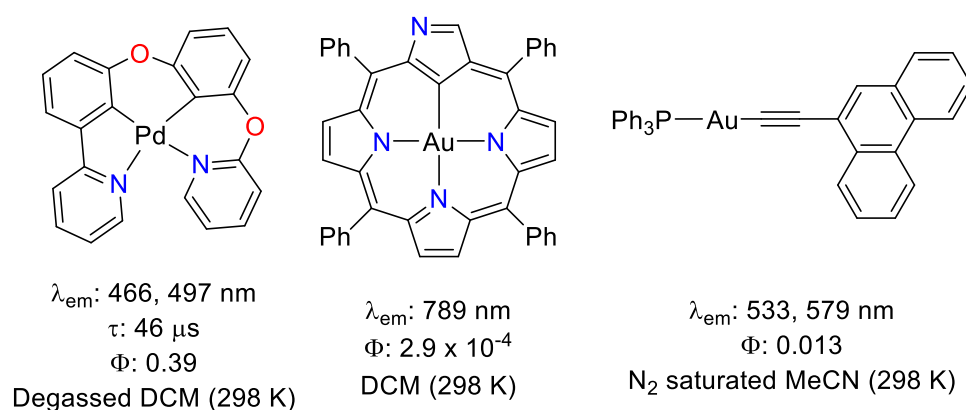


Figure 1.15 – Examples of phosphorescent Pd(II), Au(III) and Au(I) complexes^{94,96,97}.

The d^{10} complexes of gold(I), such as Au(I)-carbenes or thiolate complexes, can be emissive via $^3\text{ILCT}$ ⁹⁸ or $^3\text{LMCT}$ ⁹⁹. For example, in the 2020 publication from

Rodriguez *et al*, Au(I) ethynylphenanthrene complexes, such as the example in Figure 1.15 exhibited differing degrees of ³ILCT emission. Silver d¹⁰ complexes are less studied for their photophysical properties, typically due to the photosensitivity silver complexes exhibit³⁹.

1.4.3 Summary

The versatility of transition metal complexes to exhibit not just fluorescence but also phosphorescence, particularly the second and third row metals in the d⁶ electron configurations, is demonstrated above. The ability for conjugated polyaromatic organic ligands to directly affect the electronic transitions and allow for tuneable emission across the visible and near-IR spectrum is why these molecules have such a strong interest in many different fields of research.

1.5 References

- 1 V. Balzani and S. Campagna, *Photochemistry and Photophysics of Coordination Compounds I*, Springer Berlin Heidelberg Springer e-books, Berlin, Heidelberg, 2007.
- 2 V. Balzani and S. Campagna, *Photochemistry and Photophysics of Coordination Compounds II*, Springer Berlin Heidelberg Springer e-books, Berlin, Heidelberg, 2007.
- 3 C. Wegeberg and O. S. Wenger, *JACS Au*, DOI:10.1021/jacsau.1c00353.
- 4 K. K.-W. Lo, *Acc. Chem. Res.*, 2020, **53**, 32–44.
- 5 Q. Zhao, C. Huang and F. Li, *Chem. Soc. Rev.*, 2011, **40**, 2508–2524.
- 6 X. Zhang, Y. Hou, X. Xiao, X. Chen, M. Hu, X. Geng, Z. Wang and J. Zhao, *Coord. Chem. Rev.*, 2020, **417**, 213371.
- 7 J. Zhao, W. Wu, J. Sun and S. Guo, *Chem. Soc. Rev.*, 2013, **42**, 5323–5351.
- 8 D. M. Arias-Rotondo and J. K. McCusker, *Chem. Soc. Rev.*, 2016, **45**, 5803–5820.
- 9 M. Redrado, A. Benedi, I. Marzo, M. C. Gimeno and V. Fernández-Moreira, *Pharmaceutics*, 2021, **13**, 1382.
- 10 P. B. O'Hara, W. St. Peter and C. Engelson, *J. Chem. Educ.*, 2005, **82**, 49.
- 11 J. R. Lakowicz, *Principles of Fluorescence Spectroscopy*, Springer, New York, 3rd ed., 2006.
- 12 A. Jabłoński, *Z. Für Phys.*, 1935, **94**, 38–46.
- 13 J. Franck and E. G. Dymond, *Trans. Faraday Soc.*, 1926, **21**, 536–542.
- 14 E. Condon, *Phys. Rev.*, 1926, **28**, 1182–1201.
- 15 J. C. Koziar and D. O. Cowan, *Acc. Chem. Res.*, 1978, **11**, 334–341.
- 16 L. Wang, Z. Shang, M. Shi, P. Cao, B. Yang and J. Zou, *RSC Adv.*, 2020, **10**, 11418–11425.
- 17 G. G. Stokes, *Philos. Trans. R. Soc. Lond.*, 1852, **142**, 463–562.
- 18 M. Kasha, *Discuss. Faraday Soc.*, 1950, **9**, 14–19.
- 19 J. C. del Valle and J. Catalán, *Phys. Chem. Chem. Phys.*, 2019, **21**, 10061–10069.
- 20 M. B. Rubin and S. E. Braslavsky, *Photochem. Photobiol. Sci.*, 2010, **9**, 670–674.
- 21 A. Brouwer, *Pure Appl. Chem.*, 2011, **83**, 2213–2228.
- 22 T. Förster, *Ann. Phys.*, 1948, **437**, 55–75.
- 23 R. B. Sekar and A. Periasamy, *J. Cell Biol.*, 2003, **160**, 629–633.
- 24 D. L. Dexter, *J. Chem. Phys.*, 1953, **21**, 836–850.
- 25 A. Monguzzi, R. Tubino and F. Meinardi, *Phys. Rev. B*, 2008, **77**, 155122.
- 26 C. Schweitzer and R. Schmidt, *Chem. Rev.*, 2003, **103**, 1685–1758.
- 27 M. C. DeRosa and R. J. Crutchley, *Coord. Chem. Rev.*, 2002, **233–234**, 351–371.
- 28 J. H. Gutow, *J. Chem. Educ.*, 2005, **82**, 302.
- 29 A. Chmyrov, T. Sandén and J. Widengren, *J. Phys. Chem. B*, 2010, **114**, 11282–11291.
- 30 X.-Q. Guo, F. N. Castellano, L. Li and J. R. Lakowicz, *Biophys. Chem.*, 1998, **71**, 51–62.
- 31 B. B. Collier and M. J. McShane, *J. Lumin.*, 2013, **144**, 180–190.
- 32 L. J. Kricka, *Optical Methods: A Guide to the “-escences,”* Amer. Assoc. for Clinical Chemistry, 2003.

- 33 I. B. Berlman, *Handbook of fluorescence spectra of aromatic molecules*, Academic Press, New York, 2d ed., 1971.
- 34 D. L. Pavia, G. M. Lampman, G. S. Kriz and J. R. Vyvyan, *Introduction to spectroscopy*, Cengage Learning, Stamford, CT, Fifth edition., 2015.
- 35 X. Liu, Z. Xu and J. M. Cole, *J. Phys. Chem. C*, 2013, **117**, 16584–16595.
- 36 X. Wu, J. Xiao, Y. Han, J. Xu, W. Zhou, Y. Li, Y. Fang, Y. Chen, Q. Wu and Y. Song, *RSC Adv.*, 2021, **11**, 15952–15958.
- 37 S. S. Anufrik, S. N. Anuchin and V. V. Tarkovskii, *Opt. Spectrosc.*, 2021, **129**, 93–101.
- 38 N. Yang, S. Song, J. Ren, C. Liu, Z. Li, H. Qi and C. Yu, *ACS Appl. Bio Mater.*, DOI:10.1021/acsabm.1c00289.
- 39 R. C. Evans, P. Douglas and C. J. Winscom, *Coord. Chem. Rev.*, 2006, **250**, 2093–2126.
- 40 X. Han, L.-Z. Wu, G. Si, J. Pan, Q.-Z. Yang, L.-P. Zhang and C.-H. Tung, *Chem. – Eur. J.*, 2007, **13**, 1231–1239.
- 41 K. Li, Y. Chen, J. Wang and C. Yang, *Coord. Chem. Rev.*, 2021, **433**, 213755.
- 42 Y. Y. Chia and M. G. Tay, *Dalton Trans.*, 2014, **43**, 13159–13168.
- 43 D. S. M. Ravinson and M. E. Thompson, *Mater. Horiz.*, 2020, **7**, 1210–1217.
- 44 Z. A. Siddique, Y. Yamamoto, T. Ohno and K. Nozaki, *Inorg. Chem.*, 2003, **42**, 6366–6378.
- 45 A. Steffen, M. G. Tay, A. S. Batsanov, J. A. K. Howard, A. Beeby, K. Q. Vuong, X.-Z. Sun, M. W. George and T. B. Marder, *Angew. Chem. Int. Ed.*, 2010, **49**, 2349–2353.
- 46 W. Lu, N. Zhu and C.-M. Che, *J. Organomet. Chem.*, 2003, **670**, 11–16.
- 47 A. Cannizzo, F. van Mourik, W. Gawelda, G. Zgrablic, C. Bressler and M. Chergui, *Angew. Chem. Int. Ed.*, 2006, **45**, 3174–3176.
- 48 G. J. Hedley, A. Ruseckas and I. D. W. Samuel, *Chem. Phys. Lett.*, 2008, **450**, 292–296.
- 49 A. C. Bhasikuttan, M. Suzuki, S. Nakashima and T. Okada, *J. Am. Chem. Soc.*, 2002, **124**, 8398–8405.
- 50 G. S. M. Tong, P. K. Chow and C.-M. Che, *Angew. Chem. Int. Ed.*, 2010, **49**, 9206–9209.
- 51 A. Vogler and H. Kunkely, in *Transition Metal and Rare Earth Compounds: Excited States, Transitions, Interactions I*, ed. H. Yersin, Springer, Berlin, Heidelberg, 2001, pp. 143–182.
- 52 A. Vogler, *Inorg. Chem. Commun.*, 2016, **67**, 32–34.
- 53 A. Vogler, *Inorg. Chem. Commun.*, 2016, **65**, 39–40.
- 54 M. Dorn, J. Kalmbach, P. Boden, A. Pöpcke, S. Gómez, C. Förster, F. Kuczelinis, L. M. Carrella, L. A. Büldt, N. H. Bings, E. Rentschler, S. Lochbrunner, L. González, M. Gerhards, M. Seitz and K. Heinze, *J. Am. Chem. Soc.*, 2020, **142**, 7947–7955.
- 55 A. D. Kirk and G. B. Porter, *J. Phys. Chem.*, 1980, **84**, 887–891.
- 56 A. J. Schuman, S. F. T. Robey, E. C. Judkins, M. Zeller and T. Ren, *Dalton Trans.*, 2021, **50**, 4936–4943.
- 57 R. A. Rader, D. R. McMillin, M. T. Buckner, T. G. Matthews, D. J. Casadonte, R. K. Lengel, S. B. Whittaker, L. M. Darmon and F. E. Lytle, *J. Am. Chem. Soc.*, 1981, **103**, 5906–5912.
- 58 A. Juris and R. Ziessel, *Inorganica Chim. Acta*, 1994, **225**, 251–254.
- 59 X. Zhang, Z. Wu, J.-Y. Xu, W.-X. Li and X.-L. Li, *Polyhedron*, 2021, **202**, 115197.
- 60 A. W. Adamson and J. N. Demas, *J. Am. Chem. Soc.*, 1971, **93**, 1800–1801.
- 61 V. W.-W. Yam and K. M.-C. Wong, *Chem. Commun.*, 2011, **47**, 11579–11592.

- 62 A. J. Amoroso, R. J. Arthur, M. P. Coogan, J. B. Court, V. Fernández-Moreira, A. J. Hayes, D. Lloyd, C. Millet and S. J. A. Pope, *New J. Chem.*, 2008, **32**, 1097–1102.
- 63 M. Frank, L. Jürgensen, J. Leduc, D. Stadler, D. Graf, I. Gessner, F. Zajusch, T. Fischer, M.-A. Rose, D. N. Mueller and S. Mathur, *Inorg. Chem.*, 2019, **58**, 10408–10416.
- 64 J. Zhao, N. Liu, S. Sun, S. Gou, X. Wang, Z. Wang, X. Li and W. Zhang, *J. Inorg. Biochem.*, 2019, **196**, 110684.
- 65 R. Caspar, C. Cordier, J. B. Waern, C. Guyard-Duhayon, M. Gruselle, P. Le Floch and H. Amouri, *Inorg. Chem.*, 2006, **45**, 4071–4078.
- 66 T. Yang, A. Xia, Q. Liu, M. Shi, H. Wu, L. Xiong, C. Huang and F. Li, *J. Mater. Chem.*, 2011, **21**, 5360–5367.
- 67 M. Maestri, D. Sandrini, V. Balzani, U. Maeder and A. Von Zelewsky, *Inorg. Chem.*, 1987, **26**, 1323–1327.
- 68 Z. Hao, K. Zhang, P. Wang, X. Lu, Z. Lu, W. Zhu and Y. Liu, *Inorg. Chem.*, 2020, **59**, 332–342.
- 69 R. Bai, X. Meng, X. Wang and L. He, *Adv. Funct. Mater.*, 2020, 1907169.
- 70 K. Kalyanasundaram, *Coord. Chem. Rev.*, 1982, **46**, 159–244.
- 71 B.-Z. Shan, Q. Zhao, N. Goswami, D. M. Eichhorn* and D. P. Rillema*, *Coord. Chem. Rev.*, 2001, **211**, 117–144.
- 72 S. Hennessey, P. Farràs, J. Benet-Buchholz and A. Llobet, *Catal. Sci. Technol.*, 2019, **9**, 6760–6768.
- 73 M. R. Gill and J. A. Thomas, *Chem. Soc. Rev.*, 2012, **41**, 3179–3192.
- 74 S. Monro, K. L. Colón, H. Yin, J. Roque, P. Konda, S. Gujar, R. P. Thummel, L. Lilge, C. G. Cameron and S. A. McFarland, *Chem. Rev.*, 2019, **119**, 797–828.
- 75 M. R. Gill, S. N. Harun, S. Halder, R. A. Boghozian, K. Ramadan, H. Ahmad and K. A. Vallis, *Sci. Rep.*, 2016, **6**, 31973.
- 76 E. Cuéllar, A. Diez-Varga, T. Torroba, P. Domingo-Legarda, J. Alemán, S. Cabrera, J. M. Martín-Alvarez, D. Miguel and F. Villafañe, *Inorg. Chem.*, 2021, **60**, 7008–7022.
- 77 *Inorganica Chim. Acta*, 1996, **242**, 281–291.
- 78 K. L. Smitten, P. A. Scattergood, C. Kiker, J. A. Thomas and P. I. P. Elliott, *Chem. Sci.*, 2020, **11**, 8928–8935.
- 79 C. Ge, J. Zhu, A. Ouyang, N. Lu, Y. Wang, Q. Zhang and P. Zhang, *Inorg. Chem. Front.*, 2020, **7**, 4020–4027.
- 80 J. C. Deaton and F. N. Castellano, in *Iridium(III) in Optoelectronic and Photonics Applications*, John Wiley & Sons, Ltd, 2017, pp. 1–69.
- 81 M. G. Colombo, A. Hauser and H. U. Guedel, *Inorg. Chem.*, 1993, **32**, 3088–3092.
- 82 M. G. Colombo, T. C. Brunold, T. Riedener, H. U. Guedel, M. Fortsch and H.-B. Büergi, *Inorg. Chem.*, 1994, **33**, 545–550.
- 83 G. Calogero, G. Giuffrida, S. Serroni, V. Ricevuto and S. Campagna, *Inorg. Chem.*, 1995, **34**, 541–545.
- 84 V. W.-W. Yam and A. S.-Y. Law, *Coord. Chem. Rev.*, 2020, **414**, 213298.
- 85 J. W. Facendola, M. Seifrid, J. Siegel, P. I. Djurovich and M. E. Thompson, *Dalton Trans.*, 2015, **44**, 8456–8466.
- 86 M. Velusamy, C.-H. Chen, Y. S. Wen, J. T. Lin, C.-C. Lin, C.-H. Lai and P.-T. Chou, *Organometallics*, 2010, **29**, 3912–3921.
- 87 Q.-Z. Yang, L.-Z. Wu, Z.-X. Wu, L.-P. Zhang and C.-H. Tung, *Inorg. Chem.*, 2002, **41**, 5653–5655.

- 88 R. Ballardini, G. Varani, M. T. Indelli and F. Scandola, *Inorg. Chem.*, 1986, **25**, 3858–3865.
- 89 D. Sandrini, M. Maestri, V. Balzani, L. Chassot and A. Von Zelewsky, *J. Am. Chem. Soc.*, 1987, **109**, 7720–7724.
- 90 G. Arena, G. Calogero, S. Campagna, L. Monsù Scolaro, V. Ricevuto and R. Romeo, *Inorg. Chem.*, 1998, **37**, 2763–2769.
- 91 J. A. G. Williams, A. Beeby, E. S. Davies, J. A. Weinstein and C. Wilson, *Inorg. Chem.*, 2003, **42**, 8609–8611.
- 92 M. Manathanath, M. Xie, C. Arunkumar, Z. Wang, J. Zhao and S. Sujatha, *Dyes Pigments*, 2019, **165**, 117–127.
- 93 M. Krause, R. von der Stück, D. Brünink, S. Buss, N. L. Doltsinis, C. A. Strassert and A. Klein, *Inorganica Chim. Acta*, 2021, **518**, 120093.
- 94 P.-K. Chow, G. Cheng, G. S. Ming Tong, C. Ma, W.-M. Kwok, W.-H. Ang, C. Yik-Sham Chung, C. Yang, F. Wang and C.-M. Che, *Chem. Sci.*, 2016, **7**, 6083–6098.
- 95 C. Bronner and O. S. Wenger, *Dalton Trans.*, 2011, **40**, 12409–12420.
- 96 M. Toganoh, T. Niino and H. Furuta, *Chem. Commun.*, 2008, 4070–4072.
- 97 A. de Aquino, F. J. Caparrós, G. Aullón, J. S. Ward, K. Rissanen, Y. Jung, H. Choi, J. C. Lima and L. Rodríguez, *Chem. – Eur. J.*, 2021, **27**, 1810–1820.
- 98 H. M. J. Wang, C. Y. L. Chen and I. J. B. Lin, *Organometallics*, 1999, **18**, 1216–1223.
- 99 J. M. Forward, D. Bohmann, J. P. Fackler and R. J. Staples, *Inorg. Chem.*, 1995, **34**, 6330–6336.

**Chapter 2 - Iridium(III) Complexes of
Substituted Phenyl-Quinoxalines.**

2.1 Introduction

2.1.1 Cyclometalated iridium complexes.

Phosphorescent metal complexes have a variety of uses, from imaging agents^{1,2}, OLEDs³ (Organic Light Emitting Diodes) and LEECs⁴ (Light Emitting Electrochemical Cells). Early research into these areas focussed on the use of d^6 , d^8 , and d^{10} metals from the second and third row. These configurations display strong spin-orbit coupling interactions which lead to effective ISC and mixing of singlet and triplet excited states, as well as a stronger ligand field splitting in comparison to their first row counterparts. As a product of this, heavy metal complexes often have a strong emission band and long lifetimes⁵. In recent years, iridium has attracted great interest as a viable metal for such applications. Iridium is a group 9 transition metal and has an electronic configuration $[\text{Xe}]4f^{14}5d^76s^2$ and atomic number 77. It is commonly found in iridium(I) and iridium(III) oxidation states. This work focuses upon the use of the +3 oxidation state where the $5d^6$ configuration commonly yields octahedral and hexacoordinate complexes. When compared to other viable metal complexes, iridium(III) offers improved stability, a larger range of emission character, which can be tuned selectively as well as desirable characteristics, such as μs lifetimes and high quantum efficiency⁶⁻⁹.

2.1.1.1 Structure, synthesis and emission tuneability.

Iridium(III) cyclometalated complexes can exist as either *bis*-cyclometalated heteroleptic complexes or *tris*-cyclometalated homoleptic or heteroleptic complexes (Figure 2.5). Both synthetic routes start following the Nonoyama synthesis for bridged chloro-iridium dimers¹⁰ $[\text{Ir}(\text{N}^{\wedge}\text{C})_2(\mu\text{-Cl})]_2$. (Figure 2.1)

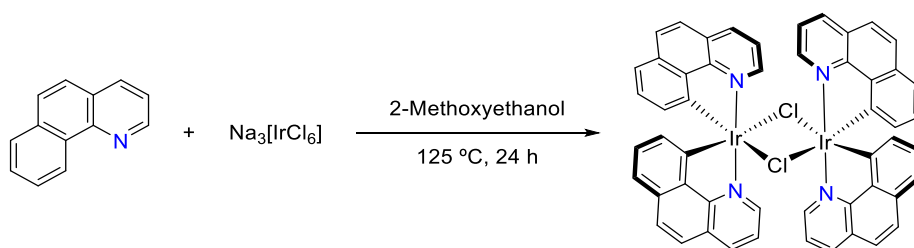


Figure 2.1 – Nonoyama’s synthesis of Benzo[h]quinoline-10-yl-N iridium dimer¹⁰.

Iridium(III) chloride (either as $\text{Na}_3[\text{IrCl}_6]$ or $\text{IrCl}_3 \cdot x\text{H}_2\text{O}$) is heated in a high boiling point solvent with two equivalents of the cyclometalating ligand ($\text{H-C}^{\wedge}\text{N}$). Complexes of low spin d^6 metals, such as iridium(III), are kinetically inert¹¹. Because of this, the use of a high boiling point solvent is required, such as 2-methoxyethanol or ethylene glycol.

The dimer can then be split to form the desired complex. Homoleptic complexes can be synthesised by heating the $[\text{Ir}(\text{N}^{\wedge}\text{C})_2(\mu\text{-Cl})]_2$ with $\text{H-C}^{\wedge}\text{N}$. Thermodynamic control of this process leads to either the *mer*-isomer (100 °C) or the *fac*-isomer (>200 °C), where typically the *fac*-isomer have a greater quantum efficiency and longer emissive lifetimes¹². *Tris*-cyclometalated complexes can also be made with a second cyclometalating ligand ($\text{H-C}^{\wedge}\text{N}'$) to yield $[\text{Ir}(\text{C}^{\wedge}\text{N})_2(\text{C}^{\wedge}\text{N}')]$, allowing small degrees of tunability over the emission wavelength.

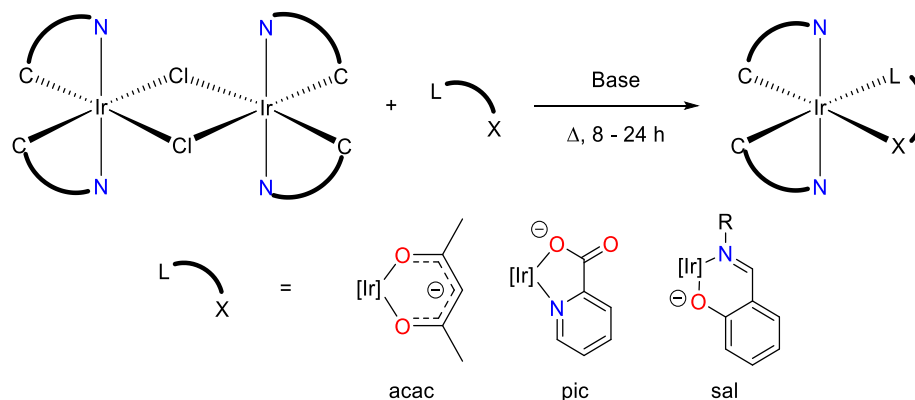


Figure 2.2 -Formation of neutral Ir(III) complexes from $[\text{Ir}(\text{N}^{\wedge}\text{C})_2(\mu\text{-Cl})]_2$ and two equivalents of $\text{L}^{\wedge}\text{X}$. Some forms of $\text{L}^{\wedge}\text{X}$ are shown below.

Heteroleptic complexes can be formed as either neutral or cationic complexes. Neutral *bis*-cyclometalated complexes are split by a monoanionic ancillary ligand, such as β -diketonates, picolinate, N-alkylsalicyliminate or a derivative of these¹³ (Figure 2.2). $[\text{Ir}(\text{N}^{\wedge}\text{C})_2(\mu\text{-Cl})]_2$ is then heated with two equivalents of the $\text{L}^{\wedge}\text{X}$ ancillary ligand in a solvent such as methanol or chloroform. Base can be added to help facilitate the deprotonation steps.

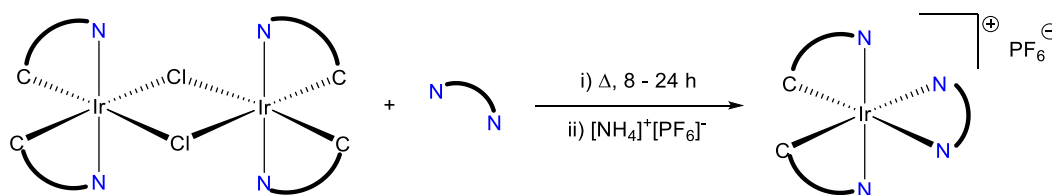


Figure 2.3 – General procedure for splitting iridium dimers to form a cationic complex.

Conversely, a cationic iridium complex typically involves a diimine based $\text{N}^{\wedge}\text{N}$ type donor, such as bpy, phen or their derivatives. Typically, $[\text{Ir}(\text{N}^{\wedge}\text{C})_2(\mu\text{-Cl})]_2$ dimer is split by heating with the $\text{N}^{\wedge}\text{N}$ ligand in a solvent such as methanol or chloroform (Figure 2.3). While in solution, a counterion exchange can take place. Typically

hexfluorophosphate salts $[X][PF_6]$ are chosen, but there is also a wide range of anions used, including, but not limited to, BF_4^- , Cl^- , $CF_3CO_2^-$ or BPh_4^- .^{2,14–16} Complexes can then be purified by chromatography, or recrystallisation.

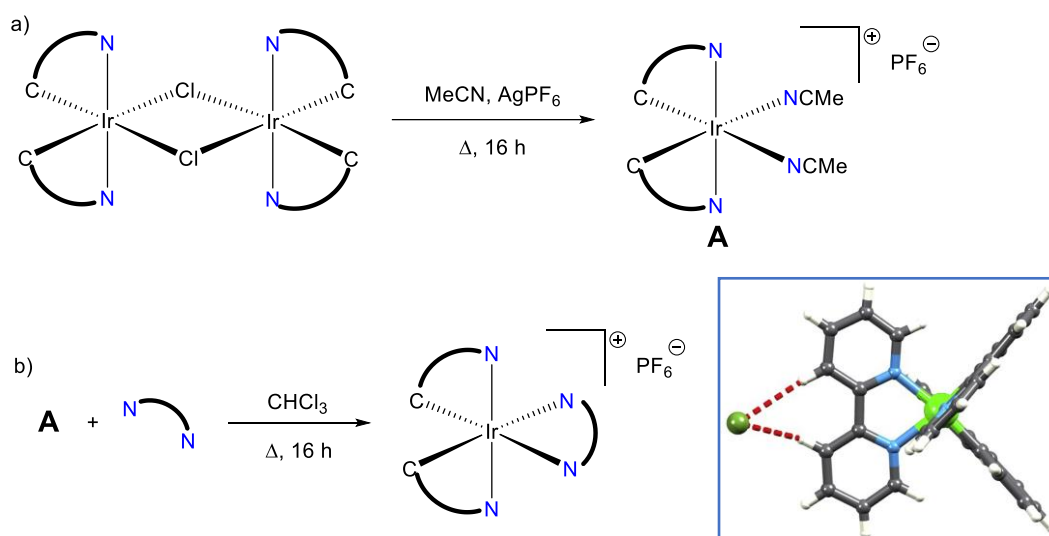


Figure 2.4 – a) Using a silver salt to abstract chlorides. b) substitution of the weakly coordinated solvent ligands in a *bis*-MeCN complex. Insert – Tight ion pairing seen by Schneider *et al* in $2\{[Ir(ppy)_2(bpy)][Cl]\} \cdot 2CH_2Cl_2 \cdot [H_3O] \cdot [Cl]$ ¹⁷ and confirmed by single crystal diffraction. Image taken from Housecroft and Constable¹⁸.

In 2013, Schneider *et al* noted that the route followed in Figure 2.3 is able to carry through a small amount of Cl^- anions. If Cl^- anions are present in the active layer of an LEEC device, they can drastically reduce performance. Crystal structure revealed a tight ion pairing between the protons on the bipyridine C-3 position and the Cl^- forming $2\{[Ir(ppy)_2(bpy)][Cl]\} \cdot 2CH_2Cl_2 \cdot [H_3O] \cdot [Cl]$ ¹⁷ (insert - Figure 2.4). To prevent this, the use of a silver salt to abstract the chlorides and form a solvent complex can be employed. This was first used by Watts *et al*¹⁹. Chlorides are precipitated as AgCl and can then be filtered to remove them from the reaction mixture. The coordinating solvent, such as MeCN or MeOH, can then be substituted by the ancillary ligand of choice by heating in chloroform overnight (Figure 2.4).

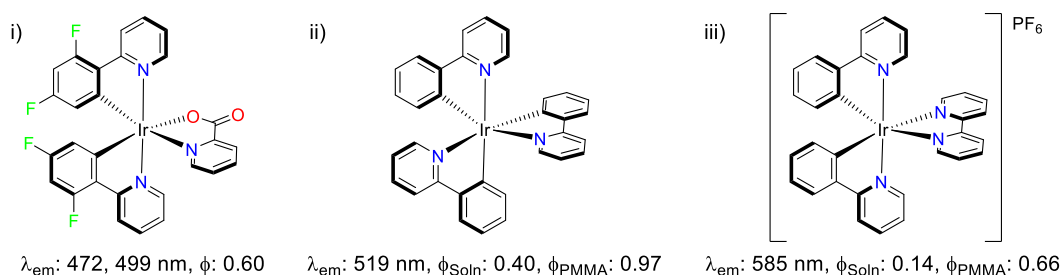


Figure 2.5 – The emission tuneability of Ir(III) come from the choice of ligands around the coordination sphere. Examples of three such complexes are seen above. i) Neutral heteroleptic blue^{20,21}, ii) homoleptic green emitter^{22,23} and iii) an orange emitting cationic complex^{24,25}.

Iridium(III) complexes can be synthesised to exhibit emission across the visible range – with some examples shown in Figure 2.5. This tuneability comes from the frontier orbitals and excited states comprising of MLCT and LC $\pi-\pi^*$ states, as opposed to the forbidden $d-d^*$ transitions. Typically, the HOMO is found to contain a mixture of Ir 5d orbitals and the π orbitals from one of the ligands. Conversely, the LUMO is normally found to be located around the π^* orbitals of another ligand²⁶. If the HOMO and LUMO character is located upon separate ligands, then the excited state may consist of mixed MLCT and LLCT^{27,28}.

The energy levels of the frontier orbitals, and therefore the absorption and emission wavelengths, can be tuned with the use of electron withdrawing or electron donating substituents on different parts of the molecule. For example, a hypsochromic shift is typically induced by using a 2,4-difluorophenylpyridine cyclometalating ligand, lowering the energy of the HOMO. Perhaps the most famous example of this is the 2001 example from Thompson and Forrest *et al* with iridium(III) bis(4,6-(di-fluorophenyl)-pyridinato-N,C2') picolinate²⁰, where the use of the difluorophenylpyridine ligand induced an emission blue shift to a λ_{max} of ca.470 nm.

A bathochromic shift is usually brought about by stabilising the LUMO energy level. Normally this is achieved via the use of extended conjugation upon either the N-Donor parts of the cyclometalating ligands or on the ancillary ligand^{16,29}.

2.1.2 Photonic applications for cationic iridium(III) complexes

The phosphorescent emission of iridium(III) complexes, brought about by the heavy metal centre and strong spin-orbit coupling, gives rise to excited state lifetimes that are relatively long compared to organic fluorophores, but short when

compared to typical phosphorescent lifetimes. The different cyclometalating ligands allow for the emission colour to be tuned to every colour of the visible spectrum. This property makes iridium(III) complexes desirable for a number of applications³⁰.

2.1.2.1 Phosphorescent Organic Light Emitting Diodes (PhOLEDs) and Light Emitting Electrochemical Cells (LEECs)

OLED technology is widely used to create digital displays, such as televisions, computer monitors or smart phone displays. Originally, OLEDs contained singlet emissive organic fluorophores. However, using quantum mechanical calculations, the ratio between singlet and triplet excited states is believed to be around 1:3. Therefore in a fluorescent emissive device, 75 % of all excited states are triplet in nature and decay via non-radiative means. This leads to a maximum quantum efficiency of only 25 %^{31,32}. To counteract this loss in efficiency, the use of triplet emissive phosphorescent complexes have been used instead, either via direct triplet excitation or ISC routes. Theoretically, the quantum efficiency of such devices is 100 %^{33–35} and hence Phosphorescent Organic Light Emitting Diodes (PhOLEDs) came to fruition.

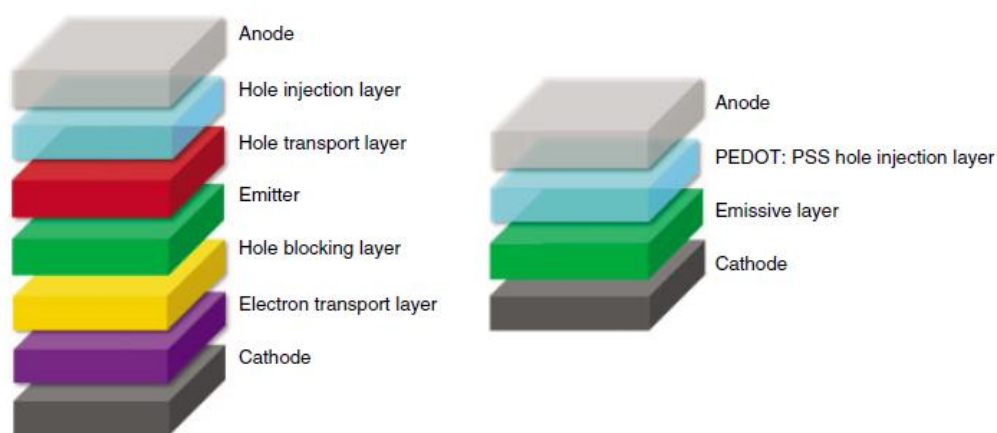


Figure 2.6 – General scheme by Henwood and Zysman-Colman³⁶ for the architecture seen in OLED (Left) and LEEC (Right). PEDOT – poly(3,4-ethylenedioxythiophene), PSS – Poly(styrenesulfonate).

Whilst the theory and physical design for OLEDs and LEECs is similar (Figure 2.6), PhOLEDs utilise an emissive layer based around neutral complexes, such as *tris*-cyclometalated iridium(III) or a *bis*-cyclometalated iridium(III) complex with a charged ancillary ligand, such as acac, while LEECs will utilise a neutral ancillary in a cationic complex^{18,37}. Though early device used a single emissive layer between an aluminium cathode and indium tin oxide (ITO) anode³⁸, later devices include a hole injecting layer consisting of poly(3,4-ethylenedioxythiophene)

(PEDOT) and poly(styrenesulfonate) (PSS). The use of an ionic liquid dopant in the emissive layer, typically [BMIM][PF₆] (1-butyl-3-methylimidazolium hexafluorophosphate), increases the charge separation and operating efficiency of the devices^{39,40}.

The archetypal literature iridium(III) LEEC device is perhaps the simplest, [Ir(ppy)₂(bpy)]PF₆²⁵ (See Figure 2.5 – iii). In photoluminescent studies, the λ_{em} in both deaerated MeCN solution and a poly(methyl methacrylate) film (PMMA) was 585 nm. Photoluminescent Quantum Yield (PLQY, Φ_{PL}) was 14 % in deaerated MeCN, which rose to 66 % in thin film. An increase in Φ_{PL} when comparing solution phase to thin film is expected. Work by Teets *et al* in 2018 on a series of 12 heteroleptic cyclometalated iridium(III) complexes, both cationic and neutral, showed a dramatic increase in Φ_{PL} in PMMA in each case⁴¹.

Since the complexes were immobilised in a polymer, removing degrees of freedom, then the decrease in k_{nr} is expected, but they also observed an increase in k_r upon immobilisation, and suggested that this phenomenon is linked with an increase in excited-state spin-orbit coupling, which has been noted previously⁴².

Perhaps the ‘holy grail’ of LEEC research would be a single component white light emitting device, but this is very difficult due to very broad emission wavelengths needed. Nevertheless, two component emitters show potential⁴³. A two-component emitter mixes a blue and an orange – red component to produce emission across the visible range, appearing white. Since [Ir(ppy)₂(bpy)]⁺ is an efficient orange emitter, the literature has predominantly focused on the development of blue emitters⁴⁴ by lowering the energy of the HOMO; typically via fluorination. Generally, red emitters tend to focus on extending the conjugation around the N^N ligand, however one of the best performing red emissive LEECs has come from research into yellow devices. Monkman *et al* synthesised devices using an 1,3,4-oxadiazole motif⁴⁵. When a 2-(pyrid-2-yl)-1,3,4-oxadiazole was used as the N^N ancillary with ppy cyclometalating ligands (Figure 2.7), emission shifted from λ_{PL} = 556 nm in a DCM solution to λ_{EL} = 624 nm as an LEEC, with an external quantum efficiency (EQE) of 9.5 %, one of the highest reported for red devices. Solid state structures revealed intermolecular π - π^* interactions between the neighbouring N^N pyridines with centroid distances of 3.62 Å, likely resulting in excimers, bringing about a bathochromic shift in emission⁴⁶.

To compare the results of extending the N^N conjugation, Thompson *et al* synthesised a series of complexes based around the 1-phenylpyrazole (ppz) cyclometalating ligand⁴⁷. Since the ³LC state can occur on either the C^N or N^N ligands, and ppy and bpy share similar ³ π - π^* transitions at 430 nm and 436 nm respectively⁴⁸, the choice of ppz (³ π - π^* = 380 nm) here was intentional to remove the ambiguity. [Ir(ppz)₂(bpy)]PF₆ (see Figure 2.7 –(A)) is a yellow green emitting complex, with a λ_{PL} = 563 nm (MeCN). Substituting bpy with 2,2'-biquinoline (biq) (see Figure 2.7 –(B)) induces a bathochromic shift to produce an orange emission at λ_{PL} = 616 nm (MeCN). This can be tuned further with the use of ^tBu groups in the 5' position of the cyclometalating ligands (see Figure 2.7 –(C)). The emission has now shifted to λ_{PL} = 627 nm (MeCN), and when LEEC are manufactured from this complex, λ_{EL} = 635 nm with an EQE of 7.4 %.

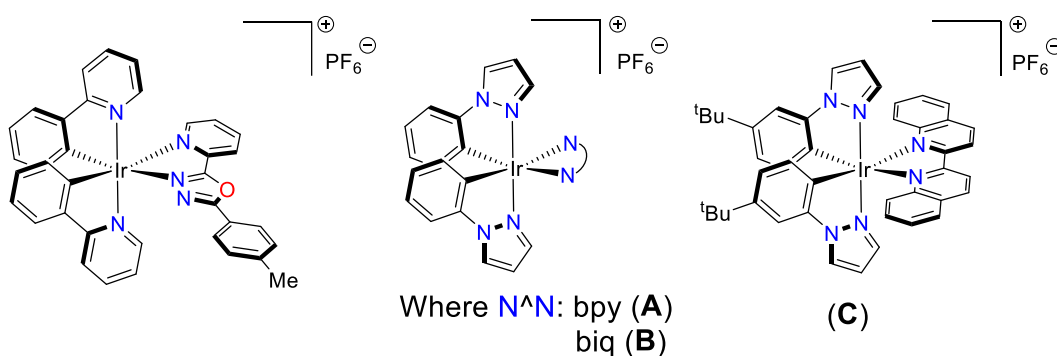


Figure 2.7 – Left: Structure of the red emitting layer for LEEC applications from Monkman *et al*⁴⁵. Middle + right: (A) + (B) Structure of ppz complexes synthesised by Thompson *et al*. (C) red emitting Ir(III) complex tested by Thompson *et al* in LEEC devices⁴⁷.

2.1.2.2 Biological cell probes, sensors and photodynamic therapy.

Once again, for cell imaging, the tuneability of iridium(III) complex emission is greatly utilised. The ability to add a variety of functional groups and moieties to ligands without negatively affecting the emission properties means iridium(III) complexes have seen a variety of potential use. By altering the functional groups on ligands, complex can probe specific ions^{49,50} or organelle⁵¹ within the cell environment. Iridium(III) complexes tend to also be sensitive to oxygen quenching, meaning they can be designed as hypoxia sensors⁵² or to generate reactive oxygen species for photo induced cytotoxicity in PDT⁵³.

One draw-back to using organic imaging agents is the short lifetimes of fluorescence. Autofluorescence from within the cell itself can mask the signals of the imaging agent, but due to the heavy atom effect inducing intersystem crossing and triplet emission, the lifetime of iridium(III) complexes tends to be in the

microsecond domain, therefore allowing the use of time gated or time resolved spectroscopies and optical microscopy techniques negating any autofluorescence⁵⁴.

In 2010, Li *et al* synthesised a series of complexes based upon the *bis*-cyclometalated 2-(2,4-difluorophenyl)pyridine ligand system⁵⁵. By varying the ancillary ligand conjugation (See complexes in Figure 2.8) from *bis*-pyridines up towards 2-(2-quinolinyl)quinoxaline they were able to bathochromically shift the emission of the complex from blue through to red emission. When HeLa cells were treated with 20 μM solutions in DMSO/PBS (pH 7, 1/49, v/v) for 10 min at 25 $^{\circ}\text{C}$, intense emission was detected upon optical microscopy techniques within the cytoplasm and not in the cell membrane or nucleus, with no signs of cytotoxicity. (See Figure 2.8 for microscopy images)

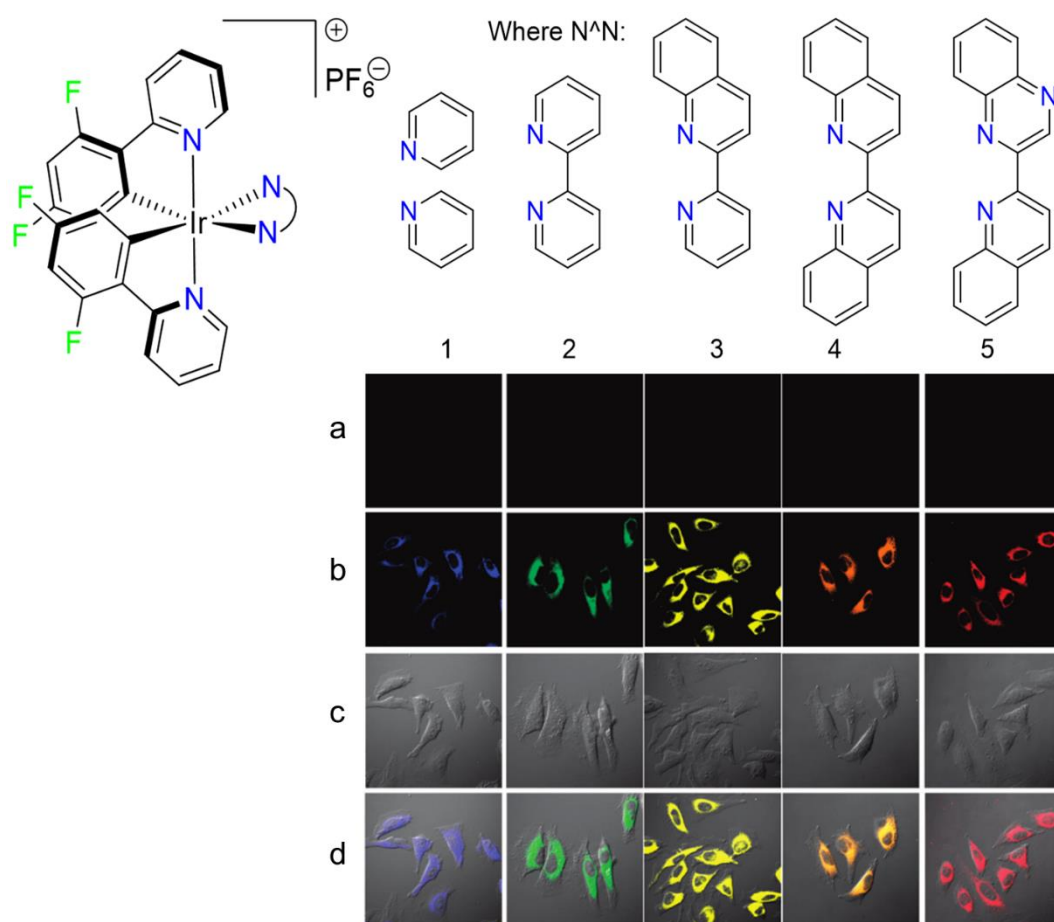


Figure 2.8 – Above – Iridium(III) complexes synthesised by Li *et al.*⁵⁵ Below: Confocal microscopy images of a) HeLa cells untreated, b) Same cells incubated with 20 μM solutions in DMSO/PBS (pH 7, 1/49, v/v) for 10 min at 25 $^{\circ}\text{C}$. c) Differential Interference

Contrast (DIC) images of b). d) Overlaid confocal and DIC microscopy showing iridium complex located in the cytoplasm of the cells.

Further functionalisation of the ligands allows for much more selectivity, such as chemodosimeter sensors. In 2014, Lu and Nabeshima synthesised a sensor for detection of HOCl in the aqueous environment⁵⁶ (See Figure 2.9). Hypochlorous acid is a natural biproduct of cellular metabolism, but a build-up may result in tissue damage. By adding an electron rich *o*-nitroaniline group to the ancillary ligand, the group were able to quench the luminescent properties of the complex via photoinduced electron transfer (PET) effects. Nitroaniline is known to undergo oxidative cleavage in the presence of HOCl, thereby removing the PET effects and creating a luminescent signal. Indeed, the complex worked as expected, and was able to be selective for HOCl compared to other reactive oxygen and reactive nitrogen species.

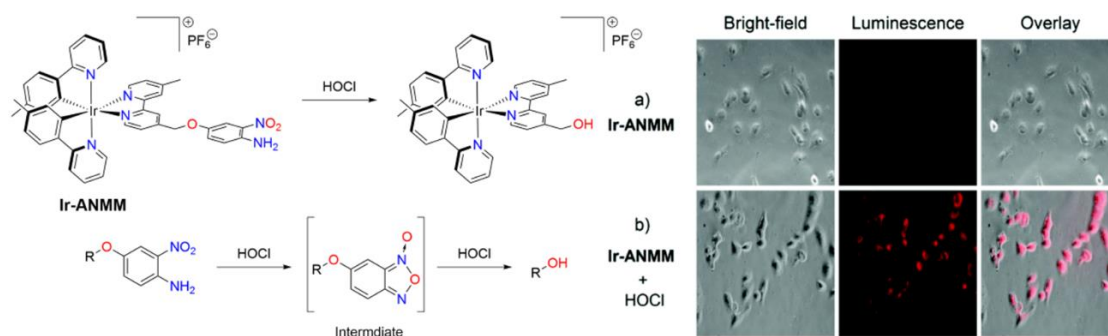


Figure 2.9 – Left Top - Complex used for chemodosimeter detection of HOCl by Lu and Nabeshima⁵⁶ showing non-emissive Ir-ANMM state and the emissive cleaved complex. Left lower – reaction between *o*-nitroaniline and HOCl. Right: Confocal microscopy images of HeLa Cells (a) incubated with 20 μ M Ir-ANMM and (b) Ir-ANMM cells treated with 50 μ M HOCl.

To obtain a stain located within the nucleus, Huang *et al* used a known DNA intercalator (tetrapyrido phenazine – tpphz) as the ancillary ligand⁵⁷ (Figure 2.10). The extended conjugation of the tpphz bathochromically shifts the emission, and as such the complex displays a λ_{em} of 597 nm in DCM, with TD-DFT calculations supporting the hypothesis of ³MLCT ($d\pi(Ir) \rightarrow \pi^*(tpphz)$) dominating the emission. Iridium(III) complexes are known to undergo quenching via interactions with molecular oxygen. This interaction is known to lower the lifetime and quantum yield of the complexes⁵⁸. This allows for the complex to be used to measure oxygen level in the cell nuclei. The study found that when oxygen levels dropped from 21 % to 2.5 % the emission intensity increased by 1.3 times and using Phosphorescent Lifetime Imaging (PLIM) they showed the average lifetime rose from 123 ns to 145 ns.

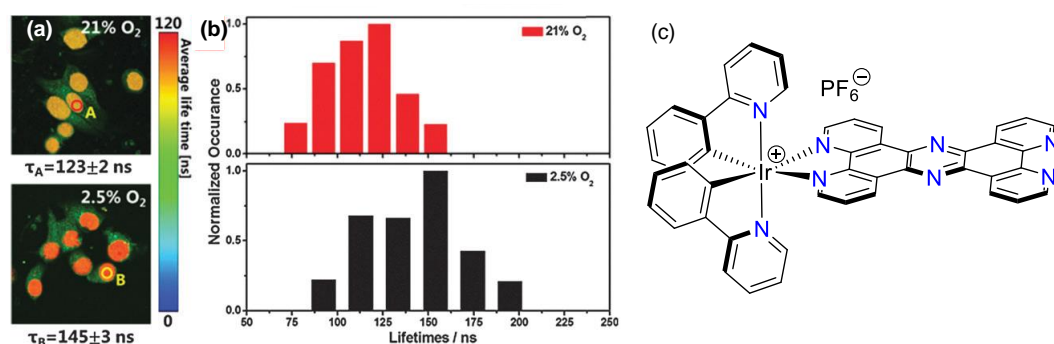


Figure 2.10 – (a) Huang *et al*⁵⁷ PLIM images with HepG 2 cells incubated with iridium(III) complex (10 μ M, λ_{ex} 405 nm) in different oxygen levels. (b) The average lifetime distributions from PLIM. (c) Complex with intercalating ancillary ligand.

The interaction with molecular oxygen can also be used to generate Reactive Oxygen Species (ROS), either as 1O_2 or radicals such as superoxide ($O_2^{\cdot-}$), hyperperoxyl (HO_2^{\cdot}) or hydroxyl (OH^{\cdot}) This process allows for the potential for the integration of diagnostic and therapeutic strategies in the battle against cancers. The generation of ROS is a complex process which can be split into two categories – Type I and Type II. Type I involves a PET process to biological substrates, generating radicals. Type II is the direct energy transfer from the excited state donor to 3O_2 generating 1O_2 species – see Figure 2.11 – Left. The generation of *in situ* ROS causes cell apoptosis or necrosis and is the basis for PDT.

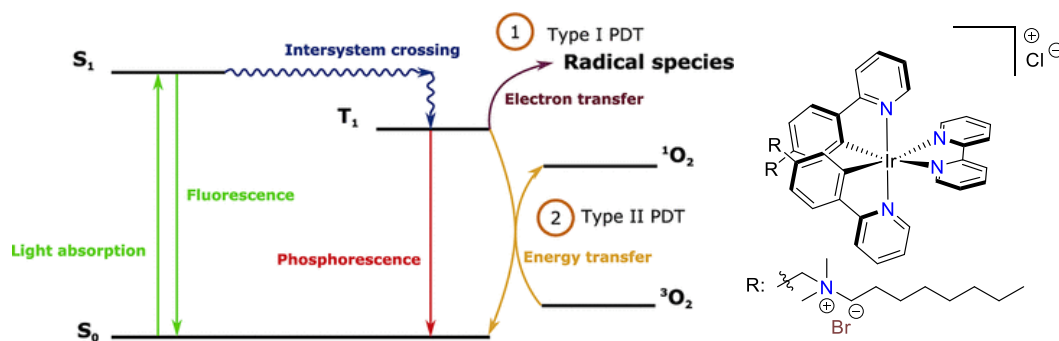


Figure 2.11 – Left: A simplified Jablonski diagram from the work of Elias *et al* summarising the generation of ROS.⁵⁹ Right: PDT Agent trailed *in vivo* by Hou *et al*.⁶⁰

In 2019, Hou *et al* published results based around a complex modified with a quaternary ammonium group⁶⁰ as a type II PDT agent. The resultant amphiphilic gemini complexes exhibited high water solubility, and self-assembly to form vesicles, as well as a good interaction with the cell membranes, due to the charge quaternary ammonium groups. The group altered the position of the ammonium functionalisation, either functionalising the ppy ligands in the 4-phenyl position

(Figure 2.11 - Right) or the bpy ligands, in the 4,4'- positions. From a photophysical viewpoint, this provides some interesting properties. If the C^N ligand is functionalised, then $\lambda_{em}(\text{H}_2\text{O}) = 540 \text{ nm}$, compared to $\lambda_{em}(\text{H}_2\text{O}) 645 - 664 \text{ nm}$ for the N^N functionalised examples. This functionalisation also affected the vesicles formation, creating 2 different forms. The N^N functionalised red vesicles displayed aggregation-based emission quenching. *In vitro* studies suggest the complex localises in the mitochondria and displays excellent PDT activity. *In vivo* studies involving an intratumoral injection in mice followed by a period of 20 minutes irradiation showed that after 14 days the tumours were severely damage and had reduced cell density, as well as being significantly smaller (~0.25 g vs ~1.25 g) when compared to control groups.

2.1.3 Quinoxalines

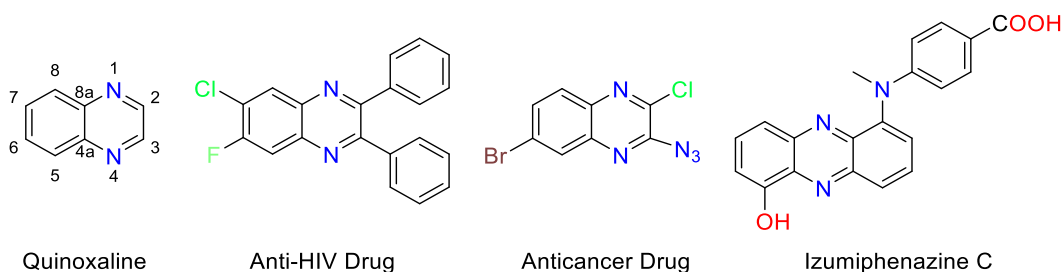


Figure 2.12 – The bicyclic heterocyclic quinoxaline and some examples of the quinoxaline motif in use against HIV⁶¹, anticancer⁶² and the isolate natural product, izumiphenazine C⁶³.

Quinoxaline is a bicyclic heterocycle, containing two imine groups in a 1,4- configuration. (Figure 2.12). It is an important group in medicinal chemistry, where compounds are used for their activity as antibiotic⁶⁴, anticancer⁶⁵, antiviral, anti-inflammatory⁶⁶ and antimicrobial^{67,68} agents. In addition to the medicinal chemistry, quinoxalines are also used as dyes⁶⁹⁻⁷¹ as well as in OLED⁷²⁻⁷⁴ applications.

From a synthetic standpoint, quinoxalines are relatively simple to synthesise. Classically, an α,β -diketone is reacted with 1,2-diaminobenzene via a di-condensation reaction in refluxing alcohol (Figure 2.13). Typically, the reaction requires a catalyst⁷⁵, such as acetic acid, and long reaction times⁷⁶. Alternatively, one may employ an oxidative cyclisation of α -hydroxy ketones⁷⁷⁻⁷⁹ or α -halo ketones⁸⁰.

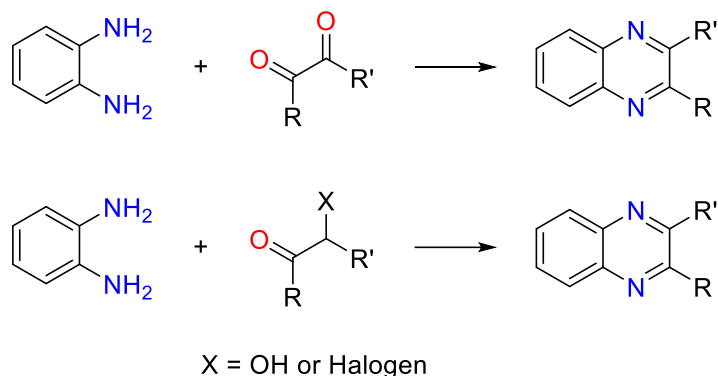


Figure 2.13 – Classical quinoxaline synthetic routes.

This simple synthetic pathway allows functionalisation to be introduced to the quinoxaline in the 2,3-positions via the functionalisation of the diketone, or in the 5,6,7,8-positions by using a functionalised diamine.

Other methods are available if the functionality desired would result in a mixture of isomers (See Figure 2.14). For example, Baohuan *et al* took mono substituted 2-iodoanilines in a three component copper catalysed reaction⁸¹. Here, 2-iodoaniline underwent condensation with 2-phenylacetaldehyde, forming an enamine. Oxidative addition of the copper follows, preceding exchange of the I⁻ with N₃⁻ before reductive elimination of the copper to give the aryl azide. Intramolecular cyclisation between the enamine and azide follows, yielding the desired single isomer with the release of N₂.

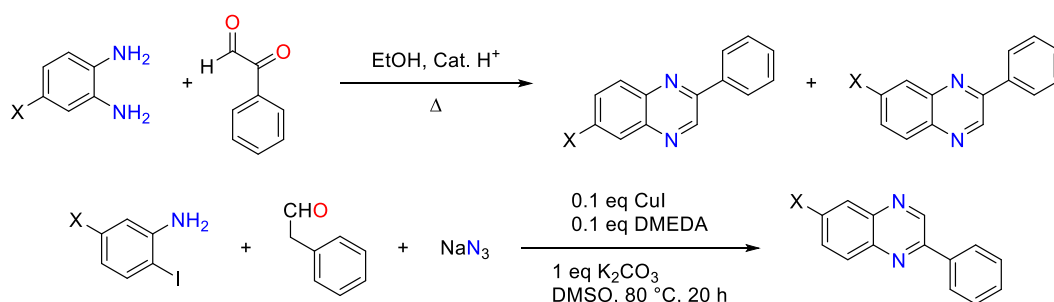


Figure 2.14 - Top: Mixed isomers that would result from the α,β -diketone condensation with 1,2-diaminobenzene. Below: One pot copper catalysed three component route to single isomers presented by Baohua *et al*⁸¹.

2-Phenylquinoxalines have been used for cyclometalation previously⁸², producing deep red emission. The additional nitrogen atom, as well as the extended conjugation, leads to a significant decrease of the LUMO energy level when compared with ppy based complexes⁸³. For example, Lee *et al* synthesised

complexes for OLED applications based around 2,3-diphenylquinoxaline – see Figure 2.15 (i) + (ii).

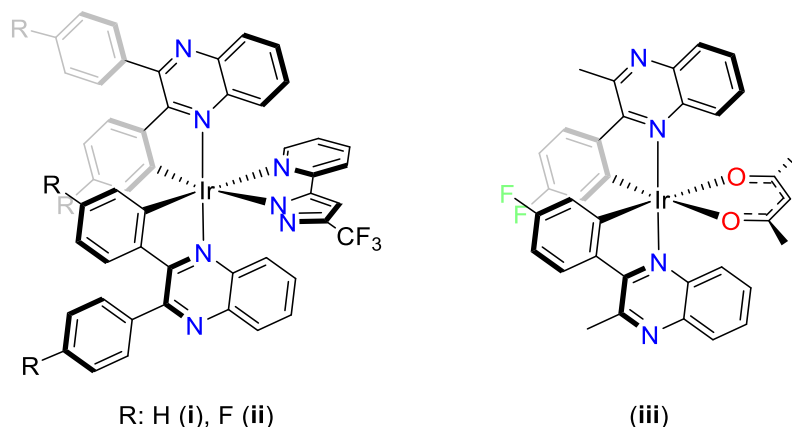


Figure 2.15 – Red emitting quinoxaline complexes for OLED use, Complexes (i) and (ii) were synthesised by Lee *et al.*⁸⁴, and complex (iii) was synthesised by Johannes *et al.*⁸⁵

Complex (i) had $\lambda_{\text{PL}} = 642$ nm. An OLED was made from this complex, and the emission spectrum of the electroluminescence was congruent with the photoluminescent spectrum. When a *para*-fluorophenyl quinoxalines (ii) were used instead, the λ_{PL} was hypsochromically shifted 630 nm, since the HOMO of the complexes is still located around the phenyl rings, much like on a ppy complex. The 2010 work of Johannes *et al* used 2-(4-fluorophenyl)-3-methylquinoxaline as cyclometalation ligands during their investigation into OLED devices.⁸⁵ By varying the ancillary ligands, the group were able to tune both the photoluminescent and electroluminescent properties, with the picolinate complex showing $\lambda_{\text{PL}} = 606$ nm and $\lambda_{\text{EL}} = 615$ nm, while the acac complex (as seen in Figure 2.15 (iii)). bathochromically shifted the emission to $\lambda_{\text{PL}} = 628$ nm and $\lambda_{\text{EL}} = 630$ nm.

Previous research from within the Pope Group started with functionalised 2,3-diphenylquinoxaline ligands (see Figure 2.16)⁸⁶. All complexes were deep red emitters, as expected. Tuneability is introduced via phenyl functionalisation, with DFT calculations showing the contribution of the phenyl moieties to the HOMO levels of the complex. λ_{em} ranges from 618 nm for the **qx**² complex with the electron withdrawing bromide substituent, to 636 nm with strongest electron donating substituent, the methoxy group on **qx**⁴. N,N'-dioctyl-2,2'-bipyridyl-4,4'-carboxamide ancillary ligands were used to help aid thin film formation. In the solution phase, the emission profile between $[\text{Ir}(\mathbf{qx}^3)(\text{bpy})]^+$ and $[\text{Ir}(\mathbf{qx}^3)(\text{Diobpy})]^+$ varied very slightly, 633 nm vs 631 nm in MeCN solutions respectively. However, upon formation of thin films by slow evaporation of DCM the emission maxima diverged,

with 688 nm and 677 nm respectively. This is likely due to the different packing arrangements in the solid state.

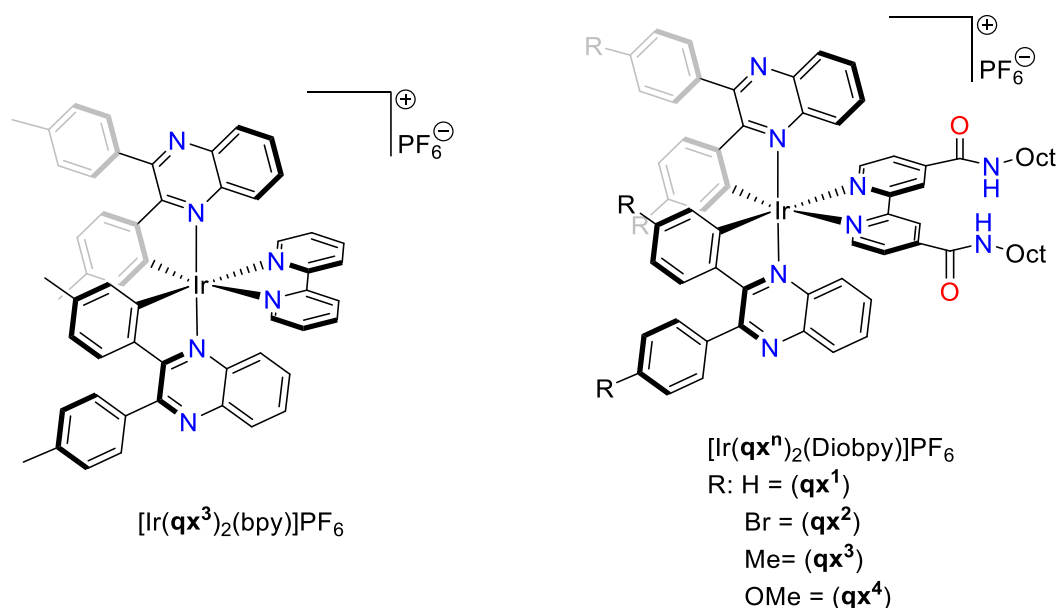


Figure 2.16 – Quinoxaline complexes synthesised by Pope et al in 2013⁸⁶.

Later, a series of ligands were synthesised to investigate the effects of substitution around the quinoxaline core in cationic⁸⁷ and neutral iridium(III) complexes⁸⁸ (See Figure 2.17). All complexes again show deep red emission, ranging from 617 nm to 680 nm in aerated chloroform. When picolinate (pic) or pyrazinoate (pyz) were used as the ancillary ligand, DFT calculations showed they contributed a modulation towards the complex HOMO levels. This manifested as an overall bathochromic shift in comparison to using a bipyridine ancillary ligand. Additionally, with the second heteroatom of the pyrazine moiety providing an additional stabilisation in direct comparison to the picolinate, a small hypsochromic shift in emission is noted.

DFT analysis on the complexes has shows that quinoxaline rings contribute orbital density towards the LUMO levels, while phenyl ring contributes to HOMO level, alongside the Ir 5d orbitals. When the quinoxaline was substituted in the 6,7-positions, the energy of emission changed from Me > H > halogen. The emission also shifted when the quinoxaline 3- position was changed, with the 3-methyl-2-phenylquinoxaline ligands giving a higher energy emission than 2,3-diphenylquinoxaline complexes.

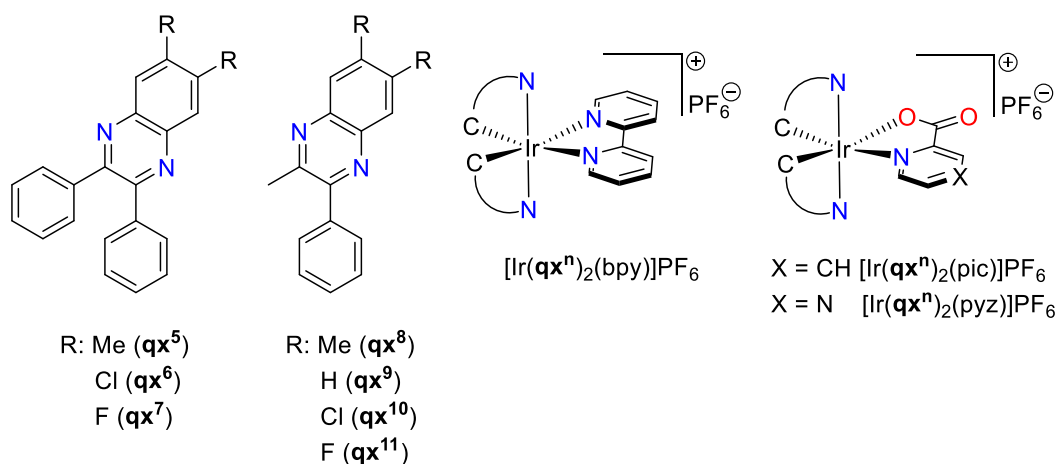


Figure 2.17 – Ligands and complexes published by Pope *et al* in investigations into tuneable red emission. ^{87,88}

2.2 Aims

Brominated acetophenones allow for a wide variety of cyclometalating ligands to be synthesised quickly, altering the substitution around the phenyl ring. As a brominating agent, dioxane dibromide offers rapid synthesis with excellent selectivity for monobrominated acetophenones. As such, this chapter sets out to synthesise and characterise a set of novel *bis*-cyclometalated iridium(III) complexes, based upon the substituted 2-phenylquinoxaline framework. The work set out to study the systematic substitution around the ligand, by using electron withdrawing groups or electron donating groups, and how this affected the photophysical properties of the resultant organometallic complexes. In total, three cationic complexes have been isolated, with two more complexes showing an unexpected mix of isomers. The data is compared with a further complex, isolated and characterised by Sophie Fitzgerald, included as a comparison to complete the series.

2.3 Results and discussions

2.3.1 Ligand synthesis and characterisation

A series of ligands was synthesised to investigate the effects of substitution on emission wavelength. First, a functionalised acetophenone underwent a selective electrophilic mono-bromination using 1.2 equivalents of dioxane dibromide, following literature methods.⁸⁹ α -Bromo ketones were then reacted with a 4,5-disubstituted-1,2-diaminobenzene derivative to form the desired polyfunctionalised quinoxaline ligands (Figure 2.18) in good yields.

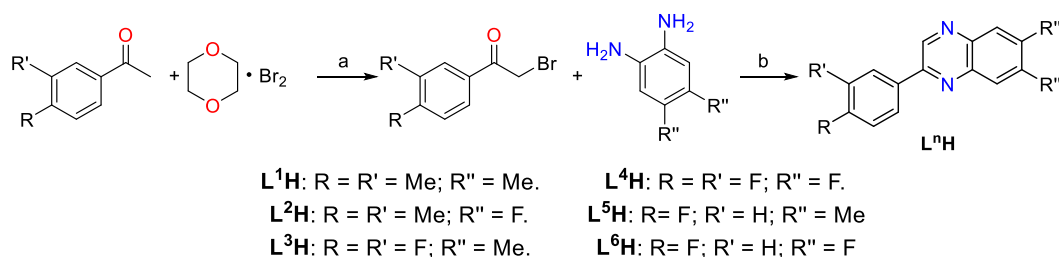


Figure 2.18 – Synthetic route used for ligand synthesis: a: 1,4-dioxane, diethyl ether, dropwise addition, 2 hours, room temperature; b: Ethanol, 24 hours, 78 °C.

The bromination step was monitored by TLC, and after two hours a proton NMR spectrum was taken, comparing the integrations of the aliphatic singlet environments. The $-\text{CH}_3$ acetal has a resonance around 2.7 ppm, $-\text{CH}_2\text{Br}$ singlet appearing around 4.5 ppm and the $-\text{CHBr}_2$ peak occurs around 6.7 ppm.⁹⁰ After two hours, the conversion was around 90 % for all tested acetophenones, with very minimal dibrominated product seen. It was noted that after 4 hours the reaction showed no improvement to the conversion and increasing the dioxane dibromide amounts increased the dibrominated product rather than the monobrominated species. Product can be isolated by triturating with petroleum ether or hexanes, however the addition of fluorine substituents to the molecule increased the solubility in these solvents, giving lower isolated yields in these cases. Since the acetal is present in low concentrations, it was not expected to hinder or compete in the second reaction with the phenylenediamine.

The crude brominated products were heated at reflux with functionalised phenylene diamines to form quinoxalines in good yields. Upon cooling a precipitate appeared, and was collected under reduced pressure, where it was washed with a minimal amount of cold ethanol and characterised by ^1H , $^{13}\text{C}\{^1\text{H}\}$, $^{19}\text{F}\{^1\text{H}\}$ NMR

spectroscopy and high-resolution mass spectrometry. The quinoxaline ring is identified in ^1H NMR spectrum by a new singlet appearing around 9.20 ppm, assigned to the proton on C3 of the quinoxaline ring. This is expected to be most downfield due to the deshielding effects from the adjacent imines.

The shifts associated with the methyl groups (Table 2.1) upon the quinoxaline ring appear to be coincidental at around 2.5 ppm. Nevertheless, it was possible to detect two separate singlets on the L^5H spectrum, which was obtained in d_6 -acetone rather than CDCl_3 . The methyl groups upon the phenyl ring are slightly more shielded with resonances at 2.36 – 2.40 ppm. $^{19}\text{F}\{^1\text{H}\}$ NMR spectra shows that once again the quinoxaline ring substituents are more deshielded than the phenyl counterparts. This can be seen by comparing the shifts of L^2H with L^3H , where the fluorine shifts from L^2H quinoxaline substituents are *ca.* -130 ppm, while L^3H fluorophenyl substituents are *ca.* -135 ppm. Each of these doublets has a $^3J_{\text{FF}}$ of 21 Hz. The effects of placing a second electronegative fluorine upon the phenyl ring is most prominent when comparing L^3H to L^5H , with a 25 ppm upfield shift induced by the second fluorine.

Ligand	^1H δ - CH_3^b / ppm	$^{19}\text{F}\{^1\text{H}\}$ δ ($^3J_{\text{FF}}$) / ppm
L^1H	2.51 (6H), 2.40, 2.36	-
L^2H	2.37, 2.40	-129.8 (d, 20.0 Hz), -131.0 (d, 21 Hz)
L^3H	2.52 (6H)	-135.8 (d, 21 Hz), -136.4 (d, 21 Hz)
L^4H	-	-128.0 (d, 21 Hz), -129.3 (d, 21 Hz), -134.3 (d, 21 Hz), -135.8 (d, 21 Hz)
L^5H^a	2.52, 2.53	-111.2 (s)
L^6H	-	-109.9 (s), -129.2 (d, 21 Hz), -130.1 (d, 21 Hz)

Table 2.1 – NMR shifts of methyl- and fluoro- substituents of ligands. All spectra obtained in CDCl_3 unless otherwise stated. ^a – spectrum obtained in d_6 -Acetone. ^b – Peak integration of 3H unless otherwise stated.

2.3.2 Complex synthesis and characterisation

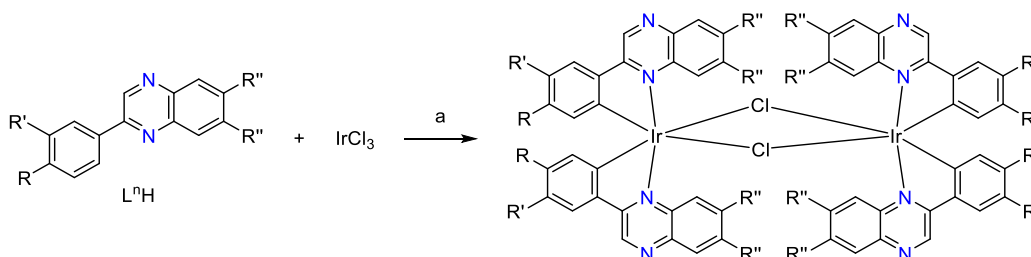


Figure 2.19 – $[(\text{L}^n)_2\text{Ir}(\mu\text{-Cl})_2\text{Ir}(\text{L}^n)_2]$ synthesis following Nonoyama route¹⁰. ^a two eq L^nH , one eq $\text{IrCl}_3 \cdot x\text{H}_2\text{O}$, 2-methoxyethanol, 125 °C, 48 hours.

With ligands in hand, cyclometalation could be attempted with IrCl₃. [(Lⁿ)₂Ir(μ-Cl)₂Ir(Lⁿ)₂] were first formed following the Nonoyama¹⁰ route (Figure 2.19). It was noted during the reflux that a yellow-orange precipitate had formed in each reaction. Initially, the iridium(III) dimer workup followed literature procedures^{25,87}, precipitation with the addition of water and collection by filtration, but, attempts to split the dimers with bpy were unsuccessful. A second attempt using AgBF₄ to abstract the chlorides also proved fruitless. During heating with the bpy, the precipitate from the dimer reaction was still present when the mixture was heated in 2-methoxyethanol, MeCN or chloroform. Since the dimer was expected to be readily soluble in each of these solvents this was identified as a potential limitation for the reaction.

The dimers were once again remade, precipitated, and collected upon a sinter. After washing with water, the solid was then washed with DCM, giving a deep red filtrate, and leaving a yellow insoluble powder on the sinter. The collected DCM fraction was dried over MgSO₄ and evaporated to dryness *in vacuo*.

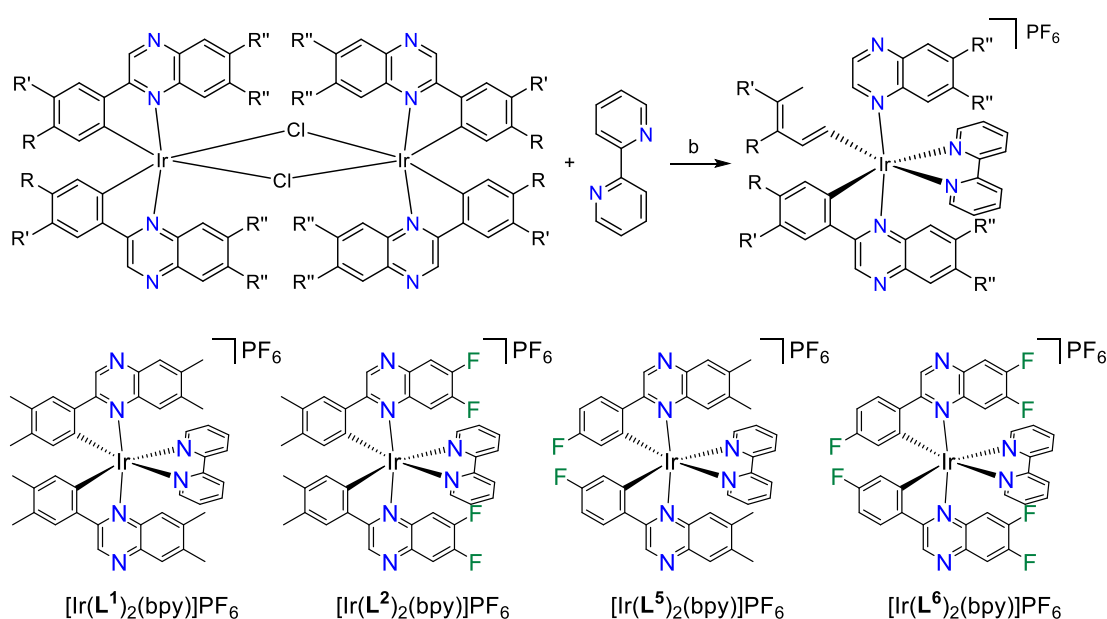


Figure 2.20 – Top: Dimer Splitting synthesis. ^b i) 2-methoxyethanol, 125 °C, 16 hours. ii) sat. NH₄PF₆ (aq). Bottom: Synthesised cyclometalated iridium(III) complexes in this work.

Having removed the insoluble side product, the dimers were split by heating in 2-methoxyethanol at reflux with two molar equivalents of bpy (Figure 2.20). Monitoring by TLC (eluted with DCM / MeOH 95:5) showed a new spot appearing over time which also showed red emission under UV irradiation. Aqueous

ammonium hexafluorophosphate was added to precipitate the desired product via counterion exchange. The crude complexes were then purified via silica gel column chromatography, eluting with DCM/MeOH (95:5) and collecting the first red band eluted. Finally, the combined red fractions were recrystallised from DCM by addition of diethyl ether. Complexes were then characterised via by ^1H , $^{13}\text{C}\{^1\text{H}\}$ and $^{19}\text{F}\{^1\text{H}\}$ NMR, UV-vis absorption, luminescence and FTIR spectroscopies.

During characterisation it became apparent that samples of $[\text{Ir}(\text{L}^3)_2(\text{bpy})]\text{PF}_6$ and $[\text{Ir}(\text{L}^4)_2(\text{bpy})]\text{PF}_6$ contained more than one species, and chromatography and recrystallisation techniques were of no use in their separation. In the case of $[\text{Ir}(\text{L}^3)_2(\text{bpy})]\text{PF}_6$, a symmetry of C_2 is expected. This would give rise to two singlet methyl environments and two fluorine doublets environments for $[\text{Ir}(\text{L}^3)_2(\text{bpy})]\text{PF}_6$. The ^1H NMR spectrum, however, showed four methyl environments, and a very complex aromatic region with overlapping resonances. The $^{19}\text{F}\{^1\text{H}\}$ NMR spectrum also showed multiple doublets (Figure 2.21) In neither case were the signals concurrent with those of the free ligand.

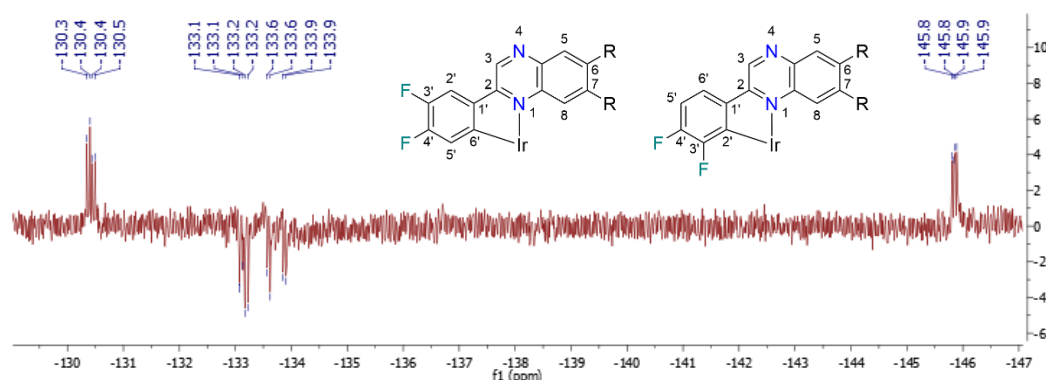


Figure 2.21 – $^{19}\text{F}\{^1\text{H}\}$ NMR spectrum for $[\text{Ir}(\text{L}^3)_2(\text{bpy})]\text{PF}_6$ – PF_6 signal (-72.6 ppm) omitted for clarity. Insert – the different coordination isomers.

Samples were run on LR MS (ES ionisation) showing a single peak at m/z 887.21 which correlates to the expected m/z for complex. The same observations were seen on the $^{19}\text{F}\{^1\text{H}\}$ NMR spectrum for $[\text{Ir}(\text{L}^4)_2(\text{bpy})]\text{PF}_6$. The aromatic positions on the ^1H NMR spectrum were again very complex. Thus, it can be postulated that the expected complex has formed a complex mixture of isomers, cyclometalating via the phenyl ring 6' position (the expected and desired position) as well as the 2' position. Complexes based around a 3,4-difluorophenyl quinoxaline ligand framework are therefore extremely challenging to isolate as pure isomers.

Since this was only seen on the 3,4-difluorophenyl based ligand systems, to obviate this isomeric mixture, two new ligands were synthesised, **L⁵H** and **L⁶H**, from 4-fluoroacetophenone.

Thus, four novel complexes were isolated and characterised, including $[\text{Ir}(\text{L}^6)_2(\text{bpy})]\text{PF}_6$ isolated and characterised by Sophie Fitzgerald.

Firstly, when looking at the ^1H NMR spectra, the expected C2 symmetry means that each of the cyclometalating ligands exhibit as equivalent environments. The singlet seen on the C3 quinoxaline position has shifted from ca. 9.2 – 9.3 ppm up to ca. 9.5 - 9.6 ppm in all isolated complexes. This is indicative of ligand cyclometalation and likely caused by an inductive effect from the positively charged iridium(III) centre. Two separate resonances also shift upfield to between 6.10 – 6.30 ppm and 6.70 – 6.80 ppm (Figure 2.22).

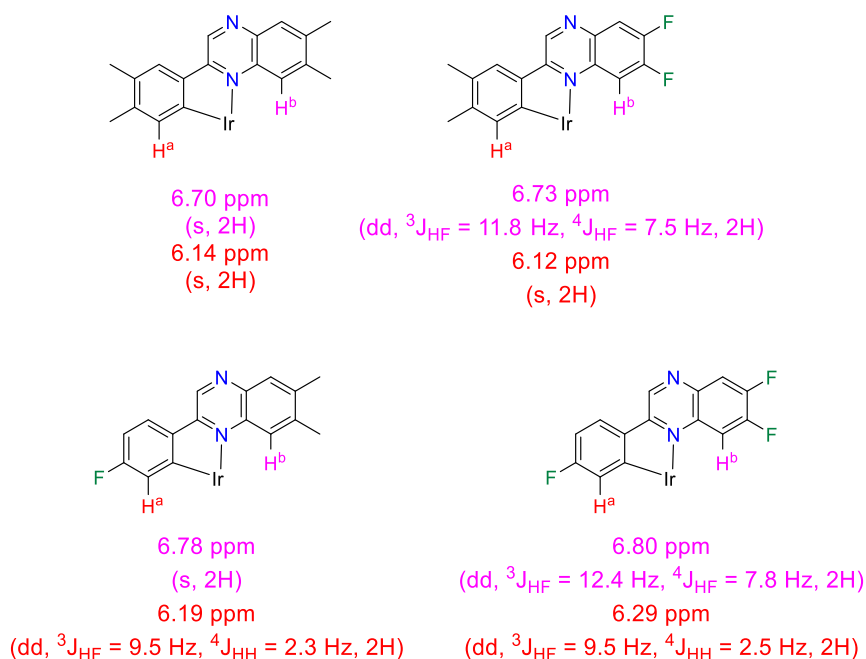


Figure 2.22 – Upfield aromatic singlet shifts seen in ^1H NMR spectra upon complexation and proposed assignments.

Secondly, in complexes $[\text{Ir}(\text{L}^1)_2(\text{bpy})]\text{PF}_6$ and $[\text{Ir}(\text{L}^2)_2(\text{bpy})]\text{PF}_6$ we see a new singlet signal appearing compared to the free ligand indicating the loss of a proton during cyclometalation. The proton *ortho*- to the site of cyclometalation (H^{a} in Figure 2.22) and the H^{b} proton have both been shifted upfield due to the overlapping aromatic ring currents from adjacent ligand quinoxaline and bipyridine ligand systems. Solid

state structures obtained (see section 2.3.3) put the average distance from adjacent ring centroids at 3.4 Å for H^a, and 2.9 Å for H^b.

Ligand	Free Ligand -CH ₃ δ _H / ppm ^a	[Ir(L ⁿ) ₂ (bpy)]PF ₆ -CH ₃ δ _H / ppm ^a
L ¹ H	2.36, 2.40, 2.52 (6H)	1.75, 1.95, 2.27, 2.23
L ² H	2.37, 2.40	1.99, 2.29
L ⁵ H	2.52, 2.53 ^b	1.76, 2.31 ^c

Table 2.2 – Aliphatic shifts from free ligand and complexes for pure synthesised complexes. ^a All spectra obtained in CDCl₃ unless otherwise indicated. ^b Spectra obtained in d₆-Acetone. ^c spectra obtained in d₃-MeCN.

Methyl group shifts have also changed upon complexation. These have been tabulated in Table 2.2 and are compared to the free ligand shifts. The coincidental shifts of the quinoxaline methyl groups seen in the free ligand have been resolved, as expected, due to the increased asymmetry from complexation, as well as close proximities to neighbouring diatropic ring currents and the iridium metal centre.

Ligand	Free Ligand ¹⁹ F{ ¹ H} δ _F / ppm	[Ir(L ⁿ) ₂ (bpy)]PF ₆ ¹⁹ F{ ¹ H} δ _F / ppm
L ² H	-129.8 (d, ³ J _{FF} = 20 Hz), -131.0 (d, ³ J _{FF} = 20 Hz)	-72.6 (d, ¹ J _{PF} = 711 Hz) (PF ₆), -123.8 (d, ³ J _{FF} = 22 Hz), -128.6 (d, ³ J _{FF} = 22 Hz)
L ⁵ H	-111.2 (s)	-72.6 (d, ¹ J _{PF} = 711 Hz) (PF ₆), -103.9 (s)
L ⁶ H	-109.9 (s), -129.2 (d, ³ J _{FF} = 21 Hz), -130.1 (d, ³ J _{FF} = 21 Hz)	-72.6 (d, ¹ J _{PF} = 711 Hz) (PF ₆), -106.2 (s), -128.2 (d, ³ J _{FF} = 21 Hz), -132.8 (d, ³ J _{FF} = 21 Hz)

Table 2.3 - ¹⁹F{¹H} NMR spectrum shifts for ligand and complexes.

¹⁹F{¹H} NMR spectrum shifts are seen in Table 2.3. Firstly, a noticeably smaller pronounced change to the shifts associate with the quinoxaline ring substitutes in comparison to the methyl substituents is seen.

In each isolated complex, the high-resolution mass spectrometry data provides a m/z peak that is expected for [M - PF₆]⁺.

2.3.3 X-ray crystal structure of $[\text{Ir}(\text{L}^1)_2(\text{bpy})]\text{PF}_6$ and $[\text{Ir}(\text{L}^2)_2(\text{bpy})]\text{PF}_6$.

Single crystal diffraction data and geometry refinements were carried out by The UK National Crystallographic Service at Southampton University. Single crystals of $[\text{Ir}(\text{L}^1)_2(\text{bpy})]\text{PF}_6$ (dark red and shard-shaped, Figure 2.23) and $[\text{Ir}(\text{L}^2)_2(\text{bpy})]\text{PF}_6$ (dark red rod-shaped, Figure 2.24) were grown by vapour diffusion of diethyl ether into DCM or chloroform solutions of each complex. In both cases, the complex displayed the expected coordination, with a *cis*-C,C and *trans*-N,N arrangement of the cyclometalating ligands around the distorted octahedral iridium(III) centre^{13,18}. In each case, there was solvent of crystallisation; for $[\text{Ir}(\text{L}^1)_2(\text{bpy})]\text{PF}_6$ disordered solvent – assumed to be diethyl ether – was removed with solvent masking. In $[\text{Ir}(\text{L}^2)_2(\text{bpy})]\text{PF}_6$ a molecule of disordered diethyl ether is still present. Each of the monocationic complexes is charged balanced by the presence of a single hexafluorophosphate ion.

When examining the bond lengths around the iridium(III) centre (Table 2.4), in both cases there is an elongation of the Ir-N bonds of the bipyridine ligand, N(41) and N(42), when compared to Ir-N bonds on the quinoxalines. This can be attributed

to the strong σ -bonding of the phenyl C-Ir organometallic bonds producing a strong trans influence upon the bipyridine Ir-N bonds.

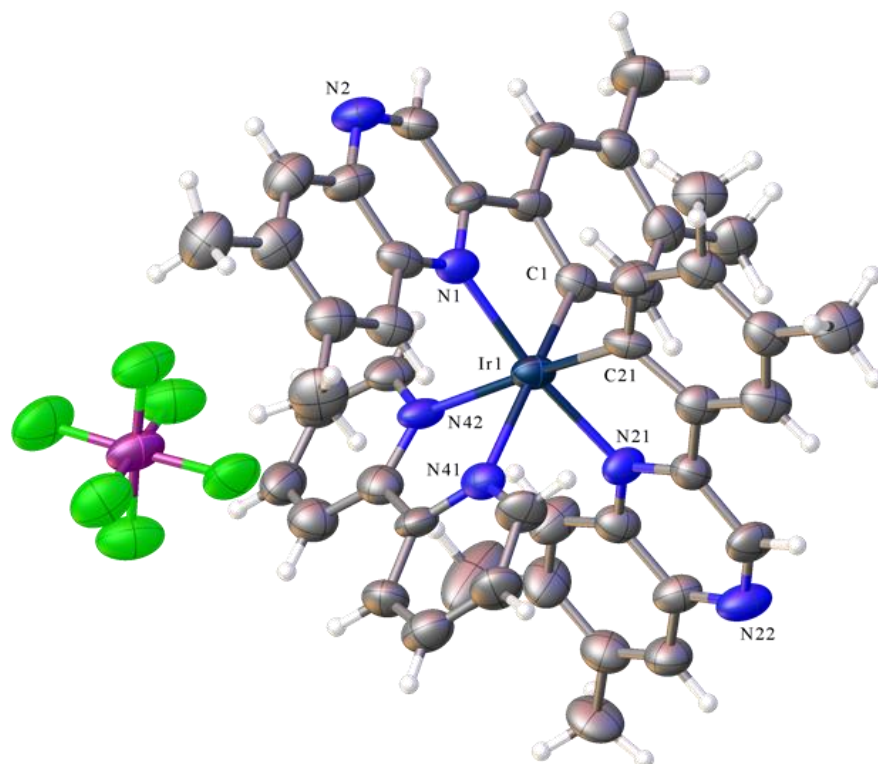


Figure 2.23 - X-ray structure of $[\text{Ir}(\text{L}^1)_2(\text{bpy})]\text{PF}_6$ ($\text{C}_{48}\text{H}_{47}\text{IrN}_6\text{O}_{0.5}\text{P}$, $M_r = 1053.08$, triclinic, $P-1$ (No. 2), $a = 10.1665(3) \text{ \AA}$, $b = 13.4268(4) \text{ \AA}$, $c = 17.3892(9) \text{ \AA}$, $\alpha = 105.700(4)^\circ$, $\beta = 100.845(3)^\circ$, $\gamma = 93.671(2)^\circ$, $V = 2227.67(16) \text{ \AA}^3$, $T = 100(2) \text{ K}$, $Z = 2$, $Z' = 1$, $m(\text{CuK}\alpha) = 6.716 \text{ mm}^{-1}$, 28306 reflections measured, 8018 unique ($R_{\text{int}} = 0.1024$) which were used in all calculations. The final wR_2 was 0.1882 (all data) and R_1 was 0.0720 ($I > 2(I)$)}

$[\text{Ir}(\text{L}^1)_2(\text{bpy})]\text{PF}_6$				$[\text{Ir}(\text{L}^2)_2(\text{bpy})]\text{PF}_6$			
Bond Length (Å)							
Ir(1)	N(1)	2.100(8)		Ir(1)	N(1)	2.079(3)	
Ir(1)	N(21)	2.090(8)		Ir(1)	N(21)	2.080(3)	
Ir(1)	N(41)	2.176(8)		Ir(1)	N(41)	2.161(3)	
Ir(1)	N(42)	2.148(8)		Ir(1)	N(42)	2.167(3)	
Ir(1)	C(1)	2.023(9)		Ir(1)	C(1)	1.992(3)	
Ir(1)	C(21)	1.974(9)		Ir(1)	C(21)	2.017(3)	
Bond Angle (°)							
N(1)	Ir(1)	N(21)	171.9(3)	N(1)	Ir(1)	N(21)	173.30(10)
N(1)	Ir(1)	N(41)	105.5(3)	N(1)	Ir(1)	N(41)	102.99(10)
N(1)	Ir(1)	N(42)	84.8(3)	N(1)	Ir(1)	N(42)	83.70(10)
N(21)	Ir(1)	N(41)	81.2(3)	N(21)	Ir(1)	N(41)	80.83(10)
N(21)	Ir(1)	N(42)	101.5(3)	N(21)	Ir(1)	N(42)	102.66(11)
N(41)	Ir(1)	N(42)	75.3(3)	N(41)	Ir(1)	N(42)	75.93(10)
C(1)	Ir(1)	N(1)	79.4(4)	C(1)	Ir(1)	N(1)	79.50(12)
C(1)	Ir(1)	N(21)	94.6(4)	C(1)	Ir(1)	N(21)	97.76(12)
C(1)	Ir(1)	N(41)	171.3(3)	C(1)	Ir(1)	N(41)	169.35(11)
C(1)	Ir(1)	N(42)	98.3(3)	C(1)	Ir(1)	N(42)	94.19(11)
C(1)	Ir(1)	C(21)	90.8(3)	C(1)	Ir(1)	C(21)	93.78(13)
C(21)	Ir(1)	N(1)	94.1(3)	C(21)	Ir(1)	N(1)	94.65(12)
C(21)	Ir(1)	N(21)	80.5(3)	C(21)	Ir(1)	N(21)	79.37(13)
C(21)	Ir(1)	N(41)	96.0(3)	C(21)	Ir(1)	N(41)	96.31(12)
C(21)	Ir(1)	N(42)	170.5(3)	C(21)	Ir(1)	N(42)	171.41(12)

Table 2.4 – Selected bond lengths and bond angles obtained from crystallographic data from complexes $[\text{Ir}(\text{L}^1)_2(\text{bpy})]\text{PF}_6$ and $[\text{Ir}(\text{L}^2)_2(\text{bpy})]\text{PF}_6$

The solid state structure shows the quinoxaline methyl group protons from $[\text{Ir}(\text{L}^1)_2(\text{bpy})]\text{PF}_6$ are in very close proximity to the centre of the bpy aromatic rings, with proton to centroid distances measured at 3.1 and 3.4 Å for each of the cyclometalated ligands. At these distances, the effects of the aromatic ring current originating from the bipyridine is likely to induce a shielding effect^{91,92}. Indeed, on the ¹H NMR spectrum this position changed from 2.5 ppm in the free ligand to 1.75 ppm once complexation has occurred.

However, in the structure seen in Figure 2.24, the distance of F1 and F21 to the centroid of the bipyridine are 4.31 and 4.60 Å which is going to be outside of any shielding effects produced by neighbouring aromatic rings. Indeed, the shifts seen on the $^{19}\text{F}\{^1\text{H}\}$ NMR spectrum have changed very little from the free ligand.

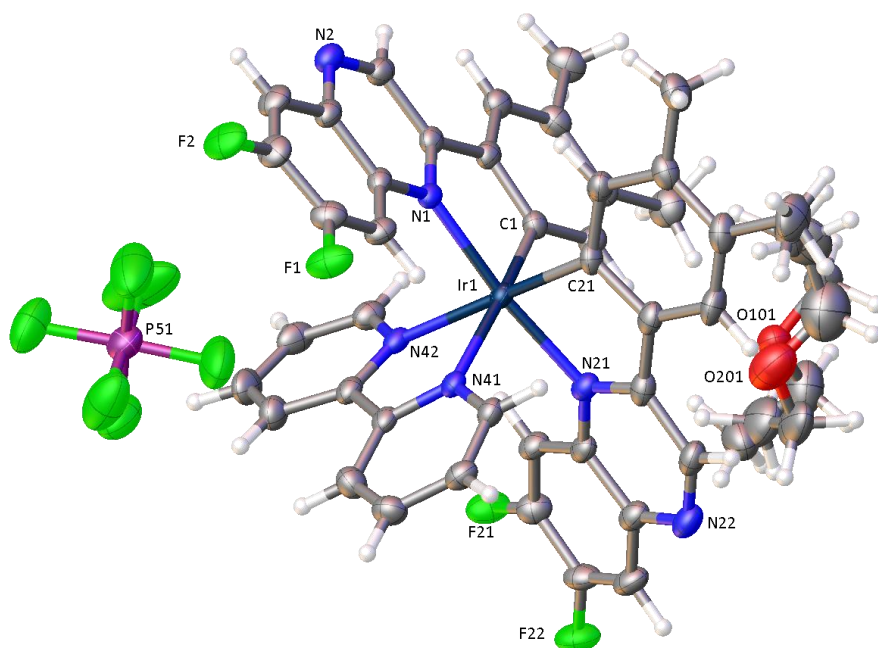


Figure 2.24 – X-ray structure of $[\text{Ir}(\text{L}^2)_2(\text{bpy})]\text{PF}_6$ $\{\text{C}_{46}\text{H}_{40}\text{F}_{10}\text{IrN}_6\text{OP}$, $M_r = 1106.01$, monoclinic, $P2_1/n$ (No. 14), $a = 10.2004(2)$ Å, $b = 21.6662(6)$ Å, $c = 18.8506(5)$ Å, $\beta = 90.842(2)^\circ$, $\alpha = \gamma = 90^\circ$, $V = 4165.61(18)$ Å³, $T = 100(2)$ K, $Z = 4$, $Z' = 1$, $m(\text{Mo } K_\alpha) = 3.335$ mm⁻¹, 189265 reflections measured, 9560 unique ($R_{\text{int}} = 0.0529$) which were used in all calculations. The final wR_2 was 0.0726 (all data) and R_1 was 0.0288 ($I > 2(I)$).

2.3.4 Electronic properties

2.3.4.1 Absorption and emission properties of the ligands

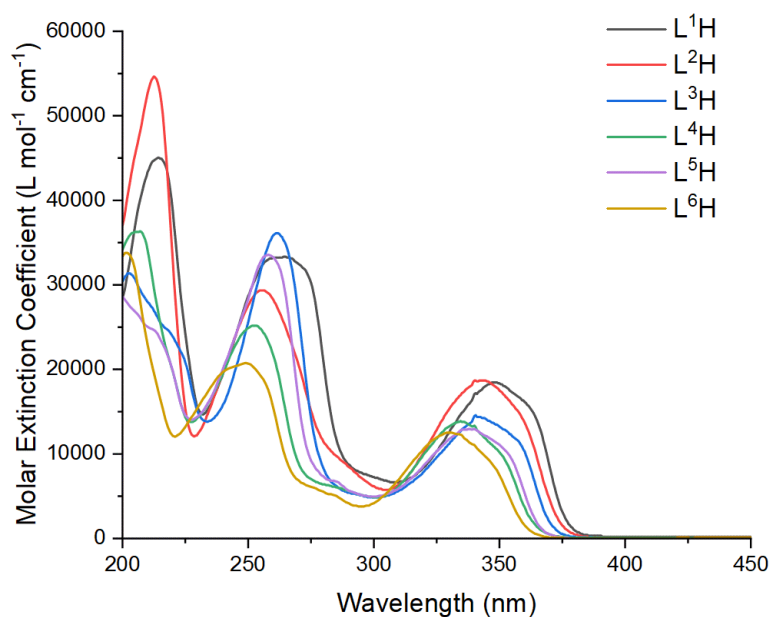


Figure 2.25 - UV-Vis spectra for **L¹⁻⁶H** recorded in MeCN at *ca.* 10⁻⁵ M.

Absorption spectra for **L¹⁻⁶H**, seen in Figure 2.25 were recorded in MeCN solution at *ca.* 10⁻⁵ M. The ligands absorb within the UV region, which can be attributed to $\pi-\pi^*$, in addition to $n-\pi^*$ transitions originating from the heteroatoms present in the quinoxaline aromatic ring. λ_{Max} shows small variations depending upon substitution with the tetramethyl quinoxaline absorbing at the highest wavelength. The effect of the second -F substituent upon the phenyl moiety induce a small (*ca.* 4 nm) bathochromic shift in absorption energies when comparing similarly substituted quinoxalines, **L³H** with **L⁵H** and **L⁴H** with **L⁶H**.

Steady state emission measurements were run in aerated MeCN for the six ligands and are shown in Figure 2.26 ($\lambda_{\text{ex}} = 330$ nm). While each ligand showed emission maxima centring around 392 nm (Table 2.1), it is clear that the degree of fluorination affects the amount of vibronic structure seen in the emission profile. With 3,4-dimethylphenyl ligands, **L¹H** and **L²H**, show a broad and featureless spectrum. The difference between the 3,4-difluorophenyl and 4-fluorophenyl ligands is more dependent upon the substitution upon the quinoxaline. Dimethylquinoxaline ligands, **L³H** and **L⁵H**, show a small shoulder at 380 nm, a sharper λ_{max} at 392nm and a broader shoulder at 407 nm. Difluoroquinoxaline

ligands, **L⁴H** and **L⁶H**, show a small feature around 370 nm, a more defined shoulder at 383 nm, a sharp λ_{max} at 392nm, and a shoulder at 407 nm.

Time resolved measurements were also made on **L¹⁻⁶H** (Table 2.5). The recorded lifetime measurements are short (between 0.5 and 5.3 ns) and are consistent with fluorescent emission. Quantum yields were calculated relative to known standards⁹³ throughout this thesis using Equation 2.1 below⁹⁴. Absorbance and fluorescent intensity were recorded across a concentration range, taking care not to exceed 0.1 absorbance at the excitation wavelength for the most concentrated sample to avoid inner filter effects⁹⁵. The results of integrated fluorescent intensity were plotted against the absorbance at the excitation wavelength, and the slope calculated.

$$\Phi_x = \Phi_{\text{std}} \left(\frac{\text{Grad}_x}{\text{Grad}_{\text{std}}} \right) \left(\frac{n_x^2}{n_{\text{std}}^2} \right) \quad \text{Equation 2.1}$$

Std and x denote the standard and sample respectively. Φ is the quantum yield and n is the refractive index of the solvents used. Grad is the gradient from a plot of integrated fluorescent intensity vs absorbance at the excitation wavelength. The error of both lifetime values and quantum yields are estimated to be no more than 10 %.

Ligand	$\lambda_{\text{abs}} (\epsilon / 10^4 \text{ M}^{-1} \text{ cm}^{-1}) / \text{nm}^a$	$\lambda_{\text{em}} / \text{nm}^b$	τ / ns^c	Φ^d
L¹H	348 (1.8), 265 (3.3), 214 (4.5)	393	5.3	0.006
L²H	343 (1.9), 256 (2.9), 213 (5.5)	397 (br)	0.5	0.008
L³H	340 (1.4), 262 (3.6), 203 (3.1)	382 (sh), 392, 407 (sh)	0.5	0.002
L⁴H	334 (1.4), 253 (2.5), 207 (3.6)	370 (sh), 382 (sh), 392, 407 (sh)	0.9	0.06
L⁵H	336 (1.3), 258 (3.3), 200 (2.9)	382 (sh), 392, 407 (sh)	0.8	0.003
L⁶H	330 (1.2), 249 (2.0), 202 (3.4)	370 (sh), 382 (sh), 392, 407 (sh)	1.4	0.002

Table 2.5 – ^a All measurements obtained at room temperature in aerated acetonitrile at ca. 1×10^{-5} M. ^b $\lambda_{\text{ex}} = 330$ nm; ^c $\lambda_{\text{ex}} = 295$ nm; ^d Vs standard Quinine Sulphate in 0.05 M H₂SO₄, $\lambda_{\text{ex}} = 350$ nm. ⁹³

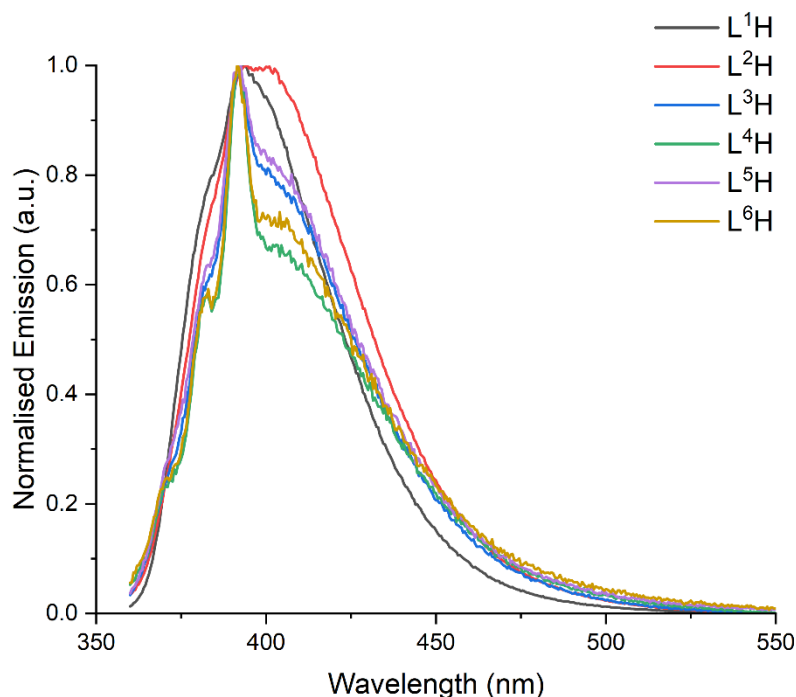


Figure 2.26 – Emission spectra for Ligands $L^{1-6}H$ obtained in aerated acetonitrile. $\lambda_{ex} = 330$ nm

2.3.4.2 Absorption and emission properties of complexes

Absorption spectra for the synthesised and isolated complexes can be seen overlaid in Figure 2.27. Measurements were made in aerated MeCN at *ca.* 10^{-5} M. Absorption bands seen between 200 and 400 nm have a large molar extinction coefficient and likely arise from spin allowed ligand centred $^1\pi-\pi^*$ transitions, from both the quinoxaline and bipyridine ligands. The heterocyclic quinoxaline ring is also likely to contribute $^1n-\pi^*$ transitions in this same region. The broad transitions occurring between 400 – 550 nm with ϵ *ca.* $5000 \text{ M}^{-1} \text{ cm}^{-1}$ typically possess some spin allowed 1MLCT character, with large differences seen between the different complexes, dominated by the substituents on the phenyl group of the quinoxaline ligands with minor differences from the quinoxaline substituents. 4-fluorophenyl ligands in $[\text{Ir}(L^5)_2(\text{bpy})]\text{PF}_6$ and $[\text{Ir}(L^6)_2(\text{bpy})]\text{PF}_6$ have narrower absorption, with a stronger ϵ when compared to the 3,4-dimethylphenyl ligands of $[\text{Ir}(L^1)_2(\text{bpy})]\text{PF}_6$ and $[\text{Ir}(L^2)_2(\text{bpy})]\text{PF}_6$. The complexes with the 6,7-difluoroquinoxalines also have a slightly bathochromically shifted absorption when compared with the 6,7-dimethylquinoxaline variants. When compared with the absorption spectrum for the free ligands, it is notable that these features from 400 nm onwards are not

seen in the ligands, and therefore are likely to occur from an MLCT process. Absorption tails off towards 600 nm with a much weaker feature, that typically is associated with spin forbidden $^3\text{MLCT}$ in iridium(III) complexes.

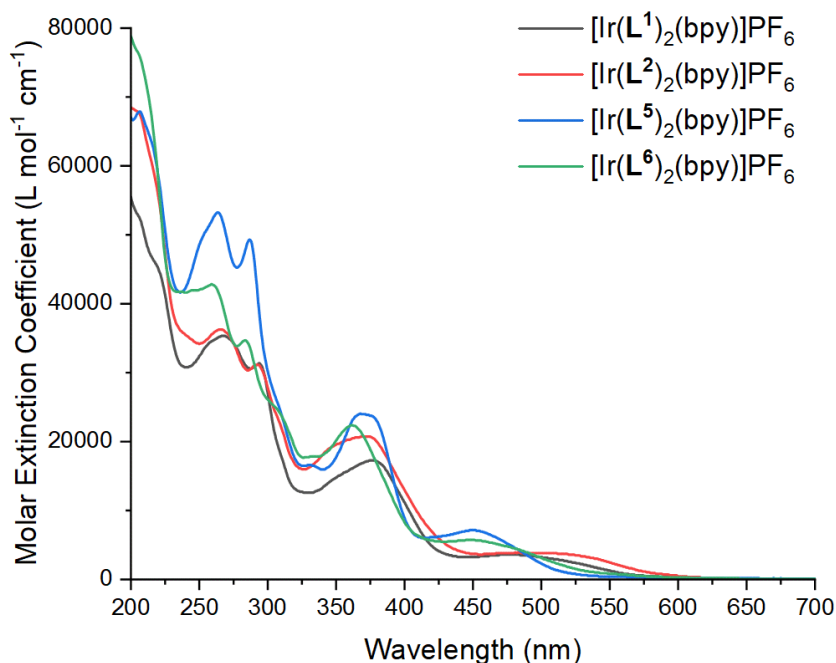


Figure 2.27 - UV-Vis spectra for isolated complexes, $[\text{Ir}(\text{L}^{1-6})(\text{bpy})]\text{PF}_6$, recorded in acetonitrile at $\text{ca.}10^{-5}\text{ M}$.

Steady state emission measurements were also run for isolated complexes in aerated MeCN solutions and can be seen in Figure 2.28. Similar to the absorbance spectrum, the substituents located upon the ligand phenyl ring show a greater effect upon the complex emission wavelength in comparison to the quinoxaline substituents. The 3,4-dimethylphenyl ligands are significantly bathochromically shifted in comparison to the 4-fluorophenyl ligands. This agrees with previous studies^{87,88} of similar red quinoxaline iridium(III) complexes, which have shown the HOMO to be located around the iridium 5d orbitals and the two cyclometalating ligands, with the ligand contribution being located upon the phenyl rings, rather than the N-donor rings. The LUMO is predominantly located across both cyclometalating ligands, with the orbital density located across both the phenyl and most predominantly, the quinoxaline moieties. Therefore, the use of the electron withdrawing -F substituents, or the electron donating -CH₃, substituents will have different effects upon the frontier orbitals depending upon the place of substitution. This is seen most clearly when comparing the spectra for $[\text{Ir}(\text{L}^1)_2(\text{bpy})]\text{PF}_6$ and $[\text{Ir}(\text{L}^2)_2(\text{bpy})]\text{PF}_6$. While both exhibit a significant bathochromic shift compared to the 4-fluorophenyl complexes, brought about by the methyl groups electron

donating effect stabilising the HOMO, $[\text{Ir}(\text{L}^2)_2(\text{bpy})]\text{PF}_6$ has a further red shift, in part by the electron withdrawing difluoro substituents on the quinoxaline destabilising the LUMO. This pattern is also seen to a lesser extent for $[\text{Ir}(\text{L}^5)_2(\text{bpy})]\text{PF}_6$ and $[\text{Ir}(\text{L}^6)_2(\text{bpy})]\text{PF}_6$.

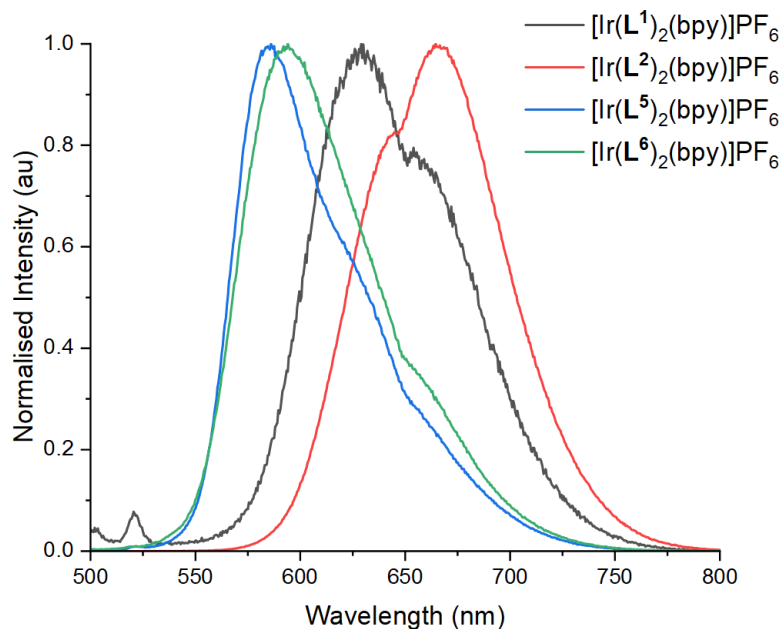


Figure 2.28 – Steady state emission spectra for isolated complexes, $[\text{Ir}(\text{L}^{1-6})(\text{bpy})]\text{PF}_6$. Samples run in MeCN at ca. 10^{-5} M. $\lambda_{\text{ex}} = 450$ nm

Complexes with mixed cyclometalation isomers, $[\text{Ir}(\text{L}^3)_2(\text{bpy})]\text{PF}_6$ and $[\text{Ir}(\text{L}^4)_2(\text{bpy})]\text{PF}_6$, would be expected to show a hypsochromic shift in comparison to $[\text{Ir}(\text{L}^1)_2(\text{bpy})]\text{PF}_6$ and $[\text{Ir}(\text{L}^2)_2(\text{bpy})]\text{PF}_6$. Indeed, samples were run on steady state emission showing one broad peak for each complex, centring around 593 nm (Figure 2.29). The shift in wavelength emission peaks appear almost congruent, suggesting the effects of the difluorophenyl group upon the frontier orbitals outweighs any effects seen by quinoxaline substitution.

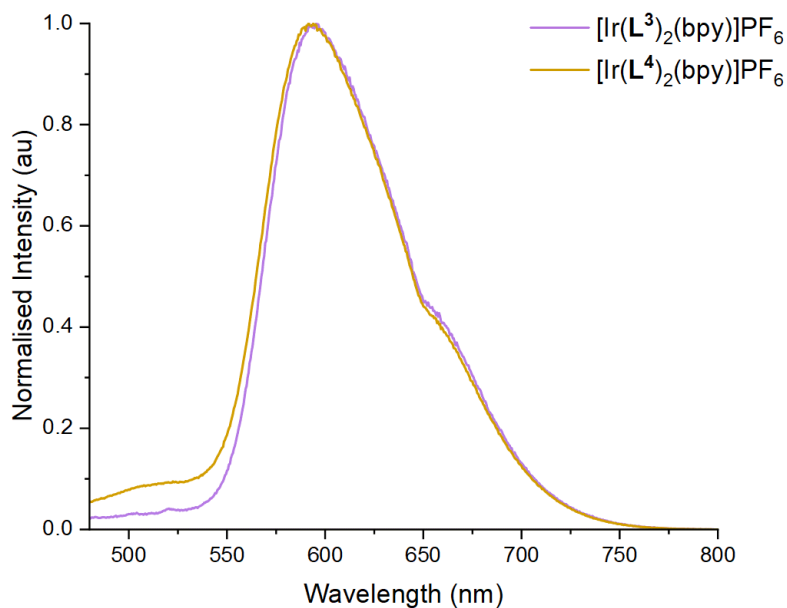


Figure 2.29 - Steady state emission spectra for mixed isomer complexes, $[\text{Ir}(\text{L}^{3-4})_2(\text{bpy})]\text{PF}_6$. Samples run in MeCN at $ca. 10^{-5} \text{ M}$. $\lambda_{\text{ex}} = 450 \text{ nm}$

Time resolved spectroscopy was also run on the isolated complexes (Table 2.6). The luminescent lifetimes were recorded in MeCN solutions. Lifetimes of all complexes showed a mono-exponential decay, which is consistent for a single emissive state. The aerated lifetimes vary from 214 – 571 ns, consistent with spin forbidden phosphorescent decay, while degassed lifetimes increased significantly to range between 659 and 4872 ns, consistent with a reduction in quenching from $^3\text{O}_2$.

Complex	$\lambda_{\text{abs}} (\epsilon / 10^4 \text{ M}^{-1} \text{ cm}^{-1}) / \text{nm}^{\text{a}}$	$\lambda_{\text{em}} / \text{nm}^{\text{b}}$	Aerated $\tau / \text{ns}^{\text{c}}$	Degassed $\tau / \text{ns}^{\text{c}}$	Φ^{d}
$[\text{Ir}(\text{L}^1)_2(\text{bpy})]\text{PF}_6$	485 (0.4), 378 (1.7), 293 (3.1), 267 (3.5)	629	230	1886	0.02
$[\text{Ir}(\text{L}^2)_2(\text{bpy})]\text{PF}_6$	518 (0.4), 373 (2.1), 292 (3.1), 266 (3.6)	666	214	659	0.01
$[\text{Ir}(\text{L}^5)_2(\text{bpy})]\text{PF}_6$	450 (0.7), 372 (2.4), 286 (4.9), 207 (6.7)	585	440	4872	0.08
$[\text{Ir}(\text{L}^6)_2(\text{bpy})]\text{PF}_6$	450 (0.6), 361 (2.2), 284 (3.5), 259 (4.2)	594	571	1387	0.09

Table 2.6 – a All measurements obtained at room temperature in aerated MeCN at ca. 1×10^{-5} M. ^b $\lambda_{\text{ex}} = 450$ nm; ^c $\lambda_{\text{ex}} = 295$ nm; Degassed lifetimes recorded by Haleema Otaif ⁹⁶; ^d Vs standard $[\text{Ru}(\text{bpy})_3][\text{PF}_6]_2$ in MeCN, $\lambda_{\text{ex}} = 450$ nm. ⁹³

2.4 Conclusions

Dioxane dibromide provides a simple synthetic methodology for the bromination of acetophenones, leading to excellent control and allowing new substituted C^N cyclometalating ligands to be synthesised with ease.

This chapter has shown the synthesis and characterisation of six novel substituted phenyl quinoxalines ligands, using a systematic design of electron withdrawing and donating groups to investigate the degree of tuneability in final complex emission.

The two iridium(III) complexes with a difluorophenyl motif upon the cyclometalating ligands exhibited mixed isomers, which were unable to be separated using standard chromatography and recrystallisation techniques.

The remaining four iridium(III) complexes were isolated, and characterised via NMR, HRMS, UV-vis and emission spectroscopies, with two examples grown as single crystals for single crystal x-ray diffraction studies. Results have shown that a bathochromic shift in emission is seen when using EDG around the phenyl ring, likely a result of a HOMO stabilisation. The effects of substitution in the quinoxaline positions were generally seen with a smaller magnitude. The use of the LUMO stabilising electron withdrawing -F substituents produced a bathochromic shift in emission. This fits with the current literature model for the predictions of the HOMO and LUMO contributions for iridium(III) quinoxaline cationic complexes.

The quantum yield and lifetime of the complexes in aerated solution appears to correlate with the emission energy, as described by the energy gap law. The aerated lifetimes *ca.* 214 – 571 ns would potentially allow for use in biological applications in oxygenated environments⁹⁷. The aerated lifetime and quantum yields are also comparable to archetypal complex, [Ir(ppy)₂bpy]⁺, where λ_{em} : 602, ϕ : 9.3 % and τ : 275 ns²⁷.

2.5 Experimental

All reactions were performed with the use of vacuum line and Schlenk techniques. Reagents were commercial grade and were used without further purification. ^1H , ^{13}C and ^{19}F NMR spectra were recorded on a Bruker fourier 300, dpx 400, or avance 500 MHz spectrometer, and were recorded in CDCl_3 , CD_3CN or d_6 -acetone solutions. ^1H and $^{13}\text{C}\{^1\text{H}\}$ NMR chemical shifts (δ) were determined relative to internal tetramethylsilane, $\text{Si}(\text{CH}_3)_4$ and are given in ppm. Low-resolution mass spectra were obtained by the staff at Cardiff University. High-resolution mass spectra were carried out by the staff at Cardiff University and the EPSRC National Mass Spectrometry Service at Swansea University, UK. All photophysical data was obtained on a JobinYvon-Horiba Fluorolog-3 spectrometer fitted with a JY TBX picosecond photodetection module in MeCN solutions. Emission spectra were uncorrected and excitation spectra were instrument corrected. The pulsed source was a Nano-LED configured for 295, 372 or 459 nm output operating at 500 kHz or 1 MHz. Luminescence lifetime profiles were obtained using the JobinYvon–Horiba FluoroHub single photon counting module and the data fits yielded the lifetime values using the provided DAS6 deconvolution software. IR spectra were recorded on an ATR equipped Shimadzu IRAffinity-1 spectrophotometer. UV-vis data was recorded as solutions on a Shimadzu UV-1800 spectrophotometer.

X-ray crystallography

Data collection and processing

Suitable crystals were selected and data collected on either a Rigaku FRE+ diffractometer equipped with VHF Varimax confocal mirrors and an AFC12 goniometer and HyPix 6000 detector, equipped with an Oxford Cryosystems low-temperature device operating at $T = 100(2)$ K (for $[\text{Ir}(\text{L}^2)_2(\text{bpy})]\text{PF}_6$) or a Rigaku 007HF diffractometer equipped with Varimax confocal mirrors and an AFC11 goniometer and HyPix 6000 detector equipped with an Oxford Cryosystems low-temperature device operating at $T = 100(2)$ K (for $[\text{Ir}(\text{L}^1)_2(\text{bpy})]\text{PF}_6$).

The structure was solved with the ShelXT⁹⁸ structure solution program using the Intrinsic Phasing solution method and by using Olex2⁹⁹ as the graphical interface. The model was refined with version 2018/3 of ShelXL¹⁰⁰ using Least Squares minimisation.

2.5.1 Synthesis of α -bromoacetophenone precursors⁸⁹

General Procedure: To a stirring solution of substituted acetophenone (1.000 g) in 1,4-dioxane (10 mL) and diethyl ether (10 mL), dioxane dibromide (1.1 eq) was added portion wise and stirred at room temperature for 2 hours. The pale yellow solution was added to water (50 mL) and extracted with diethyl ether (3 x 20 mL). The combined ether layers were dried over magnesium sulphate, and the solvent removed *in vacuo* to yield crude product. A minimum amount of hexanes were added and the resultant slurry filtered under suction to yield brominated precursors.

2.5.1.1 2-bromo-1-(3,4-dimethylphenyl)ethan-1-one

Off white solid (1.364 g, 89 %). ¹H NMR (400 MHz, CDCl₃) δ_{H} = 7.79 (s, 1H), 7.74 (d, *J* = 7.9 Hz, 1H), 7.28 (d, *J* = 3.3 Hz, 1H), 4.46 (s, 2H), 2.36 (s, 6H) ppm.

2.5.1.2 2-bromo-1-(3,4-difluorophenyl)ethan-1-one

Off white solid (0.311 g, 21 %). ¹H NMR (400 MHz, CDCl₃) δ_{H} = 7.80 – 7.74 (m, 1H), 7.73 – 7.69 (m, 1H), 7.22 (ddd, *J* = 11.4, *J* = 5.3 Hz, *J* = 4.2 Hz 1H), 4.35 (s, 2H) ppm. ¹⁹F{¹H} NMR (376 MHz, CDCl₃) δ_{F} = -127.7 (d, ³*J*_{HH} = 21 Hz), -135.1 (d, ³*J*_{HH} = 21 Hz) ppm.

2.5.1.3 2-bromo-1-(4-fluorophenyl)ethan-1-one

White crystalline solid (0.837 g, 53 %). ¹H NMR (300 MHz, CDCl₃) δ_{H} = 8.75 – 8.30 (m, 2H), 7.60 (ddd, *J* = 8.5, *J* 6.0, *J* 3.0 Hz, 2H), 4.85 (s, 2H).

2.5.2 Synthesis of phenylquinoxaline ligands

2.5.2.1 2-(3,4-dimethylphenyl)-6,7-dimethylquinoxaline (L¹H)

2-bromo-1-(3,4-dimethylphenyl)ethan-1-one (0.800 g, 3.520 mmol) and 4,5-dimethyl-1,2-phenylenediamine (0.530 g, 3.870 mmol, 1.2 eq) were dissolved in ethanol and heated to reflux for 24 hours. After cooling, the resultant precipitate was filtered under reduced pressure, washed with ice cold ethanol (3 x 5 mL), to yield the title product as a pale yellow solid (0.347 g, 40 %). ¹H NMR (400 MHz, CDCl₃) δ_{H} 9.20 (s, 1H), 7.97 (d, *J* = 0.9 Hz, 1H), 7.90 (s, 1H), 7.88 (dd, *J* = 7.8, *J* = 1.7 Hz, 1H), 7.84 (s, 1H), 7.31 (d, *J* = 7.8 Hz, 1H), 2.51 (s, 6H), 2.40 (s, 3H), 2.36 (s, 3H) ppm. ¹³C{¹H} NMR (101 MHz, CDCl₃) δ_{C} 142.7, 140.8, 139.0, 137.7, 134.9, 130.5, 128.8, 128.7, 128.3, 125.0, 20.6, 20.5, 20.2, 19.9 ppm. UV-vis (MeCN): λ_{abs} ($\epsilon/10^4$ L mol⁻¹ cm⁻¹) 214 (4.5), 265 (3.3), 348 (1.8) nm. FTIR (solid) (ATR) ν_{max} : 2972, 2945, 2907, 1628, 1605, 1570, 1528, 1483, 1447, 1362, 1317, 1283, 1234, 1209, 1121, 1053, 1022, 1003, 991, 964, 943, 885, 862, 837, 794, 737, 716, 637, 623, 546, 488, 442, 428 cm⁻¹. HRMS (EI⁺): *m/z* calc'd for [M]⁺ C₁₈H₁₈N₂ 262.1470; found: 262.1465.

2.5.2.2 2-(3,4-dimethylphenyl)-6,7-difluoroquinoxaline (L²H)

Prepared similarly from 2-bromo-1-(3,4-dimethylphenyl)ethan-1-one (0.998 g, 4.395 mmol) and 4,5-difluoro-1,2-phenylenediamine (760 mg, 1.2 eq, 5.274 mmol) to yield the product as an off-white solid (0.593 g, 50 %). ¹H NMR (400 MHz, CDCl₃) δ_H 9.27 (s, 1H), 7.96 (d, *J* = 0.6 Hz, 1H), 7.88 (dd, *J* = 7.9, *J* = 5.5 Hz, 2H), 7.86 – 7.81 (m, 1H), 7.32 (d, *J* = 7.9 Hz, 1H), 2.40 (s, 3H), 2.37 (s, 3H) ppm. ¹³C{¹H} NMR (101 MHz, CDCl₃) δ_C 152.3, 143.6, 139.8, 138.6, 137.8, 133.8, 130.6, 128.6, 125.0, 115.0, 20.0 ppm. ¹⁹F{¹H} NMR (376 MHz, CDCl₃) δ_F -129.8 (d, ³*J*_{FF} = 20 Hz), -131.0 (d, ³*J*_{FF} = 21 Hz) ppm. UV-vis (MeCN): λ_{abs} (ε/10⁴ L mol⁻¹ cm⁻¹) 213 (5.5), 256 (2.9), 343 (1.8) nm. FTIR (solid) (ATR) ν_{max}: 3067, 2978, 2922, 1636, 1609, 1545, 1493, 1449, 1433, 1385, 1350, 1315, 1283, 1225, 1167, 1165, 1128, 1051, 1016, 988, 968, 926, 880, 862, 835, 752, 731, 710, 650, 613, 602, 546, 492, 463, 440 cm⁻¹. HRMS (EI⁺): *m/z* calc'd for [M]⁺ C₁₆H₁₂F₂N₂ 270.0969; found: 270.0970.

2.5.2.3 2-(3,4-difluorophenyl)-6,7-dimethylquinoxaline (L³H)

Prepared similarly from crude 2-bromo-1-(3,4-difluorophenyl)ethan-1-one (0.311 g, 1.320 mmol) and 4,5-dimethyl-1,2-phenylenediamine (0.216 g, 1.2 eq, 1.586 mmol) to yield the product as a pale yellow solid. (0.209 g, 58 %). ¹H NMR (400 MHz, CDCl₃) δ_H = 9.17 (s, 1H), 8.07 (ddd, *J* = 11.4, *J* = 7.7, *J* = 2.2 Hz, 1H), 7.93 – 7.89 (m, 1H), 7.89 (s, 1H), 7.86 (s, 1H), 7.37 – 7.30 (m, 1H), 2.52 (s, 6H) ppm. ¹³C{¹H} NMR (101 MHz, CDCl₃) δ_C 141.7, 141.4, 141.1, 140.8, 128.7, 128.3, 123.5, 118.1, 117.9, 116.7, 116.5, 20.5, 20.5 ppm. ¹⁹F{¹H} NMR (376 MHz, CDCl₃) δ_F -135.8 (d, ³*J*_{FF} = 21 Hz), -136.4 (d, ³*J*_{FF} = 21 Hz) ppm. UV-vis (MeCN): λ_{abs} (ε/10⁴ L mol⁻¹ cm⁻¹) 203 (3.1), 262 (3.6), 340 (1.4) nm. FTIR (solid) (ATR) ν_{max}: 3040, 2978, 2355, 1616, 1604, 1520, 1518, 1487, 1472, 1442, 1369, 1364, 1323, 1290, 1273, 1254, 1213, 1188, 1165, 1113, 1049, 1007, 1003, 976, 939, 897, 876, 829, 773, 710, 638, 583, 492, 457, 434 cm⁻¹. HRMS (EI⁺): *m/z* calc'd for [M]⁺ C₁₆H₁₂F₂N₂ 270.0969; found: 270.0969.

2.5.2.4 2-(3,4-difluorophenyl)-6,7-difluoroquinoxaline (L⁴H)

Prepared similarly from crude 2-bromo-1-(3,4-difluorophenyl)ethan-1-one (1.25 g, 5.34 mmol) and 4,5-difluoro-1,2-phenylenediamine (0.923 g, 1.2 eq, 6.404 mmol) to give the product as an off-white solid. (0.450 g, 25 %). ¹H NMR (400 MHz, CDCl₃) δ_H 9.25 (s, 1H), 8.08 (ddd, *J* = 11.2, *J* 7.6 Hz, *J* 2.2 Hz, 1H), 7.95 – 7.90 (m, 1H), 7.87 (ddd, *J* = 10.2, *J* = 8.1 Hz, *J* = 2.0 Hz, 2H), 7.40 – 7.32 (m, *J* = 9.8, 8.5 Hz, 1H) ppm. ¹³C{¹H} NMR (101 MHz, CDCl₃) δ_C 154.3, 153.4, 149.8, 142.7, 139.4,

133.3, 123.7, 118.2, 116.8, 115.1 ppm. $^{19}\text{F}\{^1\text{H}\}$ NMR (376 MHz, CDCl_3) δ_{F} -128.6 (d, $^3J_{\text{FF}} = 21$ Hz), -129.3 (d, $^3J_{\text{FF}} = 21$ Hz), -134.3 (d, $^3J_{\text{FF}} = 21$ Hz), -135.8 (d, $^3J_{\text{FF}} = 21$ Hz) ppm. UV-vis (MeCN): λ_{abs} ($\epsilon/10^4 \text{ L mol}^{-1} \text{ cm}^{-1}$) 207 (3.6), 253 (2.5), 334 (1.4) nm. FTIR (solid) (ATR) ν_{max} : 3042, 1636, 1609, 1508, 1476, 1445, 1410, 1350, 1300, 1281, 1273, 1233, 1223, 1188, 1124, 968, 901, 889, 818, 779, 731, 706, 660, 611, 581, 494, 492, 451, 399 cm^{-1} . HRMS (EI⁺): m/z calc'd for $[\text{M}]^+$ $\text{C}_{14}\text{H}_6\text{F}_4\text{N}_2$ 278.0467; found: 278.0470

2.5.2.5 2-(4-fluorophenyl)-6,7-dimethylquinoxaline (L⁵H)

Prepared similarly from 2-bromo-1-(4-difluorophenyl)ethan-1-one (1.00 g, 4.61 mmol) and 4,5-dimethyl-1,2-phenylenediamine (753 mg, 1.2 eq, 5.53 mmol) to give the product as a yellow solid. (0.58 g, 50. %) ^1H NMR (400 MHz, Acetone) δ_{H} 9.38 (s, 1H), 8.42 – 8.36 (m, 2H), 7.87 (s, 1H), 7.85 (s, 1H), 7.39 – 7.33 (m, 2H), 2.53 (s, 3H), 2.52 (s, 3H) ppm. $^{13}\text{C}\{^1\text{H}\}$ NMR (101 MHz, CDCl_3) δ_{C} 165.5, 150.2, 142.2, 141.4, 141.3, 140.7, 140.5, 129.6, 129.5, 128.7, 128.3, 116.5, 116.3, 20.6, 20.6 ppm. $^{19}\text{F}\{^1\text{H}\}$ NMR (376 MHz, CDCl_3) δ_{F} -111.2 (s). UV-vis (MeCN): λ_{abs} ($\epsilon/10^4 \text{ L mol}^{-1} \text{ cm}^{-1}$) 200 (2.9), 258 (3.3), 338 (1.3) nm. FTIR (solid) (ATR) ν_{max} : 1653, 1624, 1599, 1535, 1514, 1487, 1441, 1375, 1329, 1315, 1283, 1211, 1161, 1107, 1047, 1020, 1005, 1001, 951, 935, 887, 868, 843, 814, 795, 739, 729, 723, 675, 638, 628, 611, 594, 552, 513, 488, 457, 434, 419 cm^{-1} . HRMS (EI⁺): m/z calc'd for $[\text{M}]^+$ $\text{C}_{16}\text{H}_{13}\text{FN}_2$ 252.1063; found: 252.1063

2.5.2.6 6,7-difluoro-2-(4-fluorophenyl)quinoxaline (L⁶H)

Prepared similarly from 2-bromo-1-(4-difluorophenyl)ethan-1-one (1.00 g, 4.61 mmol) and 4,5-difluoro-1,2-phenylenediamine (0.797 g, 1.2 eq, 5.53 mmol). The product was produced as an off-white solid. (0.461 g, 39 %) ^1H NMR (400 MHz, CDCl_3) δ_{H} 9.29 (s, 1H), 8.24 – 8.17 (m, 2H), 7.93 – 7.85 (m, 2H), 7.34 – 7.23 (m, 2H) ppm. $^{13}\text{C}\{^1\text{H}\}$ NMR (101 MHz, CDCl_3) δ_{C} 165.9, 163.4, 151.2, 151.0, 143.2, 143.2, 139.0, 138.9, 132.5, 129.7, 129.7, 116.7, 116.5, 115.4, 115.2, 115.0 ppm. $^{19}\text{F}\{^1\text{H}\}$ NMR (376 MHz, CDCl_3) δ_{F} -109.9 (s), -129.2 (d, $^3J_{\text{FF}} = 21$ Hz), -130.1 (d, $^3J_{\text{FF}} = 21$ Hz). UV-vis (MeCN): λ_{abs} ($\epsilon/10^4 \text{ L mol}^{-1} \text{ cm}^{-1}$) 202 (3.4), 249 (2.1), 330 (1.2) nm. FTIR (solid) (ATR) ν_{max} : 3042, 1632, 1603, 1501, 1441, 1440, 1350, 1310, 1300, 1285, 1223, 1204, 1175, 1155, 1132, 1103, 1040, 1011, 955, 924, 885, 876, 868, 831, 787, 756, 731, 718, 650, 642, 608, 579, 509, 488, 451, 442 cm^{-1} . HRMS (EI⁺): m/z calc'd for $[\text{M}]^+$ $\text{C}_{14}\text{H}_7\text{F}_3\text{N}_2$ 261.0640; found: 261.0641.

2.5.3 Synthesis of cyclometalated Ir(III) complexes

2.5.3.1 Synthesis of Ir(III) μ -chloro bridged dimers:

The chloride-bridged dimers, $[(L^n)_2Ir(\mu-Cl)_2Ir(L^n)_2]$, were synthesised by the Nonoyama route¹⁰. $IrCl_3 \cdot xH_2O$ and L^nH (2.0 eq, 0.881 mmol) were dissolved in 2-methoxyethanol and distilled water (3:1) (20 mL) and the mixture was stirred at reflux under a nitrogen atmosphere for 48 h. The reaction mixture was cooled to room temperature and precipitated by the addition of deionised water (30 mL). The solids were collected by filtration under reduced pressure, washed with water, to give the crude products as orange solids. Insoluble competing reaction products were removed by dissolving the desired dimeric species in dichloromethane (50 mL). The DCM solution was dried over $MgSO_4$, and the solvent removed *in vacuo* to give dark red solids, which were used in subsequent steps without further purification or characterisation.

2.5.3.2 $[Ir(L^1)_2(bpy)]PF_6$

$[(L^1)_2Ir(\mu-Cl)_2Ir(L^1)_2]$ (0.179 g, 0.119 mmol) and 2,2'-bipyridine (0.041 g, 2.2 eq, 0.263 mmol) were dissolved in 2-methoxyethanol (20 mL) and heated to 125 °C for 48 h under a nitrogen atmosphere. Upon cooling, saturated NH_4PF_6 solution was added, and the product precipitated as the PF_6^- salt. The product was purified by silica gel column chromatography (DCM / MeOH, 95:5), collecting the first red band that eluted. The solvent was removed *in vacuo* and then product dissolved in a minimum amount of CH_2Cl_2 and recrystallized with diethyl ether. The product was filtered under reduced pressure and dried in an oven overnight to yield a red solid (23 mg, 10 %). 1H NMR (500 MHz, $CDCl_3$) δ_H 9.36 (s, 2H), 8.53 (d, $J = 6.8$ Hz, 2H), 8.10-8.05 (m, 2H), 8.01 (d, $J = 4.9$ Hz, 2H), 7.75 (s, 2H), 7.40-7.45 (m, 2H), 6.70 (s, 2H), 6.14 (s, 2H), 2.33 (s, 6H), 2.27 (s, 6H), 1.95 (s, 6H), 1.75 (s, 6H) ppm. ^{13}C NMR (126 MHz, $CDCl_3$) δ_C 162.2, 155.9, 148.9, 147.9, 143.2, 141.8, 141.4, 140.9, 140.8, 140.5, 140.3, 139.6, 135.1, 131.9, 129.8, 128.7, 127.8, 125.5, 123.0, 20.4, 20.3, 19.8, 19.7 ppm. UV-vis (MeCN): λ_{abs} ($\epsilon/10^4$ L mol⁻¹ cm⁻¹) 267 (3.6), 293 (3.1), 378 (1.7), 485 (0.4) nm. FTIR (solid) (ATR) ν_{max} : 1597, 1518, 1447, 1342, 1314, 1281, 1215, 1148, 1074, 1005, 835 (PF_6^-), 768, 662, 640, 556 (PF_6^-), 442, 426, 417, 403 cm⁻¹. m/z calc'd for $C_{46}H_{42}IrN_6$ 871.3100; found: 871.3391 $[M - PF_6]^+$.

2.5.3.3 [Ir(L²)₂(bpy)]PF₆

Prepared as above from [(L²)₂Ir(μ-Cl)₂Ir(L²)₂] (40 mg, 0.026 mmol) and 2,2'-bipyridine (9 mg, 2.2 eq, 0.057 mmol) to yield a red solid (10 mg, 19 %). ¹H NMR (500 MHz, CDCl₃) δ_H 9.46 (s, 2H), 8.52 (d, *J* = 8.1 Hz, 2H), 8.15 – 8.11 (m, 2H), 8.00 – 7.98 (m, 2H), 7.92 (s, 2H), 7.84 (dd, *J* = 9.3, 8.3 Hz, 2H), 7.54 (ddd, *J* = 7.6, 5.5, 1.2 Hz, 2H), 6.73 (dd, *J* = 11.8, 7.5 Hz, 2H), 6.12 (s, 2H), 2.29 (s, 6H), 1.99 (s, 6H) ppm. ¹⁹F{¹H} NMR (376 MHz, CDCl₃) δ_F -72.6 (d, ¹*J*_{PF} = 711 Hz, PF₆⁻), -123.8 (d, ³*J*_{FF} = 22 Hz), -128.6 (d, ³*J*_{FF} = 22 Hz) ppm. ¹³C NMR (101 MHz, Acetone) δ 156.7, 150.7, 149.7, 145.1, 143.6, 141.8, 141.4, 136.1, 133.0, 130.3, 130.1, 126.0, 111.6, 20.1, 19.5 ppm. UV-vis (MeCN): λ_{abs} (ε/10⁴ L mol⁻¹ cm⁻¹) 266 (3.6), 292 (3.1), 373 (2.1), 518 (0.4) nm. FTIR (solid) (ATR) ν_{max}: 1599, 1523, 1506, 1446, 1396, 1328, 1240, 1151, 1006, 922, 837 (PF₆⁻), 768, 736, 638, 623, 557 (PF₆⁻), 484, 435, 422, 405 cm⁻¹. HRMS (EI+): *m/z* calc'd for C₄₂H₃₀F₄N₆Ir 885.2074; found: 885.2098 [M – PF₆]⁺.

2.5.3.4 [Ir(L⁵)₂(bpy)]PF₆

Prepared as above from [(L⁵)₂Ir(μ-Cl)₂Ir(L⁵)₂] (320 mg, 0.219 mmol) and 2,2'-bipyridine (75 mg, 2.2 eq, 0.482 mmol) to yield an orange solid (27 mg, 16 %). ¹H NMR (400 MHz, CD₃CN) δ_H 9.50 (s, 2H), 8.32 (dd, *J* = 8.7, *J* = 5.6 Hz, 2H), 8.25 (d, *J* = 8.2 Hz, 2H), 8.15 (d, *J* = 5.7 Hz, 2H), 8.02 – 8.07 (m, 2H), 7.79 (s, 2H), 7.53 – 7.58 (m, 2H), 7.05 – 6.99 (m, 2H), 6.78 (s, 2H), 6.19 (dd, *J* = 9.5, 2.3 Hz, 2H), 2.31 (s, 6H), 1.76 (s, 6H) ppm. ¹³C{¹H} NMR (101 MHz, CD₃CN) δ_C 156.5, 150.4, 143.8, 142.2, 142.0, 141.2, 130.6, 130.0, 125.6, 124.0, 20.3, 19.7 ppm. ¹⁹F{¹H} NMR (376 MHz, CDCl₃) δ_F -72.6 (d, ¹*J*_{PF} = 711 Hz), 103.9 (s) ppm. UV-vis (MeCN): λ_{abs} (ε/10⁴ L mol⁻¹ cm⁻¹) 207 (6.7), 286 (24.9), 372 (2.4), 450 (0.7) nm. FTIR (solid) (ATR) ν_{max} : 1587, 1566, 1526, 1445, 1341, 1258, 1196, 1123, 1065, 851 (PF₆⁻), 810, 775, 735, 656, 557 (PF₆⁻), 459, 446, 409 cm⁻¹. HRMS (EI+): *m/z* calc'd for C₄₂H₃₂F₂IrN₆ 849.2263; found: 849.2287 [M – PF₆]⁺.

2.6 References

- 1 A. Byrne, C. S. Burke and T. E. Keyes, *Chem. Sci.*, 2016, **7**, 6551–6562.
- 2 A. H. Day, M. H. Übler, H. L. Best, E. Lloyd-Evans, R. J. Mart, I. A. Fallis, R. K. Allemann, E. A. H. Al-Wattar, N. I. Keymer, N. J. Buurma and S. J. A. Pope, *Chem. Sci.*, 2020, **11**, 1599–1606.
- 3 H. Xia, C. Zhang, X. Liu, S. Qiu, P. Lu, F. Shen, J. Zhang and Y. Ma, *J. Phys. Chem. B*, 2004, **108**, 3185–3190.
- 4 H. Xu, R. Chen, Q. Sun, W. Lai, Q. Su, W. Huang and X. Liu, *Chem. Soc. Rev.*, 2014, **43**, 3259–3302.
- 5 T. Yang, A. Xia, Q. Liu, M. Shi, H. Wu, L. Xiong, C. Huang and F. Li, *J. Mater. Chem.*, 2011, **21**, 5360–5367.
- 6 A. F. Henwood and E. Zysman-Colman, *Chem. Commun.*, 2017, **53**, 807–826.
- 7 J. Li, P. I. Djurovich, B. D. Alleyne, M. Yousufuddin, N. N. Ho, J. C. Thomas, J. C. Peters, R. Bau and M. E. Thompson, *Inorg. Chem.*, 2005, **44**, 1713–1727.
- 8 D. Di Censo, S. Fantacci, F. De Angelis, C. Klein, N. Evans, K. Kalyanasundaram, H. J. Bolink, M. Grätzel and M. K. Nazeeruddin, *Inorg. Chem.*, 2008, **47**, 980–989.
- 9 J. M. Thomsen, D. L. Huang, R. H. Crabtree and G. W. Brudvig, *Dalton Trans.*, 2015, **44**, 12452–12472.
- 10 M. Nonoyama, *Bull. Chem. Soc. Jpn.*, 1974, **47**, 767–768.
- 11 N. N. Greenwood and A. Earnshaw, *Chemistry of the elements*, Butterworth-Heinemann, Oxford ; Boston, 2nd ed., 1997.
- 12 A. B. Tamayo, B. D. Alleyne, P. I. Djurovich, S. Lamansky, I. Tsyba, N. N. Ho, R. Bau and M. E. Thompson, *J. Am. Chem. Soc.*, 2003, **125**, 7377–7387.
- 13 S. Lamansky, P. Djurovich, D. Murphy, F. Abdel-Razzaq, R. Kwong, I. Tsyba, M. Bortz, B. Mui, R. Bau and M. E. Thompson, *Inorg. Chem.*, 2001, **40**, 1704–1711.
- 14 D. Ma, L. Duan and Y. Qiu, *Dalton Trans.*, 2015, **44**, 8521–8528.
- 15 C. D. Sunesh, M. Chandran, S. Ok and Y. Choe, *Mol. Cryst. Liq. Cryst.*, 2013, **584**, 131–138.
- 16 R. A. Smith, E. C. Stokes, E. E. Langdon-Jones, J. A. Platts, B. M. Kariuki, A. J. Hallett and S. J. A. Pope, *Dalton Trans.*, 2013, **42**, 10347–10357.
- 17 G. E. Schneider, H. J. Bolink, E. C. Constable, C. D. Ertl, C. E. Housecroft, A. Pertegàs, J. A. Zampese, A. Kanitz, F. Kessler and S. B. Meier, *Dalton Trans.*, 2013, **43**, 1961–1964.
- 18 C. E. Housecroft and E. C. Constable, *Coord. Chem. Rev.*, 2017, **350**, 155–177.
- 19 B. Schmid, F. O. Garces and R. J. Watts, *Inorg. Chem.*, 1994, **33**, 9–14.
- 20 C. Adachi, R. C. Kwong, P. Djurovich, V. Adamovich, M. A. Baldo, M. E. Thompson and S. R. Forrest, *Appl. Phys. Lett.*, 2001, **79**, 2082–2084.
- 21 E. Baranoff and B. F. E. Curchod, *Dalton Trans.*, 2015, **44**, 8318–8329.
- 22 K. A. King, P. J. Spellane and R. J. Watts, *J. Am. Chem. Soc.*, 1985, **107**, 1431–1432.
- 23 T. Hofbeck and H. Yersin, *Inorg. Chem.*, 2010, **49**, 9290–9299.
- 24 Y. Ohsawa, S. Sprouse, K. A. King, M. K. DeArmond, K. W. Hanck and R. J. Watts, *J. Phys. Chem.*, 1987, **91**, 1047–1054.
- 25 R. D. Costa, E. Ortí, H. J. Bolink, S. Graber, S. Schaffner, M. Neuburger, C. E. Housecroft and E. C. Constable, *Adv. Funct. Mater.*, 2009, **19**, 3456–3463.

- 26 A. Sinopoli, C. J. Wood, E. A. Gibson and P. I. P. Elliott, *Dyes Pigments*, 2017, **140**, 269–277.
- 27 S. Ladouceur and E. Zysman-Colman, *Eur. J. Inorg. Chem.*, 2013, **2013**, 2985–3007.
- 28 W. Wei, S. A. M. Lima, P. I. Djurovich, A. Bossi, M. T. Whited and M. E. Thompson, *Polyhedron*, 2018, **140**, 138–145.
- 29 E. Kabir, Y. Wu, S. Sittel, B.-L. Nguyen and T. S. Teets, *Inorg. Chem. Front.*, 2020, **7**, 1362–1373.
- 30 D. S. M. Ravinson and M. E. Thompson, *Mater. Horiz.*, 2020, **7**, 1210–1217.
- 31 T. Tsutsui, M.-J. Yang, M. Yahiro, K. Nakamura, T. Watanabe, T. Tsuji, Y. Fukuda, T. Wakimoto and S. Miyaguchi, *Jpn. J. Appl. Phys.*, 1999, **38**, L1502.
- 32 R. H. Friend, R. W. Gymer, A. B. Holmes, J. H. Burroughes, R. N. Marks, C. Taliani, D. D. C. Bradley, D. A. D. Santos, J. L. Brédas, M. Lögdlund and W. R. Salaneck, *Nature*, 1999, **397**, 121–128.
- 33 M. A. Baldo, D. F. O'Brien, Y. You, A. Shoustikov, S. Sibley, M. E. Thompson and S. R. Forrest, *Nature*, 1998, **395**, 151–154.
- 34 M. A. Baldo, D. F. O'Brien, M. E. Thompson and S. R. Forrest, *Phys. Rev. B*, 1999, **60**, 14422–14428.
- 35 C. Adachi, M. A. Baldo, M. E. Thompson and S. R. Forrest, *J. Appl. Phys.*, 2001, **90**, 5048–5051.
- 36 A. F. Henwood and E. Zysman-Colman, in *Iridium(III) in Optoelectronic and Photonics Applications*, ed. E. Zysman-Colman, John Wiley & Sons, Ltd, 1st edn., 2017, vol. 1 chap. 7, pp. 275–357.
- 37 E. Zysman-Colman, Ed., *Iridium(III) in Optoelectronic and Photonics Applications*, John Wiley & Sons, Ltd, Chichester, UK, 2017.
- 38 J. D. Slinker, A. A. Gorodetsky, M. S. Lowry, J. Wang, S. Parker, R. Rohl, S. Bernhard and G. G. Malliaras, *J. Am. Chem. Soc.*, 2004, **126**, 2763–2767.
- 39 Y. Shen, D. D. Kuddes, C. A. Naquin, T. W. Hesterberg, C. Kusmierz, B. J. Holliday and J. D. Slinker, *Appl. Phys. Lett.*, 2013, **102**, 203305.
- 40 S. T. Parker, J. D. Slinker, M. S. Lowry, M. P. Cox, S. Bernhard and G. G. Malliaras, *Chem. Mater.*, 2005, **17**, 3187–3190.
- 41 H. Na, P. Lai, L. M. Cañada and T. S. Teets, *Organometallics*, 2018, **37**, 3269–3277.
- 42 A. F. Rausch, M. E. Thompson and H. Yersin, *Inorg. Chem.*, 2009, **48**, 1928–1937.
- 43 J. Liu, J. Oliva, K. Tong, F. Zhao, D. Chen and Q. Pei, *Sci. Rep.*, 2017, **7**, 1524.
- 44 R. Bai, X. Meng, X. Wang and L. He, *Adv. Funct. Mater.*, 2020, 1907169.
- 45 J. Zhang, L. Zhou, H. A. Al-Attar, K. Shao, L. Wang, D. Zhu, Z. Su, M. R. Bryce and A. P. Monkman, *Adv. Funct. Mater.*, 2013, **23**, 4667–4677.
- 46 H. Y. Zhang, Z. L. Zhang, K. Q. Ye, J. Y. Zhang and Y. Wang, *Adv. Mater.*, 2006, **18**, 2369–2372.
- 47 A. B. Tamayo, S. Garon, T. Sajoto, P. I. Djurovich, I. M. Tsyba, R. Bau and M. E. Thompson, *Inorg. Chem.*, 2005, **44**, 8723–8732.
- 48 M. Maestri, D. Sandrini, V. Balzani, U. Maeder and A. Von Zelewsky, *Inorg. Chem.*, 1987, **26**, 1323–1327.
- 49 Q. Mei, J. Shu, S. Zhou, H. Zhou, B. Tong and S. Wang, *Inorg. Chem. Commun.*, 2018, **98**, 62–67.
- 50 C.-N. Ko, C. Yang, S. Lin, S. Li, Z. Dong, J. Liu, S. M.-Y. Lee, C.-H. Leung and D.-L. Ma, *Biosens. Bioelectron.*, 2017, **94**, 575–583.
- 51 Q. Tang, X. Zhang, H. Cao, G. Chen, H. Huang, P. Zhang and Q. Zhang, *Dalton Trans.*, 2019, **48**, 7728–7734.
- 52 K. Y. Zhang, P. Gao, G. Sun, T. Zhang, X. Li, S. Liu, Q. Zhao, K. K.-W. Lo and W. Huang, *J. Am. Chem. Soc.*, 2018, **140**, 7827–7834.

- 53 J. S. Nam, M.-G. Kang, J. Kang, S.-Y. Park, S. J. C. Lee, H.-T. Kim, J. K. Seo, O.-H. Kwon, M. H. Lim, H.-W. Rhee and T.-H. Kwon, *J. Am. Chem. Soc.*, 2016, **138**, 10968–10977.
- 54 E. Baggaley, J. A. Weinstein and J. A. G. Williams, *Coord. Chem. Rev.*, 2012, **256**, 1762–1785.
- 55 Q. Zhao, M. Yu, L. Shi, S. Liu, C. Li, M. Shi, Z. Zhou, C. Huang and F. Li, *Organometallics*, 2010, **29**, 1085–1091.
- 56 F. Lu and T. Nabeshima, *Dalton Trans.*, 2014, **43**, 9529–9536.
- 57 S. Liu, H. Liang, K. Y. Zhang, Q. Zhao, X. Zhou, W. Xu and W. Huang, *Chem. Commun.*, 2015, **51**, 7943–7946.
- 58 N. Hasebe, Y. Deguchi, S. Murayama, T. Yoshihara, H. Horiuchi, T. Okutsu and S. Tobita, *J. Photochem. Photobiol. Chem.*, 2016, **324**, 134–144.
- 59 R. Bevernaegie, B. Doix, E. Bastien, A. Diman, A. Decottignies, O. Feron and B. Elias, *J. Am. Chem. Soc.*, 2019, **141**, 18486–18491.
- 60 S. Yi, Z. Lu, J. Zhang, J. Wang, Z. Xie and L. Hou, *ACS Appl. Mater. Interfaces*, 2019, **11**, 15276–15289.
- 61 S. B. Patel, B. D. Patel, C. Pannecouque and H. G. Bhatt, *Eur. J. Med. Chem.*, 2016, **117**, 230–240.
- 62 A. R. Al-Marhabi, H.-A. S. Abbas and Y. A. Ammar, *Molecules*, 2015, **20**, 19805–19822.
- 63 M. S. Abdelfattah, T. Kazufumi and M. Ishibashi, *J. Nat. Prod.*, 2010, **73**, 1999–2002.
- 64 A. K. Parhi, Y. Zhang, K. W. Saionz, P. Pradhan, M. Kaul, K. Trivedi, D. S. Pilch and E. J. LaVoie, *Bioorg. Med. Chem. Lett.*, 2013, **23**, 4968–4974.
- 65 F. A. R. Rodrigues, I. da S. Bomfim, B. C. Cavalcanti, C. do Ó. Pessoa, J. L. Wardell, S. M. S. V. Wardell, A. C. Pinheiro, C. R. Kaiser, T. C. M. Nogueira, J. N. Low, L. R. Gomes and M. V. N. de Souza, *Bioorg. Med. Chem. Lett.*, 2014, **24**, 934–939.
- 66 M. M. F. Ismail, Y. A. Ammar, M. K. Ibrahim, H. S. A. El-Zahaby and S. S. Mahmoud, *ArzneimForschDrugRes*, 2005, **55**, 738–743.
- 67 M. M. Ali, M. M. F. Ismail, M. S. A. El-Gaby, M. A. Zahran and Y. A. Ammar, *Molecules*, 2000, **5**, 864–873.
- 68 A. Kamal, K. Suresh Babu, S. Faazil, S. M. Ali Hussaini and A. Basha Shaik, *RSC Adv.*, 2014, **4**, 46369–46377.
- 69 Z.-S. Huang, X.-F. Zang, T. Hua, L. Wang, H. Meier and D. Cao, *ACS Appl. Mater. Interfaces*, 2015, **7**, 20418–20429.
- 70 L.-N. Yang, S.-C. Li, Z.-S. Li and Q.-S. Li, *RSC Adv.*, 2015, **5**, 25079–25088.
- 71 World Intellectual Property Organization, WO1999051688A1, 1999.
- 72 P. Gąsiorowski, M. Matusiewicz, E. Gondek, M. Pokladko-Kowar, P. Armatys, K. Wojtasik, A. Danel, T. Uchacz and A. V. Kityk, *Dyes Pigments*, 2018, **151**, 380–384.
- 73 M. Yasa, S. Surmeli, T. Depci, L. Toppare and S. O. Hacıoglu, *Macromol. Chem. Phys.*, 2020, **221**, 1900470.
- 74 C. Zhou, X. Zhang, G. Pan, X. Tian, S. Xiao, H. Liu, S. Zhang and B. Yang, *Org. Electron.*, 2019, **75**, 105414.
- 75 S. V. More, M. N. V. Sastry, C.-C. Wang and C.-F. Yao, *Tetrahedron Lett.*, 2005, **46**, 6345–6348.
- 76 D. J. Brown and E. C. Taylor, *Quinoxalines: Supplement II*, John Wiley & Sons, Hoboken, NJ, 2004, vol. 61.
- 77 S. Y. Kim, K. H. Park and Y. K. Chung, *Chem. Commun.*, 2005, 1321–1323.

- 78 H. M. Meshram, G. Santosh Kumar, P. Ramesh and B. Chennakesava Reddy, *Tetrahedron Lett.*, 2010, **51**, 2580–2585.
- 79 J.-P. Wan, S.-F. Gan, J.-M. Wu and Y. Pan, *Green Chem.*, 2009, **11**, 1633–1637.
- 80 B. Madhav, S. Narayana Murthy, V. Prakash Reddy, K. Rama Rao and Y. V. D. Nageswar, *Tetrahedron Lett.*, 2009, **50**, 6025–6028.
- 81 H. Yuan, K. Li, Y. Chen, Y. Wang, J. Cui and B. Chen, *Synlett*, 2013, **24**, 2315–2319.
- 82 Z. Hao, K. Zhang, P. Wang, X. Lu, Z. Lu, W. Zhu and Y. Liu, *Inorg. Chem.*, 2020, **59**, 332–342.
- 83 X.-Q. Zhou, Y. Li, Y.-B. Sun and H.-X. Zhang, *J. Korean Chem. Soc.*, 2011, **55**, 354–363.
- 84 F.-M. Hwang, H.-Y. Chen, P.-S. Chen, C.-S. Liu, Y. Chi, C.-F. Shu, F.-I. Wu, P.-T. Chou, S.-M. Peng and G.-H. Lee, *Inorg. Chem.*, 2005, **44**, 1344–1353.
- 85 D. Schneidenbach, S. Ammermann, M. Debeaux, A. Freund, M. Zöllner, C. Daniliuc, P. G. Jones, W. Kowalsky and H.-H. Johannes, *Inorg. Chem.*, 2010, **49**, 397–406.
- 86 E. E. Langdon-Jones, A. J. Hallett, J. D. Routledge, D. A. Crole, B. D. Ward, J. A. Platts and S. J. A. Pope, *Inorg. Chem.*, 2013, **52**, 448–456.
- 87 S. J. Pope, T. Stonelake, K. Phillips, S. Coles, P. Horton, S. Keane, E. Stokes, I. Fallis, J. Beames, J. Zhao, K. Chen, Y. Hou, A. Hallett and S. O’Kell, *Chem. – Eur. J.*, , DOI:10.1002/chem.201801007.
- 88 T. M. Stonelake, K. A. Phillips, H. Y. Otaif, Z. C. Edwardson, P. N. Horton, S. J. Coles, J. M. Beames and S. J. A. Pope, *Inorg. Chem.*, 2020, **59**, 2266–2277.
- 89 S. J. Pasaribu and L. R. Williams, *Aust. J. Chem.*, 1973, **26**, 1327–1331.
- 90 S. Paul, V. Gupta, R. Gupta and A. Loupy, *Tetrahedron Lett.*, 2003, **44**, 439–442.
- 91 S. Klod and E. Kleinpeter, *J. Chem. Soc. Perkin Trans. 2*, 2001, 1893–1898.
- 92 C. S. Wannere and P. von R. Schleyer, *Org. Lett.*, 2003, **5**, 605–608.
- 93 A. Brouwer, *Pure Appl. Chem.*, 2011, **83**, 2213–2228.
- 94 J. R. Lakowicz, *Principles of Fluorescence Spectroscopy*, Springer, New York, 3rd ed., 2006.
- 95 C. Würth, M. Grabolle, J. Pauli, M. Spieles and U. Resch-Genger, *Nat. Protoc.*, 2013, **8**, 1535–1550.
- 96 S. A. Fitzgerald, H. Y. Otaif, C. E. Elgar, N. Sawicka, P. N. Horton, S. J. Coles, J. M. Beames and S. J. A. Pope, *Inorg. Chem.*, , DOI:10.1021/acs.inorgchem.1c02121.
- 97 D.-L. Ma, H. P. Ng, S.-Y. Wong, K. Vellaisamy, K.-J. Wu and C.-H. Leung, *Dalton Trans.*, 2018, **47**, 15278–15282.
- 98 G. M. Sheldrick, *Acta Crystallogr. Sect. Found. Adv.*, 2015, **71**, 3–8.
- 99 O. V. Dolomanov, L. J. Bourhis, R. J. Gildea, J. A. K. Howard and H. Puschmann, *J. Appl. Crystallogr.*, 2009, **42**, 339–341.
- 100 G. M. Sheldrick, *Acta Crystallogr. Sect. C Struct. Chem.*, 2015, **71**, 3–8.

**Chapter 3 - Iridium(III) Complexes of
2-(Naphthyl)Quinoxalines.**

3.1 Introduction

Chapter 2 demonstrated the quick and easy synthesis of quinoxaline ligands via dioxane dibromide. The work in this chapter builds upon the bromoacetal ligand synthesis, with naphthylquinoxaline ligands designed to induce a red shift through extended conjugation.

3.1.1 Extended conjugation in ligand design.

As seen in Chapter 2, the tuneability of the emission from Ir(III) complexes is linked to the ligand design. The complex frontier orbitals can contain a contribution from the ligands, either in the cyclometalating ligands or the ancillary ligand in the case of heteroleptic complexes. Typically the overall complex HOMO consists of a mixture of the Ir 5d orbitals and the aryl group π orbitals on the cyclometalating ligands¹, while the LUMO is predominantly on the ancillary ligand², or the heterocyclic rings of the cyclometalating ligand³. One common practice to induce a bathochromic shift in emission is by extending the conjugation of the cyclometalating ligand, such as on the heterocyclic component (Figure 3.1) where emission ranges from 585 nm for the [Ir(ppy)₂(bpy)]PF₆ up to the near IR emitters at 760 nm utilising the 2-phenylbenzo[*g*]quinoline cyclometalating ligand.

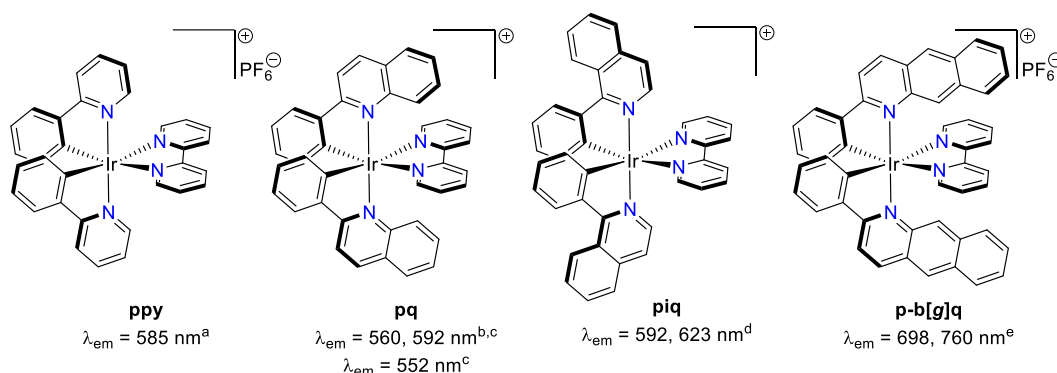


Figure 3.1 – The effect on emission of extending the cyclometalating ligand. ^a Measured in aerated MeCN ², ^b Measured in aerated MeOH ⁴, ^c Measured in aerated MeCN ⁵, ^d Degassed MeCN ⁶, ^e Measured in degassed DCM ⁷.

A second, less investigated approach focuses on extending the conjugation in the aryl group. For example, the *tris*-cyclometalated complex of 2-(naphth-1-yl)pyridine (Figure 3.2 - left) exhibits a bathochromic shift in emission of 72 nm in comparison to the [Ir(ppy)₃] complex.⁸ Heteroleptic, neutral acac complexes have been used in research as the emissive layer in OLED devices. The model green emitting complex, [Ir(ppy)₂(acac)] exhibits PL at 528 nm (deaerated MeCN solution) and EL at 525 nm when built into an OLED device.⁹ In comparison, when the aryl conjugation is extended to a naphthyl group, the emission, both PL and EL, is

bathochromically shifted. In the complex $[\text{Ir}(\text{2npy})_2(\text{acac})]$ (where $\text{2npy} = 2\text{-(naphth-2-yl)pyridine}$ – see Figure 3.2 – right) the PL $\lambda_{\text{max}} = 550 \text{ nm}$ (DCM), and EL $\lambda_{\text{max}} = 551 \text{ nm}$.¹⁰ In comparison, the 1-naphthyl complex, $[\text{Ir}(\text{1npy})_2(\text{acac})]$ (Figure 3.2 – middle) the PL and EL are even further bathochromically shifted, with the PL $\lambda_{\text{max}} = 600 \text{ nm}$ ¹¹, and the EL $\lambda_{\text{max}} = 595 \text{ nm}$ ¹².

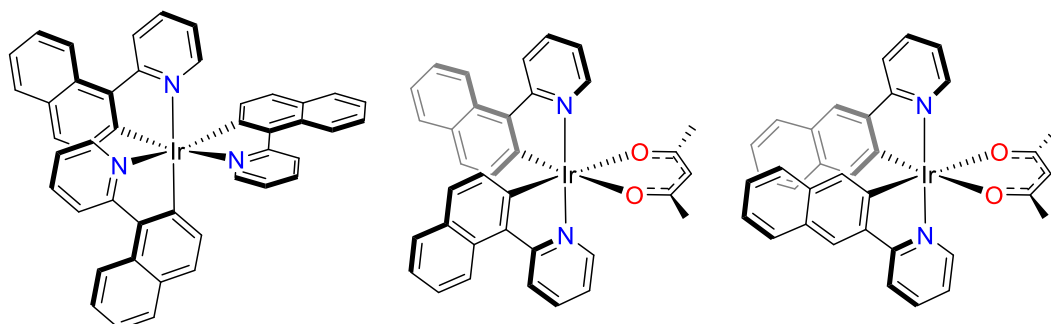


Figure 3.2 – Neutral complexes investigating increased conjugation in the aryl ring of the cyclometalating ligand. Left: $\text{Ir}(\text{1npy})_3$ from Wallentin *et al*.⁸ Middle: $[\text{Ir}(\text{1npy})_2(\text{acac})]$ from Cao *et al*.^{11,12} Right $[\text{Ir}(\text{2npy})_2(\text{acac})]$ from Lee *et al*.¹⁰

The 2014 paper from Sun *et al* focuses on the extended conjugation on heteroleptic cationic complexes, $[\text{Ir}(\text{C}^{\wedge}\text{N})_2(\text{bpy})]\text{PF}_6$ ¹³ (Figure 3.3). Of the seven complexes synthesised, two complexes were targeted to compare the emission from the structural isomers of the 2-(naphthyl)pyridine ligand. Similar to the neutral acac complexes, both isomers exhibited different λ_{max} emission profiles, although with less of a bathochromic shift that previous in comparison to the ppy derivative, where $[\text{Ir}(\text{ppy})_2(\text{bpy})]\text{PF}_6$ has its $\lambda_{\text{max}} = 685 \text{ nm}$. While the λ_{max} of $[\text{Ir}(\text{1npy})_2(\text{bpy})]\text{PF}_6$ in MeCN solution is 583 nm, the peak is very broad with a shoulder occurring at 620 nm. On comparison, the λ_{max} of $[\text{Ir}(\text{2npy})_2(\text{bpy})]\text{PF}_6$ in MeCN solution is 609 nm, and only a single peak. Sun *et al* also observed a difference in lifetimes, with the 1npy complex having a lifetime in degassed MeCN of 3.8 μs , and the 2npy complex having a lifetime of 0.1 μs , which is attributed to varying degrees of $^3\pi-\pi$ and $^3\text{MLCT}$ contributions in the excited states.

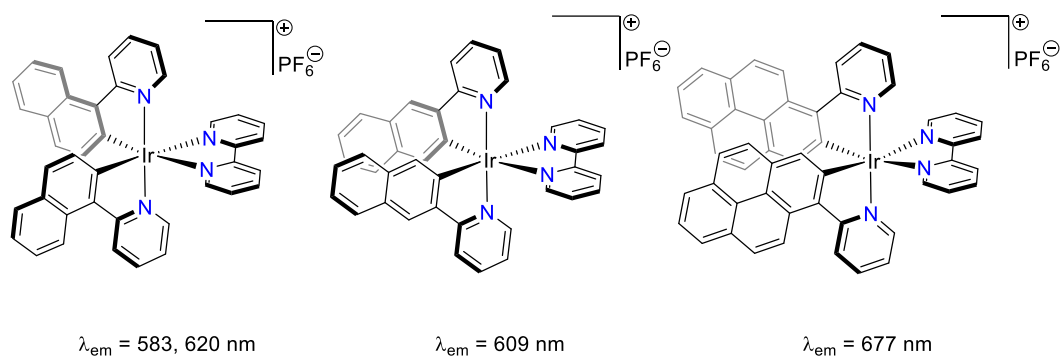


Figure 3.3 – Three complexes synthesised and characterised by Sun *et al*¹³ to explore the effects of conjugation in the aryl group of the cyclometalating ligand in cationic emitters. Emission recorded in degassed MeCN solutions.

Interest in extending conjugation of the aryl group doesn't end with naphthalene with examples including corannulene¹⁴, fluorene¹⁵ or pyrene, with the latter seen as the bpy complex from Sun *et al* in Figure 3.3. Pyrene is known for its relatively long fluorescent lifetimes and high quantum yields (0.65 in cyclohexane¹⁶), as well as accessible triplet excited states¹⁷. In a 2013 study, Beeby *et al* cyclometalated two different ligands featuring isomers of 2-(pyrene)pyridine into neutral acac complexes¹⁸. Here the complex $[\text{Ir}(1\text{pyr-py})_2(\text{acac})]$ is shown to emit at 680 nm in degassed MeCN with a lifetime of 2.5 μs , while the corresponding complex $[\text{Ir}(2\text{pyr-py})_2(\text{acac})]$ emits at 623 nm in MeCN with a lifetime of 11.6 μs , which is sensitive to the solvent used with lifetimes above 50 μs seen in toluene and EPA. It was found that the complexes mainly underwent ³LC emission, with the pyren-1-yl ligand displaying unfavourable steric interactions.

3.2 Aims

This work set out to synthesise and characterise a series of novel *bis*-cyclometalated iridium (III) complexes based around the 2-naphthyl quinoxaline ligand framework. The complexes allowed an investigation into the emissive properties based around the different structural isomers of the 1-naphthyl and 2-naphthyl ligand systems, as well as a systematic investigation onto the effects on emission from the addition of substituents around the naphthyl ring by either the electron withdrawing fluoro group, or an electron donating methoxy group.

3.3 Results and Discussion

3.3.1 Ligand synthesis and characterisation

A series of ligands was synthesised to investigate the effects of the different isomers of naphthalene and the effects of substitution on emission wavelength. First, a functionalised acetonaphthone underwent a selective electrophilic mono-bromination using 1.2 equivalents of dioxane dibromide, following literature methods.¹⁹ α -Bromo ketones were then reacted with 1,2-diaminobenzene to form the desired quinoxaline ligands (Figure 3.4) in good yields.

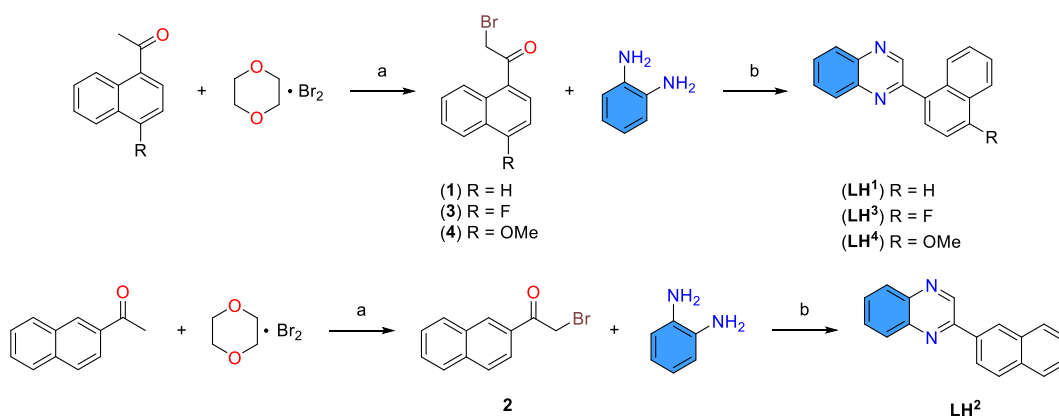


Figure 3.4 - Synthetic route used for ligand synthesis: a: 1,4-dioxane, dropwise addition, 2 hours, room temperature; b: Ethanol, 24 hours, 78 °C.

Similar to the brominations reported in Chapter 2, reactions were monitored by TLC, and after two hours, a crude ¹H NMR spectrum. ¹H NMR spectroscopy showed around 90 % conversion when integrating the proton environments relating to the acetyl -CH₃ group, seen at ca. 2.7 ppm, comparing it to the newly formed -CH₂Br group, which is seen at ca. 4.5 ppm. The dioxane was removed *in vacuo* before triturating with cold hexanes to obtain the desired brominated products (**1-4**) as off-white solids in good yields.

Brominated products (**1-4**) were then reacted with 1,2-diaminobenzene by heating at reflux in ethanol. After 24 hours a precipitate had formed, and the reaction mixture was cooled to room temperature and the solid collected by filtration. The precipitate was washed with ice cold ethanol and dried, yielding the desired ligands (LH¹⁻⁴) in good yield which were then characterised by ¹H, ¹³C{¹H}, ¹⁹F{¹H} NMR spectroscopies and high-resolution mass spectrometry. Quinoxaline formation was confirmed by the appearance of a new singlet resonance at ca. 9.15 ppm for the 1-naphthyl derivatives and 9.50 ppm for LH². This position is assigned to the proton

in the C3 position around the quinoxaline ring, being the most downfield due to the proximity to the two imines in the heterocyclic ring. $^{19}\text{F}\{^1\text{H}\}$ NMR spectra on the brominated product **3** shows a single peak at -111.9 ppm. Upon formation of the quinoxaline, this position becomes more shielded due to the mesomeric effects of the heterocyclic group in the para position, shifting to -119.7 ppm.

3.3.2 Complex synthesis and characterisation

After successful ligand synthesis, the formation of cyclometalated Ir(III) dimers was attempted following the Nonoyama route²⁰. Briefly, two equivalents of ligand were heated at reflux with $\text{IrCl}_3 \cdot \text{H}_2\text{O}$ in 2-methoxyethanol for 48 hours. After cooling to room temperature, the reaction mixture was precipitated by addition of water and collected by filtration. Much like Chapter 2, with the mono functionalisation of the quinoxaline in the 2,3-positions, the collection flask was changed, and the desired dimeric species could be dissolved in DCM, leaving behind a dark insoluble byproduct on the filter. The filtrate was dried over MgSO_4 before the solvent was removed *in vacuo*. These dimers were used without further purification. The dimers were then split by heating in 2-methoxyethanol with two equivalents of bpy overnight before cooling to room temperature and precipitating via counter ion metathesis by the addition of an excess of aqueous $[\text{NH}_4][\text{PF}_6]$. Complexes were further purified by silica gel column chromatography, collecting the first red band eluted with 95:5 (DCM / Methanol). Combined fractions were concentrated to around 2 mL before the addition of diethyl ether to crystallise out the product. This red solid was collected on a sinter and the desired complexes could then be characterised by ^1H , $^{19}\text{F}\{^1\text{H}\}$, $^{13}\text{C}\{^1\text{H}\}$ NMR, HR MS, absorption, emission, and IR spectroscopies.

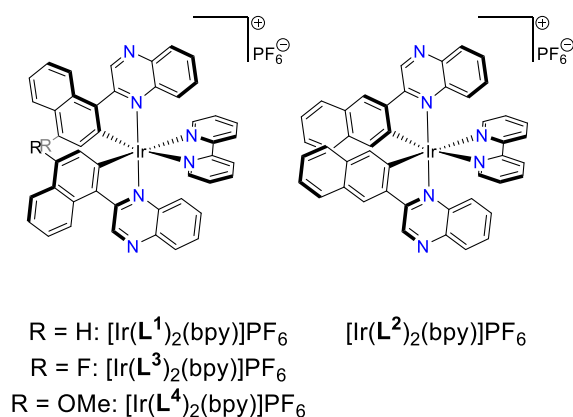


Figure 3.5 – Complexes synthesised in this chapter.

^1H NMR spectroscopy once again confirmed C_2 symmetrical complexes as expected, with equivalent environments seen on each of the cyclometalating

ligands. The proton in the C3 quinoxaline position has shifted upon chelation. In the spectrum for **LH**², this proton is seen at 9.5 ppm, and upon chelation is shifted to 9.93 ppm. In the 1-naphthyl variants, the free ligand resonances are seen at ca. 9.15 ppm, but upon chelation, [Ir(**L**¹)₂(bpy)]PF₆ shifts to 9.97 ppm from 9.17 ppm. Both [Ir(**L**³)₂(bpy)]PF₆ and [Ir(**L**⁴)₂(bpy)]PF₆ exhibit a slightly lower shift, to 9.93 and 9.84 ppm respectively. Despite the fluoro substituent being a more electronegative substituent, both substituents will exert a positive mesomeric effect in comparison to the unsubstituted complex. The combined electron withdrawing effect and weaker positive mesomeric effect of the -F substituent in comparison to the methoxy substituent is seen by the difference in the resonances between the two substituted complexes. The shifts between the free ligand and complex resonances are caused by the inductive effects of the large cationic iridium atom. The resonance *ortho*- to the site of cyclometalation is more shielded than in the free ligand. On the unsubstituted naphthyl rings, the proton resonance is seen at 6.80 ppm and 6.77 ppm for [Ir(**L**¹)₂(bpy)]PF₆ and [Ir(**L**²)₂(bpy)]PF₆ respectively. Complexes of **L**³⁻⁴ are more shielded still at 6.49 ppm and 5.94 ppm respectively. The proximity to both the Ir-C σ-bond and the methoxy group likely causes the singlet resonance in [Ir(**L**⁴)₂(bpy)]PF₆ to become the most shielded.

The methoxy group shifts from 4.1 ppm in the free ligand to 3.30 ppm upon complexation. This is again due to the proximity of the organometallic bond. A ¹⁹F{¹H} NMR spectrum was also obtained for [Ir(**L**³)₂(bpy)]PF₆. The doublet at -72.6 ppm (¹J_{FP} = 711 Hz) being associated with the hexafluorophosphate counterion, and the singlet at -112.8 ppm associated with the -F substituent.

In each isolated complex, the high-resolution mass spectrometry data provides the expected isotopic distributions and a m/z peak that is expected for [M - PF₆]⁺.

3.3.3 X-Ray crystallography

The single crystal diffraction data collection and geometry refinement was carried out by The UK National Crystallographic Service at Southampton University. A plate shaped single crystal of [Ir(**L**¹)₂(bpy)]PF₆ was grown through vapour diffusion of diethyl ether into a DCM solution of the complex. The structure included a highly disordered molecule of solvent, presumed to be diethyl ether, and as such solvent masking techniques were employed. The complex displayed the expected coordination with a *cis*-C,C and *trans*-N,N arrangement of the cyclometalating

ligands around the distorted octahedral iridium(III) centre.²¹ The repeating unit contains a single PF₆⁻ counterion to charge balance the monocationic iridium centre. There is a small degree of distortion exhibited across one of the cyclometalating ligands.

[Ir(L ¹) ₂ (bpy)]PF ₆			
Bond lengths (Å)			
Ir(1)-N(1)	2.075(3)	Ir(1)-C(1)	1.998(3)
Ir(1)-N(41)	2.163(3)	Ir(1)-N(42)	2.152(3)
Ir(1)-C(21)	2.013(8)	Ir(1)-C(21A)	2.021(11)
Ir(1)-N(21)	2.066(8)	Ir(1)-N(21A)	2.057(10)
Bond angles (°)			
N(1)-Ir(1)-N(42)	82.91(11)	C(1)-Ir(1)-N(41)	173.18(12)
N(1)-Ir(1)-N(41)	104.48(12)	C(1)-Ir(1)-N(21)	94.8(5)
N(41)-Ir(1)-N(42)	75.29(11)	C(1)-Ir(1)-C(21)	92.0(4)
N(21)-Ir(1)-N(1)	171.6(4)	C(1)-Ir(1)-N(21A)	95.7(7)
N(21)-Ir(1)-N(42)	103.7(4)	C(1)-Ir(1)-C(21A)	84.4(6)
N(21)-Ir(1)-N(41)	82.4(5)	N(21A)-Ir(1)-N(1)	173.6(7)
C(21)-Ir(1)-N(1)	95.4(4)	N(21A)-Ir(1)-N(42)	101.4(5)
C(21)-Ir(1)-N(42)	167.9(4)	N(21A)-Ir(1)-N(41)	81.3(7)
C(21)-Ir(1)-N(41)	93.6(4)	C(21A)-Ir(1)-N(1)	97.5(6)
C(21)-Ir(1)-N(21)	79.3(5)	C(21A)-Ir(1)-N(41)	100.9(6)
C(1)-Ir(1)-N(1)	78.82(14)	C(21A)-Ir(1)-N(42)	176.2(6)
C(1)-Ir(1)-N(42)	99.43(13)	C(21A)-Ir(1)-N(21A)	78.5(7)

Table 3.1 - Selected bond angles and bond lengths from refinement data for [Ir(L¹)₂(bpy)]PF₆.

Bond lengths and bond angles (Table 3.1) around the iridium centre show little difference with the phenyl quinoxalines from Chapter 2. The Ir-N atoms on the bipyridine ligand are significantly longer than quinoxaline N-Ir bond lengths, caused by the stronger trans effect of the Ir-C σ -bonds trans to the ancillary ligand. The naphthyl ring has caused an increase in torsion angle between the naphthalene and the quinoxaline rings, which was unseen in the smaller phenyl quinoxalines of Chapter 2, with the added bulk of the naphthyl rings causing the additional steric strain around the coordination sphere. For the ligand that isn't disordered, the angle of N(1), C(11), C(10) and C(1) gives a twist of -12.2(4) °. For the disordered ligand, the distortion angle between C(21), C(30), C(31) and N(21) is -14.6(13) °, and for N(21A), C(30A), C(31A), C(21A) is 15.7(8) °.

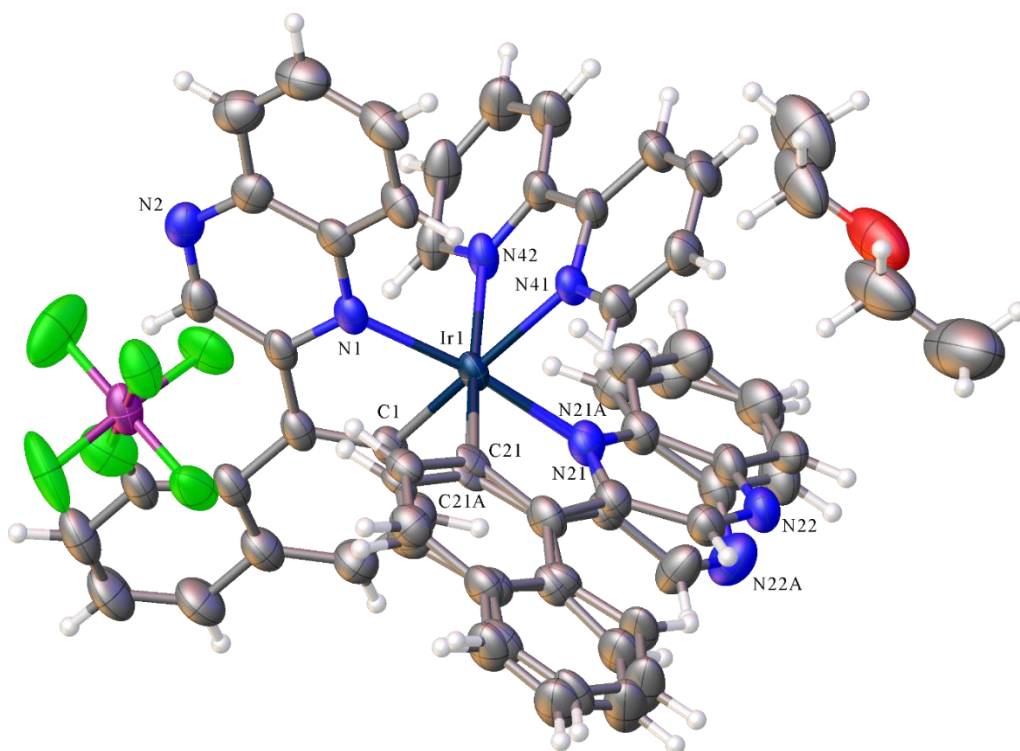


Figure.3.6 - X-ray structure of $[\text{Ir}(\text{L}^1)_2(\text{bpy})]\text{PF}_6$. Crystal Data: $\text{C}_{58}\text{H}_{60}\text{IrN}_6\text{O}_3\text{PF}_6$, $M_r = 1226.29$, triclinic, P-1 (No. 2), $a = 11.7003(3) \text{ \AA}$, $b = 14.5700(4) \text{ \AA}$, $c = 15.4795(4) \text{ \AA}$, $\alpha = 110.590(2)^\circ$, $\beta = 91.143(2)^\circ$, $\gamma = 94.368(2)^\circ$, $V = 2460.01(12) \text{ \AA}^3$, $T = 100(2) \text{ K}$, $Z = 2$, $Z' = 1$, $\mu(\text{MoK}\alpha) = 2.824$, 83320 reflections measured, 11256 unique ($R_{\text{int}} = 0.0652$) which were used in all calculations. The final wR_2 was 0.0947 (all data) and R_1 was 0.0356 ($I > 2(I)$).

3.3.4 Electrochemistry

The redox potentials of complexes $[\text{Ir}(\text{L}^1)_2(\text{bpy})]\text{PF}_6$ and $[\text{Ir}(\text{L}^2)_2(\text{bpy})]\text{PF}_6$ were studied by cyclic voltammetry (CV) and potentials can be seen in Table 3.2. Measurements were made in deoxygenated DCM using a platinum disc electrode (scan rate $u = 200 \text{ mV s}^{-1}$, $1 \times 10^{-3} \text{ M}$ solutions, $0.1 \text{ M} [\text{NBu}_4][\text{PF}_6]$ as a supporting electrolyte).

Complex	Oxidation	Reduction	
	$E_{1/2} / \text{V}$	$E_{(\text{red } 1)} / \text{V}$	$E_{(\text{red } 2)} / \text{V}$
$[\text{Ir}(\text{L}^1)_2(\text{bpy})]\text{PF}_6$	-	-1.01 ^a	-1.31 ^a
$[\text{Ir}(\text{L}^2)_2(\text{bpy})]\text{PF}_6$	+1.42	-1.05 ^a	-1.26 ^a

Table 3.2 - Electrochemical properties of the iridium(III) complexes obtained from cyclic voltammetry. Potentials measured in deaerated DCM solutions at 200 mVs^{-1} with $0.1 \text{ M} [\text{NBu}_4][\text{PF}_6]$ as supporting electrolyte calibrated with Fc/Fc^+ ; ^a $E_{1/2}$ values for fully reversible reduction process.

$[\text{Ir}(\text{L}^2)_2(\text{bpy})]\text{PF}_6$ has a single electron oxidation occurring at $E_{1/2} = +1.42$ V relative to the ferrocene / ferrocenium redox couple which is assigned to the $\text{Ir}^{4+/3+}$ couple. The $[\text{Ir}(\text{L}^1)_2(\text{bpy})]\text{PF}_6$ trace oxidation appears to have been obscured by the solvent centred processes. Each complex displays two ligand centred one electron reduction processes occurring between -1.05 and -1.31 V. Both reductions occur at different potentials for each complex, suggesting that they are occurring by the population of a π^* orbital of the different cyclometalating ligands.

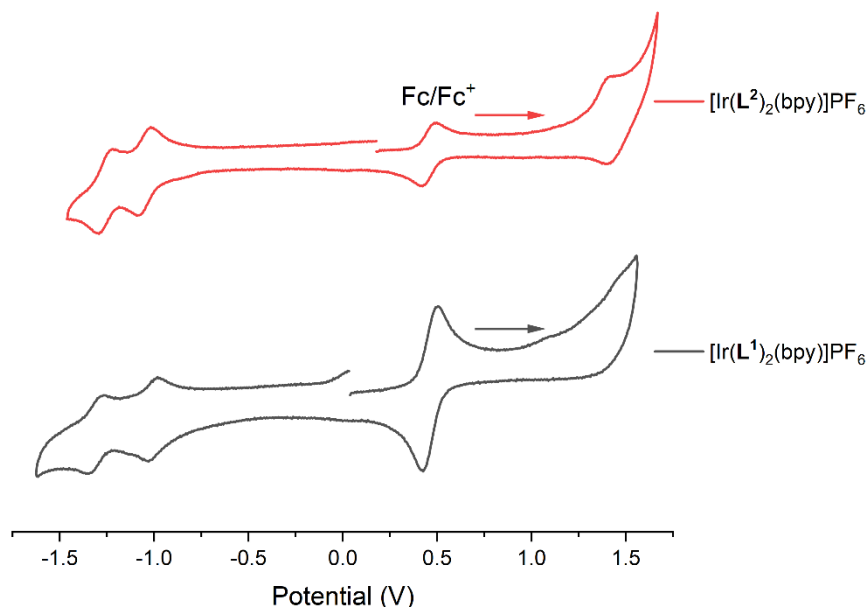


Figure 3.7 - Cyclic Voltammograms of $[\text{Ir}(\text{L}^1)_2(\text{bpy})]\text{PF}_6$ and $[\text{Ir}(\text{L}^2)_2(\text{bpy})]\text{PF}_6$. All potentials measured in deoxygenated DCM solutions at 200 mVs^{-1} with $0.1 \text{ M } [\text{NBu}_4][\text{PF}_6]$ as supporting electrolyte calibrated with Fc/Fc^+ .

3.3.5 Photophysical measurements

3.3.5.1 Ligand absorbance and emission

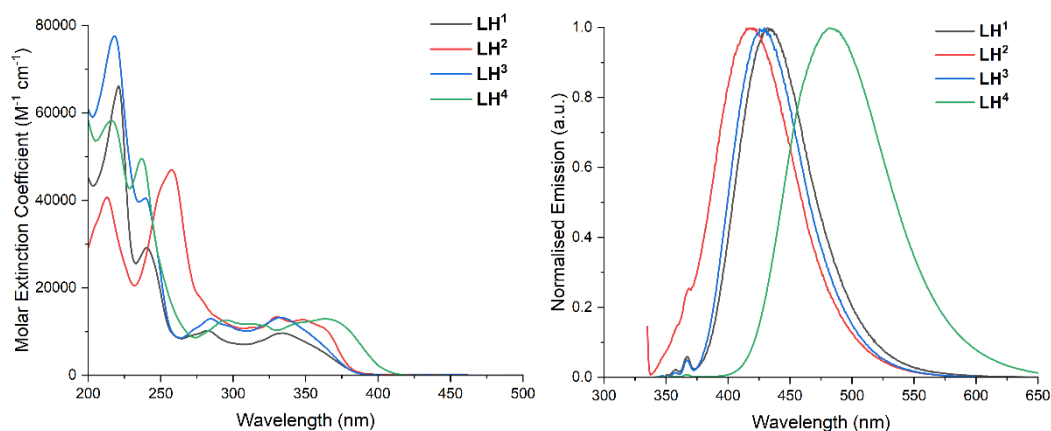


Figure 3.8 – Left: UV-Vis spectra for LH^{1-4} recorded in MeCN at $\text{ca.}10^{-5} \text{ M}$. Right: Emission spectrums for Ligands LH^{1-4} obtained in aerated acetonitrile at $\text{ca.}10^{-5} \text{ M}$. $\lambda_{\text{ex}} = 330 \text{ nm}$.

Absorbance spectra for the ligands were obtained in aerated acetonitrile at *ca.* 10^{-5} M can be seen in Figure 3.8 - Left. Strong absorbances can be seen between 200 and 300 nm, resulting from $\pi-\pi^*$ transition and the weaker $n-\pi^*$ transitions. Absorption λ_{\max} show slight differences with substitution. The **LH²** absorbance is bathochromically shifted by *ca.* 30 nm in comparison to the 1-naphthyl derivative **LH¹**. Between the 1-naphthyl ligands, **LH^{1,3,4}**, the absorbance is shifted depending upon substitution. The electron withdrawing -F group of **LH³** shifting the transition to a higher energy, while the stronger electron donating -OMe of **LH⁴** bathochromically shifts the emission to 366 nm.

Ligand	$\lambda_{\text{abs}} (\epsilon / \times 10^4 \text{ M}^{-1} \text{ cm}^{-1}) / \text{nm}^{\text{a}}$	$\lambda_{\text{em}} / \text{nm}^{\text{b}}$	$\tau / \text{ns}^{\text{c}}$	$\Phi / \%^{\text{d}}$
LH¹	335 (0.9), 282 (1.0), 239 (2.9), 221 (6.6)	432	< 1	0.021
LH²	362 (1.1), 348 (1.3), 330 (1.3), 257 (4.7), 213 (4.1)	418	< 1	0.016
LH³	332 (1.3), 284 (1.3), 239 (4.0), 218 (7.8)	428	< 1	0.018
LH⁴	366 (1.3), 319 (1.1), 293 (1.2), 237 (4.9), 215 (5.8)	483	3	0.155

Table 3.3 - ^a aerated acetonitrile, 10^{-5} M; ^b $\lambda_{\text{ex}} = 330$ nm; ^c $\lambda_{\text{ex}} = 295$ nm; ^d Vs standard Quinine Sulphate in 0.05 M H₂SO₄, $\lambda_{\text{ex}} = 330$ nm. ²²

Steady state emission spectra from the ligands were also run in aerated MeCN at *ca.* 10^{-5} M (Figure 3.8 - Left). Each of the ligands were excited at $\lambda_{\text{ex}} = 330$ nm and exhibited a single broad featureless emission peak. The emission from **LH²** has a λ_{\max} of 418 nm and is hypsochromically shifted in comparison to the 1-naphthyl **LH¹**, where $\lambda_{\max} = 432$ nm. Substitution around the 1-naphthyl ring gives some tuneability to the emission. The fluoro substituent of **LH³** gives a small hypsochromic shift in emission to $\lambda_{\max} = 428$ nm, while the methoxy substituted ligand **LH⁴** gives a larger bathochromic shift in emission to $\lambda_{\max} = 483$ nm, probably due to the increased conjugation of the latter.

Time resolved measurements were also recorded and can be seen in Table 3.3. Each of the ligands has a short lifetime, typical of fluorescent emission. The individual lifetimes of **LH¹⁻³** are below 1 ns, while **LH⁴** had a lifetime of 3 ns.

3.3.5.2 Complex absorption and emission

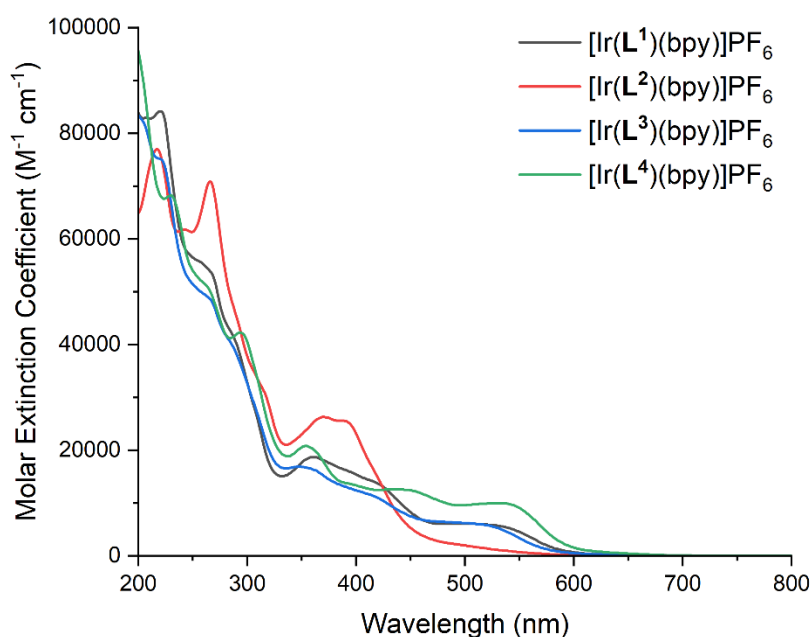


Figure 3.9 - UV-Vis spectra for $[\text{Ir}(\text{L}^{\text{H}^1-4})(\text{bpy})]\text{PF}_6$ recorded in aerated MeCN at $\text{ca. } 10^{-5}$ M.

Absorbance spectra for the complexes can be seen above in Figure 3.9. Measurements were obtained in aerated MeCN solution at $\text{ca. } 10^{-5}$ M. Strong absorbances between 200 and 370 nm are the result of the ligand centred spin allowed $^1\pi-\pi^*$ transitions. The features past 400 nm, which are not seen in the ligand spectra, are typically assigned to spin allowed $^1\text{MLCT}$ transitions, with spin forbidden $^3\text{MLCT}$ transitions tailing off towards 600 nm.²³ Substitution of the 1-naphthyl ring exhibits an effect on the absorption wavelengths in the MLCT region. Once again, the electron withdrawing -F substituent of $[\text{Ir}(\text{L}^3)_2(\text{bpy})]\text{PF}_6$ gave a higher energy transition, 516 nm, than the unsubstituted $[\text{Ir}(\text{L}^1)_2(\text{bpy})]\text{PF}_6$, where the absorbance was seen at 524 nm. The methoxy substituted $[\text{Ir}(\text{L}^4)_2(\text{bpy})]\text{PF}_6$ was the most bathochromically shifted spectrum at 544 nm and demonstrated the highest molar absorption coefficients in the visible region, tailing to $\text{ca. } 650$ nm. For $[\text{Ir}(\text{L}^2)_2(\text{bpy})]\text{PF}_6$, the MLCT region is likely to comprise both spin allowed, and spin forbidden contributions, the latter facilitated by the heavy Ir centre. The transitions are all at higher energy in comparison to the 1-naphthyl variants.

Steady state emission spectra were recorded for $[\text{Ir}(\text{L}^1-4)_2(\text{bpy})]\text{PF}_6$ in aerated acetonitrile solutions at $\text{ca. } 10^{-5}$ M. (Figure 3.10) the complexes were all excited at $\lambda_{\text{ex}} = 500$ nm, well into the MLCT absorption region. Complexes of the 1-naphthyl isomer display a single featureless emission profile, centred around λ_{max} $\text{ca. } 680$ nm. The emission profiles also exhibit tuneability based upon substitution on the

naphthyl ring. The fluoro-substituted $[\text{Ir}(\text{L}^3)_2(\text{bpy})]\text{PF}_6$ had the highest energy transition at 670 nm, while the methoxy substituted $[\text{Ir}(\text{L}^4)_2(\text{bpy})]\text{PF}_6$ transition occurred at 690 nm with the unsubstituted $[\text{Ir}(\text{L}^1)_2(\text{bpy})]\text{PF}_6$ nicely dissecting them with a λ_{max} of 678 nm. In comparison, the complex $[\text{Ir}(\text{L}^2)_2(\text{bpy})]\text{PF}_6$, with the 2-naphthyl based ligand, has a broader emission profile, with a $\lambda_{\text{max}} = 665$ nm. The tuneability of emission suggest the naphthyl rings make up a large part of the frontier orbitals of the complex.

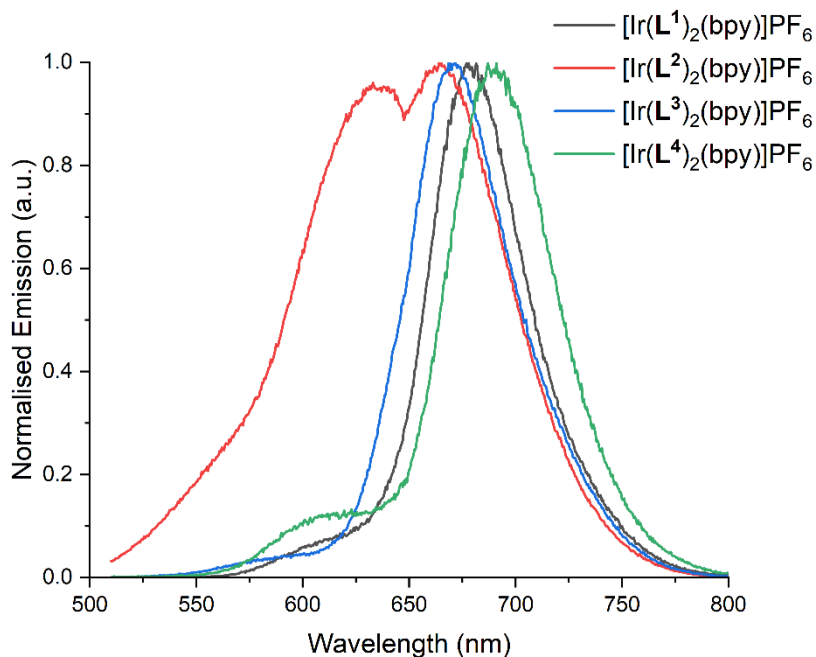


Figure 3.10 – Steady state emission spectra for complexes $[\text{Ir}(\text{L}^{1-4})_2(\text{bpy})]\text{PF}_6$, recorded in aerated MeCN at $\lambda_{\text{ex}} = 500$ nm.

Low temperature emission measurements were obtained in ethanol/methanol (4:1) glasses and are shown in Figure 3.11 (overlaid with their room temperature measurements made in MeCN). The 1-naphthyl complexes show a small, ca. 20 nm, hypsochromic shift in the λ_{max} emission, revealing a minor contributing shoulder to the emission between 700 and 730 nm. For $[\text{Ir}(\text{L}^2)_2(\text{bpy})]\text{PF}_6$ the λ_{max} has hypsochromically shifted by ca. 100 nm with a second peak at 635 nm. The increase in vibronic features for both 1- and 2-naphthyl varieties suggests a ligand-centred contribution to the excited state. Previous investigations into similar phenyl quinoxaline complexes²⁴ has shown, by both experimental and DFT analyses, that the true nature of the excited state is a combination of $^3\text{MLCT}$ and ^3LC emission, with the HOMO incorporating the phenyl moiety of the cyclometalating ligands. The data collected here would suggest this is once again the case, with a mixed $^3\text{MLCT}$

and ^3LC based excited state, and the naphthyl rings being part of the HOMO frontier orbitals.

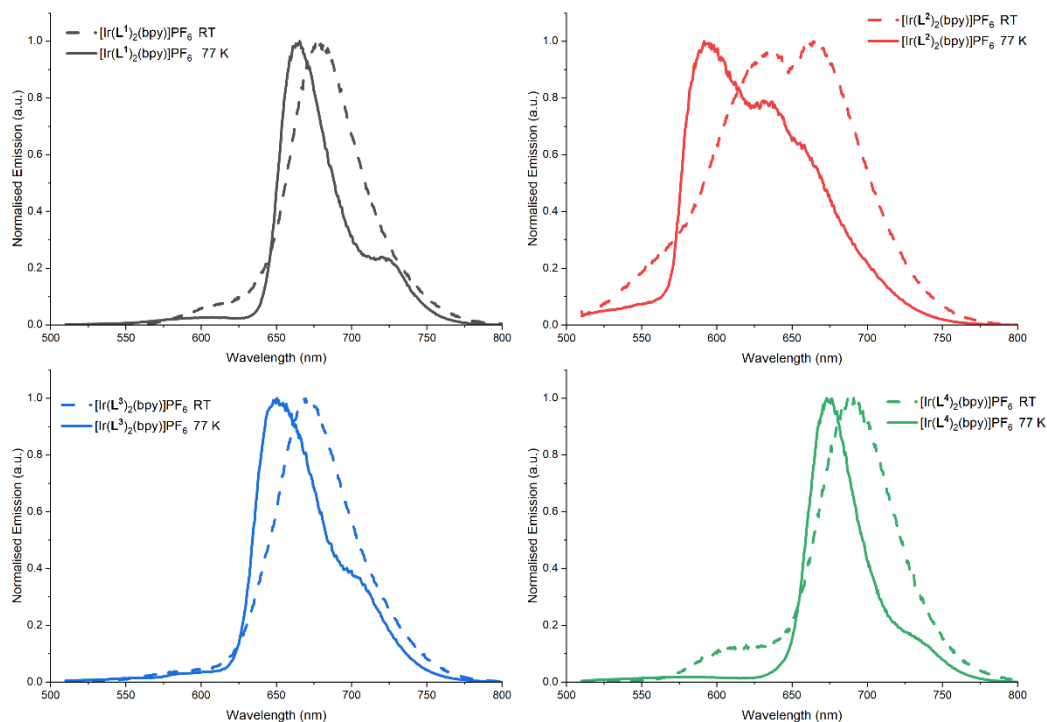


Figure 3.11 – Low temperature emission measurements (solid line), recorded in 4:1 ethanol/methanol glass, overlaid with room temperature measurements (dashed lines) recorded in MeCN solution. ($\lambda_{\text{ex}} = 500 \text{ nm}$)

Time resolved emission spectroscopy was also run on the complexes, with lifetimes were recorded in MeCN solutions (Table 3.4). Lifetimes of all complexes showed a mono-exponential decay, which is consistent for a single emissive state. The lifetimes of the 1-naphthyl based complexes are all comparable ca. 230 ns, while the 2-naphthyl complex lifetime is slightly shorter at 134 ns. Lifetimes are consistent with phosphorescent emission.

Complex	λ_{abs} ($\epsilon / \times 10^4 \text{ M}^{-1} \text{ cm}^{-1}$) / nm^{a}	λ_{em} / nm^{b}	τ / ns^{c}	Φ / $\%^{\text{d}}$
$[\text{Ir}(\text{L}^1)_2(\text{bpy})]\text{PF}_6$	524 (0.6), 420 (1.4), 361 (1.8), 255 (5.5), 219 (8.4)	678	230	0.7
$[\text{Ir}(\text{L}^2)_2(\text{bpy})]\text{PF}_6$	487 (0.2), 391 (2.5), 370 (2.6), 266(7.1), 216 (7.7)	665, 634	134	1.3
$[\text{Ir}(\text{L}^3)_2(\text{bpy})]\text{PF}_6$	516 (0.6), 410 (1.1), 348 (1.7), 264 (4.9), 220 (7.5)	670	238	0.5

$[\text{Ir}(\text{L}^4)_2(\text{bpy})]\text{PF}_6$	544 (0.9), 448 (1.2), 354 (2.1), 293 (4.2), 229 (6.8)	690	219	0.2
--	---	-----	-----	-----

Table 3.4 - ^a aerated acetonitrile, 10^{-5} M; ^b $\lambda_{\text{ex}} = 500$ nm; ^c $\lambda_{\text{ex}} = 295$ nm; ^d Vs standard $[\text{Ru}(\text{bpy})_3][(\text{PF}_6)_2]$ in aerated acetonitrile, 10^{-5} M, $\lambda_{\text{ex}} = 450$ nm. ²²

3.4 Conclusions

This chapter has shown the synthesis and characterisation of two novel ligands, which when combined with two previously reported compounds, provided a ligand series to investigate the effects of adding electron donating and withdrawing groups upon phosphorescent cyclometalated Ir(III) complexes. To this end, four novel cyclometalated complexes were isolated and characterised via ^1H , $^{19}\text{F}\{^1\text{H}\}$, $^{13}\text{C}\{^1\text{H}\}$ NMR, HRMS, UV-vis, and emission spectroscopies as well as by cyclic voltammetry. One example was grown as a single crystal of sufficient quality to allow the capture of diffraction data via single crystal XRD analysis.

In comparison to the complexes from Chapter 2, as well as literature complexes^{24,25}, where 2-phenylquinoxalines complexes of Ir(III) have been shown to emit between 580-630 nm, increasing the conjugation from phenyl to naphthyl has shifted the emission to a deeper red between 630 and 690 nm. The emissive states appear to be a mix of ^3LC and $^3\text{MLCT}$ processes, with naphthyl based contributions to the HOMO orbitals.

The small differences between 1-naphthyl and 2-naphthyl isomers λ_{em} correlated to earlier work by Sun *et al.*²⁶ with cyclometalated naphthylpyridines, where the 1-naphthyl isomer was also emitting at a lower energy. While the emission wavelength has been further redshifted by the extended conjugation of a quinoxaline group over the pyridine group, the quantum yields share the same magnitude. The lifetimes seen in this study are also longer than the previous work.

In further work it would be valuable to investigate the nature of the participating HOMO and LUMO levels using computational analysis. Such studies would help support the suggestions here that the emitting state in these phosphorescent complexes is likely to be a mixture of MLCT character and ligand centred contributions.

3.5 Experimental

All reactions were performed with the use of vacuum line and Schlenk techniques. Reagents were commercial grade and were used without further purification. ^1H , ^{13}C and ^{19}F NMR spectra were recorded on a Bruker fourier 300, dpx 400, or avance 500 MHz spectrometer, and were recorded in CDCl_3 or CD_3CN . ^1H and $^{13}\text{C}\{^1\text{H}\}$ NMR chemical shifts (δ) were determined relative to internal tetramethylsilane, $\text{Si}(\text{CH}_3)_4$ and are given in ppm. Low-resolution mass spectra were obtained by the staff at Cardiff University. High-resolution mass spectra were carried out by the staff at Cardiff University and the EPSRC National Mass Spectrometry Service at Swansea University, UK. All photophysical data was obtained on a JobinYvon-Horiba Fluorolog-3 spectrometer fitted with a JY TBX picosecond photodetection module in MeCN solutions. Emission spectra were uncorrected and excitation spectra were instrument corrected. The pulsed source was a Nano-LED configured for 295, 372 or 459 nm output operating at 500 kHz or 1 MHz. Luminescence lifetime profiles were obtained using the JobinYvon–Horiba FluoroHub single photon counting module and the data fits yielded the lifetime values using the provided DAS6 deconvolution software. IR spectra were recorded on an ATR equipped Shimadzu IRAffinity-1 spectrophotometer. UV-vis data was recorded as solutions on a Shimadzu UV-1800 spectrophotometer.

X-ray crystallography

Data collection and processing

Data collection and structural refinement was carried out by the UK national crystallographic service at the University of Southampton. Suitable crystals were selected, and data collected on a Rigaku FRE+ diffractometer equipped with VHF Varimax confocal mirrors and an AFC12 goniometer and HyPix 6000 detector. The crystal was kept at a steady $T = 100(2)$ K during data collection. The structure was solved with the ShelXT²⁷ structure solution program using the Intrinsic Phasing solution method and by using Olex2²⁸ as the graphical interface. The model was refined with version 2018/3 of ShelXL²⁹ using Least Squares minimisation.

3.5.1 2-Bromo-1-(naphthalen-1-yl)ethan-1-one (1)

To a stirring solution of 1-(naphthalen-1-yl)ethan-1-one (1.00 g, 5.88 mmol) in 1,4-dioxane (10 mL), dioxane dibromide (1.60 g, 6.46 mmol) was added portion wise

and stirred at room temperature for 2 hours. The solvent removed *in vacuo* to yield crude product. A minimum amount of cold hexanes were added and the resultant slurry filtered under suction to yield title compound as an off white solid (1.15 g, 83 %) ¹H NMR (400 MHz, CDCl₃) δ 8.63 (d, *J* = 8.8 Hz, 1H), 8.04 (d, *J* = 8.2 Hz, 1H), 7.92 (dd, *J* = 7.3, 1.1 Hz, 1H), 7.89 (dd, *J* = 8.4, 1.0 Hz, 1H), 7.63 (ddd, *J* = 8.5, 6.9, 1.5 Hz, 1H), 7.56 (ddd, *J* = 8.1, 6.9, 1.2 Hz, 1H), 7.51 (dd, *J* = 8.2, 7.3 Hz, 1H), 4.57 (s, 2H) ppm.

3.5.2 2-Bromo-1-(naphthalen-2-yl)ethan-1-one (2)

Synthesised as above from 1-(naphthalen-2-yl)ethan-1-one (1.00 g, 5.88 mmol) and dioxane dibromide (1.60 g, 6.46 mmol) to yield off white solid (1.07g, 77 %). ¹H NMR (400 MHz, CDCl₃) δ 8.52 (d, *J* = 1.2 Hz, 1H), 8.05 (d, *J* = 1.8 Hz, 1H), 8.02 (d, *J* = 1.8 Hz, 1H), 7.99 (d, *J* = 7.4 Hz, 1H), 7.94 (s, 1H), 7.91 (d, *J* = 3.9 Hz, 1H), 7.89 (s, 1H), 4.59 (s, 2H) ppm.

3.5.3 2-Bromo-1-(4-fluoronaphthalen-1-yl)ethan-1-one (3)

Synthesised as above from 1-(4-fluoronaphthalen-1-yl)ethan-1-one (1.00 g, 5.31 mmol) and dioxane dibromide (1.45 g, 5.84 mmol) to yield off white solid (1.21 g, 90 %). ¹H NMR (400 MHz, CDCl₃) δ 8.78 (d, *J* = 8.7 Hz, 1H), 8.18 (d, *J* = 8.3 Hz, 1H), 7.98 (dd, *J* = 8.1, 5.3 Hz, 1H), 7.71 (ddd, *J* = 8.6, 6.9, 1.4 Hz, 1H), 7.66 – 7.57 (m, 1H), 7.18 (dd, *J* = 9.6, 8.2 Hz, 1H), 4.54 (s, 2H) ppm. ¹⁹F{¹H} NMR (376 MHz, CDCl₃) δ -111.9 (s) ppm.

3.5.4 2-Bromo-1-(4-methoxynaphthalen-1-yl)ethan-1-one (4)

Synthesised as above from 1-(4-methoxynaphthalen-1-yl)ethan-1-one (1.00 g, 4.99 mmol) and dioxane dibromide (1.36 g, 5.49 mmol) to yield off white solid (0.95 g, 71 %). ¹H NMR (400 MHz, CDCl₃) δ 8.94 (d, *J* = 8.4 Hz, 1H), 8.32 (dd, *J* = 8.4, 0.7 Hz, 1H), 8.02 (d, *J* = 8.3 Hz, 1H), 7.65 (ddd, *J* = 8.6, 6.9, 1.4 Hz, 1H), 7.54 (ddd, *J* = 8.2, 6.9, 1.1 Hz, 1H), 6.78 (d, *J* = 8.3 Hz, 1H), 4.54 (s, *J* = 12.3 Hz, 2H), 4.06 (s, 3H).

3.5.5 2-(naphthalen-1-yl)-quinoxaline (LH¹).³⁰

1 (1.000 g, 4.25 mmol) was dissolved in ethanol (10 mL). 1,2-diaminobenzene (552 mg, 5.10 mmol) was added and the mixture heated to reflux for 16 hours. The suspension was cooled to room temperature, the precipitate collected by filtration and washed with ethanol (3 x 5 mL) before drying overnight in an oven to yield the title compound as a yellow solid (684 mg, 63 %). Spectral data conforms to those listed in the literature. ¹H NMR (400 MHz, CDCl₃) δ 9.17 (s, 1H), 8.26 – 8.19 (m, 2H), 8.19 – 8.15 (m, 1H), 8.02 (d, *J* = 8.1 Hz, 1H), 7.98 (dd, *J* = 7.2, 2.1 Hz, 1H),

7.88 – 7.81 (m, 2H), 7.78 (dd, $J = 7.1, 1.0$ Hz, 1H), 7.65 (dd, $J = 8.7, 8.0$ Hz, 1H), 7.59 – 7.51 (m, 2H) ppm.

3.5.6 2-(naphthalen-2-yl)-quinoxaline (LH²).³¹

Synthesised as LH¹ from **2** (1.070 g, 4.55 mmol) and 1,2-diaminobenzene (590 mg, 5.46 mmol) to yield title compound as a yellow solid (564 mg, 48 %). Spectral data conforms to those listed in the literature. ¹H NMR (400 MHz, CDCl₃) δ 9.50 (s, $J = 5.1$ Hz, 1H), 8.68 (d, $J = 1.4$ Hz, 1H), 8.38 (dd, $J = 8.6, 1.8$ Hz, 1H), 8.21 (dd, $J = 8.3, 1.4$ Hz, 1H), 8.15 (dd, $J = 8.2, 1.5$ Hz, 1H), 8.07 – 8.01 (m, 2H), 7.95 – 7.90 (m, 1H), 7.85 – 7.75 (m, 2H), 7.60 – 7.55 (m, 2H) ppm.

3.5.7 2-(4-fluoronaphthalen-1-yl)-quinoxaline (LH³).

Synthesised as LH¹ from **3** (1.100 g, 4.35 mmol) and 1,2-diaminobenzene (564 mg, 5.22 mmol) to yield title compound as a yellow powder (568 mg, 52 %). ¹H NMR (400 MHz, CDCl₃) δ 9.14 (s, 1H), 8.27 – 8.12 (m, 4H), 7.89 – 7.81 (m, 2H), 7.73 (dd, $J = 7.9, 5.4$ Hz, 1H), 7.67 – 7.57 (m, 2H), 7.32 (dd, $J = 10.0, 8.0$ Hz, 1H). ¹⁹F{¹H} NMR (376 MHz, CDCl₃) δ -119.7 (s). ¹³C{¹H} NMR (101 MHz, CDCl₃) δ 153.7, 146.6, 142.3, 141.5, 132.8, 132.8, 131.4, 130.7, 130.2, 129.7, 129.5, 128.9, 128.8, 128.3, 126.9, 125.3, 124.3, 121.3, 121.3, 109.6, 109.3 ppm. UV-vis (MeCN): λ_{abs} (ε/10⁴ L mol⁻¹ cm⁻¹) 218(7.8), 239 (4.0), 284 (1.3), 332 (1.3) nm. FTIR (solid) (ATR) ν_{max}: 3043, 1601, 1577, 1548, 1512, 1489, 1473, 1398, 1344, 1298, 1261, 1242, 1228, 1190, 1157, 1132, 1047, 1022, 987, 931, 831, 817, 798, 748, 711, 661, 599, 572, 557, 532, 503, 462, 449, 410 cm⁻¹. HRMS (ES) Calc'd 275.0985 for C₁₈H₁₂N₂F; found m/z 275.0978 [M + H]⁺.

3.5.8 2-(4-methoxynaphthalen-1-yl)-quinoxaline (LH⁴).

Synthesised as LH¹ from **4** (900 mg, 3.39 mmol) and 1,2-diaminobenzene (440 mg, 4.07 mmol) to yield title compound as a yellow powder (409 mg, 42 %). ¹H NMR (400 MHz, CDCl₃) δ 9.15 (s, 1H), 8.43 – 8.37 (m, 1H), 8.27 – 8.16 (m, 3H), 7.88 – 7.76 (m, 2H), 7.74 (d, $J = 8.0$ Hz, 1H), 7.63 – 7.52 (m, 2H), 6.99 (d, $J = 8.0$ Hz, 1H), 4.10 (s, 3H) ppm. ¹³C{¹H} NMR (101 MHz, CDCl₃) δ 157.1, 154.5, 147.0, 142.4, 141.2, 132.2, 130.4, 129.7, 129.7, 129.5, 129.4, 127.8, 127.7, 126.1, 125.9, 124.9, 122.7, 103.7, 55.9 ppm. UV-vis (MeCN): λ_{abs} (ε/10⁴ L mol⁻¹ cm⁻¹) 215 (5.8), 237 (4.9), 293 (1.2), 319 (1.1), 366 (1.3) nm. FTIR (solid) (ATR) ν_{max}: 3001, 1577, 1544, 1510, 1487, 1456, 1440, 1421, 1388, 1375, 1342, 1317, 1298, 1259, 1242, 1317, 1298, 1259, 1157, 1136, 1126, 1085, 1029, 1001, 974, 962, 921, 821, 802,

759, 713, 655, 626, 603, 592, 526, 505, 472, 453, 420, 411 cm^{-1} . HRMS (ES) Calc'd 287.1184 for $\text{C}_{19}\text{H}_{15}\text{N}_2\text{O}$; found m/z 287.1187 $[\text{M} + \text{H}]^+$.

3.5.9 General procedure for the synthesis of $[(\text{Ir}(\text{L}^x)_2\mu\text{-Cl})_2]$.

To a solution of LH^x (0.8 mmol) in 2-methoxyethanol (10 mL), $\text{IrCl}_3 \cdot x\text{H}_2\text{O}$ (120 mg, 0.40 mmol) was added and the mixture heated to reflux for 48 hours. The solution was cooled to room temperature and precipitated by the addition of water and collected on a sinter. After drying, the collection flask was changed, and the precipitate dissolved in DCM until the fresh filtrate was clear leaving impurities on the sinter. The organic were combined, and the solvent removed *in vacuo*. The resulting red $[(\text{Ir}(\text{L}^x)_2\mu\text{-Cl})_2]$ were used without further purification or spectroscopy.

3.5.10 $[\text{Ir}(\text{L}^1)_2(\text{bpy})]\text{PF}_6$.

2,2'-bipyridine (42 mg, 0.270 mmol) and $[(\text{Ir}(\text{L}^1)_2\mu\text{-Cl})_2]$ (200 mg, 0.135 mmol) was dissolved in 2-methoxy ethanol (10 mL) and heated to 125 °C for 24 hours. The solution was cooled to room temperature and the crude precipitated by the addition of saturated $[\text{NH}_4][\text{PF}_6]$ solution and the precipitate collected on a sinter. The crude was washed with water (2 x 20 mL) and diethyl ether (3 x 25 mL). The target compound was obtained by column chromatography, collecting the first red band eluted with 95:5 DCM / methanol solution. This was concentrated and recrystallised from DCM by the addition of diethyl ether to yield the title compound as a red powder (58 mg, 21 %). ^1H NMR (400 MHz, CDCl_3) δ 9.97 (s, 2H), 9.36 (d, $J = 8.0$ Hz, 2H), 8.64 (d, $J = 8.6$ Hz, 2H), 8.14 (app. t, $J = 7.4$ Hz, 2H), 8.03 (d, $J = 8.1$ Hz, 2H), 7.93 (d, $J = 4.5$ Hz, 2H), 7.80 (d, $J = 7.7$ Hz, 2H), 7.68 (ddd, $J = 8.4$, 7.0, 1.3 Hz, 2H), 7.58 (ddd, $J = 8.3$, 5.7, 2.5 Hz, 2H), 7.50 (dd, $J = 11.1$, 3.9 Hz, 2H), 7.33 (dd, $J = 6.9$, 6.1 Hz, 2H), 7.29 (d, $J = 8.4$ Hz, 2H), 7.09 – 7.03 (m, 4H), 6.80 (d, $J = 8.4$ Hz, 2H) ppm. $^{13}\text{C}\{^1\text{H}\}$ NMR (101 MHz, CDCl_3) δ 165.7, 159.9, 155.9, 146.8, 145.2, 141.5, 141.3, 141.2, 136.9, 132.8, 132.3, 132.0, 131.8, 130.5, 130.5, 130.1, 128.8, 127.7, 127.6, 125.1, 123.0, 121.6 ppm. UV-vis (MeCN): λ_{abs} ($\epsilon/10^4$ L mol^{-1} cm^{-1}) 219 (8.4), 255 (5.5), 361 (1.8), 420 (1.4), 524 (0.6) nm. FTIR (solid) (ATR) ν_{max} : 1604, 1573, 1548, 1523, 1498, 1471, 1423, 1375, 1350, 1311, 1255, 1205, 1126, 1095, 1026, 1014, 958, 894, 835 (PF_6^-), 756, 705, 673, 634, 578, 555 (PF_6^-), 484, 422, 414, 403 cm^{-1} . HRMS (ES) Calc'd 857.2132 for $\text{C}_{46}\text{H}_{30}\text{N}_6\text{Ir}$; found m/z 857.2124 $[\text{M} - \text{PF}_6]^+$.

3.5.11 $[\text{Ir}(\text{L}^2)_2(\text{bpy})]\text{PF}_6$.

Synthesised as before yield the title compound as a red powder (50 mg, 18 %). ^1H NMR (500 MHz, CD_3CN) δ 9.90 (s, 2H), 8.98 (s, 2H), 8.18 (d, $J = 5.6$ Hz, 2H), 8.15

(d, $J = 7.8$ Hz, 2H), 8.09 (d, $J = 8.2$ Hz, 2H), 8.00 – 7.95 (m, 4H), 7.66 – 7.61 (m, 2H), 7.50 – 7.46 (m, 2H), 7.38 – 7.34 (m, 2H), 7.34 – 7.29 (m, 2H), 7.28 (d, $J = 8.5$ Hz, 2H), 7.23 (d, $J = 8.5$ Hz, 2H), 7.17 – 7.12 (m, 2H), 6.98 (s, 2H) ppm. $^{13}\text{C}\{^1\text{H}\}$ NMR (126 MHz, CDCl_3) δ 162.8, 156.0, 148.0, 143.3, 142.9, 142.8, 142.5, 141.9, 141.3, 140.9, 136.0, 132.6, 132.3, 131.2, 130.8, 130.4, 129.6, 129.1, 128.9, 128.4, 128.3, 126.5, 125.7, 125.2, 124.0 ppm. UV-vis (MeCN): λ_{abs} ($\epsilon/10^4$ L mol $^{-1}$ cm $^{-1}$) 216 (7.7), 266 (7.1), 370 (2.6), 391 (2.5), 487 (0.2) nm. FTIR (solid) (ATR) ν_{max} : 1616, 1601, 1533, 1525, 1446, 1327, 1238, 1207, 1151, 1132, 1070, 1006, 833 (PF_6^-), 763, 638, 623, 555 (PF_6^-), 422 cm $^{-1}$. HRMS (ES) Calc'd 857.2138 for $\text{C}_{46}\text{H}_{30}\text{N}_6\text{Ir}$; found m/z 857.2125 [$\text{M} - \text{PF}_6$] $^+$.

3.5.12 $[\text{Ir}(\text{L}^3)_2(\text{bpy})]\text{PF}_6$

Synthesised as before yield the title compound as a red powder (49 mg, 10 %). ^1H NMR (500 MHz, CDCl_3) δ 9.93 (s, 2H), 8.68 (d, $J = 8.6$ Hz, 2H), 8.39 (d, $J = 8.1$ Hz, 2H), 8.10 (d, $J = 7.4$ Hz, 2H), 8.05 (dd, $J = 8.2, 1.5$ Hz, 4H), 7.99 (ddd, $J = 5.6, 1.5, 0.6$ Hz, 2H), 7.77 (ddd, $J = 8.5, 7.0, 1.3$ Hz, 2H), 7.61 (dddd, $J = 8.1, 6.7, 5.6, 1.1$ Hz, 4H), 7.39 (ddd, $J = 7.6, 5.5, 1.2$ Hz, 2H), 7.14 (ddd, $J = 8.6, 7.0, 1.5$ Hz, 2H), 7.01 (dd, $J = 8.8, 0.8$ Hz, 2H), 6.49 (d, $J = 10.1$ Hz, 2H) ppm. $^{19}\text{F}\{^1\text{H}\}$ NMR (376 MHz, CDCl_3) δ -72.6 (d, $^1J_{\text{PF}} = 711$ Hz), -112.8 (s) ppm. $^{13}\text{C}\{^1\text{H}\}$ NMR (126 MHz, CDCl_3) δ 164.9, 161.4, 159.8, 159.2, 155.5, 147.3, 144.9, 141.3, 141.2, 141.1, 133.8, 133.2, 132.4, 130.7, 130.3, 130.0, 129.2, 128.3, 125.8, 125.4, 124.8, 123.3, 122.6, 122.4, 122.3, 121.7, 116.1, 116.0 ppm. UV-vis (MeCN): λ_{abs} ($\epsilon/10^4$ L mol $^{-1}$ cm $^{-1}$) 220 (7.5), 264 (4.9), 348 (1.7), 410 (1.1), 516 (0.6) nm. FTIR (solid) (ATR) ν_{max} : 1618, 1581, 1525, 1499, 1446, 1417, 1354, 1232, 1141, 1099, 1056, 835 (PF_6^-), 758, 634, 580, 555 (PF_6^-), 470, 433 cm $^{-1}$. HRMS (ES) Calc'd 893.1977 for $\text{C}_{46}\text{H}_{28}\text{N}_6\text{F}_2\text{Ir}$; found m/z 893.1949 [$\text{M} - \text{PF}_6$] $^+$.

3.5.13 $[\text{Ir}(\text{L}^4)_2(\text{bpy})]\text{PF}_6$.

Synthesised as before yield the title compound as a red powder (69 mg, 15 %). ^1H NMR (400 MHz, CDCl_3) δ 9.84 (s, 2H), 8.59 (d, $J = 8.5$ Hz, 2H), 8.49 (d, $J = 8.2$ Hz, 2H), 8.25 (d, $J = 8.4$ Hz, 2H), 8.10 (app. t, $J = 7.8$ Hz, 2H), 8.02 (d, $J = 6.7$ Hz, 2H), 8.00 (d, $J = 9.4$ Hz, 2H), 7.69 (app. t, $J = 8.2$ Hz, 2H), 7.56 – 7.50 (m, 4H), 7.42 – 7.36 (m, 2H), 7.13 – 7.07 (m, 2H), 6.96 (d, $J = 9.0$ Hz, 2H), 5.94 (s, 2H), 3.30 (s, 6H) ppm. $^{13}\text{C}\{^1\text{H}\}$ NMR (126 MHz, CDCl_3) δ 165.6, 163.4, 158.1, 155.7, 148.2, 145.2, 141.5, 141.0, 140.4, 133.2, 131.9, 130.4, 129.7, 129.4, 129.2, 128.2, 125.6, 124.7, 124.7, 124.3, 122.6, 121.4, 110.1, 55.3 ppm. UV-vis (MeCN): λ_{abs}

($\epsilon/10^4 \text{ L mol}^{-1} \text{ cm}^{-1}$) 229 (6.8), 293 (4.2), 354 (2.1), 448 (1.2), 544 (0.9) nm. FTIR (solid) (ATR) ν_{max} : 1608, 1568, 1543, 1496, 1456, 1425, 1409, 1357, 1338, 1296, 1259, 1240, 1161, 1097, 1028, 1016, 979, 954, 837 (PF_6^-), 756, 665, 634, 557 (PF_6^-), 489, 470, 420, 407 cm^{-1} . HRMS (ES) Calc'd 917.2349 for $\text{C}_{48}\text{H}_{34}\text{N}_6\text{O}_2\text{Ir}$; found m/z 917.2374 $[\text{M} - \text{PF}_6]^+$.

3.6 References

- 1 W. Wei, S. A. M. Lima, P. I. Djurovich, A. Bossi, M. T. Whited and M. E. Thompson, *Polyhedron*, 2018, **140**, 138–145.
- 2 R. D. Costa, E. Ortí, H. J. Bolink, S. Graber, S. Schaffner, M. Neuburger, C. E. Housecroft and E. C. Constable, *Adv. Funct. Mater.*, 2009, **19**, 3456–3463.
- 3 T. M. Stonelake, K. A. Phillips, H. Y. Otaif, Z. C. Edwardson, P. N. Horton, S. J. Coles, J. M. Beames and S. J. A. Pope, *Inorg. Chem.*, 2020, **59**, 2266–2277.
- 4 L.-P. Li and B.-H. Ye, *Inorg. Chem.*, 2019, **58**, 7775–7784.
- 5 B. Tong, P. Ma, Q. Mei and Z. Hua, *Inorganica Chim. Acta*, 2014, **421**, 405–409.
- 6 D. Ma, R. Liu, Y. Qiu and L. Duan, *J. Mater. Chem. C*, 2018, **6**, 5630–5638.
- 7 G. Zhang, H. Zhang, Y. Gao, R. Tao, L. Xin, J. Yi, F. Li, W. Liu and J. Qiao, *Organometallics*, 2014, **33**, 61–68.
- 8 R. E. N. Njogu, P. Fodran, Y. Tian, L. W. Njenga, D. K. Kariuki, A. O. Yusuf, I. Scheblykin, O. F. Wendt and C.-J. Wallentin, *Synlett*, 2019, **30**, 792–798.
- 9 S. Lamansky, P. Djurovich, D. Murphy, F. Abdel-Razzaq, H.-E. Lee, C. Adachi, P. E. Burrows, S. R. Forrest and M. E. Thompson, *J. Am. Chem. Soc.*, 2001, **123**, 4304–4312.
- 10 S.-L. Lai, S.-L. Tao, M.-Y. Chan, M.-F. Lo, T.-W. Ng, S.-T. Lee, W.-M. Zhao and C.-S. Lee, *J. Mater. Chem.*, 2011, **21**, 4983–4988.
- 11 W. G. Zhu, Y. Ke, F. Wang, C. Z. Liu, M. Yuan and Y. Cao, *Synth. Met.*, 2003, **137**, 1079–1080.
- 12 W. Zhu, M. Zhu, Y. Ke, L. Su, M. Yuan and Y. Cao, *Thin Solid Films*, 2004, **446**, 128–131.
- 13 Z. Li, P. Cui, C. Wang, S. Kilina and W. Sun, *J. Phys. Chem. C*, 2014, **118**, 28764–28775.
- 14 J. W. Facendola, M. Seifrid, J. Siegel, P. I. Djurovich and M. E. Thompson, *Dalton Trans.*, 2015, **44**, 8456–8466.
- 15 W. Dang, X. Yang, Z. Feng, Y. Sun, D. Zhong, G. Zhou, Z. Wu and W.-Y. Wong, *J. Mater. Chem. C*, 2018, **6**, 9453–9464.
- 16 D. S. Karpovich and G. J. Blanchard, *J. Phys. Chem.*, 1995, **99**, 3951–3958.
- 17 D. P. Craig and I. G. Ross, *J. Chem. Soc. Resumed*, 1954, 1589–1606.
- 18 R. M. Eddins, K. Fucke, M. J. G. Peach, A. G. Crawford, T. B. Marder and A. Beeby, *Inorg. Chem.*, 2013, **52**, 9842–9860.
- 19 S. J. Pasaribu and L. R. Williams, *Aust. J. Chem.*, 1973, **26**, 1327–1331.
- 20 M. Nonoyama, *Bull. Chem. Soc. Jpn.*, 1974, **47**, 767–768.
- 21 S. Lamansky, P. Djurovich, D. Murphy, F. Abdel-Razzaq, R. Kwong, I. Tsyba, M. Bortz, B. Mui, R. Bau and M. E. Thompson, *Inorg. Chem.*, 2001, **40**, 1704–1711.
- 22 A. Brouwer, *Pure Appl. Chem.*, 2011, **83**, 2213–2228.
- 23 E. Zysman-Colman, Ed., *Iridium(III) in Optoelectronic and Photonics Applications*, John Wiley & Sons, Ltd, Chichester, UK, 2017.
- 24 S. J. Pope, T. Stonelake, K. Phillips, S. Coles, P. Horton, S. Keane, E. Stokes, I. Fallis, J. Beames, J. Zhao, K. Chen, Y. Hou, A. Hallett and S. O’Kell, *Chem. – Eur. J.*, DOI:10.1002/chem.201801007.
- 25 E. E. Langdon-Jones, A. J. Hallett, J. D. Routledge, D. A. Crole, B. D. Ward, J. A. Platts and S. J. A. Pope, *Inorg. Chem.*, 2013, **52**, 448–456.
- 26 B. Liu, L. Lystrom, S. Kilina and W. Sun, *Inorg. Chem.*, 2019, **58**, 476–488.
- 27 G. M. Sheldrick, *Acta Crystallogr. Sect. Found. Adv.*, 2015, **71**, 3–8.

- 28 O. V. Dolomanov, L. J. Bourhis, R. J. Gildea, J. A. K. Howard and H. Puschmann, *J. Appl. Crystallogr.*, 2009, **42**, 339–341.
- 29 G. M. Sheldrick, *Acta Crystallogr. Sect. C Struct. Chem.*, 2015, **71**, 3–8.
- 30 S. D. Pardeshi, P. A. Sathe, K. S. Vadagaonkar and A. C. Chaskar, *Adv. Synth. Catal.*, 2017, **359**, 4217–4226.
- 31 P. Wang, Z. Yang, Z. Wang, C. Xu, L. Huang, S. Wang, H. Zhang and A. Lei, *Angew. Chem. Int. Ed.*, 2019, **58**, 15747–15751.

**Chapter 4 - Red Emissive Iridium Complexes
Based upon 2-(Naphthyl)Quinoline Ligand
Architecture.**

4.1 Introduction

This chapter focus is on further synthesis, isolation and characterisation of extended conjugation and tuneability in cyclometalating ligand systems coordinated to iridium(III). The use of Pfitzinger synthesis allows for a facile route towards a range of ligands allowing for a comparison of different substituents around the quinoline ring and any changes to the emission properties they bring.

4.1.1 Quinolines

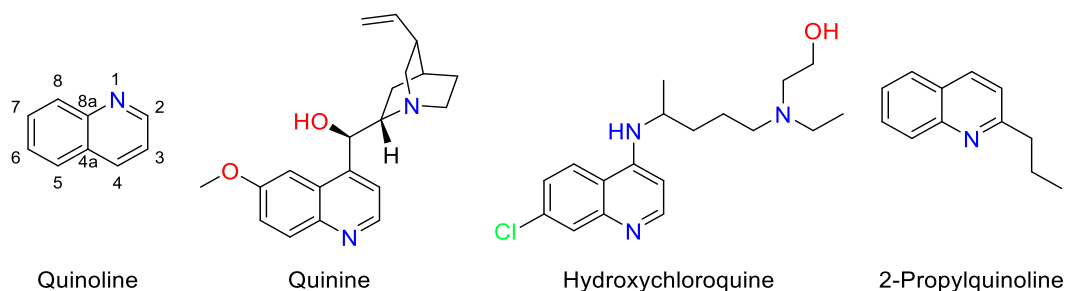


Figure 4.1 – Heterocyclic quinoline and examples of antimalarials, quinine and hydroxychloroquine¹, with natural antiparasitic 2-propylquinoline isolated from *Galipea longiflora*².

Quinoline is a bicyclic heterocycle containing a single imine in the 1-position of the aromatic ring (Figure 4.1). One structural variant exists, isoquinoline, with the imine at the 2-position. Perhaps the most famous quinoline is that of the anti-malarial quinine^{3,4}, now used primarily as an ingredient in tonic water. Quinolines are biologically active and have been harnessed by nature and medicinal chemists for many years. As well as antimalarial activity, natural and synthetic quinoline based drugs have been shown to be effective in treating cancer^{5,6}, as antibiotics⁷, antivirals^{8,9}, as anti-inflammatory agents¹⁰ and as analgesics¹¹. Outside of medicinal chemistry, quinolines are used as dyes¹² and chelates, perhaps most prominently in OLEDs where *tris*-(8-hydroxyquinolinato)aluminium is used as both a green emitter and as the electron transport layer^{13,14}.

4.1.1.1 Quinoline synthesis

As one could imagine, for such a noteworthy medicinal molecule there are many synthetic approaches adapted over the previous 150 years to produce functionalised quinolines. The reactions seen here are by no mean an exhaustive list of known quinoline synthesis, but perhaps a look at some of the more important synthetic routes.

The simplest routes to functionalising the quinoline heterocycle begins with functionalised aniline derivatives (see Figure 4.2). Skraup's synthesis from 1880¹⁵

reacts glycerol with aniline in the presence of an acid catalyst. Notably it uses nitrobenzene as both solvent and oxidant. However, the reaction requires less than a one half of a percent water content for the glycerol to react with hot concentrated H_2SO_4 producing a violent reaction with low yields. In 1881, the Doebner-Miller reaction was published¹⁶, synthesising quinolines by reaction of an aniline with α,β -unsaturated carbonyls. This method is able to incorporate and control functionality of the nitrogen containing ring in the 2 position by design. Further functionality can be obtained following the Conrad-Limpach-Knorr¹⁷⁻¹⁹ synthetic approach from 1886/7. The reaction functionalises in the 2- and 4- positions of the nitrogen containing ring, with thermodynamic control over the kinetic or thermodynamic products, allowing a wider variety of potential products to be reached.

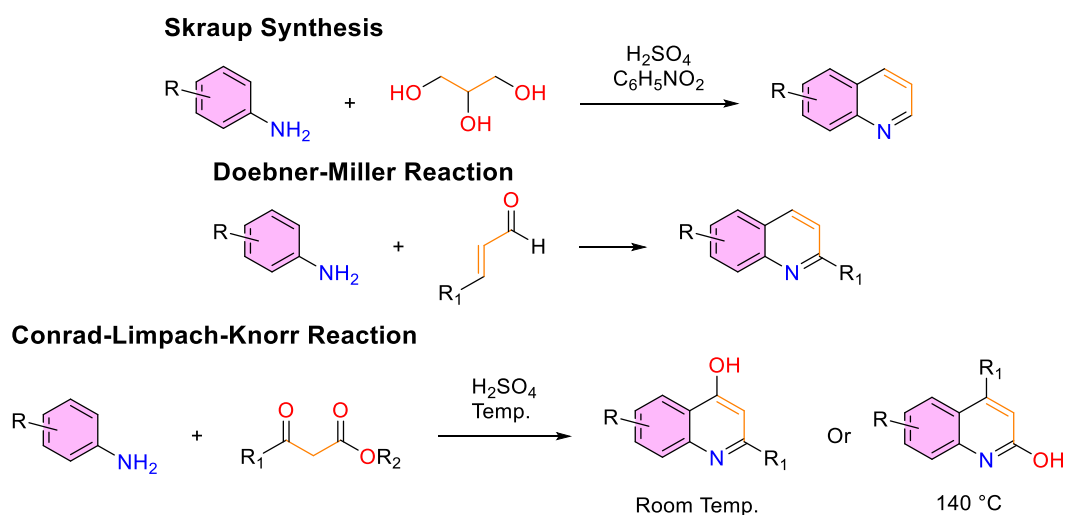


Figure 4.2 – Skarup¹⁵, Doebner-Miller¹⁶ and Conrad-Limpach-Knorr¹⁷⁻¹⁹ functionalised quinoline synthetic pathways.

Controlling the functionalising in the 2,3,4- positions of the quinoline opens even more possible syntheses and uses. *Ortho*-substituted anilines offer a variety of different approaches to this. The four examples seen in Figure 4.3 offer selective functionalisation of the 2- and 3- positions, while being each offering a separate functionality for the 4-position. Friedländers quinoline synthesis from 1883²⁰ utilises 2-aminobenzaldehyde (or keto derivative) and reacts with an asymmetric carbonyl compound. This gives a 2,3-substituted quinoline, with an the 4- position dependent upon the aniline derivative used in the synthesis – for example, the aldehyde would produce a proton in the 4 position, whereas an acetal would give

a 4-methyl substitution. In a similar vein to Friedländer's synthesis, the Niemantowski synthesis²¹ from 1894 reacts 2-aminobenzoic acid with a carbonyl to produce a 4-hydroxy-2,3-substituted quinoline.

Quinoline-4-carboxylic acids allow for a variety of different functionality to be accessed by the synthetic chemist. For this there are two slightly different routes utilised – Doebner synthesis²² and Pfitzinger synthesis²³. Doebner's 1887 synthesis reacts aniline with an aldehyde and pyruvic acid – yielding a quinoline-4-carboxylic acid, with potential for further functionalisation of the 2-position. For a 2,3-substituted quinoline-4-carboxylic acid, Pfitzinger's 1885 synthesis of cinchonic acid provides a simple and efficient synthetic pathway.

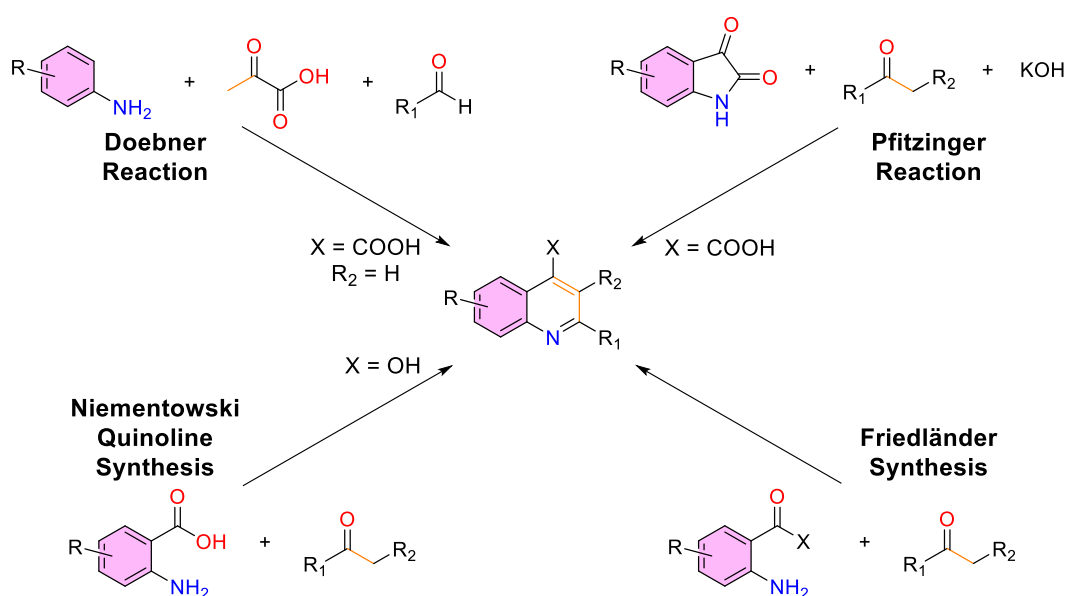


Figure 4.3 – Doebner²², Niementowski²¹, Friedländer²⁰ and Pfitzinger²³ Syntheses of 4-functionalised quinolines.

Recent developments in the synthesis of quinolines still rely heavily on the use of substituted anilines – however newer methodologies are appearing to focus on the use of cheap, reusable organocatalysts as chemists make the conscious effort to focus on greener, more environmentally friendly approaches²⁴.

4.1.1.2 Quinolines as cyclometalating ligands.

Alongside the tris(8-hydroxyquinolineato)aluminium complexes mentioned in section 4.1.1.1, cyclometalated quinolines have been synthesised for a variety of different metals, such as platinum, ruthenium or osmium^{25,26}, as well as iridium(III) complexes, predominantly for potential OLED use^{27,28}.

Iridium(III) cationic complexes tend to focus on the functionalisation of three main ligand architectures – benzo[*h*]quinoline, 2-phenylquinoline and

1-phenylisoquinoline. A comparison of complexes of the form $[\text{Ir}(\text{C}^{\wedge}\text{N})_2(\text{bpy})]\text{PF}_6$ (Figure 4.4) reveals the effects of the different quinolines upon emission wavelength. The benzo[*h*]quinoline complex was synthesised by Ma *et al* in their search for a luminescent assay for silver detection²⁹. They reported the emission of the complex at $\lambda_{\text{em}} = 588$ nm. Kwon *et al* work on potential photodynamic therapy involved the synthesis of both remaining complexes, finding $\lambda_{\text{em}} = 562$ nm for 2-phenylquinoline and $\lambda_{\text{em}} = 593$ nm for 1-phenylisoquinoline. The isoquinoline isomer was in good agreement with the work of Elias *et al*³⁰.

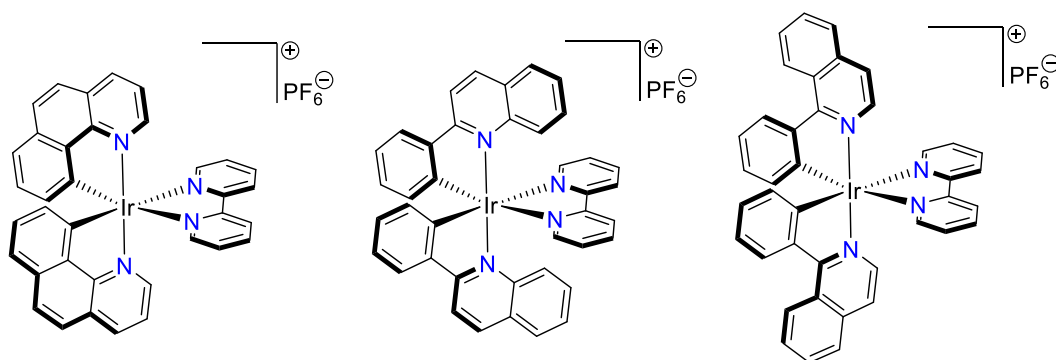


Figure 4.4 – Cationic iridium(III) complexes of Benzo[*h*]quinoline²⁹, 2-phenylquinoline³¹ and 1-phenylisoquinoline^{30,31}.

Earlier work carried out within the Pope research group on quinoline complexes of iridium(III) has focussed on the tuneability of complexes using the 2-phenylquinoline-4-carboxylate ligand system^{32–34}. Amide functionalised quinolines were complexed with iridium(III), using a bpy ancillary ligand to investigate the effects of incorporating additional functionality into the ligand architecture, and to what extent this alters the emission profile. Complexes **Ir1** - **Ir6** (Figure 4.5) exhibited a single broad emission peak, between $\lambda_{\text{em}} = 585$ nm for **Ir1** and $\lambda_{\text{em}} = 627$ nm for **Ir5**. Computational calculations found the HOMO orbitals to be located upon the quinoline cyclometalating ligands and the Ir 5d orbitals, while the LUMO was located almost entirely on the bipyridine ligands. This fits with the experimental data, where the more electron withdrawing the amide substituent, the more bathochromically shifted the emission profile became.

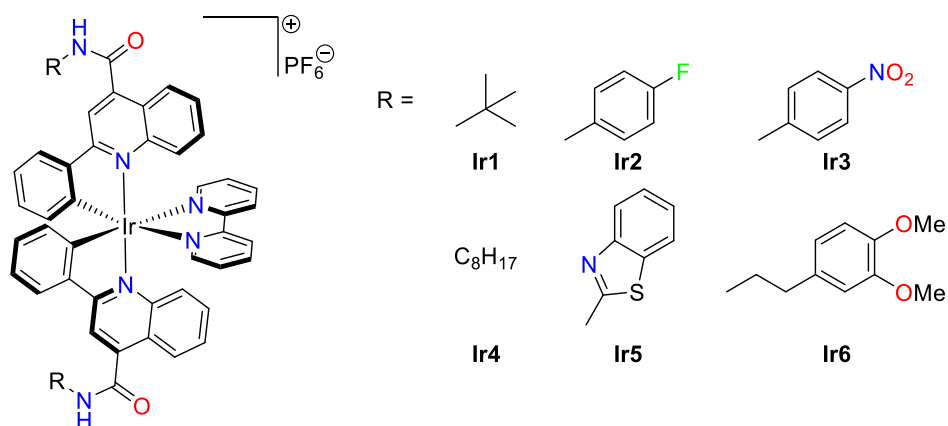


Figure 4.5 – Amide functionalised quinoline complexes, synthesised by Pope *et al*.²

As well as investigating the effects of altering the carboxylate functionality, the group has also looked at changing the ancillary, while keeping the cyclometalating quinoline the same. Several examples have been published, with a selection shown in Figure 4.6. Emission values for the complexes **Ir7** – **Ir14** are all around 620 – 630 nm in MeCN solution, except **Ir15**, where the MLCT emission is fully quenched by the anthraquinone moiety. Ethyl esters of the cyclometalating quinoline are used instead of carboxylic acid groups to aid the solubility of the ligand and intermediates in organic solvents. The ethyl ester can then be hydrolysed after the complex is isolated, and aid solubility in water. The emission of the free acid variants of **Ir7-12** and **Ir14** undergoes a hypsochromic shift of around 50 nm to *ca.* 570 nm (MeCN) and to *ca.* 590 nm in water, while maintaining long phosphorescent lifetimes. The bimetallic complexes of **Ir13** are also water soluble. With Ln³⁺ bound the emission shifts the ³MLCT bathochromically *ca.* 10 nm in the visible region, while demonstrating sensitised near IR emission from Yb³⁺.

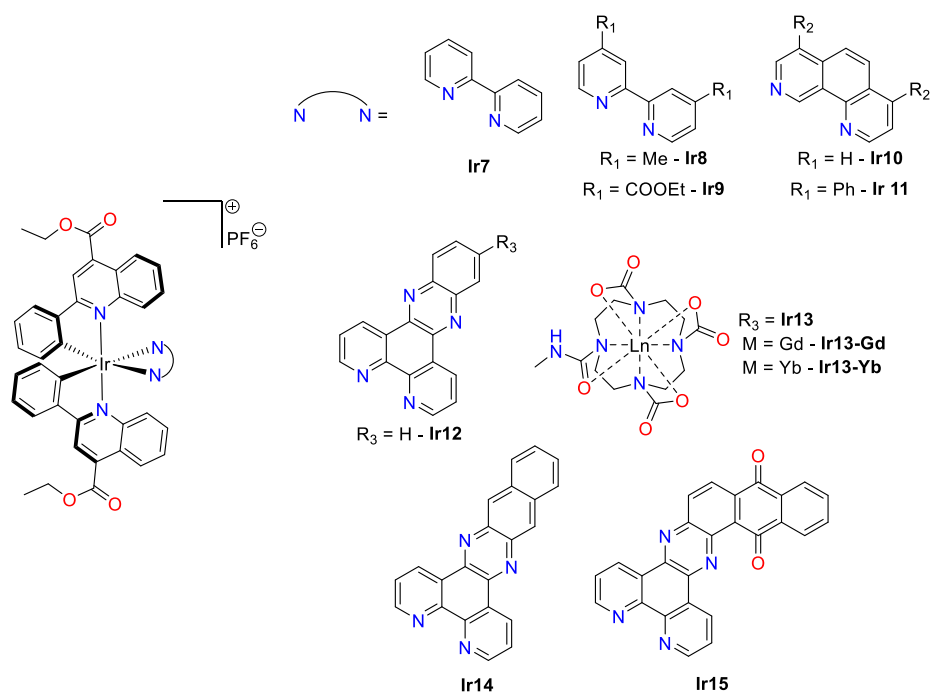


Figure 4.6 – Iridium(III) complexes featuring different ancillary ligands synthesised by Pope *et al*^{33,34}.

4.1.2 Triplet-triplet-annihilation energy up conversion

Anti-Stokes luminescent emission – where the emitted photons are of a higher energy than the absorbed photons – is known as energy upconversion (UC). The process involves the absorption of two photons which typically takes one of two forms: Lanthanide based emission (Figure 4.7) or Triplet-Triplet-Annihilation (TTA) (Figure 4.8)³⁵. Upconversion has been known about since the 1960's^{36,37}. Lanthanide based upconversion may take place via a two or three photon absorption, cooperative sensitisation, or energy transfer upconversion. Lanthanide upconversion takes place in either an inorganic host, used for example in lasers³⁸, or within upconverting nanoparticles, allowing use as *in vivo* therapeutics^{39,40}.

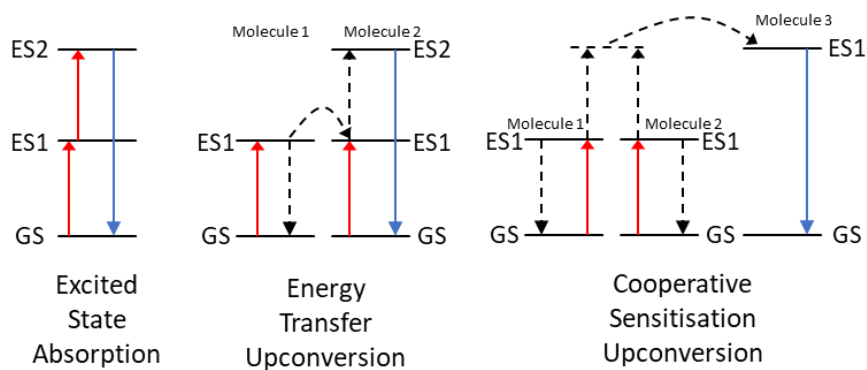


Figure 4.7 – Different types of Upconversion processes – adapted from Xu *et al*⁴¹. GS – Ground State, ES – Excited State, Red line – Photon Absorption, blue line – Photon Emission, Dashed line energy transfer processes.

More relevant to this work however is TTA upconversion. TTA upconversion is a solution phase two photon upconversion process taking place between sensitiser and annihilators. Energy is absorbed by the sensitiser, exciting typically to a singlet excited state. The molecule undergoes intersystem crossing to a triplet excited state. The system then undergoes Triplet-Triplet-Energy Transfer (TTET) to a low lying triplet level of similar energy on the emitter while the sensitiser relaxes back to ground state non radiatively. The emitter triplet levels are long lived in solution and the whole process repeats many times, before annihilating with a second triplet excited emitter. Upon annihilation, one emitter relaxes back to the ground state without emission while the second molecule is excited to a higher energy singlet excited state, which quickly gives emissive fluorescent relaxation, generating the higher energy emission.⁴²

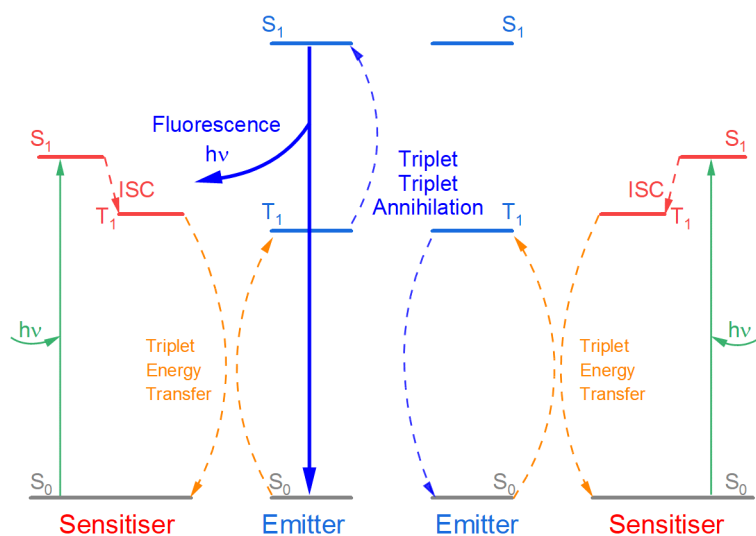


Figure 4.8 – Jablonski diagram represented the process of Triplet-Triplet Annihilation.

An annihilator needs to have a high quantum yield of fluorescence, triplet states accessible at suitable energy levels and long triplet lifetimes³⁵. To this end, there are many polycyclic aromatic hydrocarbons that fit the criteria. Commonly used in the literature are derivatives of anthracene⁴³, perylene⁴⁴ or pyrene⁴⁵.

The sensitizer should be able to absorb strongly at the excitation wavelength, undergo efficient intersystem crossing and have triplet states of comparable energy to the emitter. Importantly, the $T_1 \rightarrow S_0$ decay rate should be slow enough to enable TTET³⁵. Organic compounds may employ the use of a cyclic ketone, such as benzophenone or fluorenones, or via the use of a heavy atom, such as Br or I, to induce triplet states^{46,47} and become efficient sensitizers, while the inorganic chemist may look towards metal complexes, such as Pt⁴⁸, Ru⁴⁹, Re⁵⁰ or Ir⁵¹, some examples can be seen in Figure 4.9.

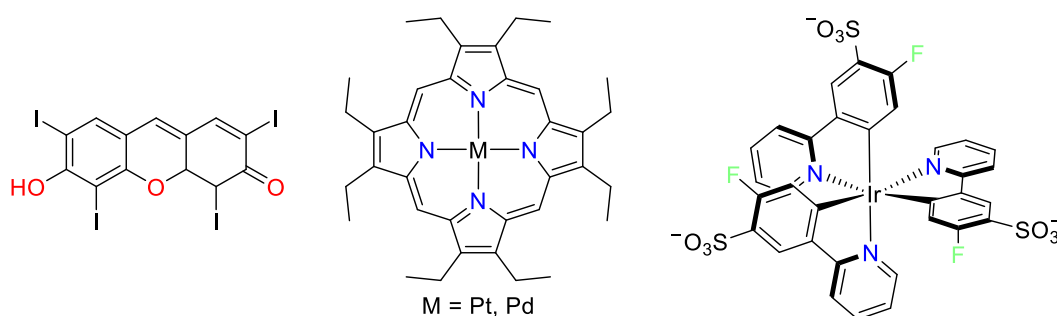


Figure 4.9 – Examples of known sensitizers – Organic tetraiodohydroxyfluorone⁴⁶, octaethylporphyrin complexes^{48,52} and an iridium(III) sensitizer⁵³, capable of upconversion in aqueous solvent.

4.1.3 Transient absorption spectroscopy

Transient absorption spectroscopy (TA) is a pump-probe technique used for measuring changes associated with excited state absorption energies. The technique first gained prominence with the seminal work of George Porter and Ronald Norrish in 1950⁵⁴, who first utilised powerful flash lamps to initiate radical chemistry⁵⁵ before applying the technique to reaction kinetics on the microsecond scale. The work earned Norrish and Porter a 25 % share each of the 1967 Nobel Prize in chemistry alongside Manfred Eigen for his work on determination of kinetics in the nanosecond domain⁵⁶.

TA spectroscopy is a pump-probe technique. Figure 4.10 shows a simple molecule with ground state G and excited states A and B. Before the photoexcitation, a reference spectrum is taken, giving information on the ground state absorption

(OD_0 where OD : optical density). At time = 0 a high-powered pump source will reach the sample, forcing the molecule into an excited state, before the probe pulse can record the transitions $A \rightarrow B$ and $G \rightarrow A$ (OD_t). The spectrum is presented as a change in absorption between OD_t and OD_0 : $\Delta OD = OD_t - OD_0$. These measurements can be presented as a function of wavelength or a function of time. A ground state bleach ($-\Delta OD$) refers to the depletion of the ground state to the excited state which occurs during the pump phase. These measurements can be on the femtosecond domain, which can be used for measuring singlet excited states such as photosystem I⁵⁷ and II⁵⁸, or in the nanosecond time frame for triplet excited states.

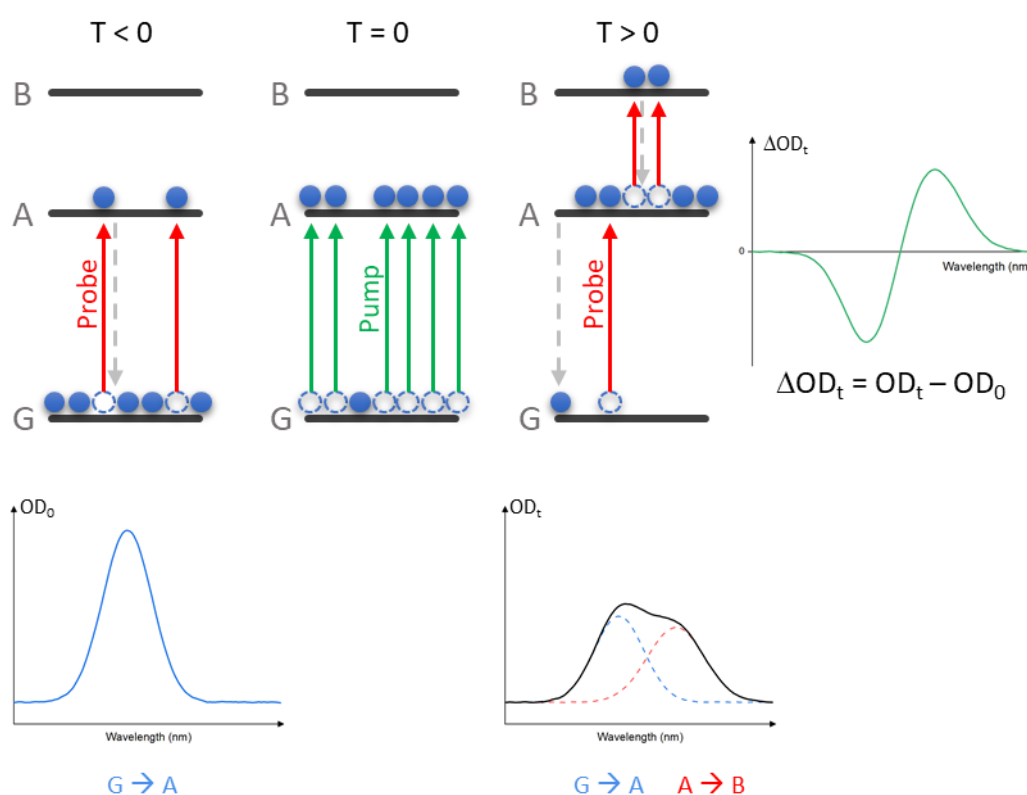


Figure 4.10 - Principles of Transient Absorption Spectroscopy adapted from Edinburgh Instruments⁵⁹. G represents ground state and A and B are distinct excited states.

4.2 Aims of the Chapter

This chapter sets out to synthesis and characterise a set of novel *bis*-cyclometalated iridium(III) complexes, based upon the novel substituted 2-naphthylquinoline framework. The work set out to study the use of electron donating and withdrawing groups have upon the quinoline ligands, as well as the difference between the two isomers of naphthalene. It will also show what effects these changes have on the photophysical properties of the resultant organometallic iridium(III) complexes. In total, seven novel cationic complexes

have been isolated and characterised with the photophysical parameters investigated.

4.3 Results and Discussions.

4.3.1 Ligand synthesis and characterisation.

A series of novel substituted 2-(naphthyl)quinoline-4-carboxylates were synthesised following Pfitzinger reaction²³. Substituted isatin underwent ring opening in the presence of base, hydrolysing the secondary amine to give a keto-acid aniline. Acetyl naphthalene is then able to form an imine with the primary amine, before tautomerizing to the enamine, which cyclises to give substituted 2-naphthyl-quinoline-4-carboxylic acids in good yields. To aid solubility, the acids underwent Fischer Esterification⁶⁰ to yield **L¹⁻⁷H** (Figure 4.11).

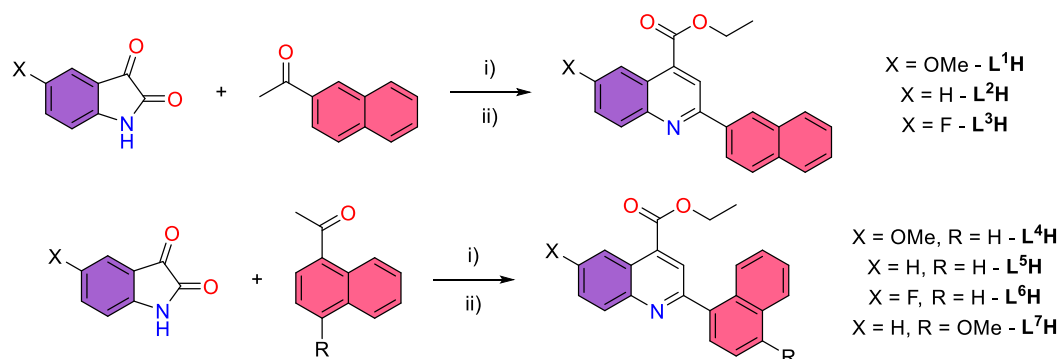


Figure 4.11 – Pfitzinger ligand synthesis and subsequent Fischer esterification: i) KOH (3 eq), EtOH, 24 hours, 78 °C; ii) Cat. H₂SO₄, EtOH, 16 hours, 78 °C.

The crude acids were precipitated from solution via neutralisation with HCl before being collected by filtration. Pure acids were isolated via an acid-base extraction as yellow solids and characterised by ¹H, ¹⁹F{¹H}, ¹³C NMR spectroscopy and HR MS. After esterification, reaction mixtures were cooled to room temperature and neutralised with 0.1 M aqueous sodium carbonate. The solvent was removed *in vacuo* before washing with water to remove salts. The ethyl esters were then purified via silica gel column chromatography, eluting with DCM. The first yellow band off the column was collected, and solvent removed *in vacuo* to yield **L¹⁻⁷H**. Ligands were once again characterised by ¹H, ¹⁹F{¹H}, ¹³C NMR spectroscopies and HR MS. For each of the 2-naphthyl ligands, a singlet centring around ca. 8.8 – 8.9 ppm in the ¹H NMR spectrum. This can be assigned to the 3 position of the quinoline ring, which is both α - to the carboxylate moiety as well as α - to the naphthyl moiety. In the 1-naphthyl complexes this peak appears at ca. 8.3 ppm. Likely the significant shielding increase could be ascribed to the through space aromatic ring current interactions increasing with the 1-naphthyl isomer. After the successful synthesis starting from 5-fluoroisatin, the same synthetic route was also attempted with 1-acetyl-4-fluoronaphthalene.

Despite literature reports for the isolation and characterisation of 2-(4-fluoronaphth-1-yl)quinoline-4-carboxylic acid⁶¹, it was noted that the ¹⁹F NMR spectrum signal was very weak after esterification. Upon examination of the ¹H NMR spectrum, a second set of the ethyl peaks were noted, suggesting a nucleophilic aromatic substitution took place during the initial synthesis. While ethanol was used in the synthesis, the peaks firstly integrate stoichiometrically and secondly are more downfield than expected for solvent peaks⁶².

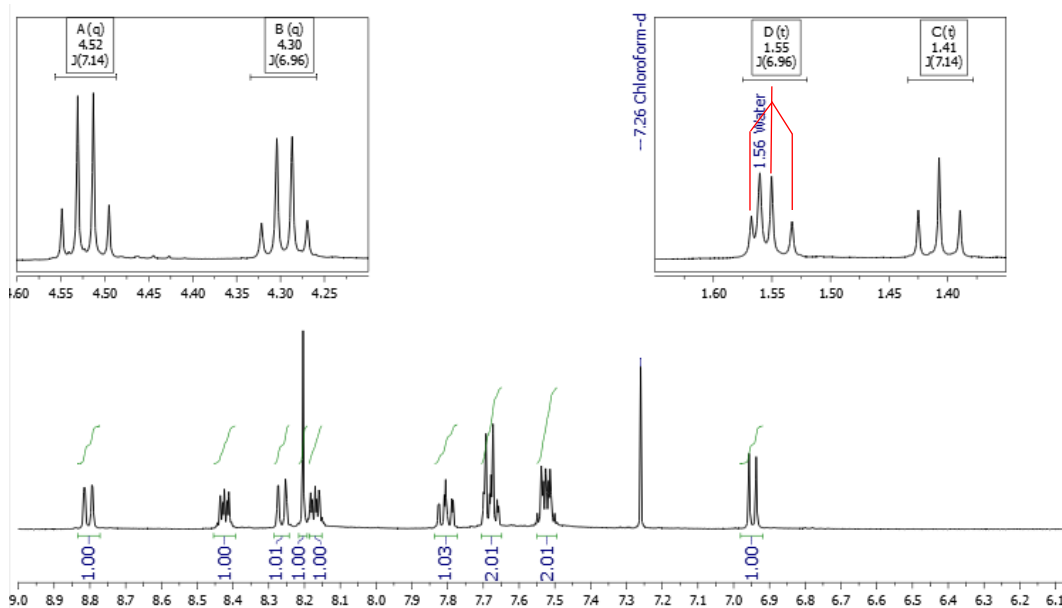


Figure 4.12 – ¹H NMR spectrum of quinoline ethyl ester, having undergone S_NAr substitution on the 4-fluoronaphthyl position.

$^{19}\text{F}\{^1\text{H}\}$ NMR spectra on L^3H , L^6H and the corresponding acids showed a single peak centred around -110 ppm. This has shifted downfield from the starting material, where the ^{19}F singlet is at -119.8 ppm (Figure 4.13).

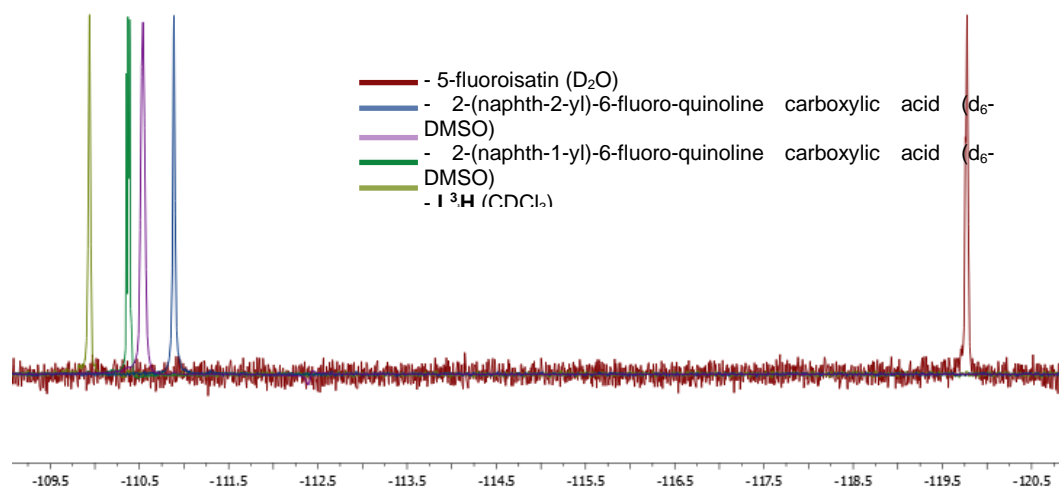


Figure 4.13 – Overlaid ^{19}F NMR spectra showing starting 5-fluoroisatin and the synthesised acids and esters.

4.3.2 Complex synthesis and characterisation.

With ligands in hand, bridged chloride iridium(III) dimers could be synthesised following the Nonoyama route⁶³. Briefly, two equivalents of ligand were heated at reflux with one equivalent of $\text{IrCl}_3 \cdot x\text{H}_2\text{O}$ in 2-methoxyethanol. Dimers were then precipitated from solution by the addition of water, collected under reduced pressure and washed with water and EtOH. In general, dimers are used without further analysis or purification, but one example was purified following the procedures set out by Sprouse *et al*⁶⁴. Crude dimer was washed with EtOH and acetone before dissolving in DCM and filtering. Toluene and hexanes were added to the filtrate, which was reduced in volume before being cooled to crystallise out the dimer. ^1H NMR spectrum of $[\{\text{Ir}(\text{L}^6)_2(\mu\text{-Cl})\}_2]$ can be seen below in Figure 4.14.

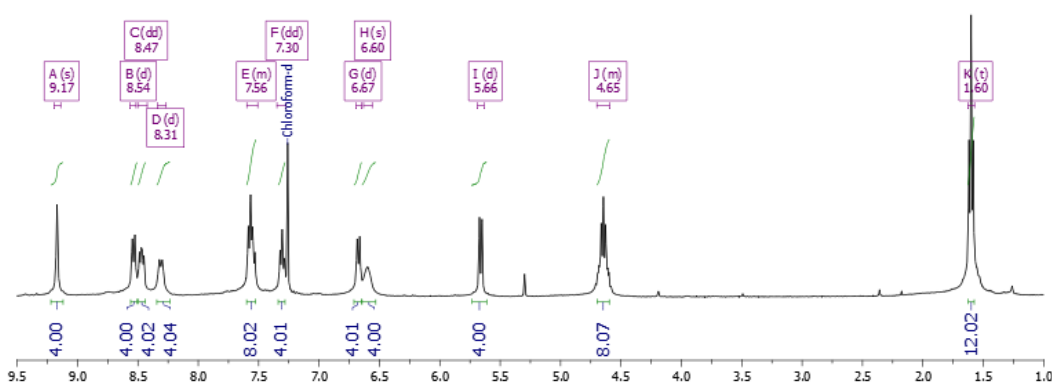
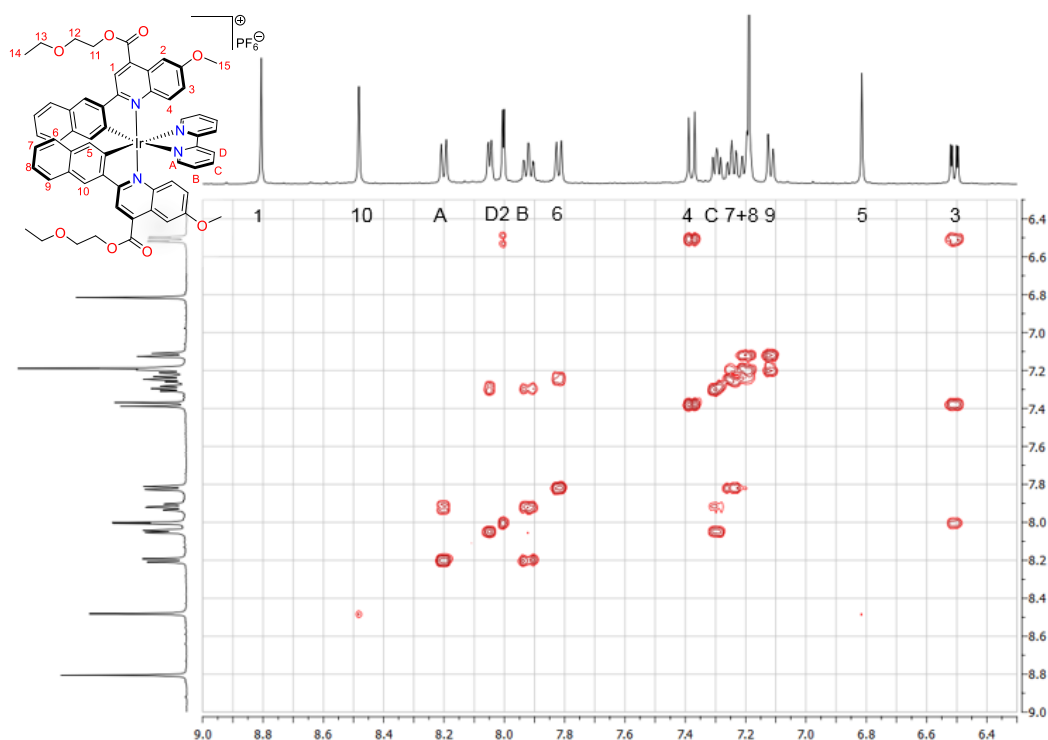


Figure 4.14 – ^1H NMR spectrum of $[\{\text{Ir}(\text{L}^6)_2(\mu\text{-Cl})\}_2]$ recorded in CDCl_3 .

The spectrum consists of 11 separate resonances (with what appears to be two overlapping signals at ca. 7.56 ppm). The free ligand contains 13 proton resonances, while a cyclometalated ligand would exhibit 12 – therefore suggesting cyclometalation has taken place. Secondly, it suggests there is only one orientation of C^N ligand chelates present. Dimeric species typically form with racemic mixture of the $\Delta\Delta/\Lambda\Lambda$ -dimeric structure⁶⁵. There is also a shift in the proton on the quinoline ring in position three. On the free ligand this proton is seen at 8.30 ppm, but it shifts to 9.17 ppm in the dimer. This is likely due to the inductive effect of the cationic iridium(III) centre. An aromatic doublet is also seen heavily shielded at 5.66 ppm. This is assigned to the proton *ortho*- to the site of cyclometalation where the adjacent aromatic ring currents from the neighbouring ligand are inducing a shielding effect⁶⁶. The multiplet at 4.65 ppm would be expected to be a -CH₂ quartet from the ethyl group. This likely brought about by a slight degree of disorder in the structure as the integration is of the magnitude expected.

The crude dimers could then be split by the addition of the bpy ancillary ligand. Initially, the same synthetic route was utilised as seen in the previous chapters; dimer was heated with two equivalents of bpy in 2-ethoxyethanol for 24 hours. The reaction was monitored by TLC before precipitation via counterion metathesis using [NH₄][PF₆]. Complexes were isolated via silica gel column chromatography, eluting first unreacted starting materials with DCM, before eluting and collecting the product as a red band using 95:5 (DCM:MeOH). Solvent was removed *in vacuo* and the red solid recrystallised from DCM with diethyl ether. When the first set of complexes (chelated with **L¹⁻³H**) was characterised by NMR spectroscopy, a degree of transesterification had taken place with the solvent, forming an ethoxy ethyl ester. The magnitude depended upon the electronic properties of the quinoline substituted ligand. For [Ir(**L¹**)₂(bpy)]PF₆ the product was entirely present as the ethoxyethyl ester – confirmed by ¹H, ¹H-¹H COSY (see Figure 4.15), ¹³C NMR spectroscopy and HR MS. [Ir(**L³**)₂(bpy)]PF₆ presented as the ethyl ester, confirmed again by ¹H and ¹³C NMR spectra as well as HR MS. [Ir(**L²**)₂(bpy)]PF₆ was a complex mixture of products on the ¹H NMR spectrum. The electron donating -OMe group resonance effects aid the stabilisation of intermediates during the transesterification. Conversely, the electron withdrawing -F substituents negative inductive effect will destabilise these intermediates.

Since the transesterification was not occurring during the dimer formation stage, as seen in ^1H NMR spectra, a change of approach for the splitting stage was needed. The complexes were synthesised via $\text{cis-}[\text{Ir}(\text{MeCN})_2(\text{L}^{1-7})_2]\text{BF}_4$ intermediate instead. Iridium(III) dimer was heated in MeCN, a weakly coordinating solvent, with two equivalents of AgBF_4 . Upon cooling to room temperature, the intermediate complexes were filtered over celite to remove the precipitated AgCl , before concentrating *in vacuo*. The *bis*-MeCN complexes were then heated in chloroform with one equivalent of bpy before counter-ion metathesis with $[\text{NH}_4][\text{PF}_6]$. Crude complexes could then be purified via silica gel chromatography, eluting unreacted ligand with DCM before collecting the complexes as a red band eluted with 95:5 (DCM/MeOH). Complexes were characterised by ^1H , $^{19}\text{F}\{^1\text{H}\}$, $^{13}\text{C}\{^1\text{H}\}$ NMR, HR MS, absorption, emission, and IR spectroscopies.



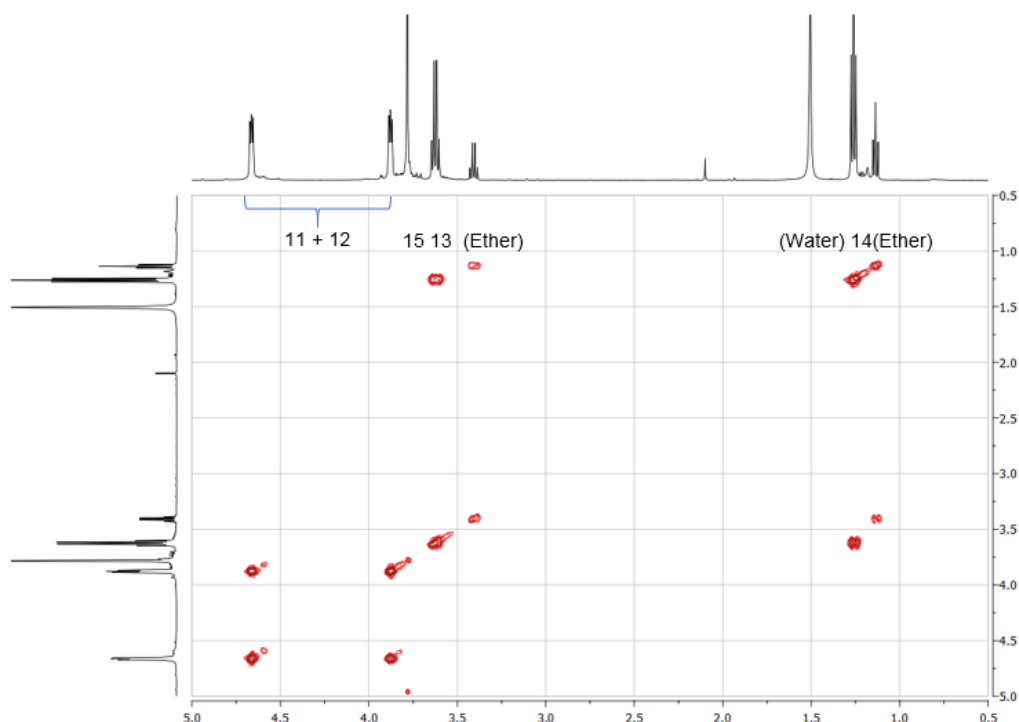


Figure 4.15 – ^1H - ^1H COSY NMR spectra for $[\text{Ir}(\text{L}^1)_2(\text{bpy})]\text{PF}_6$ (See insert). Top expanded aromatic region. Below: expanded aliphatic region.

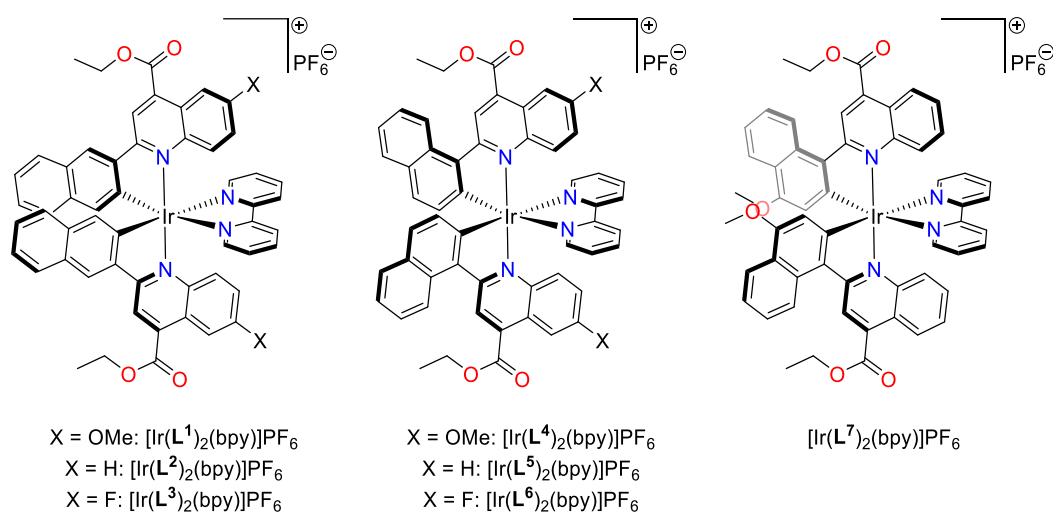


Figure 4.16 – Complexes synthesised and characterised in this work.

^1H NMR spectra once again confirms the C_2 symmetry with both cyclometalating ligands having equivalent environments. The proton in position three of the quinoline ring has shifted downfield from ca. 8.6 ppm in L^{1-3}H to ca. 8.9 ppm in the corresponding complexes. For the 1-naphthyl ligands L^{4-7}H the peak appears ca. 8.2 ppm, shifting to ca. 9.15 ppm for the unsubstituted 1-naphthyl complexes and 8.96 ppm for the 4-methoxy-1-naphthyl complex of L^7H . This shift is indicative of chelation, caused by the inductive effects of the larger cationic iridium(III) atom.

For complexes $[\text{Ir}(\text{L}^{1-6})_2(\text{bpy})]\text{PF}_6$, the proton resonance *ortho*- to the site of cyclometalation is more shielded, at ca. 6.9 ppm. This resonance is even more shifted in $[\text{Ir}(\text{L}^7)_2(\text{bpy})]\text{PF}_6$ at 6.20 ppm due to also being adjacent to both the Ir-C σ bond and a methoxy group. In the cases of L^1H and L^4H the methoxy group appears ca. 4 ppm; upon complexation there was only a minor shift of this resonance to ca. 3.85 ppm. Conversely, for L^7H the methoxy group appears at 4.08 ppm, and upon complexation shifts significantly to 3.36 ppm which is assigned to the proximity to the Ir-C σ bond.

$^{19}\text{F}\{^1\text{H}\}$ NMR spectra were also obtained for $[\text{Ir}(\text{L}^3)_2(\text{bpy})]\text{PF}_6$ and $[\text{Ir}(\text{L}^6)_2(\text{bpy})]\text{PF}_6$. (Table 4.1) The doublet at -72.6 ppm ($^1J_{\text{FP}} = 711$ Hz) is assigned to the PF_6^- counterion. A second resonance is seen around -107.5 ppm, representing the resonance of the fluorine substituent on the quinoline ring, representing a subtle shift upon complexation.

In each isolated complex, the high-resolution mass spectrometry data provides the expected isotopic distributions and a m/z peak that is expected for $[\text{M} - \text{PF}_6]^+$.

Compound	Ligand $^{19}\text{F}\{^1\text{H}\}$ δ_{F} / ppm	PF_6^- $^{19}\text{F}\{^1\text{H}\}$ δ_{F} ($^1J_{\text{FP}}$) / ppm
L^3H	-110.4 (s)	-
L^6H	-109.9 (s)	-
$[\text{Ir}(\text{L}^3)_2(\text{bpy})]\text{PF}_6$	-107.2 (s)	-72.6 (d, 711 Hz)
$[\text{Ir}(\text{L}^6)_2(\text{bpy})]\text{PF}_6$	-107.7 (s)	-72.6 (d, 711 Hz)

Table 4.1 - $^{19}\text{F}\{^1\text{H}\}$ NMR spectra shifts for ligand and complexes.

4.3.3 X-Ray crystallography

Single crystal diffraction data collection and geometry refinements were carried out by The UK National Crystallographic Service at Southampton University. Single, red plate-shaped crystals from three of the complexes, $[\text{Ir}(\text{L}^3)_2(\text{bpy})]\text{PF}_6$, $[\text{Ir}(\text{L}^5)_2(\text{bpy})]\text{PF}_6$ and $[\text{Ir}(\text{L}^6)_2(\text{bpy})]\text{PF}_6$, were successfully isolated from vapor diffusion of diethyl ether into a DCM solution of the complex and investigated using X-ray diffraction. Although of lower quality, the data for $[\text{Ir}(\text{L}^6)_2(\text{bpy})]\text{PF}_6$ was still sufficient to allow determination of the key features of the structure. In each example, there is solvent of crystallisation present, with solvent masking techniques employed in the refinement of $[\text{Ir}(\text{L}^5)_2(\text{bpy})]\text{PF}_6$ and $[\text{Ir}(\text{L}^6)_2(\text{bpy})]\text{PF}_6$. Each of the 3 structures displayed the expected coordination with a *cis*-C,C and *trans*-N,N arrangement of the cyclometalating ligands around the distorted octahedral iridium(III) centre⁶⁵. Each of the monocationic complexes is charged

balanced by the presence of a single hexafluorophosphate ion. $[\text{Ir}(\text{L}^3)_2(\text{bpy})]\text{PF}_6$ also shows a small degree of disorder over one of the ethyl esters.

[Ir(L³)₂(bpy)]PF₆							
Bond Length (Å)							
Ir(1)	N(1)	2.081(3)		Ir(1)	N(62)	2.166(3)	
Ir(1)	N(31)	2.099(3)		Ir(1)	C(1)	2.006(3)	
Ir(1)	N(61)	2.166(3)		Ir(1)	C(31)	2.007(3)	
Bond Angle (°)							
N(1)	Ir(1)	N(31)	172.09(10)	C(1)	Ir(1)	N(61)	169.08(12)
N(1)	Ir(1)	N(61)	103.88(10)	C(1)	Ir(1)	N(62)	96.16(11)
N(1)	Ir(1)	N(62)	81.40(10)	C(1)	Ir(1)	C(31)	89.75(13)
N(31)	Ir(1)	N(61)	82.58(10)	C(31)	Ir(1)	N(1)	94.16(12)
N(31)	Ir(1)	N(62)	104.93(10)	C(31)	Ir(1)	N(31)	80.10(12)
N(62)	Ir(1)	N(61)	74.94(10)	C(31)	Ir(1)	N(61)	99.75(12)
C(1)	Ir(1)	N(1)	80.59(12)	C(31)	Ir(1)	N(62)	171.90(12)
C(1)	Ir(1)	N(31)	93.87(12)				
[Ir(L⁵)₂(bpy)]PF₆							
Bond Length (Å)							
Ir(1)	N(1)	2.079(3)		Ir(1)	N(62)	2.168(3)	
Ir(1)	N(31)	2.080(3)		Ir(1)	C(1)	2.001(4)	
Ir(1)	N(61)	2.143(3)		Ir(1)	C(31)	1.994(4)	
Bond Angle (°)							
N(1)	Ir(1)	N(31)	174.57(12)	C(1)	Ir(1)	N(61)	173.49(14)
N(1)	Ir(1)	N(61)	100.87(13)	C(1)	Ir(1)	N(62)	98.41(14)
N(1)	Ir(1)	N(62)	78.44(12)	C(31)	Ir(1)	N(1)	96.52(15)
N(31)	Ir(1)	N(61)	83.60(12)	C(31)	Ir(1)	N(31)	79.70(14)
N(31)	Ir(1)	N(62)	105.83(12)	C(31)	Ir(1)	N(61)	98.02(15)
N(61)	Ir(1)	N(62)	75.37(12)	C(31)	Ir(1)	N(62)	170.58(14)
C(1)	Ir(1)	N(1)	79.48(15)	C(31)	Ir(1)	C(1)	88.37(16)
C(1)	Ir(1)	N(31)	96.43(15)				
[Ir(L⁶)₂(bpy)]PF₆							
Bond Length (Å)							
Ir(1)	N(1)	2.095(10)		Ir(1)	N(62)	2.145(10)	
Ir(1)	N(31)	2.075(10)		Ir(1)	C(1)	1.990(14)	
Ir(1)	N(61)	2.160(11)		Ir(1)	C(31)	1.991(13)	
Bond Angle (°)							
N(1)	Ir(1)	N(61)	99.9(4)	C(1)	Ir(1)	N(61)	172.1(4)
N(1)	Ir(1)	N(62)	83.1(4)	C(1)	Ir(1)	N(62)	96.9(5)
N(31)	Ir(1)	N(1)	175.2(4)	C(1)	Ir(1)	C(31)	90.2(5)
N(31)	Ir(1)	N(61)	81.3(4)	C(31)	Ir(1)	N(1)	97.4(5)
N(31)	Ir(1)	N(62)	101.6(4)	C(31)	Ir(1)	N(31)	77.9(5)
N(62)	Ir(1)	N(61)	75.3(4)	C(31)	Ir(1)	N(61)	97.6(5)
C(1)	Ir(1)	N(1)	80.4(5)	C(31)	Ir(1)	N(62)	172.9(5)
C(1)	Ir(1)	N(31)	99.0(5)				

Table 4.2 – Selected bond lengths and bond angles obtained from crystallographic data from complexes [Ir(L³)₂(bpy)]PF₆, [Ir(L⁵)₂(bpy)]PF₆ and [Ir(L⁶)₂(bpy)]PF₆.

When examining the bond lengths around the iridium(III) centre, there is notably little difference between the two isomers of naphthalene, and in fact the Ir-C bonds are comparable to those seen earlier in Chapters 2 and 3. All three complexes exhibit an elongation of the Ir-N bonds of the bipyridine ligand in comparison to the Ir-N quinoline bonds, again seen in previous chapters, due to the larger trans influence of the strong σ -bonds from the naphthyl groups. All three complexes exhibit appreciable torsion angles between the naphthyl and quinoline rings of the

cyclometalating ligands, particularly in $[\text{Ir}(\text{L}^5)_2(\text{bpy})]\text{PF}_6$ and $[\text{Ir}(\text{L}^6)_2(\text{bpy})]\text{PF}_6$ (Table 4.3).

$[\text{Ir}(\text{L}^3)_2(\text{bpy})]\text{PF}_6$				Torsion Angle / °
C(1)	C(10)	C(11)	N(1)	4.5(4)
C(31)	C(40)	C(41)	N(31)	4.3(4)
$[\text{Ir}(\text{L}^5)_2(\text{bpy})]\text{PF}_6$				
C(1)	C(1)	C(1)	C(1)	21.1(5)
C(31)	C(31)	C(31)	C(31)	12.3(5)
$[\text{Ir}(\text{L}^6)_2(\text{bpy})]\text{PF}_6$				
C(1)	C(1)	C(1)	C(1)	-19.3(18)
C(31)	C(31)	C(31)	C(31)	-13(2)

Table 4.3 – Selected torsion angles between naphthyl and quinoline rings.

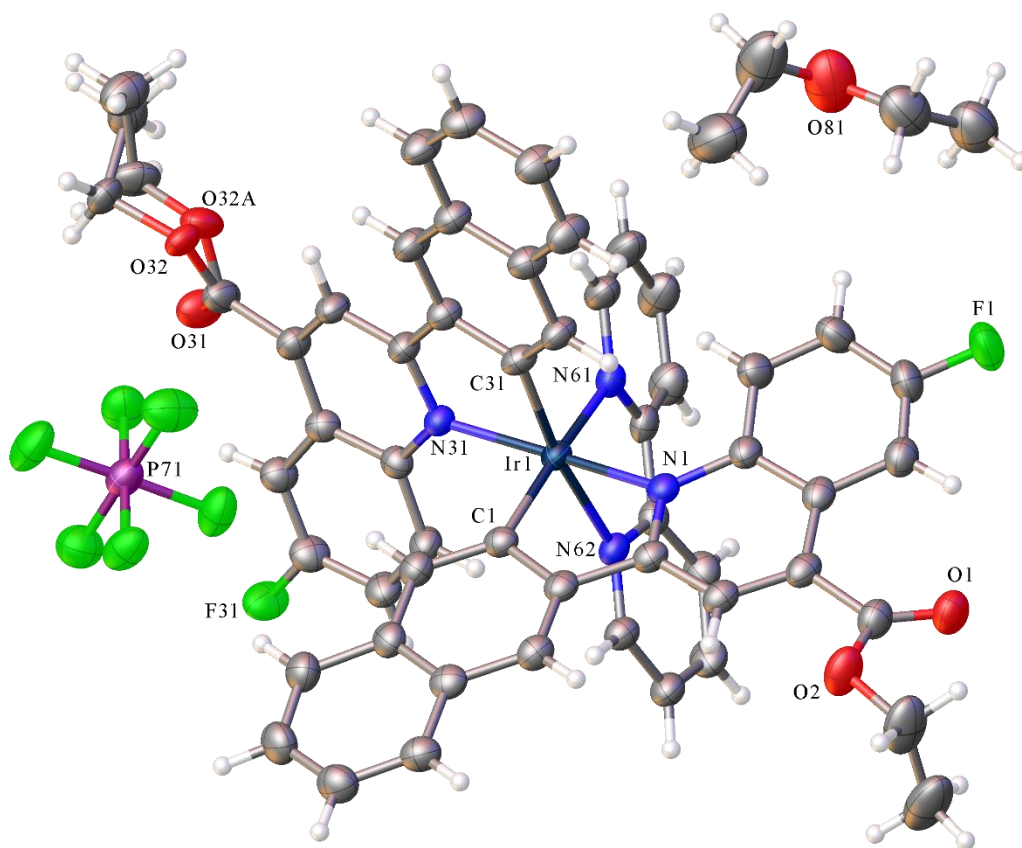


Figure 4.17 - X-ray structures of $[\text{Ir}(\text{L}^3)_2(\text{bpy})]\text{PF}_6$ ($\text{C}_{58}\text{H}_{48}\text{F}_8\text{IrN}_4\text{O}_5\text{P}$, $M_r = 1256.17$, triclinic, $P-1$ (No. 2), $a = 12.3219(3)$ Å, $b = 13.6454(2)$ Å, $c = 15.6097(3)$ Å, $\alpha = 81.489(2)^\circ$, $\beta = 86.747(2)^\circ$, $\gamma = 76.124(2)^\circ$, $V = 2519.30(9)$ Å³, $T = 100(2)$ K, $Z = 2$, $Z' = 1$, $\mu(\text{MoK}\alpha) = 2.767$ mm⁻¹, 56370 reflections measured, 11532 unique ($R_{int} = 0.0392$) which were used in all calculations. The final wR_2 was 0.0821 (all data) and R_1 was 0.0315 ($I > 2(I)$).}

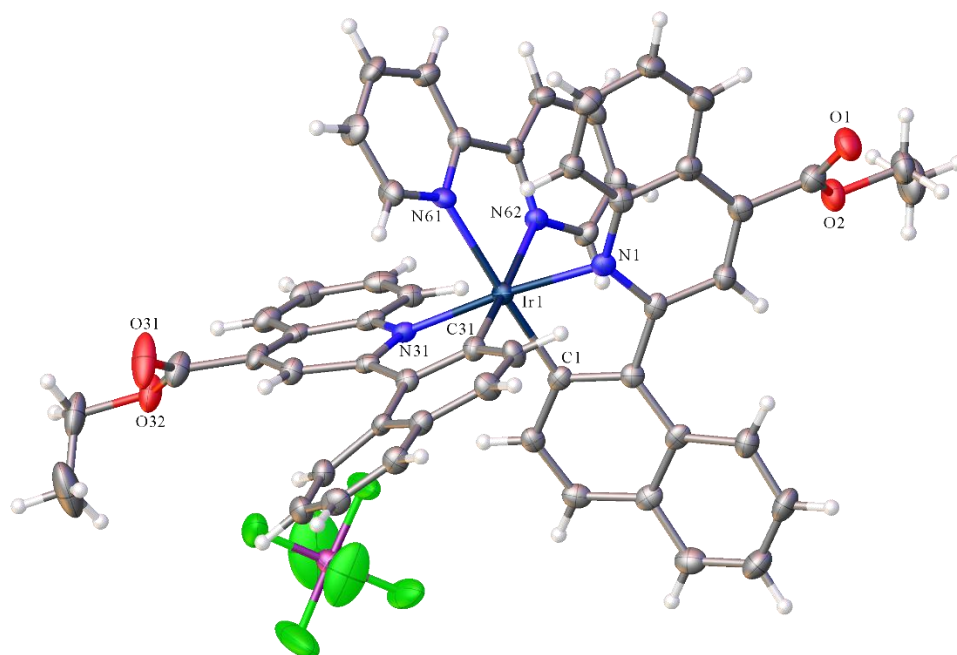


Figure 4.18 - X-ray structures of $[\text{Ir}(\text{L}^5)_2(\text{bpy})]\text{PF}_6$ $\{\text{C}_{58}\text{F}_6\text{H}_{50}\text{IrN}_4\text{O}_5\text{P}$, $M_r = 1220.19$, monoclinic, $P2_1/n$ (No. 14), $a = 14.8065(3)$ Å, $b = 16.0145(3)$ Å, $c = 21.9767(4)$ Å, $\beta = 105.323(2)^\circ$, $\alpha = \gamma = 90^\circ$, $V = 5025.84(17)$ Å³, $T = 100(2)$ K, $Z = 4$, $Z' = 1$, $\mu(\text{MoK}\alpha) = 2.766$ mm⁻¹, 54477 reflections measured, 11515 unique ($R_{\text{int}} = 0.0447$) which were used in all calculations. The final wR_2 was 0.0873 (all data) and R_1 was 0.0395 ($I > 2(I)$).}

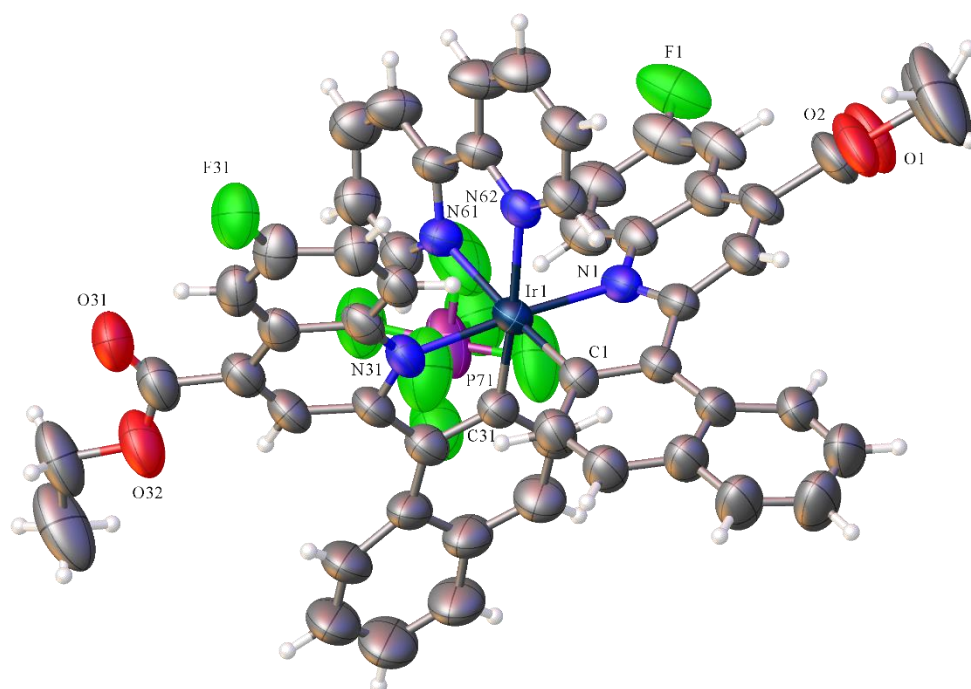


Figure 4.19 - X-ray structures of $[\text{Ir}(\text{L}^5)_2(\text{bpy})]\text{PF}_6$ $\{\text{C}_{55}\text{Cl}_2\text{F}_8\text{H}_{40}\text{IrN}_4\text{O}_4\text{P}$, $M_r = 1266.98$, monoclinic, $I2/a$ (No. 15), $a = 17.9525(6)$ Å, $b = 19.6127(9)$ Å, $c = 29.2291(9)$ Å, $\beta = 93.838(3)^\circ$, $\alpha = \gamma = 90^\circ$, $V = 10268.4(7)$ Å³, $T = 100(2)$ K, $Z = 8$, $Z' = 1$, $\mu(\text{CuK}\alpha) = 6.982$ mm⁻¹, 39479 reflections measured, 8711 unique ($R_{\text{int}} = 0.1139$) which were used in all calculations. The final wR_2 was 0.2640 (all data) and R_1 was 0.0893 ($I > 2(I)$).}

4.3.4 Electrochemical properties

The redox potential of the iridium(III) complexes was studied by cyclic voltammetry with potentials listed below in Table 3.2. Measurements were made in deoxygenated DCM using a platinum disc electrode (scan rate $\nu = 200 \text{ mV s}^{-1}$, $1 \times 10^{-3} \text{ M}$ solutions, 0.1 M $[\text{NBu}_4][\text{PF}_6]$ as a supporting electrolyte).

Complex	Oxidation	Reduction	
	$E_{1/2} / \text{V}$	$E_{(\text{red } 1)} / \text{V}$	$E_{(\text{red } 2)} / \text{V}$
$[\text{Ir}(\text{L}^1)_2(\text{bpy})][\text{PF}_6]$	+1.26	-1.14 ^a	-1.31 ^a
$[\text{Ir}(\text{L}^2)_2(\text{bpy})][\text{PF}_6]$	+1.28	-1.10 ^a	-1.27 ^a
$[\text{Ir}(\text{L}^3)_2(\text{bpy})][\text{PF}_6]$	+1.32	-0.93 ^a	-1.21 ^a
$[\text{Ir}(\text{L}^4)_2(\text{bpy})][\text{PF}_6]$	+1.29	-1.11 ^b	-1.33 ^b
$[\text{Ir}(\text{L}^5)_2(\text{bpy})][\text{PF}_6]$	+1.37	-1.05 ^b	-1.29 ^b
$[\text{Ir}(\text{L}^6)_2(\text{bpy})][\text{PF}_6]$	+1.39	-0.97 ^b	-1.22 ^b

Table 4.4 - Electrochemical properties of the iridium(III) complexes obtained from cyclic voltammetry. Potentials measured in deaerated DCM solutions at 200 mVs^{-1} with 0.1 M $[\text{NBu}_4][\text{PF}_6]$ as supporting electrolyte calibrated with Fc/Fc^+ ; ^a cathodic peak of irreversible process; ^b $E_{1/2}$ values for fully reversible process.

Each complex exhibited one fully reversible oxidation between +1.26 and +1.39 V which is ascribed to the $\text{Ir}^{3+/4+}$ couple. Differences in oxidation potential can be explained by considering the substitutions around the quinoline ring and which isomer of naphthalene is used. Ligands with a 2-naphthyl quinoline system show a lower oxidation potential when compared with their substituted counterpart on the 1-naphthyl ligands. When comparing the different substituents on the quinoline we see a lower oxidation potential for the $\text{Ir}^{3+/4+}$ with the methoxy substituent. This suggests the Ir^{3+} is more readily oxidised when the quinoline has an electron rich π -system. Conversely, the electron withdrawing fluoro substituents lead to a higher oxidation potential. All of the oxidation couples seen for naphthyl quinolines are lower than the results from Chapter 3 for naphthyl quinoxalines, due to the quinolines being better electron donors.

The 2-naphthyl variants $[\text{Ir}(\text{L}^{1-3})_2(\text{bpy})]\text{PF}_6$ each display two single electron reduction processes, which are not fully reversible (Figure 4.20). While the 1-naphthyl variants $[\text{Ir}(\text{L}^{4-6})_2(\text{bpy})]\text{PF}_6$ appear to be more electrochemically stable, with each complex showing two fully reversible reduction processes. The features vary with

substitution, which implies that all processes are associated with the cyclometalating ligands.

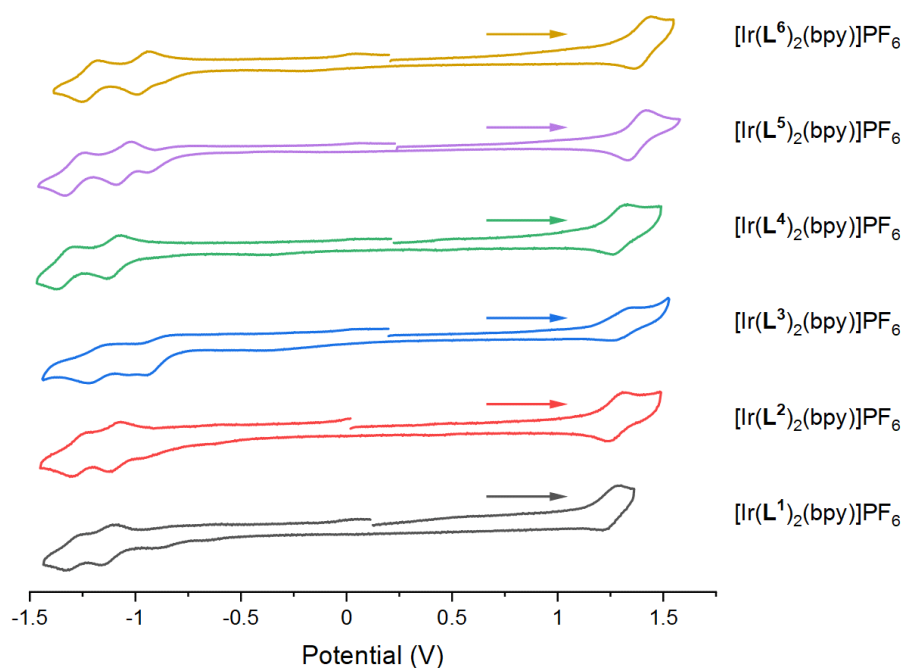


Figure 4.20 – Cyclic Voltammograms of $[\text{Ir}(\text{L}^{1-6})_2(\text{bpy})]\text{PF}_6$. All potentials measured in deoxygenated DCM solutions at 200 mVs^{-1} with $0.1 \text{ M } [\text{NBu}_4][\text{PF}_6]$ as supporting electrolyte calibrated with Fc/Fc^+ .

4.3.5 Electronic properties

4.3.5.1 Ligand absorption and emission properties

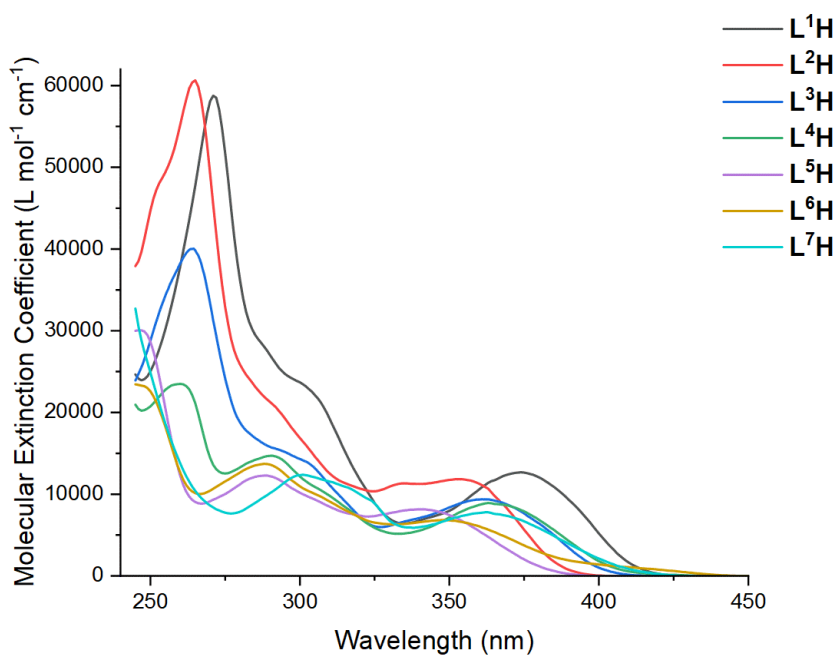


Figure 4.21 - UV-Vis spectra for ligands L^{1-7}H recorded in CHCl_3 at $\text{ca. } 10^{-5} \text{ M}$

Absorption spectra for **L¹⁻⁷H** can be seen in Figure 4.21. The ligands have a strong absorption within the UV region of the spectrum (245 – 300 nm), which can be attributed to $\pi-\pi^*$, in addition to $n-\pi^*$ transitions originating from the heteroatoms present in the quinoline aromatic ring. The wavelength of the absorption maxima varies slightly with substitution, whilst the 2-naphthyl derivatives are bathochromically shifted compared to the 1-Naphthyl derivatives by about 10 nm. The addition of the methoxy group to **L⁷H** induces a small bathochromic shift in absorption compared to **L⁵H**.

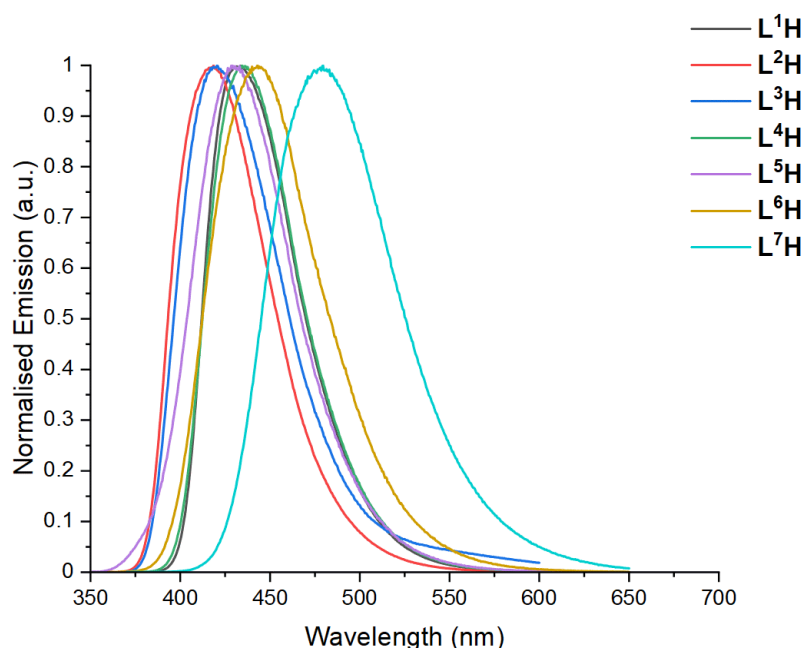


Figure 4.22 – Steady state emission spectra for ligands **L¹⁻⁷H** obtained in aerated CHCl_3 (λ_{ex} : 330 nm)

Steady state emission measurements were made in aerated CHCl_3 solution (Figure 4.22), exciting at 330 nm. Each ligand has a broad featureless emission peak. Emission maxima centre around 420-430 nm for **L¹⁻³H**. Conversely to the absorption, 1-Naphthyl ligands **L⁴⁻⁶H** are more bathochromically shifted than their 2-naphthyl counterparts, with the emission between 430-440 nm. The largest bathochromic shift in emission (ca. 50 nm), coming from the introduction of the methoxy group in the 4- position of the 1-naphthyl group in **L⁷H** can be seen by comparing the emission to **L⁵H**.

Time resolved measurements were also taken on $L^{1-7}H$ (Table 4.5). Recorded lifetimes are short (between 0.8 and 2.5 ns). This is consistent with fluorescent emission.

Ligand	$\lambda_{\text{abs}} (\epsilon / 10^4 \text{ M}^{-1} \text{ cm}^{-1}) / \text{nm}^{\text{a}}$	$\lambda_{\text{em}} / \text{nm}^{\text{b}}$	$\tau / \text{ns}^{\text{c}}$	Φ^{d}
L^1H	374 (1.2), 300 (2.3), 271 (5.8)	432	2.5	0.183
L^2H	354 (1.2), 291 (2.1), 264 (6.0)	418	1.6	0.082
L^3H	360 (0.9), 301 (1.4), 292 (1.5), 263 (4.0)	420	1.8	0.076
L^4H	367 (0.9), 290 (1.5), 259 (2.3)	434	1.5	0.082
L^5H	341 (0.8), 288 (1.2), 246 (3.0)	429	0.8	0.042
L^6H	350 (6.9), 288 (1.4), 248 (2.3)	443	0.8	0.046
L^7H	364 (0.8), 300 (1.2)	479	2.4	0.069

Table 4.5 – ^a All measurements run at room temperature in aerated CHCl_3 at *ca.* 1×10^{-5} M. ^b $\lambda_{\text{ex}} = 330$ nm; ^c $\lambda_{\text{ex}} = 295$ nm; ^d Vs standard Quinine Sulphate in 0.05 M H_2SO_4 , $\lambda_{\text{ex}} = 350$ nm. ⁶⁷

4.3.5.2 Complex absorption and emission properties

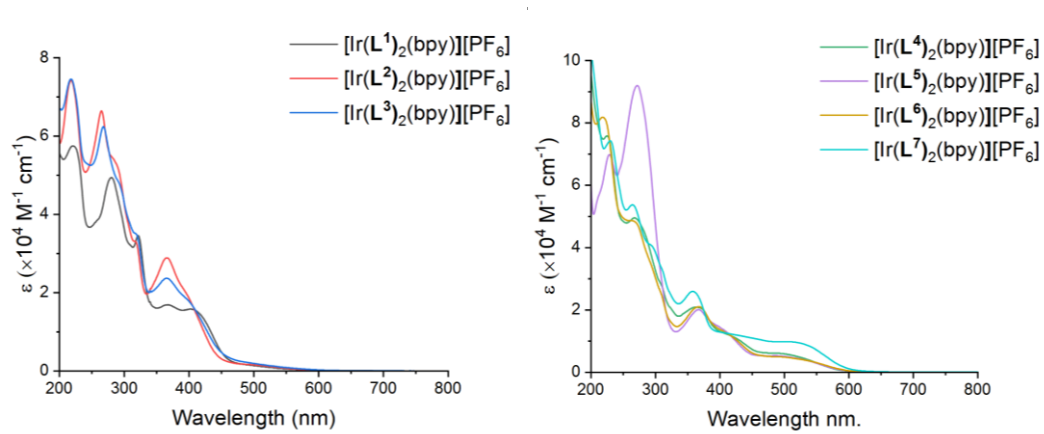


Figure 4.23 - UV-Vis spectra. R: 2-naphthyl complexes $[\text{Ir}(L^{1-3})_2(\text{bpy})]\text{PF}_6$, L: 1-naphthyl complexes $[\text{Ir}(L^{4-7})_2(\text{bpy})]\text{PF}_6$. All spectra recorded in acetonitrile at *ca.* 10^{-5} M.

Absorption spectra for the complexes are seen above in Figure 4.23. Measurements were made in aerated MeCN at *ca.* 10^{-5} M. Strong absorptions between 200 and 400 nm are likely the result of spin allowed ligand centred $^1\pi-\pi^*$ transitions, with contributions from the various aromatic components. This region is also likely to contain contributions from $^1n-\pi^*$ transitions from the heterocyclic quinoline rings. Features from 400 nm onwards typically exhibit spin allowed $^1\text{MLCT}$, with the spin forbidden $^3\text{MLCT}$ transitions tailing off towards 600 nm. It is clear that the substituents on the quinoline only exhibit a minor effect upon the absorption bands, while 1-naphthyl variants $[\text{Ir}(L^{4-7})_2(\text{bpy})]\text{PF}_6$ possess relatively

bathochromically shifted MLCT features compared to $[\text{Ir}(\text{L}^{1-3})_2(\text{bpy})]\text{PF}_6$ (Table 4.6).

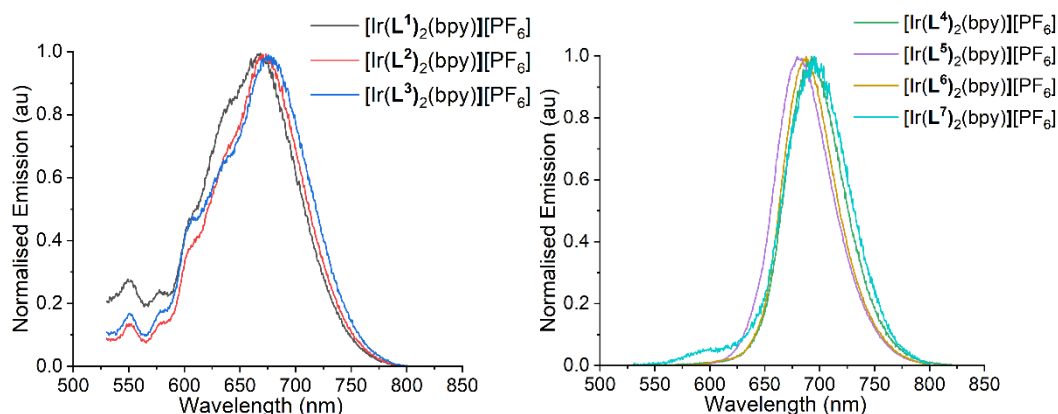


Figure 4.24 - Emission spectra complexes $[\text{Ir}(\text{L}^{1-7})_2(\text{bpy})]\text{PF}_6$. Spectra obtained as MeCN solutions at $\text{ca.}10^{-5} \text{ M}$. $\lambda_{\text{ex}} = 510 \text{ nm}$

Aerated MeCN solutions of the complexes were again used to obtain steady state emission measurements. Complexes were excited in the MLCT band (510 nm) and showed deep red emission, with emission maxima occurring between 668 and 695 nm, tailing off towards 800 nm. (Figure 4.24). 1-naphthyl complexes $[\text{Ir}(\text{L}^{4-6})_2(\text{bpy})]\text{PF}_6$ showed a greater bathochromic shift, with minor variations between the different substituents. They displayed a broad and featureless emission profile. In contrast, the emission profiles for the 2-naphthyl complexes $[\text{Ir}(\text{L}^{1-3})_2(\text{bpy})]\text{PF}_6$ display some weak vibronic features across the higher energy side of the spectra. In each case however, the emission has been bathochromically shifted when compared to earlier work on phenyl quinoline cyclometalating ligands³². $[\text{Ir}(\text{L}^7)_2(\text{bpy})]\text{PF}_6$ shows a larger bathochromic shift with the electron donating methoxy substituent on the naphthyl ring. This is consistent with the work in Chapters two and three exploring the effects of substituted quinoxalines, where the HOMO is a mixture of Ir 5d character and C^N ligand character, where the frontier orbitals lay predominantly across the phenyl and naphthyl ring moieties of the C^N ligands.

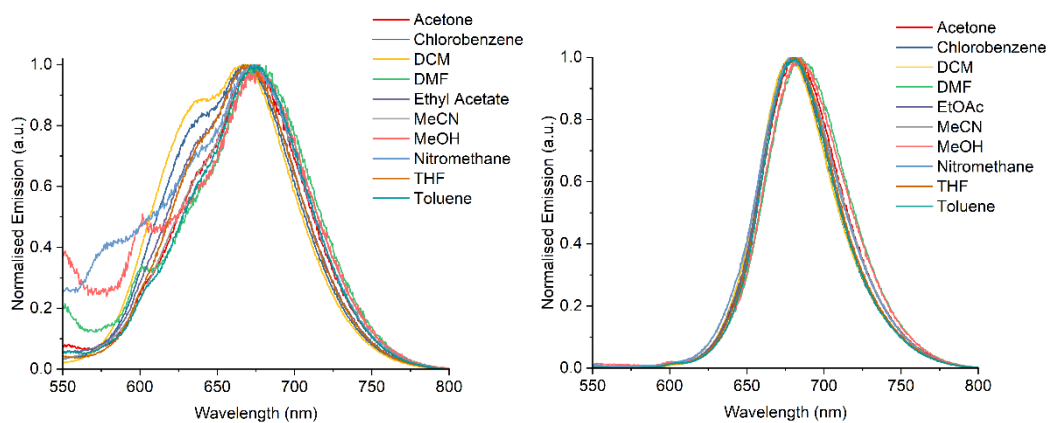


Figure 4.25 – Emission spectra for left: $[\text{Ir}(\text{L}^2)_2(\text{bpy})]\text{PF}_6$ and right: $[\text{Ir}(\text{L}^5)_2(\text{bpy})]\text{PF}_6$ in a range of solvents at $\lambda_{\text{ex}} = 500 \text{ nm}$

The emission spectra were recorded in a range of solvents with varying polarities (Figure 4.25). For both $[\text{Ir}(\text{L}^2)_2(\text{bpy})]\text{PF}_6$ and $[\text{Ir}(\text{L}^5)_2(\text{bpy})]\text{PF}_6$ the emission changed very little with solvent polarity. In a classical $^3\text{MLCT}$ species, such as $[\text{Ru}(\text{bpy})_3]^{2+}$, the emission is insensitive to solvent polarity due to the charge transfer being localised over the three ligands. This gives further evidence of the complexes displaying $^3\text{MLCT}$ emission.

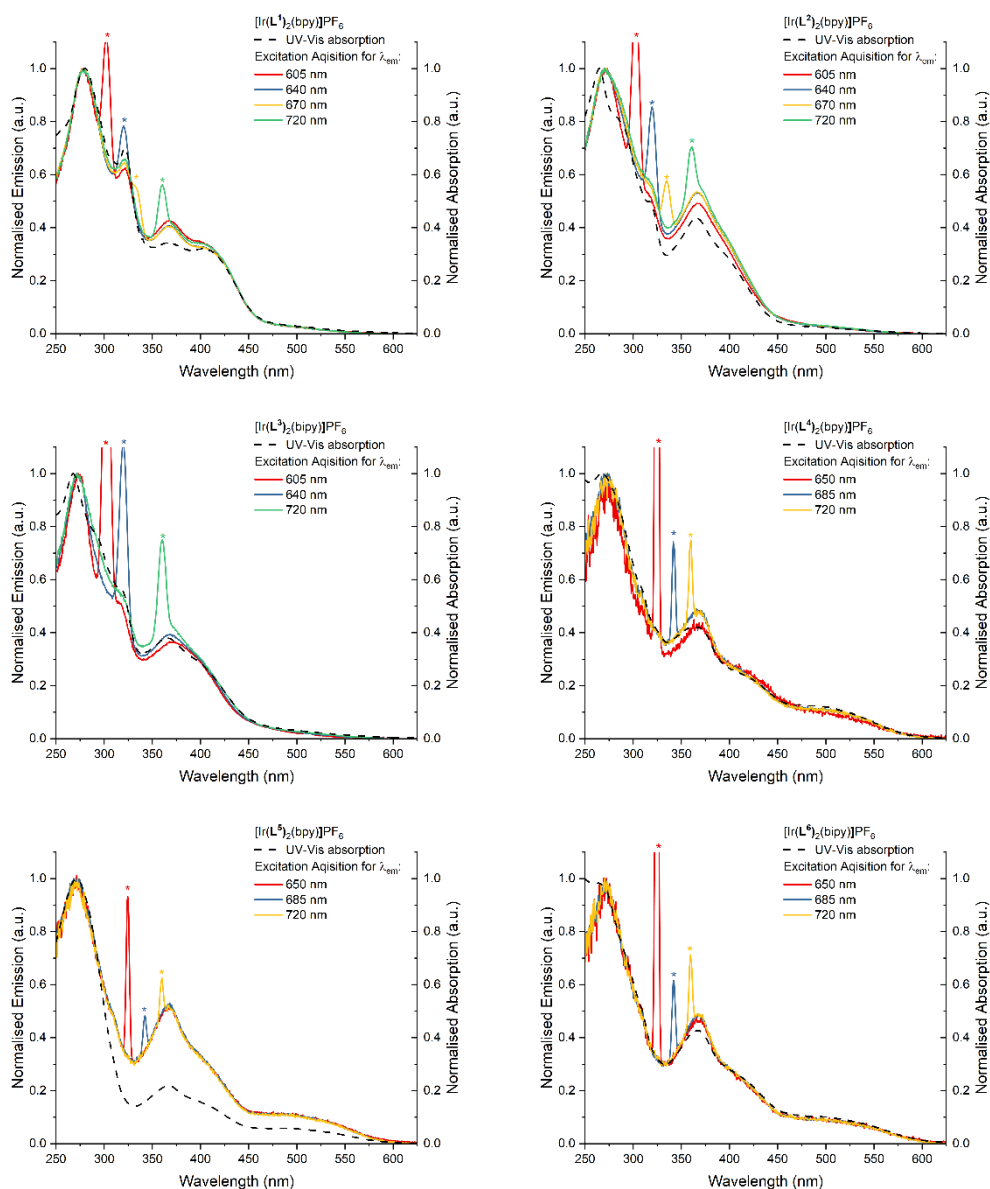


Figure 4.26 – Comparison of excitation spectra with absorption spectra (both obtained in MeCN at ca. 10^{-5} M). * indicates a harmonic from the lamp in the excitation spectra.

Excitation spectra were recorded for each of the complexes $[\text{Ir}(\text{L}^{1-6})_2(\text{bpy})]\text{PF}_6$, recording at different λ_{em} across the emission spectrum. Results have been overlaid with the absorbance spectra in Figure 4.26. Each of the excitation spectra are closely matching the absorption spectra, which shows the emissive state can be populated by both MLCT and LC transitions.

Time resolved spectroscopy was also run on the complexes. The luminescent lifetimes and quantum yields were recorded in aerated MeCN solutions. While

each complex displays mono-exponential decay, the lifetimes are shorter (17 – 89 ns) for 2-naphthyl isomers in comparison to 1-naphthyl complexes (217 – 240 ns). The quantum yields were also recorded and were quite low, albeit in aerated solvent, at $\leq 1\%$.

Complex	$\lambda_{\text{abs}} (\epsilon / 10^4 \text{ M}^{-1} \text{ cm}^{-1}) / \text{nm}^{\text{a}}$	$\lambda_{\text{em}} / \text{nm}^{\text{b}}$	$\tau / \text{ns}^{\text{c}}$	$\Phi / \%^{\text{e}}$
$[\text{Ir}(\text{L}^1)_2(\text{bpy})]\text{PF}_6$	480 (0.2), 401 (1.6), 367 (1.7), 321 (3.5), 280 (4.9), 221 (5.7)	668	89	0.4
$[\text{Ir}(\text{L}^2)_2(\text{bpy})]\text{PF}_6$	464 (0.2), 365 (2.9), 315 (3.3), 283 (5.4), 265 (6.6), 218 (7.4)	673	36	0.3
$[\text{Ir}(\text{L}^3)_2(\text{bpy})]\text{PF}_6$	483 (0.2), 399 (1.6), 365 (2.1), 268 (5.5)	675	17	0.3
$[\text{Ir}(\text{L}^4)_2(\text{bpy})]\text{PF}_6$	495 (0.6), 417 (1.2), 367 (2.1), 267 (5.0), 223 (7.6)	693	223	0.2
$[\text{Ir}(\text{L}^5)_2(\text{bpy})]\text{PF}_6$	494 (0.5), 405 (1.4), 366 (2.0), 271 (9.2)	679	240	0.6
$[\text{Ir}(\text{L}^6)_2(\text{bpy})]\text{PF}_6$	492 (0.5), 408 (1.3), 367 (2.2), 264 (5.0), 216 (8.2)	687	217	1.0
$[\text{Ir}(\text{L}^7)_2(\text{bpy})]\text{PF}_6$	514 (0.9), 359 (2.6), 292 (4.1), 264 (5.4), 229 (7.4)	695	83	0.1

Table 4.6 – Absorbance and emission data for complexes at room temperature. ^aAll measurements run at room temperature in aerated MeCN at ca. 1×10^{-5} M. ^b $\lambda_{\text{ex}} = 510$ nm; ^c $\lambda_{\text{ex}} = 295$ nm; ^d Vs standard $[\text{Ru}(\text{bpy})_3](\text{PF}_6)_2$ in MeCN, $\lambda_{\text{ex}} = 420$ nm⁶⁷.

Low temperature measurements were run at 77 K in frozen glasses (4:1 EtOH : MeOH) for complexes $[\text{Ir}(\text{L}^{1-6})_2(\text{bpy})]\text{PF}_6$ (Figure 4.27). For the 2-naphthyl complexes $[\text{Ir}(\text{L}^{1-3})_2(\text{bpy})]\text{PF}_6$, the emission maxima are hypsochromically shifted in comparison to the room temperature measurements. There is also stronger vibronic structure visible, which could be indicative of a ligand centred contribution to the emissive state. In the spectra for 1-naphthyl complexes $[\text{Ir}(\text{L}^{4-6})_2(\text{bpy})]\text{PF}_6$, the emission peaks appear much more defined, between 650 and 675 nm, and a weaker shoulder feature at lower energy. 77 K emission lifetimes were also recorded, where interestingly $[\text{Ir}(\text{L}^{1-3})_2(\text{bpy})]\text{PF}_6$ lifetime showed a significant extension to ca. 12 μs , while for $[\text{Ir}(\text{L}^{4-6})_2(\text{bpy})]\text{PF}_6$ it was lower ca. 3 μs .

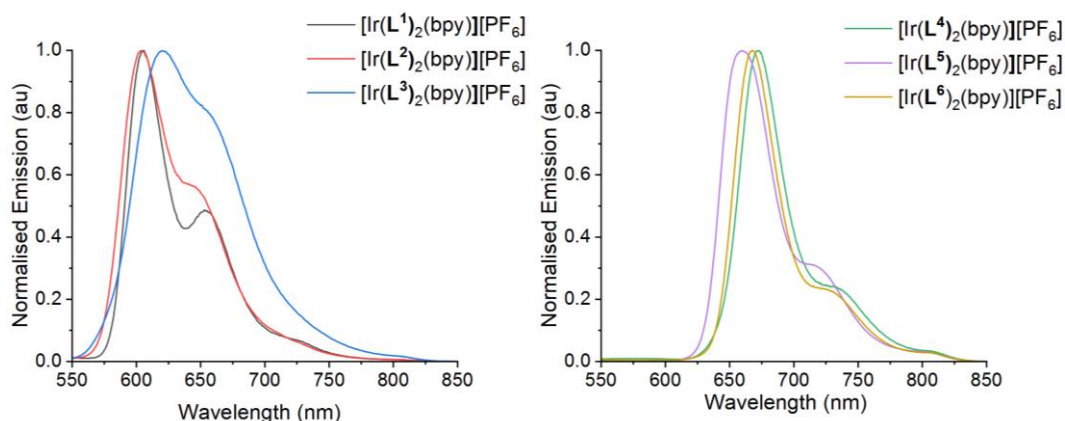


Figure 4.27 - Luminescence spectra of the complexes recorded as a frozen glass (1:4, MeOH/EtOH) ($\lambda_{\text{ex}} = 510$ nm).

4.3.5.3 Transient Absorption Spectroscopy

Time resolved transient absorption experiments in this work were carried out by Xue Zhang and Prof. Jianzhang Zhao (Dalian University of Technology). Further discussion of these points can be found in the publication related to this work.⁶⁸

For complexes $[\text{Ir}(\text{L}^{1-3})_2(\text{bpy})]\text{PF}_6$, the short triplet lifetime characteristics mean TA measurements were unable to be obtained, despite attempting measurements at various concentrations and measurement models.

However, spectra were successfully obtained for MeCN solutions of $[\text{Ir}(\text{L}^{4-6})_2(\text{bpy})]\text{PF}_6$ along with decay profiles. The profiles of complexes $[\text{Ir}(\text{L}^5)_2(\text{bpy})]\text{PF}_6$ and $[\text{Ir}(\text{L}^6)_2(\text{bpy})]\text{PF}_6$ are comparable (See Figure 4.29 and Figure 4.30). A ground state bleach is evident between $350 \text{ nm} < \lambda < 400 \text{ nm}$, with strong positive features at $400 \text{ nm} < \lambda < 500 \text{ nm}$ and $550 \text{ nm} < \lambda < 700 \text{ nm}$. The decay characteristics of these features appear to belong to triplet-to-triplet transitions as the lifetimes correlate with the presence of a long-lived species.

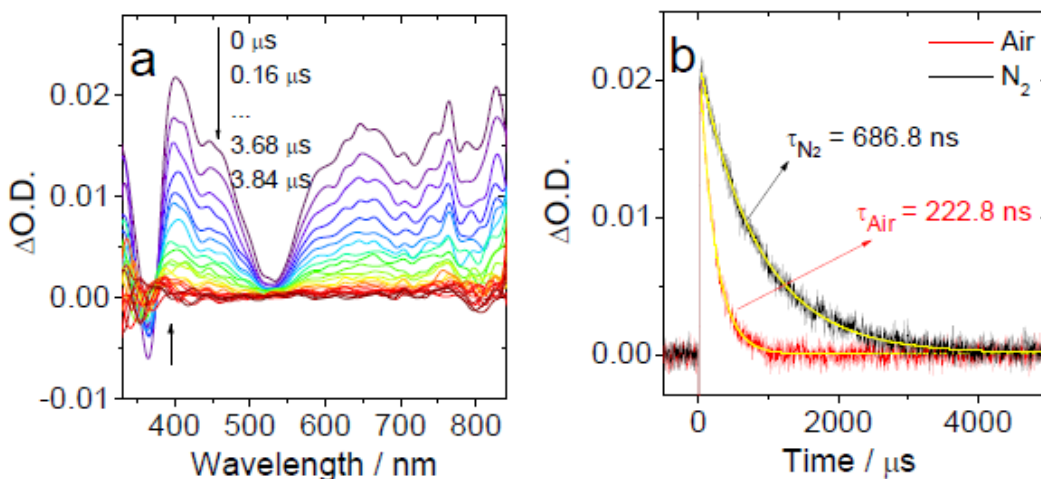


Figure 4.28 - (a) Nanosecond time-resolved transient absorption spectra of compound $[\text{Ir}(\text{L}^4)_2(\text{bpy})]\text{PF}_6$ upon pulsed laser excitation ($\lambda_{\text{ex}} = 510 \text{ nm}$, $c = 5 \times 10^{-5} \text{ M}$) and (b) decay trace of compound $[\text{Ir}(\text{L}^4)_2(\text{bpy})]\text{PF}_6$ at 645 nm in acetonitrile under air and nitrogen atmosphere, 20 °C.

Methoxy substituted complex $[\text{Ir}(\text{L}^4)_2(\text{bpy})]\text{PF}_6$ (Figure 4.28) produces a slightly different spectrum. There are strong positive features at $400 \text{ nm} < \lambda < 500 \text{ nm}$ and across the $550 \text{ nm} < \lambda < 850 \text{ nm}$ region. Once more the decay profile suggests these are triplet-to-triplet transitions.

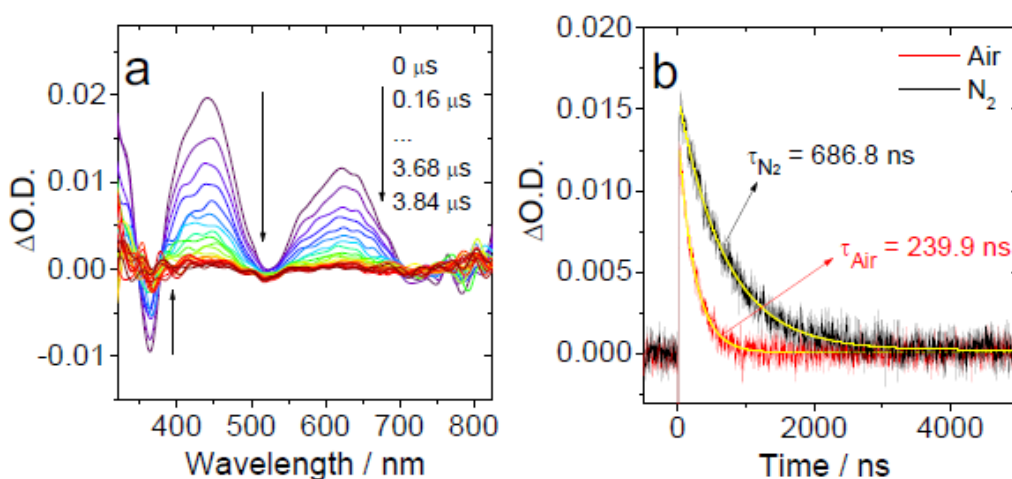


Figure 4.29 - (a) Nanosecond time-resolved transient absorption spectra of compound $[\text{Ir}(\text{L}^5)_2(\text{bpy})]\text{PF}_6$ upon pulsed laser excitation ($\lambda_{\text{ex}} = 510 \text{ nm}$, $c = 5 \times 10^{-5} \text{ M}$) and (b) decay trace of compound $[\text{Ir}(\text{L}^5)_2(\text{bpy})]\text{PF}_6$ at 625 nm in acetonitrile under air and nitrogen atmosphere, 20 °C.

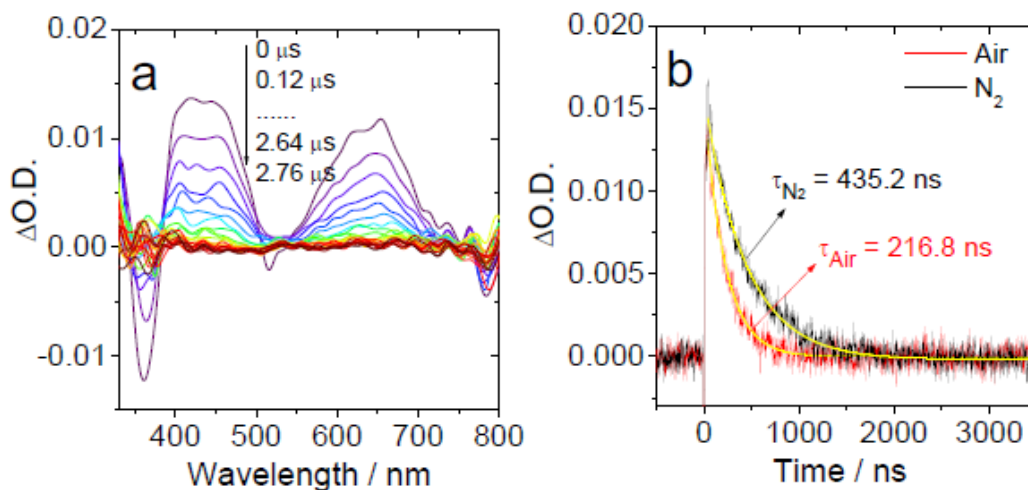


Figure 4.30 - (a) Nanosecond time-resolved transient absorption spectra of compound $[\text{Ir}(\text{L}^6)_2(\text{bpy})][\text{PF}_6]$ upon pulsed laser excitation ($\lambda_{\text{ex}} = 510 \text{ nm}$, $c = 5 \times 10^{-5} \text{ M}$) and (b) decay trace of compound $[\text{Ir}(\text{L}^6)_2(\text{bpy})]\text{PF}_6$ at 645 nm in acetonitrile under air and nitrogen atmosphere, 20 °C.

4.3.5.4 Triplet-Triplet-Annihilation Upconversion.

TTA upconversion measurements in this work were made by Xue Zhang and Prof. Jianzhang Zhao (Dalian University of Technology). Further discussion of these points can be found in the publication related to this work.⁶⁸

Solution state TTA upconversion measurements were recorded using $[\text{Ir}(\text{L}^{4-6})_2(\text{bpy})]\text{PF}_6$ as the sensitiser and 9,10-diphenylanthracene (DPA) as the annihilator. Samples were continuously excited with a 532 nm laser. This wavelength is selective for the long wavelength absorption of the complexes, correlating with the spin forbidden ($S_0 \rightarrow T_1$) MLCT transitions. Importantly, DPA does not absorb at this excitation wavelength. In each example (Figure 4.31), upon addition of DPA to the solution of iridium(III) sensitiser, the emission of the sensitiser was quenched and a new emission from DPA appeared between 400 – 500 nm.

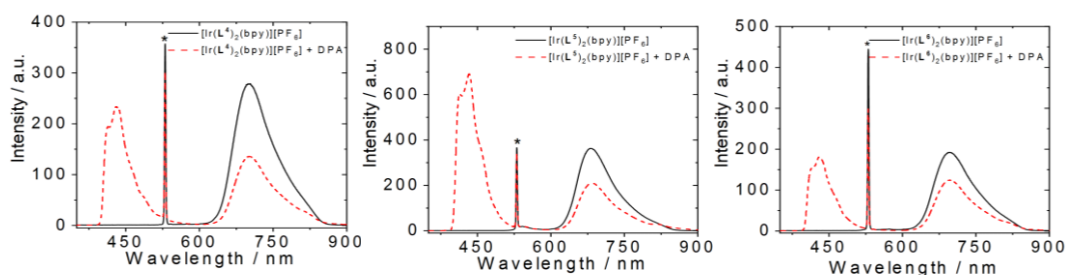


Figure 4.31 - Triplet-triplet annihilation upconversion fluorescence spectra of the photosensitisers, $[\text{Ir}(\text{L}^{4-6})_2(\text{bpy})]\text{PF}_6$, in aerated acetonitrile where DPA was used as the annihilator. Excitation was achieved with a continuous laser at $\lambda = 532 \text{ nm}$ (power density of 5.6 mW) under a deaerated atmosphere. $c(\text{sensitiser}) = 1 \times 10^{-5} \text{ M}$, $c(\text{DPA}) = 5 \times 10^{-4} \text{ M}$, $20 \text{ }^\circ\text{C}$. The asterisks indicate the scattered laser signal.

The efficiency of the TTA upconversion is given by quantum yields (Φ_{uc}) of 2.2 %, 6.7 % and 1.6 % for $[\text{Ir}(\text{L}^4)_2(\text{bpy})]\text{PF}_6$, $[\text{Ir}(\text{L}^5)_2(\text{bpy})]\text{PF}_6$ and $[\text{Ir}(\text{L}^6)_2(\text{bpy})]\text{PF}_6$ respectively. The standard used was Rose Bengal ($\Phi_{\text{F}} = 0.08$ in methanol). The effect of mixing sensitiser and annihilator is clearly seen in Figure 4.32. Upconversion efficiencies are on the lower side of literature values^{51,69–71}. Efficient TTA-UC relies upon long lived triplet lifetimes on the sensitiser⁷² to facilitate the TTET to annihilators. The nitrogen saturated lifetimes recorded in section 4.3.5.3 are all less than $1 \mu\text{s}$, which may explain the lower TTA-UC efficiencies seen here.

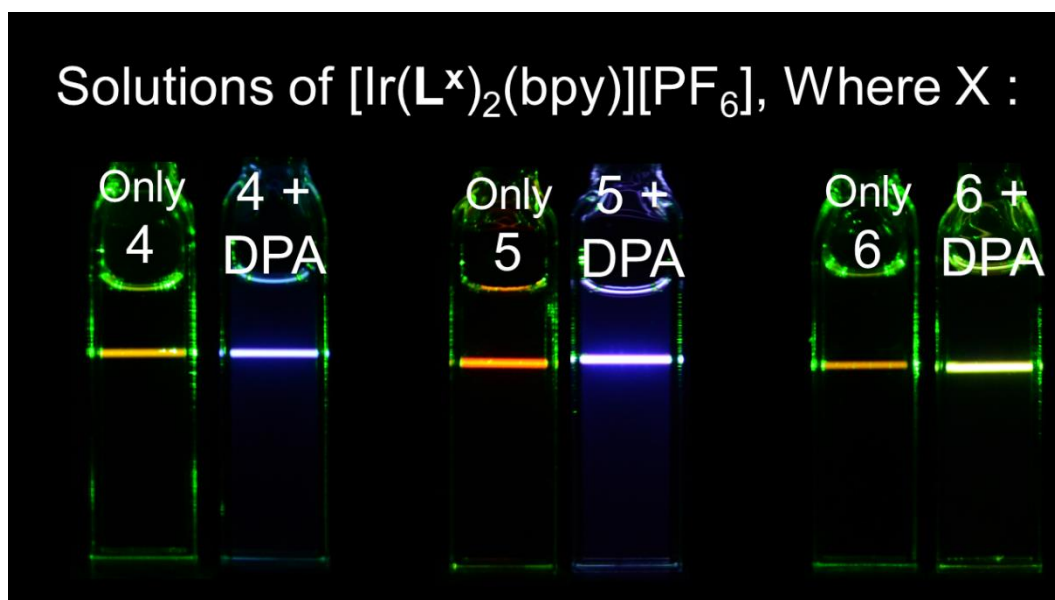
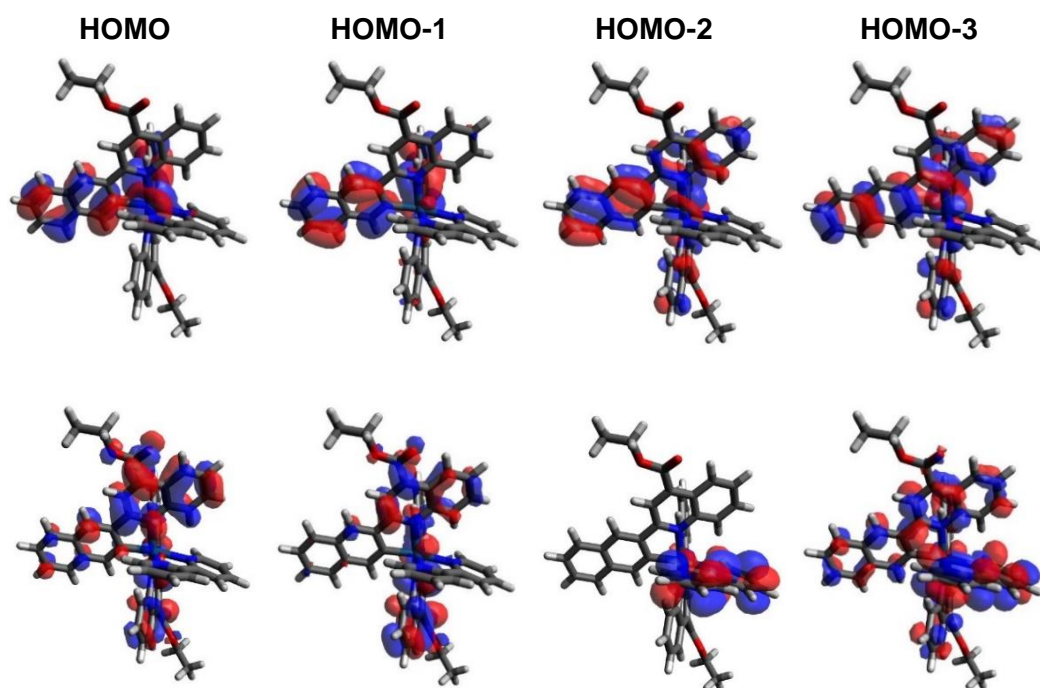


Figure 4.32 - Photographs of the emission of the selected triplet sensitizers and their upconversion with DPA in deaerated acetonitrile. Excitation was achieved with a continuous laser at $\lambda = 532 \text{ nm}$ (power density of 5.6 mW) under a deaerated atmosphere. $c(\text{sensitiser}) = 1 \times 10^{-5} \text{ M}$, $c(\text{DPA}) = 5 \times 10^{-4} \text{ M}$, $20 \text{ }^\circ\text{C}$. The photographs were taken without any filters.

4.3.6 Density Functional Theory

All computation studies in this work were carried out by Haleema Otaif and Dr Joseph Beams (Cardiff University). Further discussion of these points can be found in the publication related to this work.⁶⁸

The geometries of $[\text{Ir}(\text{L}^2)_2(\text{bpy})]^+$ and $[\text{Ir}(\text{L}^5)_2(\text{bpy})]^+$ were optimised in their lowest electronic singlet and triplet states using DFT//B3LYP/6-31G* basis sets. The resulting bond lengths and bond angles are in a good agreement with experimentally obtained results, typically differing by less than 0.05 Å and 1 °. Calculated Kohn-Sham orbitals are shown in Figure 4.33. The calculations indicate the HOMO for both complexes is a mixture of Ir 5d orbital character and naphthyl moiety π orbital character from the cyclometalating ligands. The LUMO of both complexes resides predominantly upon the quinoline moieties of both complexes. In each complex, the quinoline cyclometalating ligands form pseudo-degenerate orbitals with alternating contributions from each of the cyclometalating ligands (Table 4.7). This has been ascribed to the near C_2 symmetry of the system, causing a subtle geometric distortion, and thus causing a splitting of the orbitals. The HOMO and LUMO locations upon the molecule are in agreement with previous results for similar ligand systems⁵¹.



LUMO LUMO+1 LUMO+2 LUMO+3

Figure 4.33 – Calculated Kohn-Sham Molecular Orbitals for $[\text{Ir}(\text{L}^2)_2(\text{bpy})]^+$

TD-DFT calculations were used to predict the UV-Vis electronic transitions from the optimised ground state singlet (S_0) and lowest triplet state (T_1) geometries. Calculated transitions are in reasonable agreement with the experimental UV-Vis spectra (Figure 4.23). For $[\text{Ir}(\text{L}^2)_2(\text{bpy})]^+$, the spin forbidden $^3\text{MLCT}$ transition ($S_0 \rightarrow T_1$) is predicted to occur at 570 nm is in good agreement with the absorption tail seen around 550 nm. The more intense lowest energy spin allowed ($S_0 \rightarrow S_1$) transitions are predicted to be around 407 nm and 402 nm. These are assigned to the HOMO to LUMO and HOMO to LUMO+1 transitions respectively, showing significant amounts of $^1\text{MLCT}$ character with minor contributions from ^1LC transitions. These are in good general agreement with the experimental band *ca.* 350 nm < λ < 425 nm. In general, as the transitions move towards higher energy, they become more ligand centred transitions. The 1-naphthyl complex $[\text{Ir}(\text{L}^5)_2(\text{bpy})]^+$ displays similar features, which agree with the experimental data and occur bathochromically shifted in comparison to the 2-naphthyl complexes.

Orbital	$[\text{Ir}(\text{L}^2)_2(\text{bpy})]^+$				$[\text{Ir}(\text{L}^5)_2(\text{bpy})]^+$			
	Moiety Contribution to Orbital (%)							
	Ir (5d)	bpy	Q1	Q2	Ir (5d)	bpy	Q1	Q2
LUMO +4	1	23	17	59	2	6	46	46
LUMO +3	1	44	26	29	2	23	34	41
LUMO +2	2	97	1	1	2	97	1	1
LUMO +1	3	0	71	26	4	1	79	17
LUMO	2	1	26	71	4	1	16	78
HOMO	28	2	36	34	21	1	39	39
HOMO -1	3	1	48	49	2	0	49	49
HOMO -2	10	0	45	45	16	1	42	41
HOMO -3	9	1	45	45	37	4	51	8
HOMO -4	41	5	35	19	36	2	10	52

Table 4.7 – Calculated MO contributions for $[\text{Ir}(\text{L}^2)_2(\text{bpy})]^+$ and $[\text{Ir}(\text{L}^5)_2(\text{bpy})]^+$. Q1 and Q2 are the different quinoline ligands on each complex.

4.4 Conclusions

This chapter has shown the synthesis and characterisation of five new substituted 2-naphthylquinoline ligands, using Pfitzinger synthesis to incorporate electron withdrawing and donating groups to investigate the degree of tuneability in final

complex emission, as well as showing the effects of the two separate isomers of naphthalene have upon absorption and emission properties.

Seven novel organometallic iridium(III) complexes were isolated and characterised via ^1H , ^{19}F , ^{13}C NMR, HRMS, absorption, emission spectroscopies, as well as via cyclic voltammetry. Three examples were grown as single crystals, leading to the collection of X-ray diffraction data and solving of the solid-state structure. The resultant *bis*-cyclometalated complexes display deep red emission with subtle tuning achieved from substitution around the quinoline ring, as well as between naphthyl isomers.

Comparison with archetypal iridium complex $[\text{Ir}(\text{ppy})_2\text{bpy}]^+$ (λ_{em} : 602 nm) shows the quantum yields are of a magnitude smaller⁷³. This may be associated with energy gap law. When compared with the aerated emission ϕ and τ of the archetypal triplet emitting organometallic complex $[\text{Pt}(\text{OEP})]$, where λ_{em} : 650 nm, ϕ : $1.25 - 1.4 \times 10^{-3}$, τ : 222 - 286 ns (measurements made in aerated THF, toluene and CHCl_3) the lifetime and quantum yield are of similar magnitudes⁴⁸.

When comparing to the results obtained from spectroscopy and TD-DFT, the 2-naphthyl complexes $[\text{Ir}(\text{L}^{1-3})_2(\text{bpy})]\text{PF}_6$ clearly show they possess a stronger triplet ligand centred emission character, while the 1-naphthyl complexes $[\text{Ir}(\text{L}^{4-6})_2(\text{bpy})]\text{PF}_6$ emit from a stronger $^3\text{MLCT}$ state. $[\text{Ir}(\text{L}^{4-6})_2(\text{bpy})]\text{PF}_6$ have also been shown to be sensitiser for TTA upconversion, achieving efficiencies of up to 6.7 %.

4.5 Experimental

All reactions were performed with the use of vacuum line and Schlenk techniques. Reagents were commercial grade and were used without further purification. ^1H , ^{13}C and ^{19}F NMR spectra were recorded on a Bruker fourier 300, dpx 400, or avance 500 MHz spectrometer, and were recorded in CDCl_3 , CD_3CN or d_6 -DMSO solutions. ^1H and $^{13}\text{C}\{^1\text{H}\}$ NMR chemical shifts (δ) were determined relative to internal tetramethylsilane, $\text{Si}(\text{CH}_3)_4$ and are given in ppm. Low-resolution mass spectra were obtained by the staff at Cardiff University. High-resolution mass spectra were carried out by the staff at Cardiff University and the EPSRC National Mass Spectrometry Service at Swansea University, UK. All photophysical data was obtained on a JobinYvon-Horiba Fluorolog-3 spectrometer fitted with a JY TBX picosecond photodetection module in CHCl_3 or MeCN solutions. Emission spectra were uncorrected and excitation spectra were instrument corrected. The pulsed source was a Nano-LED configured for 295, 372 or 459 nm output operating at 500 kHz or 1 MHz. Luminescence lifetime profiles were obtained using the JobinYvon–Horiba FluoroHub single photon counting module and the data fits yielded the lifetime values using the provided DAS6 deconvolution software. IR spectra were recorded on an ATR equipped Shimadzu IRAffinity-1 spectrophotometer. UV-vis data was recorded as solutions on a Shimadzu UV-1800 spectrophotometer. TTA Energy Upconversion measurements utilized $c(\text{sensitiser}) = 1 \times 10^{-5}$ M, $c(\text{DPA}) = 5 \times 10^{-4}$ M, 20 °C; deaerated MeCN; and the upconversion quantum efficiencies were obtained using Bengal Rose as a standard ($\Phi_{\text{F}} = 0.08$ in methanol).

X-Ray Diffraction Data Collection and Refinement.

Suitable crystals were selected and mounted on a MITIGEN holder in perfluoroether oil on either a Rigaku FRE+ diffractometer equipped with VHF Varimax confocal mirrors and an AFC12 goniometer and HyPix 6000 detector, equipped with an Oxford Cryosystems low-temperature device operating at $T = 100(2)$ K (for $[\text{Ir}(\text{L}^3)_2(\text{bpy})]\text{PF}_6$ and $[\text{Ir}(\text{L}^5)_2(\text{bpy})]\text{PF}_6$) or a Rigaku 007HF diffractometer equipped with Varimax confocal mirrors and an AFC11 goniometer and HyPix 6000 detector equipped with an Oxford Cryosystems low-temperature device operating at $T = 100(2)$ K (for $[\text{Ir}(\text{L}^6)_2(\text{bpy})]\text{PF}_6$).

The structure was solved with the ShelXT⁷⁴ structure solution program using the Intrinsic Phasing solution method and by using Olex2⁷⁵ as the graphical interface. The model was refined with version 2018/3 of ShelXL⁷⁶ using Least Squares minimisation.

DFT studies

All calculations were performed within the Gaussian 09 suite of programmes⁷⁷. Geometry optimisations were carried out without constraints using the DFT//B3LYP level of theory.^{78,79} The Stuttgart-Dresden basis set was used for the iridium atoms,⁸⁰ and was invoked with pseudo-potentials for the core electrons, with a 6-31G* basis set for all remaining atoms.^{81–83} All calculations included the use of a polarized continuum model (IEFPCM) approach for the treatment of the MeCN solvent.⁸⁴ All stationary point geometries obtained by DFT method were confirmed through harmonic vibrational frequency calculations

All absorption spectra predictions, orbitals and other ground state properties were computed using the ground state minimum energy geometry. Excitation energies (absorption spectra predictions) were computed in the same manner as ground state properties, but using the long range corrected CAM-B3LYP functional for improved accuracy. For the prediction of emission energies, the triplet state was allowed to relax to its optimal geometry, prior to single point energy calculations of the ground state at this set of geometric parameters. Molecular orbital decomposition was performed using the GaussSum package.⁸⁵

4.5.1 General Synthesis of 2-(2-naphthyl)quinoline-4-carboxylic acids

Generally, isatin derivative (300 mg), 2-acetylnaphthalene (1.2 eq) and KOH pellets (3 eq) were added to a flask and dissolved in ethanol (20 mL). The resultant mixture was heated to reflux and stirred at this temperature for 24 hours. Upon cooling, the reaction mixture was diluted with water (50 mL), neutralised with 1M HCl and the resulting precipitate collected on the filter before washing with water. The crude mixture was dissolved in DCM (20 mL), and the carboxylic acid taken into the aqueous layer by shaking with 1M NaOH (20 mL x 3). The combined aqueous layers were acidified with HCl and the product extracted into fresh DCM (3 x 20 mL). Combined organic layers were dried over Na₂SO₄ and the solvents were removed to yield naphthyl quinoline carboxylic acids as yellow solids.

4.5.1.1 6-Methoxy-2-(naphthalen-2-yl)quinoline-4-carboxylic acid

Obtained as a yellow solid (58 % yield). ¹H NMR (400 MHz, d₆-DMSO) δ_H 8.82 (s, 1H), 8.66 (s, 1H), 8.47 (dd, *J* = 8.7, 1.6 Hz, 1H), 8.16 (d, *J* = 2.8 Hz, 1H), 8.14 (d, *J* = 9.1 Hz, 2H), 8.08 (d, *J* = 8.7 Hz, 1H), 8.02 – 7.96 (m, 1H), 7.59 (dd, *J* = 6.1, 3.3 Hz, 2H), 7.54 (dd, *J* = 9.1, 2.8 Hz, 1H), 3.94 (s, 3H) ppm. ¹³C{¹H} NMR (101 MHz,

d_6 -DMSO) δ_c 167.8, 158.4, 153.0, 144.8, 135.5, 135.4, 133.4, 133.2, 131.4, 128.8, 128.5, 127.6, 127.0, 126.6, 126.4, 125.0, 124.3, 122.5, 120.0, 103.8, 55.5 ppm. HRMS (ES) Calc'd 330.1125 for $C_{21}H_{16}NO_3$; found m/z 330.1128.

4.5.1.2 2-(Naphthalen-2-yl)quinoline-4-carboxylic acid⁸⁶

Obtained as a yellow solid (64 % yield). 1H NMR (400 MHz, d_6 -DMSO) δ_H 8.94 (s, 1H), 8.72 (d, J = 7.8 Hz, 1H), 8.56 (dd, J = 8.7, 1.7 Hz, 1H), 8.27 (d, J = 8.2 Hz, 1H), 8.23 – 8.18 (m, J = 6.0, 3.4 Hz, 1H), 8.15 (d, J = 8.7 Hz, 1H), 8.08 – 8.01 (m, J = 6.0, 3.3 Hz, 1H), 7.96 – 7.88 (m, 1H), 7.80 – 7.73 (m, 1H), 7.65 (dd, J = 6.2, 3.2 Hz, 2H) ppm.

4.5.1.3 6-Fluoro-2-(naphthalen-2-yl)quinoline-4-carboxylic acid

Obtained as a yellow solid (61 % yield). 1H NMR (400 MHz, d_6 -DMSO) δ_H 8.91 (s, 1H), 8.79 (s, 1H), 8.54 (s, 1H), 8.52 (s, 1H), 8.33 (dd, J = 8.6, 5.9 Hz, 1H), 8.20 (s, 1H), 8.14 (d, J = 8.6 Hz, 1H), 8.04 (s, 1H), 7.85 (dd, J = 8.8, 8.6 Hz, 1H), 7.64 (dd, J = 6.0, 2.8 Hz, 2H) ppm. $^{13}C\{^1H\}$ NMR (101 MHz, d_6 -DMSO) δ_c 167.7, 162.3, 159.9, 155.8, 146.4, 137.1, 135.4, 134.1, 133.5, 129.4, 129.1, 128.1, 127.8, 127.5, 127.2, 124.8, 121.1, 121.0, 120.7, 109.9, 109.6 ppm. $^{19}F\{^1H\}$ NMR (376 MHz, d_6 -DMSO) δ -110.9 (s) ppm. HRMS (ES) $[M + H]^+$ Calc'd 318.0925 for $C_{20}H_{12}FNO_2$; found m/z 318.0928.

4.5.1.4 6-Methoxy-2-(naphthalen-1-yl)quinoline-4-carboxylic acid

Obtained as a yellow solid (56 % yield). 1H NMR (400 MHz, d_6 -DMSO) δ_H 8.30 (d, J = 2.7 Hz, 1H), 8.23 (s, 1H), 8.18 – 8.08 (m, 4H), 7.82 (d, J = 6.2 Hz, 1H), 7.75 – 7.69 (m, 1H), 7.66 – 7.56 (m, 3H), 4.00 (s, 3H) ppm. $^{13}C\{^1H\}$ NMR (101 MHz, d_6 -DMSO) δ 167.5, 158.6, 155.4, 144.5, 137.1, 136.3, 135.0, 133.5, 131.1, 130.5, 129.2, 128.5, 128.0, 126.9, 126.2, 125.5, 125.2, 124.9, 124.3, 122.7, 103.7, 55.6 ppm. HRMS (ES) $[M - H]^-$ Calc'd 328.0979 for $C_{21}H_{14}NO_3$; found m/z 328.0977.

4.5.1.5 2-(Naphthalen-1-yl)quinoline-4-carboxylic acid⁸⁷

Obtained as a yellow solid (41 % yield). Spectral properties were in agreement with those listed in the literature.

4.5.1.6 6-Fluoro-2-(naphthalen-1-yl)quinoline-4-carboxylic acid

Obtained as a yellow solid (58 % yield). 1H NMR (500 MHz, d_6 -DMSO) δ 8.59 (d, J = 9.8 Hz, 1H), 8.29 – 8.23 (m, 2H), 8.11 (dd, J = 11.4, 9.1 Hz, 2H), 8.06 (d, J = 7.9 Hz, 1H), 7.82 (dd, J = 7.5 Hz, 1H), 7.79 (d, J = 7.0 Hz, 1H), 7.67 (dd, J = 7.6 Hz, 1H), 7.62 – 7.57 (m, 1H), 7.55 (dd, J = 7.2 Hz, 7.2 Hz 1H) ppm. $^{13}C\{^1H\}$ NMR (126 MHz, d_6 -DMSO) δ 167.0, 161.8, 159.8, 157.9, 157.9, 145.8, 137.0, 133.5, 130.4, 129.5, 128.5, 128.1, 127.0, 126.2, 125.5, 125.1, 124.9, 120.4, 120.2, 109.4,

109.2 ppm. $^{19}\text{F}\{^1\text{H}\}$ NMR (471 MHz, d_6 -DMSO) δ -110.5 (s) ppm. HRMS (EI) [M^+] Calc'd 317.0852 for $\text{C}_{20}\text{H}_{12}\text{NO}_2\text{F}$; found m/z 317.0851.

4.5.1.7 2-(4-methoxynaphthalen-1-yl)quinoline-4-carboxylic acid⁸⁸

Obtained as a yellow solid (66 % yield). ^1H NMR (400 MHz, d_6 -DMSO) δ 8.76 (d, $J = 7.9$ Hz, 1H), 8.32 – 8.28 (m, 1H), 8.28 – 8.23 (m, 1H), 8.19 – 8.13 (m, 2H), 7.91 – 7.85 (m, 1H), 7.80 – 7.72 (m, 2H), 7.61 – 7.55 (m, 2H), 7.15 (d, $J = 8.2$ Hz, 1H), 4.06 (s, 3H).

4.5.2 General synthesis of ethyl 2-(naphthalen-2-yl)quinoline-4-carboxylate derivatives

The naphthalene substituted quinoline-4-carboxylic acid was dissolved in ethanol, and a few drops of sulfuric acid were added to the flask and the mixture heated to reflux overnight. Upon cooling to room temperature, the mixture was neutralised with NaOH (2 M) and the solvent removed under vacuum. The crude product was dissolved in DCM, washed with water and the organics combined, dried over MgSO_4 and the solvents removed *in vacuo*. The product was purified by silica gel column chromatography, eluting with DCM to yield the title compounds.

4.5.2.1 Ethyl 6-methoxy-2-(naphthalen-2-yl)quinoline-4-carboxylate (L^1H)

Obtained as a yellow solid (60 % yield). ^1H NMR (400 MHz, CDCl_3) δ_{H} 8.66 (s, 1H), 8.62 (d, $J = 9.4$ Hz, 1H), 8.55 (s, 1H), 8.18 (d, $J = 2.7$ Hz, 1H), 8.12 – 7.96 (m, 3H), 7.84 (d, $J = 7.3$ Hz, 1H), 7.65 (dd, $J = 9.4, 2.7$ Hz, 1H), 7.59 – 7.50 (m, 2H), 4.55 (q, $J = 7.1$ Hz, 2H), 3.96 (s, 3H), 1.47 (t, $J = 7.1$ Hz, 3H) ppm. $^{13}\text{C}\{^1\text{H}\}$ NMR (126 MHz, d_6 -DMSO) δ_{C} 166.1, 158.6, 153.0, 144.8, 135.3, 134.7, 133.5, 133.1, 131.5, 128.9, 128.6, 127.7, 127.2, 126.7, 126.5, 124.7, 124.4, 122.9, 120.0, 103.4, 62.0, 55.6, 14.2 ppm. UV-vis (MeCN): λ_{abs} ($\epsilon/10^4$ L mol $^{-1}$ cm $^{-1}$) 374 (1.2), 300 (2.3), 271 (5.8) nm. FTIR (solid) (ATR) ν_{max} : 3134, 3057, 2974, 1718 (C=O), 1618, 1585, 1550, 1508, 1465, 1406, 1388, 1365, 1336, 1309, 1274, 1242, 1217, 1182, 1143, 1118, 1060, 1039, 1024, 954, 925, 894, 862, 783, 752, 692, 628, 549, 505, 480, 472, 408 cm $^{-1}$. HRMS (ES) [$\text{M} + \text{H}$] $^+$ Calc'd 358.1438 for $\text{C}_{23}\text{H}_{19}\text{NO}_3$; found m/z 358.1441.

4.5.2.2 Ethyl 2-(naphthalen-2-yl)quinoline-4-carboxylate (L^2H)⁸⁹

Obtained as a yellow solid (75 % yield). ^1H NMR (400 MHz, CDCl_3) δ_{H} 8.75 (d, $J = 7.7$ Hz, 1H), 8.66 (s, 1H), 8.55 (s, 1H), 8.41 (dd, $J = 8.6, 1.8$ Hz, 1H), 8.28 (d, $J = 8.5$ Hz, 1H), 8.03 (dd, $J = 6.9, 4.1$ Hz, 2H), 7.91 (dd, $J = 6.0, 3.5$ Hz, 1H), 7.80

(ddd, $J = 8.4, 6.8, 1.4$ Hz, 1H), 7.65 (ddd, $J = 8.4, 6.9, 1.3$ Hz, 1H), 7.58 – 7.48 (m, 2H), 4.59 (q, $J = 7.1$ Hz, 2H), 1.54 (t, $J = 7.1$ Hz, 3H).

4.5.2.3 Ethyl 6-fluoro-2-(naphthalen-2-yl)quinoline-4-carboxylate (L³H)

Obtained as a yellow solid (57 % yield). ¹H NMR (500 MHz, CDCl₃) δ 8.64 (d, $J = 1.2$ Hz, 1H), 8.62 (s, 1H), 8.52 (dd, $J = 10.7, 2.8$ Hz, 1H), 8.38 (dd, $J = 8.6, 1.8$ Hz, 1H), 8.27 (dd, $J = 9.2, 5.7$ Hz, 1H), 8.02 (s, 1H), 8.01 (s, 1H), 7.91 (dd, $J = 6.0, 3.5$ Hz, 1H), 7.88 (d, $J = 8.6$ Hz, 1H), 7.57 – 7.53 (m, 3H), 4.58 (q, $J = 7.1$ Hz, 2H), 1.54 (t, $J = 7.1$ Hz, 3H) ppm. ¹³C{¹H} NMR (126 MHz, CDCl₃) δ_c 166.1, 162.5, 160.5, 155.9, 155.9, 146.6, 135.8, 135.3, 135.2, 134.0, 133.5, 132.8, 132.7, 131.0, 129.3, 128.9, 128.8, 128.2, 128.1, 127.8, 127.1, 127.0, 126.6, 126.6, 125.3, 125.0, 125.0, 124.6, 121.3, 120.3, 120.1, 109.7, 109.5, 62.1, 14.4 ppm. ¹⁹F NMR (471 MHz, CDCl₃) δ -110.4 (ddd, $J = 10.8, 7.8, 5.9$ Hz) ppm. UV-vis (MeCN): λ_{abs} ($\epsilon/10^4$ L mol⁻¹ cm⁻¹) 360 (0.9), 301 (1.4), 292 (1.5), 263 (4.0) nm. FTIR (solid) (ATR) ν_{max} : 3064, 1726 (C=O), 1624, 1591, 1550, 1508, 1487, 1456, 1442, 1392, 1373, 1355, 1325, 1301, 1267, 1251, 1240, 1217, 12085, 1161, 1139, 1111, 1066, 1029, 952, 929, 898, 869, 856, 835, 812, 792, 781, 761, 742, 700, 642, 628, 607, 588, 569, 540, 520, 495, 495, 474, 435, 410 cm⁻¹. HRMS (ES) [M + H]⁺ Calc'd 346.1238 for C₂₂H₁₆FNO₂; found m/z 346.1239.

4.5.2.4 Ethyl 6-methoxy-2-(naphthalen-1-yl)quinoline-4-carboxylate (L⁴H)

Obtained as a yellow solid (60 % yield). ¹H NMR (400 MHz, CDCl₃) δ_H 8.31 (d, $J = 2.8$ Hz, 1H), 8.25 (s, 1H), 8.16 (d, $J = 9.2$ Hz, 1H), 8.10 (d, $J = 8.2$ Hz, 1H), 7.96 (d, $J = 8.2$ Hz, 1H), 7.94 (d, $J = 8.0$ Hz, 1H), 7.73 (d, $J = 7.1$ Hz, 1H), 7.63 – 7.58 (m, 1H), 7.56 – 7.43 (m, 3H), 4.51 (q, $J = 7.1$ Hz, 2H), 4.02 (s, 3H), 1.45 (t, $J = 7.1$ Hz, 3H) ppm. ¹³C{¹H} NMR (101 MHz, CDCl₃) δ_c 166.5, 159.2, 156.1, 145.6, 138.0, 134.0, 133.3, 131.7, 131.2, 129.2, 128.4, 127.8, 126.7, 126.0, 125.5, 125.4, 125.4, 124.8, 123.0, 103.2, 61.7, 55.6, 14.3 ppm. UV-vis (MeCN): λ_{abs} ($\epsilon/10^4$ L mol⁻¹ cm⁻¹) 367 (0.9), 290 (1.5), 259 (2.3) nm. FTIR (solid) (ATR) ν_{max} : 3066, 2974, 1718 (C=O), 1616, 1589, 1550, 1496, 1488, 1458, 1436, 1390, 1365, 1348, 1330, 1278, 1247, 1220, 1190, 1182, 1170, 1147, 1112, 1093, 1062, 1026, 1010, 977, 962, 914, 898, 875, 866, 844, 812, 792, 781, 736, 696, 638, 594, 561, 534, 505, 459, 422, 414 cm⁻¹. HRMS (ES) [M + H]⁺ Calc'd 358.1443 for C₂₃H₂₀NO₃; found m/z 358.1458.

4.5.2.5 Ethyl 2-(naphthalen-1-yl)quinoline-4-carboxylate (L⁵H)⁹⁰

Obtained as a yellow solid (63% yield). Spectral properties were in agreement with those reported in the literature.

4.5.2.6 Ethyl 6-fluoro-2-(naphthalen-1-yl)quinoline-4-carboxylate (L⁶H)

Obtained as a yellow solid (57 % yield). ¹H NMR (400 MHz, CDCl₃) δ_H 8.60 (dd, *J* = 10.7, 2.8 Hz, 1H), 8.30 (s, 1H), 8.27 (dd, *J* = 9.3, 5.7 Hz, 1H), 8.09 (d, *J* = 8.2, 1H), 8.01 – 7.94 (m, 2H), 7.73 (dd, *J* = 7.1, 1.2 Hz, 1H), 7.65 – 7.48 (m, 4H), 4.52 (q, *J* = 7.1 Hz, 2H), 1.46 (t, *J* = 7.1 Hz, 3H) ppm. ¹³C{¹H} NMR (101 MHz, CDCl₃) δ_C 165.9, 158.3, 146.40, 137.6, 134.7, 134.0, 132.8, 132.7, 131.1, 129.6, 128.6, 127.9, 126.9, 126.2, 125.4, 125.3, 125.3, 125.0, 120.5, 120.2, 109.7, 109.5, 62.0, 14.3 ppm. ¹⁹F{¹H} NMR (376 MHz, CDCl₃) δ -109.9 (s) ppm. UV-vis (MeCN): λ_{abs} (ε/10⁴ L mol⁻¹ cm⁻¹) 350 (6.9), 288 (1.4), 248 (2.3) nm. FTIR (solid) (ATR) ν_{max}: 3051, 2980, 1714 (C=O), 1618, 1589, 1548, 1504, 1467, 1446, 1388, 1363, 1344, 1327, 1259, 1234, 1201, 1139, 1109, 1058, 1035, 1010, 921, 879, 844, 802m 790, 771, 744, 700, 603, 592, 555, 536, 472, 445, 432, 420 cm⁻¹. HRMS (ES) [M + H]⁺ Calc'd 346.1243 for C₂₂H₁₆FNO₂; found *m/z* 346.1249.

4.5.2.7 Ethyl 2-(4-methoxynaphthalen-1-yl)quinoline-4-carboxylate (L⁷H)

Obtained as a yellow solid (47 % yield) ¹H NMR (400 MHz, CDCl₃) δ 8.80 (dd, *J* = 8.5, 0.6 Hz, 1H), 8.40 – 8.36 (m, 1H), 8.26 (d, *J* = 8.4 Hz, 1H), 8.20 (s, 1H), 8.18 – 8.15 (m, 1H), 7.84 – 7.76 (m, 1H), 7.72 – 7.64 (m, 2H), 7.59 – 7.47 (m, 2H), 6.96 (d, *J* = 8.0 Hz, 1H), 4.52 (q, *J* = 7.1 Hz, 2H), 4.08 (s, 3H), 1.46 (t, *J* = 7.1 Hz, 3H) ppm. UV-vis (MeCN): λ_{abs} (ε/10⁴ L mol⁻¹ cm⁻¹) 364 (0.8), 300 (1.2) nm. FTIR (solid) (ATR) ν_{max}: 3062, 2981, 1718 (C=O), 1581, 1546, 1514, 1481, 1471, 1429, 1388, 1377, 1363, 1346, 1309, 1265, 1228, 1188, 1145, 1107, 1085, 1033, 1024, 970, 914, 898, 867, 821, 808, 796, 773, 763, 746, 709, 698, 644, 624, 596, 580, 559, 513, 491, 468, 432, 412 cm⁻¹. HRMS (AP) [M + H]⁺ Calc'd 358.1443 for C₂₃H₂₀NO₃; found *m/z* 358.1440.

4.5.3 Iridium(III) Dimer formation⁶³

IrCl₃.xH₂O (0.5 eq) and ligand (200 mg) were placed in a flask and dissolved in 2-ethoxyethanol (10 mL). The reaction mixture was heated to 130 °C and stirred for 2 days. The mixture was allowed to cool to room temperature, and the product precipitated with the addition of distilled water. The red precipitate was collected via filtration, washed with distilled water and dried in an oven for 8 hours. The Ir(III) dimers were used in subsequent reactions without purification or characterisation.

4.5.4 General Synthesis of [Ir(L)₂(bpy)]PF₆ complexes

[Ir₂(L)₄-μ-Cl₂] (300 mg) and AgBF₄ (2.2 equivalents) were dissolved in acetonitrile (20 mL) and heated to reflux in the absence of light for 16 hours. The reaction mixture was cooled to room temperature and the precipitated AgCl was removed *via* a celite pad and washed with MeCN. The solvent was removed and redissolved in CHCl₃. 2,2'-bipyridine (2.2 equivalents) was added and mixture heated to reflux for 16 hours. The mixture was cooled to room temperature, solvent removed and resuspended in MeCN. Saturated aqueous [NH₄][PF₆] was added and stirred for 5 minutes. The solvent was removed, and product purified by silica column chromatography (DCM, 9:1 DCM/MeOH) collecting the first red band eluted, the volume was reduced to *ca.* 3 ml and recrystallised by the addition of 30 ml diethyl ether before collecting on a sinter.

4.5.4.1 Synthesis of [Ir(L¹)₂(bpy)]PF₆

Obtained as a red solid (56 % yield) Characterisation revealed that the complex was isolated as the ethoxyethyl ester. ¹H NMR (500 MHz, CDCl₃) δ 8.88 (s, 2H), 8.55 (s, 2H), 8.27 (d, *J* = 8.2 Hz, 2H), 8.12 (d, *J* = 4.7 Hz, 2H), 8.07 (d, *J* = 2.8 Hz, 2H), 7.99 (ddd, *J* = 8.0, 1.4 Hz, 2H), 7.89 (d, *J* = 8.0 Hz, 2H), 7.45 (d, *J* = 9.7 Hz, 2H), 7.38 – 7.35 (m, 2H), 7.34 – 7.29 (m, *J* = 1.2 Hz, 2H), 7.27 (dd, *J* = 8.3, 1.2 Hz, 2H), 7.19 (d, *J* = 8.1 Hz, 2H), 6.89 (s, 2H), 6.58 (dd, *J* = 9.7, 2.8 Hz, 2H), 4.75 – 4.72 (m, 4H), 3.96 – 3.94 (m, 4H), 3.85 (s, 6H), 3.70 (q, *J* = 7.0 Hz, 4H), 1.33 (t, *J* = 7.0 Hz, 6H) ppm. ¹³C{¹H} NMR (126 MHz, CDCl₃) δ_C 165.7, 165.4, 159.2, 155.5, 147.4, 144.9, 144.4, 140.8, 140.1, 136.2, 135.3, 132.4, 130.4, 129.0, 127.8, 127.7, 127.2, 126.8, 126.5, 126.3, 124.8, 124.5, 123.0, 119.9, 105.5, 68.1, 66.8, 65.7, 55.7, 15.2 ppm. UV-vis. (MeCN) λ_{abs} (ε /10⁴ M⁻¹ cm⁻¹) 480 (0.2), 401 (1.6), 367 (1.7), 321 (3.5), 280 (4.9), 221 (5.7) nm. FTIR (solid) (ATR) ν_{max}: 2980, 1726 (C=O), 1616, 1602, 1552, 1533, 1506, 1471, 1444, 1381, 1296, 1259, 1236, 1161, 1120, 1106, 1080, 1020, 873, 833 (PF₆⁻), 804, 786, 709, 646, 635, 555 (PF₆⁻) cm⁻¹. HRMS (ES) [M - PF₆]⁺ Calc'd 1149.3414 for C₆₀H₅₂IrN₄O₈; found *m/z* 1149.3396.

4.5.4.2 Synthesis of [Ir(L²)₂(bpy)]PF₆

Obtained as a red solid (90 % yield). ¹H NMR (400 MHz, CD₃CN) δ_H 8.92 (s, *J* = 23.6 Hz, 2H), 8.87 (s, 2H), 8.49 (d, *J* = 8.4 Hz, 2H), 8.26 (d, *J* = 5.4 Hz, 2H), 8.04 (d, *J* = 8.1 Hz, 2H), 8.00 (d, *J* = 8.2 Hz, 2H), 7.92 (dd, *J* = 7.7, 7.6 Hz, 2H), 7.61 (d, *J* = 9.0 Hz, 2H), 7.50 – 7.41 (m, 4H), 7.38 – 7.32 (m, 2H), 7.31 – 7.26 (m, 2H), 7.21 (d, *J* = 8.3 Hz, 2H), 7.08 – 7.00 (m, 4H), 4.61 (q, *J* = 7.0 Hz, 4H), 1.55 (t, *J* = 7.1 Hz, 6H) ppm. ¹³C{¹H} NMR (101 MHz, CD₃CN) δ_C 170.6, 166.6, 163.6, 156.6, 149.8, 149.7, 146.6, 140.8, 140.5, 136.8, 133.5, 132.3, 131.8, 130.6, 129.7, 129.5,

127.9, 127.3, 127.1, 126.1, 125.7, 125.1, 64.1, 14.9 ppm. UV-vis. (MeCN) λ_{abs} ($\epsilon / 10^4 \text{ M}^{-1} \text{ cm}^{-1}$) 464 (0.2), 365 (2.9), 315 (3.3), 283 (5.4), 265 (6.6), 218 (7.4) nm. FTIR (solid) (ATR) ν_{max} : 3074, 2981, 1734, 1718 (C=O), 1597, 1560, 1544, 1535, 1458, 1438, 1371, 1352, 1274, 1242, 1193, 1149, 875, 835 (PF_6^-), 767, 746, 555 (PF_6^-) cm^{-1} . HRMS (ES) $[\text{M} - \text{PF}_6]^+$ Calc'd 999.2650 for $\text{C}_{54}\text{H}_{40}\text{IrN}_4\text{O}_4$; found m/z 999.2659.

4.5.4.3 Synthesis of $[\text{Ir}(\text{L}^3)_2(\text{bpy})]\text{PF}_6$

Obtained as a red solid (38 % yield). ^1H NMR (500 MHz, CD_3CN) δ_{H} 8.99 (s, 2H), 8.86 (s, $J = 25.8$ Hz, 2H), 8.29 (dd, $J = 10.3, 2.5$ Hz, 2H), 8.22 (d, $J = 4.9$ Hz, 2H), 8.07 (d, $J = 8.2$ Hz, 2H), 8.01 (d, $J = 7.9$ Hz, 2H), 7.94 (dd, $J = 7.8, 7.3$ Hz, 2H), 7.66 (dd, $J = 9.6, 5.2$ Hz, 2H), 7.48 – 7.44 (m, 2H), 7.36 (d, $J = 7.2$ Hz, 2H), 7.30 (d, $J = 6.8$ Hz, 2H), 7.24 (d, $J = 8.1$ Hz, 2H), 7.05 (s, 2H), 6.88 – 6.83 (m, 2H), 4.61 (q, $J = 7.1$ Hz, 4H), 1.55 (t, $J = 7.1$ Hz, 6H) ppm. $^{13}\text{C}\{^1\text{H}\}$ NMR (126 MHz, CD_3CN) δ_{C} 170.3, 166.6, 166.2, 163.3, 156.7, 149.8, 146.4, 142.7, 140.9, 139.3, 136.9, 131.9, 130.6, 130.2, 129.9, 129.9, 129.6, 127.2, 125.9, 125.4, 122.0, 121.6, 64.3, 14.9 ppm. $^{19}\text{F}\{^1\text{H}\}$ NMR (376 MHz, CDCl_3) δ -72.6 (d, $^1J_{\text{PF}} = 711$ Hz), -107.2 (s) ppm. UV-vis. (MeCN) λ_{abs} ($\epsilon / 10^4 \text{ M}^{-1} \text{ cm}^{-1}$) 483 (0.2), 399 (1.6), 365 (2.1), 268 (5.5) nm. FTIR (solid) (ATR) ν_{max} : 3047, 2924, 1720 (C=O), 1625, 1602, 1583, 1548, 1465, 1438, 1373, 1354, 1300, 1247, 1219, 1147, 1122, 1076, 1026, 875, 837 (PF_6^-), 763, 555 (PF_6^-) cm^{-1} . HRMS (ES) $[\text{M} - \text{PF}_6]^+$ Calc'd 1035.2456 for $\text{C}_{54}\text{H}_{38}\text{IrF}_2\text{N}_4\text{O}_4$; found m/z 1035.2462.

4.5.4.4 Synthesis of $[\text{Ir}(\text{L}^4)_2(\text{bpy})]\text{PF}_6$

Obtained as a red solid (36 % yield). ^1H NMR (500 MHz, CDCl_3) δ_{H} 9.14 (s, 2H), 8.63 (d, $J = 8.7$ Hz, 2H), 8.24 (d, $J = 8.1$ Hz, 2H), 8.07 – 8.04 (m, 4H), 7.98 (dd, $J = 7.9, 7.8$ Hz, 2H), 7.80 (d, $J = 8.1$ Hz, 2H), 7.66 (dd, $J = 7.8, 7.5$ Hz, 2H), 7.48 (dd, $J = 8.0, 7.0$ Hz, 2H), 7.36 – 7.29 (m, 6H), 6.95 (d, $J = 8.5$ Hz, 2H), 6.60 (dd, $J = 9.6, 2.6$ Hz, 2H), 4.59 (q, $J = 7.1$ Hz, 4H), 3.86 (s, 6H), 1.55 (t, $J = 7.1$ Hz, 6H) ppm. $^{13}\text{C}\{^1\text{H}\}$ NMR (126 MHz, CDCl_3) δ_{C} 167.7, 165.2, 158.9, 155.1, 155.0, 146.8, 144.9, 140.3, 138.9, 135.2, 132.8, 132.0, 131.8, 131.0, 130.2, 127.8, 127.3, 126.1, 125.2, 125.0, 124.3, 123.4, 122.8, 121.2, 105.0, 62.6, 55.7, 14.3 ppm. UV-vis (MeCN): λ_{abs} ($\epsilon / 10^4 \text{ L mol}^{-1} \text{ cm}^{-1}$) 497 (0.7), 417 (1.4), 367 (2.5), 267 (6.1) nm. FTIR (solid) (ATR) ν_{max} : 2980, 1760 (C=O), 1616, 1533, 1500, 1471, 1444, 1382, 1294, 1265, 1234, 1157, 1122, 1103, 1026, 835 (PF_6^-), 786, 763, 748, 709, 648, 636, 580, 555

(PF₆⁻), 513 cm⁻¹. HRMS (ES) [M - PF₆]⁺ Calc'd 1059.2861 for C₅₆H₄₄IrN₄O₆; found *m/z* 1059.2849.

4.5.4.5 Synthesis of [Ir(L⁵)₂(bpy)]PF₆

Obtained as a red solid (38 % yield). ¹H NMR (400 MHz, CDCl₃) δ_H 9.11 (s, 2H), 8.69 (d, *J* = 4.2 Hz, 2H), 8.64 (d, *J* = 8.5 Hz, 2H), 8.55 (d, *J* = 8.2 Hz, 2H), 8.19 (d, *J* = 8.1 Hz, 2H), 8.06 (d, *J* = 5.0 Hz, 2H), 7.97 (dd, *J* = 8.0, 7.3 Hz, 2H), 7.80 (d, *J* = 7.8 Hz, 2H), 7.67 (dd, *J* = 7.8, 7.5 Hz, 2H), 7.49 (dd, *J* = 7.5, 7.3 Hz, 2H), 7.47 – 7.41 (m, 2H), 7.39 (d, *J* = 8.8 Hz, 2H), 7.34 – 7.28 (m, 4H), 6.99 (d, *J* = 8.4 Hz, 2H), 4.60 (q, *J* = 7.1 Hz, 4H), 1.54 (t, *J* = 7.1 Hz, 6H) ppm. ¹³C{¹H} NMR (101 MHz, CDCl₃) δ_C 171.0, 165.0, 156.8, 155.2, 149.2, 148.8, 146.8, 140.4, 138.8, 137.8, 137.0, 132.8, 132.3, 131.8, 131.0, 130.3, 128.1, 127.4, 126.7, 124.9, 124.6, 124.5, 123.7, 123.5, 122.8, 121.2, 121.1, 62.8, 14.3 ppm. UV-vis (MeCN): λ_{abs} (ε/10⁴ L mol⁻¹ cm⁻¹) 494 (0.5), 405 (1.4), 366 (2.0), 271 (9.2) nm. FTIR (solid) (ATR) ν_{max}: 2980, 1728 (C=O), 1600, 1558, 1531, 1471, 1444, 1396, 1381, 1296, 1267, 1238, 1161, 1101, 1018, 835 (PF₆⁻), 802, 786, 709, 555 (PF₆⁻) cm⁻¹. HRMS (ES) [M - PF₆]⁺ Calc'd 999.2650 for C₅₄H₄₀IrN₄O₄; found *m/z* 999.2628.

4.5.4.6 Synthesis of [Ir(L⁶)₂(bpy)]PF₆

Obtained as a red solid (72 % yield). ¹H NMR (400 MHz, CDCl₃) δ_H 9.21 (s, 2H), 8.62 (d, *J* = 8.5 Hz, 2H), 8.42 – 8.35 (m, 4H), 8.05 (dd, *J* = 6.6, 5.9 Hz, 4H), 7.82 (d, *J* = 7.9 Hz, 2H), 7.69 (dd, *J* = 8.5, 7.1 Hz, 2H), 7.51 dd, *J* = 7.6, 7.2 Hz, 2H), 7.42 (dd, *J* = 9.6, 5.0 Hz, 2H), 7.38 – 7.28 (m, 4H), 6.90 (d, *J* = 8.3 Hz, 2H), 6.80 – 6.73 (m, 2H), 4.60 (q, *J* = 7.1 Hz, 4H), 1.55 (t, *J* = 7.1 Hz, 6H) ppm. ¹³C{¹H} NMR (126 MHz, CDCl₃) δ_C 170.5, 164.4, 159.9, 156.3, 155.1, 149.2, 146.7, 145.8, 140.7, 138.6, 136.9, 136.5, 132.5, 132.3, 132.0, 131.8, 130.4, 128.3, 127.7, 126.9, 126.8, 125.2, 124.7, 123.9, 123.7, 121.1, 120.9, 120.7, 111.4, 111.2, 63.0, 14.3 ppm. ¹⁹F{¹H} NMR (376 MHz, CDCl₃) δ -72.6 (d, ¹J_{PF} = 711 Hz), -107.7 (s) ppm. UV-vis (MeCN): λ_{abs} (ε/10⁴ L mol⁻¹ cm⁻¹) 492 (0.5), 408 (1.3), 367 (2.2), 264 (5.0) nm. FTIR (solid) (ATR) ν_{max}: 3030, 2924, 1718 (C=O), 1624, 1597, 1577, 1552, 1533, 1500, 1473, 1458, 1444, 1425, 1396, 1363, 1354, 1321, 1294, 1261, 1240, 1220, 1199, 1170, 1179, 1105, 1028, 999, 933, 879, 840 (PF₆⁻), 790, 763, 744, 707, 665, 648, 557 (PF₆⁻), 528, 518 cm⁻¹. HRMS (ES) [M - PF₆]⁺ Calc'd 1035.2462 for C₅₄H₃₈IrF₂N₄O₄; found *m/z* 1035.2458.

4.5.4.7 Synthesis of [Ir(L⁷)₂(bpy)]PF₆

Obtained as a red solid (69 % yield). ¹H NMR (500 MHz, CDCl₃) δ_H 8.96 (s, 2H), 8.59 (d, *J* = 8.8 Hz, 2H), 8.49 (dd, *J* = 8.5, 1.1 Hz, 2H), 8.30 – 8.26 (m, 4H), 8.10 –

8.08 (m, 2H), 8.05 – 8.01 (m, 2H), 7.69 (ddd, J = 8.5, 6.9, 1.5 Hz, 2H), 7.52 (ddd, J = 8.1, 6.9, 1.0 Hz, 2H), 7.43 – 7.39 (m, 2H), 7.35 (ddd, J = 7.6, 5.5, 1.2 Hz, 2H), 7.31 (dd, J = 8.9, 0.6 Hz, 2H), 7.02 – 6.96 (m, 2H), 6.20 (s, 2H), 4.61 (q, J = 7.1 Hz, 4H), 3.36 (s, 6H), 1.55 (t, J = 7.1 Hz, 6H) ppm. $^{13}\text{C}\{^1\text{H}\}$ NMR (126 MHz, CDCl_3) δ 171.1, 165.4, 160.3, 157.2, 155.4, 148.8, 147.7, 140.4, 137.7, 133.4, 131.6, 131.0, 128.8, 127.6, 127.4, 126.7, 125.1, 124.5, 124.4, 124.3, 124.1, 123.0, 122.5, 121.1, 110.8, 62.8, 55.4, 14.5 ppm. UV-vis (MeCN): λ_{abs} ($\epsilon/10^4 \text{ L mol}^{-1} \text{ cm}^{-1}$) 526 (0.9), 358 (2.6), 264 (5.4), 229 (7.4) nm. FTIR (solid) (ATR) ν_{max} : 1722 (C=O), 1596, 1548, 1498, 1446, 1408, 1361, 1296, 1273, 1238, 1195, 1159, 1139, 1099, 1026, 975, 835 (PF_6^-), 761, 711, 642, 605, 555 (PF_6^-), 509, 408 cm^{-1} . HRMS (ES) $[\text{M} - \text{PF}_6]^+$ Calc'd 1059.2867 for $\text{C}_{56}\text{H}_{44}\text{IrN}_4\text{O}_6$; found m/z 1059.2889.

4.6 References

- 1 M. T. Hoekenga, *Am. J. Trop. Med. Hyg.*, 1954, **3**, 833–838.
- 2 A. Fournet, A. A. Barrios, V. Muñoz, R. Hocquemiller, F. Roblot, A. Cavé, P. Richomme and J. Bruneton, *Phytother. Res.*, 1994, **8**, 174–178.
- 3 J. Achan, J. K. Tibenderana, D. Kyabayinze, F. W. Mangen, M. R. Kanya, G. Dorsey, U. D'Alessandro, P. J. Rosenthal and A. O. Talisuna, *BMJ*, DOI:10.1136/bmj.b2763.
- 4 *The Lancet*, 2005, **366**, 717–725.
- 5 M. E. Wall, M. C. Wani, C. E. Cook, K. H. Palmer, A. T. McPhail and G. A. Sim, *J. Am. Chem. Soc.*, 1966, **88**, 3888–3890.
- 6 W. Cai, M. Hassani, R. Karki, E. D. Walter, K. H. Koelsch, H. Seradj, J. P. Lineswala, H. Mirzaei, J. S. York, F. Olang, M. Sedighi, J. S. Lucas, T. J. Eads, A. S. Rose, S. Charkharrin, N. G. Hermann, H. D. Beall and M. Behforouz, *Bioorg. Med. Chem.*, 2010, **18**, 1899–1909.
- 7 K. V. Rao, K. Biemann and R. B. Woodward, *J. Am. Chem. Soc.*, 1963, **85**, 2532–2533.
- 8 R. Musharrafieh, J. Zhang, P. Tuohy, N. Kitamura, S. S. Bellampalli, Y. Hu, R. Khanna and J. Wang, *J. Med. Chem.*, 2019, **62**, 4074–4090.
- 9 R. Musharrafieh, N. Kitamura, Y. Hu and J. Wang, *Bioorganic Chem.*, 2020, **101**, 103981.
- 10 C.-Y. Yang, Y.-L. Hung, K.-W. Tang, S.-C. Wang, C.-H. Tseng, C.-C. Tzeng, P.-L. Liu, C.-Y. Li and Y.-L. Chen, *Molecules*, 2019, **24**, 1162.
- 11 A. H. Abadi, G. H. Hegazy and A. A. El-Zaher, *Bioorg. Med. Chem.*, 2005, **13**, 5759–5765.
- 12 G. R. Han, D. Hwang, S. Lee, J. W. Lee, E. Lim, J. Heo and S. K. Kim, *Sci. Rep.*, 2017, **7**, 3863.
- 13 C. W. Tang and S. A. VanSlyke, *Appl. Phys. Lett.*, 1987, **51**, 913–915.
- 14 H. Kaur, S. Sundriyal, V. Pachauri, S. Ingebrandt, K.-H. Kim, A. L. Sharma and A. Deep, *Coord. Chem. Rev.*, 2019, **401**, 213077.
- 15 Z. H. Skarup, *Berichte Dtsch. Chem. Ges.*, 1880, **13**, 2086–2089.
- 16 O. Doebner and W. v. Miller, *Berichte Dtsch. Chem. Ges.*, 1881, **14**, 2812–2817.
- 17 M. Conrad and L. Limpach, *Berichte Dtsch. Chem. Ges.*, 1887, **20**, 944–948.
- 18 M. Conrad and L. Limpach, *Berichte Dtsch. Chem. Ges.*, 1887, **20**, 948–959.
- 19 L. Knorr, *Justus Liebigs Ann. Chem.*, 1886, **236**, 69–115.
- 20 P. Friedländer and C. F. Gohring, *Berichte Dtsch. Chem. Ges.*, 1883, **16**, 1833–1839.
- 21 St. Niementowski, *Berichte Dtsch. Chem. Ges.*, 1894, **27**, 1394–1403.
- 22 O. Döbner, *Justus Liebigs Ann. Chem.*, 1887, **242**, 265–289.
- 23 W. Pfitzinger, *J. Für Prakt. Chem.*, 1885, **33**, 100–100.
- 24 L.-H. Li, Z.-J. Niu and Y.-M. Liang, *Chem. – Asian J.*, 2020, **15**, 231–241.
- 25 M. Velusamy, C.-H. Chen, Y. S. Wen, J. T. Lin, C.-C. Lin, C.-H. Lai and P.-T. Chou, *Organometallics*, 2010, **29**, 3912–3921.
- 26 M. A. Esteruelas, F. J. Fernández-Alvarez and E. Oñate, *Organometallics*, 2007, **26**, 5239–5245.
- 27 Y. Miao, K. Wang, L. Gao, B. Zhao, H. Wang, F. Zhu, B. Xu and D. Ma, *J. Mater. Chem. C*, 2018, **6**, 8122–8134.
- 28 J. Ye, C.-J. Zheng, X.-M. Ou, X.-H. Zhang, M.-K. Fung and C.-S. Lee, *Adv. Mater.*, 2012, **24**, 3410–3414.
- 29 M. Wang, K.-H. Leung, S. Lin, D. S.-H. Chan, C.-H. Leung and D.-L. Ma, *J. Mater. Chem. B*, 2014, **2**, 6467–6471.

- 30 C. Lentz, O. Schott, T. Auvray, G. Hanan and B. Elias, *Inorg. Chem.*, 2017, **56**, 10875–10881.
- 31 J. S. Nam, M.-G. Kang, J. Kang, S.-Y. Park, S. J. C. Lee, H.-T. Kim, J. K. Seo, O.-H. Kwon, M. H. Lim, H.-W. Rhee and T.-H. Kwon, *J. Am. Chem. Soc.*, 2016, **138**, 10968–10977.
- 32 J. D. Routledge, A. J. Hallett, J. A. Platts, P. N. Horton, S. J. Coles and S. J. A. Pope, *Eur. J. Inorg. Chem.*, 2012, **2012**, 4065–4075.
- 33 J. E. Jones, R. L. Jenkins, R. S. Hicks, A. J. Hallett and S. J. A. Pope, *Dalton Trans.*, 2012, **41**, 10372–10381.
- 34 R. A. Smith, E. C. Stokes, E. E. Langdon-Jones, J. A. Platts, B. M. Kariuki, A. J. Hallett and S. J. A. Pope, *Dalton Trans.*, 2013, **42**, 10347–10357.
- 35 J. Zhou, Q. Liu, W. Feng, Y. Sun and F. Li, *Chem. Rev.*, 2015, **115**, 395–465.
- 36 C. A. Parker, C. G. Hatchard and E. J. Bowen, *Proc. R. Soc. Lond. Ser. Math. Phys. Sci.*, 1962, **269**, 574–584.
- 37 F. Auzel, *J. Lumin.*, 2020, **223**, 116900.
- 38 R. Scheps, *Prog. Quantum Electron.*, 1996, **20**, 271–358.
- 39 N. M. Idris, M. K. Gnanasammandhan, J. Zhang, P. C. Ho, R. Mahendran and Y. Zhang, *Nat. Med.*, 2012, **18**, 1580–1585.
- 40 Y. Ma, J. Bao, Y. Zhang, Z. Li, X. Zhou, C. Wan, L. Huang, Y. Zhao, G. Han and T. Xue, *Cell*, 2019, **177**, 243-255.e15.
- 41 C. Duan, L. Liang, L. Li, R. Zhang and Z. P. Xu, *J. Mater. Chem. B*, 2018, **6**, 192–209.
- 42 T. N. Singh-Rachford and F. N. Castellano, *Coord. Chem. Rev.*, 2010, **254**, 2560–2573.
- 43 R. Haruki, Y. Sasaki, K. Masutani, N. Yanai and N. Kimizuka, *Chem. Commun.*, 2020, **56**, 7017–7020.
- 44 C. Ye, V. Gray, K. Kushwaha, S. K. Singh, P. Erhart and K. Börjesson, *Phys. Chem. Chem. Phys.*, 2020, **22**, 1715–1720.
- 45 M. Alipour and Z. Safari, *Phys. Chem. Chem. Phys.*, 2019, **21**, 17126–17141.
- 46 H.-C. Chen, C.-Y. Hung, K.-H. Wang, H.-L. Chen, W. S. Fann, F.-C. Chien, P. Chen, T. J. Chow, C.-P. Hsu and S.-S. Sun, *Chem. Commun.*, 2009, 4064–4066.
- 47 B. Soep, J.-M. Mestdagh, M. Briant, M.-A. Gaveau and L. Poisson, *Phys. Chem. Chem. Phys.*, 2016, **18**, 22914–22920.
- 48 A. K. Bansal, W. Holzer, A. Penzkofer and T. Tsuboi, *Chem. Phys.*, 2006, **330**, 118–129.
- 49 Z.-Q. Liang, Z.-Y. Zou, G.-L. Dai, X.-M. Wang and X.-T. Tao, *Dyes Pigments*, 2020, **180**, 108489.
- 50 X. Yi, J. Zhao, J. Sun, S. Guo and H. Zhang, *Dalton Trans.*, 2013, **42**, 2062–2074.
- 51 S. J. Pope, T. Stonelake, K. Phillips, S. Coles, P. Horton, S. Keane, E. Stokes, I. Fallis, J. Beames, J. Zhao, K. Chen, Y. Hou, A. Hallett and S. O’Kell, *Chem. – Eur. J.*, , DOI:10.1002/chem.201801007.
- 52 F. Deng, J. Blumhoff and F. N. Castellano, *J. Phys. Chem. A*, 2013, **117**, 4412–4419.
- 53 B. Pfund, D. M. Steffen, M. R. Schreier, M.-S. Bertrams, C. Ye, K. Börjesson, O. S. Wenger and C. Kerzig, *J. Am. Chem. Soc.*, 2020, **142**, 10468–10476.

- 54 G.-N. Porter and R. G. W. Norrish, *Proc. R. Soc. Lond. Ser. Math. Phys. Sci.*, 1950, **200**, 284–300.
- 55 R. G. W. Norrish and G. Porter, *Nature*, 1949, **164**, 658–658.
- 56 The Nobel Prize in Chemistry 1967, <https://www.nobelprize.org/prizes/chemistry/1967/summary/>, (accessed June 29, 2020).
- 57 B. L. Gore, T. A. M. Doust, L. B. Giorgi, D. R. Klug, J. P. Ide, B. Crystall and G. Porter, *J. Chem. Soc. Faraday Trans. 2 Mol. Chem. Phys.*, 1986, **82**, 2111–2115.
- 58 S. R. Greenfield and M. R. Wasielewski, *Photosynth. Res.*, 1996, **48**, 83–97.
- 59 Granite, Pump Probe | What is Transient Absorption?, <https://www.edinst.com/blog/pump-probe-transient-absorption-spectroscopy/>, (accessed June 26, 2020).
- 60 E. Fischer and A. Speier, *Berichte Dtsch. Chem. Ges.*, 1895, **28**, 3252–3258.
- 61 N. P. BUU-HOÏ, N. D. XUONG and V. Q. YEN, *J. Org. Chem.*, 1958, **23**, 539–541.
- 62 H. E. Gottlieb, V. Kotlyar and A. Nudelman, *J. Org. Chem.*, 1997, **62**, 7512–7515.
- 63 M. Nonoyama, *Bull. Chem. Soc. Jpn.*, 1974, **47**, 767–768.
- 64 S. Sprouse, K. A. King, P. J. Spellane and R. J. Watts, *J. Am. Chem. Soc.*, 1984, **106**, 6647–6653.
- 65 S. Lamansky, P. Djurovich, D. Murphy, F. Abdel-Razzaq, R. Kwong, I. Tsyba, M. Bortz, B. Mui, R. Bau and M. E. Thompson, *Inorg. Chem.*, 2001, **40**, 1704–1711.
- 66 F. O. Garces, K. A. King and R. J. Watts, *Inorg. Chem.*, 1988, **27**, 3464–3471.
- 67 A. Brouwer, *Pure Appl. Chem.*, 2011, **83**, 2213–2228.
- 68 C. E. Elgar, H. Y. Otaif, X. Zhang, J. Zhao, P. N. Horton, S. J. Coles, J. M. Beames and S. J. A. Pope, *Chem. – Eur. J.*, 2021, **27**, 3427–3439.
- 69 X. Yi, C. Zhang, S. Guo, J. Ma and J. Zhao, *Dalton Trans.*, 2013, **43**, 1672–1683.
- 70 J. Sun, W. Wu and J. Zhao, *Chem. – Eur. J.*, 2012, **18**, 8100–8112.
- 71 L. Ma, H. Guo, Q. Li, S. Guo and J. Zhao, *Dalton Trans.*, 2012, **41**, 10680–10689.
- 72 P. Bharmoria, H. Bildirir and K. Moth-Poulsen, *Chem. Soc. Rev.*, 2020, **49**, 6529–6554.
- 73 S. Ladouceur and E. Zysman-Colman, *Eur. J. Inorg. Chem.*, 2013, **2013**, 2985–3007.
- 74 G. M. Sheldrick, *Acta Crystallogr. Sect. Found. Adv.*, 2015, **71**, 3–8.
- 75 O. V. Dolomanov, L. J. Bourhis, R. J. Gildea, J. A. K. Howard and H. Puschmann, *J. Appl. Crystallogr.*, 2009, **42**, 339–341.
- 76 G. M. Sheldrick, *Acta Crystallogr. Sect. C Struct. Chem.*, 2015, **71**, 3–8.
- 77 M. J. Frisch, G. W. Trucks, J. R. Cheeseman, G. Scalmani, M. Caricato, H. P. Hratchian, X. Li, V. Barone, J. Bloino, G. Zheng, T. Vreven, J. A. Montgomery, G. A. Petersson, G. E. Scuseria, H. B. Schlegel, H. Nakatsuji, A. F. Izmaylov, R. L. Martin, J. L. Sonnenberg, J. E. Peralta, J. J. Heyd, E. Brothers, F. Ogliaro, M. Bearpark, M. A. Robb, B. Mennucci, K. N. Kudin, V. N. Staroverov, R. Kobayashi, J. Normand, A. Rendell, R. Gomperts, V. G. Zakrzewski, M. Hada, M. Ehara, K. Toyota, R. Fukuda, J. Hasegawa, M. Ishida, T. Nakajima, Y. Honda, O. Kitao and H. Nakai, *Gaussian 09*, Revision C.01, Gaussian Inc. Wallingford CT 2009.
- 78 A. D. Becke, *J. Chem. Phys.*, 1993, **98**, 5648–5652.
- 79 C. Lee, W. Yang and R. G. Parr, *Phys. Rev. B*, 1988, **37**, 785–789.

- 80 D. Andrae, U. Häußermann, M. Dolg, H. Stoll and H. Preuß, *Theor. Chim. Acta*, 1990, **77**, 123–141.
- 81 R. Ditchfield, W. J. Hehre and J. A. Pople, *J. Chem. Phys.*, 1971, **54**, 724–728.
- 82 W. J. Hehre, R. Ditchfield and J. A. Pople, *J. Chem. Phys.*, 1972, **56**, 2257–2261.
- 83 P. C. Hariharan and J. A. Pople, *Theor. Chim. Acta*, 1973, **28**, 213–222.
- 84 J. Tomasi, B. Mennucci and R. Cammi, *Chem. Rev.*, 2005, **105**, 2999–3094.
- 85 N. M. O'boyle, A. L. Tenderholt and K. M. Langner, *J. Comput. Chem.*, 2008, **29**, 839–845.
- 86 R. D. Garrett and H. R. Henze, *J. Med. Chem.*, 1966, **9**, 976–977.
- 87 G. C. Muscia, J. P. Carnevale, A. Luczywo, M. Victoria Peláez, A. Rodríguez Ó Toole, G. Y. Buldain, J. J. Casal and S. E. Asís, *Arab. J. Chem.*, , DOI:10.1016/j.arabjc.2018.10.003.
- 88 N. P. Buu-Hoï and P. Cagniant, *Recl. Trav. Chim. Pays-Bas*, 1945, **64**, 214–218.
- 89 R. F. Brown, T. L. Jacobs, S. Winstein, M. C. Kloetzel, E. C. Spaeth, W. H. Florsheim, J. H. Robson, E. F. Levy, G. M. Bryan, A. B. Magnusson, S. J. Miller, M. L. Ott and J. A. Terek, *J. Am. Chem. Soc.*, 1946, **68**, 2705–2708.
- 90 Y. Luo, H. Sun, W. Zhang, X. Wang, S. Xu, G. Zhang, Y. Jian and Z. Gao, *RSC Adv.*, 2017, **7**, 28616–28625.

**Chapter 5 - Iridium(III) Complexes of *Bis*-
Imine Ligands; 2-(Pyridin-2-yl)Quinoline and
2-(Pyrazin-2-yl)Quinoline.**

5.1 Introduction

So far the work of this thesis has focused on tuning of emission wavelength of red emitting *bis*-cyclometalated iridium(III) complexes via modification of the cyclometalating ligand. This chapter aims to build upon this idea by the synthesis and complexation of new N^N type asymmetric ancillary ligands in an attempt to further modify the emission properties.

5.1.1 Asymmetric *bis*-cyclometalated iridium(III) complexes

Rational design of phosphorescent metal complexes to tailor the properties towards the end use is becoming more and more prevalent in the catalysis and imaging fields¹⁻³. Moreover, the need to move away from the typical D_3 and C_2 symmetrical motif for asymmetrical iridium(III) complexes grows, since this allows for further control over not just emission properties, but solubility properties of the complexes⁴. Solvent solubility is an important consideration for metal complexes in the fields of catalysis⁵ and bioimaging⁶.

For the cyclometalated iridium(III) chemists, there are a variety of options available to produce asymmetrical complexes. For example, *tris*-cyclometalated $[\text{Ir}(\text{C}^{\wedge}\text{N})_3]$ complexes can be synthesised to include either one different ligand, as $[\text{Ir}(\text{C}^{\wedge}\text{N}^1)_2(\text{C}^{\wedge}\text{N}^2)]$, or with each ligand different, $[\text{Ir}(\text{C}^{\wedge}\text{N}^1)(\text{C}^{\wedge}\text{N}^2)(\text{C}^{\wedge}\text{N}^3)]$.⁷ Synthetically, the same procedures can be applied to produce mismatched *bis*-cyclometalated complexes, $[\text{Ir}(\text{C}^{\wedge}\text{N}^1)(\text{C}^{\wedge}\text{N}^2)(\text{L})]^{0/+}$. For example, Nazeeruddin *et al* noted in 2012 the ability for picolinate or acac ancillary ligands to dissociate, reforming the bridged chloride iridium dimer while in a solution of either Brønsted or Lewis acids⁸. To obtain the pure $[\{\text{Ir}(\text{ppy})(\text{diFppy})(\mu\text{-Cl})\}_2]$ dimer, the group first reacted equimolar amounts of ppy and diFppy with $[\{\text{Ir}(\text{COD})(\mu\text{-Cl})\}_2]$ producing a mixture of different dimeric species. The dimers could be split with acetylacetone and purified by column chromatography, giving three complexes: $[\text{Ir}(\text{ppy})_2\text{acac}]$, $[\text{Ir}(\text{diFppy})_2\text{acac}]$ and the desired $[\text{Ir}(\text{ppy})(\text{diFppy})\text{acac}]$. From here, the *tris*-heteroleptic complex can be dissolved in CH_2Cl_2 and treated with 2 M HCl (in Et_2O) for 15 minutes without heating, yielding the pure mixed dimeric species at good yields (Figure 5.1). At this stage, the dimeric species $[\{\text{Ir}(\text{ppy})(\text{diFppy})(\mu\text{-Cl})\}_2]$ can be split like normal by any ancillary ligand, or third cyclometalating ligand. Emission wavelength of the $[\text{Ir}(\text{ppy})(\text{diFppy})\text{acac}]$ was found to fall between the

corresponding $[\text{Ir}(\text{diFppy})_2\text{acac}]$ (λ_{em} : 484 nm) and $[\text{Ir}(\text{ppy})_2\text{acac}]$ (λ_{em} : 520 nm) complexes at λ_{em} : 503 nm in degassed CH_2Cl_2 solutions.

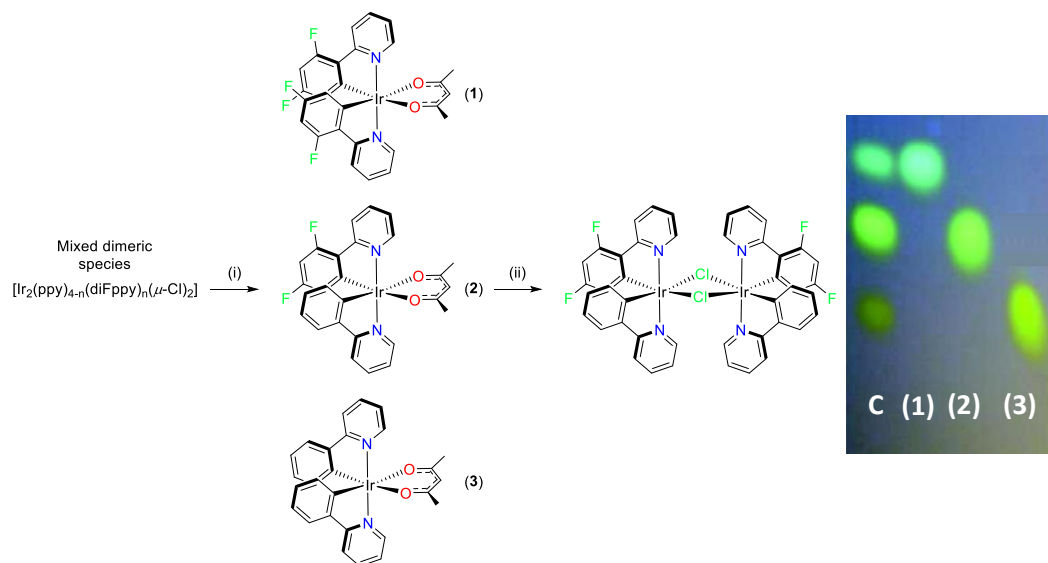


Figure 5.1 – Synthesis of pure mixed ligand Ir(III) dimers, adapted from Nazeeruddin *et al.*⁸. (i) acacH, $[\text{Bu}_4\text{N}][\text{OH}]$, CH_2Cl_2 , 40°C overnight, 44%; (ii) (2), HCl (2 M in Et_2O), CH_2Cl_2 , RT, 15 min, 86%. TLC plate of acac complexes. C: crude mix from dimer splitting followed by samples after purification.

Another methodology for asymmetric complexes involves the use of asymmetric ancillary ligands, such as picolinates⁹, β -diketonates¹⁰ or substituted *bis*-imines¹¹. These ligands can often be used for post-synthetic modification of the complex, allowing access to ligand systems that are often too sterically demanding or unstable as free ligands, as demonstrated by Beeby *et al* in 2017¹². By reacting brominated picolinic acid with an iridium dimer, the team was able to use Sonogashira coupling to then attach ethynyl TIPS groups in either the 3,4,5 or 6 positions around the picolinate ring (Figure 5.2). The effects of the position of substitution can be seen in the emission wavelengths; varying from 582 nm for complex 4 to 636 nm for complex 6 (measurements recorded in degassed CH_2Cl_2). Complex 5 showed λ_{max} at 616 nm, while this was shifted to 590 nm for complex 7. As expected, all of the emission wavelengths show a significant bathochromic shift when compared with $[\text{Ir}(\text{ppy})_2(\text{pic})]$, which has a λ_{max} at 506 nm¹³, while substitution in position 4- and 5- show the greatest effect upon the optical behaviour of the compounds.

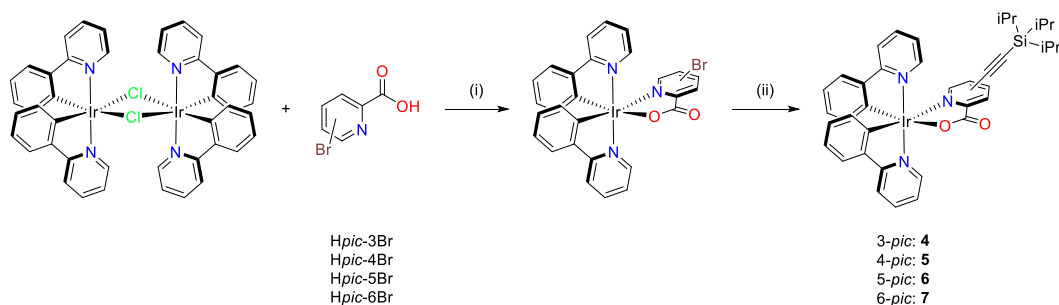


Figure 5.2 – Synthesis Hpic-Br complexes and further post-synthetic modifications employed by Beeby *et al.*¹² (i) Acetone, K₂CO₃, and bromopicolinic acid; (ii) CuI, THF, Et₃N, Pd(PPh₃)₂Cl₂ and triisopropylsilylacetylene.

Recent work by Tsai *et al* in 2020¹⁴ has shown the anti-addition of unsaturated C-C bonds into the O-H bonds of bridged hydroxo dimeric iridium species, to yield the asymmetric β -diketonates *in situ* (Figure 5.3). The group first formed the dihydroxo bridged dimer due to the amphoteric nature of the hydroxo ligands¹⁵. When heated in toluene, it is suggested that the coordination of the C-C triple bond to the iridium will occur, forming the intermediate species [Ir(C[^]N)₂(OH)(η^2 -R¹C \equiv CR²)]. This allows for the anti-addition of the OH group leading to the formation of asymmetric β -diketonate ligand, which features both electron donating and electron withdrawing groups. The same methodology can be applied to α,β -unsaturated ketones, which also form asymmetric β -diketonates.

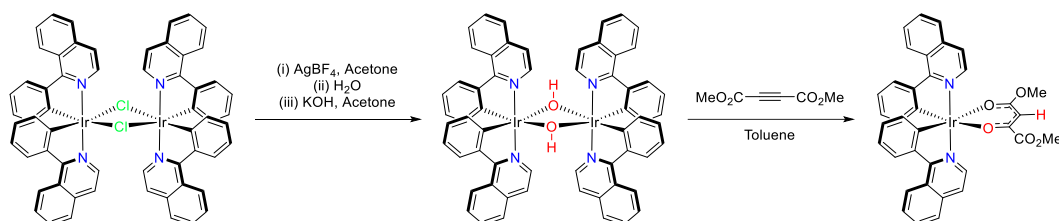


Figure 5.3 – In situ anti addition of an unsaturated bond into μ -OH bond adapted from Tsai *et al*¹⁴.

5.1.2 Bidentate chelating quinoline ligands

The quinoline analogue of bpy, 2,2'-biquinoline (biq), is the most widely used bidentate quinoline ligand system. Biq has previously been complexed with a wide variety of transition metals, including Au^{16,17}, Cu¹⁸, Co¹⁹, Ir²⁰, Ni²¹, Os²², Pd²³, Pt²⁴, Re²⁵, Ru^{26,27} and Zn²⁸. Metal biq complexes have seen uses in a wide variety of fields such as catalysis²⁹, single-molecule magnets³⁰, OLED devices³¹ and anti-cancer applications³². The extended conjugation of biq over bpy offers a bathochromic shift of the emission profile. For example, in 2005 Thompson *et al*³³

synthesised the emissive complexes $[\text{Ir}(\text{ppz})_2(\text{bpy})]\text{PF}_6$ and $[\text{Ir}(\text{ppz})_2(\text{biq})]\text{PF}_6$, as part of their work on the development of LEECs (Figure 5.4 – **8 + 9**). The emission profile was recorded in CH_2Cl_2 , where the emission λ_{max} shifted from 554 nm to 610 nm going from bpy to biq ancillary ligand, respectively. The shift in emission was attributed to the stabilisation of the LUMO orbitals, which in this series of complexes were located across the ancillary ligand.

The work of the Sun group has focused on the development and understanding of the emissive state of metal complexes bearing benzannulated ligand frameworks, from both the effects of benzannulation seen in the cyclometalating ligands³⁴, and the ancillary ligands³⁵. The 2-(pyridin-2-yl)quinoline (pyq) ligand features prominently across the group's work, with the $[\text{Ir}(\text{ppy})_2(\text{pyq})]\text{PF}_6$ complex (Figure 5.4 – **10**) producing an emission λ_{max} at 619 nm in CH_2Cl_2 ³⁶. The findings in this work complement earlier studies by Huang et al, who produced benzannulated ancillary ligands iridium complexes of phenylisoquinoline (piq)³⁷.

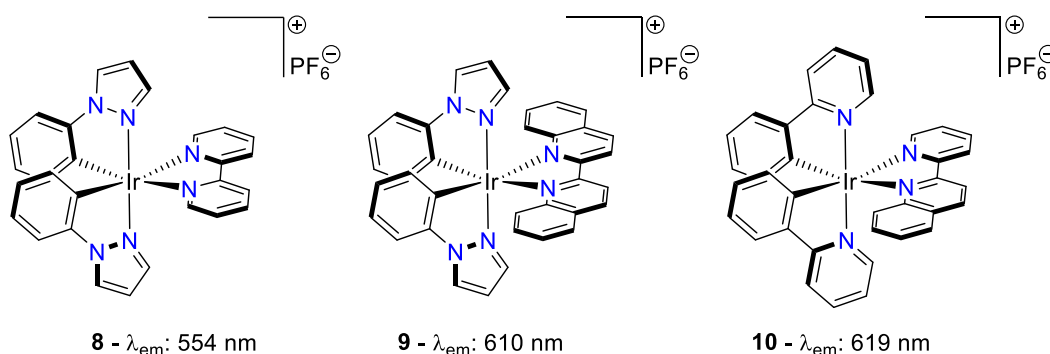


Figure 5.4 – Cationic complexes synthesised and characterised during investigations into the effects of increased conjugation of ancillary ligands. Emission wavelengths recorded in CH_2Cl_2 .^{33,36}

5.2 Aims of the Chapter

This chapter sets out to synthesise and characterise a set of novel ligands based around the substituted 2-(pyridin-2-yl)quinoline and 2-(pyrazin-2-yl)quinoline frameworks to see how the addition of a heteroatom and inherent asymmetry affects the emission properties of the resultant complexes. The ligands are to be complexed with Ir(III) as the ancillary ligand. The hope is that via the stabilisation of the ancillary antibonding orbitals from the extended conjugation as well as the additional heteroatom for the pyrazine-based ligand systems, the properties of the MLCT emission can be modulated via ligand design. A comparison to Chapter 4 complex will be made using 1nq and 2nq cyclometalating ligands. In total, 14 novel

cationic iridium complexes have also been isolated, characterised, and investigated for their photophysical properties.

5.3 Results and Discussions

5.3.1 Ligand synthesis and characterisation

A series of novel substituted 2-(pyridinyl/pyrazinyl) quinoline-4-carboxylic acids have been synthesised following a Pfitzinger reaction. Initially, conditions replicated those of the traditional Pfitzinger reaction³⁸, seen in Chapter 4, by refluxing the acetal and isatin in basic ethanol. Upon addition of KOH, the normal colour change from a yellow solution to a dark red solution was noted as the pyrrolidine ring moiety of the isatin was hydrolysed, but after work up the desired product could not be isolated. A modified version of the methodology first reported by Baker *et al*^{39,40} proved more successful. Briefly, to a pestle and mortar a 5-substituted isatin powder was added along with equimolar amounts of either 2-acetylpyridine or 2-acetylpyrazine and ground together until homogenous. 33 % aqueous NaOH solution was added and the immediate colour change to dark red was noted. Upon further stirring, the solution gradually became solid with a metallic sheen, and at this point ice cold water was added to slurry up the mixture. The resultant powder was collected on a sinter, washed with a further 1 mL of ice-cold water followed by acetone washes to leave the off-white sodium salt of the target acid. This was then dissolved into water and precipitated by the addition of 5M HCl until the supernatant became a neutral pH, and the precipitate collected via filtration to yield the desired functionalised quinoline-acid ligands in good yields. Two of the acids (**L**² and **L**⁵) were selected for further reaction via Fischer esterification with ethanol to yield the analogous ethyl esters, **L**⁷ and **L**⁸ (Figure 5.5)

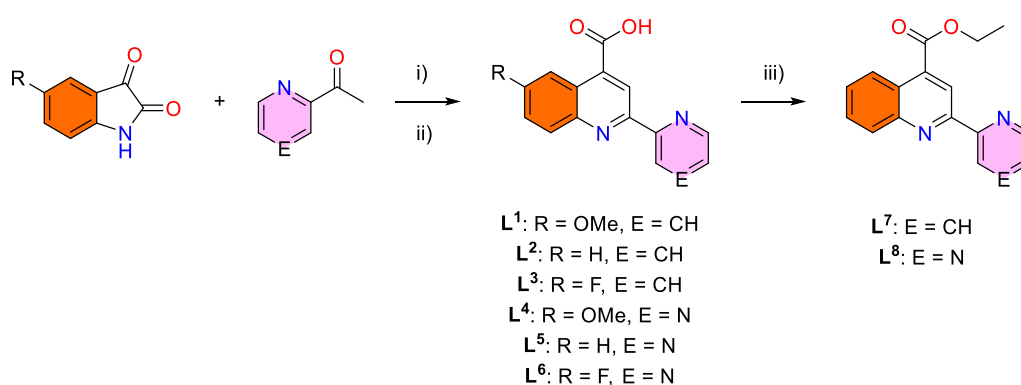


Figure 5.5 – Synthetic route towards ligand synthesis: i) 33 % NaOH_(aq) (4 eq), stir 15 minutes, room temperature. ii) H₂O, HCl (5M). iii) Cat. H₂SO₄, EtOH, 16 hours, 78 °C.

Successful acid (**L**¹⁻⁶) formation and isolation was confirmed by ¹H, ¹⁹F{¹H}, ¹³C{¹H} NMR spectroscopy as well as FTIR spectroscopy and HRMS. The formation of the ethyl esters was monitored by TLC, and after 16 hours, the reaction mixtures were

cooled to room temperature and neutralised with 0.1 M sodium carbonate solution. Desired ester products were isolated via silica gel column chromatography, eluting with DCM. The first light yellow band off the column was collected, and solvent removed *in vacuo* to yield **L**⁷⁻⁸, which were once again characterised by ¹H, ¹³C{¹H} NMR, FTIR spectroscopies and HRMS. Each of the 8 ligands displays a singlet centred around 9.0 ppm in the ¹H NMR spectrum (measured in *d*₆-DMSO). This peak is assigned to the proton in the 3-position of the quinoline ring. This result is comparable to the 2-naphth-2-yl quinoline-4-carboxylic acids seen in Chapter 4, where the spectra were also recorded in *d*₆-DMSO. The pyrazine containing ligands **L**⁴⁻⁶ all show a singlet resonance between 9.7 and 9.8 ppm. This can be assigned to the environment α - to the second pyrazine imine (position 3' around the pyrazine ring). In the case of **L**⁸ where the spectrum was recorded in CDCl₃, this signal is a doublet, appearing at 9.89 ppm, with a ⁴J_{HH} coupling of 1.5 Hz. The ¹⁹F{¹H} NMR spectra on **L**³ and **L**⁶ showed a single peak at -110.0 and -109.1 ppm respectively, which is comparable to the results obtained in Chapter 4 for fluorinated quinoline ligands.

5.3.2 Complex synthesis and characterisation

Iridium complexes were synthesised using **L**¹⁻⁸ as ancillary ligands following the same methodology seen previously in Chapter 4. Briefly, a molar excess of **L**¹⁻⁸ was added to a stirring chloroform solution of *cis*-[Ir(nq)₂(MeCN)₂]BF₄. Complexes were retained as their BF₄⁻ salts and purified via silica gel chromatography, eluting first with 95:5 (DCM/MeOH) to remove the precursor complex before eluting the desired complex as a red band using 9:1 (DCM/MeOH). Complexes were characterised by ¹H, ¹⁹F{¹H}, ¹³C{¹H} NMR, HRMS, absorption, emission, and IR spectroscopies. It became apparent the 2nq complexes had undergone a counterion metathesis during synthesis and were present as the chloride salt rather than BF₄⁻ salts as expected. Some counterions were exchanged for PF₆⁻ to aide in the growing of single crystals suitable for X-ray diffraction studies.

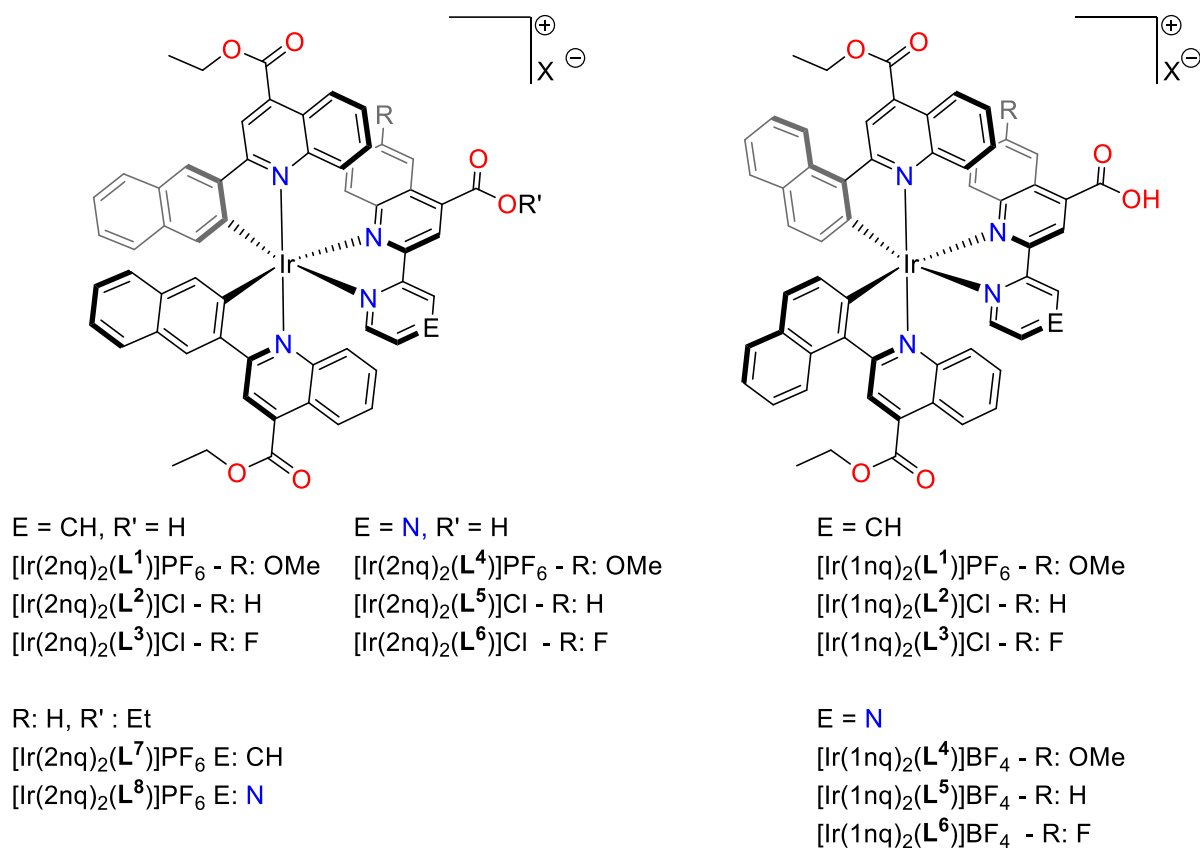


Figure 5.6 - Iridium complexes synthesised and characterised for this work.

5.3.2.1 Solid state structure of $[\text{Ir}(2\text{nq})_2(\text{L}^4)]\text{PF}_6$ and $[\text{Ir}(1\text{nq})_2(\text{L}^2)]\text{PF}_6$

Single red lath crystals of $[\text{Ir}(2\text{nq})_2(\text{L}^4)]\text{PF}_6$ (Figure 5.7) and dark red cut blade crystals of $[\text{Ir}(1\text{nq})_2(\text{L}^2)]\text{PF}_6$ (Figure 5.8) were successfully grown from vapour diffusion of isopropyl ether into a chloroform solution of the complex, and investigated by X-ray diffraction. The diffraction data was collected and solved at The UK National Crystallographic Service located at University of Southampton. $[\text{Ir}(2\text{nq})_2(\text{L}^4)]\text{PF}_6$ shows disorder across the PF_6^- anion and one ester group, and solvent masking has also been employed. For $[\text{Ir}(1\text{nq})_2(\text{L}^2)]\text{PF}_6$, no solvent masking has been used, but a molecule of isopropyl ether and a disordered chloroform molecule are present in the asymmetric cell, hydrogen bonded to a ligand and anion respectively (Figure 5.9). Both structures displayed the expected coordination with a *cis*-C,C and *trans*-N,N arrangement of the cyclometalating ligands around the distorted octahedral iridium(III) centre⁴¹. Like previous chapters, the Ir-N bonds *trans* to the Ir-C σ -bond are elongated in comparison to the cyclometalating ligand Ir-N bonds due to the stronger *trans* influence of the organometallic bond (Table 5.1). Both complexes also exhibit coordination sphere bond angles comparable to those seen for similar naphthyl quinoline complexes from Chapter 4. Both solid state structures reveal π - π interactions between the

non-heterocyclic rings of the quinoline on a cyclometalating ligand, as seen highlighted in blue on Figure 5.10.

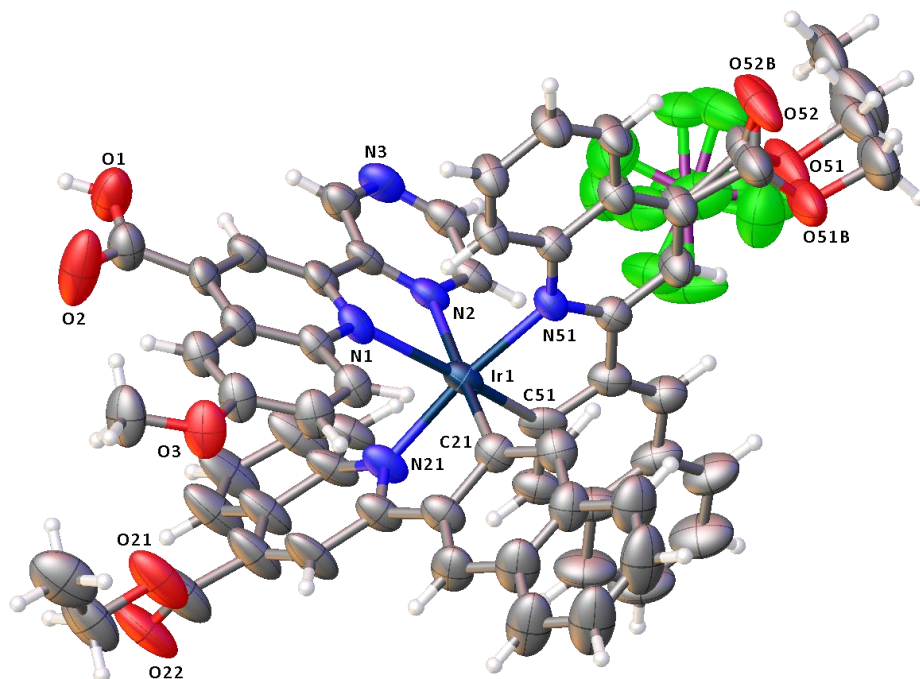


Figure 5.7 – X-ray structure of $[\text{Ir}(\text{2nq})_2(\text{L}^4)]\text{PF}_6$ - $\text{C}_{74}\text{F}_6\text{H}_{78}\text{IrN}_5\text{O}_{9.5}\text{P}$, $M_r = 1526.58$, triclinic, $P-1$ (No. 2), $a = 14.5944(3) \text{ \AA}$, $b = 15.8228(4) \text{ \AA}$, $c = 15.9735(5) \text{ \AA}$, $\alpha = 103.713(2)^\circ$, $\beta = 92.681(2)^\circ$, $\gamma = 101.881(2)^\circ$, $V = 3488.99(16) \text{ \AA}^3$, $T = 100(2) \text{ K}$, $Z = 2$, $Z' = 1$, $\mu(\text{Mo K}\alpha) = 2.014 \text{ mm}^{-1}$, 91231 reflections measured, 15993 unique ($R_{int} = 0.0803$) which were used in all calculations. The final wR_2 was 0.1337 (all data) and R_1 was 0.0551 ($I > 2(I)$).

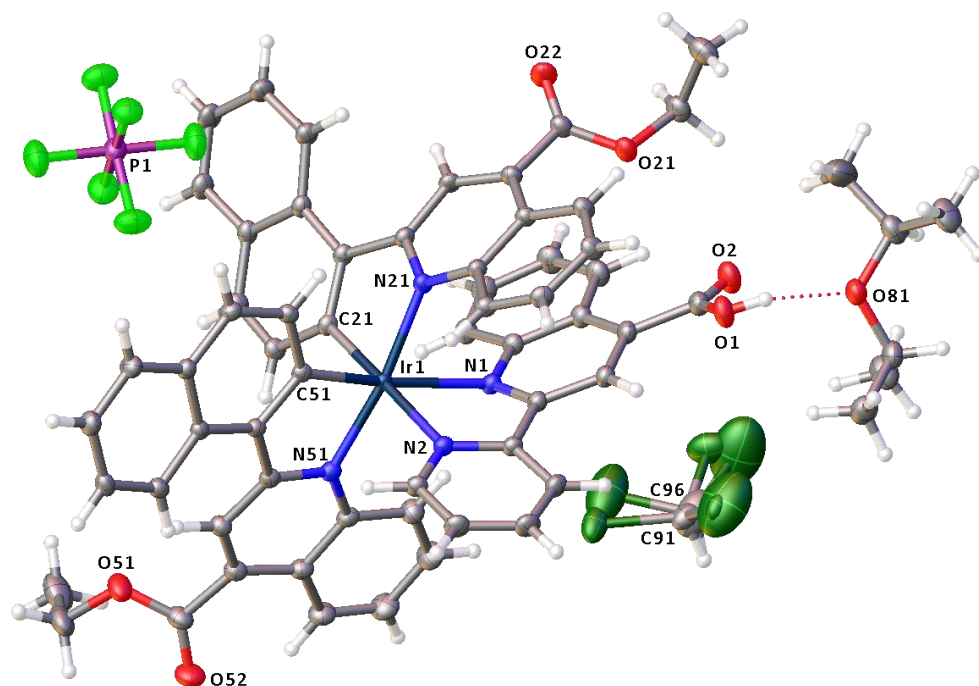


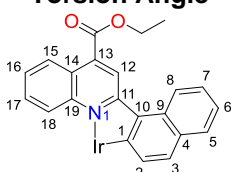
Figure 5.8 - X-ray structure of $[\text{Ir}(\text{1nq})_2(\text{L}^2)]\text{PF}_6$ - $\text{C}_{66}\text{H}_{57}\text{Cl}_3\text{F}_6\text{IrN}_4\text{O}_7\text{P}$, $M_r = 1461.67$, triclinic, *P*-1 (No. 2), $a = 13.11880(10)$ Å, $b = 15.6022(2)$ Å, $c = 16.0146(2)$ Å, $\alpha = 70.1570(10)^\circ$, $\beta = 83.6410(10)^\circ$, $\gamma = 74.2860(10)^\circ$, $V = 2967.41(6)$ Å³, $T = 100(2)$ K, $Z = 2$, $Z' = 1$, $\mu(\text{Mo K}\alpha) = 2.491$ mm⁻¹, 237955 reflections measured, 18055 unique ($R_{\text{int}} = 0.0551$) which were used in all calculations. The final wR_2 was 0.0670 (all data) and R_1 was 0.0261 ($I > 2(I)$).

$[\text{Ir}(\text{1nq})_2(\text{L}^2)]\text{PF}_6$				$[\text{Ir}(\text{2nq})_2(\text{L}^4)]\text{PF}_6$			
Bond Length (Å)							
Ir1	N1	2.2836(17)		Ir1	N1	2.284(4)	
Ir1	N2	2.1476(17)		Ir1	N2	2.151(4)	
Ir1	N21	2.0973(17)		Ir1	N21	2.070(4)	
Ir1	N51	2.0751(18)		Ir1	N51	2.080(4)	
Ir1	C21	2.0194(19)		Ir1	C21	2.009(5)	
Ir1	C51	1.9834(19)		Ir1	C51	1.991(6)	
Bond Angle (°)							
N2	Ir1	N1	73.95(6)	N2	Ir1	N1	74.73(16)
N21	Ir1	N1	75.38(6)	N21	Ir1	N1	79.26(17)
N21	Ir1	N2	102.82(6)	N21	Ir1	N2	102.29(16)
N51	Ir1	N1	110.45(6)	N51	Ir1	N1	106.05(15)
N51	Ir1	N2	85.85(7)	N51	Ir1	N2	84.06(15)
N51	Ir1	N21	170.80(6)	N51	Ir1	N21	172.75(17)
C21	Ir1	N1	104.73(7)	C21	Ir1	N1	103.80(18)
C21	Ir1	N2	177.34(7)	C21	Ir1	N2	177.37(18)
C21	Ir1	N21	78.93(7)	C21	Ir1	N21	79.5(2)

C21	Ir1	N51	92.51(7)	C21	Ir1	N51	94.32(19)
C51	Ir1	N1	165.85(7)	C51	Ir1	N1	166.00(17)
C51	Ir1	N2	97.61(7)	C51	Ir1	N2	94.28(18)
C51	Ir1	N21	95.97(7)	C51	Ir1	N21	95.0(2)
C51	Ir1	N51	79.65(7)	C51	Ir1	N51	80.89(19)
C51	Ir1	C21	84.13(8)	C51	Ir1	C21	87.5(2)

Table 5.1 – Selected bond lengths and bond angles obtained from crystallographic data for $[\text{Ir}(\text{1nq})_2(\text{L}^2)]\text{PF}_6$ and $[\text{Ir}(\text{2nq})_2(\text{L}^4)]\text{PF}_6$.

There appears to be some significant distortion of both cyclometalating ligands and ancillary ligands around the iridium centre. Firstly, Table 5.2 shows a comparison of the ligand torsion angles of the 1nq cyclometalating ligands of $[\text{Ir}(\text{1nq})_2(\text{L}^2)]\text{PF}_6$ with $[\text{Ir}(\text{1nq})_2(\text{bpy})]\text{PF}_6$ from Chapter 4. While the solid-state structure is clearly constrained, the torsion angles show very little differences. The biggest difference seen in torsion angle appears on the ancillary ligands. Around the N-C-C-N angles (or the degree of rotation between the two heterocyclic rings). For the complex $[\text{Ir}(\text{1nq})_2(\text{bpy})]\text{PF}_6$ the ancillary torsion angle is $6.2(5)^\circ$, while the comparable angle in the $[\text{Ir}(\text{1nq})_2(\text{L}^2)]\text{PF}_6$ complex is $-20.1(3)^\circ$. Secondly, as shown in Figure 5.11, there is significant strain in the quinoline rings of the ancillary ligand. The bending seen in the cyclometalating ligands, between Ir-N-*para*-C, is comparable to the $[\text{Ir}(\text{1nq})_2(\text{bpy})]\text{PF}_6$ (153° vs 151° and 164° vs 167° respectively). Difference in the ancillary ligands is more significant. In the $[\text{Ir}(\text{1nq})_2(\text{L}^2)]\text{PF}_6$ complex, the pyridine ring offers practically the same deformations as the equivalent pyridine form bpy, a small 177° bend, rotated towards the second aromatic system. The bend seen in the quinoline ancillary ring is 150° , which is greater than the equivalent ring in the bpy complex. The bend is towards the cyclometalating ligand and is reducing the two proton – ring centroid distances between the two quinolines C3-position protons and the opposite nonheterocyclic quinoline aromatic ring to 3.51 \AA and 3.79 \AA . The deformation also leads to a shortening of the distance between the ester group CH_2 moiety and the carbonyl of the acid group.

	$[\text{Ir}(\text{1nq})_2(\text{bpy})]\text{PF}_6 / ^\circ$	$[\text{Ir}(\text{1nq})_2(\text{L}^2)]\text{PF}_6 / ^\circ$	
		Cyclometalated Ligand 1	Cyclometalated Ligand 2

C1, C10, C11, N1	21.1(5) / 12.3 (5)	-21.3(3)	12.3(2)
C1, C10, C11, C12	-149.7(4) / -160.9(4)	148.6(2)	-159.67(19)
C9, C10, C11, C12	31.7(6) / 18.2(6)	31.8(3)	17.6(3)
C10, C1, C2, C3	3.2(6) / -1.9(6)	-3.4(3)	0.6(3)
C13, C14, C19, N1	-6.3(6) / 2.4(6)	5.9(3)	3.0(3)
C15, C14, C19, N1	174.2(4) / -179.8(4)	-174.45(19)	179.4(2)
C15, C16, C17, C18	-4.6(7) / 0.0(6)	2.6(3)	0.4(4)
N1, C11, C12, C13	3.4(6) / 9.1 (6)	-0.7(3)	6.1(3)

Table 5.2 – Selected torsion angles from within the cyclometalating ligands for $[\text{Ir}(\text{1nq})_2(\text{L}^2)]\text{PF}_6$. $[\text{Ir}(\text{1nq})_2(\text{bpy})]\text{PF}_6$ structure taken from the work in Chapter 4.

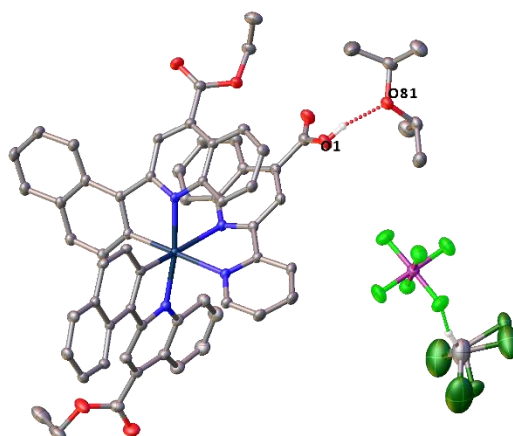


Figure 5.9 - $[\text{Ir}(\text{1nq})_2(\text{L}^2)]\text{PF}_6$ showing hydrogen bonding interactions between solvent and complex, with a maximum D-D distance of 2.84 Å.

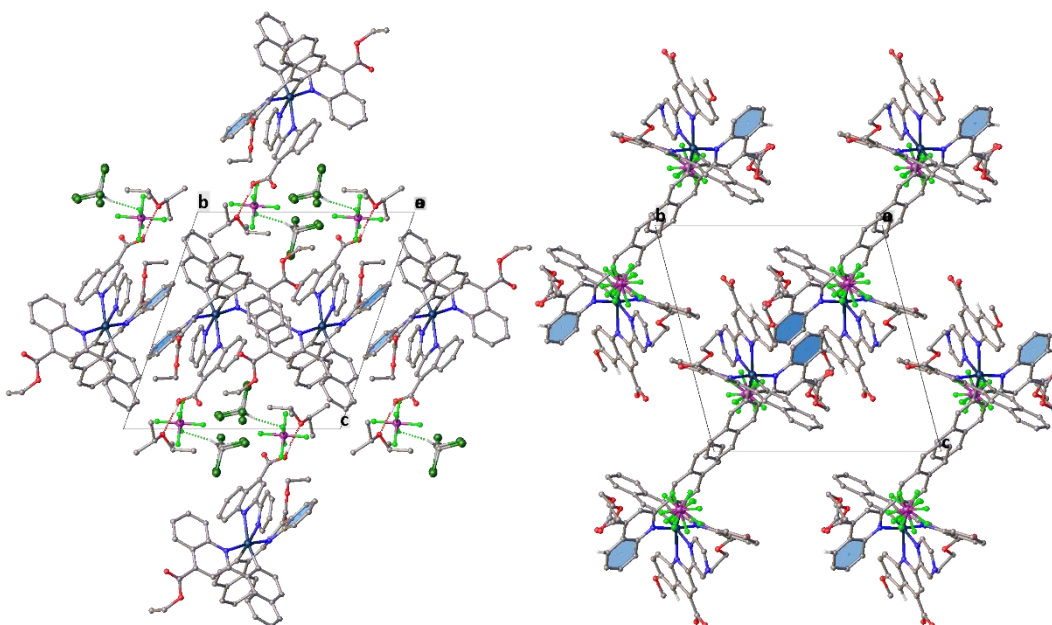


Figure 5.10 – Packing diagram of left: $[\text{Ir}(\text{1nq})_2(\text{L}^2)]\text{PF}_6$ and right: $[\text{Ir}(\text{2nq})_2(\text{L}^4)]\text{PF}_6$. Both complexes exhibit π - π interactions between aromatic rings highlighted in blue.

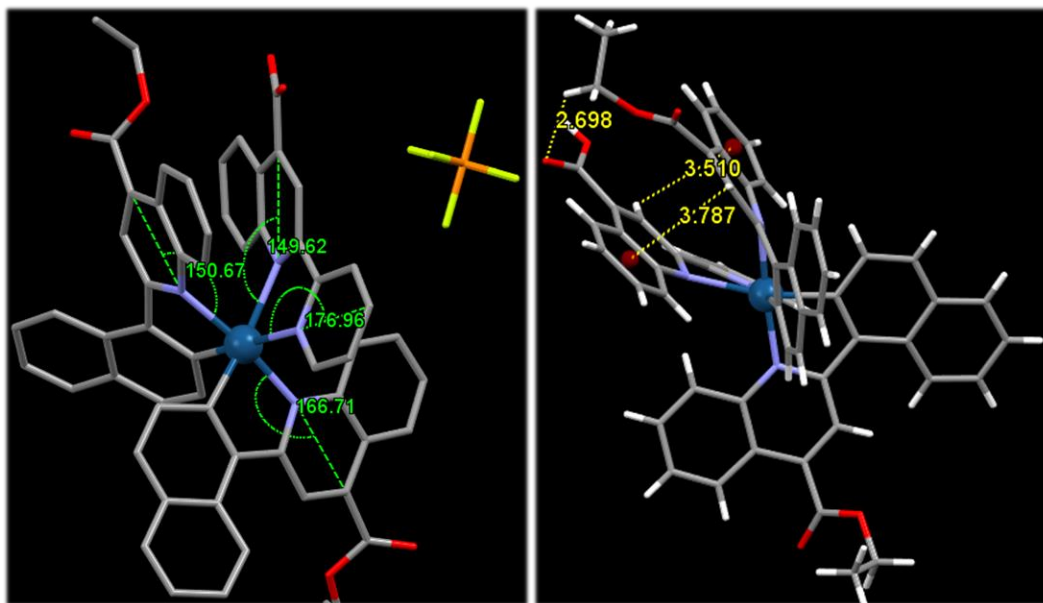


Figure 5.11 – Solid state structure of $[\text{Ir}(\text{1nq})_2(\text{L}^2)]\text{PF}_6$ showing Left: quinoline rotation after complexation. Hydrogens have been omitted for clarity. Right: Showing strain of one cyclometalating ligand and selected distances (in Å) between certain atoms and ring centroids. Counterion and solvents of crystallisation have been omitted for clarity.

5.3.2.2 Complex Characterisation

Unlike previous complexes synthesised in this thesis utilising the 2,2'-bipyridine ancillary ligand, the complexes in this chapter do not exhibit C_2 symmetry. As such each of the corresponding proton environment on both cyclometalating ligands are inequivalent to each other (see Figure 5.12). In Chapter 4, the most downfield proton resonances are due to the proton in the 3-position around the quinoline ring. For the complexes $[\text{Ir}(\text{2nq})_2(\text{bpy})]\text{PF}_6$ and $[\text{Ir}(\text{1nq})_2(\text{bpy})]\text{PF}_6$ these occur at 8.83 ppm and 9.12 ppm respectively. For the asymmetric complexes in this Chapter, there are some larger differences. Most notably $\text{L}^{4-6,8}$ see the most downfield position assigned to the pyrazine moiety, from the 3-position around *ca.* 9.5 – 9.6 ppm. This affect is likely brought about by the inductive effect of the iridium centre being induced on the aromatic ring, as well as being *ortho*- to the second imine. The singlet resonances from the cyclometalated quinoline 3-position show a large difference between each other. In the case of $[\text{Ir}(\text{1nq})_2(\text{L}^x)]^+$, the first cyclometalating ligand appears at *ca.* 9.3 ppm for both pyridine and pyrazine complexes. This is slightly more deshielded in comparison to the corresponding bpy complex. The second cyclometalating ligand 3-position proton signal is much more upfield, with the resonance appearing at around *ca.* 8.2 ppm for the pyridine complexes and 8.4 ppm for the pyrazine complexes. The 3-position proton on the ancillary quinoline can be seen at *ca.* 8.0 and 8.1 ppm for the pyridine and pyrazine complexes respectively.

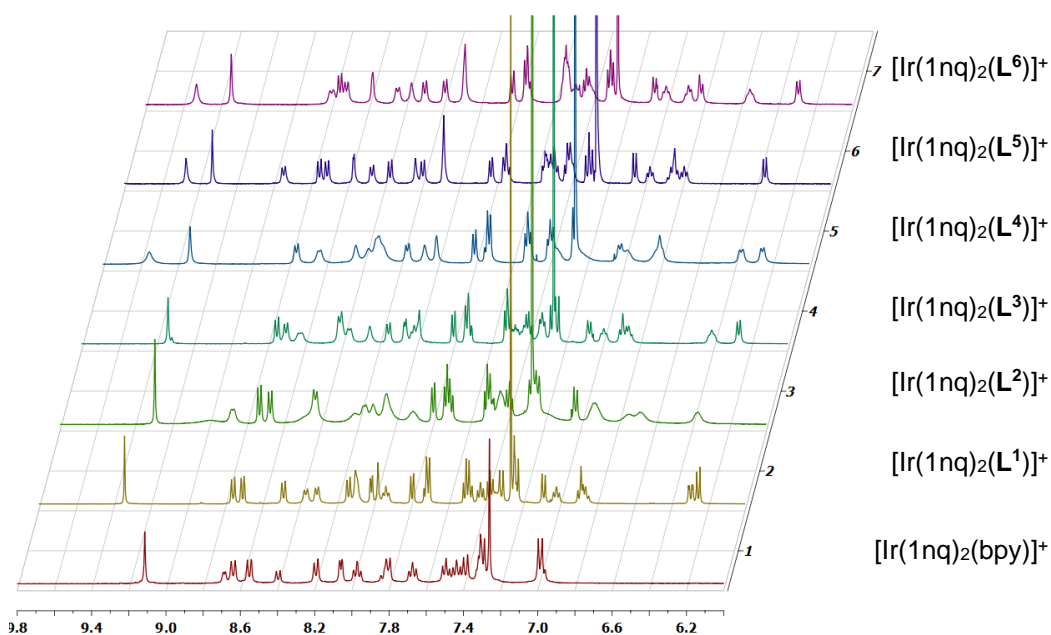


Figure 5.12 – Stacked ^1H NMR spectra of $[\text{Ir}(\text{1nq})_2(\text{L}^X)]^+$ (500 MHz, CDCl_3).

As discussed earlier, the solid-state single crystal structure of $[\text{Ir}(\text{1nq})_2(\text{L}^2)]\text{PF}_6$ (See section 5.3.2.1) reveals an excessive amount of strain in one of the cyclometalating ligands (Figure 5.11). The proton centroid distances between the 3-position protons and the opposite homocyclic quinoline aromatic ring are 3.51 Å and 3.79 Å, meaning the proton is within the aromatic ring currents inducing the extra shielding seen in the NMR spectra. The effects of the strain in one cyclometalating ligand is also seen when looking at the proton environments *ortho*-to the organometallic sigma bond. For $[\text{Ir}(\text{1nq})_2(\text{bpy})]\text{PF}_6$, this doublet is seen at 6.99 ppm in CDCl_3 with a $^3J_{\text{HH}} = 8.4$ Hz. The $[\text{Ir}(\text{1nq})_2(\text{L}^X)]^+$, has one doublet between 7.02 – 7.08 ppm ($^3J_{\text{HH}}$ between 8.2 – 8.5 Hz), while the second doublet is much more shielded around 6.3 ppm ($^3J_{\text{HH}}$ between 8.3 – 8.6 Hz). This strain also goes some way to explaining the second doublet appearing at ca. 6.4 ppm all four substituted quinoline complexes. ^1H - ^1H COSY correlation spectroscopy obtained for $[\text{Ir}(\text{1nq})_2(\text{L}^1)]\text{PF}_6$ reveals this doublet is position 8 of a naphthyl ring. The ester group NMR environments have also become inequivalent. Perhaps the most noticeable change is how one environment undergoes peak broadening or becomes a multiplet. The distortion in the cyclometalating ligand is forcing the CH_2 of the ethyl ester group towards the carbonyl of the acid group on the ancillary ligand. This is likely inducing a static interaction that is slowing down or stopping

the movement of the ethyl group, which would lead towards peak broadening and ultimately geminal $^2J_{HH}$ coupling.

The methoxy groups from **L**¹ and **L**⁴ have shifted upon complexation, from 3.94 and 3.93 ppm respectively, to 3.66 ppm (Broad) and 3.85 ppm. The broadness of this peak corresponds to the broadness seen from the CH₂ ethyl group and is likely to be caused by the same effects.

In the case of the [Ir(2nq)₂(L^x)]⁺ quinoline 3-position protons, all three protons are appearing between ca. 8.6 – 9.1 ppm (see example in Figure 5.13). This suggests less interaction with neighbouring aromatic ring currents, and indeed, the solid-state crystal structure of [Ir(2nq)₂(L⁴)]PF₆ shows a much lower degree of distortion on one of the cyclometalating ligand (see section 5.3.2.1). The positions *ortho*- to the site of cyclometalation are both closely grouped in each complex, differing typically by less than 0.1 ppm, and appearing around ca. 6.8 ppm when run in CD₃OD. Complexes [Ir(2nq)₂(L^{7,8})]PF₆ were run in CDCl₃ and showed a general agreement to the other complexes, as well as [Ir(2nq)₂(bpy)]PF₆, where this resonance occurs at 6.91 ppm. Finally, for the ¹H NMR spectra, the methoxy group upon **L**¹ and **L**⁴ have undergone a slight upfield shift upon complexation. **L**¹ has gone from 3.94 ppm (in d₆-DMSO) to 3.75 ppm (in CD₃OD), whilst **L**⁴ has shifted from 3.93 ppm (in d₆-DMSO) to 3.88 ppm (in CD₃OD). The subtle differences are likely due to the proximity to neighbouring aromatic systems.

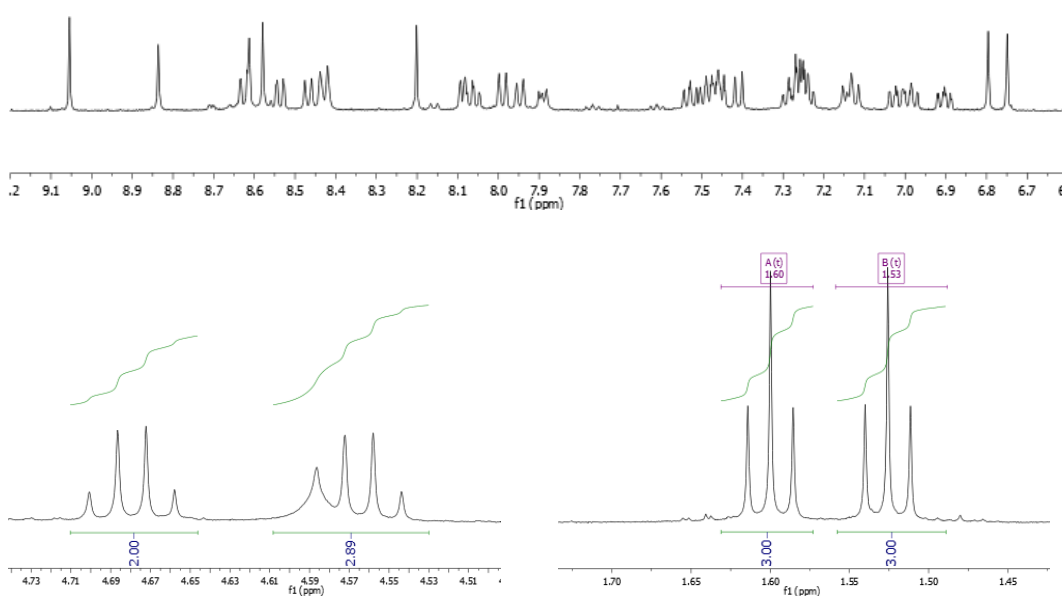


Figure 5.13 - NMR spectra for [Ir(2nq)₂(L²)]PF₆ obtained in CD₃OD. Over integration of the quartet at 4.57 ppm is likely a result of H-Bonded water appearing at 4.59 ppm. This peak is seen in each of the spectra obtained in CD₃OD. The solvent was not dried prior to use.

$^{19}\text{F}\{^1\text{H}\}$ NMR spectra were also obtained for ligands L^3 and L^6 , as well as their corresponding iridium complexes, and the data is presented in Table 5.3. Generally, upon complexation, the ligand-based singlet becomes more deshielded, which can be attributed to the inductive effects of the iridium centre. There are smaller changes between the complex and free ligand when pyridine is present rather than pyrazine. For each complex, the high-resolution mass spectrometry data provides a m/z peak that is as expected for $[\text{M} - \text{X}]^+$ (where X = counterion – PF_6^- , BF_4^- or Cl^-)

Ligand	Free Ligand $^{19}\text{F}\{^1\text{H}\} \delta_{\text{F}} / \text{ppm}^{\text{a}}$	$[\text{Ir}(\text{1nq})_2(\text{L}^{\text{n}})]^+$ $^{19}\text{F}\{^1\text{H}\} \delta_{\text{F}} / \text{ppm}^{\text{b}}$	$[\text{Ir}(\text{2nq})_2(\text{L}^{\text{n}})]\text{Cl}$ $^{19}\text{F}\{^1\text{H}\} \delta_{\text{F}} / \text{ppm}^{\text{c}}$
L^3	-110.0 (s)	-72.6 (d, $^1J_{\text{PF}}$: 712 Hz) (PF_6^-) -108.0 (s)	-110.4 (s)
L^6	-109.1 (s)	-102.5 (s) -148.0 (s) (BF_4^-)	-102.4 (s)

Table 5.3 - $^{19}\text{F}\{^1\text{H}\}$ NMR spectra shifts for ligand and complexes. ^aLigand spectra obtained in d_6 -DMSO. ^bIridium complexes of 1nq spectra obtained in CDCl_3 . ^cIridium complexes of 2nq spectra obtained in CD_3OD .

5.3.3 Electronic properties

5.3.3.1 Ligand absorption and emission properties

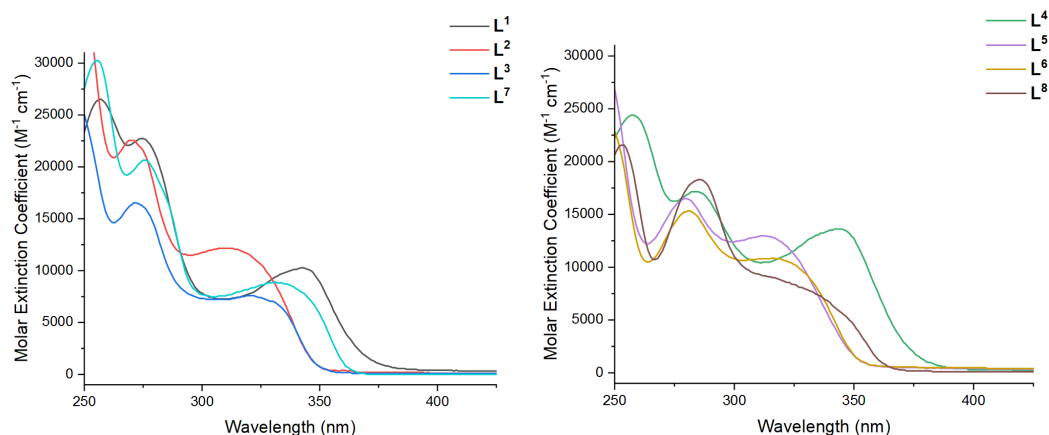


Figure 5.14 – Absorbance spectra for ligands. Spectra obtained in aqueous 0.1 M NaOH (L^{1-6}) at ca. 10^{-5} M. L^{7-8} spectra obtained in MeCN at ca. 10^{-5} M.

The absorbance spectra for L^{1-8} can be seen in Figure 5.14. strong absorbances can be seen between 250 and 300 nm, which originate from the $\pi-\pi^*$ transitions, in addition to $n-\pi^*$ transitions which occur in the same region with a weaker ϵ value. The second heteroatom in the pyrazine-based ligands induces a slight

bathochromic shift at ca. 280 nm compared to the pyridine-based systems which appear at ca. 270 nm. There is a slight variation between the absorption maxima based on substitution.

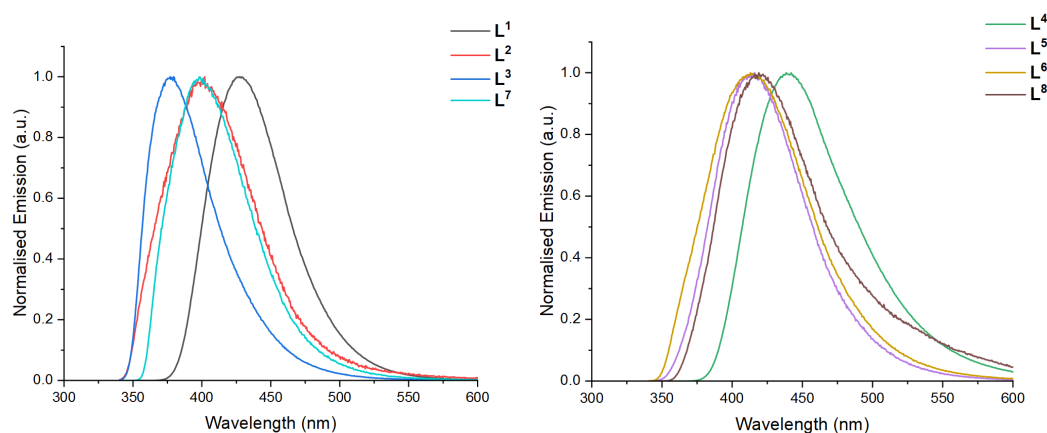


Figure 5.15 - Emission spectra for ligands. Spectra obtained in aqueous 0.1 M NaOH (L^{1-6}) at ca. 10^{-5} M. L^{7-8} spectra obtained in MeCN at ca. 10^{-5} M. $\lambda_{ex} = 325$ nm.

Steady state emission measurements were obtained (Figure 5.15) in aerated aqueous 0.1 M NaOH (L^{1-6}) or aerated MeCN (L^{7-8}). Each ligand exhibits a single broad featureless emission peak. Pyrazine based ligands have a more bathochromically shifted emission λ_{max} , between 413 – 440 nm, while the pyridine emission has a λ_{max} between 376 – 427 nm. In both cases, the electron donating methoxy-substituted quinolines showed the lowest energy emission, while the electron withdrawing fluoro substituent had the highest energy emission.

Ligand	$\lambda_{abs} (\epsilon / 10^4 M^{-1} cm^{-1}) / nm^a$	λ_{em} / nm^b	τ / ns^c	Φ^d
L^1	342 (1.0), 274 (2.2), 256 (2.6)	427	4	0.348
L^2	311 (1.2), 270 (2.3)	399	2	0.001
L^3	325 (0.7), 271 (1.6)	376	< 1	0.003
L^4	344 (1.4), 283 (1.7), 257 (2.4)	440	< 1	0.031
L^5	312 (1.3), 279 (1.7)	414	< 1	0.002
L^6	319 (1.1), 280 (1.5)	413	< 1	0.002
L^{7e}	331 (0.9), 275 (2.1), 255 (3.0)	398	2	0.001 ^f
L^{8e}	334 (0.7), 285 (1.8), 253 (2.1)	419	2	0.002 ^f

Table 5.4 - ^a All measurements obtained at room temperature in aerated aqueous 0.1 M NaOH at ca. 1×10^{-5} M unless otherwise stated. ^b $\lambda_{ex} = 325$ nm; ^c $\lambda_{ex} = 295$ nm; ^d Vs standard Quinine Sulphate in 0.05 M H_2SO_4 , $\lambda_{ex} = 310$ nm.⁴² ^e Measurements obtained in aerated MeCN. ^f Measurements obtained in aerated $CHCl_3$.

Time resolved measurements were also made on each of the ligands and can be seen in Table 5.4. Short emission lifetimes (4 ns and below) are all consistent with fluorescent emission.

5.3.3.2 Iridium complex absorption and emission properties

5.3.3.2.1 Complexes of $[\text{Ir}(\text{1nq})_2(\text{L}^n)]^+$

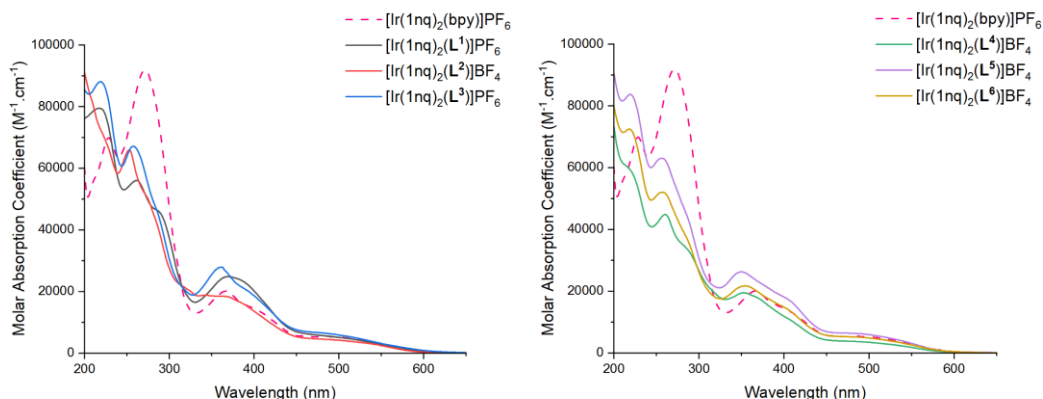


Figure 5.16 - Absorption spectra for $[\text{Ir}(\text{1nq})_2(\text{L}^x)]^+$ obtained in MeCN solution at ca. 10^{-5} M.

Absorption spectra for the complexes of $[\text{Ir}(\text{1nq})_2(\text{L}^x)]^+$ were obtained in aerated MeCN solution at ca. 10^{-5} M and can be seen above in Figure 5.16. Spectra are compared with $[\text{Ir}(\text{1nq})_2(\text{bpy})]\text{PF}_6$ from Chapter 4, seen above as the pink dashed line. Much like the bpy complex, all six new asymmetric complexes show a strong absorbance between 200 nm and 400 nm, occurring from the $^1\pi-\pi^*$ and $^1n-\pi^*$ transitions. Features past 400 nm are not seen in the ligand absorption spectra and are assigned to the MLCT absorptions, with ϵ values ca. $4000 - 6000 \text{ M}^{-1}.\text{cm}^{-1}$. The difference between the pyridine-based and pyrazine-based complexes shows no change, and the substitution on the quinoline appears to not affect the transitions. The MLCT transitions show very little variance between each other, or from the bpy complex. This is in keeping with the DFT evidence backing up the experimental results in Chapter 4 on the complex of $[\text{Ir}(\text{1nq})_2(\text{bpy})]\text{PF}_6$ that suggests the LUMO is located mainly on the cyclometalating ligands. Although the extended conjugation of the quinoline based ancillary ligand is expected to lower the energy level of the π^* orbitals in comparison to the bpy complexes.

Complex	$\lambda_{\text{abs}} (\epsilon / 10^4 \text{ M}^{-1} \text{ cm}^{-1}) / \text{nm}^{\text{a}}$	$\lambda_{\text{em}} / \text{nm}^{\text{b}}$	$\tau / \text{ns}^{\text{c}}$	Φ^{d}
$[\text{Ir}(\text{1nq})_2(\text{bpy})]\text{PF}_6$	494 (0.5), 405 (1.4), 366 (2.0), 271 (9.2), 228 (7.0)	679	240	0.006
$[\text{Ir}(\text{1nq})_2(\text{L}^1)]\text{PF}_6$	494 (0.5), 373(br) (2.4), 285 (4.6), 261 (5.6), 217 (7.9)	681	267	0.007
$[\text{Ir}(\text{1nq})_2(\text{L}^2)]\text{BF}_4$	492 (0.5), 368 (1.8), 273(sh) (5.0)	679	240	0.013
$[\text{Ir}(\text{1nq})_2(\text{L}^3)]\text{PF}_6$	490 (0.6), 391 (2.0), 361 (2.8), 257 (6.6), 219 (8.8)	682	265	0.003
$[\text{Ir}(\text{1nq})_2(\text{L}^4)]\text{BF}_4$	492 (0.4), 402(sh) (1.1), 356(br) (1.9), 282 (3.5), 260 (4.5), 217 (6.0)	677	181	0.015
$[\text{Ir}(\text{1nq})_2(\text{L}^5)]\text{BF}_4$	493 (0.6), 404(sh) (1.7), 349 (2.6), 256 (6.3), 219 (8.4)	677	244	0.014
$[\text{Ir}(\text{1nq})_2(\text{L}^6)]\text{BF}_4$	495 (0.5), 396(sh) (1.5), 355 (2.2), 256 (5.1), 218 (7.3)	678	279	0.011

Table 5.5 - ^a All measurements obtained at room temperature in aerated MeCN at *ca.* 1×10^{-5} M unless otherwise stated. ^b $\lambda_{\text{ex}} = 510$ nm; ^c $\lambda_{\text{ex}} = 295$ nm; ^d Vs standard $[\text{Ru}(\text{bpy})_3][\text{PF}_6]_2$, $\lambda_{\text{ex}} = 430$ nm.⁴²

The steady state emission measurements, seen in Figure 5.17, were obtained in aerated MeCN solution at *ca.* 10^{-5} M. Spectra are once again compared with $[\text{Ir}(\text{1nq})_2(\text{bpy})]\text{PF}_6$ from Chapter 4. Each emission is shown a single broad emission peak. All six asymmetric complexes' emission λ_{max} show minor differences, but, these differences are within the working error of the equipment used to obtain the measurements. All the emission peaks are between 677 – 682 nm, while the bpy complex sits at 679 nm. This is again suggesting the LUMO of the complexes sits over both cyclometalating ligands and not the ancillary ligand. Time resolved measurements give lifetimes of around the same timeframe as the bpy complex, with some slight variations, although complex $[\text{Ir}(\text{1nq})_2(\text{L}^4)]\text{BF}_4$ has a noticeably shorter lifetime. Quantum yields are also an order of magnitude better in general than those seen in Chapter 4. These differences could be due to the amount of strain seen in the cyclometalating ligands, as discussed earlier in section 5.3.2.1.

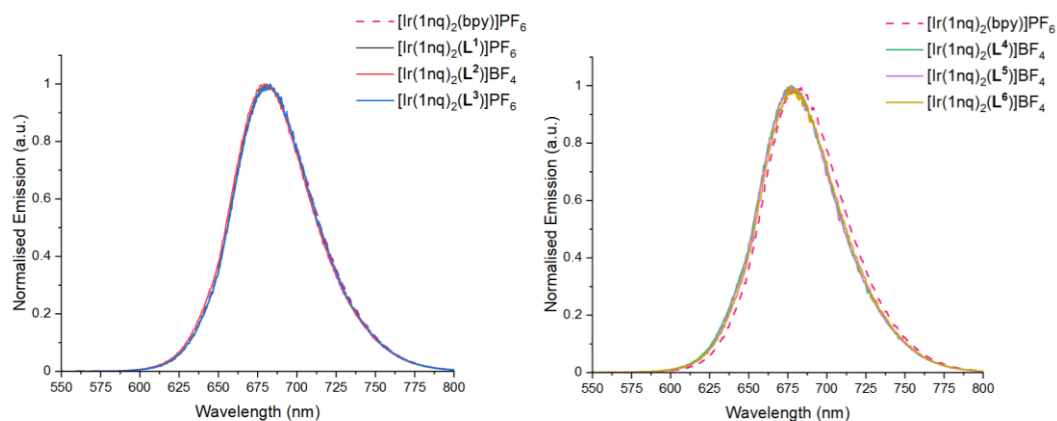


Figure 5.17 - Emission spectra for $[\text{Ir}(\text{1nq})_2(\text{L}^x)]^+$ obtained in MeCN solution at ca. 10^{-5} M ($\lambda_{\text{ex}} = 510$ nm).

Low temperature emission spectra (see Figure 5.18) were run in a 4:1 ethanol/methanol glass, exciting at 510 nm. The emission λ_{max} of each complex is again the same as for the bpy complex, at 660 nm. The shoulder at lower energy is different to the bpy complex. In the pyridine-based complexes (L^{1-3}) this peak is hypsochromically shifted by 10 nm in comparison to bpy, from 720 nm to 710 nm. For pyrazine-based ligands (L^{4-6}), the shoulder is at a slightly higher energy, 705nm. These results suggest a degree of ligand centred emission in a predominantly MLCT based emission.

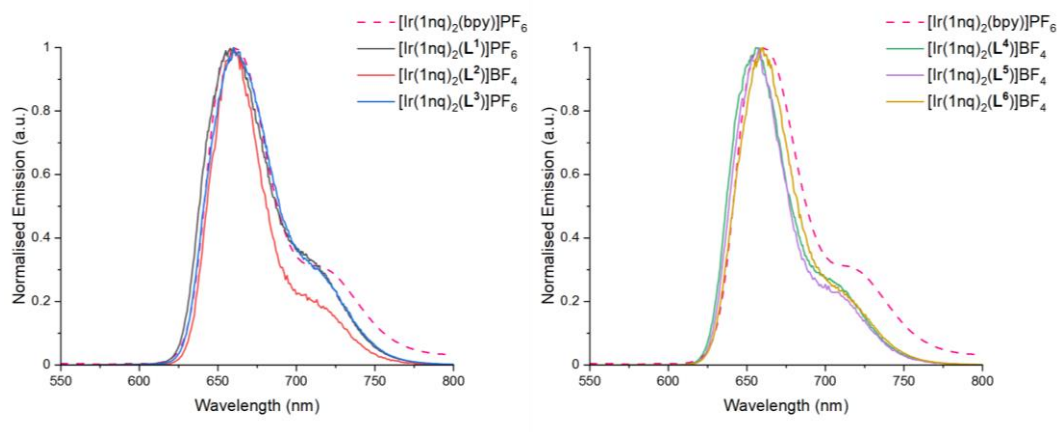


Figure 5.18 – Low temperature emission spectra recorded in a MeOH / EtOH (1:4) glass at 77 K ($\lambda_{\text{ex}} = 510$ nm).

5.3.3.2.2 Complexes of $[\text{Ir}(\text{2nq})_2(\text{L}^n)]^+$

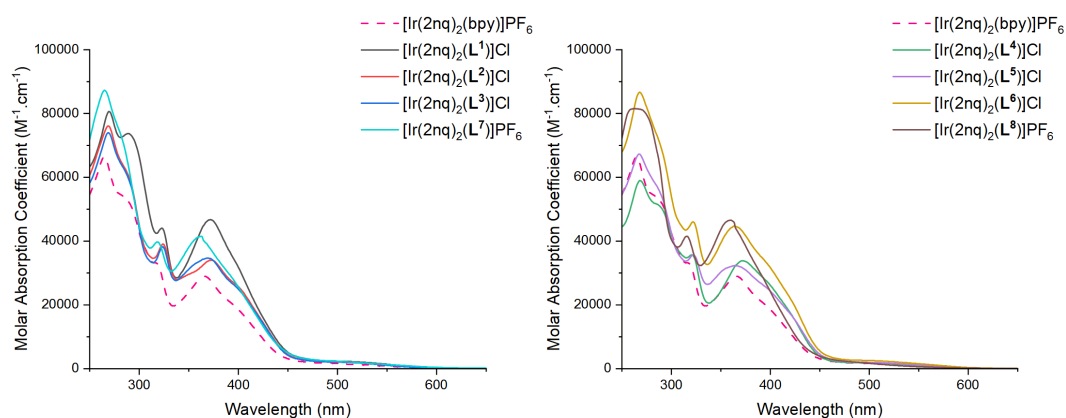


Figure 5.19 - Absorption spectra for $[\text{Ir}(\text{2nq})_2(\text{L}^x)]^+$ obtained in MeCN solution at ca. 10^{-5} M. Absorption spectra for the complexes of $[\text{Ir}(\text{2nq})_2(\text{L}^x)]^+$ were obtained in aerated MeCN solution at ca. 10^{-5} M and can be seen above in Figure 5.19. Spectra are compared with $[\text{Ir}(\text{2nq})_2(\text{bpy})]\text{PF}_6$ from Chapter 4, seen above as the pink dashed line. Once again, features between 350 – 400 nm can be ascribed to $^1\pi-\pi^*$ and $^1n-\pi^*$ transitions, with strong ϵ values. Features past 400 nm, which are not seen on the ligand absorbance spectra, are assigned to the $^1\text{MLCT}$ transitions, with the spin forbidden $^3\text{MLCT}$ and ^3LC transitions seen tailing off towards 600 nm. While the eight spectra are almost superimposable upon the bpy complex absorbance spectra, some subtle differences should be noted. Features in the region around 370 nm show a slight increase in fine structure, by either exhibiting a peak broadening, or the emergences of a lower energy shoulder feature. This could be due to the two very similar energy transitions from the two cyclometalating ligands losing their degeneracy. This could be a result of the asymmetry of the complexes due to the new more conjugated ancillary ligands.

Complex	$\lambda_{\text{abs}} (\epsilon / 10^4 \text{ M}^{-1} \text{ cm}^{-1}) / \text{nm}^{\text{a}}$	Emission $\lambda_{\text{max}} / \text{nm}^{\text{b}}$	$\tau / \text{ns}^{\text{c}}$	Φ^{d}
$[\text{Ir}(\text{2nq})_2(\text{bpy})]\text{PF}_6$	464 (0.2), 365 (2.9), 315 (3.3), 283 (5.4), 265 (6.6)	673	36	0.003
$[\text{Ir}(\text{2nq})_2(\text{L}^1)]\text{Cl}$	497 (0.2), 371 (4.6), 322 (4.4), 288 (7.4), 269 (8.0)	632	39	0.032
$[\text{Ir}(\text{2nq})_2(\text{L}^2)]\text{Cl}$	497 (0.2), 395(sh) (2.7), 372 (3.4), 324 (3.9), 286(sh) (6.2), 268 (7.6)	633	50	0.031
$[\text{Ir}(\text{2nq})_2(\text{L}^3)]\text{Cl}$	497 (0.2), 393(sh) (2.6), 369 (3.5), 323 (3.8), 283(sh) (6.3), 269 (7.4)	628	57	0.046
$[\text{Ir}(\text{2nq})_2(\text{L}^4)]\text{Cl}$	497 (0.2), 372(br) (3.3), 320 (3.5), 286(sh) (5.2), 268 (5.9)	629	21	0.034
$[\text{Ir}(\text{2nq})_2(\text{L}^5)]\text{Cl}$	497 (0.2), 362(br) (3.2), 322 (3.6), 284(sh) (5.8), 267 (6.7)	667	6	0.034
$[\text{Ir}(\text{2nq})_2(\text{L}^6)]\text{Cl}$	497 (0.2), 365(br) (4.5), 321 (4.6), 268 (8.7)	667	16	0.008
$[\text{Ir}(\text{2nq})_2(\text{L}^7)]\text{PF}_6$	497 (0.2), 360 (4.1), 318 (4.0), 265 (8.7)	673	49	0.005
$[\text{Ir}(\text{2nq})_2(\text{L}^8)]\text{PF}_6$	497 (0.2), 359 (4.6), 315 (4.1), 268 (8.1)	666	39	0.003

Table 5.6 - ^a All measurements obtained at room temperature in aerated MeCN at ca. 1×10^{-5} M unless otherwise stated. ^b $\lambda_{\text{ex}} = 510$ nm; ^c $\lambda_{\text{ex}} = 295$ nm; ^d Vs standard $[\text{Ru}(\text{bpy})_3][\text{PF}_6]_2$, $\lambda_{\text{ex}} = 430$ nm.⁴²

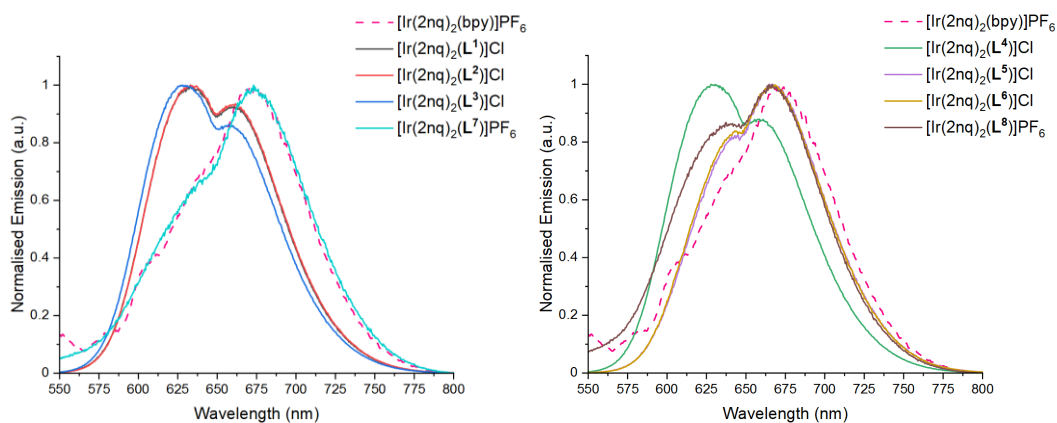


Figure 5.20 - Emission spectra for $[\text{Ir}(1\text{nq})_2(\text{L}^x)]^+$ obtained in MeCN solution at ca. 10^{-5} M ($\lambda_{\text{ex}} = 510$ nm).

Steady state emission measurements were recorded in aerated MeCN at ca. 10^{-5} M and can be seen above in Figure 5.20. Unlike the 1nq complexes earlier, the 2nq complexes show differences in comparison between the asymmetric complexes and the bpy complexes from Chapter 4. Each of the measurement presented in this Chapter are uncorrected emission spectra. A detector based anomaly at 650 nm is known to occur with the equipment used, which leads to a distortion in the peak shape. Firstly, the bpy complexes all showed an emission λ_{max} ca. 670 nm, with some higher energy weaker vibronic features, which is like the complex of L^7 , which interestingly appears to be superimposable over the bpy complex. The remaining pyridine-based carboxylic acid complexes of L^{1-3} the λ_{max} emission is seen ca. 630 nm. With the pyrazine complexes, L^4 shows a λ_{max} emission of 629 nm. While the complexes of $\text{L}^{5,6,8}$ have λ_{max} emission ca. 667 nm.

Time resolved measurements were obtained in aerated MeCN, at the λ_{max} emission (Table 5.6). Each measurement best fit a monoexponential decay, with lifetimes indicative of phosphorescent emission. Furthermore, when the lifetime was recorded at both 630 nm and 670 nm, each measurement once again was best fit using monoexponential decay, which is indicative of a single emission process, giving the same lifetime measurements for each wavelength. This is further evidence that the anomaly at 650 nm is not two separate transitions, but a single emission being modified at the detector. The quantum yields again are typically an order of magnitude larger than the bpy complex. Perhaps the difference in quantum yields seen in both the 1nq and 2nq complexes could be a result of the larger conjugated ancillary ligand removing some degree of freedom for the cyclometalating ligands to move around in the excited state as a pathway to

nonradiative relaxation. The strained rotation seen in the solid-state structure suggests the movement of this ligand is constrained.

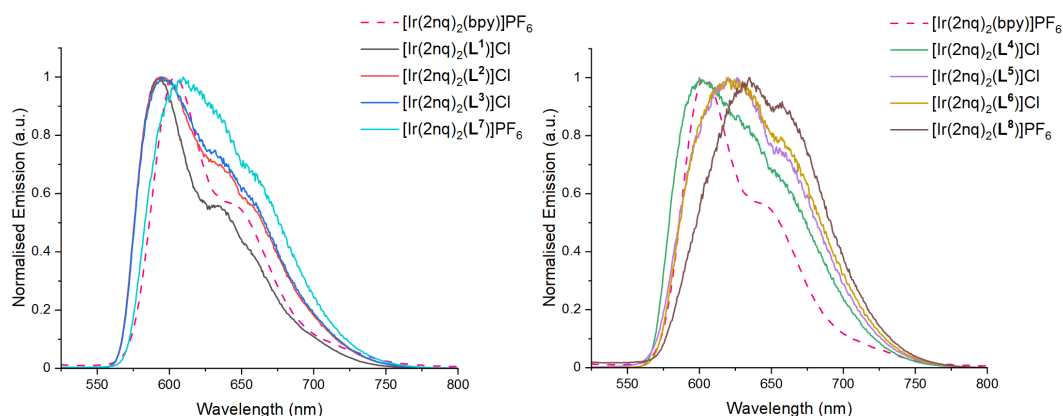


Figure 5.21 - Low temperature emission spectra recorded in a MeOH / EtOH (1:4) glass at 77 K ($\lambda_{\text{ex}} = 510$ nm).

Low temperature emission spectra (seen in Figure 5.21) were obtained in an ethanol/methanol glass (4:1). Much like in the bpy complex, a relatively large hypsochromic shift is observed at low temperature. Complexes of pyridine-based ancillary ligands are observed at higher energy than the pyrazine and bipyridine based ancillary complexes. The pyridine-based acid ligand complexes have a λ_{max} emission of 594 nm, 10 nm longer in energy than the bpy complex. All four of the emissions are observed with a lower energy shoulder, showing features at 630 nm and 655 nm. Interestingly, the complex of **L**⁷ with the ester replacing the acid group shows a λ_{max} emission of 611 nm. Once again, the pyrazine based ancillary ligand complexes are showing some subtle variations in a λ_{max} emission based upon substitution. **L**⁴ complex has an emission λ_{max} at 602 nm, while both the unsubstituted **L**⁵ and the fluoro substituted **L**⁶ have emission peaks at 623 nm. Once again, the ester group is seen to be bathochromically shifted further to 635 nm. All four of the pyrazine-based complexes show the same shoulder feature at 655 nm. The differences seen in the emission spectra suggests the presence of ³ILCT or ³LLCT emission as well as a smaller degree of ³MLCT based emission.

5.4 Conclusions

This chapter has shown the synthesis, isolation, and characterisation of five novel *bis-imine* ligands based around the substituted 2-(pyridin-2-yl)quinoline and 2-(pyrazin-2-yl)quinoline frameworks. The modified Pfitzinger synthesis employed a greener approach to the synthesis, allowing for the isolation of targeted substituted quinoline-4-carboxylic acids at good yields.

Six novel iridium(III) complexes using the cyclometalating ligand 1nq, along with eight novel iridium(III) complexes using the cyclometalating ligand 2nq were also synthesised, utilising the new *bis-imine* ligands as the ancillary ligand. Complexes were characterised via ^1H , $^{19}\text{F}\{^1\text{H}\}$, $^{13}\text{C}\{^1\text{H}\}$ NMR, HRMS, FTIR, absorption and emission spectroscopies, as well as two examples grown as single crystals allowing for the collection and refinement of single crystal x-ray diffraction data.

The 1nq complexes display the same deep red emission seen from the corresponding bpy complex in Chapter 4, a predominantly $^3\text{MLCT}$ based emission character. Photophysical properties are similar to those of archetypal red emitter $[\text{Pt}(\text{OEP})]^{43}$. The 2nq complexes that were previously shown to emit from a more ^3LC emission showed a degree of tuneability across the deep red region, especially noticeable at 77 K, suggesting the ancillary ligand π^* orbitals are approaching the same energy level as LUMO levels, located across the cyclometalating ligands.

5.5 Experimental

All reactions were performed with the use of vacuum line and Schlenk techniques. Reagents were commercial grade and were used without further purification. ^1H , ^{13}C and ^{19}F NMR spectra were recorded on a Bruker fourier 300, dpx 400, or avance 500 MHz spectrometer, and were recorded in CDCl_3 , CD_3OD or d_6 -DMSO solutions. ^1H and $^{13}\text{C}\{^1\text{H}\}$ NMR chemical shifts (δ) were determined relative to internal tetramethylsilane, $\text{Si}(\text{CH}_3)_4$ and are given in ppm. Low-resolution and high-resolution mass spectra were obtained by the staff at Cardiff University. All photophysical data was obtained on a JobinYvon-Horiba Fluorolog-3 spectrometer fitted with a JY TBX picosecond photodetection module in 0.1 M NaOH or MeCN solutions. Emission spectra were uncorrected and excitation spectra were instrument corrected. The pulsed source was a Nano-LED configured for 295, 372 or 459 nm output operating at 500 kHz or 1 MHz. Luminescence lifetime profiles were obtained using the JobinYvon-Horiba FluoroHub single photon counting module and the data fits yielded the lifetime values using the provided DAS6 deconvolution software. IR spectra were recorded on an ATR equipped Shimadzu IRAffinity-1 spectrophotometer. UV-vis data was recorded as solutions on a Shimadzu UV-1800 spectrophotometer.

X-Ray Diffraction Data Collection and Refinement.

Suitable crystals were selected and mounted on a MITIGEN holder in perfluoroether oil on either a Rigaku FRE+ diffractometer equipped with VHF Varimax confocal mirrors and an AFC12 goniometer and HyPix 6000 detector, operating at $T = 100(2)$ K during data collection.

The structure was solved with the ShelXT⁴⁴ structure solution program using dual methods and by using Olex2⁴⁵ as the graphical interface. The model was refined with version 2018/3 of ShelXL⁴⁶ using Least Squares minimisation.

5.5.1 Ligand synthesis.

5.5.1.1 6-methoxy-2-(pyridin-2-yl)quinoline-4-carboxylic acid. (**L**¹)

5-Methoxyisatin (1.00 g, 5.64 mmol) and 2-acetylpyridine (684 mg, 5.64 mg) were ground together in a pestle and mortar for 5 minutes until homogeneous. To this, 33 % aqueous NaOH solution (2 mL, 4 eq) was added, and the colour changed immediately from orange to dark red. The mixture was ground for a further 15

minutes until the solution solidified. The solid was slurried by the addition of cold water (2 mL) and collected onto a sinter, where it was washed with ice water (5 mL). The crude was then washed with plenty of acetone to remove any unreacted isatin and acetal. The off-white sodium salt was dissolved in water (500 mL) and the solution was neutralised with 5 M HCl, where upon a precipitate appeared. This was collected on a sinter and washed with water before triturating with ethanol (20 mL) to yield the title products as an off-white solid (552 mg, 33 % Yield). ^1H NMR (400 MHz, d_6 -DMSO) δ_{H} 9.02 (s, 1H), 8.75 (s, 1H), 8.57 (d, $J = 7.6$ Hz, 1H), 8.25 (s, 1H), 8.15 – 8.08 (m, 1H), 8.06 – 7.98 (m, 1H), 7.58 - 7.48 (m, 2H), 3.94 (s, 3H) ppm. $^{13}\text{C}\{^1\text{H}\}$ NMR (101 MHz, d_6 -DMSO) δ 167.7, 158.8, 154.6, 152.6, 149.4, 144.5, 137.5, 131.5, 126.2, 124.6, 122.5, 120.6, 119.9, 104.0, 55.5 ppm. UV-vis (0.1 M NaOH): λ_{abs} ($\epsilon/10^4$ L mol $^{-1}$ cm $^{-1}$) 256 (2.6), 274 (2.2), 342 (1.0) nm. FTIR (solid) (ATR) ν_{max} : 3143, 3034, 1685 (C=O), 1620, 1598, 1568, 1550, 1508, 1481, 1436, 1408, 1359, 1334, 1269, 1246, 1219, 1186, 1161, 1082, 1047, 1022, 1010, 885, 862, 825, 783, 758, 734, 704, 659, 634, 557, 524, 511, 406 cm $^{-1}$. HRMS (ES) $[\text{M} + \text{H}]^+$ Calc'd for $\text{C}_{16}\text{H}_{13}\text{N}_2\text{O}_3$ 281.0926; Found m/z 281.0930.

5.5.1.2 2-(pyridin-2-yl)quinoline-4-carboxylic acid³⁹ (L²)

Synthesised as L¹ from isatin and 2-acetylpyridine to yield an off-white solid (494 mg, 35 % Yield). Spectral properties were in agreement with those listed in the literature.

5.5.1.3 6-fluoro-2-(pyridin-2-yl)quinoline-4-carboxylic acid (L³)

Synthesised as L¹ from 5-fluoroisatin and 2-acetylpyridine to yield an off-white solid (692 mg, 46 % Yield). ^1H NMR (400 MHz, d_6 -DMSO) δ_{H} 9.09 (s, 1H), 8.79 (d, $J = 4.4$ Hz, 1H), 8.64 – 8.54 (m, 2H), 8.29 (dd, $J = 9.3, 5.9$ Hz, 1H), 8.06 (dd, $J = 8.2, 7.5$ Hz, 1H), 7.83 (ddd, $J = 9.4, 9.0, 2.5$ Hz, 1H), 7.64 – 7.53 (m, 1H) ppm. $^{19}\text{F}\{^1\text{H}\}$ NMR (376 MHz, d_6 -DMSO) δ -109.98 (s) ppm. $^{13}\text{C}\{^1\text{H}\}$ NMR (126 MHz, d_6 -DMSO) δ 167.6, 162.4, 160.5, 155.3, 154.6, 150.5, 146.1, 138.1, 133.4, 133.3, 126.2, 125.6, 121.5, 121.0, 121.0, 120.8, 110.0, 109.8 ppm. UV-vis (0.1 M NaOH): λ_{abs} ($\epsilon/10^4$ L mol $^{-1}$ cm $^{-1}$) 271 (1.6), 325 (0.7) nm. FTIR (solid) (ATR) ν_{max} : 3109, 3086, 1701 (C=O), 1624, 1600, 1591, 1550, 1508, 1481, 1446, 1344, 1327, 1286, 1238, 1211, 1163, 1151, 1101, 1083, 1014, 827, 877, 833, 821, 788, 759, 740, 707, 682, 661, 640, 611, 590, 511, 478, 443, 403 cm $^{-1}$. HRMS (ES) $[\text{M} + \text{H}]^+$ Calc'd for $\text{C}_{15}\text{H}_{10}\text{FN}_2\text{O}_2$ 269.0726; Found m/z 269.0746.

5.5.1.4 6-methoxy-2-(pyrazin-2-yl)quinoline-4-carboxylic acid (L⁴)

Synthesised as L¹ from 5-methoxyisatin and 2-acetylpyrazine to yield an off-white solid (803 mg, 51 % Yield). ¹H NMR (400 MHz, d₆-DMSO) δ_H 9.70 (s, 1H), 8.95 – 8.73 (m, 3H), 8.26 (s, 1H), 8.14 (s, 1H), 7.56 (s, 1H), 3.94 (s, 3H) ppm. ¹³C{¹H} NMR (101 MHz, d₆-DMSO) δ 167.6, 159.0, 150.8, 149.8, 145.2, 144.5, 144.1, 142.5, 131.6, 126.5, 122.8, 119.7, 104.1, 55.6 ppm. UV-vis (0.1 M NaOH): λ_{abs} (ε/10⁴ L mol⁻¹ cm⁻¹) 257 (2.4), 283 (1.7), 344 (1.4) nm. FTIR (solid) (ATR) ν_{max}: 3120, 3064, 1701 (C=O), 1622, 1527, 1504, 1485, 1438, 1421, 1359, 1338, 1288, 1263, 1226, 1184, 1151, 1089, 1062, 1016, 929, 912, 852, 833, 790, 765, 736, 719, 673, 646, 603, 557, 526, 493, 405 cm⁻¹. HRMS (ES) [M + H]⁺ Calc'd for C₁₅H₁₂N₃O₃ 282.0879; Found *m/z* 282.0882.

5.5.1.5 2-(pyrazin-2-yl)quinoline-4-carboxylic acid (L⁵)

Synthesised as L¹ from isatin and 2-acetylpyrazine to yield an off-white solid (456 mg, 32 % Yield). Spectral properties were in agreement with those listed in the literature ⁴⁷.

5.5.1.6 6-fluoro-2-(pyrazin-2-yl)quinoline-4-carboxylic acid (L⁶)

Synthesised as L¹ from 5-fluoroisatin and 2-acetylpyrazine to yield an off-white solid (521 mg, 34 % Yield). ¹H NMR (400 MHz, d₆-DMSO) δ_H 9.74 (s, 1H), 8.98 (s, 1H), 8.83 (dd, *J* = 8.3, 1.8 Hz, 2H), 8.58 (d, *J* = 10.7 Hz, 1H), 8.36 – 8.30 (m, 1H), 7.86 (dd, *J* = 9.6, 8.2 Hz, 1H) ppm. ¹⁹F{¹H} NMR (376 MHz, d₆-DMSO) δ -109.09 (s) ppm. ¹³C NMR (126 MHz, d₆-DMSO) δ 166.9, 162.3, 160.3, 153.1, 153.1, 149.2, 145.8, 145.6, 144.3, 142.89, 136.3, 136.2, 133.1, 133.0, 125.9, 125.8, 120.8, 120.6, 120.5, 109.6, 109.4 ppm. UV-vis (0.1 M NaOH): λ_{abs} (ε/10⁴ L mol⁻¹ cm⁻¹) 280 (1.5), 319 (1.1) nm. FTIR (solid) (ATR) ν_{max}: 3109, 3072, 1718 (C=O), 1654, 1649, 1622, 1560, 1527, 1508, 1481, 1460, 1421, 1363, 1336, 1325, 1274, 1236, 1226, 1207, 1182, 1145, 1083, 1060, 1016, 935, 916, 881, 852, 833, 790, 763, 738, 723, 673, 646, 547, 503, 489, 437, 420, 408 cm⁻¹. HRMS (ES) [M + H]⁺ Calc'd for C₁₄H₉N₃O₂ 270.0679; Found *m/z* 270.0680.

5.5.1.7 Ethyl 2-(pyridin-2-yl)quinoline-4-carboxylate (L⁷)

To a stirring solution of L² (500 mg, 2 mmol) in ethanol (10 mL), H₂SO₄ (6 drops) was added slowly before heating to 78 °C for 16 hours. The solution was cooled to room temperature and neutralised with Na₂CO₃ (0.1 M). solvents were removed and the product purified by column chromatography, eluting with dichloromethane

before solvents removed *in vacuo* to yield the title compound as a white powder (476 mg, 1.71 mmol, 86 %). Spectral properties were in agreement with those listed in the literature⁴⁸.

5.5.1.8 Ethyl 2-(pyrazin-2-yl)quinoline-4-carboxylate (L⁸)

Synthesised as above from L⁵, yielding an off white solid (456 mg, 82 %). ¹H NMR (400 MHz, CDCl₃) δ 9.89 (d, J = 1.5 Hz, 1H), 8.97 (s, 1H), 8.79 (dd, J = 8.6, 0.8 Hz, 1H), 8.71 (dd, J = 2.5, 1.5 Hz, 1H), 8.68 (d, J = 2.5 Hz, 1H), 8.27 (ddd, J = 8.5, 1.3, 0.6 Hz, 1H), 7.82 (ddd, J = 8.4, 6.9, 1.4 Hz, 1H), 7.70 (ddd, J = 8.4, 6.9, 1.4 Hz, 1H), 4.56 (q, J = 7.1 Hz, 2H), 1.51 (t, J = 7.1 Hz, 3H) ppm. ¹³C NMR (101 MHz, CDCl₃) δ 166.4, 153.9, 150.8, 149.0, 145.1, 144.1, 143.7, 136.7, 130.7, 130.3, 129.0, 125.8, 125.4, 120.0, 62.1, 14.5 ppm. UV-vis (MeCN): λ_{abs} (ε/10⁴ L mol⁻¹ cm⁻¹) 253 (2.1), 285 (1.8), 334 (0.7) nm. FTIR (solid) (ATR) ν_{max}: 3053, 2993, 1732, 1712 (C=O), 1585, 1521, 1506, 1477, 1423, 1388, 1363, 1334, 1274, 1246, 1226, 1190, 1138, 1111, 1085, 1033, 1014, 910, 854, 794, 773, 740, 675, 578, 557, 524, 514, 460 cm⁻¹. HRMS (AP) [M + H]⁺ Calc'd for C₁₆H₁₄N₃O₂ 280.1086; Found *m/z* 280.1085.

5.5.2 General procedure for the synthesis of [Ir(L)₂(MeCN)₂]BF₄

Synthesised following the same procedure used in Chapter 4 from IrCl₃.xH₂O, ethyl 2-(naphth-1-yl)quinoline-4-carboxylate (1nq) or Ethyl 2-(naphth-2-yl)quinoline-4-carboxylate (2nq) to yield [Ir(1nq)₂(MeCN)₂]BF₄ and [Ir(2nq)₂(MeCN)₂]BF₄ respectfully. Complex [Ir(2nq)₂(MeCN)₂]BF₄ was found to contain excess silver salts. The product was dissolved in chloroform (15 mL) and stirred with brine (15 mL) for 2 hours. The chloroform layer was separated, washed with water (3 x 10 mL) and dried over MgSO₄ and passed through a celite pad. Solvent was removed to yield a red solid which was used without further purification.

5.5.3 General procedure for the synthesis of [Ir(1/2nq)₂(L¹⁻⁸)]⁺

[Ir(1/2nq)₂(MeCN)₂]BF₄ (30 mg) was dissolved in chloroform (10 mL). Ligand (1.1 eq) was added, and the solution stirred at reflux for 16 hours. the solvent was removed and the and the product purified by silica gel column chromatography, eluting first with DCM followed by DCM / Methanol (9:1), collecting the second red fraction.

5.5.3.1 [Ir(1nq)₂(L¹)]PF₆

Obtained as a red solid (45 %). ¹H NMR (500 MHz, CDCl₃) δ 9.34 (s, 1H), 8.75 (d, J = 8.6 Hz, 1H), 8.70 (d, J = 7.6 Hz, 1H), 8.48 (d, J = 9.0 Hz, 1H), 8.36 (d, J = 8.3 Hz, 1H), 8.30 (d, J = 8.1 Hz, 1H), 8.13 (d, J = 8.6 Hz, 1H), 8.10 (s, 2H), 8.01 (d, J

= 5.5 Hz, 1H), 7.97 (s, $J = 9.8$ Hz, 1H), 7.95 – 7.91 (m, 1H), 7.79 (d, $J = 7.6$ Hz, 1H), 7.73 – 7.69 (m, 2H), 7.52 – 7.46 (m, 2H), 7.44 – 7.40 (m, 1H), 7.39 – 7.34 (m, 2H), 7.31 (d, $J = 9.5$ Hz, 1H), 7.26 – 7.20 (m, 3H), 7.08 (d, $J = 8.5$ Hz, 1H), 7.04 – 6.99 (m, 1H), 6.91 – 6.83 (m, 2H), 6.29 (dd, $J = 9.5, 2.7$ Hz, 1H), 6.25 (d, $J = 8.4$ Hz, 1H), 4.66 (q, $J = 7.1$ Hz, 2H), 4.48 (q, $J = 7.1$ Hz, 2H), 3.66 (s, 3H), 1.59 (t, $J = 7.1$ Hz, 3H), 1.38 (t, $J = 7.1$ Hz, 3H) ppm. ^{13}C NMR (126 MHz, CDCl_3) δ 172.0, 171.2, 170.9, 165.4, 165.1, 159.2, 159.1, 153.9, 149.7, 147.6, 147.4, 142.0, 140.7, 140.0, 138.1, 137.8, 136.4, 132.4, 132.3, 132.2, 131.9, 131.8, 131.4, 130.7, 130.6, 130.4, 130.1, 129.8, 128.6, 128.3, 128.0, 128.0, 126.9, 126.7, 126.4, 126.2, 124.6, 124.4, 123.8, 123.8, 123.2, 123.1, 123.0, 121.6, 121.1, 105.9, 63.1, 63.0, 56.0, 14.5, 14.1 ppm. UV-vis (MeCN): λ_{abs} ($\epsilon/10^4 \text{ L mol}^{-1} \text{ cm}^{-1}$) 217 (7.9), 261 (5.6), 285 (4.6), 373 (2.4), 494 (0.5) nm. FTIR (solid) (ATR) ν_{max} : 1716 (C=O), 1614, 1575, 1533, 1506, 1487, 1456, 1436, 1296, 1271, 1234, 1195, 1124, 1099, 1024, 837 (PF_6^-), 785, 746, 713, 557 (PF_6^-), 446, 410, 403 cm^{-1} . HRMS (ES) $[\text{M} - \text{PF}_6]^+$ Calc'd for $\text{C}_{60}\text{H}_{44}\text{N}_4\text{O}_7\text{Ir}$ 1125.2839; Found m/z 1125.2893.

5.5.3.2 $[\text{Ir}(\text{1nq})_2(\text{L}^2)]\text{PF}_6$

Obtained as a red solid (75 %). ^1H NMR (500 MHz, CDCl_3) δ 9.29 (s, 1H), 8.87 (s, 1H), 8.73 (d, $J = 8.5$ Hz, 1H), 8.67 (d, $J = 8.5$ Hz, 1H), 8.43 (d, $J = 8.6$ Hz, 2H), 8.26 – 8.09 (m, 3H), 8.04 (s, 2H), 7.90 (s, 1H), 7.79 (d, $J = 8.0$ Hz, 1H), 7.74 – 7.68 (m, 2H), 7.53 – 7.46 (m, 2H), 7.46 – 7.40 (m, 2H), 7.40 – 7.35 (m, 2H), 7.29 – 7.21 (m, 4H), 7.03 (d, $J = 8.5$ Hz, 1H), 6.96 – 6.88 (m, 2H), 6.74 (s, 1H), 6.68 (s, 1H), 6.37 (s, 1H), 4.66 (q, $J = 7.1$ Hz, 2H), 4.58 – 4.39 (m, 2H), 1.59 (t, $J = 7.2$ Hz, 3H), 1.53 – 1.35 (m, 3H) ppm. ^{13}C NMR (126 MHz, CDCl_3) δ 171.9, 170.7, 165.2, 164.7, 149.4, 140.5, 138.0, 137.8, 132.2, 131.9, 131.7, 131.7, 131.3, 130.6, 130.3, 129.9, 128.4, 128.1, 127.8, 127.5, 126.8, 126.4, 126.3, 124.5, 124.2, 123.6, 123.6, 122.9, 121.9, 121.4, 121.2, 62.8, 14.4, 14.2 ppm. UV-vis (MeCN): λ_{abs} ($\epsilon/10^4 \text{ L mol}^{-1} \text{ cm}^{-1}$) 273 (5.0), 368 (1.8), 492 (0.5) nm. FTIR (solid) (ATR) ν_{max} : 1722 (C=O), 1595, 1575, 1533, 1456, 1436, 1325, 1269, 1238, 1195, 1153, 1124, 1099, 1025, 837 (PF_6^-), 790, 769, 748, 713, 657, 557 (PF_6^-), 497, 445, 432, 412 cm^{-1} . HRMS (ES) $[\text{M} - \text{PF}_6]^+$ Calc'd for $\text{C}_{59}\text{H}_{42}\text{N}_4\text{O}_6\text{Ir}$ 1093.2710; Found m/z 1093.2697.

5.5.3.3 $[\text{Ir}(\text{1nq})_2(\text{L}^3)]\text{PF}_6$

Obtained as a red solid (76 %). ^1H NMR (500 MHz, CDCl_3) δ 9.33 (s, 1H), 8.75 (d, $J = 8.6$ Hz, 1H), 8.70 (d, $J = 8.4$ Hz, 1H), 8.62 (d, $J = 9.1$ Hz, 1H), 8.45 – 8.39 (m, 2H), 8.36 (d, $J = 7.5$ Hz, 1H), 8.25 (s, 1H), 8.15 (d, $J = 8.1$ Hz, 1H), 8.06 (d, $J = 4.8$

Hz, 1H), 8.03 – 7.96 (m, 2H), 7.80 (d, $J = 7.9$ Hz, 1H), 7.75 – 7.69 (m, 2H), 7.53 – 7.37 (m, 5H), 7.35 – 7.30 (m, 2H), 7.28 (s, 1H), 7.23 (s, 1H), 7.09 – 7.04 (m, 1H), 7.01 – 6.96 (m, 1H), 6.92 – 6.81 (m, 2H), 6.44 – 6.36 (m, 1H), 6.26 (d, $J = 8.4$ Hz, 1H), 4.66 (q, $J = 7.1$ Hz, 2H), 4.55 – 4.45 (m, 2H), 1.59 (t, $J = 7.1$ Hz, 3H), 1.41 (t, $J = 6.5$ Hz, 3H) ppm. ^{19}F NMR (471 MHz, CDCl_3) δ -72.58 (d, $J = 712$ Hz, PF_6^-), -107.98 (s) ppm. ^{13}C NMR (126 MHz, CDCl_3) δ 171.9, 165.3, 164.8, 160.0, 149.6, 147.6, 140.7, 138.2, 137.8, 132.3, 132.2, 132.1, 131.9, 131.9, 131.5, 130.6, 130.4, 128.6, 128.1, 127.2, 126.6, 126.6, 126.4, 124.7, 124.5, 123.9, 123.8, 123.3, 123.2, 121.6, 121.2, 63.0, 63.0, 14.5, 14.2 ppm. UV-vis (MeCN): λ_{abs} ($\epsilon/10^4$ L mol $^{-1}$ cm $^{-1}$) 219 (8.8), 257 (6.6), 361 (2.8), 391 (2.0), 490 (0.6) nm. FTIR (solid) (ATR) ν_{max} : 1720 (C=O), 1595, 1575, 1533, 1498, 1483, 1436, 1384, 1325, 1296, 1269, 1232, 1193, 1153, 1124, 1099, 1024, 937, 891, 839 (PF_6^-), 785, 746, 711, 665, 624, 557 (PF_6^-), 518, 493, 472, 433, 410, 403 cm $^{-1}$. HRMS (ES) $[\text{M} - \text{PF}_6]^+$ Calc'd for $\text{C}_{59}\text{H}_{41}\text{N}_4\text{O}_6\text{Ir}$ 1113.2639; Found m/z 1113.2689.

5.5.3.4 $[\text{Ir}(\text{1nq})_2(\text{L}^4)]\text{BF}_4$

Obtained as a red solid (43 % yield). ^1H NMR (500 MHz, CDCl_3) δ 9.44 (s, 1H), 9.29 (s, 1H), 8.72 (d, $J = 8.7$ Hz, 1H), 8.69 (d, $J = 8.4$ Hz, 1H), 8.56 – 8.35 (m, 5H), 8.34 – 8.24 (m, 3H), 8.22 (s, 2H), 8.00 (s, 1H), 7.81 (d, $J = 8.0$ Hz, 1H), 7.73 (d, $J = 8.0$ Hz, 1H), 7.72 (d, $J = 7.9$ Hz, 1H), 7.52 (dd, $J = 9.2, 7.4$ Hz, 2H), 7.50 – 7.44 (m, 1H), 7.44 – 7.38 (m, 2H), 7.30 (s, 1H), 7.28 (s, 1H), 7.01 (s, 1H), 6.99 (s, 1H), 6.83 (s, 2H), 6.40 (s, 1H), 6.34 (s, 1H), 4.66 (q, $J = 7.1$ Hz, 2H), 4.57 – 4.48 (m, 2H), 3.85 (s, 3H), 1.59 (t, $J = 7.1$ Hz, 4H), 1.51 – 1.44 (m, 3H) ppm. ^{13}C NMR (126 MHz, CDCl_3) δ 171.9, 170.6, 166.9, 165.2, 164.8, 149.3, 147.4, 147.0, 140.6, 138.5, 137.8, 132.4, 132.2, 132.1, 131.9, 131.6, 130.4, 130.1, 129.6, 128.5, 128.2, 127.3, 126.7, 125.0, 124.6, 123.8, 123.5, 121.7, 121.3, 63.1, 63.0, 56.1, 14.5, 14.2 ppm. UV-vis (MeCN): λ_{abs} ($\epsilon/10^4$ L mol $^{-1}$ cm $^{-1}$) 217 (6.0), 260 (4.5), 282 (3.5), 356 (1.9), 402 (1.1), 492 (0.4) nm. FTIR (solid) (ATR) ν_{max} : 1734 (C=O), 1716, 1683, 1653, 1647, 1635, 1577, 1558, 1541, 1533, 1508, 1498, 1489, 1473, 1458, 1436, 1419, , 1271, 1232, 1217, 1151, 1022 (BF_4^-), 835, 669, 518 (BF_4^-), 472, 457, 433, 418, 412, 403 cm $^{-1}$. HRMS (ES) $[\text{M} - \text{BF}_4]^+$ Calc'd for $\text{C}_{59}\text{H}_{43}\text{N}_5\text{O}_7\text{Ir}$ 1124.2768; Found m/z 1124.2789.

5.5.3.5 $[\text{Ir}(\text{1nq})_2(\text{L}^5)]\text{BF}_4$

Obtained as a red solid (40 % yield). ^1H NMR (500 MHz, CDCl_3) δ 9.47 (s, 1H), 9.33 (s, 1H), 8.94 (d, $J = 8.7$ Hz, 1H), 8.75 (d, $J = 8.5$ Hz, 1H), 8.71 (d, $J = 8.6$ Hz, 1H), 8.56 (s, 1H), 8.47 (d, $J = 8.2$ Hz, 1H), 8.37 (d, $J = 8.9$ Hz, 1H), 8.23 (s, 1H), 8.19 (d, $J = 8.6$ Hz, 1H), 8.08 (s, 2H), 7.83 (d, $J = 7.8$ Hz, 1H), 7.77 – 7.71 (m, 2H),

7.56 – 7.45 (m, 4H), 7.44 – 7.37 (m, 3H), 7.34 – 7.27 (m, 2H), 7.05 (d, $J = 8.4$ Hz, 1H), 6.97 (dd, $J = 9.4, 8.0$ Hz, 1H), 6.90 – 6.81 (m, 2H), 6.79 (dd, $J = 8.0, 7.9$ Hz, 1H), 6.35 (d, $J = 8.6$ Hz, 1H), 4.67 (q, $J = 7.2$ Hz, 2H), 4.60 – 4.45 (m, 2H), 1.60 (t, $J = 7.1$ Hz, 3H), 1.50 (t, $J = 7.0$ Hz, 3H) ppm. ^{13}C NMR (126 MHz, CDCl_3) δ 171.9, 170.6, 165.2, 165.8, 164.7, 149.2, 147.7, 140.4, 138.6, 137.8, 132.4, 132.2, 132.1, 131.9, 131.6, 131.5, 130.8, 130.5, 130.4, 130.1, 128.8, 128.5, 128.3, 128.2, 128.0, 127.7, 127.0, 126.7, 126.3, 125.0, 124.6, 124.3, 123.8, 123.2, 122.2, 121.6, 121.4, 77.1, 63.1, 63.0, 62.9, 14.5, 14.4 ppm. UV-vis (MeCN): λ_{abs} ($\epsilon/10^4 \text{ L mol}^{-1} \text{ cm}^{-1}$) 219 (8.4), 256 (6.3), 349 (2.6), 404 (1.7), 493 (0.6) nm. FTIR (solid) (ATR) ν_{max} : 1716 (C=O), 1683, 1575, 1558, 1533, 1506, 1473, 1456, 1436, 1269, 1234, 1151, 1099, 1024 (BF_4^-), 891, 813, 767, 748, 518 (BF_4^-), 443, 432 cm^{-1} . HRMS (ES) $[\text{M} - \text{BF}_4]^+$ Calc'd for $\text{C}_{58}\text{H}_{41}\text{N}_5\text{O}_6\text{Ir}$ 1094.2662; Found m/z 1094.2663.

5.5.3.6 $[\text{Ir}(\text{1nq})_2(\text{L}^6)]\text{BF}_4$

Obtained as a red solid (33 % yield). ^1H NMR (500 MHz, CDCl_3) δ 9.53 (s, 1H), 9.34 (s, 1H), 8.80 (d, $J = 8.4$ Hz, 1H), 8.75 (d, $J = 8.7$ Hz, 1H), 8.72 (d, $J = 8.5$ Hz, 1H), 8.58 (s, 1H), 8.44 (d, $J = 8.0$ Hz, 1H), 8.37 (s, 1H), 8.30 (d, $J = 9.1$ Hz, 1H), 8.19 (d, $J = 8.5$ Hz, 1H), 8.08 (s, 2H), 7.83 (d, $J = 7.9$ Hz, 1H), 7.77 – 7.72 (m, 2H), 7.58 – 7.51 (m, 3H), 7.48 (d, $J = 9.8$ Hz, 1H), 7.45 – 7.37 (m, 2H), 7.33 – 7.27 (m, 2H), 7.06 (d, $J = 8.5$ Hz, 1H), 7.00 (dd, $J = 10.5, 7.1$ Hz, 1H), 6.91 – 6.84 (m, 1H), 6.81 (d, $J = 8.5$ Hz, 1H), 6.55 (s, 1H), 6.29 (d, $J = 8.3$ Hz, 1H), 4.67 (q, $J = 7.1$ Hz, 2H), 4.60 – 4.46 (m, 2H), 1.59 (t, $J = 7.2$ Hz, 3H), 1.50 (t, $J = 6.9$ Hz, 3H) ppm. ^{19}F NMR (471 MHz, CDCl_3) δ -102.5 (s), -148.0 (s, BF_4^-) ppm. ^{13}C NMR (126 MHz, CDCl_3) δ 171.8, 170.5, 165.0, 164.5, 160.2, 154.0, 149.2, 147.6, 146.7, 143.5, 143.5, 140.7, 140.5, 138.6, 138.1, 137.7, 132.2, 132.0, 131.8, 131.6, 130.4, 130.2, 130.0, 128.8, 128.5, 128.3, 127.9, 126.7, 126.0, 124.9, 124.7, 123.7, 123.2, 121.8, 121.5, 121.3, 63.0, 63.0, 14.4, 14.2 ppm. UV-vis (MeCN): λ_{abs} ($\epsilon/10^4 \text{ L mol}^{-1} \text{ cm}^{-1}$) 218 (7.3), 256 (5.1), 355 (2.2), 396 (1.5), 495 (0.5) nm. FTIR (solid) (ATR) ν_{max} : 1718 (C=O), 1593, 1550, 1531, 1498, 1475, 1436, 1382, 1296, 1267, 1236, 1193 (BF_4^-), 1168, 1151, 1151, 1124, 1099, 1022 (BF_4^-), 935, 891, 862, 815, 785, 767, 746, 713, 682, 582, 518 (BF_4^-), 495, 426, 412, 403 cm^{-1} . HRMS (ES) $[\text{M} - \text{BF}_4]^+$ Calc'd for $\text{C}_{58}\text{H}_{40}\text{N}_5\text{O}_6\text{Ir}$ 1112.2569; Found m/z 1112.2583.

5.5.3.7 $[\text{Ir}(\text{2nq})_2(\text{L}^1)]\text{PF}_6$

Obtained as a red solid (50 % yield). ^1H NMR (500 MHz, CD_3OD) δ 8.95 (s, 1H), 8.73 (s, 1H), 8.56 – 8.50 (m, 3H), 8.44 (d, $J = 8.3$ Hz, 1H), 8.31 (d, $J = 8.3$ Hz, 2H),

8.09 (s, 1H), 7.98 – 7.92 (m, 2H), 7.85 (d, $J = 8.5$ Hz, 1H), 7.83 – 7.79 (m, 1H), 7.77 (d, $J = 6.5$ Hz, 1H), 7.76 (s, 1H), 7.42 – 7.30 (m, 4H), 7.21 – 7.12 (m, 4H), 7.04 (d, $J = 7.3$ Hz, 1H), 7.02 (d, $J = 8.8$ Hz, 1H), 6.95 – 6.90 (m, 1H), 6.86 – 6.82 (m, 1H), 6.66 (d, $J = 17.0$ Hz, 2H), 6.47 (dd, $J = 9.6, 2.9$ Hz, 1H), 4.58 (q, $J = 7.1$ Hz, 2H), 4.51 – 4.44 (m, 2H), 3.75 (s, 2H), 1.50 (t, $J = 7.2$ Hz, 3H), 1.43 (t, $J = 7.2$ Hz, 3H) ppm. ^{13}C NMR (126 MHz, CDCl_3) δ 169.7, 169.0, 168.2, 165.2, 164.9, 159.5, 158.9, 153.1, 148.6, 148.1, 147.8, 146.0, 144.1, 143.5, 142.3, 138.8, 138.7, 138.4, 135.6, 132.1, 130.8, 130.6, 130.3, 130.2, 129.4, 129.3, 129.1, 128.9, 128.2, 128.1, 128.0, 128.0, 127.4, 127.1, 126.4, 126.4, 126.3, 125.0, 124.9, 124.7, 124.7, 124.3, 124.2, 119.3, 118.9, 118.7, 106.8, 63.0, 62.9, 56.0, 14.5, 14.4 ppm. UV-vis (MeCN): λ_{abs} ($\epsilon/10^4 \text{ L mol}^{-1} \text{ cm}^{-1}$) 269 (8.0), 288 (7.4), 322 (4.4), 371 (4.6), 497 (0.2) nm. FTIR (solid) (ATR) ν_{max} : 1720 (C=O), 1616, 1598, 1585, 1544, 1508, 1483, 1438, 1371, 1354, 1296, 1273, 1236, 1199, 1149, 1078, 1022, 833 (PF_6^-), 792, 773, 746, 723, 659, 557 (PF_6^-), 468 cm^{-1} . HRMS (ES) $[\text{M} - \text{PF}_6]^+$ Calc'd for $\text{C}_{60}\text{H}_{44}\text{N}_4\text{O}_7\text{Ir}$ 1123.2816; Found m/z 1123.2863.

5.5.3.8 $[\text{Ir}(\text{2nq})_2(\text{L}^2)]\text{Cl}$

Obtained as a red solid (50 % yield). ^1H NMR (500 MHz CD_3OD) δ 9.07 (s, 1H), 8.86 (s, 1H), 8.66 – 8.63 (m, 2H), 8.60 (s, 1H), 8.56 (dd, $J = 8.6, 1.1$ Hz, 1H), 8.49 (d, $J = 8.1$ Hz, 1H), 8.46 – 8.43 (m, 2H), 8.22 (s, 1H), 8.12 – 8.09 (m, 1H), 8.07 (dd, $J = 7.9, 1.5$ Hz, 1H), 8.01 (d, $J = 8.6$ Hz, 1H), 7.97 (d, $J = 8.3$ Hz, 1H), 7.93 – 7.89 (m, 1H), 7.58 – 7.45 (m, 4H), 7.43 (d, $J = 9.0$ Hz, 1H), 7.33 – 7.23 (m, 4H), 7.18 – 7.12 (m, 2H), 7.07 – 6.98 (m, 2H), 6.95 – 6.90 (m, 1H), 6.81 (s, 1H), 6.77 (s, 1H), 4.70 (q, $J = 7.1$ Hz, 2H), 4.58 (q, $J = 7.1$ Hz, 2H), 1.62 (t, $J = 7.2$ Hz, 3H), 1.54 (t, $J = 7.2$ Hz, 3H) ppm. ^{13}C NMR (126 MHz, CD_3OD) δ 182.2, 170.8, 170.2, 168.8, 165.1, 164.7, 158.2, 157.2, 153.5, 148.9, 148.2, 147.8, 146.9, 146.2, 144.1, 139.5, 139.4, 138.8, 135.7, 131.1, 131.0, 130.6, 130.4, 130.1, 130.0, 129.0, 128.5, 128.3, 128.0, 127.8, 127.7, 127.7, 126.8, 126.6, 126.4, 126.3, 125.8, 125.6, 125.1, 124.6, 124.4, 124.2, 123.9, 121.7, 119.0, 118.4, 117.2, 62.6, 62.4, 13.2, 13.1 ppm. UV-vis (MeCN): λ_{abs} ($\epsilon/10^4 \text{ L mol}^{-1} \text{ cm}^{-1}$) 268 (7.6), 286 (6.2), 324 (3.9), 372 (3.4), 395 (2.7), 497 (0.2) nm. FTIR (solid) (ATR) ν_{max} : 1722 (C=O), 1598, 1579, 1544, 1514, 1456, 1438, 1392, 1371, 1350, 1330, 1300, 1276, 1249, 1193, 1149, 1078, 1024, 985, 871, 813, 773, 746, 663, 624, 611, 570, 526, 466 cm^{-1} . HRMS (ES) $[\text{M} - \text{Cl}]^+$ Calc'd for $\text{C}_{59}\text{H}^{+} \quad {}_{42}\text{N}_4\text{O}_6\text{Ir}$ 1093.2710; Found m/z 1093.2758.

5.5.3.9 $[\text{Ir}(\text{2nq})_2(\text{L}^3)]\text{Cl}$

Obtained as a red solid (51 % yield). ^1H NMR (500 MHz, CD_3OD) δ 9.32 (s, 1H), 9.10 (s, 1H), 8.85 (d, $J = 1.1$ Hz, 1H), 8.83 (s, 1H), 8.75 (s, 1H), 8.70 (s, 1H), 8.69

(s, 1H), 8.66 (d, $J = 8.7$ Hz, 1H), 8.56 (d, $J = 8.1$ Hz, 1H), 8.49 (s, 1H), 8.36 (d, $J = 5.5$ Hz, 1H), 8.32 (dd, $J = 8.8, 1.9$ Hz, 1H), 8.21 – 8.15 (m, 2H), 8.11 – 8.08 (m, 1H), 7.75 – 7.65 (m, 4H), 7.59 (d, $J = 8.4$ Hz, 1H), 7.52 – 7.42 (m, 5H), 7.37 – 7.32 (m, 2H), 7.27 – 7.23 (m, 1H), 7.23 – 7.18 (m, 1H), 7.05 (s, 1H), 7.03 – 6.98 (m, 2H), 4.78 – 4.73 (m, 2H), 1.80 (t, $J = 7.2$ Hz, 3H), 1.72 (t, $J = 7.2$ Hz, 3H) ppm. ^{19}F NMR (471 MHz, CD_3OD) δ -110.4 (s) ppm. ^{13}C NMR (126 MHz, CDCl_3) δ 169.6, 168.2, 165.2, 164.8, 148.6, 147.8, 146.0, 143.9, 135.6, 130.9, 130.4, 130.2, 129.3, 129.1, 128.9, 128.3, 128.1, 128.0, 127.5, 127.1, 126.9, 126.60, 126.3, 126.3, 124.9, 124.8, 124.7, 124.5, 120.2, 119.0, 63.1, 63.0, 14.5, 14.3 ppm. UV-vis (MeCN): λ_{abs} ($\epsilon/10^4 \text{ L mol}^{-1} \text{ cm}^{-1}$) 269 (7.4), 283 (6.3), 323 (3.8), 369 (3.5), 293 (2.6), 497 (0.2) nm. FTIR (solid) (ATR) ν_{max} : 1718 (C=O), 1616, 1597, 1583, 1543, 1510, 1483, 1480, 1440, 1396, 1373, 1354, 1327, 1296, 1274, 1246, 1228, 1197, 1153, 1134, 1080, 1022, 935, 875, 829, 790, 775, 746, 705, 661, 626, 615, 570, 526, 509, 466, 418 cm^{-1} . HRMS (ES) $[\text{M} - \text{Cl}]^+$ Calc'd for $\text{C}_{59}\text{H}_{41}\text{N}_4\text{O}_6\text{FIr}$ 1111.2616; Found m/z 1111.2667.

*nb CH_2 ^1H quartet believed to be obscured by residual H_2O peak from solvent.

5.5.3.10 $[\text{Ir}(\text{2nq})_2(\text{L}^4)]\text{PF}_6$

Obtained as a red solid (73 % yield). ^1H NMR (500 MHz, CD_3OD) δ 9.64 (d, $J = 1.2$ Hz, 1H), 9.10 (s, 1H), 8.89 (s, 1H), 8.66 (s, 1H), 8.65 – 8.61 (m, 2H), 8.54 (dd, $J = 8.5, 1.1$ Hz, 1H), 8.37 (d, $J = 8.5$ Hz, 1H), 8.34 (s, 1H), 8.09 (dd, $J = 3.1, 1.2$ Hz, 1H), 7.99 (d, $J = 7.9$ Hz, 1H), 7.94 – 7.89 (m, 2H), 7.87 (d, $J = 9.6$ Hz, 1H), 7.55 – 7.47 (m, 2H), 7.34 – 7.24 (m, 4H), 7.18 – 7.08 (m, 3H), 7.00 – 6.94 (m, 1H), 6.79 (s, 1H), 6.76 (s, 1H), 6.64 (dd, $J = 9.6, 2.9$ Hz, 1H), 4.70 (q, $J = 7.1$ Hz, 2H), 4.58 (q, $J = 7.1$ Hz, 2H), 3.88 (s, 3H), 1.61 (t, $J = 7.2$ Hz, 2H), 1.54 (t, $J = 7.2$ Hz, 2H) ppm. ^{13}C NMR (126 MHz, CDCl_3) δ 169.6, 168.0, 165.1, 164.7, 159.4, 150.5, 148.3, 146.9, 146.3, 145.7, 144.0, 143.6, 140.6, 139.2, 138.8, 135.6, 135.6, 131.1, 130.8, 130.4, 130.3, 129.3, 129.1, 128.7, 128.5, 128.4, 128.2, 127.7, 126.7, 126.7, 126.5, 126.4, 125.1, 124.9, 124.8, 124.6, 124.5, 119.0, 118.8, 106.9, 63.1, 63.0, 56.1, 14.5, 14.4 ppm. UV-vis (MeCN): λ_{abs} ($\epsilon/10^4 \text{ L mol}^{-1} \text{ cm}^{-1}$) 268 (5.9), 286 (5.2), 320 (3.5), 372 (3.3), 497 (0.2) nm. FTIR (solid) (ATR) ν_{max} : 17126 (C=O), 1616, 1598, 1581, 1541, 1508, 1481, 1473, 1458, 1436, 1396, 1371, 1352, 1298, 1273, 1240, 1197, 1153, 1107, 1024, 835 (PF_6^-), 771, 742, 557 (PF_6^-), 526, 484, 470, 441 cm^{-1} . HRMS (ES) $[\text{M} - \text{PF}_6]^+$ Calc'd for $\text{C}_{59}\text{H}_{43}\text{N}_5\text{O}_7\text{Ir}$ 1124.2468; Found m/z 1124.2808.

5.5.3.11 [Ir(2nq)₂(L⁵)]Cl

Obtained as a red solid (62 % yield). ¹H NMR (500 MHz, CD₃OD) δ 9.63 (d, *J* = 1.0 Hz, 1H), 9.05 (s, 1H), 8.82 (s, 1H), 8.61 – 8.56 (m, 4H), 8.51 (s, 1H), 8.48 (dd, *J* = 8.5, 1.2 Hz, 1H), 8.41 (d, *J* = 7.6 Hz, 1H), 8.33 (d, *J* = 8.9 Hz, 1H), 8.30 (s, 1H), 8.05 (dd, *J* = 3.1, 1.2 Hz, 1H), 7.93 (d, *J* = 8.6 Hz, 1H), 7.89 (d, *J* = 7.9 Hz, 1H), 7.82 – 7.78 (m, 1H), 7.54 – 7.50 (m, 1H), 7.47 – 7.40 (m, 3H), 7.26 – 7.16 (m, 4H), 7.08 (d, *J* = 7.0 Hz, 2H), 7.06 – 7.03 (m, 1H), 7.00 – 6.94 (m, 1H), 6.89 – 6.84 (m, 1H), 6.73 (d, *J* = 13.3 Hz, 2H), 4.63 (q, *J* = 7.3 Hz, 2H), 4.51 (qd, *J* = 7.1, 1.1 Hz, 2H), 1.55 (t, *J* = 7.2 Hz, 3H), 1.47 (t, *J* = 7.2 Hz, 3H) ppm. ¹³C NMR (126 MHz, CDCl₃) δ 169.7, 168.6, 168.1, 165.2, 164.9, 154.2, 153.6, 148.4, 147.8, 146.8, 145.9, 143.7, 141.2, 141.0, 139.3, 138.9, 137.0, 135.7, 132.5, 131.8, 131.2, 131.0, 130.5, 129.3, 128.9, 128.7, 128.4, 127.9, 127.4, 126.9, 126.5, 125.2, 124.8, 124.5, 119.1, 118.9, 118.6, 63.3, 63.1, 14.6, 14.5 ppm. UV-vis (MeCN): λ_{abs} (ε/10⁴ L mol⁻¹ cm⁻¹) 267 (6.7), 284 (5.8), 322 (3.6), 362 (3.2), 497 (0.2) nm. FTIR (solid) (ATR) ν_{max}: 1714 (C=O), 1581, 1568, 1539, 1440, 1396, 1371, 1336, 1296, 1246, 1195, 1151, 1080, 1024, 950, 871, 815, 775, 744, 721, 650, 646, 611, 570, 524, 468 cm⁻¹. HRMS (ES) [M – Cl]⁺ Calc'd for C₅₈H₄₁N₅O₆Ir 1094.2663; Found *m/z* 1094.2704.

5.5.3.12 [Ir(2nq)₂(L⁶)]Cl

Obtained as a red solid (32 % yield). ¹H NMR (500 MHz, CD₃OD) δ 9.66 (s, 1H), 9.15 (s, 1H), 8.92 (s, 1H), 8.67 (d, *J* = 7.7 Hz, 1H), 8.64 (d, *J* = 3.0 Hz, 1H), 8.59 (s, 1H), 8.54 – 8.50 (m, 2H), 8.42 – 8.38 (m, 2H), 8.34 (dd, *J* = 9.9, 2.4 Hz, 1H), 8.14 (d, *J* = 2.0 Hz, 1H), 8.00 – 7.95 (m, 2H), 7.83 (dd, *J* = 6.0, 3.4 Hz, 1H), 7.54 – 7.47 (m, 2H), 7.33 – 7.22 (m, 6H), 7.18 – 7.08 (m, 4H), 7.04 – 6.99 (m, 1H), 6.89 – 6.82 (m, 2H), 6.73 (s, 1H), 4.70 (q, *J* = 7.1 Hz, 2H), 4.59 – 4.54 (m, 2H), 1.62 (t, *J* = 7.1 Hz, 3H), 1.53 (t, *J* = 7.2 Hz, 3H) ppm. ¹⁹F NMR (471 MHz, CD₃OD) δ -102.4 ppm. ¹³C NMR (126 MHz, CDCl₃) δ 169.6, 168.2, 165.1, 164.8, 148.4, 147.9, 145.8, 144.7, 143.6, 141.0, 139.4, 139.0, 135.8, 135.7, 132.5, 131.3, 130.6, 130.6, 130.5, 130.0, 129.4, 129.3, 129.3, 128.7, 128.6, 128.5, 128.4, 128.3, 127.0, 126.7, 126.6, 125.3, 125.0, 124.7, 124.5, 119.3, 118.7, 77.1, 63.3, 63.2, 14.6, 14.5 ppm. UV-vis (MeCN): λ_{abs} (ε/10⁴ L mol⁻¹ cm⁻¹) 268 (8.7), 321 (4.6), 365 (4.5), 497 (0.2) nm. FTIR (solid) (ATR) ν_{max}: 1716 (C=O), 1614, 1600, 1583, 1544, 1519, 1475, 1485, 1440, 1388, 1371, 1350, 1334, 1433, 1276, 1238, 1193, 1166, 1151, 1130, 1101, 1078, 1024, 935, 873, 831, 794, 773, 744, 721, 682, 640, 570, 526, 464, 418 cm⁻¹. HRMS (ES) [M – Cl]⁺ Calc'd for C₅₈H₄₀N₅O₆Flr 1112.2569; Found *m/z* 1112.2621.

5.5.3.13 [Ir(2nq)₂(L⁷)]PF₆

Obtained as a red solid (50 % yield). ¹H NMR (500 MHz, CDCl₃) δ 8.95 (s, 1H), 8.74 (dd, *J* = 8.6, 1.2 Hz, 1H), 8.68 (dd, *J* = 8.6, 1.1 Hz, 1H), 8.64 (s, 1H), 8.53 (d, *J* = 8.1 Hz, 1H), 8.50 (d, *J* = 8.6 Hz, 1H), 8.42 (dd, *J* = 8.6, 1.2 Hz, 1H), 8.33 (s, 1H), 8.25 – 8.21 (m, 2H), 8.11 (s, 1H), 7.98 (dd, *J* = 5.5, 0.9 Hz, 1H), 7.93 (d, *J* = 8.0 Hz, 1H), 7.88 (d, *J* = 8.4 Hz, 1H), 7.82 – 7.79 (m, 1H), 7.58 – 7.53 (m, 1H), 7.53 – 7.48 (m, 2H), 7.40 (ddd, *J* = 7.6, 5.5, 1.1 Hz, 1H), 7.33 (ddd, *J* = 8.2, 6.8, 1.3 Hz, 1H), 7.30 – 7.26 (m, 3H), 7.21 (dd, *J* = 5.5, 4.1 Hz, 1H), 7.19 – 7.15 (m, 2H), 7.06 – 7.02 (m, 1H), 7.01 – 6.95 (m, 2H), 6.82 (s, 1H), 6.65 (s, 1H), 4.73 (q, *J* = 7.2 Hz, 2H), 4.59 (q, *J* = 7.2 Hz, 2H), 4.55 (qd, *J* = 7.1, 1.6 Hz, 2H), 1.65 (t, *J* = 7.2 Hz, 3H), 1.56 (t, *J* = 7.2 Hz, 3H), 1.51 (t, *J* = 7.1 Hz, 3H) ppm. ¹³C NMR (126 MHz, CDCl₃) δ 169.6, 168.4, 165.3, 164.9, 164.1, 157.6, 157.5, 148.6, 148.0, 147.4, 146.7, 146.1, 143.6, 141.5, 141.1, 139.1, 139.0, 138.4, 137.1, 135.8, 135.6, 132.1, 131.8, 131.5, 131.2, 130.6, 130.5, 130.4, 130.0, 129.4, 129.3, 129.0, 129.0, 128.9, 128.6, 128.4, 128.2, 127.9, 127.4, 127.2, 126.9, 126.9, 126.6, 126.5, 126.4, 125.9, 125.1, 125.0, 125.0, 124.6, 124.1, 121.1, 119.5, 118.0, 63.3, 63.2, 62.9, 14.6, 14.5, 14.1 ppm. UV-vis (MeCN): λ_{abs} (ε/10⁴ L mol⁻¹ cm⁻¹) 265 (8.7), 318 (4.0), 360 (4.1), 467 (0.2) nm. FTIR (solid) (ATR) ν_{max}: 1720 (C=O), 1618, 1597, 1583, 1544, 1516, 1458, 1440, 1373, 1354, 1298, 1249, 1197, 1149, 1024, 875, 837 (PF₆⁻), 792, 771, 746, 557 (PF₆⁻), 468, 418 cm⁻¹. HRMS (ES) [M – PF₆]⁺ Calc'd for C₆₁H₄₆N₄O₆Ir 1121.3023; Found *m/z* 1121.3026.

5.5.3.14 [Ir(2nq)₂(L⁸)]PF₆

Obtained as a reddish brown solid (54 % yield). ¹H NMR (500 MHz, CDCl₃) δ 9.56 (s, 1H), 9.01 (s, 1H), 8.74 – 8.68 (m, 4H), 8.44 – 8.39 (m, 2H), 8.38 (s, 1H), 8.29 (s, 1H), 8.14 (s, 1H), 8.07 – 8.04 (m, 1H), 7.97 (d, *J* = 8.1 Hz, 1H), 7.92 (d, *J* = 8.7 Hz, 1H), 7.84 (dd, *J* = 6.1, 3.4 Hz, 1H), 7.65 – 7.61 (m, 1H), 7.53 – 7.46 (m, 2H), 7.35 – 7.27 (m, 4H), 7.23 – 7.18 (m, 1H), 7.16 (d, *J* = 8.3 Hz, 1H), 7.11 – 7.05 (m, 3H), 7.02 – 6.96 (m, 1H), 6.77 (s, 1H), 6.63 (s, 1H), 4.72 (q, *J* = 7.1 Hz, 2H), 4.61 – 4.53 (m, 4H), 1.64 (t, *J* = 7.2 Hz, 3H), 1.55 (t, *J* = 7.2 Hz, 3H), 1.50 (t, *J* = 7.1 Hz, 3H) ppm. ¹³C NMR (126 MHz, CDCl₃) δ 169.5, 168.3, 165.1, 164.7, 163.9, 155.1, 152.5, 149.3, 148.2, 147.2, 147.1, 147.1, 145.8, 143.1, 141.5, 140.4, 139.4, 139.3, 138.6, 135.8, 135.7, 135.3, 132.4, 132.2, 131.8, 131.3, 130.8, 130.8, 130.7, 130.6, 129.7, 129.4, 129.3, 129.1, 128.9, 128.9, 128.7, 128.4, 128.2, 127.3, 127.2, 126.9, 126.7, 126.6, 126.4, 126.2, 125.3, 125.1, 124.9, 124.8, 124.2, 120.8, 112.0, 118.3,

63.4, 63.3, 63.0, 14.5, 14.5, 14.2 ppm. UV-vis (MeCN): λ_{abs} ($\epsilon/10^4 \text{ L mol}^{-1} \text{ cm}^{-1}$) 268 (8.1), 315 (4.1), 359 (4.6), 497 (0.2) nm. FTIR (solid) (ATR) ν_{max} 1718 (C=O), 1618, 1583, 1544, 1458, 1440, 1373, 1354, 1298, 1249, 1197, 1153, 1024, 873, 835 (PF_6^-), 794, 773, 746, 555 (PF_6^-), 468, 418, 412, 406 cm^{-1} . HRMS (ES) $[\text{M} - \text{PF}_6]^+$ Calc'd for $\text{C}_{60}\text{H}_{45}\text{N}_5\text{O}_6\text{Ir}$ 1124.2999; Found m/z 1124.3042.

5.6 References

- 1 Z. Fan, J. Jiang, L. Ai, Z. Shao and S. Liu, *ACS Appl. Mater. Interfaces*, 2019, **11**, 47894–47903.
- 2 W. Zheng, Y. Zhao, Q. Luo, Y. Zhang, K. Wu and F. Wang, *Sci. China Chem.*, 2016, **59**, 1240–1249.
- 3 C. Jin, R. Guan, J. Wu, B. Yuan, L. Wang, J. Huang, H. Wang, L. Ji and H. Chao, *Chem. Commun.*, 2017, **53**, 10374–10377.
- 4 Y. Hisamatsu, S. Kumar and S. Aoki, *Inorg. Chem.*, 2017, **56**, 886–899.
- 5 W. A. Herrmann and C. W. Kohlpaintner, *Angew. Chem. Int. Ed. Engl.*, 1993, **32**, 1524–1544.
- 6 J. Karges, S. Kuang, F. Maschietto, O. Blacque, I. Ciofini, H. Chao and G. Gasser, *Nat. Commun.*, 2020, **11**, 3262.
- 7 Y. Tamura, Y. Hisamatsu, S. Kumar, T. Itoh, K. Sato, R. Kuroda and S. Aoki, *Inorg. Chem.*, 2017, **56**, 812–833.
- 8 E. Baranoff, B. F. E. Curchod, J. Frey, R. Scopelliti, F. Kessler, I. Tavernelli, U. Rothlisberger, M. Grätzel and Md. K. Nazeeruddin, *Inorg. Chem.*, 2012, **51**, 215–224.
- 9 M. Zhang, Y.-Y. Hu, M. Pan, B.-H. Tong, S. Wang, H.-D. Zhou, P. Shi and Q.-F. Zhang, *Dyes Pigments*, 2019, **165**, 11–17.
- 10 X. Liu, Y. Liu, T. Yu, W. Su, Y. Niu, Y. Li, Y. Zhao and H. Zhang, *Inorg. Chem. Front.*, 2018, **5**, 2321–2331.
- 11 Y. Kataoka, K. Okuno, N. Yano, H. Ueda, T. Kawamoto and M. Handa, *J. Photochem. Photobiol. Chem.*, 2018, **358**, 345–355.
- 12 R. Davidson, Y.-T. Hsu, C. Bhagani, D. Yufit and A. Beeby, *Organometallics*, 2017, **36**, 2727–2735.
- 13 M. Xu, R. Zhou, G. Wang, Q. Xiao, W. Du and G. Che, *Inorganica Chim. Acta*, 2008, **361**, 2407–2412.
- 14 P.-L. T. Boudreault, M. A. Esteruelas, A. M. López, E. Oñate, E. Raga and J.-Y. Tsai, *Inorg. Chem.*, 2020, **59**, 15877–15887.
- 15 A. Antiñolo, M. A. Esteruelas, C. García-Yebra, J. Martín, E. Oñate and A. Ramos, *Organometallics*, 2019, **38**, 310–318.
- 16 A. P. Shaw, M. K. Ghosh, K. W. Törnroos, D. S. Wragg, M. Tilset, O. Swang, R. H. Heyn and S. Jakobsen, *Organometallics*, 2012, **31**, 7093–7100.
- 17 A. N. Chernyshev, M. V. Chernysheva, P. Hirva, V. Y. Kukushkin and M. Haukka, *Dalton Trans.*, 2015, **44**, 14523–14531.
- 18 Y. Saito, M. Nishikawa and T. Tsubomura, *New J. Chem.*, 2018, **43**, 277–283.
- 19 N. A. Torbati, A. R. Rezvani, H. Saravani, V. Amani and H. R. Khavasi, *Synth. React. Inorg. Met.-Org. Nano-Met. Chem.*, 2011, **41**, 507–512.
- 20 C. Wu, G. Li, Q.-B. Han, R.-J. Pei, J.-B. Liu, D.-L. Ma and C.-H. Leung, *Dalton Trans.*, 2017, **46**, 17074–17079.
- 21 D. C. Powers, B. L. Anderson and D. G. Nocera, *J. Am. Chem. Soc.*, 2013, **135**, 18876–18883.
- 22 P. G. Hoertz, A. Staniszewski, A. Marton, G. T. Higgins, C. D. Incarvito, A. L. Rheingold and G. J. Meyer, *J. Am. Chem. Soc.*, 2006, **128**, 8234–8245.
- 23 Q. Cao, N. L. Hughes and M. J. Muldoon, *Chem. – Eur. J.*, 2016, **22**, 11982–11985.
- 24 V. Anbalagan and T. S. Srivastava, *Polyhedron*, 2004, **23**, 3173–3183.
- 25 P. Kurz, B. Probst, B. Spingler and R. Alberto, *Eur. J. Inorg. Chem.*, 2006, **2006**, 2966–2974.

- 26 H. Chan, J. B. Ghayche, J. Wei and A. K. Renfrew, *Eur. J. Inorg. Chem.*, 2017, **2017**, 1679–1686.
- 27 J. Zhao, N. Liu, S. Sun, S. Gou, X. Wang, Z. Wang, X. Li and W. Zhang, *J. Inorg. Biochem.*, 2019, **196**, 110684.
- 28 A. E. Ozel, S. Kecel and S. Akyuz, *Vib. Spectrosc.*, 2008, **48**, 238–245.
- 29 A. de Palo, G. La Ganga, F. Nastasi, M. Guelfi, M. Bortoluzzi, G. Pampaloni, F. Puntoriero, S. Campagna and F. Marchetti, *Eur. J. Inorg. Chem.*, 2021, **2021**, 861–869.
- 30 L. Smolko, J. Černák, M. Dušek, J. Miklovič, J. Titiš and R. Boča, *Dalton Trans.*, 2015, **44**, 17565–17571.
- 31 Y. Nishikitani, T. Cho, S. Uchida, S. Nishimura, K. Oyaizu and H. Nishide, *ChemPlusChem*, 2018, **83**, 463–469.
- 32 L. Li, J. Zhang, L. Ma, Z. Zhang, S. Wang, S. Li and G. Zhou, *J. Coord. Chem.*, 2013, **66**, 638–649.
- 33 A. B. Tamayo, S. Garon, T. Sajoto, P. I. Djurovich, I. M. Tsyba, R. Bau and M. E. Thompson, *Inorg. Chem.*, 2005, **44**, 8723–8732.
- 34 B. Liu, L. Lystrom, S. Kilina and W. Sun, *Inorg. Chem.*, 2019, **58**, 476–488.
- 35 B. Liu, L. Lystrom, S. Kilina and W. Sun, *Inorg. Chem.*, 2017, **56**, 5361–5370.
- 36 R. Liu, N. Dandu, J. Chen, Y. Li, Z. Li, S. Liu, C. Wang, S. Kilina, B. Kohler and W. Sun, *J. Phys. Chem. C*, 2014, **118**, 23233–23246.
- 37 Q. Zhao, S. Liu, M. Shi, C. Wang, M. Yu, L. Li, F. Li, T. Yi and C. Huang, *Inorg. Chem.*, 2006, **45**, 6152–6160.
- 38 W. Pfitzinger, *J. Für Prakt. Chem.*, 1885, **33**, 100–100.
- 39 Y. Bass, R. J. Morgan, R. J. Donovan and A. D. Baker, *Synth. Commun.*, 1997, **27**, 2165–2169.
- 40 United States, US5874587A, 1999.
- 41 S. Lamansky, P. Djurovich, D. Murphy, F. Abdel-Razzaq, R. Kwong, I. Tsyba, M. Bortz, B. Mui, R. Bau and M. E. Thompson, *Inorg. Chem.*, 2001, **40**, 1704–1711.
- 42 A. Brouwer, *Pure Appl. Chem.*, 2011, **83**, 2213–2228.
- 43 A. K. Bansal, W. Holzer, A. Penzkofer and T. Tsuboi, *Chem. Phys.*, 2006, **330**, 118–129.
- 44 G. M. Sheldrick, *Acta Crystallogr. Sect. Found. Adv.*, 2015, **71**, 3–8.
- 45 O. V. Dolomanov, L. J. Bourhis, R. J. Gildea, J. A. K. Howard and H. Puschmann, *J. Appl. Crystallogr.*, 2009, **42**, 339–341.
- 46 G. M. Sheldrick, *Acta Crystallogr. Sect. C Struct. Chem.*, 2015, **71**, 3–8.
- 47 A. Shafiee, N. Tavasoli, K. Abdolahnegat, and F. Kamal, *J. Sci. Islam. Repub. Iran*, 1993, **4**, 118.
- 48 M. Ya. Goikhman, I. V. Podeshvo, N. L. Loretsyan, T. D. Anan'eva, R. Yu. Smyslov, T. N. Nekrasova, M. A. Smirnov, E. N. Popova and A. V. Yakimanskii, *Polym. Sci. Ser. B*, 2011, **53**, 89–95.

**Chapter 6 - Rhenium(I) Complexes of *Bis*-
Imine Ligands; 2-(Pyridin-2-yl)Quinoline and
2-(Pyrazin-2-yl)Quinoline.**

6.1 Introduction

The N^N type quinoline ligands synthesised in the previous chapter are, by design, able to chelate to a variety of metals, not just iridium(III). The following chapter explores the coordination chemistry of the N^N type quinolines in tricarbonylrhenium(I) complexes.

6.1.1 Rhenium(I) tricarbonyl chemistry

Rhenium was first described in 1925 by Ida and Walter Noddack and is one of the rarest metals found on Earth¹. It is commonly isolated as a by-product of the molybdenum industry and is not known as a free metal. It occurs as two isotopes ¹⁸⁵Re (37.4%) and ¹⁸⁷Re (62.6%), of which ¹⁸⁷Re is a weak β emitter. Rhenium is a group 7 metal that can be found in a large variety of oxidation states, from +7 to -1². Interest in luminescent species of Re focuses on Re(I) carbonyls. Carbon monoxide is a widely utilised and studied ligand in the field of organometallic chemistry, due to its synergistic bonding to metals³. Bonding of the carbonyl ligand consists of two components. Firstly, a carbon lone pair donation to a vacant metal $d\sigma$ -orbital, and secondly a back donation from a filled metal d-orbital into a vacant CO π^* orbital. In the Re(I) oxidation state, the metal centre is low spin d^6 offering excellent stability and kinetic inertness. Despite this stability, diimine tricarbonyl luminescent complexes can be synthesised rather simply, starting from dirhenium decacarbonyl (Figure 6.1). Rhenium pentacarbonyl halogen species were first synthesised in 1941 by Hieber, Schuh and Fuchs^{4,5}, typically employing the use of CCl₄, although more recently, the dirhenium species have been split using solvents such as CS₂ or DCM instead⁶. The diimine species began to see interest around the 1970s^{7,8} where the focus lay in photocatalysis. Typically, diimine ligand is heated with the pentacarbonyl rhenium species to give the *fac*-[Re(L)(CO)₃X] species (where X = halogen).

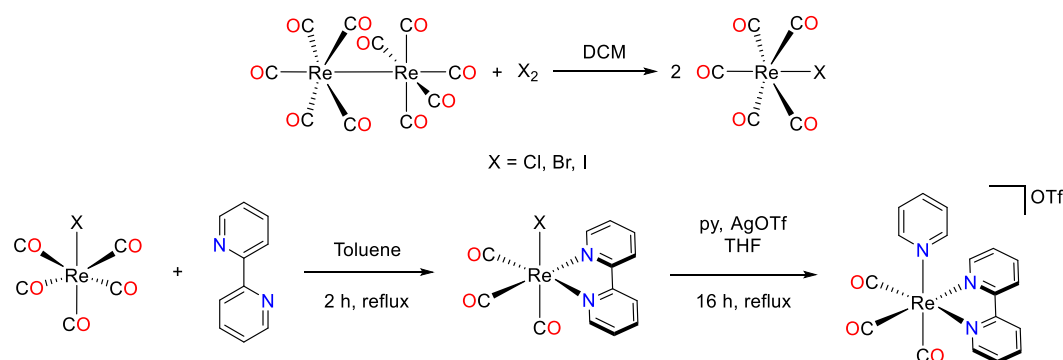


Figure 6.1 – Example of a synthetic pathway towards a luminescent [Re(CO)₃(bpy)(py)]OTf species starting from the dirheniumdecacarbonyl⁹.

Metal complexes, such as $[\text{Re}(\text{CO})_3(\text{N}^{\wedge}\text{N})(\text{L})]^{0/+1}$ can exhibit two types of conformational isomerism, facial and meridional. Due to the strong trans effect of the CO ligands, the first and second coordination of a bidentate ligands occur *cis*-to the axial halide (Figure 6.2), resulting in the *fac*- $[\text{Re}(\text{CO})_3(\text{N}^{\wedge}\text{N})(\text{L})]$ product.

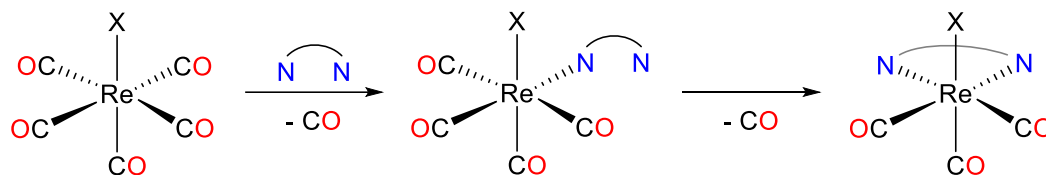


Figure 6.2 – Bidentate ligand coordination, directed by the trans effect resulting in the *fac*- $[\text{Re}(\text{CO})_3(\text{N}^{\wedge}\text{N})(\text{X})]$ product.

The *mer*- $[\text{Re}(\text{CO})_3(\text{bpy})\text{Cl}]$ was first isolated in 2007 by Ishitani *et al*¹⁰. The *fac*- isomer was dissolved in THF and irradiated under a CO atmosphere at 313 nm for three hours to give the meridional isomer in an isolated 33 % yield (Figure 6.3). The authors also noted the rearrangement proceeds under an argon atmosphere at a lower yield. Further irradiation of the meridional complex did not facilitate the reverse isomerisation, but the complex was seen to decompose. The absorption band related to the MLCT transition was bathochromically shifted by 100 nm in DCM solution for the meridional complex. Although in solution, the meridional isomer was non emissive, which the authors attributed to the lower excitation energy of the MLCT state.

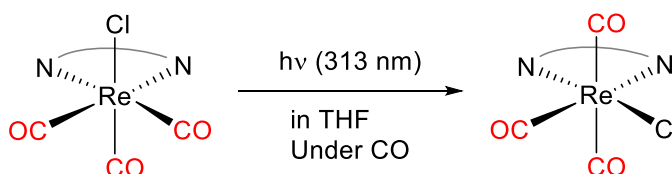


Figure 6.3 - Photoisomerisation of *fac*- $[\text{Re}(\text{CO})_3(\text{bpy})\text{Cl}]$ to form *mer*- $[\text{Re}(\text{CO})_3(\text{bpy})\text{Cl}]$ by Ishitani *et al*. $\text{N}^{\wedge}\text{N}$: bpy.¹⁰

6.1.2 Photonic applications for Re(I) complexes

6.1.2.1 Effects of ligand design

For tricarbonyl complexes, there are two main ways to functionalise; functionalisation of the diimine ligand and substitution of the axial halide. One of the simplest ways to modulate the emission if the diimine is to extend the conjugation, as seen in Figure 6.4. In 1986 Kalyanasundaram¹¹ investigated the nature of the excited state for a variety of $[\text{Re}(\text{CO})_3(\text{N}^{\wedge}\text{N})\text{Cl}]$ complexes. It was

noted that subtle modulation of the bidentate ligands has only a small effect on the absorption and emission wavelengths, with the five ligands tested showing a ca. 20 nm difference between 4,4'-dimethyl-2,2'-bipyridine at 592 nm as the highest energy emitter and 5-chloro-1,10-phenanthroline at 614 nm as the lowest energy emitter. When the ligand was changed to bpz, the absorption and emission underwent a bathochromic shift of ca. 50 nm in comparison to the bpy complex in MeCN solutions (612 vs 660 nm for bpy vs bpz emission respectively), although the emission was considerably shorter and weaker. Cyclic voltammetry measurements were able to show the ligand reduction potentials to lower than the bpy derivatives accounting for the lower energy transition since the ligand π^* orbitals are easier to access. The differences in metal centre oxidation and ligand reduction potentials are of similar values to those seen in other complexes, suggesting the excited state is of MLCT character.

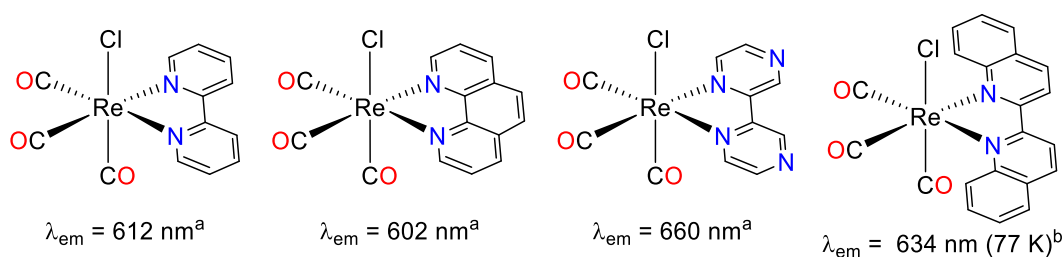


Figure 6.4 – Room temperature emission effects from extended conjugation of the diimine ligands in ^adegassed MeCN.¹¹ ^bBisquinoline complex is non emissive at rt in solution – λ_{em} = 634 nm at 77 K in an EPA glass.^{12,13}

As conjugation is increase towards the 2,2'-biquinoline ligand (Figure 6.4 – far right) the λ_{max} absorption is bathochromically shifted to 435 nm (measured in DMF)¹². Interestingly, the complex isn't emissive at room temperature in a variety of solvents¹³, and it was reasoned by Alberto *et al* that this is due to the small gap between ground and excited state, bringing about an increase in k_{nr} following the energy gap law¹⁴.

L:	$\lambda_{max} / \text{nm}$
Cl ⁻	621 ^a
4-(N,N-dimethylamino)pyridine	610 ^a
4-Aminopyridine	597 ^a
N-Methylimidazole	588 ^a
4-Ethylpyridine	566 ^a
Pyridine	558 ^a
PMe ₃	544 ^a
MeCN	535 ^a

L:	$\lambda_{max} / \text{nm}$
4-Hydroxypyridine	692 ^b
4-Benzylpyridine	686 ^b
Pyridine	675 ^b
4-Cyanopyridine	671 ^b
MeCN	629 ^c

Figure 6.5 – Tuneability of emission from changing the axial ligands. ^a Spectra recorded as PF₆⁻ salts in deoxygenated DCM solution¹⁵. ^b Spectra recorded in MeCN as ClO₄⁻ salts¹⁶. ^c Recorded in EPA as a CF₃SO₃⁻ salt¹³.

The second method for modulating the emission properties is by changing the axial halide for a second coordinating ligand. Caspar and Meyer's paper from 1983 investigated the effects of altering the chloride axial ligand for a variety of different ligands including a series of 4-substituted pyridines on the $[\text{Re}(\text{CO})_3(\text{bpy})(\text{L})]^{0/+1}$ complex (Figure 6.5 - Left)¹⁵. Similarly, the effects of 4-substituted pyridines as the axial ligand were also investigated by Garland *et al* in 2005 on the $[\text{Re}(\text{CO})_3(\text{biq})(\text{L})]^+$ complex (Figure 6.5 - Right). In both examples, the emission is modulated by the properties of the ligand. For the series of 4-substituted pyridines, it is apparent that the stronger the electron withdrawing effects of the moiety in the pyridine 4-position increases the energy of the transition. Interestingly, all complexes of the 2,2'-biquinoline ligands are emissive in solution in comparison to the chloride complex, due to the stronger ligand field effect of the new ligands compared with the chloride. Wrighton *et al* noted when using the MeCN axial ligand, the complex has an emission of 629 nm (recorded in EPA solution)¹³. Both the halo complex and MeCN complex were emissive in low temperature, with spectra recorded at 77 K in EPA glass. For the MeCN there was a small hypsochromic shift to 613 nm. The chloride complex was also emissive at 634 nm. The hypsochromic shift observed at low temperature is known as rigidochromism, and was first described in 1973 by Wrighton and Morse who reported measurements on functionalised phenanthroline ligands in $[\text{Re}(\text{CO})_3(\text{phen})\text{Cl}]$ complexes¹⁷. Measurements were recorded as either an EPA solution or in an EPA glass. The authors noted that in general, the room temperature emission measurements were less intense, they exhibited quantum yields and emissive lifetimes that was one order of magnitude smaller than when recorded at 77 K, due to an increase in k_{nr} . The characteristic $^3\text{MLCT}$ emission also independent of excitation wavelength. Upon cooling the emission spectra shifted *ca.* 50 nm hypsochromically. The emission was also more intense and longer lasting across a variety of different rigid media – EPA (77 K), pure solid and in polyester at room temperature. It was noted this was not a phenomenon caused by photochemical decay since the effects of temperature were reversible for the EPA samples. Raman analysis has since shown the MLCT transition to be mostly $^3\text{MLCT}$, and this is important for the rigidochromic effect^{18–20}, since the phosphorescent lifetime is longer lived than the $^1\text{MLCT}$ counterpart. In the $^3\text{MLCT}$ excited state, the molecular dipole direction is reversed in comparison to the ground state molecule.

In solution, the solvation sphere can reorientate to accommodate the new dipole moment. As the solvent viscosity is increased, the ability to reorientate diminishes causing a destabilisation of the $^3\text{MLCT}$ levels and a hypsochromic shift in emission²¹.

6.1.2.2 Re(I) tricarbonyls as biological imaging molecules

As luminescent imaging dyes, rhenium tricarbonyls offer a big advantage over other metal-based triplet emitters, since the properties of the molecule are based on the different ligands. The diimine ligand largely controls the photophysical properties²², while the axial ligand can be functionalised to control the cellular uptake and localisation²³ with only a minor modulation of the emission wavelength. For example, the work of Massi *et al* has focused on the axial functionalisation of rhenium(I) tetrazolato complexes^{24–26} (see Figure 6.6). Each of the potential imaging agents was tested against multiple live cell lines using two photon excitations to limit cell damage from the laser. The λ_{max} emission from the complexes was around 570 nm. During confocal microscopy studies, the complex **Re-3py** was seen to localise on the lysosomes, whereas the **Re-4py** localises itself within the endoplasmic reticulum, while **Re-4CN** localised in polar lipid droplets.

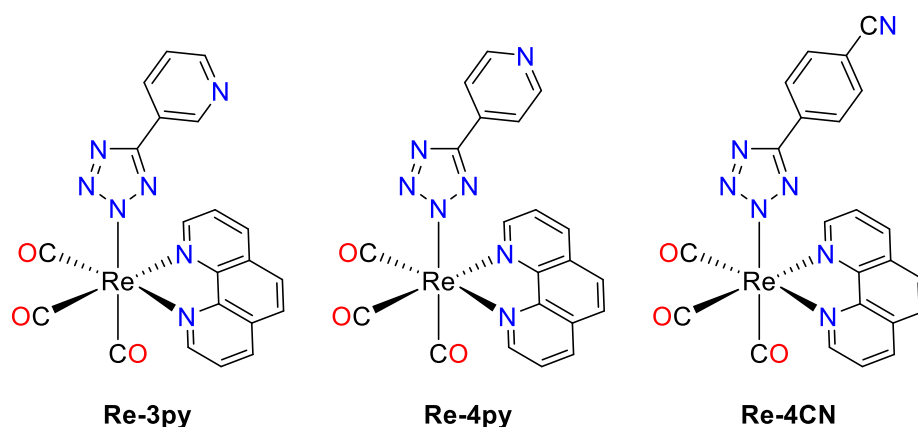


Figure 6.6 - Rhenium (I) imaging agents synthesised by Massi *et al* ^{24–26}.

Rhenium tricarbonyls have also been shown to be effective at treating cancers, through the use of three main pathways; (i) Targeting specific cellular compartments²⁷, (ii) generating $^1\text{O}_2$,²⁸ and finally (iii) photoinduced CO releasing molecules²⁹.

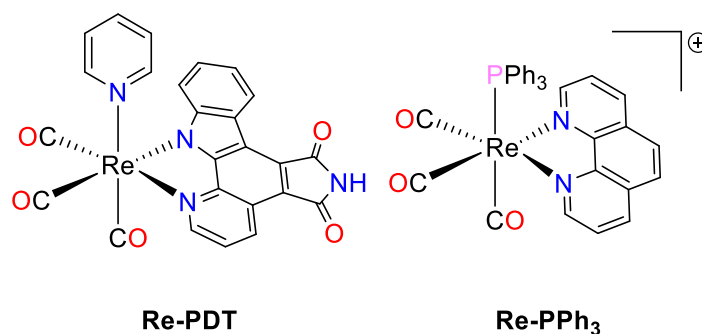


Figure 6.7 - Examples of rhenium(I) tricarbonyls with anticancer properties ^{30,31}

The rhenium indolato complex **Re-PDT** (Figure 6.7) was synthesised by Meggers *et al* as a photo dynamic therapy agent³⁰. **Re-PDT** was incubated with HeLa cells in the dark and showed no effect on cell survivability with an EC₅₀ at 100 μM. When the cell lines were treated with **Re-PDT** and illuminated at λ_{ex} > 505 nm, the cell survivability dropped dramatically, with the EC₅₀ at 0.1 μM. Confocal microscopy studies revealed the complex to locate within the cell membrane, and the generation of ¹O₂ responsible for the cell death.

The use of CO as a cause of cell apoptosis has been known about for over a century³². The targeted delivery and administration of CO to cancerous cells is possible through the use metal carbonyl complexes³³. The complex **Re-PPh₃** (Figure 6.7), synthesised by Mascharak *et al*³¹, exhibits excellent release of CO; with a *k*_(CO) rate of 1.59 ± 0.02 min⁻¹ (4.5 × 10⁻⁴ M MeCN solution, λ_{ex} = 370 nm). The complex was shown by confocal microscopy to localise in the nucleus as well as the cytosol. When the complex releases a CO molecule, the MLCT transition disappears and the ¹LC transitions remain.

6.1.2.3 Re(I) CO₂ reduction catalysis

The use of rhenium tricarbonyls as a photocatalyst was first reported in 1983 by Ziesel *et al*³⁴, who showed that [Re(CO)₃(L)X] (Where X = Cl⁻ or Br⁻; L = bpy or phen) was able to reduce CO₂ to CO when irradiated. The direct reduction of CO₂ towards CO₂⁻ requires a large potential, +1.9 V (vs NHE), with an overpotential of +0.6 V required for the rapid reduction^{35,36}. This high potential can be overcome by photocatalytic processes invoking multielectron, multi-proton reductions for the formation of chemically useful reactants such as formic acid and carbon monoxide (Figure 6.8). The reduction potentials for the two proton, two electron reductions of CO₂ towards the CO and H₂CO₂ are -0.77 and -0.85 V (Vs SCE) respectively³⁵.

Upon excitation, in the presence of a sacrificial amine – such as Et₃N – the excited state can be quenched to form the anion radical [Re(CO)₃(L[•])X]⁻ followed by the loss of the axial halide, forming the solvato complex. The solvato ligand can be replaced by a hydride before a CO₂ insertion into the Re–H bond forming the formate. The formation of CO is postulated³⁷ to go via a metal carboxylate intermediate, which could be protonated to yield H₂O and [Re(CO)₄(L)]⁺, before the halide substitutes into the axial position, returning to the original [Re(CO)₃(L)X] species.

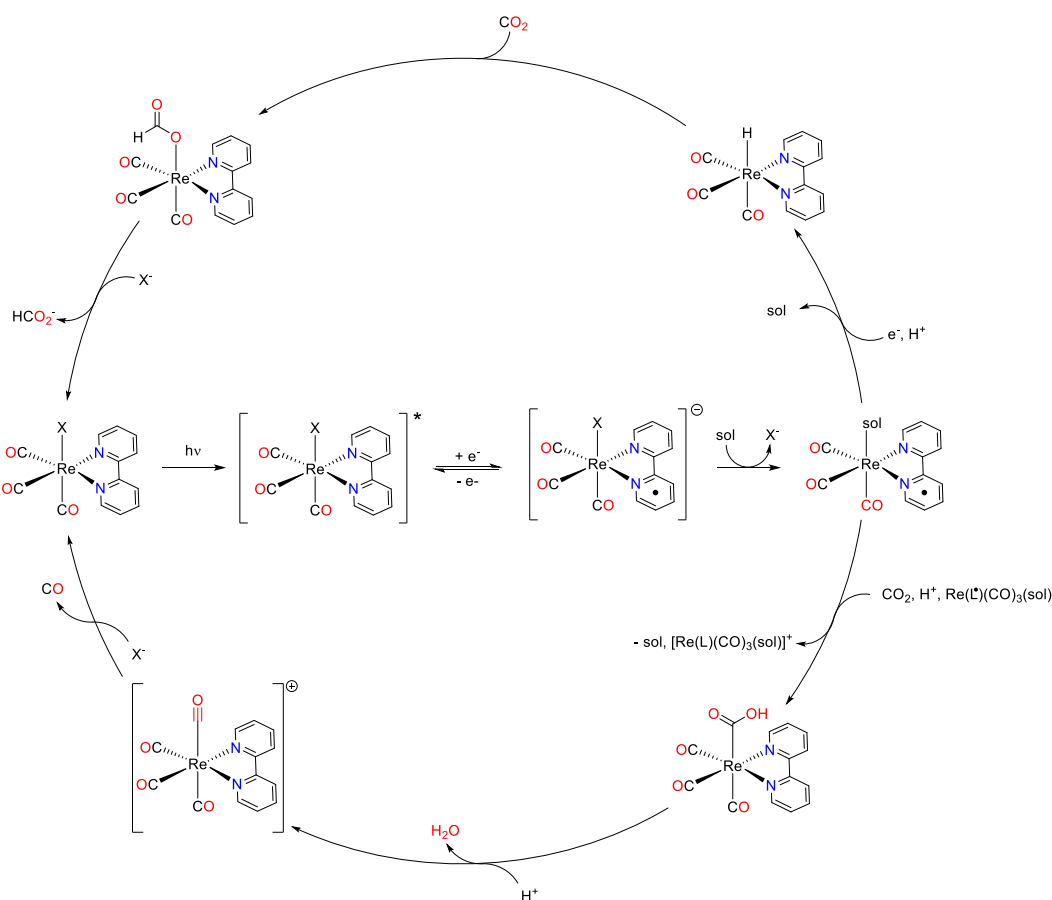


Figure 6.8 – Photocatalytic multi-proton, multielectron reduction of CO₂ ^{36,38}

6.2 Aims of the chapter.

This chapter sets out to synthesise and characterise a set of novel *fac*-tricarbonyl(*bis*-imine)rhenium(I) complexes based around the substituted 2-(pyridin-2-yl)quinoline and 2-(pyrazin-2-yl)quinoline ligand framework from Chapter 5 and investigate the emissive properties of the complexes. A total of eight novel neutral rhenium complexes have been isolated and characterised.

6.3 Results and Discussions

6.3.1 Rhenium tricarbonyl complex synthesis and characterisation

Using the N^N quinoline ligands synthesised in Chapter 5, neutral diimine Re(I) complexes were synthesised according to literature procedures³⁹ (Figure 6.9). Equimolar amounts of pentacarbonylbromorhenium(I) and ligand **L**¹⁻⁸ were heated in toluene overnight producing a red precipitate. The solids were collected on a sinter and washed with toluene before recrystallised from DCM by diethyl ether addition. Complexes were then characterised via ¹H, ¹³C{¹H} and ¹⁹F{¹H} NMR, UV-vis absorption, luminescence, and IR spectroscopies. As expected with the addition of the bidentate ligand, the resultant complex forms in only the facial isomer, due to the strong trans effect of the CO ligands.

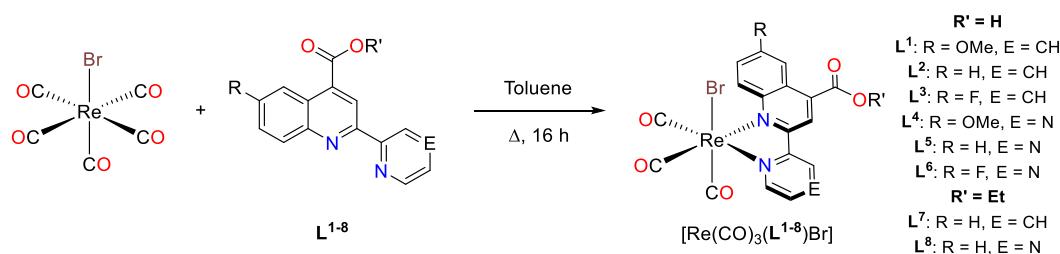


Figure 6.9 – Synthetic route for rhenium tricarbonyl complexes and the complexes isolated and characterised in this work.

6.3.1.1 X-Ray crystallography of [Re(CO)₃(L⁷)Br]

Single crystal diffraction data and geometry refinements were carried out by the National Crystallographic Service at Southampton University. A single red blocked shaped crystal of [Re(CO)₃(L⁷)Br] was successfully grown by vapour diffusion of diisopropyl ether into a chloroform solution of the complex (Figure 6.10). The complex has two unique molecules within the asymmetric unit with each displaying expected *fac*-tricarbonyl coordination around the rhenium core. Each Re centre displays a distorted octahedral geometry, with the trans bond angles ranging between 169.45 ° and 179.60 °, a minor deviation from the ideal octahedral arrangement. The ligand is coordinated via the nitrogen atoms of the 2-(pyrid-2-yl)quinoline unit. The axial positions are filled by the Br and a CO. Bond lengths and bond angles seen around the Re(I) core (Table 6.1) are typical for the coordination sphere for this type of complex.^{40,41} Ligand torsion angle shows a lower degree of strain than in the examples seen in Chapters 4 and Chapter 5 where 2-(Naphthyl)quinolines coordinate to Iridium.

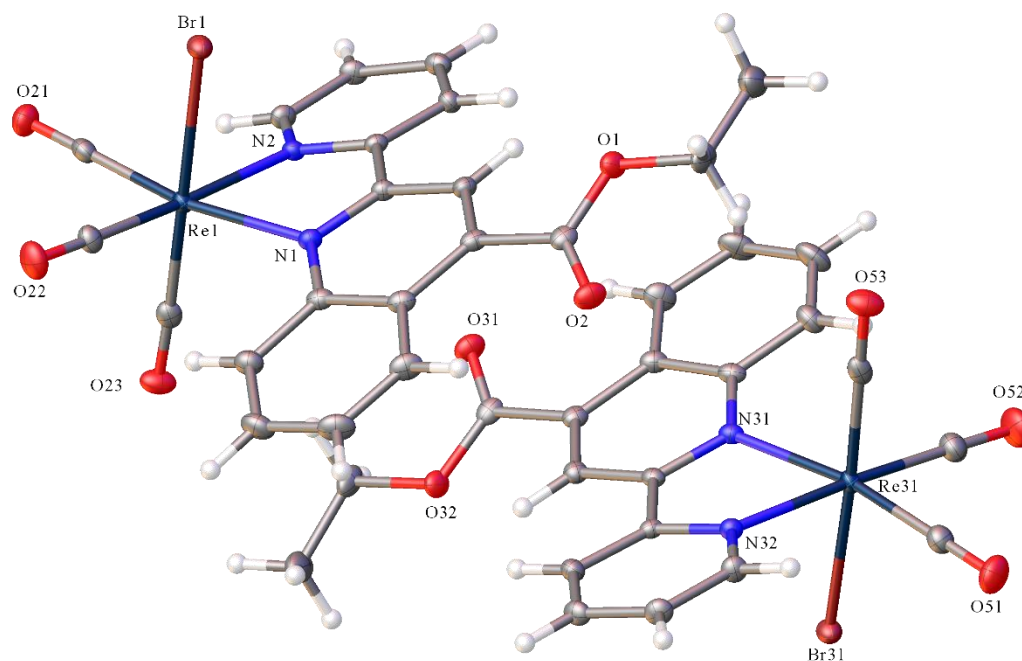


Figure 6.10 – X-ray structure of $[\text{Re}(\text{CO})_3(\text{L}^7)\text{Br}] - \text{C}_{20}\text{H}_{14}\text{BrN}_2\text{O}_5\text{Re}$, $M_r = 628.44$, triclinic, $P-1$ (No. 2), $a = 8.37400(10) \text{ \AA}$, $b = 13.6124(2) \text{ \AA}$, $c = 18.4796(2) \text{ \AA}$, $\alpha = 107.9060(10)^\circ$, $\beta = 94.6350(10)^\circ$, $\gamma = 102.7330(10)^\circ$, $V = 1929.95(4) \text{ \AA}^3$, $T = 100(2) \text{ K}$, $Z = 4$, $Z' = 2$, $\mu(\text{MoK}\alpha) = 8.402 \text{ mm}^{-1}$, 85283 reflections measured, 9971 unique ($R_{int} = 0.0332$) which were used in all calculations. The final wR_2 was 0.0379 (all data) and R_1 was 0.0170 ($I > 2(I)$)

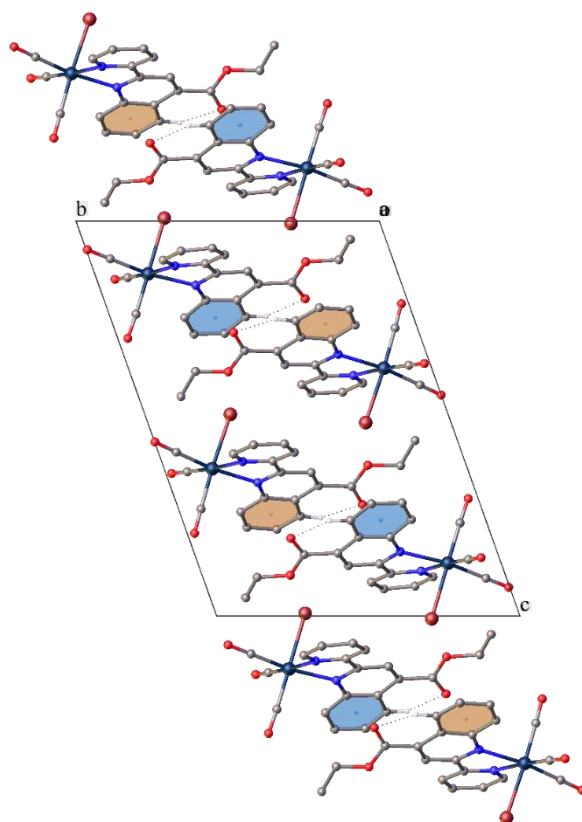


Figure 6.11 – Packing diagram for $[\text{Re}(\text{CO})_3(\text{L}^7)\text{Br}]$, also showing two separate $\pi-\pi$ interactions of aromatic rings highlighted in blue and red.

Bond Length (Å)					Bond Angle (°)			
Re(1)	Br(1)	2.6274(2)			N(1)	Re(1)	Br(1)	84.01(5)
Re(1)	N(1)	2.2097(18)			N(2)	Re(1)	Br(1)	84.65(5)
Re(1)	N(2)	2.1606(17)			N(2)	Re(1)	N(1)	74.14(7)
Re(1)	C(21)	1.921(2)			C(21)	Re(1)	Br(1)	90.06(7)
Re(1)	C(22)	1.912(2)			C(21)	Re(1)	N(1)	169.45(8)
Re(1)	C(23)	1.908(2)			C(21)	Re(1)	N(2)	96.66(8)
Re(31)	Br(31)	2.6240(2)			C(22)	Re(1)	Br(1)	89.32(7)
Re(31)	N(31)	2.2109(18)			C(22)	Re(1)	N(1)	101.94(8)
Re(31)	N(32)	2.1550(18)			C(22)	Re(1)	N(2)	173.10(8)
Re(31)	C(51)	1.925(2)			C(22)	Re(1)	C(21)	86.67(9)
Re(31)	C(52)	1.915(2)			C(23)	Re(1)	Br(1)	179.60(7)
Re(31)	C(53)	1.911(2)			C(23)	Re(1)	N(1)	96.38(8)
Torsion Angles (°)					C(23)	Re(1)	N(2)	95.52(8)
N(1)	C(9)	C(10)	N(2)	5.4(3)	C(23)	Re(1)	C(21)	89.56(9)
N(31)	C(39)	C(40)	N(32)	-3.2(3)	C(23)	Re(1)	C(22)	90.53(9)
					N(31)	Re(31)	Br(31)	83.29(5)
					N(32)	Re(31)	Br(31)	84.06(5)
					N(32)	Re(31)	N(31)	74.51(7)
					C(51)	Re(31)	Br(31)	91.49(7)
					C(51)	Re(31)	N(31)	170.05(8)
					C(51)	Re(31)	N(32)	96.58(8)
					C(52)	Re(31)	Br(31)	90.39(7)
					C(52)	Re(31)	N(31)	103.21(9)
					C(52)	Re(31)	N(32)	174.19(9)
					C(52)	Re(31)	C(51)	85.23(10)
					C(53)	Re(31)	Br(31)	177.02(7)
					C(53)	Re(31)	N(31)	93.87(8)
					C(53)	Re(31)	N(32)	94.33(8)
					C(53)	Re(31)	C(51)	91.18(10)
					C(53)	Re(31)	C(52)	91.14(10)

Table 6.1 - Selected bond lengths, bond angles and ligand torsion angles obtained from crystallographic data from complex $[\text{Re}(\text{CO})_3(\text{L}^7)\text{Br}]$.

6.3.1.2 NMR and FTIR characterisation

Upon complexation, each ^1H NMR resonance has been shifted downfield. For example, in the spectra comparing L^2 with $[\text{Re}(\text{CO})_3(\text{L}^2)\text{Br}]$ (both recorded in d_6 -DMSO) the range of the resonance is between 7.5 ppm and 9.0 ppm in the free ligand. Upon complexation, this shifts to between 7.8 ppm and 9.2 ppm, which is in agreement with other facial isomers¹⁰. This is due to the large inductive effect of the 5d metal centre, as well as having *trans* CO of the facial isomer. More significantly, a 2H multiplet at 8.75 ppm in L^2 has been resolved into two doublets. A total of four doublets are now seen in the spectra, with two being significantly shifted downfield to 9.07 and 9.24 ppm. ^1H - ^1H COSY Correlation spectroscopy of $[\text{Re}(\text{CO})_3(\text{L}^8)\text{Br}]$ provides us with further evidence towards assignment (Figure 6.12).

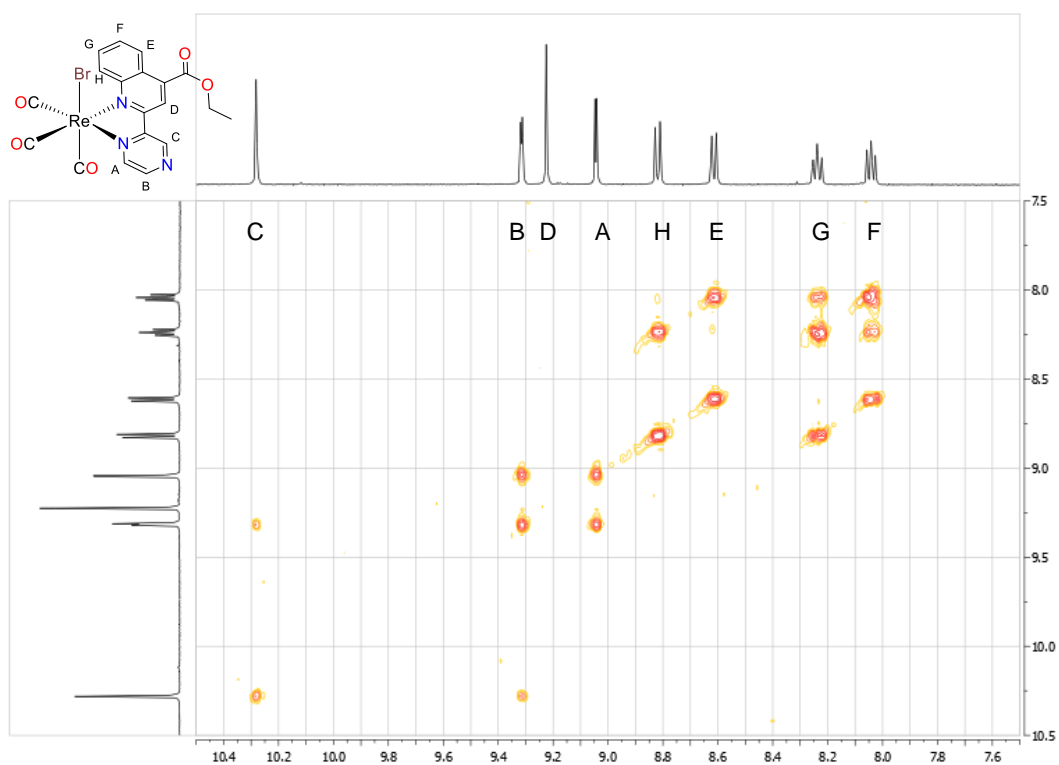


Figure 6.12 - 2D ^1H - ^1H COSY Correlation spectra of $[\text{Re}(\text{CO})_3(\text{L}^8)\text{Br}]$ (Full aromatic region shown)

Protons on the non-heterocyclic ring of the quinoline can all be seen between ca. 8.0 and 8.8 ppm. The single environment on the quinoline is seen at 9.2 ppm in the example above. The pyrazine environments sit between ca. 9.0 and 10.3 ppm. The singlet at 10.3 ppm shows correlation to one of the doublets, despite seeing no splitting in the 1D spectrum. This has been assigned as the $^4J_{\text{HH}}$ *meta*-coupling

as was seen in the free ligand. The larger shifts of the pyrazine resonances suggest a stronger interaction between the rhenium atom and the pyrazine coordinating nitrogen than for the quinoline nitrogen. This conjecture is backed up by the solid-state structure (Table 6.1) where the Re-N bond lengths are elongated for the quinoline ring compared with the pyridine counterpart, with 2.2097(18) and 2.2109(18) Å for the two Re – quinoline bonds in the asymmetric unit and 2.1606(17) and 2.1550(18) Å for the two pyridine - Re bonds respectively. Re-N bond angles are in agreement with those seen in the literature for quinoline and pyridine groups.^{42–44} With regards to the ¹³C{¹H} NMR spectra, when the results were recorded in *d*₆-acetone, three weak resonances were present between 188.0 and 198.4 ppm. These are assigned to the M-CO resonances⁴⁵. (Table 6.2). There appears to be no difference in the shifts when comparing the pyridine or pyrazine ligands. It is worth noting how weak these signals are, and for the [Re(CO)₃(L⁸)Br] spectra, measurements were made in both *d*₆-acetone and *d*₆-DMSO, running 1024 scans on a 500 MHz NMR spectrometer and both spectra the carbonyl peaks were not observable.

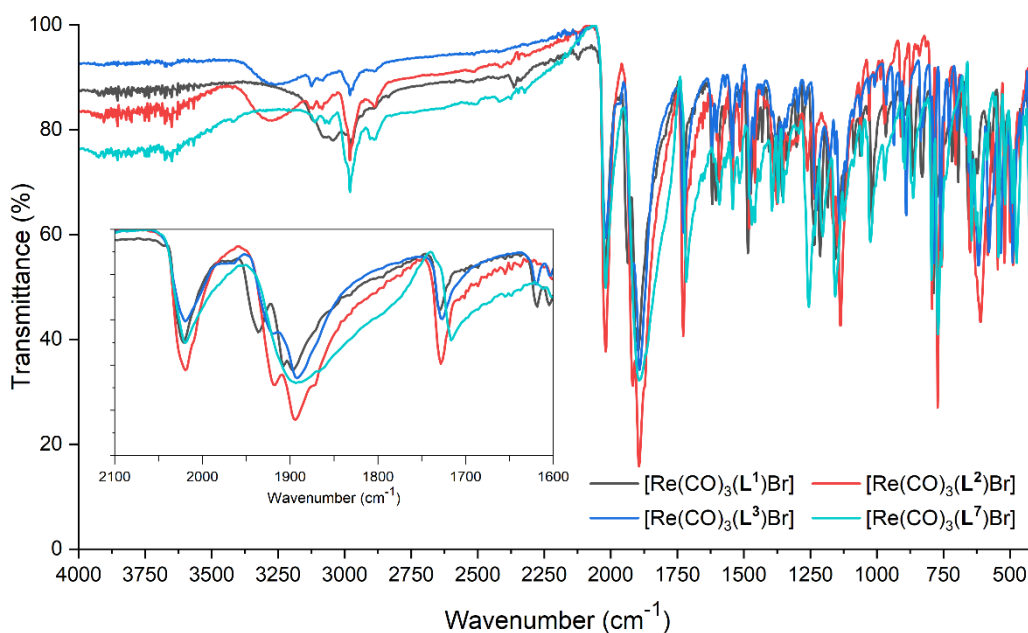


Figure 6.13 - FTIR spectra showing rhenium complexes of 2-(pyridin-2-yl)quinoline ligands. Inserts – expanded look at the carbonyl region.

The FTIR spectra for the eight [Re(CO)₃(L)Br] complexes were recorded, and the carbonyl stretching bands tabulated (Table 6.2). An example of the spectra can be seen in Figure 6.13. The organic carbonyl of the ligand carboxylic acids or esters groups appears between ca. 1710 – 1730 cm⁻¹, this is a small shift from the free ligand of around 30 cm⁻¹. The metal carbonyls appear as two features. A strong

band at $\sim 2020\text{ cm}^{-1}$ corresponds to the $A'(1)$ stretching mode, while the broader features between $1890 - 1920\text{ cm}^{-1}$ are assigned to the $A'(2)$ and A'' modes of the C_s symmetrical complexes. These second peaks are closely matched in energy and on some of the spectra taken are indistinguishable⁴⁶⁻⁴⁹. It is expected that the weaker coordinating pyrazine complexes would result in less π -backbonding between the Re centre and the carbonyl groups, shifting the absorbance bands to a higher energy, however if this is happening it is below the resolution of the spectrometer, 4 cm^{-1} .

Complex	$^{13}\text{C}\{^1\text{H}\}_{\text{CO}}, \delta / \text{ppm}^a$	$\nu_{\text{CO}} / \text{cm}^{-1}$
$[\text{Re}(\text{CO})_3(\text{L}^1)\text{Br}]$	198.4, 197.9, 189.9	2021, 1907, 1896
$[\text{Re}(\text{CO})_3(\text{L}^2)\text{Br}]$	198.4, 197.9, 189.7	2019, 1917, 1894
$[\text{Re}(\text{CO})_3(\text{L}^3)\text{Br}]$	198.2, 197.8, 189.6	2019, 1919(sh), 1891(br)
$[\text{Re}(\text{CO})_3(\text{L}^4)\text{Br}]$	198.2, 197.1, 188.0	2019, 1917, 1892
$[\text{Re}(\text{CO})_3(\text{L}^5)\text{Br}]$	198.2, 197.0, 188.7	2026, 1906(br)
$[\text{Re}(\text{CO})_3(\text{L}^6)\text{Br}]$	198.1, 197.0, 188.6	2018, 1915, 1895
$[\text{Re}(\text{CO})_3(\text{L}^7)\text{Br}]$	198.4, 197.9, 189.7	2020, 1893(br)
$[\text{Re}(\text{CO})_3(\text{L}^8)\text{Br}]$		2026, 1923, 1898

Table 6.2 – Metal carbonyl $^{13}\text{C}\{^1\text{H}\}$ NMR spectrum shifts and FTIR peaks assigned to Metal carbonyls for $[\text{Re}(\text{CO})_3(\text{L}^{1-8})\text{Br}]$ complexes. ^aSpectra obtained in d_6 -acetone.

6.3.2 Electrochemical properties

Complex	Oxidation	Reduction	
	$E_{\text{p}^{\text{ox}}} / \text{V}$	$E_{(\text{red } 1)} / \text{V}$	$E_{(\text{red } 2)} / \text{V}$
$[\text{Re}(\text{CO})_3(\text{L}^1)\text{Br}]$	+1.49	-1.30 ^a	--
$[\text{Re}(\text{CO})_3(\text{L}^2)\text{Br}]$	+1.50	-1.20 ^a	--
$[\text{Re}(\text{CO})_3(\text{L}^3)\text{Br}]$	+1.55, +1.43	-1.22 ^a	--
$[\text{Re}(\text{CO})_3(\text{L}^4)\text{Br}]$	+1.62	-1.02 ^a	-0.55 ^a
$[\text{Re}(\text{CO})_3(\text{L}^5)\text{Br}]$	+1.58	-1.00 ^b	-0.53 ^b
$[\text{Re}(\text{CO})_3(\text{L}^6)\text{Br}]$	+1.67	-0.99 ^b	-0.46 ^b
$[\text{Re}(\text{CO})_3(\text{L}^7)\text{Br}]$	+1.50	-0.87 ^a	--

The	$[\text{Re}(\text{CO})_3(\text{L}^{\text{a}})\text{Br}]$	+1.63	-0.99 ^a	-0.70 ^a
-----	--	-------	--------------------	--------------------

redox potential of the eight rhenium(I) complexes has been studied by cyclic voltammetry with potentials listed below in Table 6.3. Measurements were made in deoxygenated DCM using a platinum disc electrode (scan rate $\nu = 200 \text{ mV s}^{-1}$, $1 \times 10^{-3} \text{ M}$ solutions, 0.1 M $[\text{NBu}_4][\text{PF}_6]$ as a supporting electrolyte).

Table 6.3 - Electrochemical properties of the rhenium(I) complexes obtained from cyclic voltammetry. Potentials measured in deaerated DCM solutions at 200 mVs^{-1} with 0.1 M $[\text{NBu}_4][\text{PF}_6]$ as supporting electrolyte calibrated with Fc/Fc^+ ; ^a $E_{1/2}$ values for fully reversible process; ^b Cathodic peak of irreversible process.

Each complex exhibits a single irreversible oxidation centred around *ca.* +1.5 V and *ca.* +1.6 V for the pyridine and pyrazine complexes, respectively. This oxidation is typically assigned to the one electron oxidation of $\text{Re}^{\text{I}} \rightarrow \text{Re}^{\text{II}}$.^{50,51} The molecule then undergoes a fast intramolecular Re – ligand redox process where typically the halide undergoes an exchange with the solvent^{52–54}. In this case, however, the solvent used is not coordinating, and as such it is likely there is an electrochemically mediated chemical process happening preventing the reversible reaction. The differences between the two ligand systems can likely be ascribed towards pyrazine being a weaker donor, meaning the Re^{1+} is less readily oxidised. The substitution around the quinoline in general follows the same patterns as seen in Chapter 4; the electron donating methoxy substituted quinolines tend to give the lowest oxidation potential, while the electron withdrawing fluoro substituted quinoline lead to a higher oxidation potential.

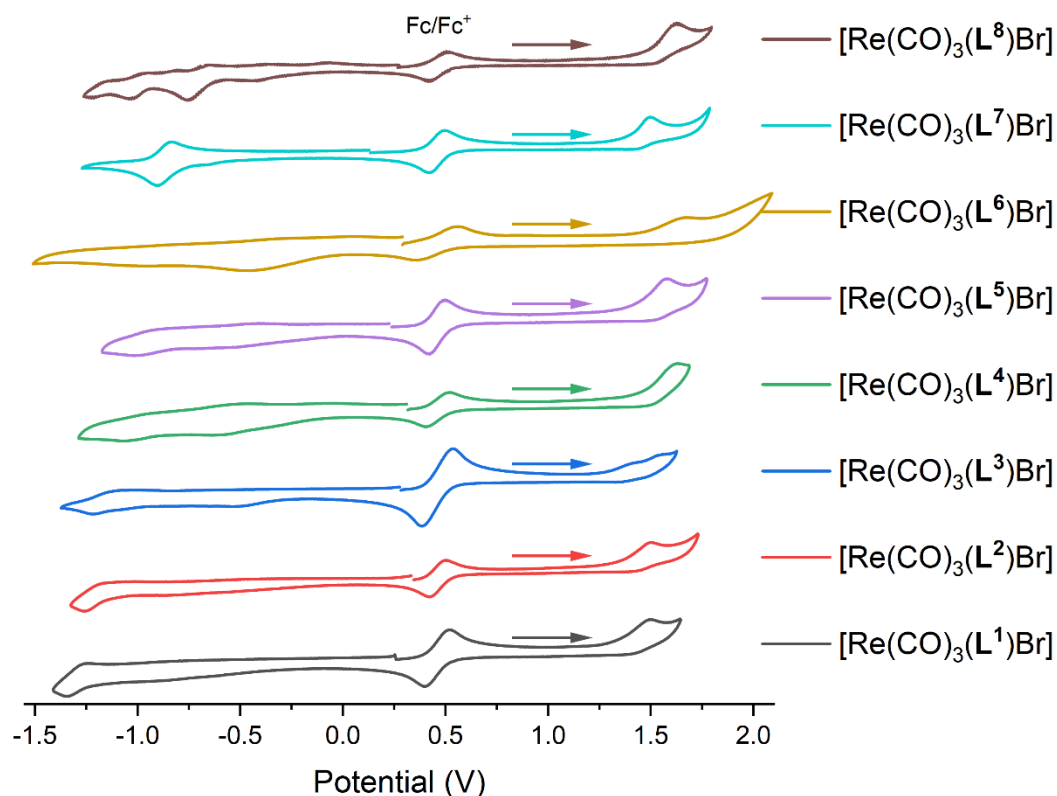


Figure 6.14 - Cyclic Voltammograms. $[\text{Re}(\text{CO})_3(\text{L}^{1-8})\text{Br}]$. All potentials measured in deoxygenated DCM solutions at 200 mVs^{-1} with $0.1 \text{ M } [\text{NBu}_4][\text{PF}_6]$ as supporting electrolyte calibrated with Fc/Fc^+ .

All complexes exhibit a reversible reduction around -1.2 V (pyridyl) or -1.0 V (pyrazinyl), similar to the work of Fontecave *et al*⁵⁵. The reduction shows anodic shift in comparison to the archetypal $[\text{Re}(\text{CO})_3(\text{bpy})\text{Cl}]$, brought about by the extended conjugation offered by the quinoline ring, suggesting the process is a ligand-based reduction. A second reduction is found upon the pyrazine based ligand complexes, *ca.* -0.5 V , and corresponds to a pyrazine based reduction⁵⁶, occurring at the second imine position.

6.3.3 Rhenium complex absorption and emission properties

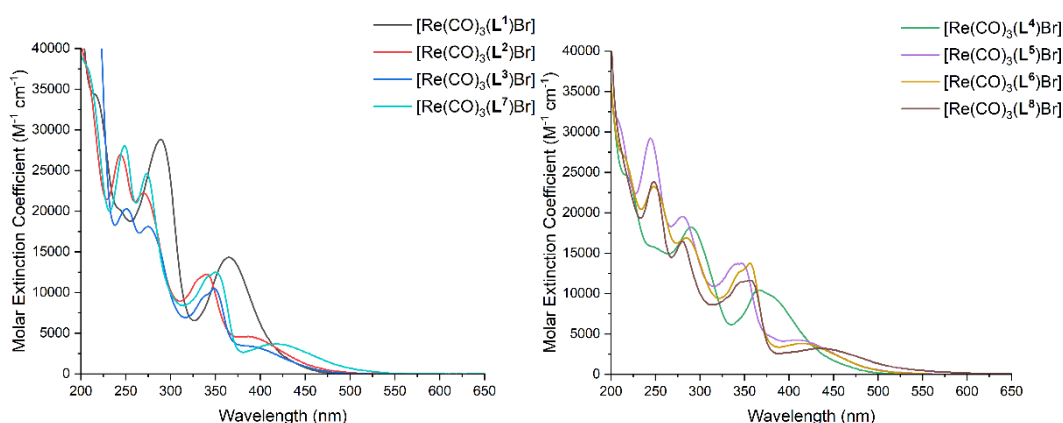


Figure 6.15 - Absorption spectra for rhenium complexes obtained in MeCN solution at *ca.* 10^{-5} M.

Absorption spectra for the rhenium tricarbonyl bromide complex of L^{1-8} can be seen above in Figure 6.15. Spectra were recorded in aerated acetonitrile at *ca.* 10^{-5} M. Between 250 nm and around 370 nm, spectra appear very similar to the free ligand absorbances. These strong absorbances are the result of spin allowed ligand centred $^1\pi-\pi^*$ transition. This region is also likely to contain contributions from $^1n-\pi^*$ transitions from the heterocyclic components. From around 370 nm onwards there is a weaker transition not present in the ligand spectra. This absorbance is assigned to the spin allowed 1MLCT absorbance with the spin forbidden 3MLCT processes tailing off towards 550 nm. Between similar functionalised pyridine or pyrazine-based ligands there is a *ca.* 20 nm bathochromic shift in the pyrazine-based ligands. Similarly, there is a 29 nm shift between the pyridine complexes of L^2 and L^7 , and a 24 nm shift between the pyrazine complexes of L^5 and L^8 , with the ester functionalised ligands inducing the bathochromic shift. Quinoline functionalisation shows a 30 – 40 nm bathochromic shift between the electron donating methoxy- functionalised quinolines to the electron withdrawing fluoro- functionalised quinoline complexes. Interestingly, the Methoxy substituted complexes, $[Re(CO)_3(L^1)Br]$ and $[Re(CO)_3(L^4)Br]$, the lowest energy transition appears to be from the mixing of the 1LC and 1MLCT states, making the absorption broader and with a larger ϵ than the differently substituted quinolines.

Complex	$\lambda_{abs} (\epsilon / 10^4 M^{-1} cm^{-1}) / nm^a$	λ_{em} / nm^b
$[Re(CO)_3(L^1)Br]$	364 (1.4), 289 (2.9), 214 (3.4)	662

[Re(CO) ₃ (L ²)Br]	390 (0.5), 339 (1.2), 269 (2.2), 243 (2.7)	681
[Re(CO) ₃ (L ³)Br]	395 (0.3), 348 (1.0), 339 (0.9), 274 (1.8), 250 (2.0)	678
[Re(CO) ₃ (L ⁴)Br]	381 (1.0), 366 (1.0), 289 (1.8), 246 (1.6), 217 (2.4)	663
[Re(CO) ₃ (L ⁵)Br]	413 (0.4), 343 (1.4), 280 (1.9), 243 (2.9), 205 (3.2)	684
[Re(CO) ₃ (L ⁶)Br]	418 (0.4), 356 (1.4), 343 (1.3), 285 (1.7), 248 (2.3), 212 (2.7)	690
[Re(CO) ₃ (L ⁷)Br]	419 (0.4), 350 (1.2), 273 (2.5), 248 (2.8), 206 (3.8)	677
[Re(CO) ₃ (L ⁸)Br]	437 (0.3), 357 (1.2), 346 (1.1), 280 (1.6), 248 (2.4)	668

Table 6.4 - ^a All measurements obtained at room temperature in aerated MeCN *ca.* 1x10⁻⁵ M. ^b Measurements obtained in the solid state, λ_{ex} = 420 nm.

Emission measurements were attempted in MeCN solutions at *ca.* 10⁻⁶, 10⁻⁵ and 10⁻³ M, but the complexes were not emissive in solution at these concentrations, similar to the [Re(CO)₃(biq)Cl] complexes discussed in section 6.1.2.1. The Re complexes were emissive however in the solid state, and the emission spectra can be seen in Figure 6.16. The pyridine complexes all exhibit a single broad featureless emission peak, centred around *ca.* 680 nm, with [Re(CO)₃(L¹)Br] slightly higher energy. The emission peak is typical for ³MLCT emission. The pyrazine complexes also show a single featureless emission profile, that varies dependent upon ligand substitution. With the methoxy complex at higher energy, and the fluoro complex at the lowest energy. The pyrazines emission is also at a lower energy than the same substituted pyridine complexes, which follows the patterns seen in the cyclic voltammetry measurements where the pyrazine complexes have a lower reduction potentials suggesting a lower lying LUMO⁵⁷.

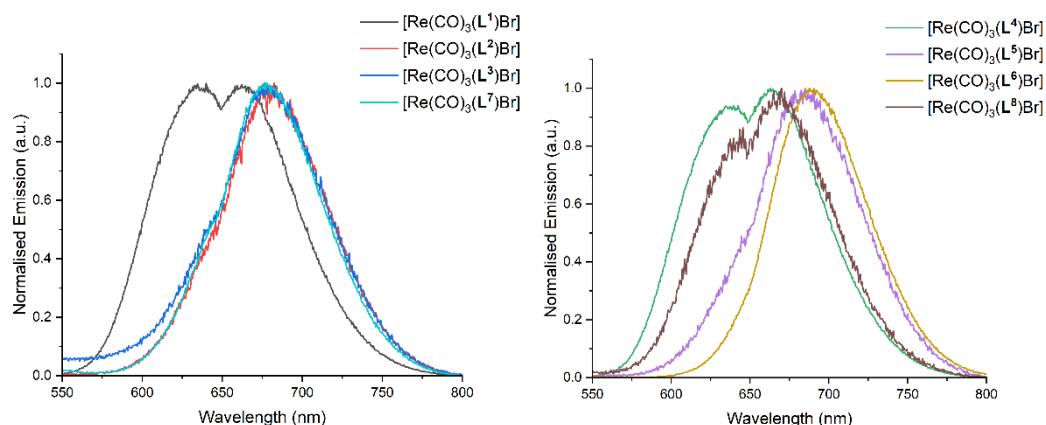


Figure 6.16 - Emission spectra for rhenium Complexes. Spectra obtained from the solid state. $\lambda_{ex} = 420$ nm.

6.4 Conclusions

This Chapter has shown eight novel organometallic *fac*-tricarbonyl(L^x) bromorhenium(I) complexes have been isolated and characterised via 1H , $^{19}F\{^1H\}$, $^{13}C\{^1H\}$ NMR, HRMS, FTIR, absorption, emission spectroscopies, as well as via cyclic voltammetry. One example was also able to be grown as a single crystal, allowing for the collection, and solving of x-ray diffraction data revealing the solid-state structure. The resultant red organometallic complexes showed red emission in the solid state, with the quinoline pyrazine complexes displaying a degree of tuneability depending upon the ligand substitution. Pyrazine complexes were also shown to have a lower reduction potential from the cyclic voltammetry results, which together suggests the lowering of the LUMO levels from the addition of the second imine position in the ligand ring.

6.5 Experimental

All reactions were performed with the use of vacuum line and Schlenk techniques. Reagents were commercial grade and were used without further purification. ^1H , ^{19}F and ^{13}C spectra were recorded on a Bruker fourier 300, dpx 400, or avance 500 MHz spectrometer, and were recorded in d_6 -acetone or d_6 -DMSO solutions. ^1H and $^{13}\text{C}\{^1\text{H}\}$ NMR chemical shifts (δ) were determined relative to internal tetramethylsilane, $\text{Si}(\text{CH}_3)_4$ and are given in ppm. Low-resolution mass spectra were obtained by the staff at Cardiff University. High-resolution mass spectra were carried out by the staff at Cardiff University. All photophysical data was obtained on a JobinYvon-Horiba Fluorolog-3 spectrometer fitted with a JY TBX picosecond photodetection module in MeCN solutions. Emission spectra were uncorrected and excitation spectra were instrument corrected. The pulsed source was a Nano-LED configured for 295, 372 or 459 nm output operating at 500 kHz or 1 MHz. Luminescence lifetime profiles were obtained using the JobinYvon–Horiba FluoroHub single photon counting module and the data fits yielded the lifetime values using the provided DAS6 deconvolution software. IR spectra were recorded on an ATR equipped Shimadzu IRAffinity-1 spectrophotometer. UV-vis data was recorded as solutions on a Shimadzu UV-1800 spectrophotometer.

6.5.1 $[\text{Re}(\text{CO})_3(\text{L}^1)\text{Br}]$.

To a stirring solution of $[\text{Re}(\text{CO})_5\text{Br}]$ (100 mg, 0.25 mmol) in toluene (5 mL), L^1 (76 mg, 0.27 mmol) was added, and the solution heated to reflux for eight hours. The solution was then cooled to room temperature and the red precipitate was collected on a sinter and washed with toluene (20 mL). Red Solid (147 mg, 95 % Yield). ^1H NMR (500 MHz, d_6 -Acetone) δ 9.29 (ddd, $J = 5.5, 1.5, 0.7$ Hz, 1H), 9.06 (s, 1H), 8.95 (d, $J = 9.6$ Hz, 1H), 8.94 (d, $J = 8.2$ Hz, 1H), 8.43 – 8.38 (m, 2H), 7.88 – 7.81 (m, 2H), 4.08 (s, 3H) ppm. $^{13}\text{C}\{^1\text{H}\}$ NMR (126 MHz, d_6 -Acetone) δ 198.4, 197.9, 189.9, 166.6, 161.7, 158.0, 156.6, 154.1, 145.6, 140.9, 138.3, 133.7, 128.7, 128.4, 126.4, 125.7, 122.4, 105.6, 56.6 ppm. UV-vis (MeCN): λ_{abs} ($\epsilon/10^4$ L mol $^{-1}$ cm $^{-1}$) 214 (3.4), 289 (2.9), 364 (1.4) nm. FTIR (solid) (ATR) ν_{max} : 3078 (br), 3041, 2978, 2021 (M-CO), 1907 (M-CO), 1896 (M-CO), 1730 (C=O), 1618, 1604, 1544, 1483, 1473, 1404, 1381, 1355, 1340, 1300, 1274, 1234, 1215, 1155, 1145, 1122, 1018, 964, 862, 829, 786, 694, 655, 634, 569, 528, 495, 482 cm $^{-1}$. HRMS (ES) $[\text{M} - \text{Br}]^+$ Calc'd for $\text{C}_{19}\text{H}_{12}\text{N}_2\text{O}_6\text{Re}$ 551.0253; Found m/z 551.0258.

6.5.2 [Re(CO)₃(L²)Br].

Made as above from [Re(CO)₅Br] (100 mg, 0.25 mmol) and L² (68 mg, 0.27 mmol) to give a red Solid (138 mg, 94 % Yield) ¹H NMR (500 MHz, d₆-DMSO) δ 9.24 (d, *J* = 4.9 Hz, 1H), 9.07 (d, *J* = 8.2 Hz, 1H), 9.03 (s, 1H), 8.83 (d, *J* = 8.7 Hz, 1H), 8.67 (d, *J* = 8.5 Hz, 1H), 8.42 – 8.37 (m, 1H), 8.21 – 8.17 (m, 1H), 8.02 – 7.96 (m, 1H), 7.88 – 7.84 (m, 1H) ppm. ¹³C{¹H} NMR (126 MHz, d₆-Acetone) δ 198.4, 197.9, 189.7, 166.5, 159.7, 157.8, 154.3, 149.3, 141.0, 133.6, 132.0, 131.3, 128.9, 127.5, 127.1, 126.7, 121.6 ppm. UV-vis (MeCN): λ_{abs} (ε/10⁴ L mol⁻¹ cm⁻¹) 243 (2.7), 269 (2.2), 339 (1.2), 390 (0.5) nm. FTIR (solid) (ATR) ν_{max}: 3269 (br), 2981, 2019 (M-CO), 1917 (M-CO), 1894 (M-CO), 1728 (C=O), 1591, 1543, 1512, 1479, 1458, 1375, 1263, 1236, 1166, 1138, 1062, 1029, 970, 908, 873, 792, 771, 756, 704, 650, 609, 584, 545, 520, 499, 487, 426 cm⁻¹. HRMS (ES) [M + Na]⁺ Calc'd for C₁₈H₁₀N₂O₅BrReNa 620.9200; Found *m/z* 620.9208.

6.5.3 [Re(CO)₃(L³)Br].

Made as above from [Re(CO)₅Br] (100 mg, 0.25 mmol) and L³ (73 mg, 0.27 mmol) to give a red Solid (72 mg, 47 % Yield) ¹H NMR (500 MHz, d₆-Acetone) δ 9.34 (ddd, *J* = 5.5, 1.5, 0.8 Hz, 1H), 9.16 (s, 1H), 9.10 (dd, *J* = 9.7, 5.2 Hz, 1H), 9.04 (d, *J* = 8.2 Hz, 1H), 8.74 (dd, *J* = 10.2, 2.9 Hz, 1H), 8.45 (ddd, *J* = 8.2, 7.7, 1.6 Hz, 1H), 8.08 (ddd, *J* = 9.7, 7.6, 2.9 Hz, 1H), 7.92 (ddd, *J* = 7.6, 5.5, 1.2 Hz, 1H) ppm. ¹⁹F NMR (471 MHz, d₆-Acetone) δ -108.6 (ddd, *J* = 10.1, 7.5, 5.6 Hz) ppm. ¹³C{¹H} NMR (126 MHz, d₆-Acetone) δ 198.2, 197.8, 189.6, 166.1, 164.4, 162.4, 159.4, 159.3, 157.6, 154.3, 146.7, 141.1, 139.6, 139.5, 135.2, 135.1, 129.0, 128.1, 128.0, 127.2, 123.5, 123.3, 123.0, 111.5, 111.3. ppm. UV-vis (MeCN): λ_{abs} (ε/10⁴ L mol⁻¹ cm⁻¹) 250 (2.0), 274 (1.8), 339 (0.9), 348 (1.0), 395 (0.3) nm. FTIR (solid) (ATR) ν_{max}: 3285 (br), 3122, 2980, 2019 (M-CO), 1917 (M-CO), 1891 (M-CO), 1726 (C=O), 1618, 1602, 1544, 1479, 1460, 1371, 1352, 1296, 1226, 1174, 1139, 114, 964, 937, 912, 889, 835, 825, 785, 759, 727, 686, 648, 617, 580, 532, 489 cm⁻¹. HRMS (ES) [M - Br]⁺ Calc'd for C₁₈H₉N₂O₅FRe 539.0053; Found *m/z* 539.0051.

6.5.4 [Re(CO)₃(L⁴)Br].

Made as above from [Re(CO)₅Br] (100 mg, 0.25 mmol) and L⁴ (73 mg, 0.27 mmol) to give a red Solid (150 mg, 97 % Yield). ¹H NMR (500 MHz, d₆-Acetone) δ 10.12 (d, *J* = 1.3 Hz, 1H), 9.22 (dd, *J* = 3.1, 1.3 Hz, 1H), 9.15 (s, 1H), 8.93 (d, *J* = 3.0 Hz, 1H), 8.83 (d, *J* = 9.6 Hz, 1H), 8.31 (d, *J* = 2.9 Hz, 1H), 7.76 (dd, *J* = 9.6, 2.9 Hz, 1H), 4.00 (s, *J* = 3.9 Hz, 3H) ppm. ¹³C{¹H} NMR (126 MHz, d₆-Acetone) δ 198.2, 197.1, 188.0, 166.1, 162.1, 154.6, 153.1, 148.6, 147.8, 147.0, 145.8, 138.4, 133.6, 129.0, 126.1, 122.4, 105.7, 56.6 ppm. UV-vis (MeCN): λ_{abs} (ε/10⁴ L mol⁻¹ cm⁻¹) 217

(2.4), 246 (1.6), 289 (1.8), 366 (1.0), 381 (1.0) nm. FTIR (solid) (ATR) ν_{\max} : 3053, 2976, 2019 (M-CO), 1919 (M-CO), 1891 (M-CO), 1712 (C=O), 1620, 1552, 1483, 1452, 1440, 1417, 1404, 1365, 1294, 1274, 1247, 1207, 1166, 1136, 1106, 1058, 1051, 1024, 935, 889, 856, 846, 823, 779, 738, 724, 686, 669, 651, 644, 619, 567, 640, 480, 432 cm^{-1} . HRMS (ES) $[\text{M} + \text{H}]^+$ Calc'd for $\text{C}_{18}\text{H}_{12}\text{N}_3\text{O}_6\text{BrRe}$ 631.9467; Found m/z 631.9459.

6.5.5 $[\text{Re}(\text{CO})_3(\text{L}^5)\text{Br}]$.

Made as above from $[\text{Re}(\text{CO})_5\text{Br}]$ (100 mg, 0.25 mmol) and L^5 (68 mg, 0.27 mmol) to give a red Solid (139 mg, 94 % Yield). ^1H NMR (400 MHz, d_6 -Acetone) δ 10.29 (s, 1H), 9.36 (dd, $J = 3.0, 1.0$ Hz, 1H), 9.23 (s, 1H), 9.08 (d, $J = 3.0$ Hz, 1H), 8.98 (d, $J = 8.8$ Hz, 1H), 8.90 (d, $J = 8.3$ Hz, 1H), 8.21 (ddd, $J = 8.6, 7.0, 1.2$ Hz, 1H), 8.06 – 8.01 (m, 1H) ppm. $^{13}\text{C}\{^1\text{H}\}$ NMR (126 MHz, d_6 -Acetone) δ 198.2, 197.0, 188.7, 166.4, 157.9, 152.9, 149.4, 149.2, 148.3, 147.3, 141.4, 133.9, 131.8, 131.7, 127.7, 126.9, 121.5 ppm. UV-vis (MeCN): λ_{abs} ($\epsilon/10^4$ L mol $^{-1}$ cm $^{-1}$) 205 (3.2), 243 (2.9), 280 (1.9), 343 (1.4), 413 (0.4) nm. FTIR (solid) (ATR) ν_{\max} : 3143 (br), 2978, 2893, 2019 (M-CO), 1912 (M-CO), 1892 (M-CO), 1724 (C=O), 1703, 1589, 1544, 1508, 1475, 1458, 1375, 1332, 1267, 1246, 1172, 1147, 1109, 1058, 1001, 893, 844, 798, 785, 775, 715, 650, 628, 617, 586, 553, 516, 482, 464 cm^{-1} . HRMS (ES) $[\text{M} + \text{H}]^+$ Calc'd for $\text{C}_{17}\text{H}_{10}\text{N}_3\text{O}_5\text{BrRe}$ 601.9361; Found m/z 601.9349.

6.5.6 $[\text{Re}(\text{CO})_3(\text{L}^6)\text{Br}]$.

Made as above from $[\text{Re}(\text{CO})_5\text{Br}]$ (100 mg, 0.25 mmol) and L^6 (73 mg, 0.27 mmol) to give a red Solid (138 mg, 91 % Yield). ^1H NMR (500 MHz, d_6 -Acetone) δ 10.30 (d, $J = 1.3$ Hz, 1H), 9.37 (dd, $J = 3.0, 1.3$ Hz, 1H), 9.35 (s, 1H), 9.09 (d, $J = 3.1$ Hz, 1H), 9.07 (d, $J = 5.2$ Hz, 1H), 8.76 (dd, $J = 10.2, 2.9$ Hz, 1H), 8.12 (ddd, $J = 9.7, 7.6, 3.0$ Hz, 1H) ppm. ^{19}F NMR (471 MHz, d_6 -Acetone) δ -107.7 (ddd, $J = 10.0, 7.5, 5.4$ Hz) ppm. $^{13}\text{C}\{^1\text{H}\}$ NMR (126 MHz, d_6 -Acetone) δ 198.1, 197.0, 188.6, 166.0, 164.6, 162.6, 157.5, 152.7, 149.3, 148.4, 147.3, 146.8, 139.8, 135.0, 134.9, 128.4, 128.3, 123.9, 123.7, 122.9, 111.7, 111.4 ppm. UV-vis (MeCN): λ_{abs} ($\epsilon/10^4$ L mol $^{-1}$ cm $^{-1}$) 212 (2.7), 248 (2.3), 285 (1.7), 343 (1.3), 356 (1.4), 418 (0.4) nm. FTIR (solid) (ATR) ν_{\max} : 3047, 2978, 2018 (M-CO), 1915 (M-CO), 1895 (M-CO), 1697 (C=O), 1620, 1550, 1517, 1479, 1440, 1419, 1357, 1296, 1238, 1166, 1136, 1103, 1060, 1022, 935, 891, 846, 821, 785, 759, 738, 686, 651, 619, 585, 532, 478, 432 cm^{-1} . HRMS (ES) $[\text{M} + \text{H}]^+$ Calc'd for $\text{C}_{17}\text{H}_9\text{N}_3\text{O}_5\text{FBrRe}$ 619.9267; Found m/z 619.9276.

6.5.7 [Re(CO)₃(L⁷)Br].

Made as above from [Re(CO)₅Br] (100 mg, 0.25 mmol) and L⁷ (76 mg, 0.27 mmol) to give a red solid (142 mg, 92 %). ¹H NMR (500 MHz, d₆-DMSO) δ 9.25 – 9.23 (m, 1H), 9.07 – 9.02 (m, 2H), 8.84 (dd, J = 8.8, 0.4 Hz, 1H), 8.59 (dd, J = 8.5, 1.0 Hz, 1H), 8.42 (ddd, J = 8.5, 8.1, 1.5 Hz, 1H), 8.20 (ddd, J = 8.9, 7.0, 1.7 Hz, 1H), 8.00 (ddd, J = 8.9, 6.9, 1.2 Hz, 1H), 7.87 (ddd, J = 7.6, 5.5, 1.1 Hz, 1H), 4.58 (qd, J = 7.1, 1.1 Hz, 2H), 1.47 (t, J = 7.1 Hz, 3H) ppm. ¹³C NMR (126 MHz, d₆-Acetone) δ 198.4, 197.9, 189.7, 165.7, 159.7, 157.8, 154.3, 149.3, 141.1, 141.0, 133.7, 132.0, 131.3, 128.9, 127.4, 127.1, 126.4, 121.4, 63.6, 14.4 ppm. UV-vis (MeCN): λ_{abs} (ε/10⁴ L mol⁻¹ cm⁻¹) 206 (3.8), 248 (2.8), 273 (2.5), 350, (1.2), 419 (0.4) nm. FTIR (solid) (ATR) ν_{max}: 3111, 3062, 2981, 2020 (M-CO), 1893 (br, M-CO), 1714 (C=O), 1591, 1543, 1517, 1469, 1460, 1436, 1394, 1371, 1352, 1255, 1203, 1157, 1122, 1026, 975, 894, 864, 794, 769, 644, 615, 543, 518, 491, 476, 726 cm⁻¹. HRMS (ES) [M + H]⁺ Calc'd for C₂₀H₁₄N₂O₅BrReNa 648.9513; Found *m/z* 648.9511.

6.5.8 [Re(CO)₃(L⁸)Br].

Made as above from [Re(CO)₅Br] (100 mg, 0.25 mmol) and L⁸ (76 mg, 0.27 mmol) to give a red solid (132 mg, 85 %). ¹H NMR (500 MHz, d₆-DMSO) δ 10.28 (s, 1H), 9.31 (d, J = 3.0 Hz, 1H), 9.22 (s, 1H), 9.04 (d, J = 3.0 Hz, 1H), 8.82 (d, J = 8.8 Hz, 1H), 8.61 (d, J = 8.5 Hz, 1H), 8.23 (ddd, J = 9.8, 7.2, 1.6 Hz, 1H), 8.04 (dd, J = 8.2, 7.2 Hz, 1H), 4.59 (q, J = 7.1 Hz, 2H), 1.48 (t, J = 7.1 Hz, 3H) ppm. ¹³C NMR (126 MHz, d₆-DMSO) δ 164.8, 157.1, 151.2, 148.6, 147.7, 147.6, 146.4, 140.6, 133.5, 131.0, 130.2, 126.5, 124.9, 120.3, 63.0, 14.0. UV-vis (MeCN): λ_{abs} (ε/10⁴ L mol⁻¹ cm⁻¹) 248 (2.4), 280 (1.6), 346 (1.1), 357 (1.2), 437 (0.3) nm. FTIR (solid) (ATR) ν_{max}: 2981, 2026 (M-CO), 1923 (M-CO), 1898 (M-CO), 1735 (C=O), 1591, 1544, 1477, 1456, 1394, 1373, 1301, 1265, 1236, 1201, 1172, 1141, 1095, 1018, 889, 840, 815, 773, 684, 653, 621, 530, 499, 457 cm⁻¹. HRMS (ES) [M + H]⁺ Calc'd for C₁₉H₁₄N₃O₅BrRe 627.9646; Found *m/z* 627.9647.

6.6 References

- 1 E. Scerri, *Nat. Chem.*, 2010, **2**, 598–598.
- 2 N. N. Greenwood and A. Earnshaw, *Chemistry of the elements*, Butterworth-Heinemann, Oxford ; Boston, 2nd ed., 1997.
- 3 F. Aubke and C. Wang, *Coord. Chem. Rev.*, 1994, **137**, 483–524.
- 4 W. Hieber and H. Fuchs, *Z. Für Anorg. Allg. Chem.*, 1941, **248**, 256–268.
- 5 W. Hieber, R. Schuh and H. Fuchs, *Z. Für Anorg. Allg. Chem.*, 1941, **248**, 243–255.
- 6 G. D. Michels and H. J. Svec, *Inorg. Chem.*, 1981, **20**, 3445–3447.
- 7 M. S. Wrighton, D. L. Morse and L. Pdungsap, *J. Am. Chem. Soc.*, 1975, **97**, 2073–2079.
- 8 L. Wallace and D. P. Rillema, *Inorg. Chem.*, 1993, **32**, 3836–3843.
- 9 B. L. Murphy, S. C. Marker, V. J. Lambert, J. J. Woods, S. N. MacMillan and J. J. Wilson, *J. Organomet. Chem.*, 2020, **907**, 121064.
- 10 S. Sato, T. Morimoto and O. Ishitani, *Inorg. Chem.*, 2007, **46**, 9051–9053.
- 11 K. Kalyanasundaram, *J. Chem. Soc. Faraday Trans. 2 Mol. Chem. Phys.*, 1986, **82**, 2401–2415.
- 12 P. Kurz, B. Probst, B. Spingler and R. Alberto, *Eur. J. Inorg. Chem.*, 2006, **2006**, 2966–2974.
- 13 S. M. Fredericks, J. C. Luong and M. S. Wrighton, *J. Am. Chem. Soc.*, 1979, **101**, 7415–7417.
- 14 G. J. Kavarnos, *Fundamentals of photoinduced electron transfer*, VCH Publishers, New York, NY, 1993.
- 15 J. V. Caspar and T. J. Meyer, *J. Phys. Chem.*, 1983, **87**, 952–957.
- 16 S. A. Moya, J. Guerrero, F. J. Rodriguez-Nieto, E. Wolcan, M. R. Féliz, R. F. Baggio and M. T. Garland, *Helv. Chim. Acta*, 2005, **88**, 2842–2860.
- 17 M. Wrighton and D. L. Morse, *J. Am. Chem. Soc.*, 1974, **96**, 998–1003.
- 18 A. J. Lees, *Comments Inorg. Chem.*, 1995, **17**, 319–346.
- 19 G. Ferraudi, M. Feliz, E. Wolcan, I. Hsu, S. A. Moya and J. Guerrero, *J. Phys. Chem.*, 1995, **99**, 4929–4934.
- 20 W. K. Smothers and M. S. Wrighton, *J. Am. Chem. Soc.*, 1983, **105**, 1067–1069.
- 21 M. K. Itokazu, A. S. Polo and N. Y. M. Iha, *J. Photochem. Photobiol. Chem.*, 2003, **160**, 27–32.
- 22 L. C.-C. Lee, K.-K. Leung and K. K.-W. Lo, *Dalton Trans.*, 2017, **46**, 16357–16380.
- 23 F. L. Thorp-Greenwood, M. P. Coogan, L. Mishra, N. Kumari, G. Rai and S. Saripella, *New J. Chem.*, 2011, **36**, 64–72.
- 24 C. A. Bader, R. D. Brooks, Y. S. Ng, A. Sorvina, M. V. Werrett, P. J. Wright, A. G. Anwer, D. A. Brooks, S. Stagni, S. Muzzioli, M. Silberstein, B. W. Skelton, E. M. Goldys, S. E. Plush, T. Shandala and M. Massi, *RSC Adv.*, 2014, **4**, 16345–16351.
- 25 C. A. Bader, A. Sorvina, P. V. Simpson, P. J. Wright, S. Stagni, S. E. Plush, M. Massi and D. A. Brooks, *FEBS Lett.*, 2016, **590**, 3051–3060.
- 26 C. A. Bader, E. A. Carter, A. Safitri, P. V. Simpson, P. Wright, S. Stagni, M. Massi, P. A. Lay, D. A. Brooks and S. E. Plush, *Mol. Biosyst.*, 2016, **12**, 2064–2068.
- 27 I. Kitanovic, S. Can, H. Alborzinia, A. Kitanovic, V. Pierroz, A. Leonidova, A. Pinto, B. Spingler, S. Ferrari, R. Molteni, A. Steffen, N. Metzler-Nolte, S. Wölfel and G. Gasser, *Chem. – Eur. J.*, 2014, **20**, 2496–2507.

- 28 F. Zhong, X. Yuan, J. Zhao and Q. Wang, *Sci. China Chem.*, 2016, **59**, 70–77.
- 29 I. Chakraborty, J. Jimenez and P. K. Mascharak, *Chem. Commun.*, 2017, **53**, 5519–5522.
- 30 A. Kastl, S. Dieckmann, K. Wähler, T. Völker, L. Kastl, A. L. Merkel, A. Vultur, B. Shannan, K. Harms, M. Ocker, W. J. Parak, M. Herlyn and E. Meggers, *ChemMedChem*, 2013, **8**, 924–927.
- 31 I. Chakraborty, J. Jimenez, W. M. C. Sameera, M. Kato and P. K. Mascharak, *Inorg. Chem.*, 2017, **56**, 2863–2873.
- 32 R. Motterlini and L. E. Otterbein, *Nat. Rev. Drug Discov.*, 2010, **9**, 728–743.
- 33 M. N. Pinto and P. K. Mascharak, *J. Photochem. Photobiol. C Photochem. Rev.*, 2020, **42**, 100341.
- 34 J. Hawecker, J.-M. Lehn and R. Ziessel, *J. Chem. Soc. Chem. Commun.*, 1983, 536–538.
- 35 E. Fujita, *Coord. Chem. Rev.*, 1999, **185–186**, 373–384.
- 36 A. J. Morris, G. J. Meyer and E. Fujita, *Acc. Chem. Res.*, 2009, **42**, 1983–1994.
- 37 D. H. Gibson and X. Yin, *J. Am. Chem. Soc.*, 1998, **120**, 11200–11201.
- 38 Y. Hayashi, S. Kita, B. S. Brunschwig and E. Fujita, *J. Am. Chem. Soc.*, 2003, **125**, 11976–11987.
- 39 T. Morimoto, T. Nakajima, S. Sawa, R. Nakanishi, D. Imori and O. Ishitani, *J. Am. Chem. Soc.*, 2013, **135**, 16825–16828.
- 40 R. O. Bonello, M. B. Pitak, S. J. Coles, A. J. Hallett, I. A. Fallis and S. J. A. Pope, *J. Organomet. Chem.*, 2017, **841**, 39–47.
- 41 F. L. Thorp-Greenwood, M. P. Coogan, A. J. Hallett, R. H. Laye and S. J. A. Pope, *J. Organomet. Chem.*, 2009, **694**, 1400–1406.
- 42 E. Hevia, J. Pérez, V. Riera, D. Miguel, S. Kassel and A. Rheingold, *Inorg. Chem.*, 2002, **41**, 4673–4679.
- 43 C. Triantis, A. Shegani, C. Kiritsis, C. P. Raptopoulou, V. Psycharis, M. Pelecanou, I. Pirmettis and M. Papadopoulos, *Acta Crystallogr. Sect. E Crystallogr. Commun.*, 2016, **72**, 114–116.
- 44 B. Machura, A. Świtlicka, M. Wolff, D. Tabak, R. Musioł, J. Polański and R. Kruszynski, *J. Organomet. Chem.*, 2011, **696**, 731–738.
- 45 L. Rotundo, E. Azzi, A. Deagostino, C. Garino, L. Nencini, E. Priola, P. Quagliotto, R. Rocca, R. Gobetto and C. Nervi, *Front. Chem.*, , DOI:10.3389/fchem.2019.00417.
- 46 P. A. Anderson, F. R. Keene, E. Horn and E. R. T. Tiekink, *Appl. Organomet. Chem.*, 1990, **4**, 523–533.
- 47 D. R. Gamelin, M. W. George, P. Glyn, F.-W. Grevels, F. P. A. Johnson, W. Klotzbuecher, S. L. Morrison, G. Russell, K. Schaffner and J. J. Turner, *Inorg. Chem.*, 1994, **33**, 3246–3250.
- 48 A. Vlček, in *Photophysics of Organometallics*, ed. A. J. Lees, Springer, Berlin, Heidelberg, 2010, pp. 115–158.
- 49 G. J. Stor, F. Hartl, J. W. M. van Outersterp and D. J. Stufkens, *Organometallics*, 1995, **14**, 1115–1131.
- 50 J. C. Canales, A. Carreño, D. Oyarzún, J. M. Manríquez, I. Chávez, J. C. Canales, A. Carreño, D. Oyarzún, J. M. Manríquez and I. Chávez, *J. Chil. Chem. Soc.*, 2017, **62**, 3765–3771.
- 51 T. Y. Kim, A. B. S. Elliott, K. J. Shaffer, C. John McAdam, K. C. Gordon and J. D. Crowley, *Polyhedron*, 2013, **52**, 1391–1398.
- 52 R. Czerwieńiec, A. Kapturkiewicz, J. Lipkowski and J. Nowacki, *Inorganica Chim. Acta*, 2005, **358**, 2701–2710.
- 53 J. P. Bullock, E. Carter, R. Johnson, A. T. Kennedy, S. E. Key, B. J. Kraft, D. Saxon and P. Underwood, *Inorg. Chem.*, 2008, **47**, 7880–7887.

- 54 F. Paolucci, M. Marcaccio, C. Paradisi, S. Roffia, C. A. Bignozzi and C. Amatore, *J. Phys. Chem. B*, 1998, **102**, 4759–4769.
- 55 H. Y. V. Ching, X. Wang, M. He, N. Perujo Holland, R. Guillot, C. Slim, S. Griveau, H. C. Bertrand, C. Policar, F. Bedioui and M. Fontecave, *Inorg. Chem.*, 2017, **56**, 2966–2976.
- 56 L. N. Klatt and R. L. Rouseff, *J. Am. Chem. Soc.*, 1972, **94**, 7295–7304.
- 57 W. Kaim, H. E. A. Kramer, C. Vogler and J. Rieker, *J. Organomet. Chem.*, 1989, **367**, 107–115.

**Chapter 7 - Towards an Intramolecular
Energy Upconverting Assembly.**

7.1 Introduction

Photon upconversion is of technological importance across a range of disciplines, from bioimaging to efficient energy transfer from solar capture. Solar cell technology based around inorganic-organic lead halide perovskites is able to capture photons up to around 800 nm¹⁻³, meaning most of the NIR photons are wasted. Photocatalytic water splitting requires a potential of at least 1.23 V, more for the over potential for efficient hydrogen generation. This requires higher energy photons, meaning the lower energy and NIR photons are once again wasted^{4,5}. It has been estimated that the use of UC methods in solar energy capture can increase the efficiency of photovoltaics by 50 % and of water splitting by up to 100 %⁶. The use of photosensitisers to generate ROS for PDT is limited by the depth of tissue visible light can penetrate. The use of NIR is advantageous since it is non ionising, harmless to normal cells and can penetrate a few cm into tissue⁷. This allows the selective irradiation of cancer cells, where upconverting PDT agents can generate the ROS locally⁸.

7.1.1 TTA-UC efficiency

Energy transfer from the sensitiser triplet energy levels (T_S) to the annihilator triplet energy levels (T_A) follows a short range Dexter energy transfer process^{9,10}, with efficient energy transfer being seen with low energy difference, $|\Delta E_{A,S}| = |E_{T_A} - E_{T_S}|$. However, a small $\Delta E_{A,S}$ will allow for backwards triplet – triplet energy transfer¹¹, lowering the efficiency of the upconverting system.

The overall quantum yield of the up-conversion process (Φ_{UC}) is calculated by the following¹²:

$$\Phi_{UC} = \frac{1}{2} f \Phi_{ISC} \Phi_{TTET} \Phi_{TTA} \Phi_A \quad \text{Equation 7.1}$$

Where the factor one half represents the process being an overall two photon excitation, one photon emission, and f representing the statistical likelihood a TTA event results in a singlet excited state annihilator. Φ_{ISC} = quantum efficiency of inter system crossing, Φ_{TTET} = quantum efficiency of triplet-triplet energy transfer, Φ_{TTA} = quantum efficiency of triplet-triplet annihilation and Φ_A = quantum efficiency of annihilator photoluminescence. From Equation 7.1, the Φ_{UC} is dependent upon the photophysical properties of the sensitisers and annihilators, via f , Φ_{ISC} , Φ_A , while Φ_{TTET} , and Φ_{TTA} shows a dependence upon the distance between molecules,

concentration, and mobility in solution, but Equation 7.1 does not take into consideration the rate of back energy transfer, or quenching by $^1\text{O}_2$, for example. In organic solvents, one of the limiting factors for efficiency of energy transfer between excited molecules is the rate of diffusion throughout the system¹³. This becomes a larger issue when looking at the use of TTA-UC systems in high viscosity systems or the solid state.

The theoretical efficiency of TTA-UC, and hence the factor f above in Equation 7.1, is 11.1 %. Upon annihilation events, two $^3\text{A}^*$ come together to form an encounter complex, $(^3\text{A}^3\text{A})^*$. The encounter complexes are formed as either singlet, triplet or quintet dimer, in a 1:3:5 ratio respectively^{14,15}. Only the $^1(^3\text{A}^3\text{A})^*$ encounter complex is able to disassociate into the desired $^1\text{A}^*$ needed for fluorescent emission. However, since there are no accessible quintet states for the encounter complex $^5(^3\text{A}^3\text{A})^*$ to dissociate into, it must split back into two triplet excited states¹⁶. The triplet encounter complex, $^3(^3\text{A}^3\text{A})^*$, will also yield a $^3\text{A}^*$ which can then go on to form another encounter complex. As such, yields larger than 11.1 % are reported^{17,18}, with a theoretical maximum above 40 % efficiency¹⁹. All of this indicates that the annihilation units must be as efficient as possible to translate any generated $^1\text{A}^*$ into emission.

7.1.2 Intramolecular TTA-UC

Intramolecular TTA-UC is the incorporation of the sensitiser and annihilator required for upconversion into the same molecule. Materials that incorporate the sensitiser and annihilator components for TTA-UC has been shown to work in Polymers^{20,21}, MOFs²², self-assembly systems^{23,24} as well as metal complexes^{25,26}.

Early methods that combined the annihilator to the sensitiser focused on the use of polymers^{27,28}. Polyfluorenes are important electrochromic materials, capable of displaying emission across the visible spectrum and have a high quantum yield, as well as good thermal and electrochemical stability²⁹. This makes them excellent candidates for flexible OLED devices³⁰. In 2001, Scherf *et al* showed that polyfluorene films can exhibit two photon absorption³¹, making them potential candidates for upconversion. Wegner *et al* used this property when they doped the polyfluorene film with 3 wt% [Pd(OEP)]²⁷ (OEP: octaethylporphyrin). [Pd(OEP)] is a well-known triplet sensitiser^{15,21}, and when the film was excited at $\lambda_{\text{ex}} = 532$ nm, which is outside of the absorbance spectrum for the polyfluorene, the film showed TTA-UC emission. Later work by the group introduced the palladium macrocycle as an end cap for the polymers²⁸ (Figure 7.1). This was intended to reduce the

separation of the dopant and the matrix that was believed to be limiting the efficiency of earlier doped systems. After covalent linking of porphyrin complex to the polymer, the efficiency of the TTA-UC was increased as well as enhancing the operational stability of the systems.

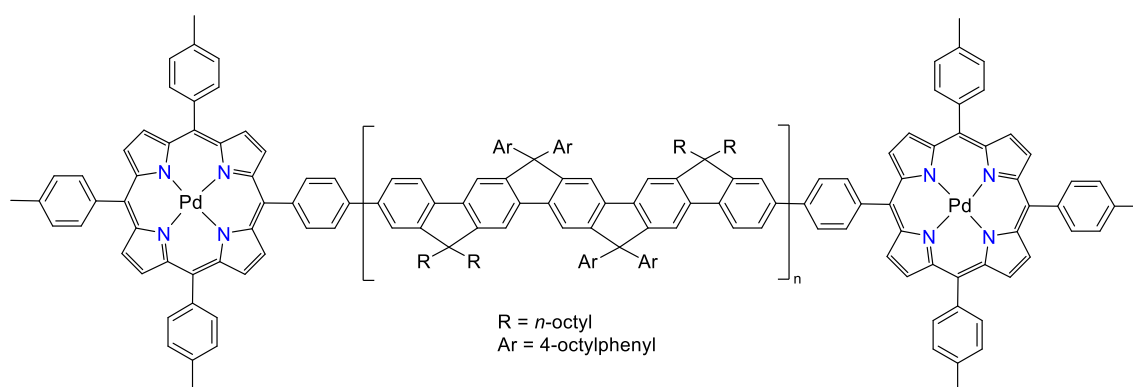


Figure 7.1 - TTA-UC polyfluorene polymers end capped with Pd(II) porphyrin complexes used in the work by Wegner *et al.*²⁸

The crystalline PCN-222(Pd) type MOF³² (Figure 7.2) was synthesised by Heinze *et al.* The triplet sensitising unit [Pd(TCCP)] was incorporated into the MOF by utilising secondary binding units, $[Zr_6(\mu_3\text{-OH})_8(\text{OH})_8]$ (where TCCP: tetrakis(carboxy)phenylporphyrin). The channels in the MOF are rather polar environments, with terminal OH groups, which were capped by a film of octanoic acid in the cavity, providing a non-polar environment. The cavities could then host DPA molecules, and crucially, the octanoic acid allowed the DPA molecules a degree of movement while not in solution. This provided the conditions for TTA-UC to occur, with an estimated efficiency of 4.3 %.

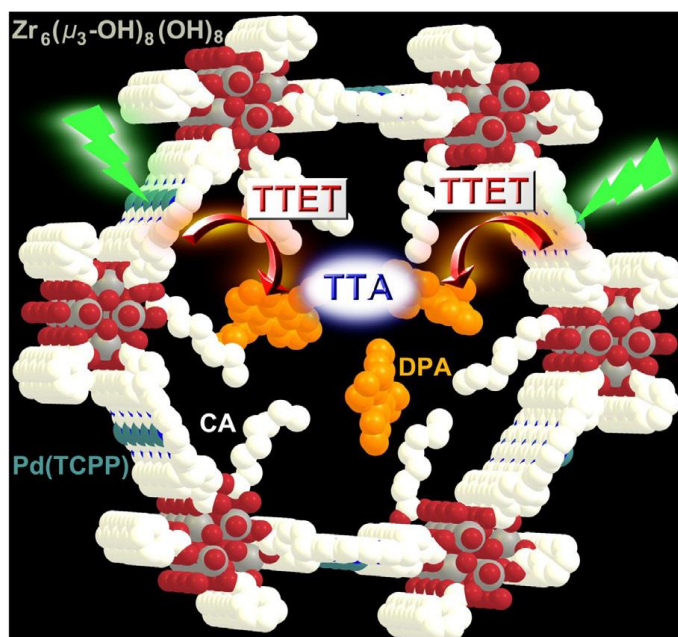


Figure 7.2 – Upconverting MOF design taken from Heinze *et al*³². Light Blue atoms are the Pd from the [Pd(TCPP)] linker units, grey atoms are Zr of the $[Zr_6(\mu_3-OH)_8(OH)_8]$ secondary binding units, red atoms are oxygen. CA – Caprylic (octanoic) acid.

Self-assembly systems can be designed to incorporate ordered arrays of annihilator units in high concentrations around sensitiser units. TTA-UC has been observed in solvent free liquids³³, ionic liquids³⁴, molecular crystals³⁵, and gels³⁶. Due to the high concentration of annihilators the excited triplet states are able to migrate across the arrays. This is referred to as Triplet Energy Migration (TEM)^{37,38}. As mentioned earlier, the Φ_{TTET} term from Equation 7.1 is distance dependent, since it is a Dexter type energy transfer^{26,39}. Self-assembly systems by design incorporate the close proximity of annihilator units, generally at less than 1 nm apart. This enables the efficient triplet energy transfer across a system until finally, two excitations can meet and annihilate producing anti-Stokes shifted emission. The dense array of annihilator units can also exclude molecular oxygen from the matrix, thereby allowing TTA-UC to take place in air⁴⁰. Similarly, the self-assembly design may incorporate O₂ scavenger molecules into the matrix, such as unsaturated double bonds of oleic acid and linoleic acid⁴¹, or hyperbranched unsaturated phosphates⁴².

Transition metal complexes featuring both sensitisers and annihilators are rarer, perhaps first demonstrated in 2016, by Moth-Poulsen *et al*, through the coordination of a series of 4-(10-phenylanthracen-9-yl)pyridines to [Zn(II)(OEP)] complex²⁵ (Figure 7.3). Replacing a phenyl group with a pyridyl group in the annihilator had minimal effect on the photophysical characteristics of the molecule, and as such it was still able to undergo TTA-UC⁴³. The coordination of the

annihilator to the Zn(II)(OEP) was confirmed by a bathochromic shift in emission of the complex. While all the tested systems showed TTA-UC, the efficiency was lower than mixing annihilator and complex in solution. This was attributed to two processes. Firstly, a >95 % singlet back energy transfer from the annihilator to the complex upon excitation, and secondly dissociation of the annihilator upon excitation. In theory, the FRET back energy transfer pathway would not be possible if the annihilator was perfectly perpendicular to the plane of the porphyrin ring. However, due to the low binding constant of 6000 M^{-1} , this rarely was the case. By substituting the metal, the binding constant could be increased. Therefore the group changed the Zn(II) metal centre for a [Ru(OEP)(CO)L], which has a binding constant estimated to be of the magnitude of $10^6 - 10^7 \text{ M}^{-1}$ for pyridyl chelation. This meaning in a 1:1 mix of annihilator and sensitiser, > 90 % of the metal centres are bound⁴⁴. This gives a Φ_{UC} of 4.5 %, three times larger than [Ru(OEP)(CO)Py] complex in solution with DPA.

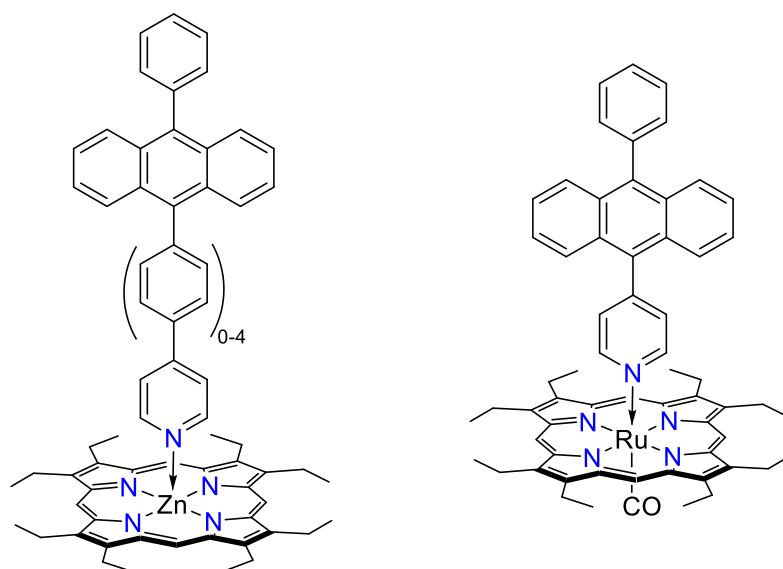


Figure 7.3 – [Zn(II)OEP] and [Ru(CO)(OEP)] TA UC complexes synthesised by Moth--Poulsen *et al*^{25,44}

7.1.3 Functionalisation strategies of DPA

As talked about previously in Chapter 4 the annihilator needs to have a high quantum yield of fluorescence, triplet states accessible at suitable energy levels, a good Stokes shift and long triplet lifetimes⁴⁵. Typically, polyaromatic molecules fit this description, such as DPA with a high quantum efficiency ($\Phi = 0.95$)⁴⁶. DPA is a common choice over the unsubstituted anthracenes due to the twisted nature of

the phenyl rings relative to the aromatic plane of the anthracene. This stops the DPA from π -stacking, which can lead to concentration-dependent quenching in solutions of polyaromatic hydrocarbons⁴⁷. Anthracenes readily undergo photochemical cycloaddition reactions (Figure 7.4), such as the [4+4]cycloaddition photodimerization of anthracene⁴⁸, or a [4+2]cycloaddition photoperoxide formation with $^1\text{O}_2$ ⁴⁹. The addition of the phenyl rings in DPA prevents the formation of these while maintaining the favourable properties of the anthracene. DPA is known to be an efficient annihilator for red emitting iridium complexes^{50,51}, and an obvious choice to incorporate into a single molecular upconverter. Therefore, the functionalisation of DPA to allow either coordination to the metal centre or attachment to a ligand system is very important.

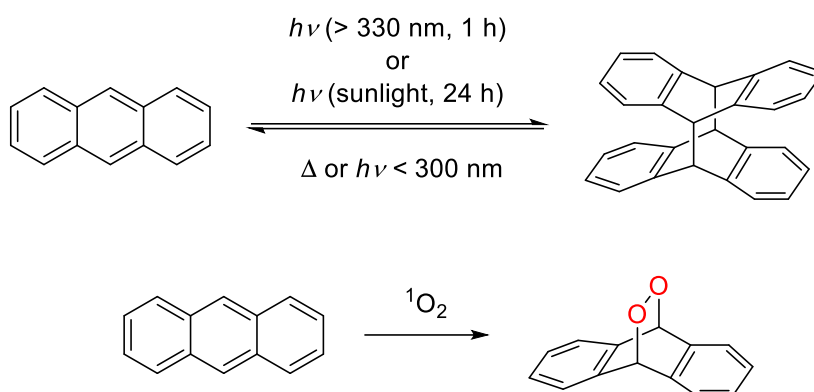


Figure 7.4 - Anthracene cycloaddition pathways

The two main routes used in the preparation of functionalised DPA molecules allow for functionalisation of either the phenyl rings or the anthracene core. A Grignard's reaction or a Suzuki-Miyaura cross coupling reaction are both frequently used, with the retrosynthetic pathways of both shown in Figure 7.5. In the first route, a diarylanthracene molecule can be synthesised via a Grignard reaction; arylmagnesium bromide is reacted with anthraquinone forming a 9,10-diaryl-9,10-dihydroxydihydroanthracene, which can then be reduced to the corresponding functionalised 9,10-diarylanthracene molecule^{52,53}. The second pathway involves a Suzuki-Miyaura cross coupling reaction between dibromoanthracene and arylboronic acids using a palladium catalyst⁵⁴⁻⁵⁶ to yield the functionalised diarylanthracene.

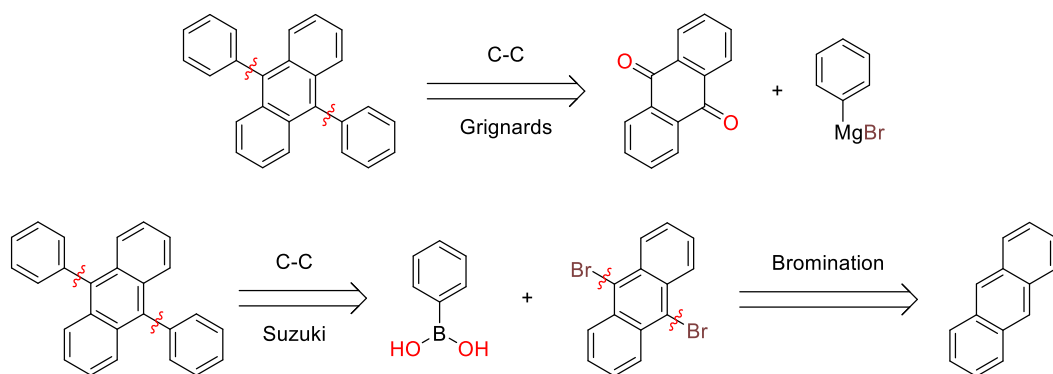


Figure 7.5 – Retrosynthetic analysis for the synthesis of amino-DPA molecule showing 2 separate routes – a Grignard's reaction with an amino anthraquinone, or a Suzuki cross coupling between a dibromo species and phenyl boronic acid.

One of the advantages of the Suzuki-Miyaura cross coupling method is it allows the synthesis of asymmetric 9,10-diarylanthracene derivatives⁵⁷. For example, Nitschke *et al* used an asymmetric 4-(10-(pyridin-4-yl)anthracen-9-yl)aniline as a linker in their work on metal – organic self-assembly structures⁵⁸ (Figure 7.6). 9-Bromoanthracene first underwent a first Suzuki-Miyaura cross coupling to form a pyridin-4-yl-anthracene. This was then brominated via NBS to yield the 10-bromo-9-pyridin-4-yl anthracene which could then undergo a second cross coupling to give the desired dual functional asymmetric diarylanthracene derivative.

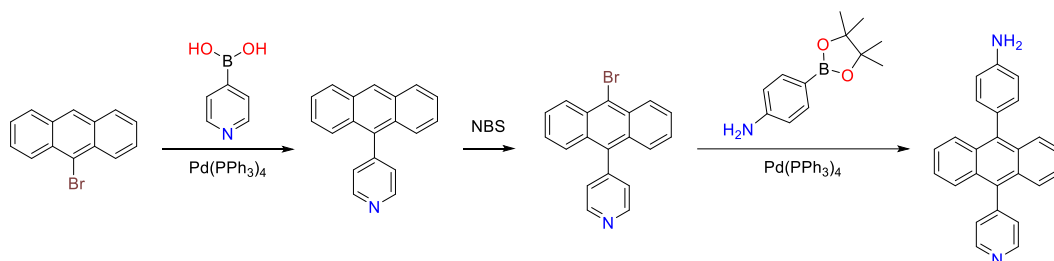


Figure 7.6 – Synthesis of 4-(10-(pyridin-4-yl)anthracen-9-yl)aniline by Nitschke *et al.*⁵⁸

7.2 Aims of the Chapter

Ir(III) compounds are known to be efficient TTA photosensitisers, and therefore have the potential for annihilator functionalisation to be incorporated by design, either as part of the cyclometalating ligands or the ancillary ligand. Furthermore, The $\Delta E_{A,S}$ between the potential Ir(III) complex and the DPA should be small enough to allow favourable triplet – triplet energy transfer, while large enough to prevent triplet back energy transfer. Previously, 2-phenylquinoline-4-amide based

Ir(III) complexes have exhibited red emission with the triplet band being approximated to at 2.10 eV (590 nm, 16938 cm⁻¹) from the emission onset.⁵⁹ For the sensitiser, 9,10-diphenylanthracene (DPA) exhibits triplet levels at 14290 cm⁻¹ (1.77 eV, 700 nm) ⁶⁰. Therefore, this chapter sets out the design, synthesis, and characterisation of N-(9,10-diphenylanthracen-2-yl)-2-phenylquinoline-4-carboxamide ligand and the associated iridium (III) *bis*-cyclometalated complex. The combination of the sensitiser and annihilator within a single molecule was the key aim in an effort to investigate intramolecular triplet-triplet-annihilation upconversion in solution. This work has produced and characterised a novel ligand Ir(III) organometallic complex that integrates a covalently linked DPA unit.

7.3 Results and Discussions

7.3.1 Design strategies

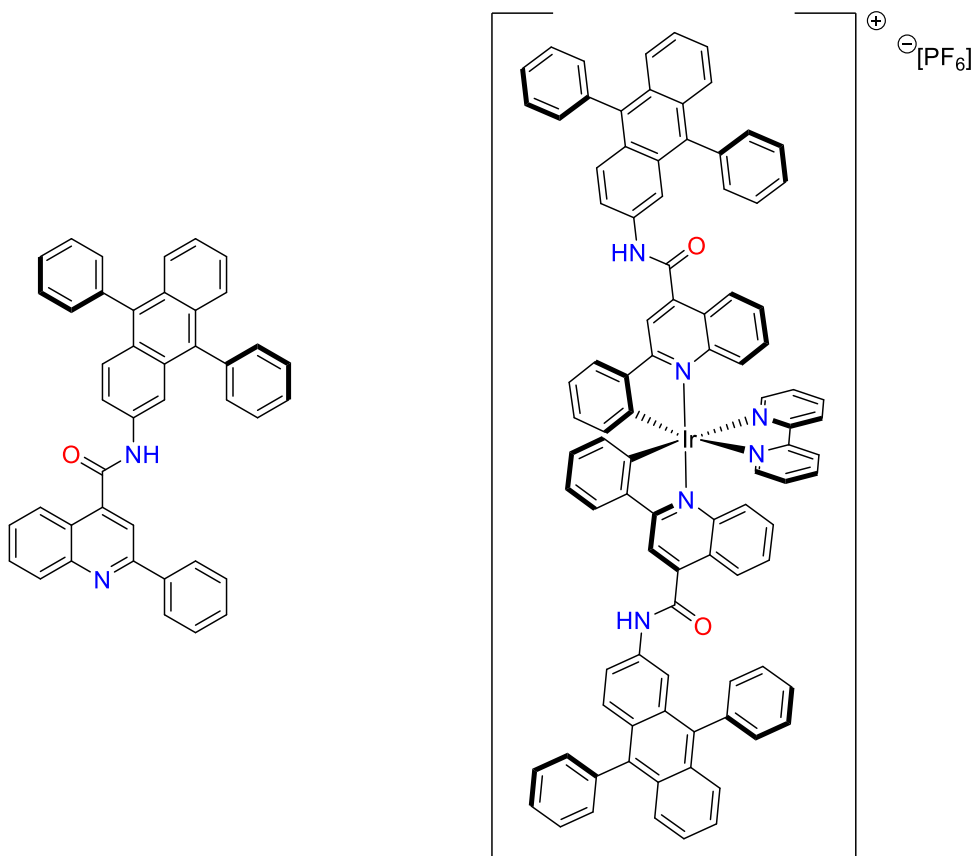


Figure 7.7 – Target ligand design and complex design for the potential of single molecule TTA UC.

Previous work of the Pope group⁵⁹ has shown the amide functionalisation of 2-phenylquinoline-4-carboxylates to be achievable via a nucleophilic substitution reaction between the corresponding acyl chloride and primary amines. Therefore, the first target was to synthesise 2-amino-9,10-diphenylanthracene. Both the Grignard and Suzuki-Miyaura cross coupling methods discussed in Section 7.1.3 need careful consideration for the incorporation of a primary amine.

During the Grignard reaction, the phenylmagnesium bromide could also potentially deprotonate the amine to yield benzene and the corresponding amine salt, meaning the reaction would require protection via a tertiary amine. The use of a Pd catalyst during the Suzuki-Miyaura cross coupling procedure with the aryl bromide and aryl amines leads to the possibility of also forming the Buchwald-Hartwig C-N cross-coupling product.⁶¹ This would also require the use

of a tertiary amine protecting group to limit the possibility of side reactions. Possible protecting groups could be a double BOC protection⁶², dibenzyl protection⁶³, or by reacting with phthalic anhydride to form the phthalimide⁶³. Deprotection can be achieved via stirring with dilute HCl and gentle warming for the BOC groups. Dibenzyl groups can be removed by hydrogenation over Pd/C catalyst while the phthalimide deprotection can be achieved by heating with hydrazine hydrate. For the synthesis, the Suzuki-Miyaura cross coupling method seen in Figure 7.8 was employed. Overall, the phthalimide protecting group chemistry employs less harmful reagents and conditions needed for both protection and deprotection in comparison with the BOC and dibenzylamine protection method.

7.3.2 Synthesis and characterisation of 2-amino-9,10-diphenylanthracene

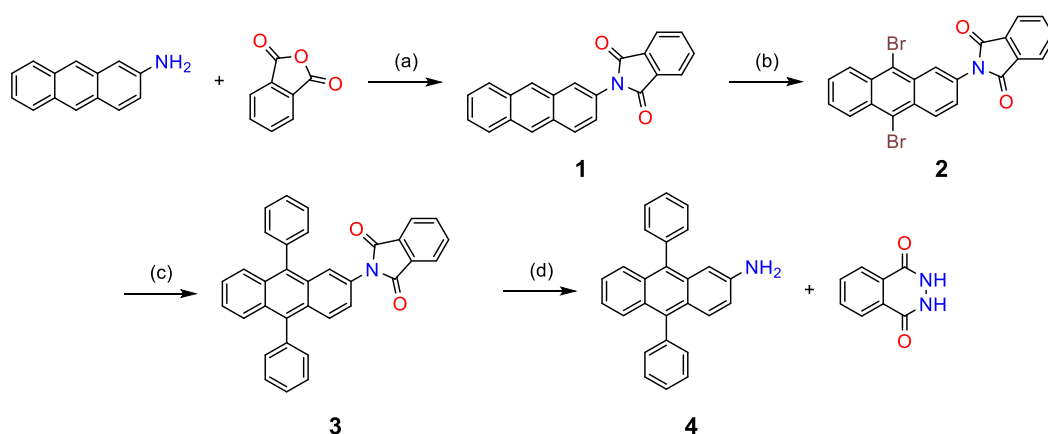


Figure 7.8 – Synthetic pathway designed for the synthesis of aminoDPA (**4**). (a) 2-Ethoxyethanol, triethylamine, 80 °C, 16 h. (b) CHCl₃, Br₂, rt, 1 h. (c) Phenyl boronic acid, [Pd(PPh₃)₄], toluene, THF, water, Na₂CO₃, 85 °C, 16 h. (d) N₂H₄•H₂O, 1,4-dioxane, 101 °C, 16 h.

2-Amino-9,10-diphenylanthracene (**4**) was synthesised from 2-aminoanthracene. Firstly the amine was protected by a condensation reaction with phthalic anhydride in basic 2-ethoxyethanol. The crude product was recrystallised from nitrobenzene to yield pure **1** as a cream-coloured powder and characterised by ¹H, ¹³C{¹H} NMR spectroscopy and HR MS. The protected amine could then undergo bromination in the 9,10- positions of the anthracene, using dropwise addition of bromine in chloroform to a solution of **1** in CHCl₃.⁶⁴ The solvent was removed, and the product crystallised from xylenes to give the desired dibromo product **2** as an off-white solid. Due to solubility issues in all common solvents, the product was only characterised by ¹H NMR spectroscopy and mass spectrometry. The ¹H NMR spectrum singlets assigned to the 9- and 10- positions (at 8.48 and 8.47 ppm) of **1** have disappeared, and instead there are two resonances now above 8.7 ppm. These are assigned to the protons in position

5- and 8- around the anthracene core, due to the proximity to the bromides in the molecule. The protons in position 1- and 4- are also likely shifted downfield, however not to the same magnitude due to the added mesomeric effects of the phthalimide group.

With bromination successful, **2** was then suspended in a 1:1 mixture of THF and toluene with stirring. Phenyl boronic acid (three equivalents) and $[\text{Pd}(\text{PPh}_3)_4]$ (7 mol%) were added to the flask alongside Na_2CO_3 in water. The suspension was heated at reflux overnight in the absence of light,⁵⁷ and after cooling a yellow solution remained. After the solvents were removed, the product was washed with water and brine before being purified by silica gel column chromatography, eluting with 10 % EtOAc in petroleum ether to yield **3** as a yellow solid. **3** was characterised by ^1H , $^{13}\text{C}\{^1\text{H}\}$ NMR spectroscopy and HR MS. As well as the improved solubility, the ^1H NMR spectrum showed all resonances were found below 8 ppm, meaning the effects seen from the dibromide substitutions in **2** are no longer present. For the deprotection, **3** was dissolved in 1,4-dioxane, and hydrazine hydrate was added slowly. After heating overnight at 101 °C, a new emissive green spot appeared on TLC, showing the hydrazinolysis was complete. After the reaction was cooled, the solvent was removed and the solution triturated in acetone, where 2,3-dihydrophthalazine-1,4-dione was precipitated and removed via filtration. The crude species could then be purified by column chromatography, eluting first with 1:1 DCM + hexanes to remove remaining starting materials, before the brightly green emissive product was eluted from the base line using DCM to give the desired 2-amino-9,10-diphenylanthracene in good yields. The light-yellow powder of **4** was characterised by ^1H , $^{13}\text{C}\{^1\text{H}\}$ NMR spectroscopy and HR MS. ^1H NMR spectrum has a broad singlet resonance of the primary amine at 3.80 ppm, as well as resonances below 7.0 ppm, belonging to the protons on the aniline ring due to the large mesomeric effect of the primary amine in comparison to the imide.

7.3.3 Ligand synthesis and characterisation

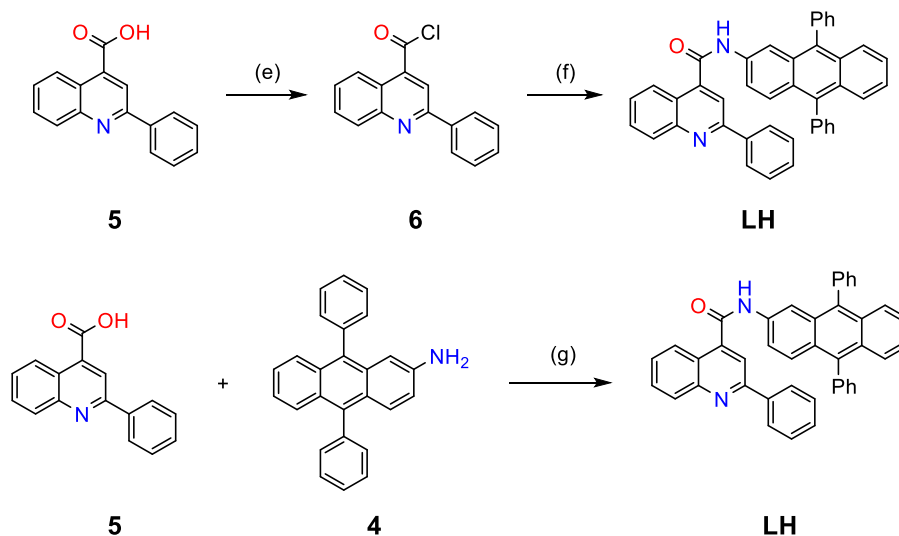


Figure 7.9 – Unsuccessful synthetic routes tried towards **LH**. (e) SOCl_2 , rt, 16 h, (f) **4**, CHCl_3 , DIPEA (2eq), rt, 16 h. (g) MeCN / DCM (1:1), EDC•HCl (5 eq), NHS (5 eq), TEA (0.1 eq), 16 hours, rt.

With the successful synthesis of **4**, a coupling reaction could now take place. Two methods of amide coupling were attempted as shown in Figure 7.9. Firstly, following the acid chloride route previously used within the Pope Group⁵⁹. To a stirring solution of **6** in CHCl_3 , **4** (1 eq) was added alongside a few drops of a base. The mixture was stirred at rt for 16 hours. No product was detected after work up. Therefore, a second attempt was made to form the amide following EDC/NHS coupling procedures. Once again, only starting materials were recovered. It appears the added conjugation and resonance stability from the two additional phenyl rings thoroughly deactivated the amine's nucleophilicity. It is possible that the steric bulk from the DPA and the phenylquinoline are also hindering the reaction.

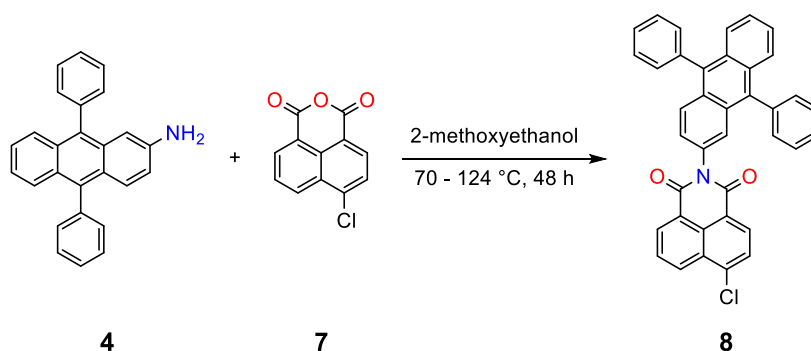


Figure 7.10 – Reactions of **4** to test reactivity; attempted naphthalimide synthesis.

Therefore, one final reaction, shown in Figure 7.10, was attempted – the formation of naphthalimide **8**, a compound that would also be expected to show interesting photophysical properties. 4-Chloro-1,8-naphthalic anhydride was dissolved in 2-methoxyethanol before **4** was added. The reaction was left overnight for 16 hours at 70 °C. The next morning TLC analysis showed no change to the reaction. The temperature was increased to heat the mixture at reflux for a further 32 hours and monitored by TLC. After a total of 48 hours heating, the TLC revealed no new spots. Therefore, the mixture was cooled to room temperature, and the solvent was removed before the components were separated by silica gel column chromatography to ensure the naphthalimide and the starting materials were not co-eluting. ¹H NMR spectroscopy on the fractions confirmed only starting materials were recovered.

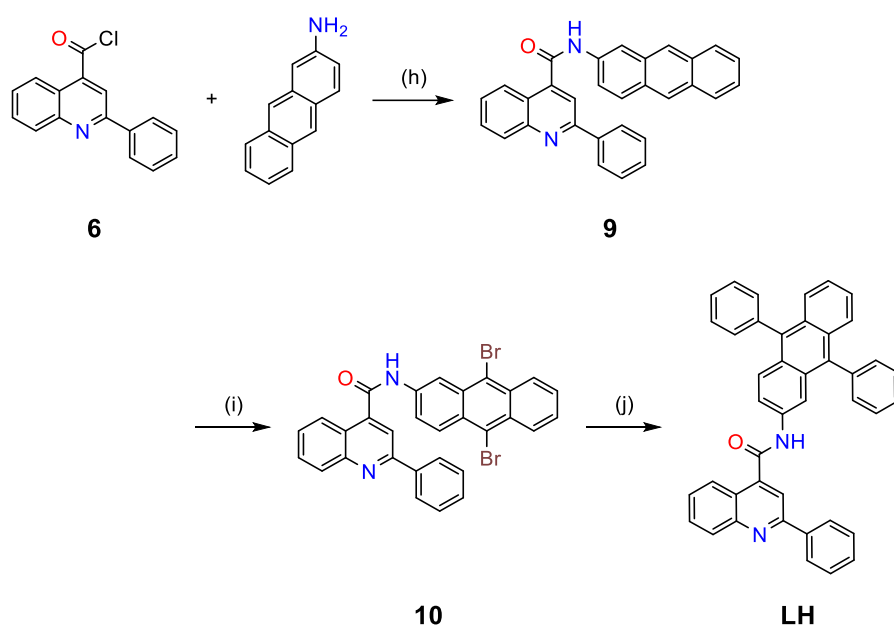


Figure 7.11 – Suzuki-Miyaura cross coupling method used for the final synthesis of **LH**. (h) TEA (2.1 eq), CHCl₃, 16 h, rt. (i) Br₂, CHCl₃, 4 h, rt. (j) Phenyl boronic acid, [Pd(PPh₃)₄], toluene, THF, water, Na₂CO₃, 16 h, 85 °C.

Since **4** was showing no signs of nucleophilicity, a new approach was adopted. The revised synthetic route is shown in Figure 7.11. Firstly, acyl chloride **6** was synthesised, and added to a stirring solution of 2-aminoanthracene to give amide **9**. After the solvent was removed, the crude solid was suspended in a minimum amount of CHCl₃, collected upon a sinter and washed with ice cold CHCl₃ before the resulting yellow powder was analysed by ¹H and ¹³C{¹H} NMR spectroscopy alongside HR MS. The dibromide species **10** was successfully synthesised by slow

addition of Br₂ into a stirring solution of **9** in CHCl₃. After stirring for four hours, the solvents were removed and the red solid of **10** was washed with cold CHCl₃, before analysis by ¹H and ¹³C{¹H} NMR spectroscopy alongside HR MS. Finally, the Suzuki-Miyaura cross coupling reaction was utilised as before; **10** was dissolved in a mixture of THF and toluene (1:1) before the addition of phenyl boronic acid, aqueous Na₂CO₃ and [Pd(PPh₃)₄]. The reaction was left overnight at 85 °C before the organic solvents were removed and the product washed with water to finally yield the ligand **LH** as a yellow solid.

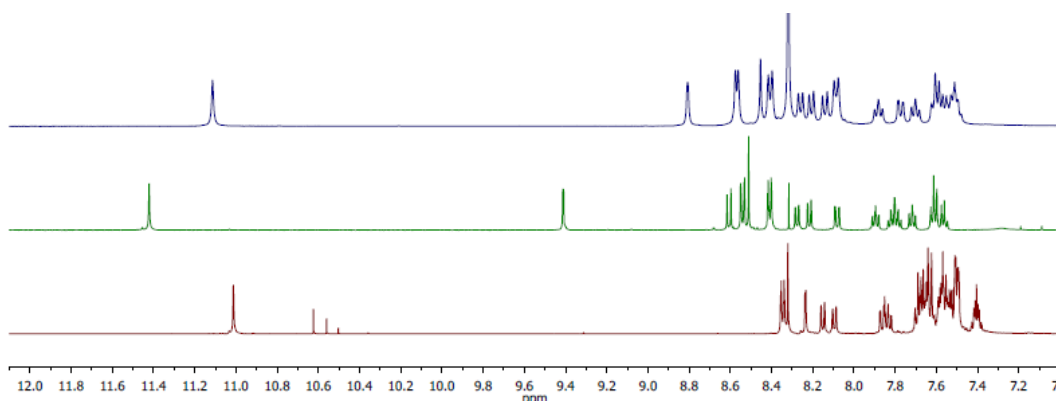


Figure 7.12 – NMR (500 MHz) spectra obtained in d₆-DMSO. Top – **9**, Middle – **10**, Bottom – **LH**.

The aromatic regions from the ¹H NMR spectra of the compounds **9**, **10** and **LH** recorded in d₆-DMSO can be seen in Figure 7.12. All three spectra display the broad singlet of the amide proton, integrating to 1H, meaning none of the potential side reactions occurred in this position during the cross coupling. There are subtle differences in the shifts depending upon the nature of the anthracene substituents, with the shift varying between 11.01 – 11.42 ppm. The addition of the bromides on **10** shift the amide proton resonance to its most deshielded position (11.42 ppm), while the added conjugation of the diphenyl substitution on **LH** are enough to show a slight difference over the unsubstituted **9** (11.01 vs 11.11 ppm respectively). Upon bromination, the two singlets from the 9,10- positions of the anthracene disappear from **10**, having previously been seen at 8.08 and 8.10 ppm respectively in compound **9**. One resonance became very deshielded at 9.41 ppm, likely a combination of the proximity to nearby aromatic ring currents and the large bromide atoms. After the successful cross coupling, new added resonances for the two phenyl rings were centred around 7.6 ppm.

7.3.4 Complex synthesis and characterisation

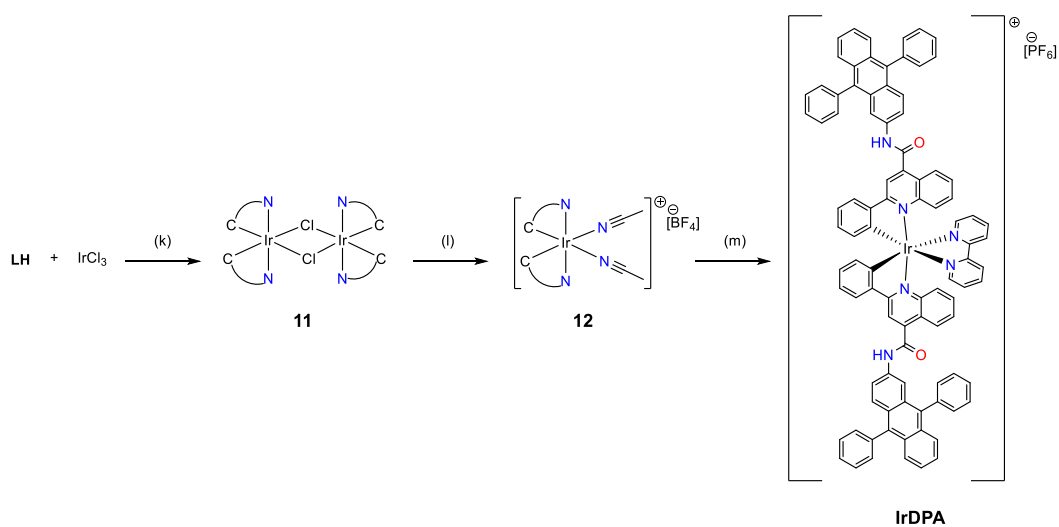


Figure 7.13 – Synthetic approach to complex synthesis following the Nonoyama iridium dimer formation⁶⁵. (k) 2-methoxyethanol, 48 h, 124 °C. (l) AgBF₄ (2 eq), MeCN, 16 h, 82 °C. (m) i) 2,2'-bipyridine (1.2 eq), CHCl₃, 70 °C, 8 h, ii) MeCN, [NH₄][PF₆], 10 minutes, rt.

With ligand in hand, the synthesis of the *bis*-cyclometalated Ir(III) complex was attempted following the procedures outlined in Figure 7.13. IrCl₃·xH₂O was heated in 2-methoxyethanol with two equivalents of **LH** to form the dimeric cyclometalated Ir(III) species, **11**⁶⁵. The dimer was precipitated by addition of distilled water before collection on a sinter. Crude dimer **11** was washed with water (2 x 10 mL) and allowed to dry in an oven before being used in the subsequent reaction without purification or further analysis. The chlorides were then abstracted by heating in MeCN solution with AgBF₄ to give the *bis*-MeCN Ir(III) complex, **12**. Precipitated AgCl salt was removed by filtration through a celite pad, before collecting the red filtrate and removing the solvent *in vacuo*. Crude complex **12** was then stirred in refluxing CHCl₃ with an excess of bpy overnight. The resulting complex then underwent counterion metathesis with PF₆⁻ before recrystallisation from DCM by diethyl ether addition to yield the desired complex [Ir(L)₂(bpy)]PF₆ (**IrDPA**). **IrDPA** was analysed by ¹H, ¹³C{¹H} NMR spectroscopy as well as mass spectrometry.

In the ¹H NMR spectra, the amide protons were a singlet at 11.11 ppm. As seen in previous chapters, the quinoline singlet from position 3 shifted to become the most downfield aromatic environment, from 8.32 ppm in the free ligand to 8.71 ppm upon complexation. This is characteristic for these complexes, caused by the inductive effects of the larger cationic iridium (III) atom. Resonances were shifted upfield into

more shielded positions, such as the multiplet seen at 6.34 – 6.48 ppm, which is typically assigned to the quinoline positions which are positioned close to the ancillary ligand's aromatic ring currents, causing the extra shielding, and giving further evidence of complexation. Mass spectrometry was obtained, with the low-resolution spectrum showing clusters of peaks for $[M]^+$, $[M+MeOH]^+$ and $[M+2MeOH]^+$ (see Figure 7.14)

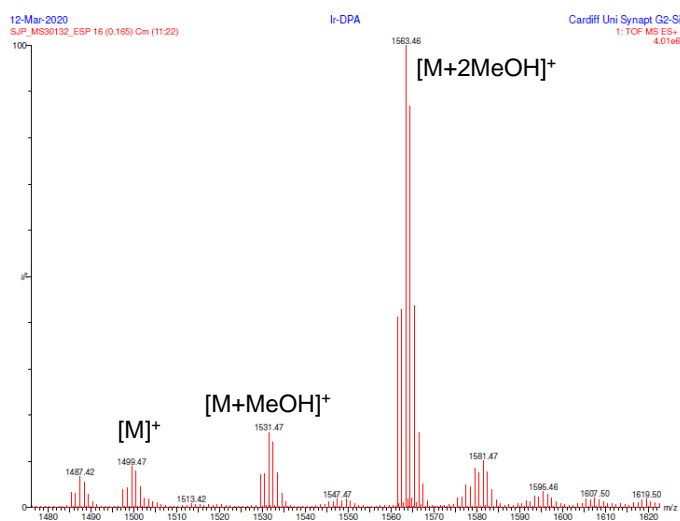


Figure 7.14 – Low resolution ES+ mass spectrum for IrDPA.

When run in high-resolution mode, the perceived $[M+2MeOH]^+$ adduct peak was once again dominant. When the elemental composition of the peak was analysed, the isotopic distribution looks consistent with the formulation, but the m/z deviates by 43 ppm (see Figure 7.15). Since HR MS is not regarded as reliable for $m/z > 1000$ this error may simply reflect the limitations of the measurement.

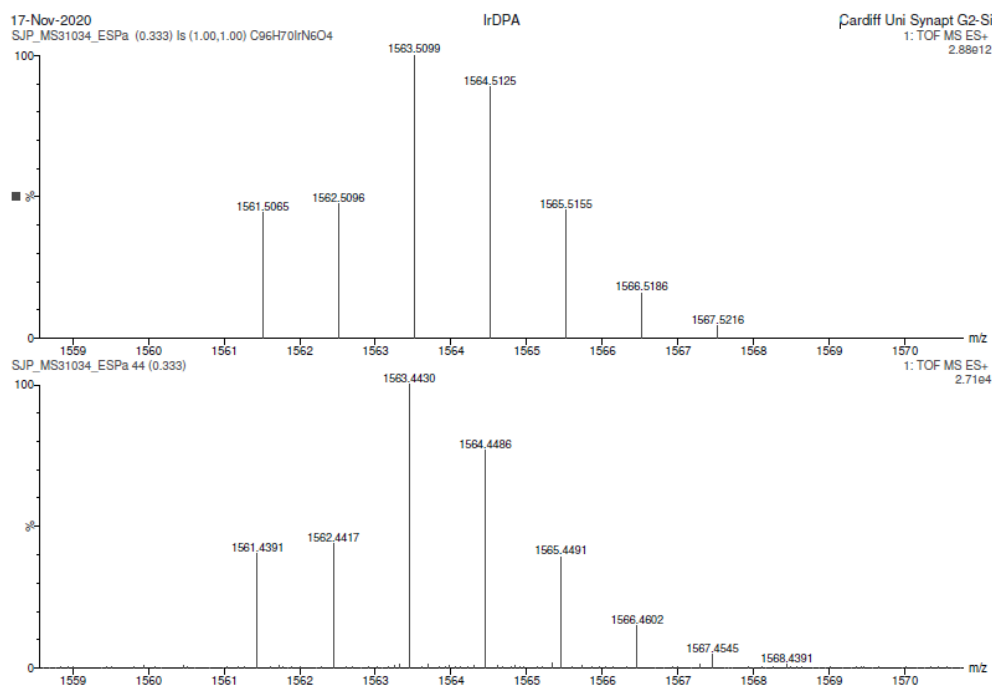


Figure 7.15 – Top: projected spectra for **IrDPA** $[M+2MeOH]^+$ adduct. Below: experimental results.

7.3.5 Ligand absorption and emission properties

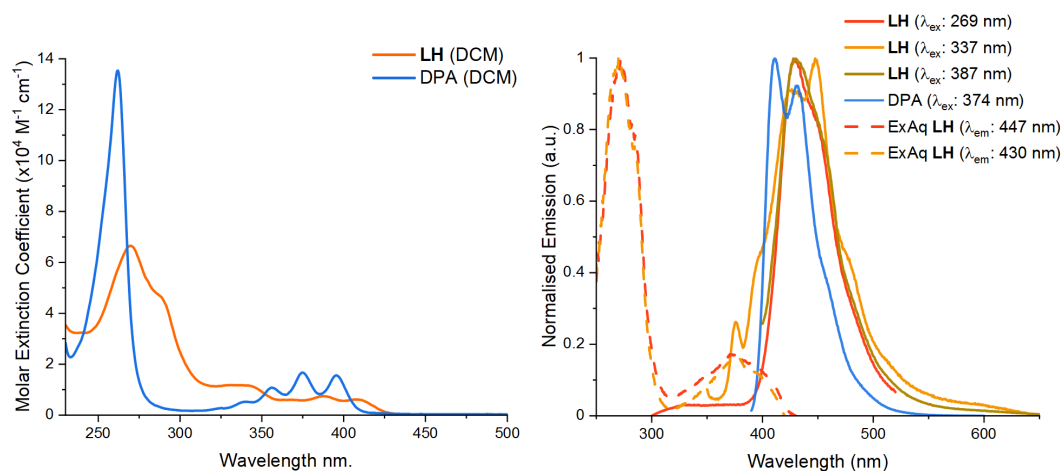


Figure 7.16 – Left: UV-VIS spectra for **LH** and **DPA** recorded in aerated DCM at ca. 10^{-5} M. Right: Emission spectra (solid lines) and excitation acquisitions (dotted lines) for **LH** and **DPA** recorded in aerated DCM at ca. 10^{-5} M.

Absorption and emission spectra for **LH** were recorded in aerated DCM solutions at ca. 10^{-5} M (Figure 7.16). Absorptions between 270 and 340 nm are likely dominated by the 2-phenylquinoline $\pi-\pi^*$ transitions, and only show a slight bathochromic shift in comparison to alkyl substituted 2-phenylquinoline amides⁵⁹. The region past 450 nm is more likely due to the **DPA** amide feature of the ligand.

The spectrum of DPA shows three features at 356, 374 and 395 nm, and while **LH** features in this region are less well-defined at 367, 386 and 480 nm. This bathochromic shift from DPA is likely caused by the addition of the amide functionality to the anthracene core.

Emission spectra show overlapping bands centring around 430 nm with some shoulder features of both lower energy and higher energy transitions. The excitation spectra for 430 nm and 447 nm show two featureless overlapping excitations in the region of ca. 310 – 420 nm, showing the emission is associated with contributions from the quinoline and the amide DPA moieties. The lifetime of **LH** (Table 7.1) was also mono exponential at 7.3 ns. While the lifetime is longer than the quinolines seen earlier in this work, it is comparable to the DPA lifetimes. The quantum yield of **LH** is significantly lower than reported for DPA (0.95⁴⁶).

	$\lambda_{\text{abs}} (\epsilon / 10^4 \text{ M}^{-1} \text{ cm}^{-1}) / \text{nm}^{\text{a}}$	$\lambda_{\text{em}} / \text{nm}$	$\lambda_{\text{ex}} / \text{nm}^{\text{d}}$	$\tau / \text{ns}^{\text{e}}$	Φ
LH	408 (0.6), 386 (0.7), 367 (0.7), 340 (1.2), 285 (4.7) 270 (6.6)	430 450 (sh) ^b	270, 284, 377, 393	7.3	0.003 ^f
DPA	395 (1.5), 374 (1.6), 356 (1.1), 340 (0.5), 262 (13.5),	411 430 ^c	-	6.4 6.5	0.95 ⁴⁶

Table 7.1 – ^a All measurements run at room temperature in aerated CH₂Cl₂ at ca. 1x10⁻⁵ M. ^b $\lambda_{\text{ex}} = 387 \text{ nm}$; ^c $\lambda_{\text{ex}} = 374 \text{ nm}$; ^d $\lambda_{\text{em}} = 447 \text{ nm}$; ^e $\lambda_{\text{ex}} = 295 \text{ nm}$; ^f Vs standard quinine sulfate in 0.05 M H₂SO₄, $\lambda_{\text{ex}} = 350 \text{ nm}$.⁶⁶

When the same emission experiments were repeated on a more concentrated solution (10⁻³ M), the emission shifted to a single peak at 460 nm. In the excitation spectrum, the transitions between 350 nm and 450 nm became dominant, showing three sharp transitions from the DPA moiety (Figure 7.17 and Table 7.2). This aggregated modulated emission and excitation profile shows that the DPA moiety on **LH** is becoming more efficient as the concentration increases in line with the larger quantum efficiency.

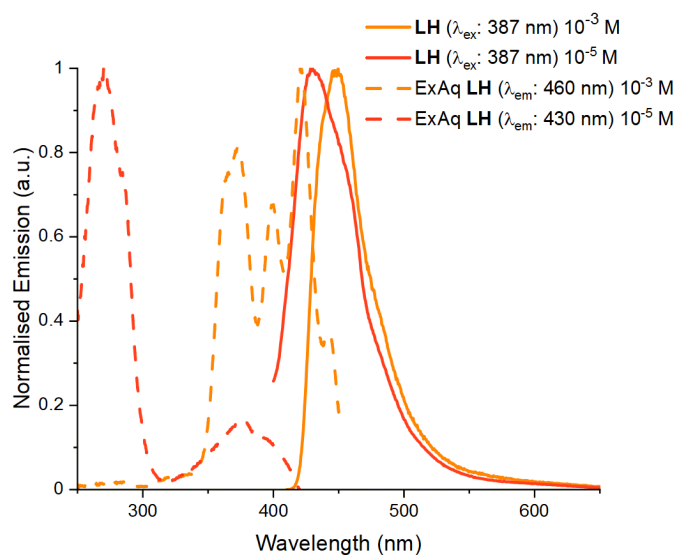


Figure 7.17 – Left: Emission and excitation spectra for **LH** showing dependence upon concentration. Right: 10^{-3} M excitation acquisition compared to the absorption of DPA.

[LH] / M	λ_{em} / nm ^a	λ_{ex} / nm
10^{-3}	460	442, 421, 399, 372, 363(sh) ^b
10^{-5}	430, 450 (sh)	393, 377, 284, 270 ^c

Table 7.2 – ^a All measurements recorded in aerated CH_2Cl_2 . $\lambda_{ex} = 387$ nm; ^b Recorded at $\lambda_{em} = 460$ nm; ^c $\lambda_{em} = 430$ nm

7.3.6 Complex absorption and emission properties

7.3.6.1 Absorption spectrum

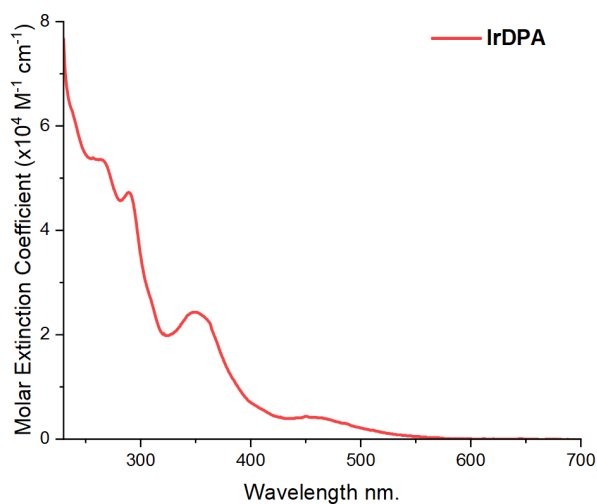


Figure 7.18 - Absorption spectrum of **IrDPA** recorded in aerated DCM at ca. 10^{-5} M.

The absorption spectrum for **IrDPA** can be seen above in Figure 7.18. Strong absorbances between 240 and 300 nm are assigned to $^1\pi-\pi^*$ transitions, with weaker contributions from the heteroatomic $^1n-\pi^*$ transitions. Weaker features past 430 nm are normally assigned to the spin allowed 1MLCT transitions, with the feature tailing off towards 600 nm including the spin forbidden 3MLCT absorbances.

7.3.6.2 Aerated emission measurements

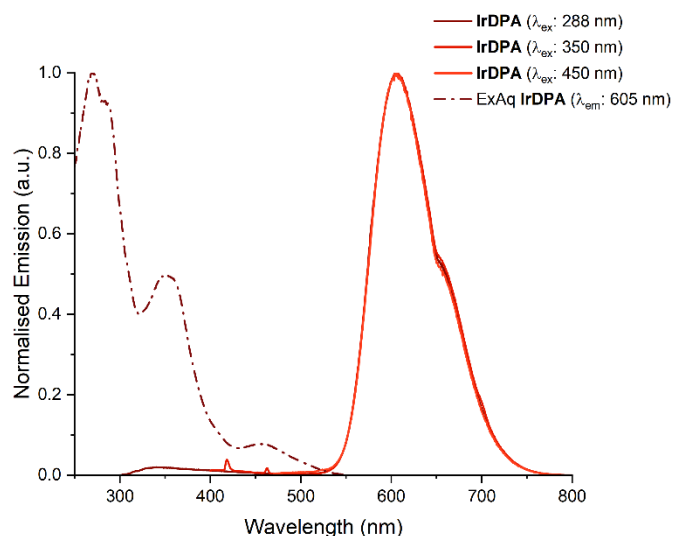


Figure 7.19 – Emission (solid line) and excitation (dashed line) spectra for **IrDPA** recorded in aerated CH_2Cl_2 at ca. 10^{-5} M

Steady state emission measurements of **IrDPA** can be seen in Figure 7.19, and were recorded in an aerated DCM solution at ca. 10^{-5} M. Emission shows a λ_{max} at 605 nm, independent of excitation wavelength. The excitation spectrum shows a distinct similarity to the absorption spectra both in peak positions and relative intensities. The emission λ_{max} and the excitation spectra follow the trends seen for previous cyclometalated Ir(III) amide complexes of 2-phenylquinolines.⁵⁹ The system does, however, exhibit a quantum yield which is an order of magnitude larger than those seen in Chapters 4 and 5.

	$\lambda_{abs} (\epsilon / 10^4 M^{-1} cm^{-1}) / nm^a$	λ_{em} / nm^b	λ_{ex} / nm^c	Φ^d
IrDPA	463 (0.3), 351 (2.4), 289 (4.7), 261 (5.3)	605	456, 353, 284, 269	0.167

Table 7.3 - ^a All measurements run at room temperature in aerated CH_2Cl_2 at ca. 10^{-5} M. ^b $\lambda_{ex} = 450$ nm; ^c $\lambda_{em} = 605$ nm; ^d Vs standard $[Ru(bpy)_3](PF_6)_2$ in MeCN, $\lambda_{ex} = 430$ nm. ⁶⁶

Time resolved measurements are seen below in Table 7.4. The lifetime at 430 nm (3.0 ns) is around half that seen for the ligand and free DPA in solution (7.3 and 6.5 ns respectively) and shows a k_r value typical of fluorescence. For the lower energy emission, the lifetime is 405 ns which is indicative of phosphorescent emission.

		$(\lambda_{\text{ex}} = 295 \text{ nm})$			
		$\lambda_{\text{em}} / \text{nm}$	τ / ns	k_r / s^{-1}	$k_{\text{nr}} / \text{s}^{-1}$
IrDPA	411	2.7	6.2×10^7	3.1×10^8	
	430	3.0	5.6×10^7	2.8×10^8	
	605	405	4.1×10^5	2.1×10^6	

Table 7.4 – **IrDPA** complex lifetime recorded in aerated CH_2Cl_2 at ca. 10^{-5} M.

Finally, the ligand and complex underwent emission studies at 77 K in a 4:1 methanol / ethanol matrix. Spectra can be seen below in Figure 7.7. All three compounds display more fine structure to their emission profiles. DPA and **LH** once again have transitions at the same wavelength, as also seen at RT. The main emission peak from **IrDPA** has shifted hypsochromically to 570 nm, while there are smaller features at 610 and 666 nm, likely due to rigidochromic effects.

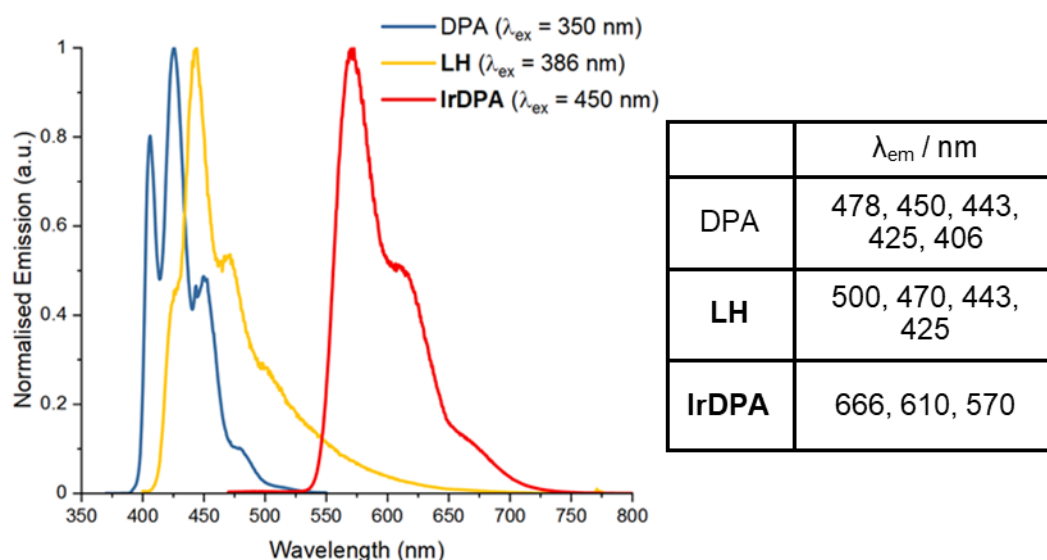


Figure 7.20 – 77 K emission spectra recorded in 4:1 EtOH : MeOH glass.

When compared with the results of the RT measurements, both steady state and time resolved, the results all tie together showing energy transfer from the DPA moiety towards the emissive state (Figure 7.21), which is seen ultimately in the increased QY performance of the complex in comparison to similar ligand systems seen in Chapter 4 and earlier work by Pope *et al*⁶⁹.

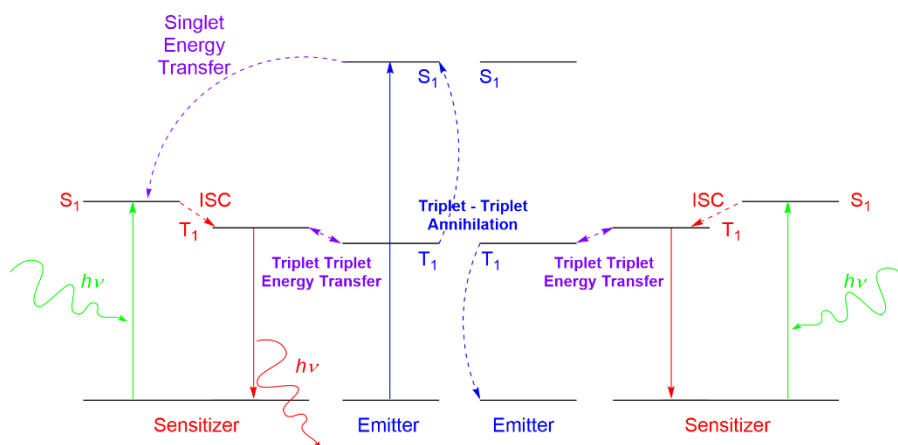


Figure 7.21 – Possible energy transfer processes seen in the IrDPA molecule. Here, sensitizer refers to the cyclometalated iridium complex, and emitter references to the amino DPA moiety.

7.3.7 Degassed emission measurements

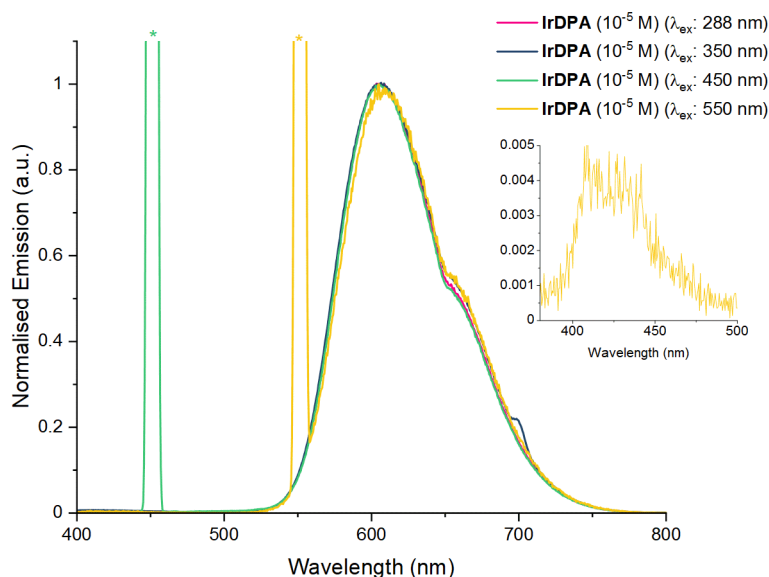


Figure 7.22 - Emission spectra for IrDPA recorded in degassed CH₂Cl₂. Insert: Expanded DPA emission region showing upconversion emission from 550 nm excitation. * Indicates scattering from the lamp.

Steady state emission spectra were recorded in degassed DCM solutions using differing excitation wavelengths (see Figure 7.22). λ_{max} emission remains consistent with aerated samples from the previous section at 605 nm. When excited at 550 nm, which is selective for the MLCT features and away from the

DPA absorption, the complexes display a small degree of upconversion performance (see insert, Figure 7.22). To investigate this more, further solutions were made up with additional DPA, using 10^{-6} , 10^{-5} and 10^{-4} M additions of DPA to a 10^{-5} M **IrDPA** solution in DCM (See Figure 7.23).

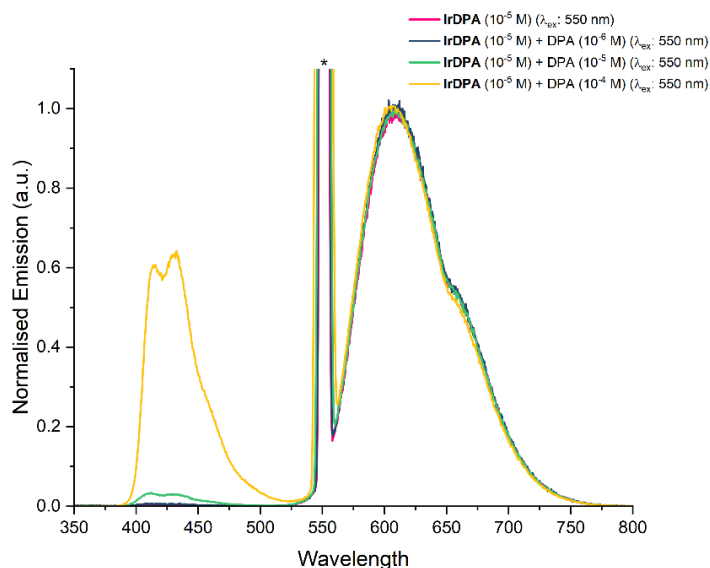


Figure 7.23 – TTA-UC between **IrDPA** and DPA at indicated concentrations. * indicated signal from the scattered lamp.

Firstly, as the acceptor concentration is increased from 10^{-5} M to 10^{-4} M, the degree of TTA-UC increases significantly⁶⁷. Showing that TTA-UC is occurring, excitation spectra were obtained for each of the solution at 660 nm and 411 nm (see Figure 7.24). The excitation spectra for $\lambda_{em} = 660$ nm show a decrease in signal strength as the concentration of the acceptor is increased. This is indicative of energy transfer occurring from the triplet excited state, as expected in a TTA-UC process. Interestingly, they also reveal an increase in the fine structure of the spectra in the 330 – 400 nm region, which is likely occurring from the increase in DPA, which may suggest there is also back triplet-triplet energy transfer also occurring.

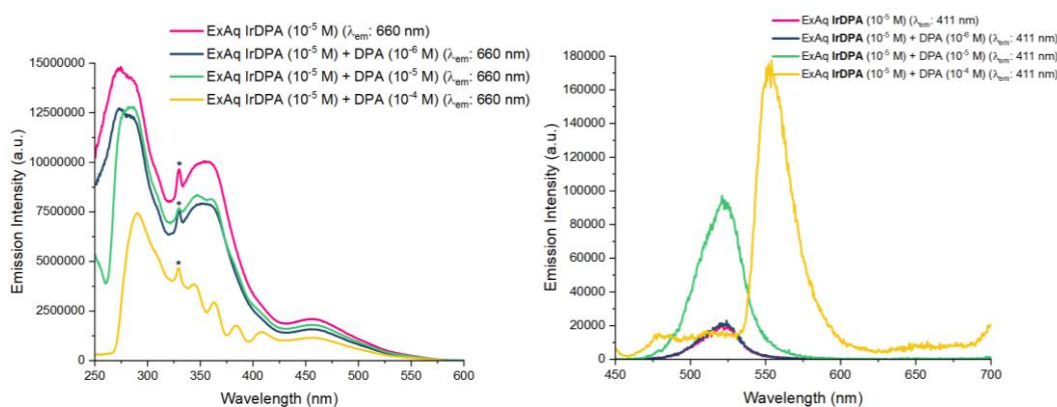


Figure 7.24 – Degassed excitation acquisition spectra for **IrDPA** + added DPA. Left: $\lambda_{em} = 660$ nm, Right $\lambda_{em} = 411$ nm.

In the $\lambda_{em} = 411$ nm excitation spectrum, a transition at 523 nm is occurring for each solution, with increasing intensity as the concentration of DPA is increased up until + 10^{-5} M DPA solution. As the concentration is increased to 10^{-4} M, an excitation transition at 550 nm appears, and the 523 nm transition becomes a minor component. When the sample with + 10^{-5} M DPA is run a $\lambda_{ex} = 523$ nm the emission signal intensity at 411 / 430 nm is increased in comparison to the $\lambda_{ex} = 550$ nm (Figure 7.25).

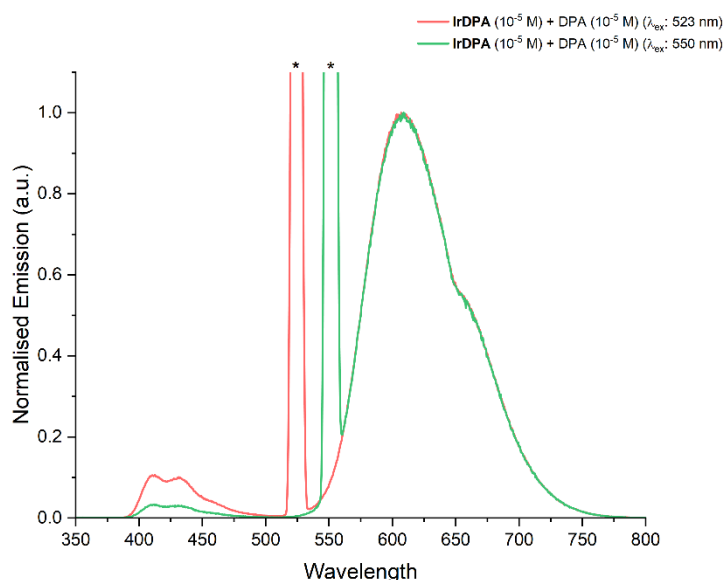


Figure 7.25 - Emission spectra for **IrDPA** with DPA addition at differing λ_{ex} .

Time resolved measurements for the degassed solutions are seen below in Table 7.5. For **IrDPA**, the lack of oxygen in solution has increased the lifetimes of the triplet emissive state considerably. When additional DPA is added to the solution, the lifetimes of the $^3\text{MLCT}$ level drop significantly. This is likely the effect of efficient

triplet-triplet energy transfer towards the DPA molecules in solution that effectively quenches the donor ³MLCT level.

	τ ($\lambda_{em} = 411$ nm) / ns	τ ($\lambda_{em} = 605$ nm) / ns
IrDPA (10^{-5} M)	6.4	1016
IrDPA (10^{-5} M) + DPA (10^{-4} M)	8.3	24

Table 7.5 – Complex lifetimes recorded in degassed CH₂Cl₂ solution. $\lambda_{ex} = 295$ nm.

7.4 Conclusions

This chapter has shown the design, synthesis, and characterisation of both the novel 2-amino-9,10-diphenylanthracene, and the novel N-(9,10-diphenylanthracen-2-yl)-2-phenylquinoline-4-carboxamide ligand. The initial synthetic route towards amino DPA proved successful, but the further reactions of the primary amine were unsuccessful, with the additional stability offered from the increased conjugation deactivating the nucleophilicity of the amine. The target ligand was finally synthesised but first forming the amide with amino anthracene before bromination and cross coupling chemistry were used. The ligand was successfully cyclometalated upon Ir(III) and the resultant complex has been characterised by NMR, UV vis and emission spectroscopies.

The complex has been shown to produce triplet-triplet annihilation upconversion performance in deaerated solution, and as the concentration of DPA is increased the performance is increased significantly.

In aerated solution, the complex has shown a remarkable increase in quantum yield and lifetime in comparison to similar complexes⁵⁹, showing the energy transfer pathways between the ligand and the DPA moieties exist in both directions.

7.5 Experimental

All reactions were performed with the use of vacuum line and Schlenk techniques. Reagents were commercial grade and were used without further purification. ^1H and ^{13}C spectra were recorded on a Bruker fourier 300, dpx 400, or avance 500 MHz spectrometer, and were recorded in CDCl_3 or d_6 -DMSO solutions. ^1H and $^{13}\text{C}\{^1\text{H}\}$ NMR chemical shifts (δ) were determined relative to internal tetramethylsilane, $\text{Si}(\text{CH}_3)_4$ and are given in ppm. Low-resolution mass spectra were obtained by the staff at Cardiff University. High-resolution mass spectra were carried out by the staff at Cardiff University. All photophysical data was obtained on a JobinYvon-Horiba Fluorolog-3 spectrometer fitted with a JY TBX picosecond photodetection module in CH_2Cl_2 or MeCN solutions. Emission spectra were uncorrected and excitation spectra were instrument corrected. The pulsed source was a Nano-LED configured for 295, 372 or 459 nm output operating at 500 kHz or 1 MHz. Luminescence lifetime profiles were obtained using the JobinYvon-Horiba FluoroHub single photon counting module and the data fits yielded the lifetime values using the provided DAS6 deconvolution software. IR spectra were recorded on an ATR equipped Shimadzu IRAffinity-1 spectrophotometer. UV-vis data were recorded as solutions on a Perkin Elmer Lambda20 spectrophotometer. TTA Energy Upconversion measurements utilized $c(\text{sensitiser}) = 1 \times 10^{-5}$ M, $c(\text{DPA}) = 5 \times 10^{-4}$ M, 20 °C; deaerated CH_2Cl_2 .

7.5.1 2-(anthracen-2-yl)isoindoline-1,3-dione (1)

2-aminoanthracene (2.5 g, 12.9 mmol), phthalic anhydride (2.3 g, 16.0 mmol) and triethylamine (0.15 mL, 1.1 mmol) were dissolved in 2-ethoxyethanol (30 mL) with stirring. The flask was wrapped in foil to protect from light and heated to 80 °C for 16 hours. Upon cooling, the solvent was removed *in vacuo* and the crude was purified by recrystallised from nitrobenzene. The precipitate was collected upon a sinter, washed with cold ethanol (3 x 10 mL) and dried to yield beige solid (2.54 g, 61 %). ^1H NMR (400 MHz, CDCl_3) δ 8.48 (s, 1H), 8.47 (s, 1H), 8.15 – 8.11 (m, 2H), 8.05 – 7.99 (m, 4H), 7.84 (d, $J = 3.0$ Hz, 1H), 7.83 (d, $J = 3.1$ Hz, 1H), 7.54 (dd, $J = 8.9, 2.0$ Hz, 1H), 7.50 (dd, $J = 6.6, 3.2$ Hz, 2H) ppm. $^{13}\text{C}\{^1\text{H}\}$ NMR (126 MHz, d_6 -DMSO) δ 168.3, 134.8, 131.7, 131.6, 131.5, 130.5, 130.0, 129.9, 128.9, 128.1, 128.0, 126.5, 126.0, 125.0, 123.5 ppm. HRMS (ES) $[\text{M} + \text{H}]^+$ Calc'd for $\text{C}_{22}\text{H}_{14}\text{NO}_2$ 324.1025; Found m/z 324.1021.

7.5.2 2-(9,10-dibromoanthracen-2-yl)isoindoline-1,3-dione (2)

2-(anthracen-2-yl)isoindoline-1,3-dione (500 mg, 1.55 mmol) was suspended in chloroform (40 mL). The flask was covered in foil and then a solution of bromine (0.16 mL, 3.12 mmol) in chloroform (20 mL) was added dropwise over the space of one hour. After this time, the solvent was removed *in vacuo* to give the crude product, which was purified by recrystallisation from xylenes to afford a yellow solid (670 mg, 90 %). ¹H NMR (300 MHz, CDCl₃) δ 8.77 (d, J = 5.3 Hz, 1H), 8.75 (d, J = 12.7 Hz, 1H), 8.64 – 8.58 (m, 2H), 8.04 (d, J = 3.1 Hz, 1H), 8.03 (d, J = 3.0 Hz, 2H), 7.89 – 7.84 (m, 2H), 7.77 (d, J = 1.9 Hz, 1H), 7.74 (d, J = 1.6 Hz, 1H), 7.69 (d, J = 3.2 Hz, 1H), 7.67 (d, J = 3.2 Hz, 1H) ppm. HRMS (ES) [M + H]⁺ Calc'd for C₂₂H₁₂NO₂Br₂ 479.9235; Found *m/z* 479.9226.

7.5.3 2-(9,10-diphenylanthracen-2-yl)isoindoline-1,3-dione (3)

2-(9,10-dibromoanthracen-2-yl)isoindoline-1,3-dione (100 mg, 0.208 mmol), phenyl boronic acid (76 mg, 0.624 mmol) and [Pd(PPh₃)₄] (16 mg, 0.015 mmol, 7 mol%) were suspended in a 1:1 mixture of THF and Toluene (6 mL). To this, sodium carbonate (88 mg, 0.833 mmol) solution in water (1 mL) was added and the mixture was heated for 16 hours at 85 °C. Upon cooling the mixture was diluted with water and extracted into diethyl ether (3 x 20 mL). The combined organics are washed with water (3 x 10 mL), brine (3 x 15 mL) and dried over MgSO₄. the solvent was removed, and the resultant crude was purified by silica gel column chromatography (ethyl acetate in petroleum ether 1:9, RF: 0.1) to yield a yellow solid (93 mg, 94 %). ¹H NMR (500 MHz, CDCl₃) δ 7.94 – 7.89 (m, 2H), 7.83 (d, J = 9.3 Hz, 1H), 7.78 – 7.74 (m, 3H), 7.72 (dd, J = 6.8, 3.3 Hz, 2H), 7.64 – 7.57 (m, 4H), 7.55 – 7.47 (m, 6H), 7.39 – 7.34 (m, 3H) ppm. ¹³C{¹H} NMR (126 MHz, CDCl₃) δ 167.5, 138.8, 138.6, 137.8, 137.5, 134.5, 134.5, 132.0, 131.5, 131.4, 130.5, 130.4, 129.7, 129.0, 128.7, 128.6, 128.6, 128.6, 128.5, 128.4, 127.8, 127.8, 127.2, 127.2, 125.6, 125.1, 123.8, 123.6 ppm. HRMS (ES) [M + H]⁺ Calc'd for C₃₄H₂₂NO₂ 476.1651; Found *m/z* 476.1639.

7.5.4 2-amino-9,10-diphenylanthracene (4)

Hydrazine Hydrate (0.15 mL, 0.309 mmol) was added to a stirring solution of 2-(9,10-diphenylanthracen-2-yl)isoindoline-1,3-dione (100 mg, 0.210 mmol) in 1,4-dioxane (2 mL) and the mixture was heated at reflux for 16 hours in the absence of light. Upon cooling, the solvent was removed *in vacuo*, and triturated in acetone (5 mL). The precipitate was removed by filtration and the filtrate

concentrated before the crude was purified by silica gel column chromatography (1:1 DCM/ Hex → DCM), collecting the strong yellow band to yield a yellow powder (61 mg, 84 %) ^1H NMR (500 MHz, CDCl_3) δ 7.62 – 7.50 (m, 10H), 7.48 – 7.45 (m, 4H), 7.23 – 7.18 (m, 1H), 6.85 (dd, $J = 9.2, 2.3$ Hz, 1H), 6.72 (d, $J = 2.3$ Hz, 1H), 3.80 (s (br), 2H) ppm. $^{13}\text{C}\{^1\text{H}\}$ NMR (126 MHz, CDCl_3) δ 143.2, 139.9, 139.4, 137.4, 133.6, 131.6, 131.5, 131.4, 130.7, 130.1, 128.8, 128.6, 128.6, 128.4, 128.1, 127.5, 127.3, 127.2, 126.4, 126.3, 125.9, 125.1, 123.7, 119.8, 119.6, 105.3 ppm. HRMS (ES) $[\text{M} + \text{H}]^+$ Calc'd for $\text{C}_{26}\text{H}_{20}\text{N}$ 346.1596; Found m/z 346.1606.

7.5.5 N-(anthracen-2-yl)-2-phenylquinoline-4-carboxamide (9)

2-phenylquinoline-4-carboxylic acid (500 mg, 2 mmol) was stirred in an excess of SOCl_2 (5 mL) for 16 hours in the absence of light. The mixture was concentrated *in vacuo* before redissolving in CHCl_3 (10 mL). To the stirring mixture, 2-aminoanthracene (387 mg, 2 mmol) and triethylamine (0.6 mL, 4.21 mmol) were added to the flask and the resultant mixture was stirred for 16 hours at room temperature in the absence of light. The resultant precipitate was collected on a sinter and washed with cold CHCl_3 (3 x 10 mL) to yield a dark yellow powder (720 mg, 85 %). ^1H NMR (400 MHz, $\text{d}_6\text{-DMSO}$) δ 11.11 (s, 1H), 8.81 (s, 1H), 8.57 (d, $J = 5.5$ Hz, 2H), 8.45 (s, 1H), 8.41 (d, $J = 7.3$ Hz, 2H), 8.26 (d, $J = 8.3$ Hz, 1H), 8.21 (d, $J = 8.4$ Hz, 1H), 8.14 (d, $J = 9.1$ Hz, 1H), 8.10 (s, 1H), 8.08 (s, 1H), 7.88 (app. t, $J = 7.6$ Hz, 1H), 7.77 (dd, $J = 9.1, 1.4$ Hz, 1H), 7.70 (app. t, $J = 7.5$ Hz, 1H), 7.63 – 7.46 (m, 5H) ppm. $^{13}\text{C}\{^1\text{H}\}$ NMR (101 MHz, $\text{d}_6\text{-DMSO}$) δ 165.7, 155.9, 148.0, 142.9, 138.2, 135.9, 131.8, 131.5, 130.7, 130.4, 130.0, 129.7, 129.0, 128.8, 128.1, 127.8, 127.5, 127.4, 126.0, 125.7, 125.4, 125.2, 125.2, 123.2, 121.3, 117.0, 115.3 ppm. HRMS (ES) $[\text{M} + \text{H}]^+$ Calc'd for $\text{C}_{30}\text{H}_{21}\text{N}_2\text{O}$ 425.1654; Found m/z 425.1656.

7.5.6 N-(9,10-dibromoanthracen-2-yl)-2-phenylquinoline-4-carboxamide (10)

N-(anthracen-2-yl)-2-phenylquinoline-4-carboxamide (170 mg, 0.400 mmol) was dissolved in CHCl_3 (10 mL). Bromine (0.05 mL, 1.00 mmol) in CHCl_3 (10 mL) was added dropwise over one hour, and the mixture was stirred in the absence of light for 4 hours. the solvent was removed *in vacuo* and the mixture was triturated in fresh CHCl_3 (5 mL), and the resultant solid was collected via filtration and washed with cold CHCl_3 (3 x 2 mL) to yield a red powder (217 mg, 93 %). ^1H NMR (500 MHz, $\text{d}_6\text{-DMSO}$) δ 11.42 (s, 1H), 9.41 (d, $J = 1.9$ Hz, 1H), 8.61 (d, $J = 9.4$ Hz, 1H), 8.55 (d, $J = 1.1$ Hz, 1H), 8.53 (d, $J = 1.2$ Hz, 1H), 8.51 (s, 1H), 8.42 – 8.39 (m, 2H), 8.28 (d, $J = 7.7$ Hz, 1H), 8.22 (d, $J = 8.1$ Hz, 1H), 8.08 (dd, $J = 9.5, 2.0$ Hz, 1H), 7.90 (ddd, $J = 8.4, 6.9, 1.3$ Hz, 1H), 7.85 – 7.76 (m, 2H), 7.72 (ddd, $J = 8.2, 6.9, 1.2$ Hz, 1H), 7.63 – 7.59 (m, 2H), 7.58 – 7.54 (m, 1H) ppm. $^{13}\text{C}\{^1\text{H}\}$ NMR (126 MHz,

d_6 -DMSO) δ 166.0, 155.8, 147.8, 142.6, 138.5, 138.0, 131.1, 130.8, 130.5, 130.1, 129.6, 129.6, 129.0, 128.6, 127.9, 127.9, 127.6, 127.6, 127.4, 125.1, 123.6, 123.1, 122.7, 121.7, 117.2, 114.7 ppm. HRMS (ES) $[M + H]^+$ Calc'd for $C_{30}H_{19}N_2OBr_2$ 580.9864; Found m/z 580.9871.

7.5.7 N-(9,10-diphenylanthracen-2-yl)-2-phenylquinoline-4-carboxamide (LH)

Synthesised using the same procedure as 2-(9,10-diphenylanthracen-2-yl)isoindoline-1,3-dione above, from N-(9,10-dibromoanthracen-2-yl)-2-phenylquinoline-4-carboxamide (200 mg, 0.343 mmol), phenyl boronic acid (167 mg, 1.37 mmol), $[Pd(PPh_3)_4]$ (40 mg, 0.034 mmol) and Na_2CO_3 (145 mg, 1.37 mmol) to yield title compound as a yellow solid (160 mg, 81 %). 1H NMR (500 MHz, $CDCl_3$) δ 11.01 (s, 1H), 8.17 (d, $J = 8.6$ Hz, 2H), 8.09 (d, $J = 6.6$ Hz, 2H), 7.99 (s, 1H), 7.94 (s, 1H), 7.92 (dd, $J = 9.4, 2.1$ Hz, 1H), 7.82 (dd, $J = 12.3, 5.6$ Hz, 2H), 7.76 – 7.67 (m, 3H), 7.66 – 7.62 (m, 2H), 7.61 – 7.56 (m, 2H), 7.48 (ddd, $J = 9.4, 9.0, 4.9$ Hz, 10H), 7.37 – 7.32 (m, 2H) ppm. $^{13}C\{^1H\}$ NMR (126 MHz, $CDCl_3$) δ 148.9, 138.9, 138.7, 137.6, 136.7, 134.6, 131.4, 131.4, 130.6, 130.5, 130.2, 130.0, 129.8, 129.1, 128.9, 128.8, 128.6, 128.0, 127.8, 127.7, 127.6, 127.2, 126.9, 125.6, 125.1, 125.0, 123.2, 120.3, 116.7, 115.4 ppm. UV-vis (CH_2Cl_2): λ_{abs} ($\epsilon/x10^4$ L mol $^{-1}$ cm $^{-1}$) 270 (6.6), 285 (4.7), 340 (1.2), 367 (0.7), 386 (0.7), 408 (0.6) nm. HRMS (ES) $[M + H]^+$ Calc'd for $C_{42}H_{29}N_2O$ 577.2280; Found m/z 577.2800.

7.5.8 $[Ir(L)_2(\mu-Cl)]_2$ (11)

Synthesis followed the Nonoyama route⁶⁵. **LH** (100 mg, 0.173 mmol) and $IrCl_3 \cdot xH_2O$ (26 mg, 0.086 mmol) were added to a flask containing 2-methoxyethanol (15 mL) and heated at reflux for 48 hours. Upon cooling, the mixture was precipitated by addition of distilled water (20 mL) and collected on a sinter. The crude red solid was used in the subsequent step without further purification or analysis.

7.5.9 $[Ir(L)_2(MeCN)_2]BF_4$ (12)

$[Ir(L)_2(\mu-Cl)]_2$ (116 mg, 0.042 mmol) and $AgBF_4$ (17 mg, 0.085 mmol) were dissolved in MeCN (10 mL) and the flask was covered in foil. The mixture was heated at reflux for 17 hours in the absence of light. After cooling to room temperature, the mixture was passed through a celite pad to remove the precipitated $AgCl$, and the solvent removed *in vacuo*. The crude red solid was used in the subsequent step without further purification or analysis.

7.5.10 [Ir(L)₂(bpy)]PF₆ (IrDPA)

To a stirring solution of 2,2'-bipyridine (15 mg, 0.096 mmol) in CHCl₃ (10 mL), [Ir(L)₂(MeCN)₂]BF₄ was added. The mixture was heated at reflux for 16 hours before being allowed to cool to RT. The solvent was removed *in vacuo* and the solid was dissolved in MeCN. Saturated aqueous [NH₄][PF₆] (1 mL) was added and the mixture was stirred at RT for 1 hour. Excess MeCN was removed *in vacuo* and the crude mixture was dissolved in DCM (15 mL), washed with water (3 x 10 mL) and the organics dried over MgSO₄. The mixture was concentrated to ca. 1 mL, crystallised by the addition of diethyl ether (20 mL) and collected on a sinter to yield the title compound as a red solid (66 mg, 61%). ¹H NMR (500 MHz, d₆-DMSO) δ 11.11 (s, 2H), 8.71 (s, 2H), 8.51 (s, 2H), 8.38 (d, *J* = 7.9 Hz, 2H), 8.18 – 8.04 (m, 4H), 7.94 – 7.55 (m, 24H), 7.51 – 7.37 (m, 4H), 7.36 – 7.22 (m, 6H), 7.20 – 7.04 (m, 12H), 6.85 (d, *J* = 6.9 Hz, 2H), 6.48 – 6.34 (m, 2H) ppm. ¹³C{¹H} NMR (126 MHz, d₆-DMSO) δ 169.7, 164.1, 154.9, 151.0, 147.4, 146.9, 145.6, 145.2, 140.8, 140.7, 140.1, 139.6, 139.5, 138.1, 135.6, 133.6, 132.3, 132.3, 131.2, 131.0, 128.9, 128.9, 128.7, 128.6, 128.5, 128.3, 128.2, 128.0, 127.9, 127.7, 127.1, 126.4, 126.1, 125.3, 124.5, 124.4, 123.9, 123.6, 123.2, 122.9, 118.9, 116.3, 115.4 ppm. UV-vis (CH₂Cl₂): λ_{abs} (ε/x10⁴ L mol⁻¹ cm⁻¹) 261 (5.3), 289 (4.7), 351 (2.4), 463 (0.3) nm.

7.6 References

- 1 S. Kazim, M. K. Nazeeruddin, M. Grätzel and S. Ahmad, *Angew. Chem. Int. Ed.*, 2014, **53**, 2812–2824.
- 2 M. A. Green, A. Ho-Baillie and H. J. Snaith, *Nat. Photonics*, 2014, **8**, 506–514.
- 3 A. K. Jena, A. Kulkarni and T. Miyasaka, *Chem. Rev.*, 2019, **119**, 3036–3103.
- 4 S. Chu, W. Li, Y. Yan, T. Hamann, I. Shih, D. Wang and Z. Mi, *Nano Futur.*, 2017, **1**, 022001.
- 5 J. Luo, J.-H. Im, M. T. Mayer, M. Schreier, M. K. Nazeeruddin, N.-G. Park, S. D. Tilley, H. J. Fan and M. Grätzel, *Science*, 2014, **345**, 1593–1596.
- 6 S. Hoseinkhani, R. Tubino, F. Meinardi and A. Monguzzi, *Phys. Chem. Chem. Phys.*, 2015, **17**, 4020–4024.
- 7 H. Kobayashi and P. L. Choyke, *Acc. Chem. Res.*, 2019, **52**, 2332–2339.
- 8 S. Y. Lee, R. Lee, E. Kim, S. Lee and Y. I. Park, *Front. Bioeng. Biotechnol.*, DOI:10.3389/fbioe.2020.00275.
- 9 D. L. Dexter, *J. Chem. Phys.*, 1953, **21**, 836–850.
- 10 M. Inokuti and F. Hirayama, *J. Chem. Phys.*, 1965, **43**, 1978–1989.
- 11 D. Meroni, A. Monguzzi and F. Meinardi, *J. Chem. Phys.*, 2020, **153**, 114302.
- 12 A. Monguzzi, R. Tubino, S. Hoseinkhani, M. Campione and F. Meinardi, *Phys. Chem. Chem. Phys.*, 2012, **14**, 4322–4332.
- 13 S. H. C. Askes, P. Brodie, G. Bruylants and S. Bonnet, *J. Phys. Chem. B*, 2017, **121**, 780–786.
- 14 J. Saltiel and B. W. Atwater, in *Advances in Photochemistry*, John Wiley & Sons, Ltd, 1988, vol. 14, pp. 1–90.
- 15 V. Gray, K. Moth-Poulsen, B. Albinsson and M. Abrahamsson, *Coord. Chem. Rev.*, 2018, **362**, 54–71.
- 16 S. M. Bachilo and R. B. Weisman, *J. Phys. Chem. A*, 2000, **104**, 7711–7714.
- 17 Y. Y. Cheng, T. Khoury, R. G. C. R. Clady, M. J. Y. Tayebjee, N. J. Ekins-Daukes, M. J. Crossley and T. W. Schmidt, *Phys. Chem. Chem. Phys.*, 2009, **12**, 66–71.
- 18 C. Fan, L. Wei, T. Niu, M. Rao, G. Cheng, J. J. Chruma, W. Wu and C. Yang, *J. Am. Chem. Soc.*, 2019, **141**, 15070–15077.
- 19 Y. Y. Cheng, B. Fückel, T. Khoury, R. G. C. R. Clady, M. J. Y. Tayebjee, N. J. Ekins-Daukes, M. J. Crossley and T. W. Schmidt, *J. Phys. Chem. Lett.*, 2010, **1**, 1795–1799.
- 20 R. R. Islangulov, J. Lott, C. Weder and F. N. Castellano, *J. Am. Chem. Soc.*, 2007, **129**, 12652–12653.
- 21 T. N. Singh-Rachford, J. Lott, C. Weder and F. N. Castellano, *J. Am. Chem. Soc.*, 2009, **131**, 12007–12014.
- 22 J. M. Rowe, J. Zhu, E. M. Soderstrom, W. Xu, A. Yakovenko and A. J. Morris, *Chem. Commun.*, 2018, **54**, 7798–7801.
- 23 C. Healy, L. Hermanspahn and P. E. Kruger, *Coord. Chem. Rev.*, 2021, **432**, 213756.
- 24 X. Qin, J. Han, D. Yang, W. Chen, T. Zhao, X. Jin, P. Guo and P. Duan, *Chin. Chem. Lett.*, 2019, **30**, 1923–1926.
- 25 V. Gray, K. Börjesson, D. Dzebo, M. Abrahamsson, B. Albinsson and K. Moth-Poulsen, *J. Phys. Chem. C*, 2016, **120**, 19018–19026.

- 26 F. Edhborg, B. Küçüköz, V. Gray and B. Albinsson, *J. Phys. Chem. B*, 2019, **123**, 9934–9943.
- 27 P. E. Keivanidis, S. Balushev, T. Miteva, G. Nelles, U. Scherf, A. Yasuda and G. Wegner, *Adv. Mater.*, 2003, **15**, 2095–2098.
- 28 S. Balushev, J. Jacob, Y. S. Avlasevich, P. E. Keivanidis, T. Miteva, A. Yasuda, G. Nelles, A. C. Grimsdale, K. Müllen and G. Wegner, *ChemPhysChem*, 2005, **6**, 1250–1253.
- 29 L. Yu, J. Liu, S. Hu, R. He, W. Yang, H. Wu, J. Peng, R. Xia and D. D. C. Bradley, *Adv. Funct. Mater.*, 2013, **23**, 4366–4376.
- 30 J. Lin, B. Liu, M. Yu, X. Wang, Z. Lin, X. Zhang, C. Sun, J. Cabanillas-Gonzalez, L. Xie, F. Liu, C. Ou, L. Bai, Y. Han, M. Xu, W. Zhu, T. A. Smith, P. N. Stavrinou, D. D. C. Bradley and W. Huang, *Adv. Mater.*, 2019, **31**, 1804811.
- 31 R. Schroeder, B. Ullrich, W. Graupner and U. Scherf, *J. Phys. Condens. Matter*, 2001, **13**, L313–L318.
- 32 S. Gharaati, C. Wang, C. Förster, F. Weigert, U. Resch-Genger and K. Heinze, *Chem. – Eur. J.*, 2020, **26**, 1003–1007.
- 33 T. Ogawa, N. Yanai, A. Monguzzi and N. Kimizuka, *Sci. Rep.*, 2015, **5**, 10882.
- 34 S. Hisamitsu, J. Miyano, K. Okumura, J. K.-H. Hui, N. Yanai and N. Kimizuka, *ChemistryOpen*, 2020, **9**, 14–17.
- 35 M. Hosoyamada, N. Yanai, T. Ogawa and N. Kimizuka, *Chem. – Eur. J.*, 2016, **22**, 2060–2067.
- 36 D. F. Barbosa de Mattos, A. Dreos, M. D. Johnstone, A. Runemark, C. Sauvée, V. Gray, K. Moth-Poulsen, H. Sundén and M. Abrahamsson, *J. Chem. Phys.*, 2020, **153**, 214705.
- 37 A. Ajayaghosh, V. K. Praveen and C. Vijayakumar, *Chem. Soc. Rev.*, 2007, **37**, 109–122.
- 38 F. Würthner, T. E. Kaiser and C. R. Saha-Möller, *Angew. Chem. Int. Ed.*, 2011, **50**, 3376–3410.
- 39 S. S. Skourtis, C. Liu, P. Antoniou, A. M. Virshup and D. N. Beratan, *Proc. Natl. Acad. Sci.*, 2016, **113**, 8115–8120.
- 40 P. Duan, N. Yanai and N. Kimizuka, *J. Am. Chem. Soc.*, 2013, **135**, 19056–19059.
- 41 Q. Liu, B. Yin, T. Yang, Y. Yang, Z. Shen, P. Yao and F. Li, *J. Am. Chem. Soc.*, 2013, **135**, 5029–5037.
- 42 F. Marsico, A. Turshatov, R. Peköz, Y. Avlasevich, M. Wagner, K. Weber, D. Donadio, K. Landfester, S. Balushev and F. R. Wurm, *J. Am. Chem. Soc.*, 2014, **136**, 11057–11064.
- 43 V. Gray, D. Dzebo, A. Lundin, J. Alborzpour, M. Abrahamsson, B. Albinsson and K. Moth-Poulsen, *J. Mater. Chem. C*, 2015, **3**, 11111–11121.
- 44 V. Gray, B. Küçüköz, F. Edhborg, M. Abrahamsson, K. Moth-Poulsen and B. Albinsson, *Phys. Chem. Chem. Phys.*, 2018, **20**, 7549–7558.
- 45 J. Zhou, Q. Liu, W. Feng, Y. Sun and F. Li, *Chem. Rev.*, 2015, **115**, 395–465.
- 46 R. R. Islangulov, D. V. Kozlov and F. N. Castellano, *Chem. Commun.*, 2005, 3776–3778.
- 47 T. Förster and K. Kasper, *Z. Für Phys. Chem.*, 1954, **1**, 275–277.
- 48 H. Ihmels and J. Luo, *J. Photochem. Photobiol. Chem.*, 2008, **200**, 3–9.
- 49 H. H. Wasserman and J. R. Scheffer, *J. Am. Chem. Soc.*, 1967, **89**, 3073–3075.
- 50 Y. Lu, J. Wang, N. McGoldrick, X. Cui, J. Zhao, C. Caverly, B. Twamley, G. M. Ó Máille, B. Irwin, R. Conway-Kenny and S. M. Draper, *Angew. Chem. Int. Ed.*, 2016, **55**, 14688–14692.

- 51 S. J. Pope, T. Stonelake, K. Phillips, S. Coles, P. Horton, S. Keane, E. Stokes, I. Fallis, J. Beames, J. Zhao, K. Chen, Y. Hou, A. Hallett and S. O’Kell, *Chem. – Eur. J.*, , DOI:10.1002/chem.201801007.
- 52 T. Serevičius, R. Komskis, P. Adomėnas, O. Adomėnienė, V. Jankauskas, A. Gruodis, K. Kazlauskas and S. Juršėnas, *Phys. Chem. Chem. Phys.*, 2014, **16**, 7089–7101.
- 53 W. J. Yang, D. Y. Kim, M.-Y. Jeong, H. M. Kim, Y. K. Lee, X. Fang, S.-J. Jeon and B. R. Cho, *Chem. – Eur. J.*, 2005, **11**, 4191–4198.
- 54 M. M. Talukder, J. M. O. Cue, J. T. Miller, P. L. Gamage, A. Aslam, G. T. McCandless, M. C. Biewer and M. C. Stefan, *ACS Omega*, 2020, **5**, 24018–24032.
- 55 B. Balaganesan, W.-J. Shen and C. H. Chen, *Tetrahedron Lett.*, 2003, **44**, 5747–5750.
- 56 S. Kotha and A. K. Ghosh, *Synlett*, 2002, **2002**, 0451–0452.
- 57 S. Kotha, A. K. Ghosh and K. D. Deodhar, *Synthesis*, 2004, **2004**, 549–557.
- 58 W. J. Ramsay, F. T. Szczypiński, H. Weissman, T. K. Ronson, M. M. J. Smulders, B. Rybtchinski and J. R. Nitschke, *Angew. Chem. Int. Ed.*, 2015, **54**, 5636–5640.
- 59 J. D. Routledge, A. J. Hallett, J. A. Platts, P. N. Horton, S. J. Coles and S. J. A. Pope, *Eur. J. Inorg. Chem.*, 2012, **2012**, 4065–4075.
- 60 J. S. Brinen and J. G. Koren, *Chem. Phys. Lett.*, 1968, **2**, 671–672.
- 61 M. Fitzner, G. Wuitschik, R. J. Koller, J.-M. Adam, T. Schindler and J.-L. Reymond, *Chem. Sci.*, , DOI:10.1039/D0SC04074F.
- 62 E. A. Englund, H. N. Gopi and D. H. Appella, *Org. Lett.*, 2004, **6**, 213–215.
- 63 T. W. Greene and P. G. M. Wuts, *Protective Groups in Organic Synthesis*, John Wiley & Sons, Inc., New York, USA, 1999.
- 64 A. Slodek, M. Filapek, E. Schab-Balcerzak, M. Grucela, S. Kotowicz, H. Janeczek, K. Smolarek, S. Mackowski, J. G. Malecki, A. Jedrzejowska, G. Szafraniec-Gorol, A. Chrobok, B. Marcol, S. Krompiec and M. Matussek, *Eur. J. Org. Chem.*, 2016, **2016**, 4020–4031.
- 65 M. Nonoyama, *Bull. Chem. Soc. Jpn.*, 1974, **47**, 767–768.
- 66 A. Brouwer, *Pure Appl. Chem.*, 2011, **83**, 2213–2228.
- 67 V. Gray, D. Dzebo, M. Abrahamsson, B. Albinsson and K. Moth-Poulsen, *Phys. Chem. Chem. Phys.*, 2014, **16**, 10345–10352.

Chapter 8 - Summary and Future Work

8.1 Summary

The work in this thesis has shown the synthesis, isolation, and characterisation of several $^3\text{MLCT}$ based red emissive organometallic complexes. The work has covered both cyclometalating ligands in iridium (III) systems, as well as novel *bis*-chelating diimine ligands, coordinated both with iridium (III) and rhenium (I).

Chapter 2 looked at what effects of substitution around phenylquinoxaline cyclometalating ligands have on Ir (III) emission. The ligands were synthesised via bromination of an acetophenone by using dioxane dibromide, introducing a potentially fast route to a large library of ligand motifs. The emissive properties of the complexes were found to be tuneable over a range 45 nm. The work in Chapter 3 expanded on the ligand substitution of Chapter 2 by introducing naphthyl quinoxaline ligand systems. This extension to the conjugation of the cyclometalation ligand further bathochromically shifted the emission of the corresponding complexes. It was also found that the isomer of naphthalene had an influence on emission wavelength. For example, the Ir (III) complex of 2-(naphth-2-yl)-quinoxaline is emissive at 630 nm, while for 2-(naphth-1-yl)-quinoxaline, the emission as seen at 678 nm.

The remaining chapters focus on the use of quinoline ligands for complexation. In Chapter 4, a series of substituted 2-naphthylquinoline-4-carboxylic acids were synthesised before cyclometalating with iridium (III). A difference emission wavelength between isomers of naphthalene was seen again, with 1-naphthalene variants emitting at lower energy, with all complexes emitting between 668 and 695 nm.

In Chapter 5, a series of novel diimine ligands were synthesised for use as ancillary ligands in red emitting complexes. The pyridine and pyrazine quinoline ligands were coordinated with *bis*-cyclometalated iridium (III) complexes of 2-(naphth-1-yl)quinoline and 2-(naphth-2-yl)quinoline. The emissive properties were similar to the bipyridine complexes of Chapter 4. In Chapter 6, the same series of ligands was then coordinated with rhenium for a series of tricarbonylbromiderhenium(I) complexes. The red complexes were non emissive in solution, likely down to the weak field bromide ligand. Each complex was emissive in the solid state, between 662 and 690 nm.

Finally, Chapter 7 say synthesis of a ligand featuring a DPA moiety, intended to produce TTA-UC from a single molecule. The complex did show very low TTA-UC, although more impressively, generating a quantum yield in aerated conditions of over 16 %. When additional DPA was added to deaerated solutions, the efficiency of TTA-UC was also increased.

8.2 Future Work

8.2.1 2-(Pyridin-2-yl)quinoline and 2-(pyrazin-2-yl)quinoline ligands.

The simple facile nature of the asymmetric N^N type quinoline ligand synthesis provides an interesting new pathway towards substituted iridium (III) complexes. The availability of the carboxylic acid group for pre- or post-complexation modification without significant modulation of the absorption and emissive properties has vast potential for application specific modifications, for example in bioconjugate chemistry.

The degree of emission tuneability is worth further investigation with some smaller archetypal cyclometalated ligands, such as seen in Figure 8.1, where the LUMO levels are known to reside over the ancillary ligands.

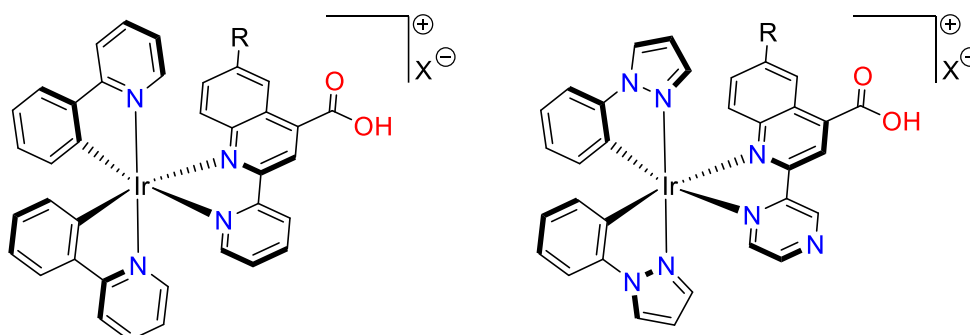


Figure 8.1 - Possible future complexes to investigate the degree of tuneability from ligand functionalisation.

8.2.2 [Re(CO)₃(L^x)Br]

The Re(I) complexes presented in this work are not emissive in solution, similar to other complexes with benzannulated ligands, such as [Re(CO)₃(biq)Cl]. When the halide is substituted for a stronger field ligand, such as MeCN or pyridine, it is expected that the complexes will become emissive in solution (Figure 8.2).

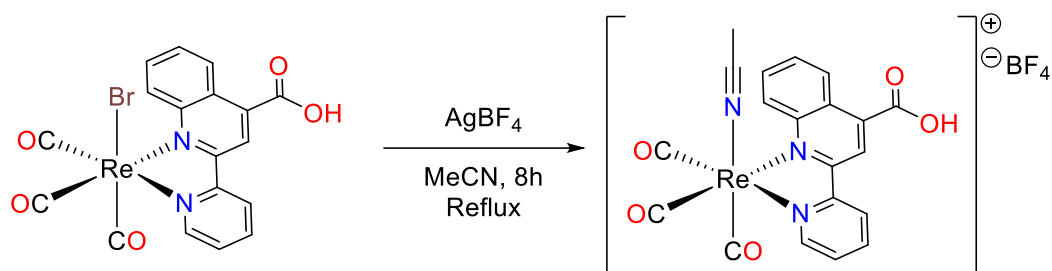


Figure 8.2 – Synthetic route for the substitution of axial halides.

8.2.3 Ir-DPA

Firstly, while the increase in quantum yield and apparent energy transfer processes involved with this molecule as is, understanding would be improved by both computational investigations and transient-absorption spectroscopy.

Secondly, to try and limit the degree of back energy transfer between the DPA and the quinoline moieties of the ligand, an alkyl linker could be added, such as seen below in . The amide-based linker I believe could be synthesised in a similar manner as used in this work with a small alkyl-based linker, perhaps up to a butyl sized linker.

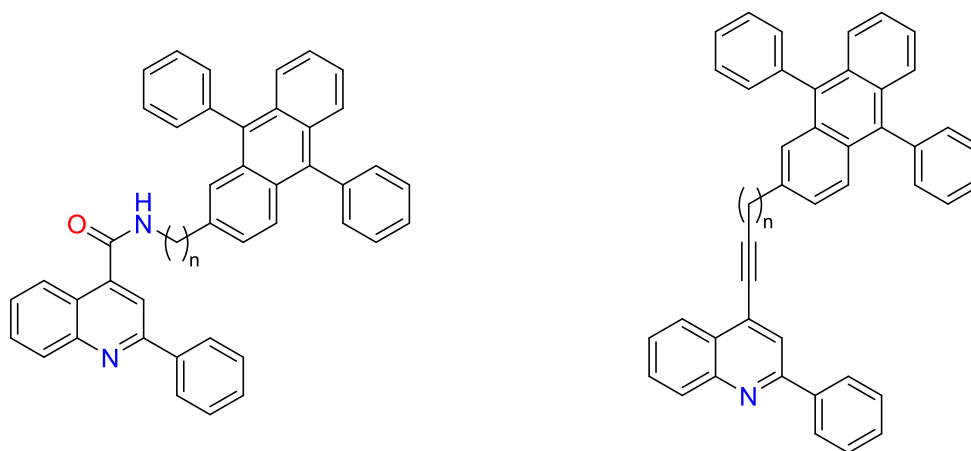


Figure 8.3 - Possible future ligand designs.

